



Citation for published version:

Johnston, DN, Burrows, CR & Edge, KA 2005, Power Transmission and Motion Control (PTMC 2005). John Wiley & Sons.

Publication date:
2005

Document Version
Publisher's PDF, also known as Version of record

[Link to publication](#)

University of Bath

General rights

Copyright and moral rights for the publications made accessible in the public portal are retained by the authors and/or other copyright owners and it is a condition of accessing publications that users recognise and abide by the legal requirements associated with these rights.

Take down policy

If you believe that this document breaches copyright please contact us providing details, and we will remove access to the work immediately and investigate your claim.

Quit



Professional
Engineering
Publishing

Power Transmission and Motion Control

Click here to Continue

Produced by

**CONFERENCE
DATA
SERVICES**

www.conferencedataservices.co.uk



UNIVERSITY OF
BATH



Professional
Engineering
Publishing



Centre for
Power Transmission
and Motion Control

Power Transmission and Motion Control

Power Transmission and Motion Control

(PTMC 2005)

Edited by

Dr D N Johnston

Workshop Organizer

Professor C R Burrows

Director

and

Professor K A Edge

Deputy Director

*Centre for Power Transmission and Motion Control
University of Bath, UK*



John Wiley & Sons, Ltd

Copyright © With The Centre for Power Transmission and Motion Control

Email (for orders and customer service enquiries): cs-books@wiley.co.uk

Visit our Home Page on www.wiley.com

All Rights Reserved. No part of this publication may be reproduced, stored in a retrieval system or transmitted in any form or by any means, electronic, mechanical, photocopying, recording, scanning or otherwise, except under the terms of the Copyright, Designs and Patents Act 1988 or under the terms of a licence issued by the Copyright Licensing Agency Ltd, 90 Tottenham Court Road, London W1T 4LP, UK, without the permission in writing of the Publisher. Requests to the Publisher should be addressed to the Permissions Department, John Wiley & Sons Ltd, The Atrium, Southern Gate, Chichester, West Sussex PO19 8SQ, England, or emailed to permreq@wiley.co.uk, or faxed to (+44) 1243 770620.

Designations used by companies to distinguish their products are often claimed as trademarks. All brand names and product names used in this book are trade names, service marks, trademarks or registered trademarks of their respective owners. The Publisher is not associated with any product or vendor mentioned in this book.

This publication is designed to provide accurate and authoritative information in regard to the subject matter covered. It is sold on the understanding that the Publisher is not engaged in rendering professional services. If professional advice or other expert assistance is required, the services of a competent professional should be sought.

Other Wiley Editorial Offices

John Wiley & Sons Inc., 111 River Street, Hoboken, NJ 07030, USA

Jossey-Bass, 989 Market Street, San Francisco, CA 94103-1741, USA

Wiley-VCH Verlag GmbH, Boschstr. 12, D-69469 Weinheim, Germany

John Wiley & Sons Australia Ltd, 42 McDougall Street, Milton, Queensland 4064, Australia

John Wiley & Sons (Asia) Pte Ltd, 2 Clementi Loop #02-01, Jin Xing Distripark, Singapore 129809

John Wiley & Sons Canada Ltd, 22 Worcester Road, Etobicoke, Ontario, Canada M9W 1L1

Wiley also publishes its books in a variety of electronic formats. Some content that appears in print may not be available in electronic books.

British Library Cataloguing in Publication Data

A catalogue record for this book is available from the British Library

ISBN-13 978-0-470-01677-0

ISBN-10 0-470-01677-9

Printed and bound in Great Britain by Antony Rowe Ltd, Chippenham, Wiltshire

This book is printed on acid-free paper responsibly manufactured from sustainable forestry in which at least two trees are planted for each one used for paper production.

Contents

Preface	ix
<u>Systems and Control</u>	
A high performance force control system for dynamic loading of fast moving actuators <i>G Jacazio and G Balossini</i>	3
Knowledge based tools for the design of servo-hydraulic closed loop control <i>M Liermann and H Murrenhoff</i>	17
Low-order robust controller for flexible hydraulic manipulators <i>M Linjama and T Virvalo</i>	29
Hybrid control with on/off electropneumatic standard valve for tracking positioning <i>X Legrand, M Smaoui, X Brun, D Thomasset, J-M Retif and X-F Lin Shi</i>	45
Comparing different control strategies of timber sawing process <i>T Virvalo and J Inberg</i>	59
Closed-loop velocity control for an electrohydraulic impact test system <i>A R Plummer</i>	75
Pressure peak phenomenon in digital hydraulic systems – a theoretical study <i>A Laamanen, M Linjama and M Vilenius</i>	91
<u>Water Hydraulic Systems</u>	
Control of water hydraulic manipulator with proportional valves <i>H Sairiala, K T Koskinen and M Vilenius</i>	107
Development of a novel water hydraulic vane actuator applied for control of a two-links test manipulator <i>F Conrad and F Roli</i>	117
<u>Fault Analysis and Diagnosis</u>	
Analysis of fault tolerance of digital hydraulic valve system <i>L Siivonen, M Linjama and M Vilenius</i>	133
Experiences on combining fault tree analysis and failure mode, effects and criticality analysis for fault diagnosis of hydrostatic transmission <i>H Rusanen, T Koivula and J Rinkinen</i>	147

System Modelling and Simulation

- Model identification of the electrohydraulic actuator for small signal inputs 163
E Sampson, S Habibi, Y Chinniah and R Burton
- An efficient numerical method for solving the dynamic equations of complex fluid power systems 179
S Esqué and A Ellman
- Dynamic modelling of a pilot-operated pressure relief valve 193
C Hös and L Kullmann

Component Design and Analysis

- A computer aided conceptual design method for hydraulic components 209
B Steiner and R Scheidl
- Determining the steady state flow forces in a rim spool valve using CFD analysis 223
N Okungbowa, D Bergstrom and R Burton
- Design of valve solenoids using the method of finite elements 243
A Schultz
- Virtual design of high dynamic pneumatic valves 255
M Fiedler, F Rüdiger and S Helduser

Smart fluids

- A micro artificial muscle actuator using electro-conjugate fluid 269
K Takemura, S Yokota and K Edamura
- A magneto-rheological valve-integrated cylinder and its application 277
K Yoshida, T Soga, S Yokota, M Kawachi and K Edamura
- Systematic experimental studies and computational perspectives of the non-linear squeeze mode behaviour of magneto-rheological fluids 291
N Gstöttenbauer, A Kainz, B Manhartgruber and R Scheidl

Vehicle systems

- An adaptable hydraulic system for tractors 307
T Fedde, T Lang and H-H Harms
- Design of a hybrid vehicle powertrain using an inverse methodology 317
E Bideaux, J Laffite, A Derkaoui, W Marquis-Favre, S Scavarda, and F Guillemard
- CPS hybrid vehicle with flywheel for energy storage 333
S-K Lee, K Ichiryu, K Kawamura, S Ikeo, E Koyabu, K Ito and H Shimoyama

Pneumatics

- Bilateral control of multi DOFs forceps using a pneumatic servo system 351
K Kawashima, K Tadano and T Kagawa

Experimental identification and validation of a pneumatic positioning servo-system <i>M Sorli, S Pastorelli, G Figliolini and P Rea</i>	365
Performances of cam-follower systems with pneumatic return spring <i>S Pastorelli, A Almondo and M Sorli</i>	379
Motion simulator with 3 D.o.F pneumatically actuated <i>G Mattiazzo, S Pastorelli and M Sorli</i>	395
<u>Fluid Dynamics and Noise</u>	
Elucidation of the noise generating mechanism produced by a hydrodynamic source associated with cavitation in an oil hydraulic valve orifice <i>E Kojima, T Yamazaki, A Terada and K A Edge</i>	409
An experimental result on the measurement of concentrated flow resistances <i>B Manhartgruber</i>	427
The dynamics of hydraulic fluids – significance, differences and measuring <i>J-P Karjalainen, R Karjalainen, K Huhtala and M Vilenius</i>	437
Measurements of elasto-hydrodynamic pressure field in the gap between piston and cylinder <i>M Ivantysynova, C Huang and R Behr</i>	451
Authors' Index	467

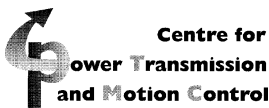
Preface

The Power Transmission and Motion Control Workshop was held on 7–9 September 2005 and is the latest in a series which has been held annually at the University of Bath since 1988. The event had a strong international flavour with authors from 11 countries. All papers have been thoroughly reviewed. The focus of the papers is principally on motion control systems, with particular emphasis on hydraulic and pneumatic systems and components, including water hydraulics and ‘smart’ fluids.

As ever, we are very grateful to the authors for their contributions. Without the continued support and enthusiasm of authors, reviewers, delegates and staff, it would not be possible to maintain such a long-running and successful series of events.

Special thanks are also due to Jane Phippen and Barbara Terry for their considerable assistance in compiling the material for this book and for organising and ensuring the smooth running of the event. We are also grateful for the support and understanding of staff at John Wiley and Sons, Ltd.

Dr D N Johnston, *Workshop Organiser*
Professor C R Burrows, *Director*
Professor K A Edge, *Deputy Director*
Centre for Power Transmission and Motion Control
Bath, September 2005



Systems and Control

A high performance force control system for dynamic loading of fast moving actuators

Giovanni Jacazio

Politecnico di Torino (Italy), Department of Mechanics; giovanni.jacazio@polito.it

Gualtiero Balossini

Microtecnica s.r.l., Torino (Italy); gualtiero.balossini@hs.utc.com

ABSTRACT

This paper presents a description of a hydraulic force control system that was recently developed as a part of the test rig of the flight control system of the Aermacchi M346 advanced trainer aircraft. In this test rig commands are provided to the flight control actuators as in real flight while they are simultaneously loaded by appropriate forces varying in time as defined by a load control computer. The force control system is comprised of servovalve controlled hydraulic actuators, force and speed sensors, and a high speed digital controller performing a complex and adaptive control law. An excellent accuracy of the load control was achieved for all combinations of actuator movements and load changes, such as those occurring during fast aircraft manoeuvres or when the aircraft is flying while subjected to gusts or turbulence.

1 THE PROBLEM OF CONTROLLING A FORCE

Force control systems have been used in many industrial and scientific applications: from tension control systems, to loading systems, to test equipments. Both hydraulic and electrical systems have been used for developing the controlled force in combination with a large variety of control architectures, ranging from simple open-loop control to complex feedback systems, depending on the required static and dynamic accuracy for the controlled force.

Whichever technology is used for developing the force (hydraulic or electromechanical), a good accuracy of the force control can generally be achieved without major difficulties if the mechanical component onto which the force must be applied is either stationary, or moving at low speed, and a control law based on a conventional PID controller is normally acceptable. In these cases three factors are needed to obtain a good accuracy: high stiffness of the device developing the force, optimization of the gains of the PID controller and good accuracy of the force measuring device.

However, when a controlled force must be applied to a mechanical component moving at a fast speed, the accuracy of the force control system can become dramatically worse unless the whole system architecture is specifically devised to compensate for the errors induced by the moving component. Controlling with a high accuracy the force acting on mechanical components moving at high speeds was exactly the case of the load control system for testing the primary flight control actuators of the M-346, an advanced trainer aircraft which first flew in July 2004 and is now undergoing an intense flight schedule. The load control system for the primary flight controls of this aircraft is a significant part of a complex Integration, Validation and Verification Rig, known as the “Iron Bird”, which was built to test the entire aircraft hydraulic system and its components.

2 HYDRAULIC FORCE CONTROL SYSTEMS

A simple hydraulic force control system can be obtained by controlling the pressure differential to a hydraulic actuator by means of two pressure control valves, each valve controlling the pressure on one of the two sides of a hydraulic actuator (figure 1). These valves are equipped with an internal pressure feedback device such that the controlled pressure (p_1, p_2) is proportional to the input signal (V_1, V_2); the pressure differential $\delta p = (p_1 - p_2)$ acts upon the hydraulic actuator whose ram is therefore subjected to a force $F = A \cdot p$ which is eventually is a function of the two input signals V_1 and V_2 . This type of force control system has the advantage of being simple and of requiring a minimum number of components, but it suffers from a few drawbacks:

- The output force is not directly controlled since the internal feedback loop is built on the pressure differential. The output force is only approximately proportional to the pressure differential because of the friction and inertia forces of the hydraulic actuator.
- The accuracy obtained by pressure transducers of these pressure control valves is poorer than that obtainable by load cells.
- A good linearity between the pressures p_1, p_2 and their input signals V_1, V_2 , occurs only when the hydraulic actuator is stationary or it is moving at low speed, but it is poor at large actuation speeds.

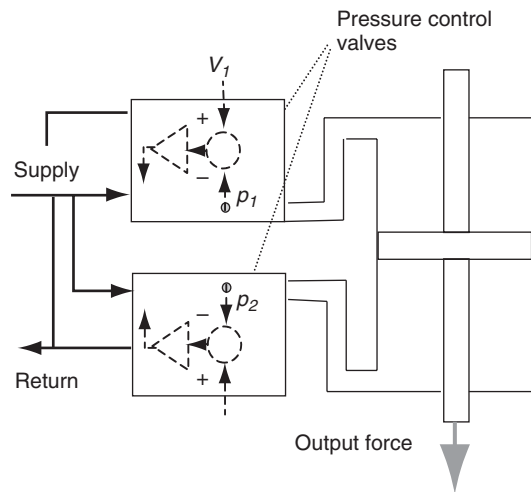


Figure 1: Hydraulic force control system based on pressure control

A different solution (figure 2) is to create a force control system making use of a flow control servovalve and to build a force control loop by direct measurement of the output force provided by the hydraulic actuator. Such system partly reduces the accuracy errors previously outlined, but it is still affected by the error created by the actuator movement, as it will be shown in the following of this paper, which will also describe a solution that was devised for overcoming this problem.

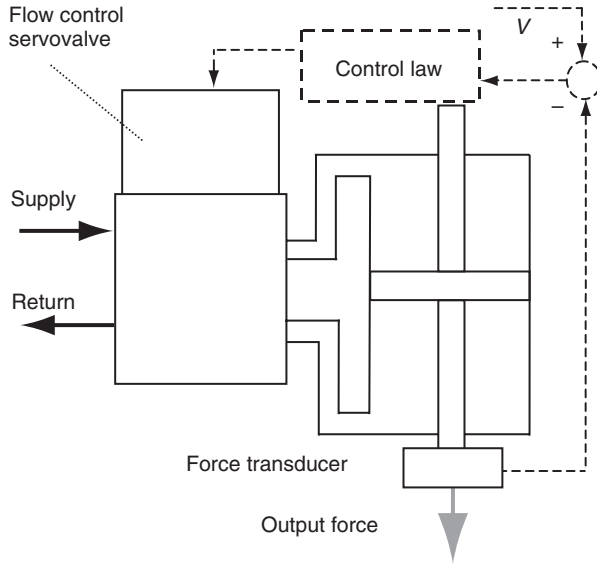


Figure 2: Hydraulic force control system based on a flow control servovalve

3 THE SPEED AS AN ERROR SOURCE IN A FORCE CONTROL SYSTEM

The force control system based upon the flow controlled servovalve of figure 2 is outlined in the block diagram of figure 3. This block diagram refers to a linear model of the system, which, though based on some approximation of the actual behaviour of the system components, is accurate enough for showing the mutual relationships among the system state variables.

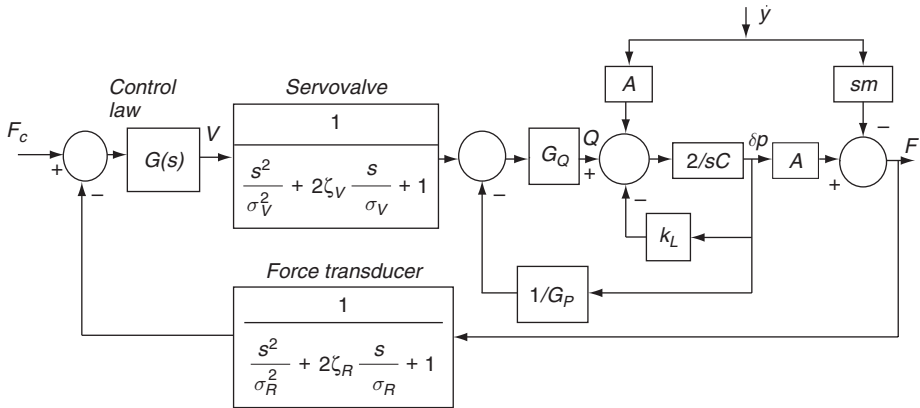


Figure 3: Simplified block diagram of a force control system based on a flow control servovalve

In the block diagram of figure 3, F_C is the force command, F is the actual force, V is the servovalve command, Q is the servovalve flow, δp is the pressure differential between the controlled ports, \dot{y} is the speed at which the actuator is driven. In the same block diagram, σ_V is the servovalve resonant frequency and ζ_V its damping factor, σ_R and ζ_R the similar quantities for the force transducer, G_Q and G_P the servovalve flow and pressure gains, A the actuator area, C the hydraulic capacitance of each actuator chamber, k_L a leakage coefficient due to the presence (if any) of a restrictor across the control lines, m the mass of the actuator piston and s the Laplace variable.

Looking at this block diagram it can be clearly seen that in a force control system the actuator speed is a source of error; a second error source is caused by the inertia force of the actuator piston. This contribution is nil if the speed is constant, but it can increase to a large value under rapid variations of the the speed, such as the case of an actuator cycling at high frequency.

In order to emphasise the effect of the speed on the accuracy of the force control system, the dynamics of the servovalve and of the force transducer can be neglected as a first approximation, since their frequency response is much faster than that of the whole force control system. Under this approximation, the transfer function between the servovalve command V , the output force F and the output speed \dot{y} becomes:

$$F = \frac{k_1 V}{s+1} - \frac{k_2 + ms + ms^2}{s+1} \dot{y} \quad [1]$$

$$\text{where: } k_1 = \frac{G_Q A}{k_L + G_Q / G_P} \quad [2]; \quad k_2 = \frac{A^2}{k_L + G_Q / G_P} \quad [3];$$

$$= \frac{C}{2(k_L + G_Q / G_P)} \quad [4]$$

If the closed loop control is performed with a conventional PID control law, the closed loop transfer function [5] is obtained that is written below. In this relationship, K_P is the proportional gain, K_I is the integrator gain, while the derivative gain has not been considered for its contribution is instrumental in slightly improving the stability margin, but has almost no effect on the system accuracy.

$$F = \frac{F_C \left(1 + \frac{K_P}{K_I} s \right) - \frac{s}{k_1 K_I} (k_2 + ms + ms^2) \dot{y}}{\frac{s^2}{k_1 K_I} + \frac{s}{k_1 K_I} (1 + k_1 K_P) + 1} \quad [5]$$

It is apparent from this transfer function that under steady state conditions, with constant speed \dot{y} , the integrator of the control law eventually brings to zero the error caused by the speed. However, the integrator gain K_I must be limited to a relatively low value in order to maintain safe stability margins, therefore when the speed varies continuously, the force error that cannot be corrected by the integrator gain; clearly, this error increases with the rate

of change of the output speed. Under such dynamic conditions, for which $s = j\omega$ in [5] is relatively large, the contribution of the integrator gain K_I becomes actually negligible, and equation [5] can be rewritten as:

$$F \cong \frac{F_C \frac{K_p k_1}{1 + K_p k_1} - \frac{k_2 + ms + ms^2}{1 + K_p k_1} \dot{y}}{\frac{s + 1}{1 + K_p k_1}} \quad [6]$$

In order to reduce the effect of the output speed \dot{y} on the error of the force control system, the factor $\frac{k_2 + ms + ms^2}{1 + K_p k_1}$ multiplying the output speed must be made as little as possible.

Of the three terms at the numerator, k_2 is the prevailing one while ms^2 is little for most applications and can generally be neglected. It thus turns out that to minimize the error of the force control system, the term

$$k_y = \frac{k_2}{1 + K_p k_1} = \frac{A^2}{k_L + \frac{G_Q}{G_P} + K_p G_Q A} \quad [7]$$

must be made as little as possible. Since the area A is established by the output force requirements and the values of flow gain G_Q and proportional gain K_p are limited by the servoloop stability requirements, the only way to greatly reduce the force error created by the output speed is to increase the term k_L , which actually means to increase the system internal leakage. This is certainly an effective way to proceed, but at the expense of a large flow consumption.

4 SPEED COMPENSATION

A control technique for reducing the error of a force control system caused by the output speed was developed, which mainly consists of measuring the actuator speed and adapting the servovalve input as a function of the measured speed. By doing that, the simplified block diagram of figure 3 is modified into the one shown in figure 4. The measured speed is multiplied by a gain and a lead network to obtain the compensation signal V' ; the actual transfer function between V' and \dot{y} used in the force control system described in this paper was a little more complex because it included appropriate filtering, but the effect of the speed compensation can well be explained without introducing these secondary factors.

When the speed compensation is introduced, as shown in figure 4, the transfer function [1] is modified into the following equation [8], which is derived under the same assumptions made for getting [1]:

$$F = \frac{k_1 V'}{s + 1} - \frac{k_2 + ms + ms^2 - k_3 (s + 1)}{s + 1} \dot{y} \quad [8]$$

In this equation the parameters k_1, k_2 and τ are those defined in [1], [2] and [3], while k_3 is

$$\text{given by: } k_3 = \frac{G_Q A a}{k_L + \frac{G_Q}{G_P}} \quad [9]$$

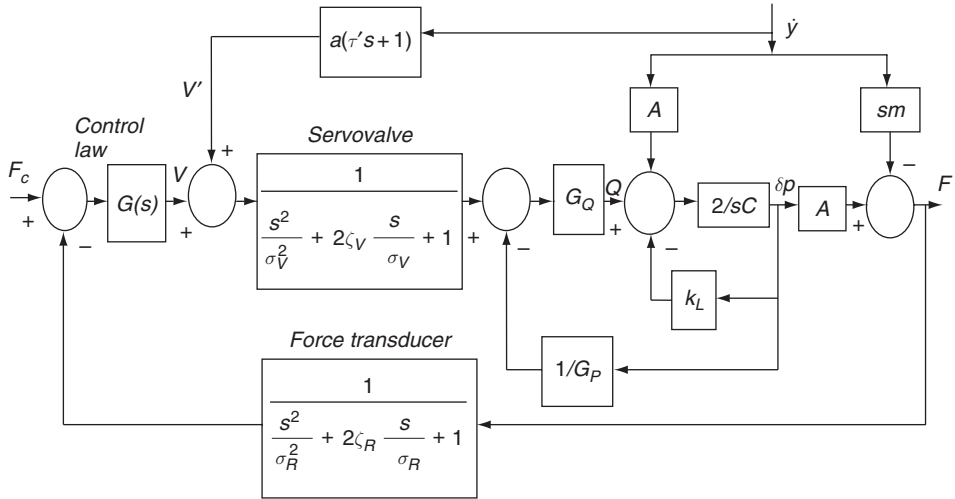


Figure 4: Simplified block diagram of a force control system based on a flow control servovalve and a speed compensation network.

Looking now at equation [8] it can be easily seen that if the parameters a and τ' of the speed compensation transfer function are taken such that:

$$k_3 = k_2, \text{ thus: } a = A/G_Q \quad [10]; \quad k_3 \tau' = m, \text{ thus: } \tau' = \frac{m \left(k_L + \frac{G_Q}{G_P} \right)}{A^2} \quad [11]$$

the effect of the speed on the force developed by the actuator becomes negligible and a very good accuracy of the force control system can be obtained under dynamic conditions, while the controlled element is moving at fast speed, and without resorting to a large power dissipation.

This control technique proved effective and it was further enhanced by using a non-linear control law to make up for the non-linearities of the physical parameters such as the servovalve flow and pressure gains and the internal leakage coefficient. In the following of this paper, a description of a specific application of this control technique is presented.

5 THE M346 “IRON BIRD”

The I, V & V rig ("Iron Bird") is the major ground facility of the M-346 aircraft for testing the flight controls, hydraulics and landing gear systems. It is designed to allow to perform all the necessary tests activities needed to allow the issue of the flight clearance and to permit testing, and troubleshooting of the problems that may arise during prototype ground and flight tests. The flight controls, landing gear and hydraulic systems components are connected together on the rig in the same way as on the aircraft to ensure that the systems as a whole operate as expected and exhibit no erroneous operation characteristics. A flight mechanics simulation computer (FMSC), which is part of the rig, is capable of closing the aerodynamic loop, simulating sensors and driving the “outside world”. Using either the aircraft pumps or with an external ground hydraulic power supply it is possible to supply the complete left-hand and right-hand hydraulic systems as in the aircraft.

The I, V & V rig is housed within a dedicated soundproof enclosure and directly communicates with a control room from which all the tests are conducted, controlled and monitored. Figure 5 shows the structure of the “iron bird”, while figure 6 shows the control room.

The flight control and landing gear subsystems are each installed within its own dedicated structural module mounted at the appropriate location on a platform. Each structural module consists of a steel framework and provides mounting for a loading actuator which is designed to apply the required load to the relevant aircraft actuator. Since the flight control and loading actuators are mounted as opposing pairs within the structural modules, these act as closed loop structures and no load is transmitted to the supporting platform to which they are bolted.

The primary control surfaces and the airbrake are represented on the rig by dummies, each having the same inertia referred to the hinge axis as the corresponding aircraft control surface. Each control surface is connected to its relevant actuator by means of a linkage and torsion bar whose stiffness is equivalent to that of the actual aircraft surface from the actuator to the hinge line, as shown in figure 7.

6 LOAD GENERATION

Load on the flight control actuators and on landing gear is generated by servovalve controlled hydraulic actuators, housed in structural modules and supplied by a dedicated hydraulic power supply. Within the structural module the rod end of the flight control actuator is connected to a lever rotating about a hinge, as in the actual aircraft.

The lever is also connected to the loading actuator which generates the required aerodynamic loading. In order to perform an accurate simulation of the inertia loading of the flight control actuator, the required system inertia is obtained by a disc located at the end of a torsion bar. The torsion bar provides the required stiffness, such that the resulting spring / mass system has the same resonant frequency as the actual actuator / aerodynamic surface of the aircraft system

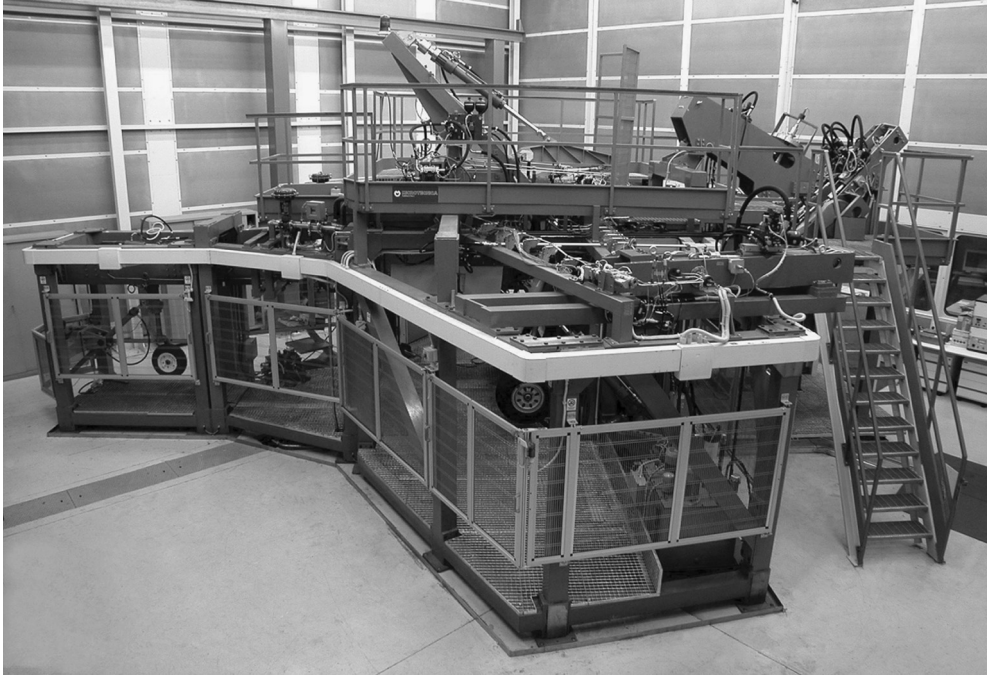


Figure 5: "Iron bird" structure



Figure 6: "Iron bird" control room

Each load actuator is comprised of a hydraulic ram, a valve module, speed and force transducers. The hydraulic ram is a double acting, equal area piston jack with extremely low friction guaranteed by the use of hydrostatic bearings; the actuator has a high side-load capability and is hinge mounted with zero backlash spherical joints. The actuator operates at 28 MPa and is capable of a stall force of 65000 N, with an internal friction of about only 30 N.

The valve module is comprised of a five ports electrohydraulic servovalve with internal electrical feedback, pilot flow lines for the hydrostatic bearings, by-pass valve for actuator floating and emergency unloading, two cross-port pressure differential limiting valves for actuator load limiting, pressure and return accumulators for minimising the effect of the hydraulic line dynamics on the transient response of the force control system. Moreover, the valve module includes a calibrated orifice for creating an internal cross port leakage, as required to optimise the force control dynamic performance.

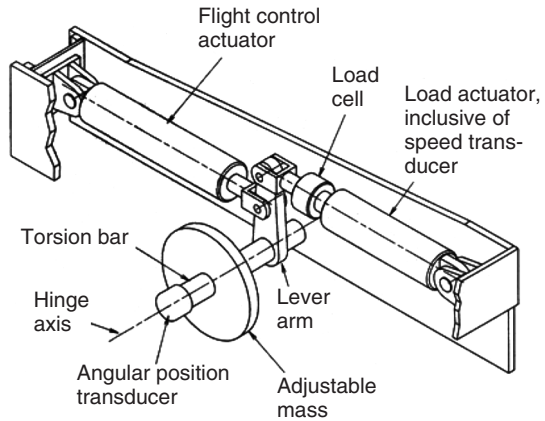


Figure 7: Configuration of a structural module

The structural module transducers are: a load cell of a strain gage type, suitable for dynamic loading, an integrally mounted LVT type speed transducer, and a rotary position transducer located at the end of the torsion bar. A three-dimensional view of the structural module is shown in figure 8, while figure 9 shows its hydraulic diagram.

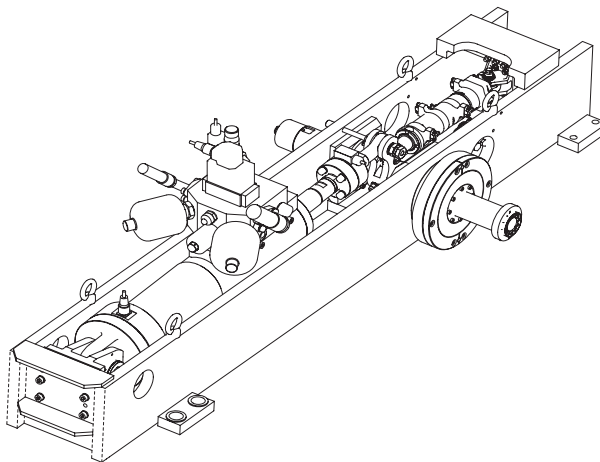


Figure 8: 3-D view of a structural module

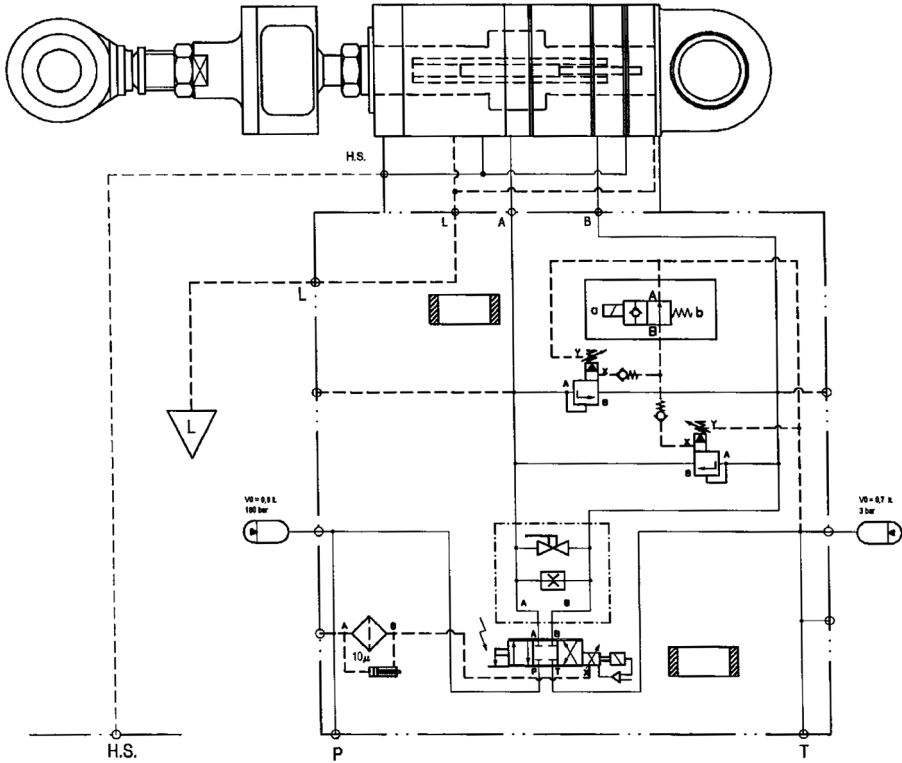


Figure 9: Hydraulic diagram

7 LOAD CONTROL

The control of the force that the hydraulic load actuator exerts onto the flight control actuator is basically obtained by closing a force feedback loop with the addition of a speed compensation network as outlined before in this paper. However, some further enhancements were introduced in the force control law to make up for the components non-linearities and for reducing the time delay to rapidly changing force commands. The block diagram of the resulting control law is illustrated in figure 10. The control law is organized such that only an integrator is present in the forward path of the control loop, while a proportional and a derivative feedback loop are created; this arrangement provides a good combination of stability margins and system accuracy, though it requires a fast recursion rate from the computer that closes the feedback loop. For this application the computer had a recursion rate of 4 kHz with a computation time of 0.3 ms and the analogue/digital converters were of 16 bit accuracy. The reduction of time delay following a fast changing force command is obtained by creating a feed-forward line with transfer function $G_F(s)$.

In order to get the best performance of the load control system over its whole operational range, the control loop gains were made adaptive both to the rate of change of the force command and to the actual force developed by the actuator. With reference to figure 10,

the rate of change of the force command determines the value of a gain X , which increases with the force command rate while the actual value of the force developed by the actuator, which on its turn is dependent on the pressure differential across the actuator ram, determines the value of gain Y according to a function $F(F_{ACT})$ that was appropriately selected to make the overall system gain almost independent of the operating condition.

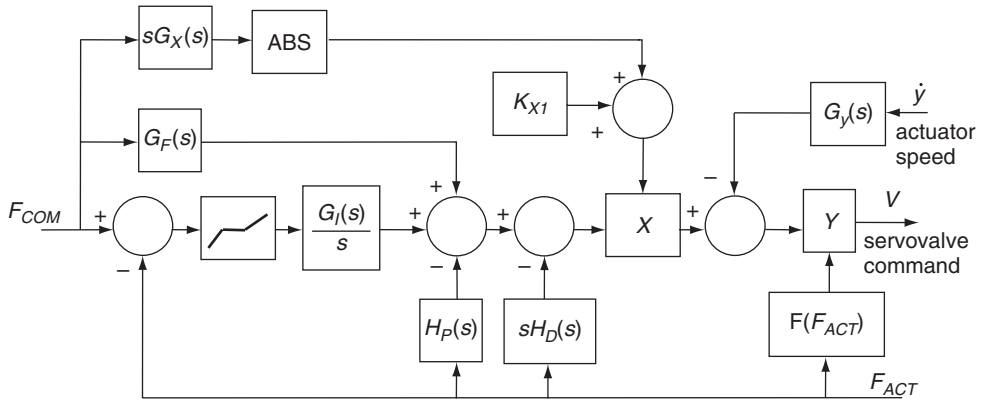


Figure 10: Block diagram of the control law for the load control system of the M346 “Iron Bird”

8 PERFORMANCE RESULTS

After a proper tuning of the control parameters and an accurate mounting of all mechanical and hydraulic hardware, an excellent performance of the load control system was achieved, that allowed dynamic loading of the M346 flight control actuators under the entire range of simulated flight conditions. As an example, two different flight cases are reported in figures 11 and 12. Figure 11 refers to the case of an aircraft turn requiring a fast aileron manoeuvre; in this figure curve 1 corresponds to the commanded aileron angle determined by the pilot stick position, curve 3 is the actual aileron angle resulting from the movement of the aileron flight control actuator, curve 2 is the load command generated by the aircraft models embedded in the Flight Mechanics Simulation Computer, curve 4 is the actual force developed by the load control actuator and 5 is the command to the load control actuator servovalve. It can be seen from this figure that during this test the actuator load was required to change rapidly while the flight control actuator was moving fast. For instance, in the time frame from 4.5 s to 4.7 s the aileron command request a change of approximately 10 deg, with a rate of about 50°/s, while the force on the actuator is simultaneously commanded with a rate of change of 90000 N/s. Curves 2 and 4, representing commanded and actual force are practically superimposed, show the capability of the force control system to accurately follow the demands, satisfying the requirement. (The difference between the commanded (1) and actual (3) position of the flight control actuator is due to an offset in the acquisition system and is not relevant to the force control system.)

Figure 12 refers to the case of the aircraft on a level flight in an atmosphere with turbulence. The pilot stick is at a fixed position (not shown in this figure.) Also in this case the two curves corresponding to the load commanded by the FMSC and the actual load are practically coincident, which allowed the system to correctly load the flight control actuators with the identical loading experienced by the same actuators during real flight.

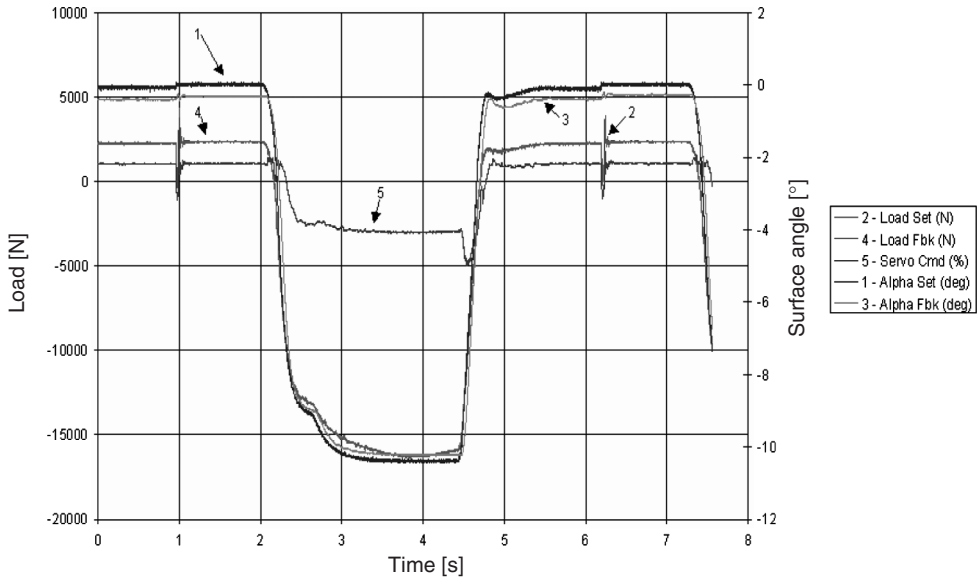


Figure 11: Force control system response for the case of fast aileron manoeuvre

9 CONCLUSIONS

The force control system described in this paper was developed as a part of the Integration, Validation and Verification Rig for the hydraulic system, flight controls and landing gear of the Aermacchi M346 advanced trainer aircraft. The highly demanding accuracy requirements for the system generating the actuators loads both in static and dynamic conditions were met by developing a system which made use of state-of-the-art hydraulic components and technology, accurate force and speed sensors and of an adaptive control law.

The force control system described in this paper referred in particular to the load control of the aircraft primary flight control actuators which required to be loaded by a hydraulic ram. For the load control of the aircraft secondary flight controls (leading and trailing edge flaps), the same control philosophy was adopted, though with some difference because of the different loading mechanism. The aircraft actuation systems for its secondary flight controls consist of centrally located Power Drive Units (PDUs) that drive transmission shafts running parallel to the leading and trailing edges of the wing; the shafts, on their turn drive either rotary or linear mechanical actuators which are connected to the aircraft flaps.

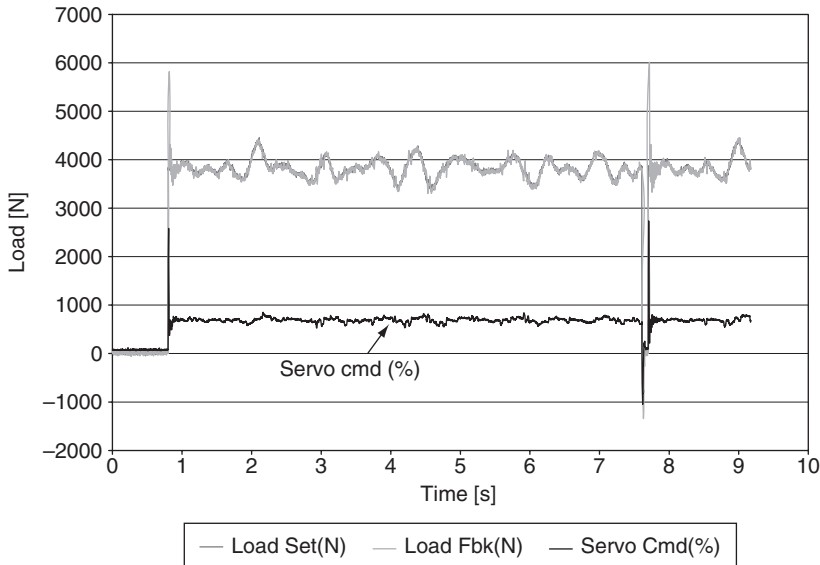


Figure 12: Force control system response for the case of level flight in turbulence

In order to simplify the already complex "iron bird", and due to the lower criticality of the secondary flight controls, a load control system was made that controls the total torque at the PDU outlet, rather than the individual loads on the single flap actuators. Therefore, in this case a servovalve controlled reversible pump was used as a device to create the controlled torque on the PDU. Though the large internal friction of the pump made the entire torque control system less accurate than the one described in this paper, still the maximum accuracy error for that application was within 5% of the maximum load torque for all type of simulated aircraft flight conditions.

10 ACKNOWLEDGMENT

The Authors wish to thank AerMacchi for having granted the permission of reproducing the pictures contained herein and for their encouragement in the preparation of this paper.

Knowledge based tools for the design of servo-hydraulic closed loop control

Matthias Liermann, Hubertus Murrenhoff
Institute for Fluid Power Drives and Controls (IFAS) - RWTH Aachen
University

ABSTRACT

The design process of hydraulic drives requires a lot of knowledge and experience although many computer tools are available that aid in various aspects of the design. One of these aspects is the selection of a suitable control strategy and its parameterisation. While being a significant key for the performance of servo-hydraulic drives it is nevertheless often neglected because of lack of knowledge in control theory. Only for very demanding applications design engineers use specialised and often complex simulation programs to analyse the system's static and dynamic behaviour prior to its implementation. Also application engineers need assistance in applying and tuning controllers that use more advanced control concepts taking user-defined constraints into account such as the performance of the given hardware.

Starting from observations of the general design process of hydraulic drives and an overview about which design steps are already computer supported, results of a literature search about knowledge based control design approaches for hydraulic drives are presented and evaluated in this paper.

1 INTRODUCTION

1.1 Challenges for hydraulic drive solutions

Fluid power drives are increasingly challenged by electrical drive solutions. Reasons for that are the accessibility of electrical power through the electricity network as well as their putative cleanliness and reduced noise emission. Since system responsibility is more and more passed on towards component suppliers a major advantage is also the growing demand for plug and play solutions. Customers wish to select the optimum drive principle for each axis without having to switch between operator controls. Thus, aspects like simple integration of hydraulic axes into automation concepts, simplified installation,

commissioning and maintenance play a key role for users today. The performance of the closed loop control should meet predefined requirement specifications with as little effort on commissioning as possible. A simulation of the drive in combination with the machine dynamics would be necessary for choosing and parameterising the controller structure and hardware. This is difficult especially for tailor made machinery and small series where the effort to physically model or to identify machinery dynamics is too cost-intensive.

Many suppliers have introduced “intelligent” electro-hydraulic linear axes to their product range. They consist of a servo-cylinder in combination with a servo-valve with integrated sensors, built in controller hardware and field bus-capability /Drec/. Nevertheless the design engineer either from the component supplier or from the user must choose a control strategy that suits his special requirements and boundary conditions and parameterise it either in a first step with the help of simulation or in the phase of commissioning the plant. This requires much experience and expert knowledge in the field of control systems. Especially smaller manufacturers often do not have this expertise.

1.2 Need for support in controller design

Due to the high power to weight ratio of hydraulic drives the actuated mass inertia has strong influence on controller parameters. The mechanical damping depends to a large degree on the actual operating pressure and the position of the piston. The largely used PID controllers do not exploit the whole potential of servo hydraulic drives while generally achieving good performance for electrical drives. The background of control theory is available and has been applied to hydraulics in many publications but it takes a long time of study and experience for a user to be able to employ more advanced control concepts in his application.

A variety of simulation tools (e.g. AMESim, DSHplus, ITISim, Simulink) are at hand helping to lay out more sophisticated systems. They facilitate the analysis of the static and dynamic behaviour of a hydraulic circuit design. In interaction with the simulation tool different control strategies can be applied and examined. Even so they do not offer intelligent support in the choice of control strategy, leaving the user to his own experience and knowledge.

Support in this design aspect would be greatly appreciated by manufacturers and users of hydraulic systems. It would help the sales engineer of hydraulic components to estimate the feasibility of a customer inquiry concerning dynamic requirements and calculating the costs for controller equipment at an early stage. The designer wishing to integrate hydraulic axes in his plant needs support in setting up the controller suiting the specified requirements best and in choosing the appropriate sensors. Also in the phase of commissioning the same knowledge domain is needed. A tool is required helping to adjust the control parameters towards optimum (or satisfying) performance without requiring in-depth knowledge of the control theory background. Such a tool would speed up commissioning and also reveal the potential of the hydraulic unit to the user.

It appears to be obvious that these different tasks cannot be performed by a single conventional software tool. Conventional software processes data in an algorithmic

fashion. The knowledge encoded in the program is intermixed with the control of this knowledge. It is encoded in functions. The fact that the different needs of a sales engineer, a designer and a commissioning engineer inquire the same domain of knowledge leads to the approach of knowledge based systems, wherein the knowledge is separated from its control.

2 COMPUTER AIDED DESIGN OF HYDRAULIC CIRCUITS

In the first section this chapter gives a brief overview of the general design process of hydraulic circuits. Subsequently a discussion is presented on which design step software tools are state of the art. Special attention shall be given in a third section to approaches of knowledge based tools and expert systems.

2.1 The general design process of hydraulic systems

In this section the general process of designing a hydraulic circuit shall be outlined. It will be examined how the different design steps can be supported by software tools.

/Pahl/ describes the principle steps of a technical design process as an iterative procedure outlined by the following steps.

- definition of problem
- conceptual design
- embodiment
- detailing

For the following it shall be assumed that a hydraulic cylinder has been chosen as the working principle with which to realise certain motion or force trajectories. By this the first two design steps have already been almost completed. The designer has examined the problem and through abstraction isolated functions to be realised by his design. From his experience with this kind of problem or because of additional boundary conditions he decided to solve the problem with a hydraulic cylinder and came to a *conceptual design*. He is sure that the problem is generally solvable and begins with the *embodiment* of this conceptual design. This involves to set up a structure of functional elements interacting with each other to realise the main function. For hydraulics this means to decide on a certain configuration of basic functional elements like fluid, pumps, valves, actuators, filters, hoses, controller hardware, sensors, etc. The result of this process is the hydraulic scheme that has to be *detailed* in the last step by precise definition of each part, creating parts lists and producing all documents for manufacturing.

So far the dynamic behaviour of the systems has not yet been considered very much. The dynamic behaviour is described by characteristic values concerning the stability and the quality of the closed loop control. Among considered criteria are rise time, transient time, smoothness, stiffness, damping and energy consumption of control. The controller plays the central role for the dynamics of a hydraulic system. It determines the kind of feedback of motion, pressure or force to the controlling element, the valve. Optimally the feedback design should succeed and overlap with the hydraulic design to allow the estimation or simulation of closed loop behaviour prior to plant set up. **Figure 1** shows the described formalised design process of hydraulic systems.

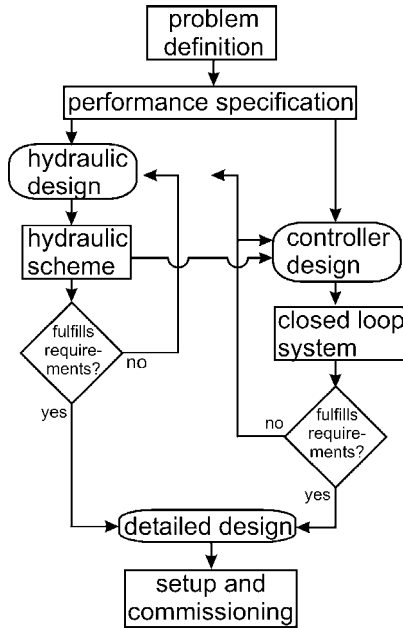


Figure 1: Formalised design process of hydraulic systems

2.2 Difficulties of concurrent controller design

Especially for smaller projects, there is rarely paid much attention to the dynamic behaviour of the system. Static characteristics have the advantage that their fulfilment can be ensured by separate design parameters. If, for example, the maximum velocity is to be increased, the nominal flow of the valve or the nominal pressure should be enlarged. The effect of these actions on other characteristics of the plant is limited, plausible and can be analysed fairly easily.

This is not the case with dynamics. The demands on dynamics always contradict each other. At the same time the performance characteristics of actors, sensors and controller hardware clearly limit the systems' dynamic potential. That means the requirements in most cases cannot be faced separately. Within these limits the task of the controller is to find a compromise between contradicting preferences and to ensure the fulfilment of all demands.

In most cases the controller is not designed concurrently to the hydraulic system. One of a few standard control algorithms is applied and parameterised when the plant is put into operation. Because of lack of understanding the resulting dynamic characteristics are accepted in favour of process stability. A problem is that control theory has a very mathematical view of the motion problem using a complete different language to describe the system's behaviour. This makes it extremely difficult to consider issues of dynamics earlier in the embodiment phase of the hydraulic design.

2.3 Automation of hydraulic system design – state of the art

Computerised support generally aims at accelerating the development by automating well defined routines as well as at cost reduction by omission of laboratory tests and by deploying different or less qualified personnel. Several classes of tools offer support in the design process. A detailed overview with references is found in /Vier/.

1. Tools that support the drawing of connection schemes according to standards or tools that automate the construction of hydraulic components within conventional CAD. This class of tools is widely used, /Foit/ and /Feus/ give an overview over such systems.
2. The majority of tools support the designer in special aspects of the iterative design process, primarily behavioural analysis and simulation. Among these are AMESim, Bathfp, DSHplus, ITISim /Feus/.

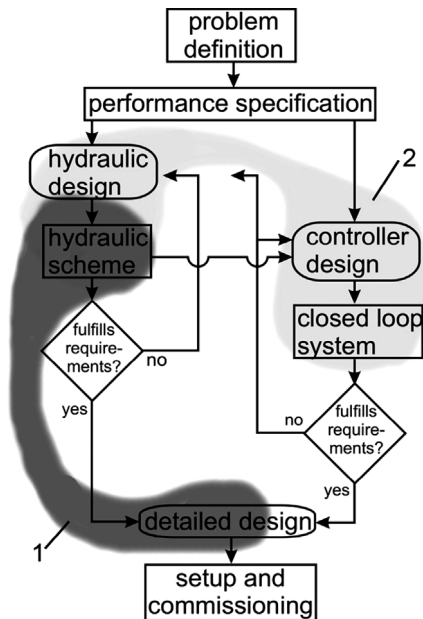


Figure 2: Association of different classes of software tools to areas in the design process

Figure 2 associates these classes to design steps in the formalised design process shown in Figure 1. The objective of the first class of tools is automation of time consuming procedures that lie between a conceptual hydraulic design and the detailed plant documents. The automated procedures are well known and straightforward. The functionality of the created systems is not verified. The question whether requirements are fulfilled or not is not answered by the system.

The design tools of the second class focus mainly on behavioural analysis of given hydraulic elements, circuits and controllers. The designer uses them to gain insight into the physical behaviour of his design. Through his knowledge and experience he can modify the design to improve its behaviour. To modify the design the designer can exchange components or change their physical parameters. By numerical computation of the behaviour he can evaluate the modifications. Some tools offer optimisation routines.

Concluding one can say that common to all design tools today is that the relevant steps of evaluating and consequent system change are left to the user /Vier/.

2.4 Automation of hydraulic system design - Knowledge based approaches

Figure 2 shows that for important parts of hydraulic circuit design automation is not yet state of the art. The reason for this is that a computer does not understand the nature of what is being processed. Nevertheless, as shall be presented in this section, a number of approaches have more recently been made with the use of expert system techniques.

The process of design is creative in its core. That means that there is no recipe how to proceed in order to generate a (hydraulic) circuit design that behaves exactly according to a given set of demands. The question in design has to do with the structure and the behaviour of a system /Steil/. Modern design tools focus mainly on one of the two facets behaviour and structure. CAD-software, for example, is a helpful tool in the design process. It can automate design steps by making use of feature-techniques. But it focuses exclusively on the structure of the component or circuit. A simulation tool on the other hand focuses mainly on the behaviour of a system, given a fixed structure. The following sections present some recent knowledge based approaches.

2.4.1 Assisted controller development and automated commissioning in hydraulics

Controller design demands a high degree of expertise in control systems which the plant operators often do not have. In his thesis Schoppel has developed a framework in which the setting into operation of control-systems for servo-hydraulic drives can be assisted /Scho/. As he observes, specialists in control systems are usually needed in two stages: For

- controller design and
- plant commissioning.

For the controller design the expert chooses a control strategy, deploys it on the plant's system model and parameterises it respective given specifications. This kind of controller

design is called model based controller design. A mathematical model of the (open loop) hydraulic system and the driven masses must be available to apply this approach.

In putting the plant into operation the control system expert proceeds according to the following steps. First he makes functional tests to check that all components and their connections are fault-free. Then the sensor signals must be calibrated to match corresponding physical values. In a next step he must identify the characteristic system parameters that he used for modelling the plant. With those, the controller can finally be parameterised based on the controller design which has been done in the first stage.

Schoppel concludes that the second stage, the setting into operation of the plant, could be largely automated because the commissioning strategy can already be defined in the first stage of designing the controller.

To reduce the expenditure of the control systems expert, Schoppel describes an assistance tool which, adapted by an expert in control systems for the specific plant configuration, enables the application engineer to put the plant into operation without requiring knowledge of control systems. The basic idea is to provide a development tool with powerful routines for applying a specific controller design. At the same time this tool is the basis for the operator assistance in the phase of commissioning. For this the control designer defines a commissioning strategy.

In contrast to the approach of an expert system that is to carry out decisions by itself on the basis of inference from structured knowledge /Durk/, the assistance tool presented by Schoppel leaves decisions in the design-process to the human expert.

The assistance tool merely assists the application engineer by guiding him through a preset sequence of operations to a controller configuration yielding the desired behaviour. Functional tests, experiments to identify characteristic parameters needed in the system model and calibration of sensor signals can be automated. The user also gets valuable support in adjusting the plant's behaviour by tuning artificial parameters that have an intuitive meaning. For safety reasons the assistance tool runs a simulation with every new set of parameters before applying them to the controller.

Difficulties with this approach arise if the customised commission strategy fails at any point. In this case the operator cannot proceed because he does not understand what the assistance tool is doing. The educational value of the system is very low for the operator as well as for the system designer. He strictly applies a certain control strategy.

2.4.2 Knowledge based commissioning and adaptive control in pneumatics

Keller's work deals with the application of expert systems in the area of controller design /Kell/. The intention of such an expert system is to emulate human knowledge and behaviour in the design of control systems. It becomes apparent that this is an extremely difficult task with systems such as pneumatic or hydraulic cylinders, where the synthesis of model based controllers is complex and involves many restrictions such as quality of signals, variable friction, controller hardware etc.

A main characteristic of expert systems is that knowledge must be separated from the processing of this knowledge. The advantage of this is that the knowledge and the processing strategy can be modified and extended independently from each other. Keller implements analytical knowledge in the form of routines and heuristic knowledge in the form of rules. The analytical part contains specific algorithms for the application of a special control strategy, for example identification of process parameters and input/output routines. The rules consist of if-then expressions (e.g. IF NOT(*coefficient is given*), THEN *estimate parameter*). These rules are executed in a certain order, defined by the inference strategy. In this case the inference strategy is monotonous forward chaining. In forward chaining every rule is checked for already fulfilled premises. A rule with fulfilled premise is fired and its conclusion may lead to the fulfilment of other rules' premises. The implemented rules though are strictly sequential so that they directly determine the order of execution.

Keller has deployed his Expert-System only on one test object, a small pneumatic piston with two two-port servo-valves and a real-time interface. A large part of his thesis deals with the difficulties in designing the controller especially for this system. The expert knowledge and experience necessary to design the controller for the servo-pneumatic system is not implemented in the knowledge base. But the application of this controller design is encoded in algorithms which by a set of rules are executed in a predefined order. A person with less knowledge about control systems is thus led through the commissioning of the pneumatic drive.

This leads to the conclusion that Keller's expert system can only be understood as a structure with potential to be extended. It supports only one possible controller structure. Different performance criteria are difficult to handle. One has to consider that by extending the proposed structure by different options of controller structures, performance criteria and boundary conditions, decisions would have to be made between these options. This problem is not discussed in his thesis.

2.4.3 Adaptive controller design via expert system

The theory of control systems is very abstract. It can be applied to social and economical issues as well as to every technical plant. While the control systems research is rapidly growing, bringing forth more powerful control strategies, these results are implemented only in a very narrow area of technology due to their high complexity. The implementation of advanced control concepts by non-experts requires computerised tools. These have to fulfil at least four demands in order to be accepted :

- simplicity of use
- simplicity of concept
- few tuneable parameters
- evidence of applicability

The expert tool ADEX presented by Jüttner is not implemented for any particular application /Jütt/. Its objective is to help applying adaptive control on arbitrary system automation.

The starting point for controller development is the linear time invariant description of the open loop behaviour of the system at a number of system states. This set of models is either fed in directly by the user via user interface or automatically identified by identification algorithms.

The system supports a cyclic process that a designer would intuitively choose. First a performance criteria can be edited with the option of consulting a knowledge base. Then the following steps are repeated until the desired performance is achieved.

- For the models of each system state a controller must be designed. The set of controllers will be blended into one adaptive control. Five different control methods are available. Each method has a set of degrees of freedom that have to be tuned in order to achieve the desired performance. The inexperienced user can consult the knowledge base that automatically tunes the parameters.
- With the new parameters the closed loop system behaviour is simulated.
- The performance of the system is evaluated by the expert system according to the performance criteria. The evaluation is the basis for enhancing the parameters in the next iteration.

Jüttner's basic idea is to integrate all design-options into one closed-loop control configuration that can be switched active/inactive. In effect the task to be solved is choosing a controller and going through its parameterisation, which is much easier to accomplish than the problem of design and configuration.

The expert system approach of ADEX is very interesting for hydraulic design, too. It shows, for example, how the controller parameterisation can be supported by knowledge base consultation. This knowledge has been collected by interpretation of the underlying control theory, by simulation studies and laboratory tests. It must be a concern to build such knowledge bases also for closed loop hydraulic systems. Furthermore it will be important to predict the performance of different control methods and to choose the best one on the basis of knowledge bases. An interesting aspect of ADEX is also that it supports different operator modes for more or less experienced users. It would frustrate a more experienced user to be led through the whole consultation as much it would overcharge a less experienced one without consultation.

2.4.4 Automated controller design modifications

On the basis of case based reasoning and making use of graph grammar design techniques Hoffmann has developed an expert system that automates the creation of hydraulic schemes /Hoff/. This approach is suitable for problems that can be solved on a component level /Schu/. It has been realised in combination with the simulation tool *art*deco. It has not been used for synthesis of controller structures, which is why it shall not be discussed here. But

/Vier/ has progressed on this work, taking the closed loop behaviour of the automatically generated schemes into account. Within this holistic expert system approach very interesting issues are discussed. For example a general problem in design is that usually a number of possible system modifications can improve the behaviour. With heuristic knowledge it is possible to estimate the probable improvement of each modification. This information can be stored in a “improvement-by-modification”-matrix. At the same time it has to be considered that a modification improving on one characteristic might change another for worse. A priority list has to be defined as a basis for deciding which of possibly improving changes to the system has to be employed. Together this leads to a proposed sequence of modifications.

This approach is very comprehensive, tackling the whole design from creation of the hydraulic scheme up to the controller and its parameterisation. It will be crucial for the implementation of this approach that the user has influence on the priority lists and boundary conditions to be considered.

2.5 Discussion of knowledge based approaches

A certain system representation often implies a certain approach to the problem. This becomes evident when looking on the different knowledge based approaches presented above. Schoppel and Keller build their thesis on a linear system model description. This model is derived from a nonlinear physical model with boundary conditions and friction. A state space control approach is applied to the linearised system model. The rules to tune this controller require experience and knowledge about the control method. For the user who does not have this knowledge a translation must be available from terms with which he describes behavioural demands into corresponding controller modifications. Such a translation is what Schoppel describes for state space control tuning. He defines a relation between certain pole placement and behavioural description of the closed loop behaviour.

From the viewpoint of the commissioning engineer it seems ridiculous to start running the plant with what are believed to be the optimal parameters. This could be dangerous and maybe harm the machine. He will start with small parameters, gradually increasing them. It maybe that the prior calculated parameters work well, if the plant was accurately modelled, but they might not if the modelling was incomplete. This is why Schoppel, Keller and Jüttner propose the identification of system parameters through experiments in order to adjust the model and get better controller parameters. But identification requires sensors to measure system behaviour. This leads to the conclusion that the approaches of Schoppel and Keller suit manufacturers of complete drive solutions who know their own components very well but not for tailor made machinery and small series, where the effort to assimilate the model to the behaviour of the plant is too costly or impossible because of lack of sensors.

Jüttner’s approach does not discuss the problem of commissioning, he assumes that open loop behaviour can be identified from measurements. But he shows how heuristic knowledge can be used to tune a controller towards desired behaviour.

Vier also uses heuristic knowledge. He shows how the control design can be integrated into the automated design of the whole system. For the decision which control method matches a particular problem best the discussed “improvement-by-modification”-matrix is a valuable contribution.

3 CONCLUSION AND FUTURE PROSPECTS

Expert system engineers are taught that a knowledge based system always has to focus on a specific problem in a specific domain /Durk/. This is important to bear in mind while judging on expert system approaches. A knowledge base has to be developed, maintained and should be expandable. And the effort on this has to be in a balanced relation to the task that is solved by inquiring this knowledge base.

The examination in this paper constitutes the beginning of the author’s efforts to establish a new knowledge base for controller design. This knowledge base should be versatile for controller design as well as for commissioning. It has to be examined what kind of structure the knowledge base must have, so that it can be used for both cases. It should be able to reason logically with behavioural criteria instead of depending only on the exact mathematical modelling of the plant in the area of decisions where neither human experts need the mathematical equations as a basis for decision making. Studies have to be made, on how empirical as well as analytical knowledge that has been accumulated in many research projects in this field could be possibly integrated in this knowledge base. It should give support in choosing and tuning a control strategy respective given constraints and performance criteria.

In this paper some knowledge based approaches have been reviewed. On the basis of this, not meant to be exhaustive, literature research some goals for the next steps in knowledge based controller design shall be derived.

4 REFERENCES

- | | | |
|--------|--------------|---|
| /Drec/ | R. Drechsler | Hydraulische NC-Linearantriebe positionieren μm genau, Konstruktion, 2004, Issue 11/12, p18-20 |
| /Durk/ | J. Durkin | Expert systems – design & development, 1994, Prentice Hall |
| /Feus/ | A. Feuser | Simulation technology in research, development and applications for fluid power, 2004, Proceedings of 4 th International Fluid Power Conference, Dresden, p29-46 |

- /Foit/ B. Foitzik “Planen mit System. Computerunterstützung bei der Schaltplanerstellung.”, 1991, *Fluid*, August, p38-39, “Designing systematically . Computer support for scheme building”
- /Hoff/ M. Hoffmann Zur Automatisierung des Designprozesses fluidischer Systeme, 1999, University of Paderborn Germany, Department of Mathematics and Computer Science, “On automated design of fluidic systems”
- /Jütt/ T. Jüttner Der Entwurf adaptiver Regler durch Einsatz eines Expertensystems, 1997, Dissertation, VDI-Verlag Düsseldorf, “Expert system aided design of adaptive closed loop control “
- /Kell/ H. Keller Wissenbasierte Inbetriebnahme und adaptive Regelung eines pneumatischen Linearantriebs, 1994, VDI-Verlag, Düsseldorf, “Knowledge-based commissioning and adaptive closed loop control of a pneumatic linear drive”
- /Pahl/ G. Pahl, W. Beitz Engineering Design: a systematic approach, 1999, 2nd ed. Springer, London
- /Scho/ G. Schoppel Beiträge zur automatischen Inbetriebsetzung und Regelung hydraulischer Zylinderantriebe, 2004, Dissertation, Shaker Verlag, “Contribution to automated commissioning and closed loop control of hydraulic linear drives”
- /Schu/ A. Schulz, B. Stein, A. Kurzok On Automated Design of Technical Systems, 2001, Notes in Computer Science tr-ri-00-218, University of Paderborn Germany, Department of Mathematics and Computer Science
- /Stei/ B. Stein Model Construction in Analysis and Synthesis Tasks, Habilitation, University of Paderborn Germany, Department of Mathematics and Computer Science, 2001.
- /Vier/ E. Vier Automatisierter Entwurf geregelter hydrostatischer Systeme, 1999, Fortschritt-Berichte VDI, Reihe 8, Nr. 795 “Automated design of servo-hydraulic systems”

LOW-ORDER ROBUST CONTROLLER FOR FLEXIBLE HYDRAULIC MANIPULATORS

Matti Linjama and Tapio Virvalo

Institute of Hydraulics and Automation

Tampere University of Technology

ABSTRACT

A filtered P-controller (gain plus first order lag) is suggested for position control of actuators of hydraulic manipulators. Analytical and simulated results show that this controller gives good performance together with robustness against modelling errors and disturbances. The achieved closed-loop natural frequency is 42 percent of the lowest natural frequency of the system, and response speed is two to three times faster than with traditional P-controller. The main conclusion is that although hydraulic manipulators are complex and non-linear, a fixed-parameter, low-order and linear controller can deliver satisfactory control performance over the whole operation range.

KEYWORDS: Hydraulic manipulators, robust control

NOTATION

d	vector of disturbance signals
e	vector of error signals
F_i	Force of i th cylinder
$G(s)$	transfer function matrix of controlled system
I	Identity matrix
K	gain of control loops when all gains are equal
$K(s)$	transfer function matrix of controller
K_{cr}	largest K such that the closed-loop system is stable
K_p	gain matrix of P-controller
$K_{pF}(s)$	transfer function matrix of filtered P-controller
K_{pi}	gain of i th controller
K_{PN}	nominal gain matrix
K_r	parameter in model of modelling error
K_{vi}	velocity gain of i th cylinder-valve combination
r	vector of reference signals
$S(s)$	sensitivity operator
$T(s)$	complementary sensitivity operator
u	vector of control signals of valves

u_i	control signal of i th valve
\mathbf{y}	vector of piston displacements
y_i	displacement of i th piston
$\Delta_M(s)$	transfer function matrix of multiplicative perturbation
θ_2	angle between horizontal line and link 2
θ_3	angle between links 2 and 3
$\sigma_1(\cdot)$	largest singular value
τ	time constant of controllers when selected equal
τ_i	time constant of i th controller
τ_r	parameter in model of modelling error
ω_B	bandwidth of closed-loop system
ω_i	i th natural frequency of the example manipulator
ω_{PF}	closed-loop natural frequency with filtered P-control
$\omega_{1,\min}$	minimum value of first natural frequency
$\omega_{1,\max}$	maximum value of first natural frequency
ζ_{PF}	closed-loop damping factor with filtered P-control
ζ	gain matrix multiplier

1 INTRODUCTION

Hydraulic manipulators are used in various heavy-duty lifting tasks e.g. in log loading. These robust machines work under difficult working conditions; loads are big and temperature may vary between -30 and $+50$ degrees centigrade. The manipulator must be reliable because productivity is an important topic. Reliability requirements cause that the simple open-loop control solutions are used. A smooth open-loop operation requires simultaneous and continuous adjustment of several valves. The closed-loop control solutions are rare because of increased cost and lack of simple control solutions. The cost increase is significant if high-quality servo valves and sensors must be used. The benefits of the closed-loop control are clear: it allows coordinated control of several actuators (e.g. straight movements), automated tasks, faster and smoother motions and improved accuracy.

Hydraulic manipulators are difficult systems from the control design point of view. The flexibility of hydraulic actuators and structure causes lightly damped vibrations in the system response. The static and dynamic properties are strongly non-linear and orientation dependent. Furthermore, many key parameters of mechanism and hydraulic circuit are poorly known. Typical examples are the mass and stiffness properties of links, the load mass, friction forces, effective bulk modulus and valve dynamics. Linjama and Virvalo (1) analysed characteristics of a commercial three-link manipulator. They found that interactions and multi-input multi-output nature of the system makes the traditional tuning rules of 1-DOF servo systems useless.

Adaptive control can address above-mentioned problems and it has been used in the control of hydraulic manipulators with some success (2,3). The main difficulty is that extremely fast adaptation is required because the dynamics change continuously during the motion. Adaptive control strategy requires high-quality sensors (low measurement noise), good

valves (less identified parameters) and additional measurements (faster adaptation). Reliability in all situations is also difficult to guarantee. Model based control has also been used (4), but it requires an accurate dynamic model. An additional sensor is needed at least for the load mass measurement. Robust control theory yields a controller which is reliable and robust against uncertainties, but whose control performance is not necessarily as good as with adaptive or model-based controllers. The drawback is that robust control synthesis tools, such as H_∞ -control or μ -synthesis, yield complicated controllers (5). Linjama and Virvalo (6) studied the robustness of some low-order controllers in an electrohydraulic position servo. They found that filtered P-controller (P-controller plus first order lag) is a robust and high performance control solution. Further benefits of this control solution are easy tuning and need for position feedback only.

The aim of this paper is to study the robustness of filtered P-controller in a hydraulic manipulator and to develop tuning rules for it. The multivariable loop-shaping techniques are used and normal P-controller is used as a reference controller. The design and simulations are based on accurate non-linear and linearised models of a commercial three-link manipulator with significant mechanical flexibility (7, 8).

2 EXAMPLE MANIPULATOR AND DYNAMIC MODELS

2.1 Example manipulator

The results of this paper are based on the analysis of a commercial hydraulic manipulator shown in Fig. 1. The manipulator is used in log loading and it is actuated by three cylinders and one rotary actuator. Only the motions of cylinders 1 and 2 are studied here and the telescopic extension of link 3 is fixed into the shortest position. The manipulator model therefore contains three flexible links and two cylinders. The cylinders are driven by high-response proportional valves and measurements consist of the supply pressure, pressures at cylinder chambers, displacements of pistons and stress at the point shown in Fig. 1.

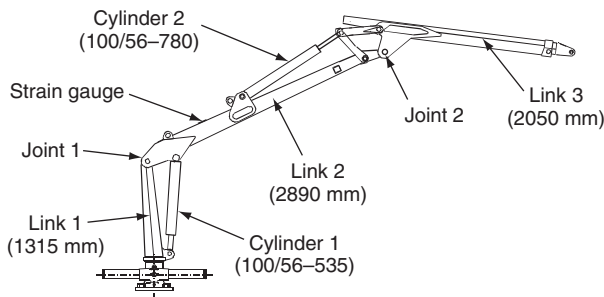


Figure 1. Example manipulator.

2.2 Dynamic models of example manipulator

A non-linear model was developed for the example manipulator in (7). The manipulator was modelled including structural flexibility by using the assumed modes method with special mode shapes. The results showed that the flexibility of links must be considered in the modelling. Good accuracy was achieved when in total five degrees of freedom (DOF) were used to model flexibility of links. The non-linear model was linearised in (8).

Variations in generalised Coriolis, centrifugal and gravitational forces were neglected in linearisation and resulting state-space model had 16 states. It was found that some tuning of damping parameters is needed in order to achieve correct damping.

2.4 Verification results

Figure 2 shows one measured and simulated open-loop response of the example manipulator with the load mass 200 kg. There is good agreement between the responses. The model can describe rather well also the complicated high-frequency response of F_2 as shown in the zoomed clip. Additional results in (7) shows that modelling accuracy is even better with bigger load mass. Figure 3 presents one step-response with non-linear and linearised models near the operation point $y_1=0.1$ m and $y_2=0.4$ m. The agreement between the responses is good but there is small error in damping. So the linearised model is adequate for analysis and control design.

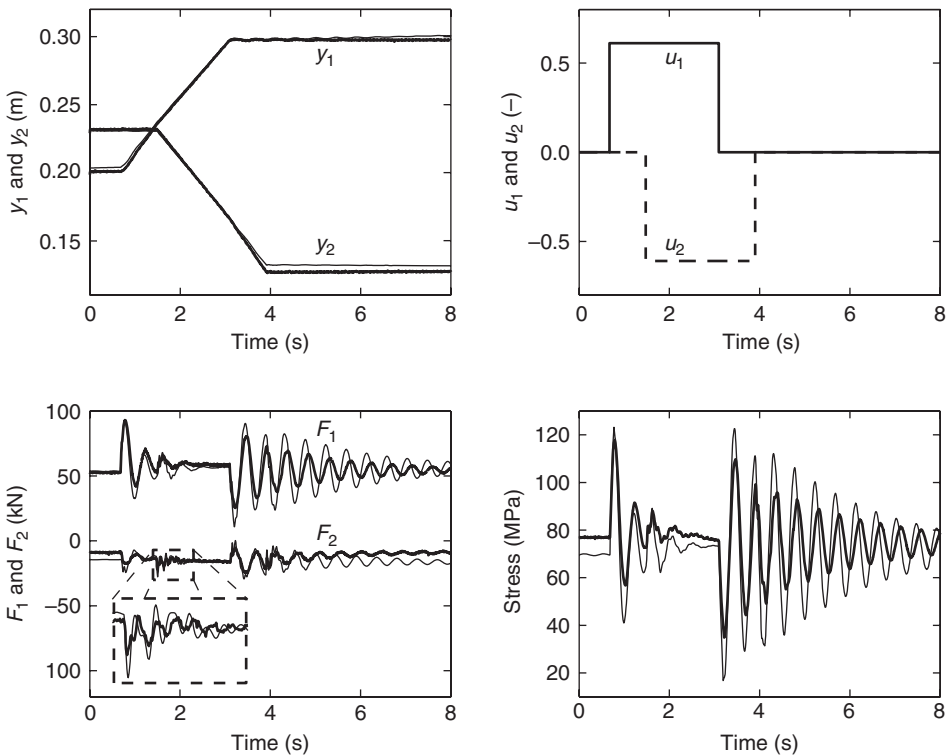


Figure 2. Measured and simulated open-loop responses of the example manipulator with a load mass 200 kg: —, measured responses; —, simulated responses

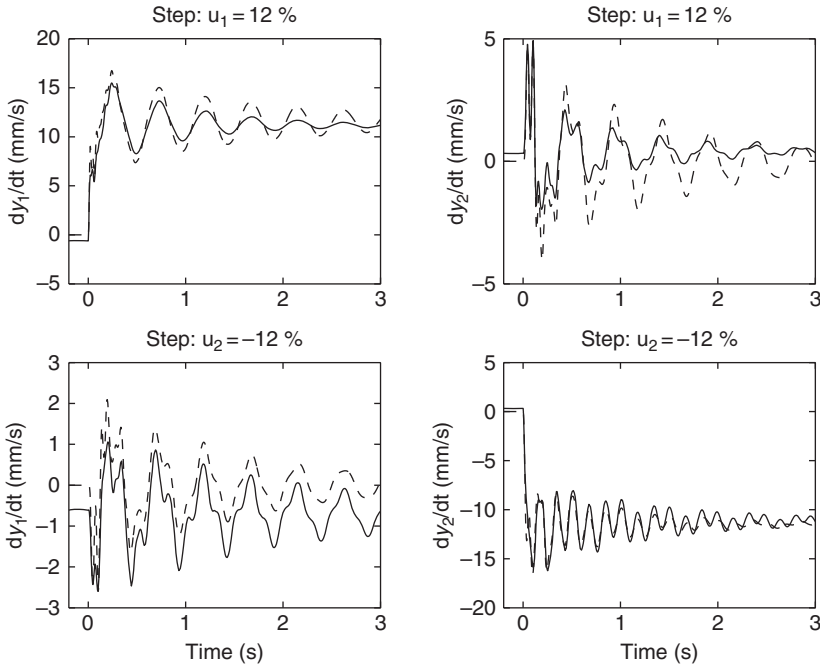


Figure 3. Step responses of non-linear and linearised models at the operation point $y_1=0.1$ m and $y_2=0.4$ m with a load mass 390 kg: —, non-linear model; - - -, linearised model

3 CONTROL APPROACH

3.1 Problems in the control of hydraulic manipulators

It is well known that hydraulic manipulators are difficult to control. This is mainly caused by four reasons: poor damping, non-linearities, uncertainties and multivariable nature of the system. The poor damping is seen in Fig. 2 in which the motion is characterised by lightly damped vibrations. The friction forces of cylinders, although significant, are not sufficient to damp vibrations. The structural flexibility also weakens the interaction between the motion of mechanism and actuators.

The dynamic equations of any manipulator with rotational joints are strongly non-linear. Hydraulic circuit and actuators are additional sources of non-linearity, the most important ones being:

- The stiffness of hydraulic cylinders varies with the displacement of the piston.
- Linear actuators are used to perform rotational movement of joints, which causes that the mapping from cylinder forces to generalised forces of the mechanism is non-linear and orientation dependent.
- Cylinders have high static and Coulombic friction forces.
- Relations between valve inputs and cylinder forces are non-linear and indirect.

Non-linearity causes among other things that the natural frequencies of hydraulic manipulators depend on the manipulator orientation. Figure 4 shows the calculated lowest natural frequency ω_1 of the example manipulator as a function of the orientation with the maximum load mass of 400 kg. In the figure, θ_2 is the angle between a horizontal line and link 2 and θ_3 is the angle between links 2 and 3. The minimum and maximum values of ω_1 are: $\omega_{1,\min} = 5.9$ rad/s and $\omega_{1,\max} = 18.9$ rad/s.

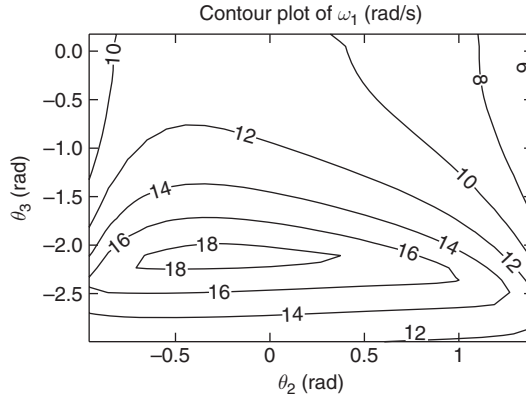


Figure 4. The calculated lowest natural frequency of the example manipulator with a load mass 400 kg.

Typical sources of uncertainty in the dynamic model are:

- The effective bulk moduli of oil volumes are uncertain because of hoses and unknown amount of entrapped air.
- The inertial and stiffness properties of links are known only with limited accuracy.
- In practical situation, the load mass is unknown or estimated with limited accuracy.
- The static and dynamic properties of mobile proportional valves are poorly known.
- Unmodelled dynamics such as high-frequency vibration modes, pipeline dynamics, and motion of the load or base of the manipulator.

The uncertainty in the load mass is especially harmful because it has an effect on both the gain of valves and dynamic behavior of the manipulator. The multivariable nature of the manipulator dynamics is seen clearly in Fig. 3. When one valve is suddenly opened, vibration occurs also in the other cylinder, and the amplitude of vibration is at the same level in both cylinders. The interactions are analysed in (1) where it is shown that interactions are significant in the frequency range above half of the lowest natural frequency. According to discussion above and more detailed analysis in (1), the dynamics of hydraulic manipulators can be characterised as follows:

- Lightly damped vibrations that occur at natural frequencies dominate the motion.
- Vibrations occur simultaneously at several frequencies. The motion is not necessarily dominated by the lowest vibration mode.
- Due to non-linearity, natural frequencies depend strongly on the manipulator orientation.

- (d) It is difficult to achieve an accurate model because of uncertainties. Even the lowest natural frequency is difficult to calculate accurately. The high-frequency response of hydraulic manipulators is highly unpredictable because of unknown high-frequency dynamic components.
- (e) Strong interactions occur between actuators at natural frequencies. Interactions are weak at the frequency range below half of the lowest natural frequency.

3.2 Robustness and performance criteria

The robustness and performance of controllers studied are analysed using frequency domain singular value plots of various transfer function matrices of the system (9). A general multi-input multi-output (MIMO) system is shown in Fig. 5a. In the figure, $\mathbf{G}(s)$ and $\mathbf{K}(s)$ are the transfer function matrices of the controlled system and controller, and the signals r , e , u , d and y are the reference, error, control, disturbance and output signals, respectively.

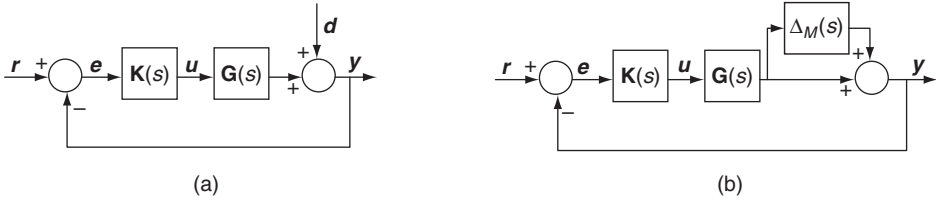


Figure 5. A closed-loop MIMO-system with disturbance (a) and with multiplicative perturbation (b).

Some important transfer function matrices are the sensitivity operator $\mathbf{S}(s)$ and complementary sensitivity operator $\mathbf{T}(s)$ which are given by

$$\begin{aligned} \mathbf{S}(s) &= (\mathbf{I} + \mathbf{G}(s)\mathbf{K}(s))^{-1} \\ \mathbf{T}(s) &= \mathbf{G}(s)\mathbf{K}(s)(\mathbf{I} + \mathbf{G}(s)\mathbf{K}(s))^{-1} = \mathbf{I} - \mathbf{S}(s) \end{aligned} \quad (1)$$

Good tracking and disturbance attenuation are achieved in the frequency range where the gain of $\mathbf{S}(s)$ is small and good sensor noise attenuation is achieved in the frequency range where the gain of $\mathbf{T}(s)$ is small. Commonly used gain measure is the largest singular value as a function of frequency and is denoted by $\sigma_1(\cdot)$. The bandwidth of a closed-loop MIMO-system is defined as the largest frequency ω_B that satisfies

$$\sigma_1(\mathbf{S}(j\omega)) \leq \varepsilon \quad \forall \omega \in [0, \omega_B] \quad (2)$$

where $\varepsilon < 1$. A value $\varepsilon = 0.5$ or -6 dB is used in this paper. Uncertainties are expressed as a multiplicative modelling error $\Delta_M(s)$ as shown in Fig. 5b. If the closed-loop system is stable when $\Delta_M(s)$ is zero, the system remains stable if (9)

$$\sigma_1(\mathbf{T}(j\omega)) \leq 1 / \sigma_1(\Delta_M(j\omega)) \quad \forall \omega \in \mathbb{R}^+ \quad (3)$$

The limit is often conservative because Δ_M is an unstructured uncertainty. In SISO systems the robustness is usually measured by gain and phase margins. The guaranteed gain margin (GGM) and guaranteed phase margin (GPM) for MIMO systems are given by (5)

$$\begin{aligned} \text{GGM} &= 1 \pm 1/\|\mathbf{T}\|_\infty \\ \text{GPM} &= \pm 2 \sin^{-1}\left(1/\left(2\|\mathbf{T}\|_\infty\right)\right) \end{aligned} \quad (4)$$

where $\|\cdot\|_\infty$ denotes an infinity norm i.e. the least upper bound of $\sigma_1(\cdot)$. The equations are valid if $\|\mathbf{T}\|_\infty$ is greater than one as is normally the case. The interpretation of Eq. 4 is that the MIMO system remains stable although gains or phases of all loops vary within given limits. These limits are only lower bounds of allowable variations and the situation can be better in practice.

The controller tuning is so that after the selection of suitable Δ_M , the controller is tuned such that Eq. 3 is satisfied. It is a difficult task to define the allowable modelling error as a function of frequency, $\sigma_1(\Delta_M(j\omega))$. Too big Δ_M yields conservative controller tuning while too small Δ_M does not give sufficient robustness. In the low-frequency area (much below the lowest natural frequency) interactions are weak and each actuator behaves like an integrator. So the low-frequency uncertainty of the model is mainly in the gain of valves. The gain of valve is with high probability within 0.5...1.5 times the nominal gain (6). This set the requirement for GGM to be at least from -6 dB to 3.5 dB. The interactions are significant in the frequency range above half of the lowest natural frequency. Therefore the modelling error is allowed to increase at the frequencies above half of the minimum of the lowest natural frequency with a slope 10 dB/decade where the slope is selected rather arbitrarily. The maximum magnitude of the modelling error is assumed to be

$$\sigma_1(\Delta_M(j\omega)) = K_r \sqrt[4]{1 + \tau_r^2 \omega^2} \quad (5)$$

The parameter τ_r is selected equal to $2/\omega_{1,\min}$, which gives in the example manipulator case $\tau_r = 0.34$ s. The parameter K_r is selected to be 0.8 that gives the GGM from -14 dB to 5.1 dB and GPM $\pm 47^\circ$. These gain and phase margins are commonly acceptable for hydraulic servosystems.

4 P-CONTROL

P-control is the simplest possible controller consisting only a static gain. If the system consists of a single actuator loaded by a pure inertia, P-control has many good properties. The stability limit is proportional to the natural frequency of the system and so the tuning for the minimum value of the natural frequency is good tuning for all other operation points also. The tuning is easy because of single tuning parameter. The P-control is also known to be robust against modelling errors.

In the multivariable P-control, the transfer function matrix of the controller is a static matrix, $\mathbf{K}(s) = \mathbf{K}_p$. The gain matrix \mathbf{K}_p is in the most general case non-diagonal but in this

study a diagonal gain matrix is assumed i.e. all actuators are controlled separately by a P-controller. The first question is how to select the gains of controllers. In order to maximise the bandwidth, the largest and smallest singular values of \mathbf{S} should be equal at low frequencies. This is achieved if each control loop has an equal open-loop gain, which yields also the maximal value of the smallest open-loop gain. Therefore the controller gains are selected so that

$$K_{P1}K_{v1} = K_{P2}K_{v2} = \dots = K_{Pn}K_{vn} \hat{=} K \quad (6)$$

where K_{P_i} are the gains of the P-controllers, i.e. the diagonal elements of \mathbf{K}_P , and K_{v_i} is velocity gain of the i th cylinder-valve combination. The critical open-loop gain, K_{cr} , is defined as the greatest value of K such that the system remains stable.

According to Section 3.3, the tuning should be such that the robustness criterion of Eq. 3 is satisfied with all load masses and all orientations of the manipulator. In practice, it is impossible to verify the criterion at all operation points. Here it is assumed that the most critical situation occurs with maximum load mass at the orientation in which the critical open-loop gain of the system is smallest. To summarise, following tuning rule is suggested for the P-control:

- 1 Select a nominal diagonal gain matrix \mathbf{K}_{PN} that satisfies Eq. 6.
- 2 Calculate the scalar ζ with the maximum load and all orientations such that the tuning $\mathbf{K}_P = \zeta \times \mathbf{K}_{PN}$ is marginally stable. Find the critical orientation where ζ is smallest.
- 3 At the critical orientation, adjust ζ such that the robustness criterion of Eq. 3 is satisfied.

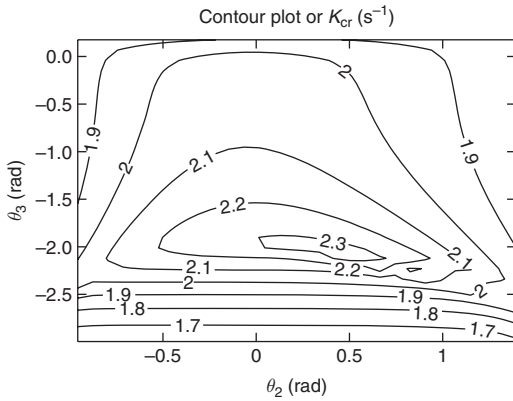


Figure 6. Critical open-loop gain of the linearised model of the example manipulator with P-control and load mass 400 kg

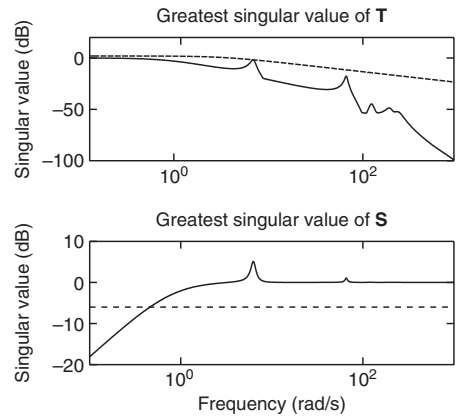


Figure 7. Singular value plot of the linearised model with P-control and load mass 400 kg. The open-loop gain is $K = 0.8 \text{ s}^{-1}$.

Figure 6 shows the calculated critical open-loop gain of the example manipulator with the maximum load mass 400 kg. It is seen that the gain is almost constant and not proportional to the lowest natural frequency (Fig. 4). The low value predicts also a sluggish response. The smallest critical open-loop gain occurs when the angle between links 2 and 3 has the smallest possible value. This area is not used in normal operation and the operation point $\theta_2 = 1.35$ rad and $\theta_3 = 0.15$ rad is selected as the most critical orientation. The critical open-loop gain at this orientation is 1.83 s^{-1} and the robustness criterion is satisfied with $K = 0.80 \text{ s}^{-1}$. The tuning is not conservative, because the gain is 43 percent of the critical gain. Figure 7 shows the singular value plot for this tuning. The inverse of $\sigma_1(\Delta_M)$ is shown by a broken line in the same plot as $\sigma_1(\mathbf{T})$ and the bandwidth limit is shown by a broken line in the same plot as $\sigma_1(\mathbf{S})$.

5 FILTERED P-CONTROL

The transfer function matrix of this filtered P-controller is

$$\mathbf{K}_{PF}(s) = \text{diag} \left(\frac{K_{P1}}{\tau_1 s + 1}, \dots, \frac{K_{Pn}}{\tau_n s + 1} \right) \quad (7)$$

where again a diagonal controller structure is used. It is seen that there are two tuning parameters for each actuator: the gain and time constant. Again it is advantageous to use same parameter values for each actuator. From this there are only two tuning parameters for the entire manipulator: the open-loop gain K and the time constant τ .

The principal idea of the filtering is to “let sleeping dogs to sleep”, i.e. not to excite vibration modes of the system. Therefore the time constant τ should be greater than $1/\omega_{1,\min}$. As a limit case, if the time constant is very large, the open-loop transfer function matrix becomes

$$\mathbf{G}(s) \mathbf{K}_{PF}(s) \approx K \text{diag} \left(\frac{1}{s(\tau s + 1)}, \dots, \frac{1}{s(\tau s + 1)} \right) \quad (8)$$

The unity feedback around $\mathbf{G}(s) \mathbf{K}_{PF}(s)$ yields separated second order transfer functions with a natural frequency and damping factor

$$\omega_{PF} = \sqrt{K/\tau} \quad , \quad \xi_{PF} = 1/(2\sqrt{K\tau}) \quad (9)$$

These equations give the relation between the dominant dynamics of the closed-loop system and the controller parameters. Solving K from the equation of the damping factor gives

$$K = 1/(4\xi_{PF}^2 \tau) \quad (10)$$

It is seen that τ should be as small as possible in order to achieve fast response and good damping. On the other hand, Eq. 8 is valid only if τ is remarkably greater than $1/\omega_{1,\min}$ and a good compromise for τ is $(1.5 \dots 3)/\omega_{1,\min}$. Figure 8 shows the calculated critical open-loop gain of the example manipulator with filtered P-control and maximum load mass 400 kg. The parameter τ is 0.34 s which refers to $2/\omega_{1,\min}$. When compared to Fig. 4, the critical gain is almost proportional to the lowest natural frequency, implying that the tuning can be done at the point where the lowest natural frequency is at its minimum. The critical open-loop gain is also much higher than with P-control (Fig. 6).

The tuning rule for the filtered P-control can be stated as follows:

- 1 Calculate $\omega_{1,\min}$ using the maximum load mass. Select $\tau = 2/\omega_{1,\min}$ as an initial value.
- 2 Select a suitable damping factor ξ_{PF} from the range 0.55 to 0.9 for the dominant dynamics of the closed-loop system and calculate K from Eq. 10.
- 3 Calculate controller gains from Eq. 6 and verify if the robustness criterion of Eq. 3 is satisfied at the orientation where ω_1 has a minimum value.
- 4 If the robustness criterion of Eq. 3 is not satisfied, increase τ , otherwise decrease it.
- 5 Repeat steps 2 to 4 until the smallest τ that satisfies the robustness criterion is found.

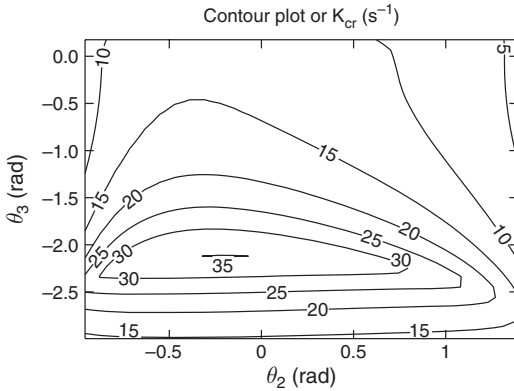


Figure 8. Critical open-loop gain of the linearised model of the example manipulator with filtered P-control and load mass 400 kg. The time constant of the controller is 0.34 s.

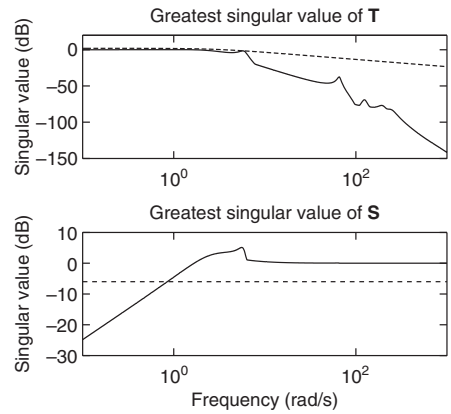


Figure 9. Singular value plot of the linearised model with filtered P-control and load mass 400 kg. The controller parameters are $K = 1.75 \text{ s}^{-1}$, $\tau = 0.29 \text{ s}$.

In the example manipulator, $\omega_{1,\min}$ occurs at the operation point $\theta_2 = 1.35 \text{ rad}$ and $\theta_3 = 0.15 \text{ rad}$, and the critical open-loop gain is 4.6 s^{-1} at this point. If the damping factor ξ_{PF} is selected to be 0.7, the above tuning rule gives $\tau = 0.29 \text{ s}$, which in turn gives $K = 1.75 \text{ s}^{-1}$ and $\omega_{PF} = 2.5 \text{ rad/s}$. The open-loop gain is almost as large as the critical open-loop gain with P-control and the closed-loop natural frequency ω_{PF} is 42 percent of $\omega_{1,\min}$. Figure 9 shows the singular value plot for this tuning. It is seen that $\sigma_1(\mathbf{S})$ is smaller in the low-

frequency range and $\sigma_1(\mathbf{T})$ is smaller in the high-frequency range than with P-controller indicating improved bandwidth and immunity for sensor noise.

6 CONTROL RESULTS

This section analyses the control performance of the example manipulator with P-control and filtered P-control. The non-linear simulation model is used with stepwise references as test signals. The controllers are implemented in the simulation model in discrete time using Tustin's approximation with 50 ms sampling time.

Figure 10 shows simulated step responses of cylinders with P-control near the most critical orientation $\theta_2 = 1.35$ rad and $\theta_3 = 0.15$ rad. It is seen that the responses are slow but there are large amplitude vibrations in the cylinder forces. Figure 11 shows the same step response with filtered P-control. The responses are much faster and force vibrations are more damped. The cost of improved speed is seen in the force response of the cylinder 1, where the amplitude has increased. The force peak can be reduced by smoothing reference signals. The force peak decreases also rapidly when the orientation of the manipulator deviates from the most critical orientation.

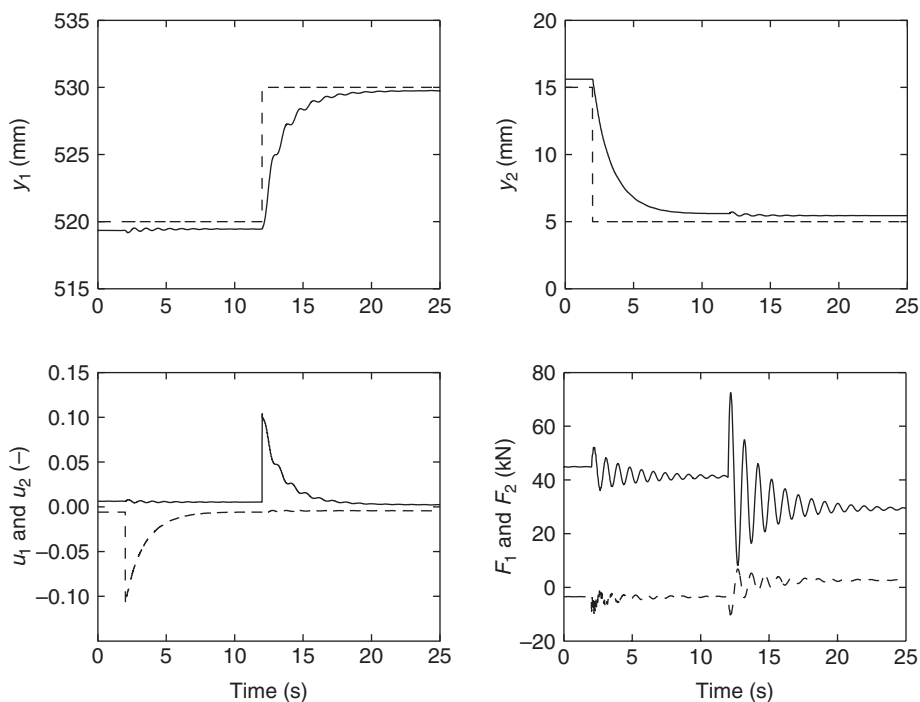


Figure 10. Simulated small step responses with P-control and load mass 400 kg. The open-loop gain is $K = 0.8 \text{ s}^{-1}$ and the final orientation is $\theta_2 = 1.35$ rad, $\theta_3 = 0.15$ rad.

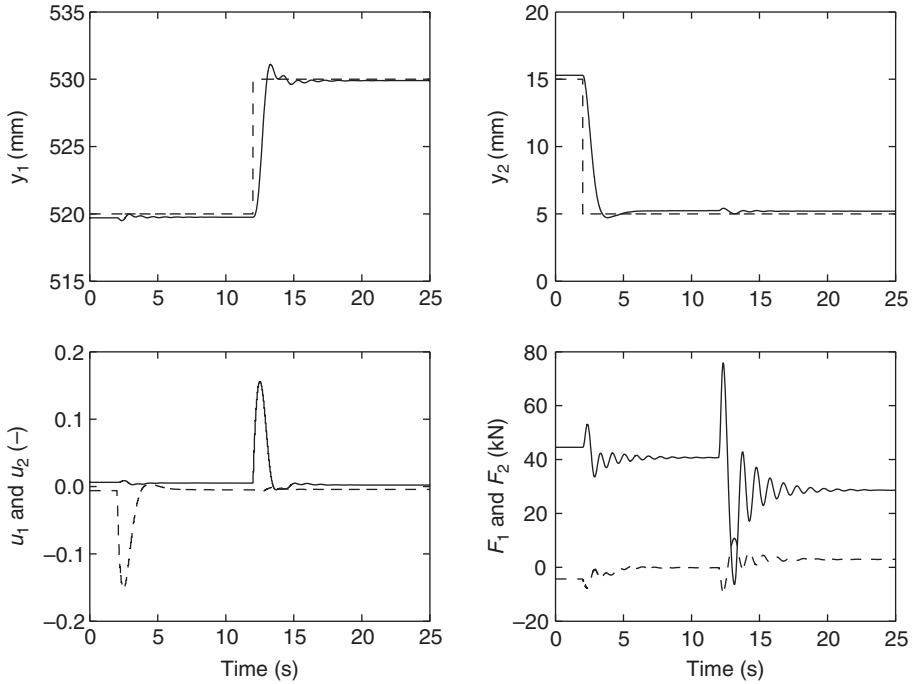


Figure 11. Simulated small step responses with filtered P-control and load mass 400 kg. The controller parameters are $K = 1.75 \text{ s}^{-1}$, $\tau = 0.29 \text{ s}$ and the final orientation is $\theta_2 = 1.35 \text{ rad}$, $\theta_3 = 0.15 \text{ rad}$.

Table 1 compares the control performance with P-control and filtered P-control. The bandwidth is determined according to Eq. 2. In the determination of rise and settling times, simulated responses are shifted so that steady-state errors are zero. The rise time from zero to 90 percent and the settling time of ± 2 percent are used. The table shows that the filtered P-controller gives much faster response and smaller error. Figures 7 and 9 show also that the filtered P-controller is more robust against high frequency modelling errors and sensor noise. However, P-controller is more robust against modelling errors in the frequency range below the first natural frequency.

Table 1. Achieved control performance with P-control and filtered P-control.

	P-control	Filtered P-control
Open-loop gain $K \text{ (s}^{-1}\text{)}$	0.8	1.75
Bandwidth $\omega_B \text{ (rad/s)}$	0.46	0.85
Rise time, cylinder 1 (s)	3.5	0.9
Rise time, cylinder 2 (s)	3.2	1.1
Settling time, cylinder 1 (s)	6.4	3.0
Settling time, cylinder 2 (s)	5.4	3.0
Steady-state error, cylinder 1 (mm)	0.23	0.10
Steady-state error, cylinder 2 (mm)	0.45	0.20

7 CONCLUSIONS

The main conclusion is that a fixed-parameter, low-order and linear controller can deliver satisfactory control performance over the whole operation range despite complicated multivariable dynamics and strong non-linearity of hydraulic manipulators. The achieved closed-loop natural frequency is 42 percent of the lowest natural frequency of the system and this performance combined with easy tuning, robustness and requirement for piston position measurement only, makes the filtered P-controller practical control solution for hydraulic manipulators. It is also important to note that no high-bandwidth valves or high-quality sensors are needed and so the cost increase due to closed-loop control is minimal. On the other hand, results show that normal P-controller cannot be recommended for hydraulic manipulators.

The results have been obtained by simulations and despite of careful verification of the model, it is important to test the proposed controller with a real machine. Initial laboratory tests with a smaller scale manipulator have shown expected performance but real manipulators have several additional uncertainties, such as counterbalance valves, temperature variations as well as load and vehicle dynamics, which are difficult to arrange in laboratory. Therefore, the field tests are the next step of the research.

ACKNOWLEDGEMENT

The research was supported by the Foundation of Technology in Finland.

REFERENCES

- 1 Linjama, M., and Virvalo, T., 1999, "Analysis of Multi-Input Multi-Output Nature of Hydraulic Cranes," *Power Transmission and Motion Control, PTMC 99*, C.R. Burrows, and K.A. Edge, eds., Professional Engineering Publishing Ltd., London and Bury St Edmunds, pp. 15–29.
- 2 Krus, P., and Gunnarsson, S., 1993, "Adaptive Control of a Hydraulic Crane Using On-line Identification," *Proceedings of the Third Scandinavian International Conference on Fluid Power*, J.-O. Palmberg, ed., Linköping University, Linköping, Sweden, **2**, pp. 363–388.
- 3 Sepehri, N., Dumont, G.A.M., Lawrence, P.D., and Sassani, F., 1990, "Cascade Control of Hydraulically Actuated Manipulators," *Robotica*, **8**, pp. 207–216.
- 4 Mattila, J., and Virvalo, T., 1997, "Computed force control of hydraulic manipulators," *Proceedings of the Fifth Scandinavian International Conference on Fluid Power*, J.-O. Palmberg, ed., Linköping University Linköping, Sweden, **1**, pp. 139–154.
- 5 Chiang, R.Y., and Safonov, M.G., 1992, *Robust control toolbox user's guide*, The MathWorks, Inc., Natick, MA.
- 6 Linjama, M., and Virvalo, T., 2001, "Robustness of Some Low-Order Controller in an Electrohydraulic Position Servo Drive," *Power Transmission and Motion Control, PTMC 2001*, C.R. Burrows, and K.A. Edge, eds., Professional Engineering Publishing Ltd., London and Bury St Edmunds, pp. 309–323

- 7 Linjama, M., and Virvalo, T., 1999, "Low-Order Dynamic Model for Flexible Hydraulic Cranes," *Proceedings of the Institution of Mechanical Engineers, Part I*, **213** (I1), pp. 11–22.
- 8 Linjama, M., and Virvalo, T., 1999, "State-Space Model for Control Design of Multi-Link Flexible Hydraulic Cranes," *Proceedings of the Sixth Scandinavian International Conference on Fluid Power*, K.T. Koskinen, M. Vilenius, and K. Tikka, eds., Tampere University of Technology (TUT) Print, Tampere, Finland, **2**, pp. 981–998.
- 9 Green M., and Limebeer, D.J.N., 1995, *Linear robust control*, Prentice Hall, Englewood Cliffs, NJ.

Hybrid control with on/off electropneumatic standard valve for tracking positioning.

Xavier LEGRAND*, Jean-Marie RETIF**, Mohamed SMAOUI*, Xavier BRUN*, Daniel THOMASSET*, Xue-Fang LIN SHI**

*Laboratoire d'Automatique Industrielle, INSA Lyon, Bâtiment Saint Exupéry, 25 Avenue Jean Capelle, 69621 Villeurbanne Cedex, France, <http://www-lai.insa-lyon.fr>
Email contact: xavier.brun@insa-lyon.fr

**Centre Génie Electrique de Lyon, INSA Lyon, Bâtiment Léonard de Vinci, 21 Avenue Jean Capelle, 69621 Villeurbanne Cedex, France, <http://cegely.cnrs.fr/>

ABSTRACT

This paper presents a new method of control applied in electropneumatic field. This strategy is issued from hybrid control theory recently applied in control of asynchronous or synchronous electrical motor (1, 2). The interest of these procedure concerns the possibility of controls the position of an electropneumatic piston all along the cylinder stroke with standard on/off valve. Nowadays the industrial electropneumatic process used on/off valve for point to point aim with displacement from one extremity of cylinder to the other one. When different desired positions are required the constructors used specific components issued from proportional technology: servovalve or servodistributor for example. The evolution in the automation process is moving towards a need of obtaining greater versatility and increased precision in compressed air driven equipment. This means obtaining proportional operation of the power element as a function of an electric control signal. Nevertheless, when the desired precision is near the millimetre and not very good performances are need during dynamic stage, the useful of proportional technology can be debatable. Indeed the system cost and its complexity to tune can be two drawbacks that on/off technology with the proposed algorithm, can be concurrence.

Based on both the models of cylinder and valves, the hybrid control presented here determines the best state of valves by tracking reference values of the cylinder states in the state space. Then a simplified model of electropneumatic system is presented and used to synthesised hybrid control algorithm. Experimental results are presented and discussed.

Keywords: Hybrid Control, standard valve, electropneumatic, experimental results.

NOMENCLATURE

		x	state vector
		y	position (m)
b	viscous coefficient (N/m/s)	ΔT	sample time
F	force (N)		
k	polytropic constant		<i>Subscripts and superscripts</i>
M	moving load (kg)	d	desired

p	pressure (Pa)	e	equilibrium
q_m	mass flow rate (kg/s)	ext	external
r	perfect gas constant (J/kg/K)	E	exhaust
S	area of the piston cylinder (m ²)	N	chamber N
t	time (s)	P	chamber P
T	temperature (K)	PNEU	pneumatic
U	valve input voltage (V)	S	supply
v	velocity (m/s)	t0	time value at each sample time
V	volume (m ³)		

1 INTRODUCTION

At the present time, the majority of the pneumatic cylinders controlled in position use servodistributors to control the mass flow rates delivered into the cylinder chambers in spite of the fact that distributors are less expensive than standard valve. The first control laws applied in Fluid Power concerned classical state feedback and were proposed by Shearer et al (3) and Burrows (4). The manufacturers of the first electropneumatic positioning systems such as Martonair (5) and GAS initially adopted it. Since then new sophisticated algorithms have been applied to electropneumatic systems: adaptive (6, 7), sliding mode control (8, 9, 10, 11), H_∞ (12), fuzzy control (13), neural control (14), flatness (15), backstepping (16)... All of them lead to more or less good results in position tracking but none of them is applicable to systems with on/off electropneumatic valves. The aim of this paper is to offer a cheaper alternative to classic pneumatic systems controlled in position which need a static precision around millimetre but for whose the position tracking error can be high in dynamic. The control must also lead to weak overshoot (around five percent of the total increase) and have few oscillations.

Using on/off electropneumatic valves for tracking positioning leads to a system with a discrete control and a continuous process: the on/off valves can take two or three discrete states even though the state variables of the cylinder are continuous. Such systems, which combine a discrete control and a continuous process, are called in this paper 'hybrid systems' and take many shapes.

Hybrid control is an efficient approach to control this kind of systems. For example, in electrical engineering, hybrid control has been developed to control electrical synchronous and asynchronous machines (1,2). In this case, synchronous and asynchronous machines modelled by continuous state equations are controlled by inverters, which can take eight discrete states. This approach can be expanded to a lot of hybrid systems.

The idea of the hybrid control is to choose at each sample time the best state of the discrete control to follow several variables of interest. Using a control model of the system, the algorithm must calculate, for each possible state of the control, the values of the variables of interest at the next sample time. Then the control state that leads to follow quickly the variables of interest will be chosen. This control state will be applied during one sample time.

In the case of an on/off electropneumatic standard valve for tracking positioning, the variables of interest are p_N and p_P . Indeed the control of the two pressures means the control of pneumatic force. Once the pneumatic force is controlled, a speed feedback and a position feedback will permit to obtain good performances in term of position tracking.

The study began with the system modelling: a control model will be defined from the knowledge model. The approximations used to define this model concern the sample time and the variables of interest chosen. Notice that the problem is very different from the electrical machine control due to a great difference of the time constants, which is equal to few microseconds in electrical field and equal to few milliseconds in pneumatic area. In next section the control algorithm will be developed. Finally, two series of experimental tests will be presented and analysed.

2 FROM KNOWLEDGE MODEL TO CONTROL MODEL

2.1 Knowledge model

The studied process is an in-line electropneumatic servodrive using a simple rod double acting linear pneumatic cylinder (Fig. 1). Two 3/3 standard valves delivered the mass flow rates into the cylinder chambers. The rod of the actuator is connected to one side of a carriage. The aim is to control its position.

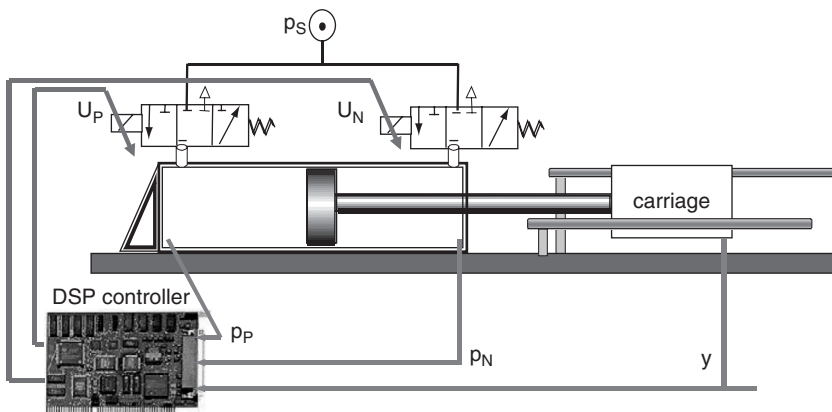


Figure 1: Electropneumatic system

Following classical assumptions (3), the model can be described by equation (1), in which:

- the dynamics of the valves are neglected,
- the evolutions in each cylinder chamber are supposed to be polytropic,
- the temperature variation in each chamber is neglected,
- the dry frictions are neglected,

$$\left. \begin{aligned} & \left. \begin{aligned} \frac{dp_P}{dt} & \frac{krT}{V_P(y)} \left[q_{mP}(U_P, p_P) - \frac{S_P}{rT} p_P v \right] \\ \frac{dp_N}{dt} & \frac{krT}{V_N(y)} \left[q_{mN}(U_N, p_N) - \frac{S_N}{rT} p_N v \right] \end{aligned} \right\} \text{pneumatic part} \\ & \left. \begin{aligned} \frac{dv}{dt} & \frac{1}{M} [S_P p_P - S_N p_N - f_v v - F_{ext}] \\ \frac{dy}{dt} & v \end{aligned} \right\} \text{mechanical part} \end{aligned} \right\} \quad (1)$$

The valve input can take three discrete values: -10V (exhaust pressure); 0V (closed); 10V (input pressure). For energetic reasons, the two input voltages are never set to +10V simultaneously. So eight combinations of control values will be considered:

control index	c1	c2	c3	c4	c5	c6	c7	c8
U_P	+10V	-10V	-10V	+10V	0V	-10V	0V	0V
U_N	-10V	+10V	-10V	0V	+10V	0V	-10V	0V

Table 1: Eight discrete possible states of control

To obtain position equilibrium, the valves need to be closed: $U_P^e = U_N^e = 0$. Indeed if a chamber is connected to the supply or exhaust pressure, the pneumatic force F_{PNEU} defined by equation (2) leads to a displacement to an extremity of the cylinder stroke.

$$F_{PNEU} = S_P p_P - S_N p_N \quad (2)$$

Considering these remarks and relation (1), the set equilibrium imposed relation (3) and so (p_P^e, p_N^e) is imposed by valves but not by cylinder. This result is right exclusively if the pneumatic force is equal to external force (see relation (1) with null equilibrium velocity). This condition is less restrictive if dry friction force is considered, and in a lot of experimental case, this condition is respected.

$$q_{mP}(U_P^e, p_P^e) = q_{mN}(U_N^e, p_N^e) = 0 \quad (3)$$

2.2 Model simplification

Dynamic of mechanical variables (position and velocity) is slower a lot than dynamic of pneumatic variables (the two pressures). Then, in pneumatic equations, position and velocity can be considered constant during a sample time ΔT chosen small enough compared to mechanical time constant:

$$\left\{ \begin{array}{l} \frac{dp_P}{dt} = \frac{krT}{V_P(y_{t0})} \left[q_{mP}(U_P, p_P) - \frac{S_P}{rT} p_P v_{t0} \right] \\ \frac{dp_N}{dt} = \frac{krT}{V_N(y_{t0})} \left[q_{mN}(U_N, p_N) + \frac{S_N}{rT} p_N v_{t0} \right] \end{array} \right\} \text{Pneumatic part} \quad (4)$$

Simulations show that the evolution of the nonlinear system (equation (1)) in the plane (p_P, p_N) is linear all over the physical domain ($1 \text{ bar} < P < 7 \text{ bar}$) excepted when the piston is initially near an extremity. In the following results, the initial position of the piston is considered near of the central position.

The linearity of the evolution of the system in the plane (p_P, p_N) involves that for each initial position in (p_P, p_N) , it is possible to calculate the eight reachable points in (p_P, p_N) corresponding to the eight control values. Indeed considering the evolution of the pressure in a chamber during ΔT as linear and knowing the state of the system at time t_0 , the pressures values can be determined at time $t_0 + \Delta T$ as given by equation (5) where the continuous model is transform in a discrete one.

$$\left\{ \begin{array}{l} p_P(k+1) = \left[\frac{d}{dt}(p_P(t)) \Big|_{t=t_0} \right] \times \Delta T + p_P(k) \\ p_N(k+1) = \left[\frac{d}{dt}(p_N(t)) \Big|_{t=t_0} \right] \times \Delta T + p_N(k) \end{array} \right. \quad (5)$$

In these expressions $\left[\frac{d}{dt}(p_P(t)) \right]_{t=t_0}$ is a function of p_P, y, v and U_P , and $\left[\frac{d}{dt}(p_N(t)) \right]_{t=t_0}$ is a function of p_N, y, v and U_N . At each sample step p_N, p_P, y are measured, v is estimate by numerical derivation so for each one of eight couples $(U_P, U_N), (p_P(k+1), p_N(k+1))$ can be calculated.

The choice of the sample time ΔT has been made by many simulations using the nonlinear model (mentioned in equation (1)). For each one of eight control values and for different simple times and different initial condition values of the system, the results show that:

- for a simple time greater than 100 milliseconds, pneumatic variables saturate before the end of the simulation.
- for a simple time lower than 10 milliseconds, the nonlinear model is not true because the dynamic of valve is not negligible anymore.

So the sample time has been chosen equal to $\Delta T = 10$ ms.

Figure 2 presents the evolution of the nonlinear system during ten milliseconds for the eight control values in (p_P, p_N) plane and the eight points determined with the discrete linear model. These figure has been studied for different initial positions in (p_P, p_N) plane all over the physical domain. The conclusion is that the discrete time linear model is very good in direction and good in amplitude.

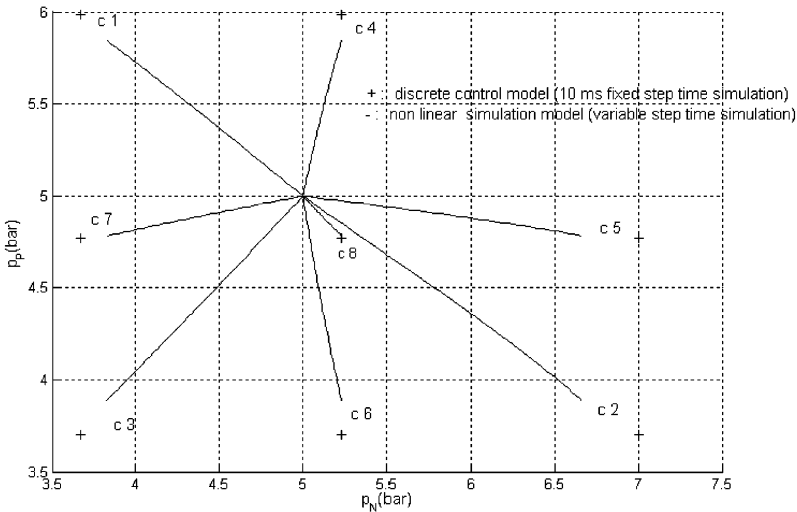


Figure 2: Validation of linear discrete time model used for control synthesis

3 CONTROL SYNTHESIS

3.1 Hybrid force control

As underlined previously, it is possible to control position if the pneumatic force tracking is correct, adding for example a speed control feedback and a position control feedback. The mechanical equations show that pneumatic force can be following by controlling pressures p_P and p_N . So a desired force generated by the position loop can be translated in a target point in (p_P, p_N) . The hybrid control algorithm consists of choosing the best state for each valve at each sample time in order to reach a target point in (p_P, p_N) .

The target will be fixed at each sample time in view of these two constraints:

- it must corresponds to the desired pneumatic force, so to respect equation (2) it must belong to the line of equation (6) with constant pneumatic force:

$$p_P = \frac{S_N}{S_P} p_N + \frac{F_{PNEU}}{S_P} \quad (6)$$

- it must be as near as possible of the partial pneumatic equilibrium set (p_P^e, p_N^e) in order to reach the equilibrium set in static stage. This constraint is not necessary in dynamic stage and could be harmful to dynamic performances, but as explain in introduction the most important aim concerns static performances.

The target in (p_P, p_N) plane is calculated each sample time to be the nearest point of (p_P^e, p_N^e) belonging on the line of equation (6) (see bold line in figures 4 and 5) and inside the physical domain (see rectangle in figures 3 and 4).

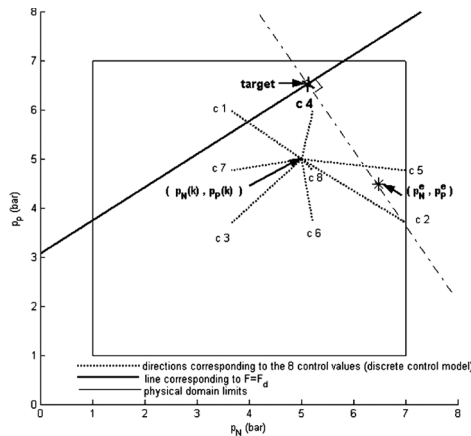


Figure 3: target in (p_P, p_N) plane when $F_d = 100$ N

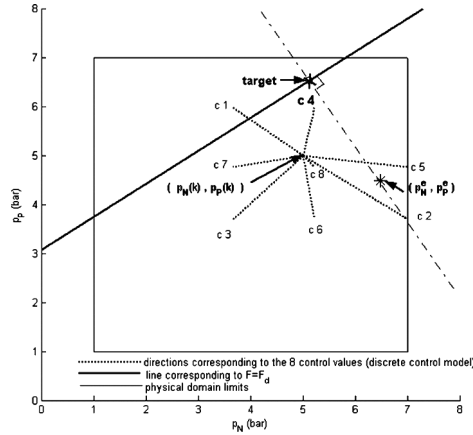


Figure 4: target in (p_P, p_N) plane when $F_d = 350$ N

For each sample time, the algorithm:

- calculate the eight reachable points in (p_N, p_P) plane corresponding to the eight control values thanks to the discrete model (5),
- calculate the target point corresponding to the desired force,
- calculate the Euclidean distance between the eight reachable points and the target point,
- choose the control that leads to the fewest Euclidean distance. For examples control c4 in figure 3 and control c1 in figure 4.

The chosen control is then applied during ten milliseconds. Thanks to this algorithm, good performances of the force tracking have been obtained.

3.2 Position control

The figure 5 presents the general structure for position control.

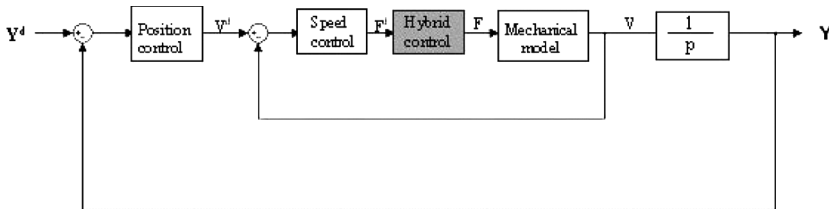


Figure 5: General structure for position control

To simplify the determination of the position and speed controllers, the force response will be considered as perfect so in the following:

$$\frac{F}{F_d} = 1 \tag{7}$$

The figure 6 presents the discrete time position control scheme.

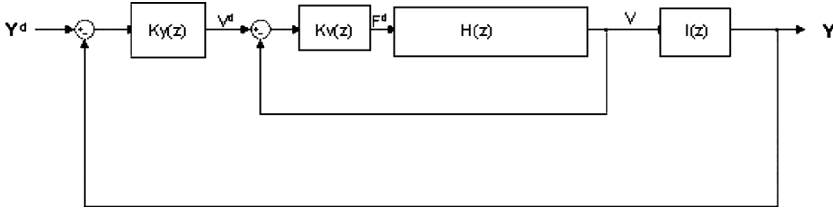


Figure 6: Discrete time position control scheme

A classical approach (18) permits to determine $K_v(z)$ and $K_y(z)$ by chosen the closed-loop dynamic behaviour in speed and position as an equivalent classic second order filter response:

$$\frac{V(p)}{V_d(p)} = \frac{1}{1 + 2\frac{\xi_v}{\omega_v}p + \frac{1}{(\omega_v)^2}p^2} \quad \text{and} \quad \frac{Y(p)}{Y_d(p)} = \frac{1}{1 + 2\frac{\xi_y}{\omega_y}p + \frac{1}{(\omega_y)^2}p^2}$$

In the following experimentation, $\omega_v = 30$ rad/s, $\xi_v = 0.9$, $\omega_y = 10$ rad/s, $\xi_y = 0.9$.

4 EXPERIMENTAL RESULTS

The following results give an illustration of the overall control performance. The test bench is presented in figure 1. In this case, the two valves are two servodistributors for which the input voltage take discrete values $-10V$, $+0V$ or $+10V$ (see table 1). The exhaust pressure value (1 bar) and the supply pressure (7 bar) limit the pressures. The dry friction force induces $p_P^e = 4.49$ bar and $p_N^e = 6.49$ bar.

The desired trajectory has been synthesised to reduce the energy consumption (17) on the same test bench so as it is easy to compare the results with those other control algorithm using control values included between plus or minus ten volt (11, 15, 17).

Two experimental results are shown:

- in the first case (figure 7), the position loop is closed all time and the hybrid algorithm works even in steady state: the aim is to minimise the steady state position error.
- in the second case (figure 8) when the absolute value of position error is less than three millimetres the position loop is open and the control is fixed to c8 (both servovalves closed): the aim is to minimise valves switching occurrences during steady state.

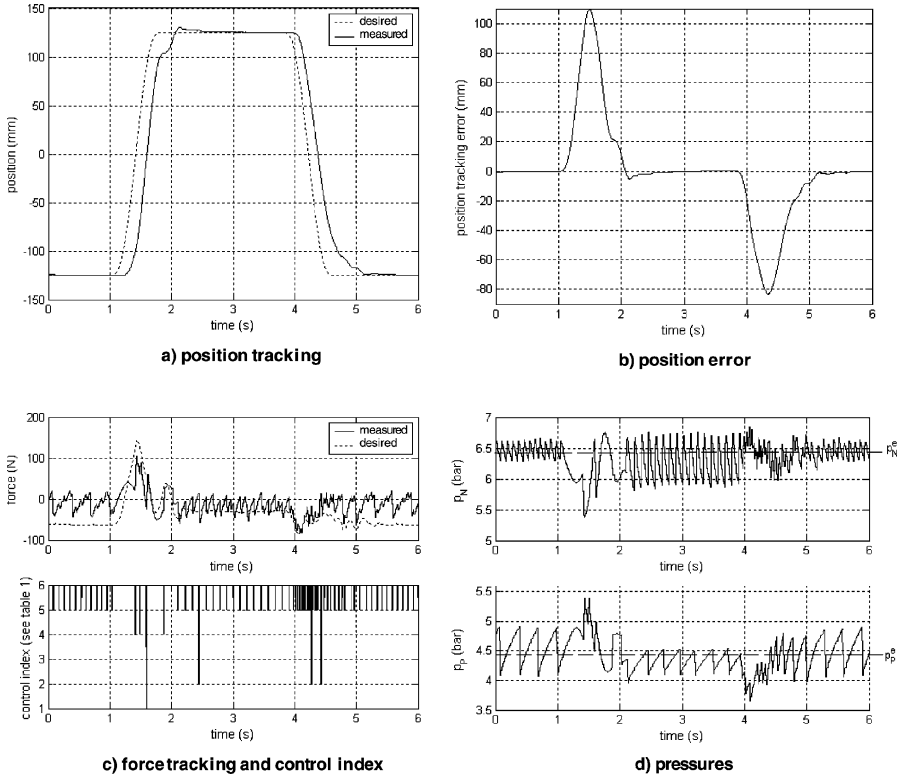


Figure 7: First case of experimental results

In these two cases, the desired position is followed with a tracking error near to 100 millimetres in dynamic stage. The pneumatic force tracking is good, excepted in steady state for second case (see figure 8c) because in steady state the hybrid algorithm is not used.

In the first case the position error in steady state is less than 0.8 millimetres, the input voltage U_P switches 47 times and the input voltage U_N switches 90 times during six seconds. In the second case, the position error in steady state can reach 2 millimetres but input valve voltages switching is limited: 31 switching for U_P and 32 for U_N .

If the application needs a great precision in position tracking, the first case will be chosen whereas the second case is less precise but the valves are less excited and so the energy consumption decreases.

Notice that the figures show two of the many tests that have been done. But we remark generally a good repeatability of experimental results when the correctors are good tuned.

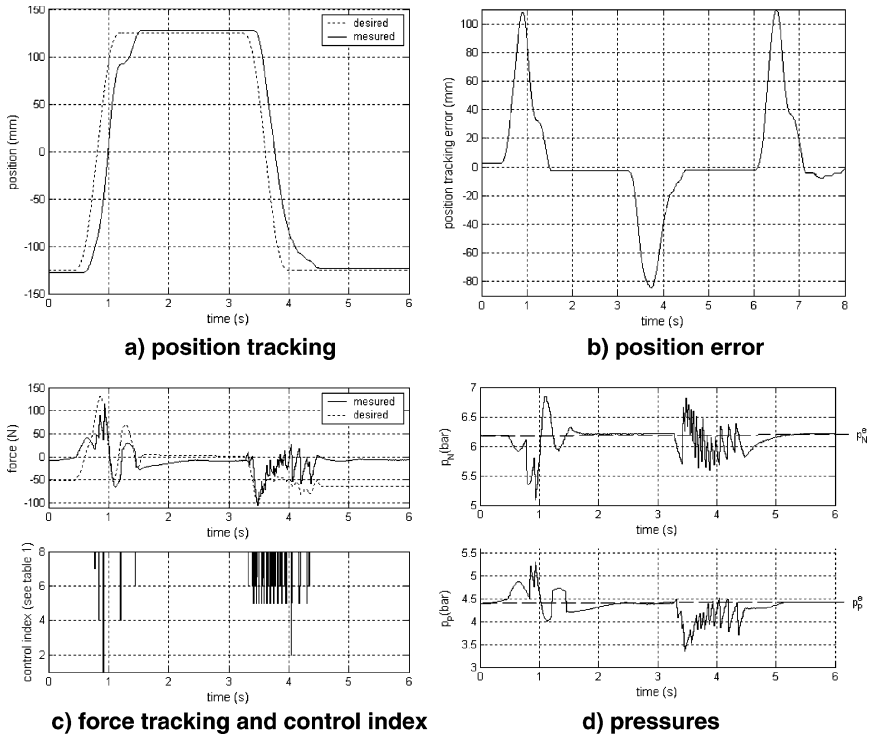


Figure 8: Second case of experimental results

5 CONCLUSION

Firstly, the first contribution of this paper concerns the transfer of the hybrid method developed for control electrical engines (1, 2) to a system composed by a pneumatic cylinder and two on/off valves. Notice that the on/off property of the valves is interesting because on/off valves are less expensive than servo valves used in classical approaches. The algorithm built with the hybrid approach, which uses a very simple control model, allows the tracking of the pneumatic force. Secondly, a speed feedback and a position feedback have been designed to control the position. Finally, the experimental tests lead to encouraging results to continue to explore this new strategy. The tuning of the correctors permits to fit the method to many applications for which the position tracking precision is less than one millimetre and the dynamic behaviour is not critical. If the precision in position tracking is less restrictive, a threshold for position tracking error under which the valves will be closed can permit to limit valve switching.

The main problem with this approach due to important number of the switching control is the valve life. Today the first results permit to solve this problem in steady state, it will be interesting to test specific hybrid control algorithm issued from electrical motor control (19) to increase dynamic performances. Future works will focus also on a more complex design of position and velocity controllers.

REFERENCES

- 1 **RETIF, J.M., LIN SHI, X.F., LLOR, A., ARNALTE, S.,** *New control for a synchronous machine, the hybrid control*, EPE-11th International Power Electronics and Motion Control Conference, 2004.
- 2 **RETIF, J.M., LIN SHI, X.F., LLOR, A.,** *A new hybrid direct-torque control for a winding rotor synchronous machine*, PESC'2004: 35th IEEE Power Electronics Specialists Conference, 2004.
- 3 **SHEARER, J.L.,** *Study of pneumatic processes in the continuous control of motion with compressed air*. Parts I and II. Trans. Am. Soc. Mech. Eng. 1956, Vol. 78, p. 233-249.
- 4 **BURROWS, C.R.** *Fluid Power Servomechanisms*. London: Van Nostrand Reinhold Company, 1972. 237 p.
- 5 **MORGAN, G., HÜBL, W.,** *Positionieren mit kleinrechnern von Pneumatikzylindern*. In: 6th Aachener fluid technisches kolloquium, Aachen, 1984, p. 121-157.
- 6 **EDGE, K.A, FIGEREDO, K.R.A.,** *An adaptively controlled electrohydraulic servomechanism: Part 1: Adaptive controller design - Part 2: Implementation*. In: Proc. Instn. Mech. Engrs. Part B, 1987, Vol 201, N°3n p 175-180 and p. 181-189.
- 7 **NORISTUGU, T., WADA, T., YANOSAKA, M.,** *Adaptive control of electropneumatic servo system*. In: 2nd Int. Symp. On Fluid -Control, Measurement, Mechanics and flow visualisation. Sheffield, England, 1988, p. 285-289.
- 8 **VAUGHAN, N. D., GAMBLE, J. B.,** *Sliding mode control of a proportional solenoid valve*. Fluidpower Systems Modelling and Control. Burrows C. R. and Edge K. A. Eds. Taunton : Research Studies Press, 1992, p. 95-107.
- 9 **BOURI, M., THOMASSET, D., SCAVARDA, S.,** *Integral sliding mode controller of a rotational servodrive*. Third Japan Hydraulics and Pneumatics Society, Tokyo, November 1996. p 145-150.
- 10 **SURGENOR, B.W., VAUGHAN N.D., UEBING, M.,** *Continuous sliding mode control of a pneumatic positioning system*. 8th Bath Int. Fluidpower Workshop, UK., Sept. 1995.
- 11 **LAGROUCHE, S., SMAOUI, M., BRUN, X. PLESTAN, F.,** *Robust second order sliding mode controller for electropneumatic actuator*, American Control Conferences, Boston, USA, June 30–July 2nd 2004, p 5090-5095.
- 12 **PICHE, R., POHJOLAINEN, S., VIRVALO, T.,** *Design of robust controllers for position servos using H-infinity theory*. Proc. Instn Mech Engrs, Part I, 1991, 205(14), p. 299-306.
- 13 **KLEIN, A. BACK, W.,** *An intelligent optimisation of a state loop controller with fuzzy-set-logic*. In Circuit Component and System Design, Proceedings of Fifth Bath International Fluid Power Workshop (Eds Burrows and Edge), 1995, pp 381-399.
- 14 **LIU, P., DRANSFIELD, P.,** *Intelligent control of air servodrives using neural networks*. Proc. of Second Japan Hydraulics and Pneumatics Society, Tokyo, 1993, p. 381-399.
- 15 **BRUN, X. THOMASSET, D., BIDEAUX, E.** *Influence of the process design on the control strategy: application in electropneumatic field*, Control Engineering Practice, Volume 10, Issue 7, July 2002, Pages 727-735.

- 16 **SMAOUI, M., BRUN, X. THOMASSET, D.,** *A robust multivariable control for an electropneumatic system using backstepping design*, Symposium on Nonlinear Control Systems, NOLCOS 6th IFAC symposium, Stuttgart, 1-3 September 2004
- 17 **BRUN, X. THOMASSET, D., SESMAT, S., SCAVARDA, S.** *Limited energy consumption in positioning control of electropneumatic actuator*, Power Transmission & Motion Control, Bath, UK, Sept. 1999, pp 199-211.
- 18 **DOYLE, J.C, FRANCIS, B.A, TANNENBAUM, A.R,** *Feedback control theory*, Ed. Maxwell Macmillan International Editions, 1992, 227 p.
- 19 **MOREL, F., RETIF, J.M., LIN SHI, X.F., LLOR, A.,** Fixed switching frequency hybrid control for a permanent *synchronous machine*, IEEE International Conference on Industrial Technology (ICIT'04), Tunisia, 8-10 December 2004.

COMPARING DIFFERENT CONTROL STRATEGIES OF TIMBER SAWING PROCESS

Tapio Virvalo* and Juha Inberg**

*Institute of Hydraulics and Automation, Tampere University of Technology, Finland

**Ponsse Oyj, 74200 Vieremä, Finland

ABSTRACT

In timber cutting applications (harvester head) a hydraulic motor drives a saw chain and the feed force to a saw bar is generated by a hydraulic cylinder. Sawing conditions vary very much due to different environment conditions as well as quality and diameters of timbers. This study is based on simulation with a well verified model. Compared control strategies are: open loop control, torque control of the saw motor, speed control of the saw motor and a method to maximize the penetration of the saw bar. Comparison criterions are total motion time of the saw bar and consumed energy of hydraulic pump.

1. INTRODUCTION

In timber cutting applications (harvester head) a hydraulic motor drives a saw chain and the feed force to a saw bar is generated by a hydraulic cylinder, Fig.1. There are many reasons why the cutting should be done as quickly as possible. One important reason is the effectiveness of the cutting process and other one is the quality of cutting. Sawing conditions vary very much due to different environment conditions as well as quality and diameters of timbers.

In timber cutting applications (harvester head) a hydraulic motor drives a saw chain and the feed force to a saw bar is generated by a hydraulic cylinder, Fig.1. There are many reasons why the cutting should be done as quickly as possible. One important reason is the effectiveness of the cutting process and other one is the quality of cutting. Sawing conditions vary very much due to different environment conditions as well as quality and diameters of timbers.

In a typical application a bent axis piston type hydraulic motor is used with very high rotation speed. The hydraulic motor drives the saw chain with a certain gearing. The saw chain is assembled around the saw bar. The saw bar is pressed against a timber to be cut by a hydraulic cylinder with the help of a certain gearing. Best cutting quality is achieved as fast cutting as possible. In practice there are many limitations and so the best results are

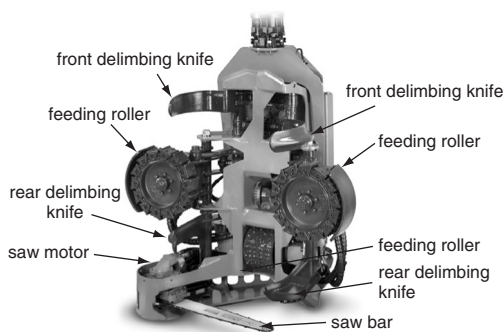


Figure 1. Harvester head, example of commercial product

achieved with the suitable combination of the saw chain speed and the feed force acting on the saw bar.

The quality of cutting is the most significant feature in wood cutting. Trees are expected to be cross-cut without longitudinal splits being caused in the end of the log. Although the timber cutting process is quick, cutting damage is a serious problem in today's forest industry. The most significant cutting damage is the end check, which appears when the tree is supported by the harvester head and the log to be cut is hanging freely. The gravitational force of the log causes bending torque on the cutting point. The bending creates high stresses in the wood, and these stresses cause the log to split before the log has been totally cut off. The damage resulting from the cutting process reduces the amount of useful material and causes considerable financial loss to sawmills and veneer industries.

An interesting question is how fast a log should be cut to avoid end checks. The only clear answer to this question is given by Swedish researchers, who claim that with constant feed rate a log with a diameter of 250 mm should be cut within 0.3s to avoid end checks [1]. This result means the cutting rate of $1636\text{cm}^2/\text{s}$. They do not discuss how this result has been derived and in addition the effect of the length of the log has not been mentioned. However, the authors claim that even a tenth of a second saved in the cutting time has a positive effect on reducing longitudinal splits. Another answer to this question is given by Myhrman, who states that the cutting rate should be at least $900\text{cm}^2/\text{s}$ for wood with a diameter of 300mm to achieve cutting without end checks [2]. Unfortunately he has not either discussed the effect of the length of the log.

2. STATE OF ART OF CHAIN SAWING CONTROL

The first developments in cutting control were based on hydraulic feedback and were publicized over 25 years ago [3]. When hydraulic feedback is used, the control principle is typically a constant torque method. There are known methods which aim to control the feed force of the saw bar as a function of the load of the saw motor and thus keep the torque of the saw motor substantially constant. Because direct measurement of the torque is quite cumbersome, measurement of the hydraulic motor load pressure is used in the estimation of the torque produced by the motor. The main advantage of this control principle is that control is independent of the dimensions and the properties of wood. However, the disadvantage of the hydraulic feedback is the dependency on the viscosity of the fluid. The

viscosity of fluid changes the outlet pressure of the saw motor and thus the supply pressure of the saw cylinder. In addition, the efficiency is very low because of the control principle. The outlet flow of the saw motor has to be throttled in order to increase cylinder pressure, causing pressure losses, and as a result heat is generated. Additionally, pressure difference in the hydraulic motor becomes smaller, causing a reduction in the torque of the hydraulic motor.

The load on the saw motor is used as a feedback also by Eaton [4]. He presents a development, in which the system is realised by a special hydraulic valve which is connected between the cylinder chamber and the motor inlet port. The aim of the valve is to control the cylinder supply pressure as a function of the inlet pressure of the saw motor. The development of Larsson's has a saw unit in which the idea is to control the feed rate of the saw bar stepwise using several feed velocities [5]. The hydraulic pressure of the motor is sensed and when an upper power limit is reached, the feed speed is set to the next lower level. However, nowadays this stepwise control is not of interest, because proportional valves enable continuous adjustment of feed rate.

Modd has introduced a development, in which the main principle is to maintain the cylinder piston velocity inversely proportional to the inlet pressure of the saw motor [6]. The system consists of a pressure transducer which measures the inlet pressure of the saw motor. The measured information is processed in a central processing unit which controls the directional and the velocity of a cylinder with a proportional direction control valve. Modd has also explained the general principle of a control method. At the beginning of the sawing operation, cylinder piston velocity has to be quite high. When the chain touches the wood and it starts to move on towards the inner portions of the log, cylinder piston velocity has to be slowed down. After the thickest part of the wood, cylinder piston velocity should be increased. Modd also mentions that the system performance characteristics are in this case related to the pump size, the motor size, the design of the hydraulic system, and especially the design of the motor inlet conduit, and thus the cutting controller takes them into consideration. This development of Modd's has already become a commercial product, *Sawcontrol RM 2100*. It has been shown that the *Sawcontrol RM 2100* system makes possible 0.2 seconds shorter cutting time compared with a system with constant feed rate [1]. However, the weakness of Modd's development is the dependency on the viscosity of the fluid.

Timperi et al present the method to keep chain speed constant by controlling the feed force of the saw bar during the cut [7]. The rotational speed of the saw motor is measured by an electric speed sensor. This measured data is processed in the electric control unit which controls the cylinder feed force. The operating principle of the system is to decrease the supply pressure of the cylinder with a proportional pressure reducing valve when the rotational speed of the saw motor drops. Correspondingly, if the motor speed is going to rise too high, the cylinder pressure will be increased. This control principle is presented also in reference [8], in which the fuzzy logic controller is developed to control the cutting process. The system developed is compared with a conventional P-type controller. The control results showed, however, that the proposed fuzzy controller does not necessarily produce shorter cutting time compared with a well tuned P- or PI-type controller.

3. MOTIVATION

An open loop control system is a commonly used control method in the sawing process of harvester heads. Figure 2 shows a typical example of the hydraulic circuit of a sawing system. Both saw motor and feed cylinder are controlled with on/off-valves. A pressure reducing valve is used to set suitable feed pressure (feed force) and a flow control/check valve is used to set feed rate. Both are manually controlled.

Simulation [9] and experimental results [10] show that remarkably better sawing results could be achieved with a closed loop control. Three different interesting closed loop control methods are presented. Timber [7] and Timber et al [8] has introduced the method to keep chain speed constant by controlling the feed force of the saw bar during the cut. The rotational speed of the saw motor is measured by an electric speed sensor. Inberg [11] has studied the control method to maximize the penetration rate of the saw bar. Promising results have been achieved in this study, but the problem is the relatively high costs of valves. Virvalo & Inberg have simulated both open and closed loop controlled sawing process [9] and made experimental tests also both open and closed loop control [10]. A constant torque closed loop control has been used in these studies. Both simulated and measured results are quite promising.

However there are several factors which influence strongly the performance of the sawing process. Long hoses between the pump and the harvester head and the timing between the starting of the saw motor and the motion of the saw bar are related to each other quite complicated way. Rushing of the saw motor at the end of the sawing is also a typical phenomenon. These problems can be clearly seen in open loop measurements presented in Fig. 2-5. The measured and simulated responses are presented in these figures. The meter-in pressure of the saw motor drops remarkably at the starting stage of the saw motor rotation. If the saw bar is pushed too strongly against a timber at this stage there is a significant risk of jamming.

The basic idea behind this study is to find with the help of simulations influences of different control strategies on the performance of the sawing process. Experimental tests are time consuming and tedious. The use of simulation is justified, because a quite well verified model exists [9]. Compared control strategies are: open loop control, torque control of the saw motor, speed control of the saw motor and a method to maximize the penetration of the saw bar. In addition interesting questions are the influences of locations of control valves (meter-in, meter-out), shape of reference signals (for instance time-ramps in the control of the saw motor) as well as different realization of supply pressure control on effectiveness, quality, and energy consumption of sawing process.

4. SPECIFICATION OF TEST CONDITIONS

The simulation model is based on the specification of a real harvester. The main basic data of the studied systems are (the same in every case):

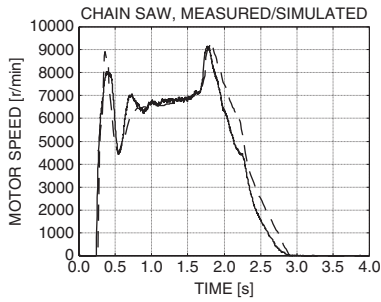


Figure 2. Rotation speed of saw motor, simulated and measured

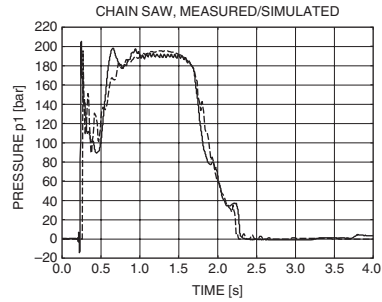


Figure 3. Meter-in pressure of saw motor, simulated and measured

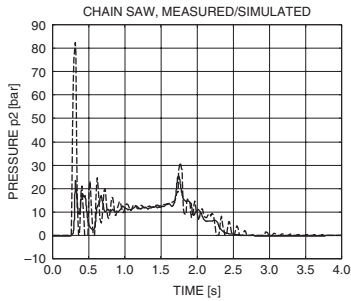


Figure 4. Meter-out pressure of saw motor, simulated and measured

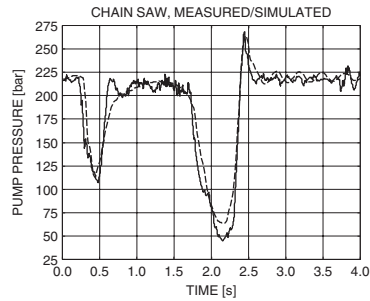


Figure 5. Supply pressure, simulated and measured

- * Constant pressure pump, maximum flow rate 230l/min,
- * Pump output pressure 240bar
- * Supply line 1" pipe and hose, total length 20m
- * Return line 1" pipe and hose, total length 20m
- * Saw motor bent-axis piston type, specific volume 30cm³
- * Feed cylinder 40/20-145
- * Stroke of feed cylinder 145mm making possible to saw up to 700mm timber diameters
- * Resolution of position sensor of feed cylinder 4mm corresponding resolution of 20mm of timber diameter

System sensitive parameters (components) of hydraulics as well as controllers are presented case by case. The nominal diameter of timbers is 320mm which is assumed to be the exact measured result. Due to branch and roughness of timbers it is assumed that the actual shape of cross sections of timbers vary randomly. As an example the variation of timber diameters around the nominal value in five simulation runs are presented in Fig.6. Because the quality of timbers influences the torque of the saw motor, the variations of torque are included as random disturbances. The standard deviation is 30%. As an example the relative variation of the torque in six simulation runs are shown in Fig.7. This variation is added to the basic torque caused by timbers.

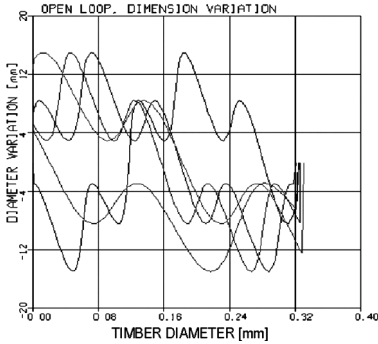


Figure 6. Timber dimension random variation around nominal dimension

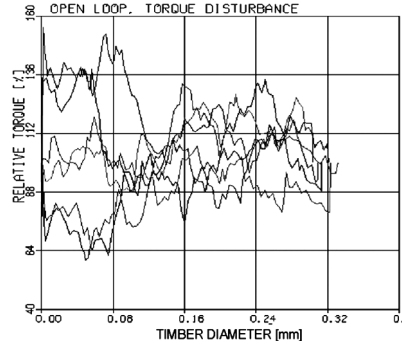


Figure 7. Torque disturbance random variation around nominal torque

Because of random disturbances several simulation are made with each system and some features are computed for comparisons. The following criteria are used in evaluating the performance of each system:

- * Sawing time, time of back-and-forth movement of saw bar,
- * Minimum rotation speed of saw motor,
- * Maximum rush speed of saw motor,
- * Energy consumption,
- * Overview of behavior.

5. OPEN LOOP CONTROL

The hydraulic system of the open loop case is depicted in Fig.8. The saw motor as well as the feed cylinder is controlled with an electrically controlled on/off-valve. The feed force is

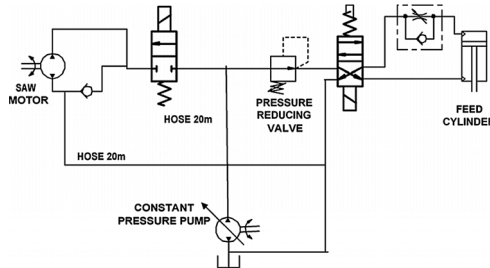


Figure 8. Hydraulic diagram, open loop control

set with a manually adjustable pressure reducing valve and the feed rate with a manually adjustable flow control valve. The feed rate and feed force of the feed cylinder are tuned so that the sawing of the 600mm diameter timbers takes place without jamming of the saw motor in repeated simulations (20 simulations). The basic simulation parameters are chosen so that the overall behavior is like shown in Fig. 2-5. The basic simulation parameters are chosen so that the overall behavior is like shown in Fig. 2-5.

Users have only two tuning parameters in a typical open loop control system of the sawing process. It is possible to adjust manually both the pressure reducing valve (maximum feed force) and flow control valve (feed rate) of the feed cylinder. Tuning of these settings is a real trial-and-error affair and an off-line method because the valves are located in the harvester head and all actions are controlled from the cabin of the harvester. From a designer's point of view there are more tuning parameters like:

- * Sizes of components
- * Supply pressure
- * Time ramps of control valves
- * Timing between the saw bar and the saw motor at starting and ending of the sawing process

The basic tuning is made with 600mm diameter timbers. It has been tried to minimize the sawing time without considerable risk of jamming. The following parameters are varied in the tuning: feed force, feed rate and timing between the saw bar motion and the starting of the saw motor. The final results are shown in Fig.9 and 10.

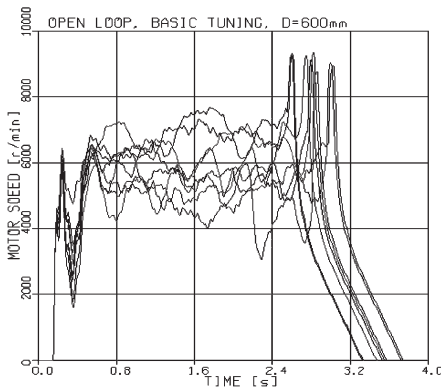


Figure 9. Saw motor rotation speed, diameters 600mm

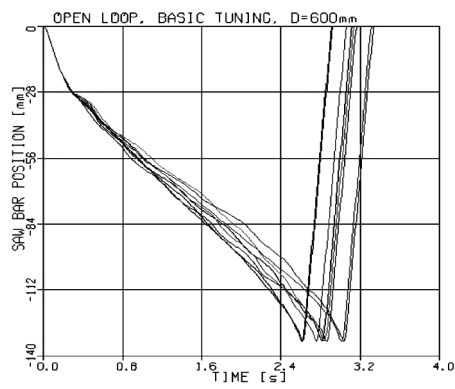


Figure 10. Saw bar movement, diameters 600mm

Figures 11 and 12 show as an example some results of the rotation speed of the saw motor and the movement of the saw bar with the basic tuning made with 600mm diameter timbers.

The rotation speed of the saw motor varies quite remarkably at the starting stage and rotation speed rushing is very high at the end. The sawing time varies in 20 simulations between 1.5-1.62s. Hydraulic energy required from the pump varies from 78 to 85kJ.

In order to study influences of parameters which users can tune, the disturbances in the model are set zero. The influence of the feed rate is shown in Fig.13, when the feed pressure is kept constant. The initial tuning (with 600mm timbers) causes the longest sawing time. The increasing the feed rate shortens the sawing time into a certain limit. Too

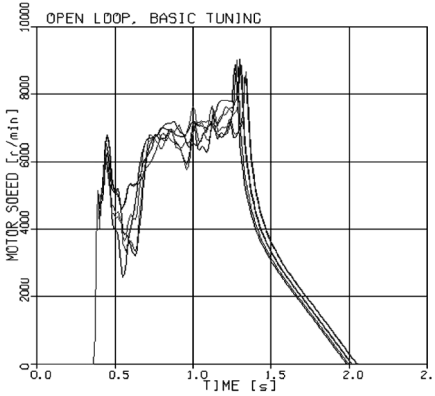


Figure 11. Saw motor rotation speeds with 320mm diameter timbers, basic tuning

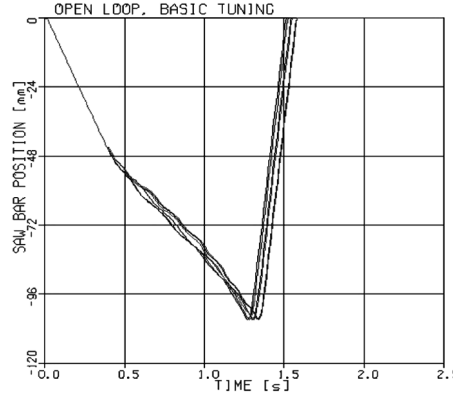


Figure 12. Saw bar movements with 320mm diameter timbers, basic tuning

high feed rate causes the decrease of the rotation speed of the saw motor and so results in longer sawing times. If the maximum feed force (feed pressure) is under a certain limit the risk to jamming is low. The influence of the feed force is shown in Fig.14, when the feed rate setting is kept constant. The initial tuning (with 600mm timbers) causes the shortest sawing time. The increasing the feed force shortens the sawing time into a certain limit. Too high feed force causes the decreasing of the rotation speed of the saw motor and so results in longer sawing times. The risk of jamming is relatively sensitive to the feed force. When no pressure compensation is used in the flow control valve, the feed rate changes also somewhat due to the change of the feed force. It seems that if retuning had to be done it is better to tune the feed rate than the feed force.

Because strength and life time of saw chains set the limit to the maximum chain velocity there are no reasons to change radically the sizes of the main components. There might be some possibilities to optimize the size and type of components mainly from cost and design points of view. The maximum volume flow is quite high, more than 210l/min, which means that pressure losses are also relatively high. There might be some benefits if the supply pressure would be around 10-20% higher than nowadays. Then the same rotation speed of the saw motor could be achieved with a little higher feed force.

According to simulations open loop control system is sensitive to the feed pressure (feed force), the approach velocity of the saw bar to timbers, and the timing between the saw bar movement and the starting of the saw motor.

6. SPEED CONTROL OF SAW MOTOR

The hydraulic diagram of the speed control system of the saw motor is depicted in Fig.15. The saw motor as well as the feed cylinder are controlled with on/off-valves. The rotation speed of the saw motor is measured with an analog tachometer and a 12 bits ADC. The feed force is controlled with a proportional pressure reducing valve.

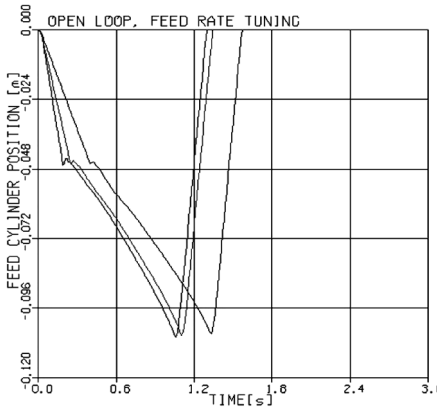


Figure 13. Influence of feed rate on sawing time, constant feed pressure, without disturbances, diameter 320mm

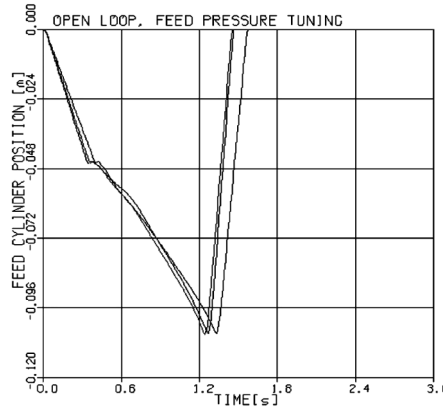


Figure 14. Influence of feed pressure on sawing time, constant feed rate setting, without disturbances, diameter 320mm

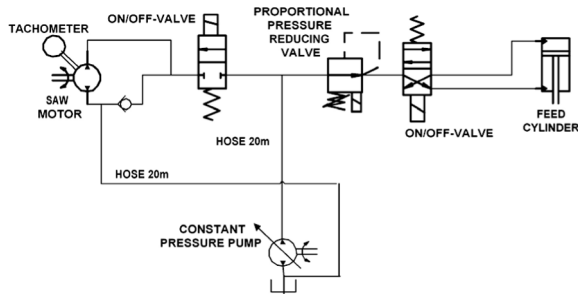


Figure 15. Speed control of saw motor, hydraulic circuit

The basic ideas of this control method are as follows

- * If a constant motor speed can be kept over the sawing process, it guarantees that
 - * Saw motor rotates all the time,
 - * Rotation speed of the saw motor does not depend on diameter and quality of timber,
 - * It is not possible to load the saw motor by the feed force too much causing it to stop which causes jamming problems, and
 - * Simple on/off valve can be used to control the saw motor.

The method is to keep the rotation speed of the saw motor constant by controlling the feed force acting on the saw bar. A rotation speed sensor and an electrically controlled pressure reducing valve are needed in the control loop, Fig.15. The principal structure of the control system is shown in Fig.16.

The parameters of the controller have been tuned by the manufacture. In principle there is no need of the re-tuning by users. In order to achieve short sawing time, avoid jamming, and utilize energy effectively the manufacturer tunes the following parameters:

- * Gains of the controller

- * Feed pressure in approaching stage. Approach velocity of the saw bar to timbers is set with this setting
- * Timing between the saw bar movement and the starting of the saw motor

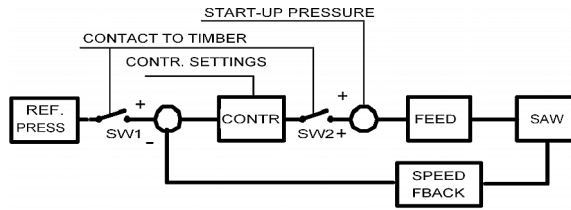


Figure 16. Principle of constant speed control of saw motor

- * Time ramps of the saw motor control valve
- * Timing between the saw bar movement and the stopping of the saw motor

The basic controller is a PI-controller. The initial tuning of the controller gains is done based on the estimated time constant of pressurized volume of the feed cylinder [12].

Because a pressure reducing and directional control valves are used to control the force and movement of the saw bar the approach velocity to timbers has to be set carefully. The movement of the feed cylinder is started at quite low setting of the pressure reducing valve in order to keep approach velocity low enough.

Because the on/off directional control valve of the saw motor is two-stage valve there is possible to achieve reasonable time ramps of the main spool with simple restrictions between the first and second stages. Slight time ramps, especially at the stopping stage of the motor, might improve energy utilization somewhat. Timings between the saw bar movement and the starting as well as stopping of the saw motor are done with try-and-error method. The saw motor is started when the saw bar is at a certain distance from timbers. The saw motor stopping is started when a certain part of timbers is still under sawing.

The responses of the saw motor rotation speed and saw bar position in five simulations are shown as an example in Fig.17 and 18. The sawing time varies between 1.25-1.5s. Hydraulic energy required from the pump varies from 72 to 92kJ.

7. TORQUE CONTROL OF SAW MOTOR

The hydraulic diagram of the torque control system of the saw motor is depicted in Fig.19. The saw motor is controlled with on/off-valves. The feed cylinder is controlled by a 3-way proportional directional control valve. The meter-in pressure of the saw motor is measured with a pressure transducer and a 12 bits ADC. The basic ideas behind this method are as follows

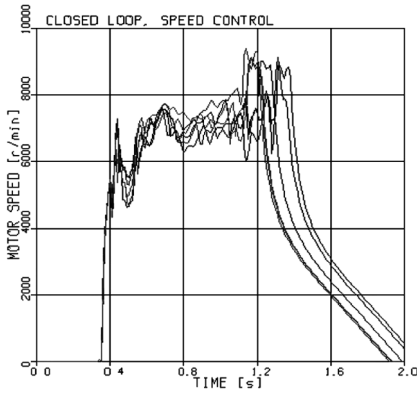


Figure 17. Rotation speed of saw motor, speed control, basic diameter 320mm

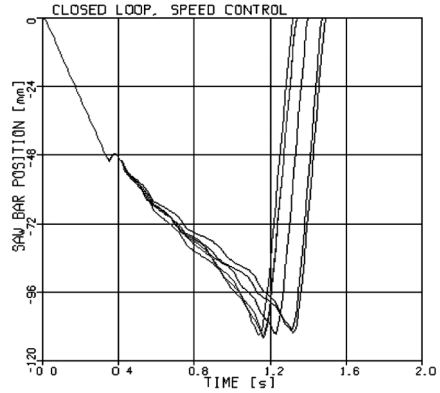


Figure 18. Saw bar position, speed control, basic diameter 320mm

- * If a constant pressure difference can be kept over the saw motor, it guarantees that
 - * Saw motor rotates all the time,
 - * Rotation speed of the saw motor does not depend on diameter and quality of timber,
 - * It is not possible to load the saw motor by the feed force too much causing it to stop which causes jamming problems, and
 - * Simple (on/off valve) can be used to control the saw motor.

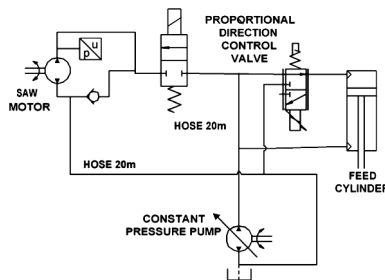


Figure 19. Torque control of saw motor, hydraulic circuit

The method is to keep the torque (meter-in pressure) of the saw motor constant by controlling the feed force acting on the saw bar. In principle only one pressure sensor and a relatively small proportional three way directional control valve are needed in the control loop. The principal structure of the control system is shown in Fig.20.

When the parameters of the controller have been tuned by the manufacture there is no need of the re-tuning by users. In order to achieve short sawing time and good energy utilization the manufacturer has to tune the following parameters:

- * Gains of the controller
- * Velocity profile and maximum approaching velocity of the saw bar when approaching timbers

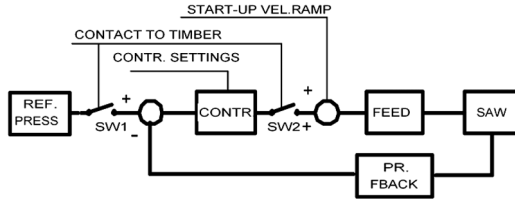


Figure 20. Principle of constant torque control of saw motor

- * Timing between the saw bar movement and the starting of the saw motor
- * Time ramps of the saw motor control valve
- * Timing between the saw bar movement and the stopping of the saw motor

The basic controller is a PI-controller. The initial tuning of gains is done based on the estimated time constant of pressurized volume of the feed cylinder [12].

Because a directional control valve is used as a control valve of the feed force it also enables reasonable velocity control of the feed cylinder. The movement of the feed cylinder is started quite high velocity and the velocity is decreased with the inverse function of the distance between the saw bar and a timber. Slight time ramps in the control valve of the saw motor improve energy utilization also in this control method somewhat. Timings between the saw bar movement and the starting as well as stopping of the saw motor are done with try-and-error method also in this case. The responses of the saw motor rotation speed and saw bar position in five simulations, as an example, are shown in Fig.21 and 22. The sawing time varies between 1.05-1.3s. Hydraulic energy required from the pump varies from 70 to 75kJ

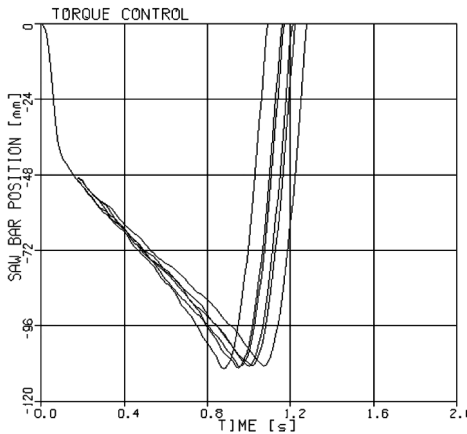


Figure 21. Rotation speed of saw motor, torque control, diameter 320mm

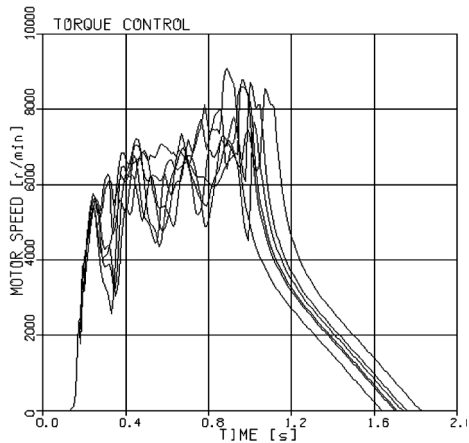


Figure 22. Saw bar position, torque control, diameter 320mm

8. MAXIMIZING PENETRATION OF SAW BAR

There are some weaknesses in the control of the constant rotation speed of the saw motor as well as in the control of the constant torque of the saw motor. In both cases the reference

value of the controlled object has to be fixed after some tests. The second common feature is the rushing of the saw motor in the starting as well as in the stopping stage. Based on these features the following control idea is studied: Closed loop speed control of the saw motor and maximizing penetration rate of the saw bar.

In practice there is a serious limiting factor in the sawing realization. When the saw chain is pressed against a timber cutting bits can penetrate only a certain depth into a timber. Saw chains can only be driven with the maximum speed allowed by manufacturers. Due to these facts the feed force is the only controlled parameter. The closed loop speed control of the saw motor can be utilized to reduce rushing of the saw motor and to improve timing. Some benefits in energy consumption can be achieved in this way.

Hydraulic diagram is depicted in Fig.23. The saw motor as well as the feed cylinder is controlled with a proportional direction control valve. A speed sensor is used to measure the rotation speed of the saw motor and a position sensor to measure the position of the feed cylinder.

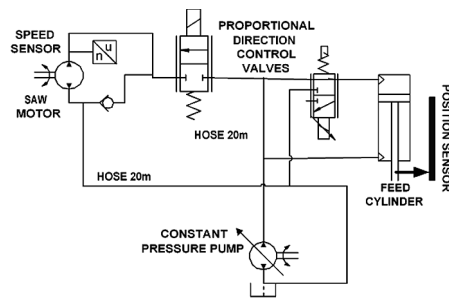


Figure 23. Penetration rate control of saw bar, hydraulic circuit

Simulation results are shown in Fig.24 and 25, as an example, when the PI-speed-controller of the saw motor and the simple open loop control of the feed cylinder are used. The reference speed profile of the saw motor includes slight time ramps at the starting and stopping stages. The velocity reference profile of the feed cylinder has firstly the high value (approach velocity) which is down-time-ramped to the constant value. The supply pressure of the feed cylinder is set to the suitable value by a trial-and-error method. The tuning is tested with the large diameter range of timbers. The sawing time varies between 1.05-1.15s. Hydraulic energy required from the pump varies from 67-70kJ.

Simulation results are shown in Fig.26 and 27, as an example, when a simple maximizing of the penetration rate of the saw bar is used with the closed loop control of the rotation speed of the saw motor. Otherwise the reference signals are the same kinds as in the previous case. The tuning is tested with the large diameter range of timbers. The sawing time varies between 0.85-1.1s. Hydraulic energy required from the pump varies from 52-56kJ.

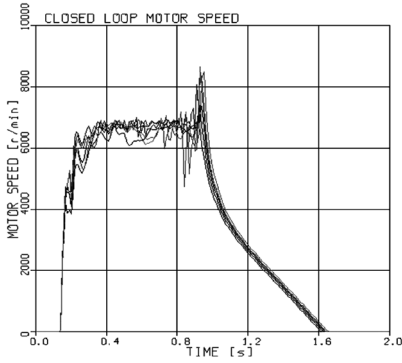


Figure 24. Saw motor rotation speed, speed control of saw motor, open loop control of feed cylinder, diameter 320mm

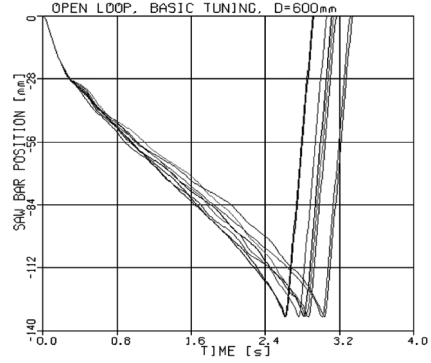


Figure 25. Saw bar position, speed control of saw motor, open loop control of feed cylinder, diameter 320mm

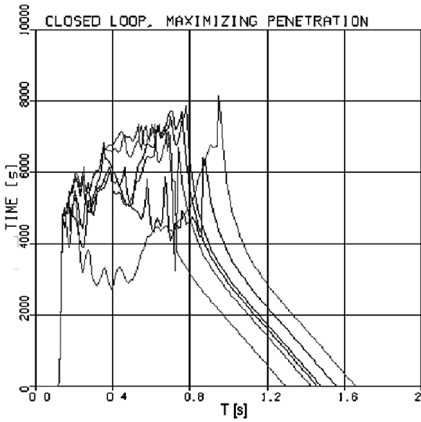


Figure 26. Saw motor rotation speed, speed control of saw motor, maximizing penetration rate of saw bar, diam. 320mm

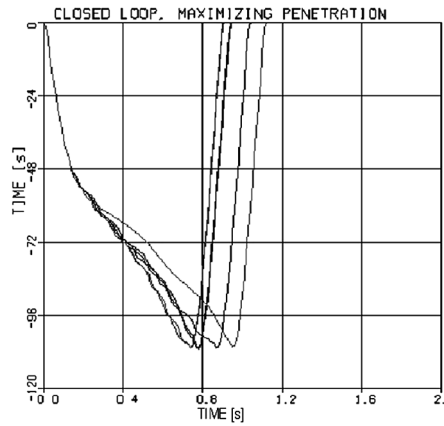


Figure 27. Saw bar position, speed control of saw motor, maximizing penetration rate of saw bar, diam. 320mm

Some remarks about results presented in Fig.24-27:

- * The change of an on/off control valve of the saw motor to a proportional direction control valve improves significantly the behavior of the saw motor.
- * The rushing of the saw motor at the stopping stage is still a problem. It can be eliminated with more accurate timing of the saw motor stopping. However the end part of cutting should be done fast due to the quality of cutting. Some improvements might be achieved with a meter-out control of the saw motor.
- * The use of a proportional direction control valve instead of a proportional pressure reducing valve in the control of the feed cylinder shortens the sawing time.
- * The penetration rate maximizing method requires a quite high resolution position sensor of the feed cylinder because the penetration rate is computed by differentiating.

9. COMPARING OF RESULTS

The comparison is based on the following simulation situations:

- * The model is the same in all cases except that the controller is realized case by case
- * Randomly varying torque and timber diameter are included to each simulation.
- * Simulations are repeated twenty times in every case.
- * The tuning is based on successful performance also with timbers of 600mm diameter.

The simulation results are summarized in the following Table1. The average of the sawing time and pump energy consumption are computed and the minimum and maximum of twenty simulations are presented. The following remarks can be made:

- * The sawing time is shorter in closed loop control methods than in the open loop case.
- * Constant speed and torque controls of the saw motor are in principle the same kinds. The torque control method uses a pressure sensor which is simpler to use and more cost effective than to speed sensor used in the speed control. A proportional direction control valve used in the control of the feed cylinder makes the velocity control of the feed cylinder significantly better than the use of a proportional pressure reducing valve. The shorter sawing time is achieved in the constant torque control method than in the constant speed control method.
- * The constant speed control of the saw motor and the open loop control of the feed cylinder give reasonable good results, but reliable behavior requires quite low supply pressure of the feed cylinder control valve. This means an extra pressure reducing valve. This means that the tuning is quite tedious and risk of jamming rises.
- * The maximizing of the penetration rate of the saw bar is an effective way from the sawing time and energy consumption points of view but it is also quite costly to realize. Two proportional valves and two sensors are required. The resolution of the saw bar position sensor should be high, because the penetration rate is computed by differentiating from the position measurement.

Table 1	Open loop		Speed contr.		Torque contr.		Const. speed		Max. penetr,	
	Av.	Lim.	Av.	Lim.	Av.	Lim.	Av.	Lim.	Av.	Lim.
Sawing time [s]	1.55	1.5-1.62	1.4	1.25-1.5	1.15	1.05-1.3	1.1	1.05-1.15	0.95	0.85-1.1
Energy [kNm]	81	78-85	84	72-92	72	70-75	68	67-70	54	52-56

10. CONCLUSIONS

The following main conclusions can be made:

- * Considerable improvements can be achieved with a closed loop control both in shortening of sawing time and reducing energy consumption.
- * Risk of jamming can be reduced significantly with closed loop control methods.
- * Good performance can be achieved with the constant torque control of the saw motor. It is also most cost effective solution compared to other closed loop control methods.
- * Very good performance and energy utilization can be achieved with the maximizing the penetration rate of the saw bar, but this solution is also quite costly.

11. FURTHER WORKS

It is necessary to do more simulations. For example the following issues and questions might be interesting to study:

- * What is the influence of the supply pressure variation (Fig.5) on the performance of sawing process? Can it be utilized or compensated somehow?
- * Can meter-out control of the saw motor improve the performance and energy utilization?
- * What kinds of requirements should be set on the sampling time, resolution of measurements (feedbacks), valve dynamics and pump dynamics?

Sawing process is very complicated and influence of environment is strong so it is necessary to make also a lot of experimental tests. Some experimental tests have already been done in laboratory conditions. These tests will be continued and after that tests in real forest are necessary.

12. REFERENCES

1. Hallonborg U. and Granlund P. Correct Technique Reduces Bucking Splits. Skogforsk Resultat No. 19/1999. 4 p. (in Swedish)
2. Myhrman D. Good Technology Must Be Better – If All Final Felling to Be Done by Single-Grip Harvesters. Skogforsk Resultat No. 22/1995. 4 p. (in Swedish)
3. Inberg J. and Virvalo T. On Control of Timber Cutting Process in Forest Machines. SICFP'01, Vol 2. 30 May - 1 June, 2001. Linköping, Sweden. pp. 247-261
4. Eaton G. Apparatus for Controlled Cutting Down of Trees. US Patent 4368763, 1983
5. Larsson L. Device for Cross-Cutting Tree Trunks. Patent SE 388752, 1978
6. Modd R. A Device for Operating a Machining Apparatus. International patent application WO 99/12410, 1999
7. Timperi A., Tågmark L. and Carlsson L. System to Automatically Set Rotation Speed of Saw Blade. Patent FI 97918B, 1997
8. Timperi A. Modern Engineering in the Development of Hydraulics and Control Systems for Forest Machines. Doctoral Thesis. Tampere University of Technology, Institute of Hydraulics and Automation, 1997. pp. 123-180
9. Virvalo, T. & Inberg, J. Feed force based constant torque control of hydraulic motor in chainsaw application. Bath Workshop on Power Transmission and Motion Control (PTMC2004) pp. 173-186 2004
10. Virvalo T., Inberg J. and Lammila M. Closed Loop Control Improves Timber Sawing Process. SICFP'05 June 1-3, 2005 p. 12
11. Inberg J. On Eliminating Cutting Damages by Advanced Control of Timber Cutting Process. Acta Polytechnica Scandinavia, ME 158, Espoo 2002, 117 p.
12. Virvalo, T. Comparing pressure control methods. Proceedings of the Fourth International Symposium on Fluid Power Transmission and Control, ISFP'2003, April 8-10, 2003, Wuhan, China, pp. 25-30.

Closed-loop velocity control for an electrohydraulic impact test system

A.R. Plummer

Manager – Control and Analysis, Instron Ltd, UK

Abstract

This paper concerns the design of a controller for an electrohydraulic pedestrian impact test system. The system is designed to launch dummy human body parts at the surfaces of a car body as required for crash safety testing. The launch velocity must be very tightly controlled. The dummy body parts are instrumented to measure acceleration signals experienced during the impact.

Previous systems of this type have used open-loop control. The valve drives required for a number of different target velocities are recorded, and used in the form of a look up table. Such an approach is prone to disturbances – for example the angle of launch and the impactor mass affect the results and so reduce accuracy.

In this work a closed-loop controller is proposed. A very high bandwidth controller is required in order to correct the actuator velocity before launch, given that the test motion typically lasts less than 0.1s. The proposed controller uses an inverse non-linear actuator model to linearize the response, together with a combined feedback/feedforward strategy. Theoretical, simulation, and experimental results are presented.

1 INTRODUCTION

The automotive regulatory authorities in many countries required new vehicle designs to have proven standards of safety for pedestrian impact. This includes leg impact for the front of the vehicle, and head impact on the bonnet. In order to test for safety, an instrumented dummy headform or legform is fired at the vehicle at a prescribed location and velocity. The deceleration of the dummy body part (impactor) is monitored to ensure it is within the required limits.

Typically, the body part must impact the vehicle with a target velocity up to 13.9m/s (50km/h). The impactor leaves the launcher when the actuator reaches its peak velocity

and starts to decelerate. This velocity must be achieved within an accuracy of 0.2m/s for the test to be valid, but there is a desire to make the tolerance smaller. In current industrial practice, in order to achieve this accuracy the launch mechanism must be calibrated for every target velocity, angle of launch, and mass of head or legform. This is a laborious trial-and-error process.

State-of-the-art launch mechanisms use servovalve-controlled hydraulic actuators. In order to accelerate the impactor using a compact device with small stroke, the acceleration period is short – usually between 10ms and 100ms. The response time of a simple closed-loop controller for a servohydraulic actuator is such that closed-loop control has not improved velocity accuracy in the past, so, being easier to implement, open-loop control has been used. An open-loop controller for another high speed electrohydraulic impact application is described in [1].

The development of a high bandwidth closed-loop velocity controller for a pedestrian impact test system is described in this paper. The controller uses position and acceleration feedback, a command feedforward path, and linearization of the valve pressure/flow relationship. A review of electrohydraulic control systems, including velocity control and the use of linearization techniques is contained in [2]. In the present work, a theoretical development is carried out, and simulation results are presented. Experimental results which validate the approach are also included. The emphasis is on a practical controller which can be implemented reliably for real industrial systems.

2 SERVOHYDRAULIC LAUNCH MECHANISM MODEL

The launch mechanism is a hydraulic cylinder supplied by a servovalve as shown in Figure 1. Flow for each shot is mostly supplied from an accumulator; pump flow is just sufficient to cover valve and cylinder leakage and to recharge the accumulator between shots. The main force generated by the actuator is that required to accelerate the combined mass M of the piston and impactor. Weight (the launcher can be rotated to any angle) and friction forces are relative small and will be neglected in the model. The model includes fluid compressibility, leakage across the piston, and the valve orifice equations. The valve spool movement X is assumed to have second order dynamics.

$$\begin{aligned} \text{Valve orifice equations:} \quad Q_1 &= k_v X \sqrt{P_{acc} - P_1} \quad \text{for positive } X & (1) \\ Q_2 &= k_v X \sqrt{P_2 - P_r} \quad \text{for positive } X \end{aligned}$$

(2)

$$\text{Cylinder flow equations:} \quad Q_1 = A\dot{y} + \frac{\dot{P}_1}{k_1} + (P_1 - P_2)c_l \quad (3)$$

$$Q_2 = A\dot{y} - \frac{\dot{P}_2}{k_2} + (P_1 - P_2)c_l \quad (4)$$

Piston force balance: $(P_1 - P_2)A = M\ddot{y}$ (5)

Valve spool dynamics: $X = \frac{e^{-sD}}{V(s)}U$ (6)

where $V(s) = \left(\frac{s}{n}\right)^2 + 2\left(\frac{s}{n}\right) + 1$

and where the fluid stiffness on each side of the cylinder is represented by $k_1 = \frac{B}{V_1}$,

and $k_2 = \frac{B}{V_2}$, B being the bulk modulus; k_v is a valve orifice constant, and c_l is a leakage coefficient. The control signal is U , and D , n and ζ are delay, natural frequency and damping ratio parameters in the valve model respectively. The differential operator is denoted s .

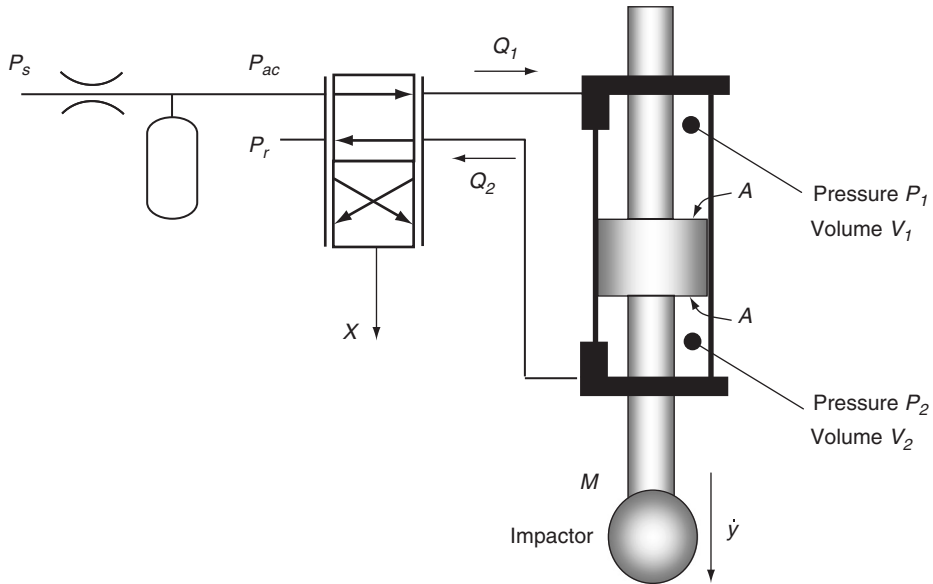


Fig 1. Electrohydraulic launcher schematic

Inverse actuator model

Using the following approximations:

$$V_1 = V_2 = V \quad (7)$$

$$k_1 = k_2 = k \quad (8)$$

each side of the system is the same (symmetrical) and it can be shown that:

$$Q_1 = Q_2 = Q \quad (9)$$

$$P_{acc} - P_1 = P_2 - P_r \quad (10)$$

Summing equations (3) and (4):

$$Q = A\dot{y} + \frac{\dot{P}_1 - \dot{P}_2}{2k} + (P_1 - P_2)c_l \quad (11)$$

Substituting for the pressure difference using equation (5):

$$Q = \frac{M}{2kA} \ddot{y} + \frac{Mc_l}{A} \dot{y} + A\dot{y} \quad (12)$$

or

$$Q = A \left(\frac{M}{2kA^2} s^2 + \frac{Mc_l}{A^2} s + 1 \right) \dot{y}$$

$$Q = A \left(\frac{1}{nr} s^2 + \frac{2}{nr} r s + 1 \right) \dot{y} \quad (13)$$

where

$$nr = \sqrt{\frac{2kA^2}{M}} \quad (14)$$

and

$$r = \frac{c_l}{A} \sqrt{\frac{Mk}{2}} \quad (15)$$

are the cylinder natural frequency and damping ratio respectively.

From (1) or (2) the cylinder flow is given by:

$$Q = k_v X \sqrt{\frac{(P_{acc} - P_r) - (P_1 - P_2)}{2}}$$

$$Q = k_v X \sqrt{\left(1 - \frac{P_1 - P_2}{P_{acc} - P_r}\right) \frac{(P_{acc} - P_r)}{2}}$$

$$Q = k_v X \sqrt{\left(1 - \frac{F_h}{R_s F_{stall}}\right) \frac{R_s (P_s - P_r)}{2}} \quad (16)$$

where $F_h = (P_1 - P_2)A$ (so $F_h = M\ddot{y}$) (17)

$$F_{stall} = (P_s - P_r)A \quad (18)$$

and $R_s = \frac{P_{acc} - P_r}{P_s - P_r}$ (19)

Gathering together the constant terms in (16):

$$\frac{Q}{A} = \frac{k_v}{A} \sqrt{\frac{P_s - P_r}{2}} X \sqrt{R_s \left(1 - \frac{F_h}{R_s F_{stall}}\right)} \quad (20)$$

$$\frac{Q}{A} = X_v \sqrt{R_s \left(1 - \frac{F_h}{R_s F_{stall}}\right)} \quad (21)$$

where X_v is the valve spool position scaled to be in units of equivalent actuator velocity.

Equations (13) and (21) can be combined to give an actuator inverse model, i.e. to calculate valve spool position from piston motion:

$$X_v = \frac{1}{\sqrt{R_s \left(1 - \frac{F_h}{R_s F_{stall}}\right)}} \left(\frac{1}{nr^2} s^2 + \frac{2}{nr} s + 1 \right) \dot{y} \quad (22)$$

or $X_v = \frac{1}{b} \left(\frac{1}{nr^2} s^2 + \frac{2}{nr} s + 1 \right) \dot{y}$ (23)

where $b = \sqrt{R_s \left(1 - \frac{F_h}{R_s F_{stall}}\right)}$ (24)

The variable b is dependent on the accumulator pressure (via R_s) and the hydraulic force F_h , both of which vary. The accumulator pressure can be modelled as a linear reduction in pressure with position during the launch (see Section 4.4), and the hydraulic force is dependent on acceleration (equation 17).

3 CONTROLLER DESIGN

3.1 Velocity Controller

There are two parts to the proposed controller. An inverse model based approach is used for developing a closed-loop velocity control system; and a command generation part is used to provide a velocity command which is appropriate for this application.

From Section 2, the spool position of the valve is related to the control signal by a second order model plus delay, and when linearised the actuator velocity is related to the spool position by another second order model. To invert the whole relationship would require differentiation of feedback signals giving unacceptable sensitivity to measurement noise (and the delay could not be inverted). Instead, only the spool to actuator model is inverted. Non-linear terms are included in this inverse as shown in equation (22) to account for the variation in pressure drop across the valve which changes the valve flow gain.

If the valve dynamics are sufficiently fast, the valve spool command can be used as the valve control signal. This is shown in Figure 2. A feedforward path directly feeds the inverse actuator model with the velocity command signal. If the achieved velocity just differs from the command velocity by the known residual dynamics of the system – i.e. the valve dynamics – then the feedback part has no effect (the output of the lower summing junction is zero). However if the actual velocity deviates from the expected, then the error is integrated and scaled by gain K to give a correction signal which is summed with the command velocity.

In the implementation of the control system, in order to keep sensitivity to measurement noise low, it is important that feedback signals are not differentiated. This can be achieved in this case if acceleration feedback is included, as shown in Figure 3.

Note that the actuator velocity is not measured directly. It is generated by combining position and acceleration signals using matched composite filters. This approach has been used in the testing industry for many years; the principle is described in [3].

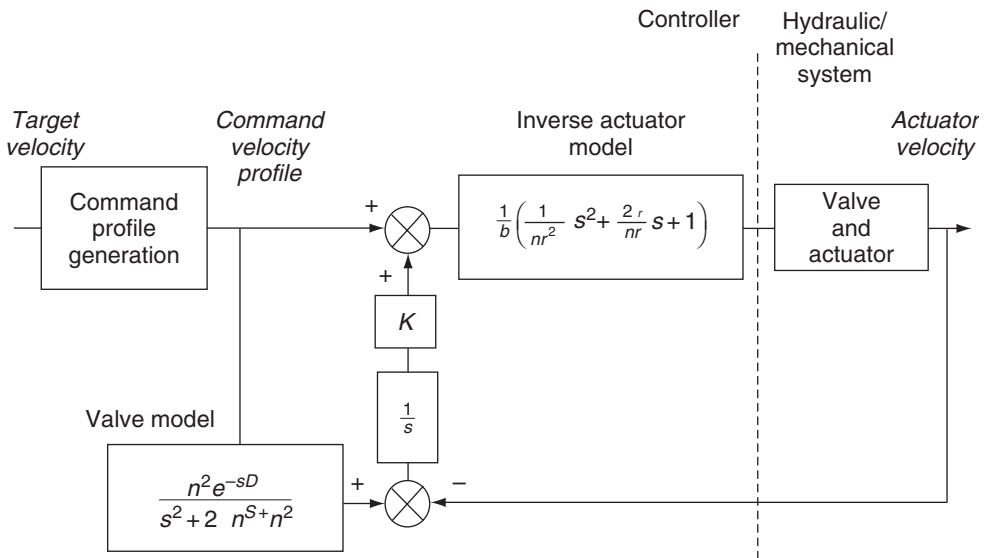


Fig. 2 Velocity control system

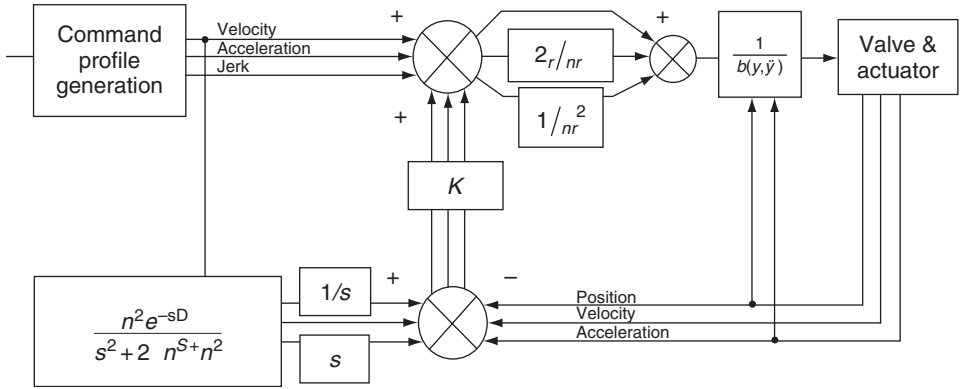


Fig. 3 Velocity control system, showing individual signals

The control system is illustrated in Figure 4 in a Simulink simulation model. The reference to ‘motion’ implies a vector signal which contains position (or velocity) and its first and second derivatives.

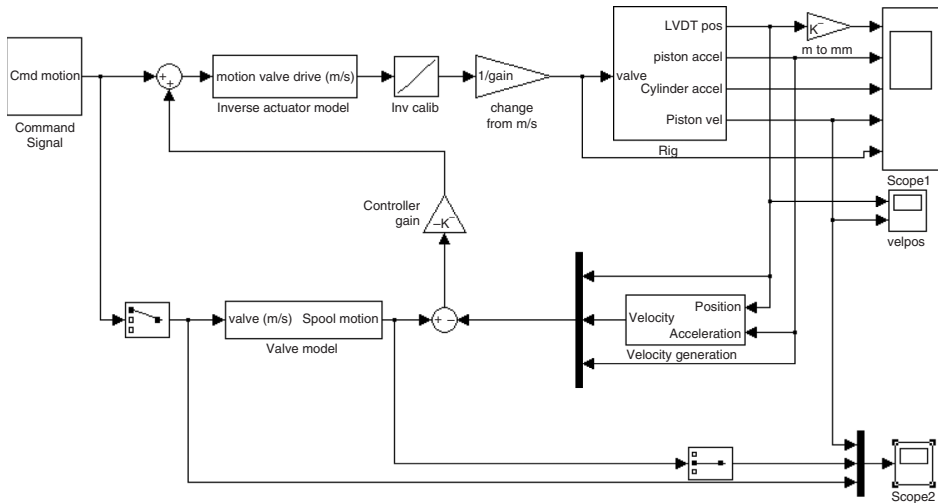


Fig. 4 Simulink simulation model

3.2 Command generation

For this application, the peak velocity is the critical value. Once the actuator starts to decelerate, the impactor will carry on at the same velocity and strike the vehicle. The command profile chosen to reach the target peak velocity is a haversine. This is unlikely to excite high frequency dynamics where modelling error will be larger. Thus the command velocity is given by:

$$\frac{V_t}{2}(1 - \cos(\omega t)) \quad (25)$$

where V_t is the target velocity. Expressions for the first and second derivatives of this are easy to find. The frequency ω is determined so that the target velocity is achieved after a specified actuator travel. A deceleration period follows so that the piston has slowed by the time it enters a buffer at the end of stroke.

There will be a small amplitude error due to the response characteristics of the valve which remain present in the whole system response. As the valve model is known, the amplitude ratio at the command haversine frequency can be used to correct for this.

4 RESULTS

4.1 Simulation results

Some key parameters of a trial launch system are contained in Table 1. A simulation model of this system has been developed which is more detailed than that described in Section 2; in particular it includes valve overlap, valve slew rate limit, pressure drop in valve body and manifold, and stroke-related stiffness variation. Figure 5 and Table 2 show that the simulation results for the proposed controller driving this more detailed model indicate good velocity accuracy.

Table 1 Specification for trial electrohydraulic launcher

Actuator	Cross-section area	5 cm ²
	Stall force (at 210 bar)	10.5 kN
	Stroke	100 mm
	Piston plus impactor mass	5kg
	Buffer length	18 mm
	Total trapped volume	58 cm ³
Servovalves	Two x D765 Moog 2-stage valves	
	Nominal rated flow (each valve)	40 l/min
	Nominal natural frequency	500 Hz
	Opening time at max slew rate	2.65 ms
Hydraulic supply	Supply pressure	210 bar
	Bulk modulus	0.9 GN/m ²

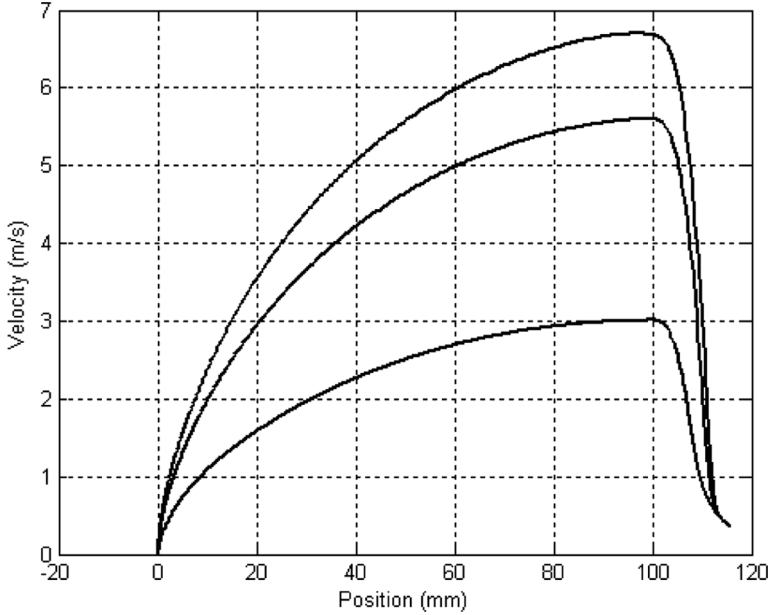


Fig. 5 Simulation results: target velocities 3, 5.6, 6.8m/s

Table 2 Peak velocity errors

Target velocity	Error (actual – target)
3.0 m/s	+0.01 m/s
5.6 m/s	0.00 m/s
6.8 m/s	-0.10 m/s

Table 3 Peak velocity error with 1000N load disturbance

Target velocity	Closed-loop	Open-loop
3.0 m/s	+0.01 m/s	-0.08 m/s
5.6 m/s	+0.01 m/s	-0.23 m/s
6.8 m/s	-0.13 m/s	-0.39 m/s

The closed-loop controller is expected to give accurate velocity control even in the presence of unmodelled disturbances; this is the key improvement required compared to open-loop control. To test this, a 1000N load disturbance acting on the piston is included in the simulation model for the duration of the launch. From Table 3 it can be seen that the improvement is significant.

4.2 Experimental controller tuning

A frequency response from valve drive to piston velocity was determined from a random excitation of the real system. The excitation signal was chosen so that the non-linear behaviour relating to accumulator and cylinder pressure drop would not be significant. Then a combined valve and actuator model (transfer function) was fitted to the frequency response. The actuator natural frequency is fixed by the known parameters of the system, but the actuator damping, which is related to piston leakage, was adjusted manually to fit the frequency response ($\zeta = 0.17$). A least squares fit then gave the following valve model: 504Hz natural frequency ($\omega_n = 3170$ rad/s), damping ratio $\zeta = 1.25$, and delay $D = 0.0012$ s. Figure 6 shows there is a good fit between the model to the actual frequency response.

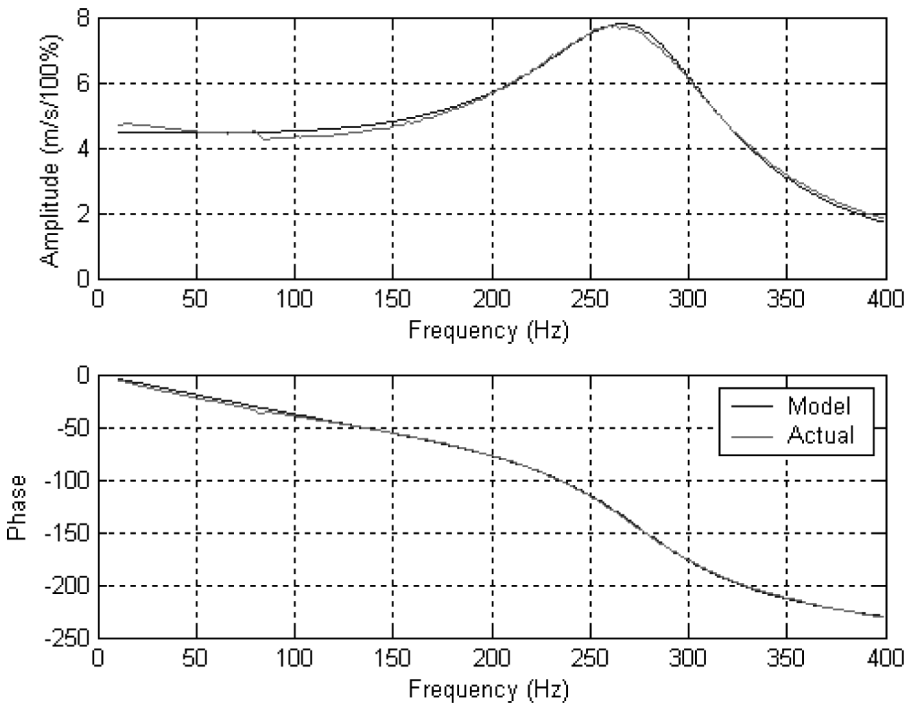


Fig 6 Fit of linear valve/actuator dynamics to measured frequency response

4.3 Experimental results from the trial system

Figures 7 to 9 show results for 2 and 3m/s target velocities; the first two use 50mm travel for the launch acceleration, the last one uses 30mm. The equivalent velocity plots generated by the detailed simulation model are also shown. Note that in Figure 9 the actual velocity trace deviates from the simulation during the deceleration phase because the accelerometer which contributes to the velocity calculation saturates at this point. Table 4 contains the peak velocity errors.

Table 4 Experimental peak velocity errors

Target velocity	Acceleration stroke	Error (actual – target)
2.0 m/s	50 mm	+0.01 m/s
3.0 m/s	50 mm	+0.02 m/s
3.0 m/s	30 mm	-0.03 m/s

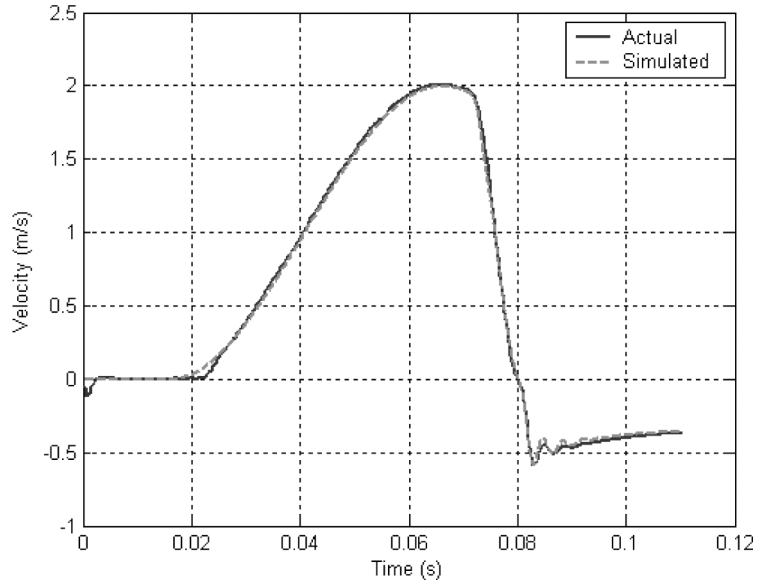


Fig 7
2m/s launch over
50mm stroke

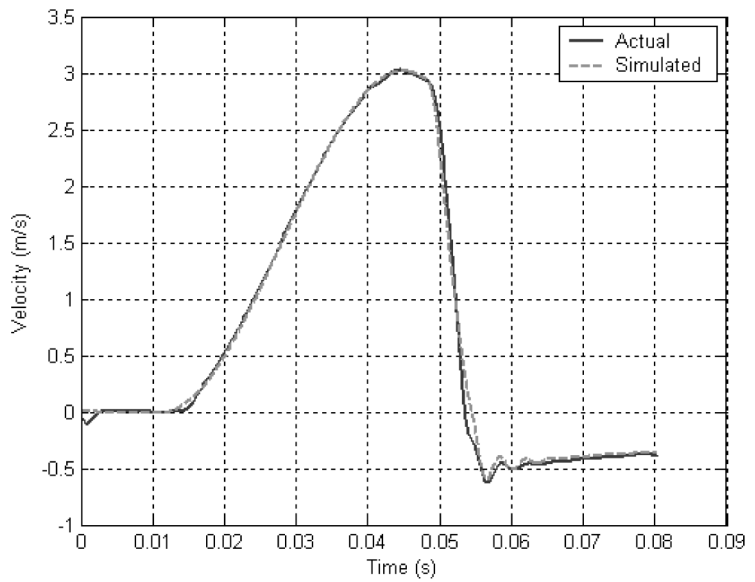


Fig 8
3m/s launch over
50mm stroke

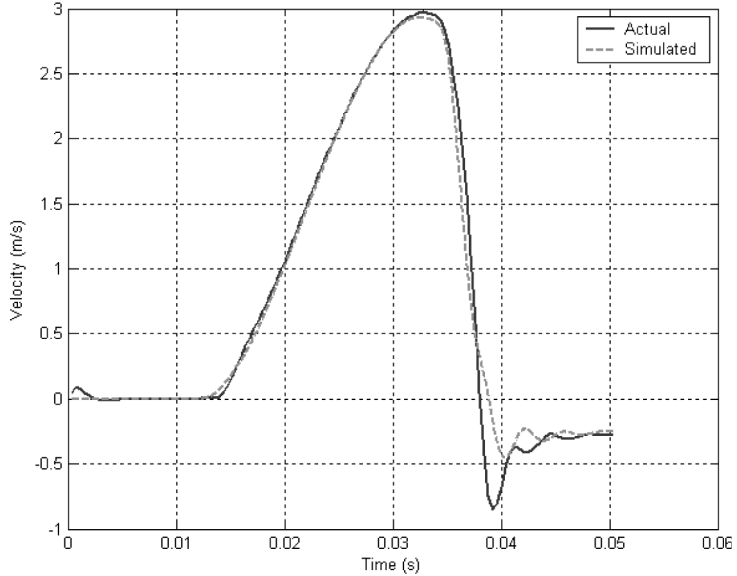


Fig 9
3m/s launch over
30mm stroke

4.4 Experimental results from the final system

The results presented thus far are for a trial system which has a limited velocity range. The final production launcher can achieve 15m/s, and some results are presented in this section. This launcher has a 20kN stall force actuator, a 3-stage 630 l/min valve, and a stroke of 350mm. Figure 10 shows the command velocity profile, the actual velocity achieved, and the predicted velocity (the output of the valve model in Figure 2), for a test with a 11.1m/s (40 km/h) target velocity. For comparison, Figure 11 shows the equivalent test with the non-linear pressure compensation term in the controller removed (i.e. $b = 1$). The actual velocity falls behind the predicted from around 0.04s, but towards the end of the launch the disturbance rejection ability of the closed-loop controller can be seen to be correcting the error.

Figure 12 shows the size of the non-linear pressure compensation term b during the 11.1m/s launch of Figure 10, and the accumulator discharge factor R_s from which it is partially derived, as calculated by the controller during the test. The simple linear accumulator model referred to in Section 2 (pressure drop proportional to actuator movement) is also shown to be close to the more conventional adiabatic discharge model in this Figure.

5 CONCLUSIONS

A closed-loop controller for a high-speed pedestrian impact test system has been designed and tested. Simulation and experimental results indicate that the required launch velocity is

achieved more accurately than open-loop control systems which have been used in the past. The experimental velocity errors are within 1% of the target velocity.

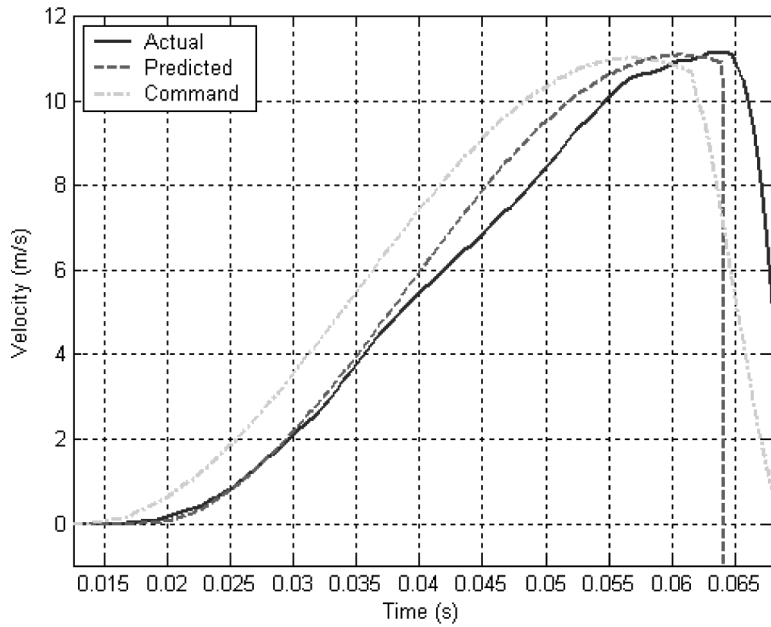
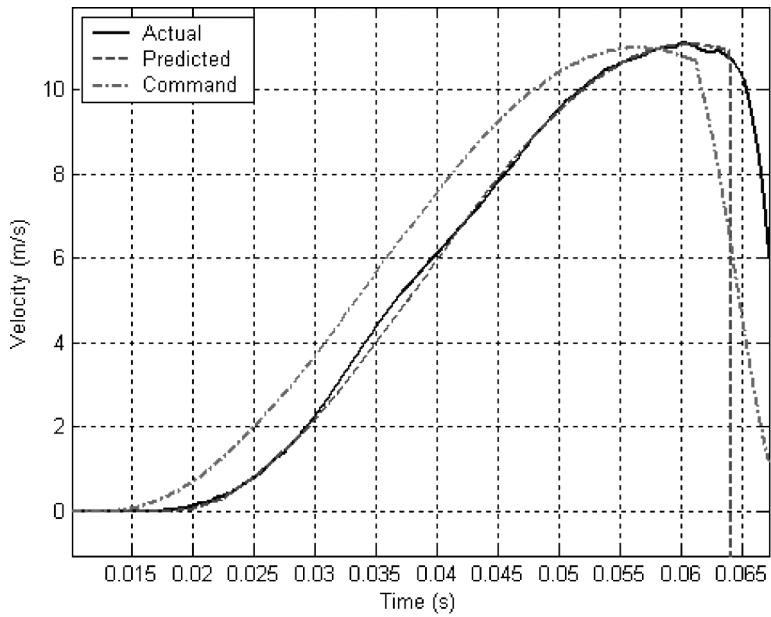


Fig. 11 11.1 m/s launch over 240mm stroke without non-linear pressure compensation

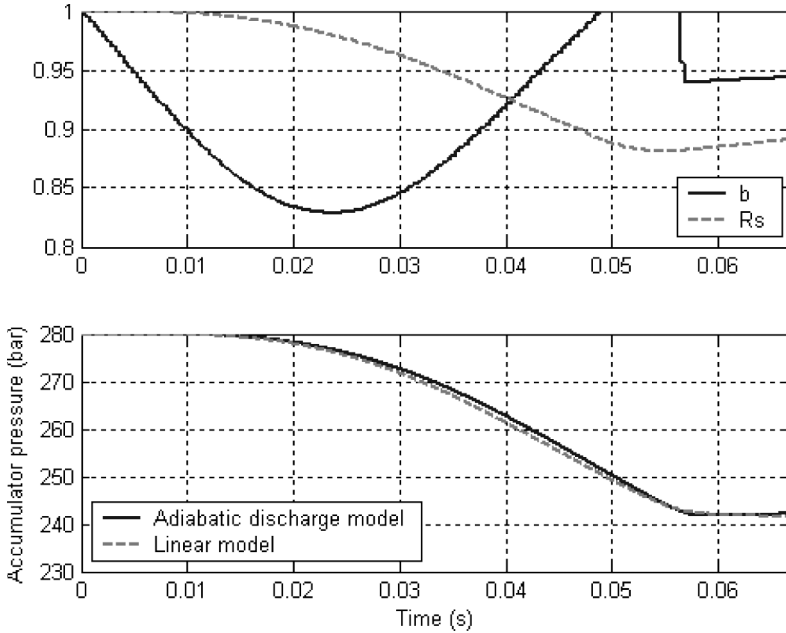


Figure 12 Pressure compensation term (b) and accumulator discharge for 11.1m/s launch

A non-linear correction of the flow gain is used to account for the varying pressure drop across the valve. A key approximation used in the development of the controller is to neglect the valve dynamics in relation to this correction. Hence the correction is effectively delayed. However, the results indicate that this makes little difference in this application because the variation in pressure is relatively low frequency compared to the bandwidth of the valve.

To use the controller for more general velocity control applications, two issues would have to be addressed. As in this application the load force is purely an inertial one, the cylinder pressure is easy to predict; in other applications this may not be the case. Secondly a command velocity has been chosen for which first and second derivatives are easy to derive; more generally this flexibility is not available.

REFERENCES

1. Plummer, A R (2001) "Iterative velocity control for a high speed hydraulic actuator". PTMC 2001, Bath, September 2001, 339-354.

2. Edge, K A (2003) "On the Control of Electrohydraulic Systems – Some Recent Research Contributions". The 8th Scandinavian International Conference on Fluid Power (SICFP03), Tampere, Finland, May 03.
3. Stoten, D P (2001) "Fusion of kinetic data using composite filters". Proc Instn Mech Engrs Vol 215 Part I, 483-497.

Pressure Peak Phenomenon in Digital Hydraulic Systems – a Theoretical Study

Arto Laamanen, Matti Linjama and Matti Vilenius

Institute of Hydraulics and Automation

Tampere University of Technology

ABSTRACT

This paper studies pressure peak phenomenon in modern on/off control systems based on the PCM control method. In PCM control systems, pressure peaks may occur because several valves are opened and closed simultaneously. In the ideal case, timing happens perfectly but in practice, switching times of the valves vary more or less. Due to this effect, valve or valves are sometimes closed before the next ones open (or vice versa), and a pressure peak occurs. Pressure peaks cause noise, may damage system and motion can be jerky and therefore, pressure peak minimization methods are worth thinking. Fundamental theory of the pressure peak phenomenon is discussed and different solutions to prevent pressure peaks are introduced based on the theory. One interesting option is Fibonacci coding which can be used instead of traditional binary coding in PCM control systems.

Keywords: Digital hydraulics, pressure peak, PCM control, Fibonacci coding

NOMENCLATURE

A_A, A_B	piston areas of the cylinder [m ²]
b	viscous friction [Ns/m]
K_h	hydraulic fluid spring constant [N/m]
L	stroke of the cylinder [m]
m	load mass [kg]
n	number of valves [-]
p_A, p_B	chamber pressures of the cylinder [Pa]
p_s	supply pressure [Pa]
p_t	tank pressure [Pa]
\dot{Q}	net flow rate into the volume [m ³ /s]
\dot{V}	pressurized volume [m ³]
v_0	initial velocity of the piston [m/s]
x	piston position [m]
β_{eff}	effective bulk modulus of the pressurized volume [Pa]
τ	error of the switching times [s]

- DFCU Digital Flow Control Unit
- PCM Pulse Code Modulation
- SMISMO Separate Meter In and Separate Meter Out

1. INTRODUCTION

A common stereotype has been that the on/off control technology is already antiquated and the old-fashioned on/off valves have nothing to do with the demanding motion control systems. However, the truth is divergent and modern on/off control systems with intelligent controllers have several suitable applications. These systems can even offer some new characteristics which are not available with the conventional control valves.

Basics of the modern on/off control strategies dates back to the early 20th century, but the longest steps have been taken in on/off control methods during the last decades due to significant enhancements both in digital hardware technology and signal processing. There are several ways to use on/off valves in hydraulic motion control systems, but only some of them have got more attention lately. One of them is Pulse Code Modulation (PCM) control method which was introduced in some patents already in 1960's [1, 2]. Although technology has improved a lot since those days, the basic idea is still the same: PCM control system consists of a number of parallel connected on/off valves whose flow capacities are not equal but for example in the ratios of $2^0:2^1:2^2:2^3:2^4$ etc. (see Figure 1). This kind of valve system is the key component of digital hydraulics and it is called Digital Flow Control Unit (DFCU).

PCM control allows stepwise flow control. The number of flow steps depends on the coding method, but for example binary coded valve series offers 2^n-1 different steps where n is the number valves. Different states of the DFCU with four valves are shown in table 1.

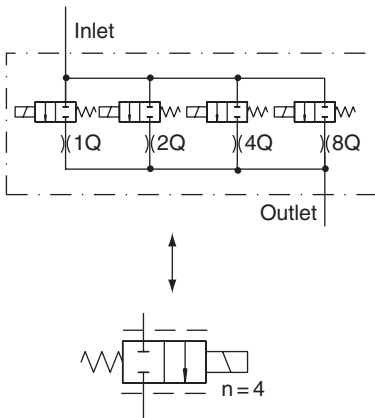


Figure 1. Digital Flow Control Unit (DFCU) and its simplified drawing symbol [3]. Q is one flow unit and n is the number of valves.

Table 1. Different states of the DFCU with 4 valves.

Net flow	Valve 1, Q	Valve 2, $2Q$	Valve 3, $4Q$	Valve 4, $8Q$	State
0	0	0	0	0	0
1xQ	1	0	0	0	1
2xQ	0	1	0	0	2
3xQ	1	1	0	0	3
4xQ	0	0	1	0	4
5xQ	1	0	1	0	5
6xQ	0	1	1	0	6
7xQ	1	1	1	0	7
8xQ	0	0	0	1	8
9xQ	1	0	0	1	9
10xQ	0	1	0	1	10
11xQ	1	1	0	1	11
12xQ	0	0	1	1	12
13xQ	1	0	1	1	13
14xQ	0	1	1	1	14
15xQ	1	1	1	1	15

0 = Valve is closed
 1 = Valve is open

Digital hydraulic motion control system can basically consist of one, two or four DFCUs depending on the control strategy. Separate Meter In and Separate Meter Out (SMISMO) control requires DFCUs both in pressure and in tank side as shown in figure 2.

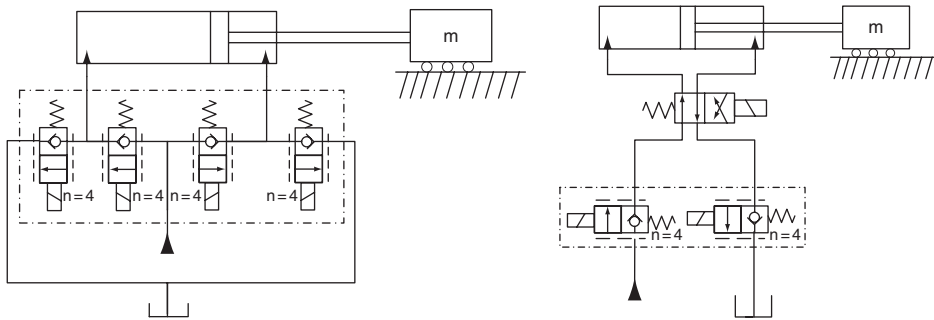


Figure 2. Two different ways to implement a SMISMO controlled cylinder application.

Systems of this type (figure 2) have been used for example in a mobile hydraulic boom mock-up and in a water hydraulic cylinder test bench. The results have been encouraging and the controllability of the digital hydraulic systems has been comparable with proportional or even with servo valves. One important factor in these digital hydraulic motion control systems is cost function based controller, which calculates steady state values for piston velocity and chamber pressures with all different valve combinations and then chooses the optimal valve combination. Controllers of this type enables for example to adjust flow area ratio during operation, which is not possible with traditional control valves. [3-6]

Modern on/off control systems have sophisticated characteristics nowadays, but they also have some drawbacks. A case in point is the pressure peak phenomenon, which has been associated to on/off valves over the years. If PCM control is compared to the basic bang-bang control, pressure peaks are in a more reasonable level in the PCM control systems. However, they are disadvantageous in any range since they cause noise, may damage components and motion can be jerky in control systems. Earlier studies have shown that pressure peaks occur only occasionally in digital hydraulics, but the risk of pressure peaks exists always when on/off valves are used with PCM control. Therefore, it is important to find a solution to minimize pressure peaks.

A traditional way to limit pressure peaks is to use pressure relief valves or different kind of accumulators. One unconventional but low-cost approach is so called hose accumulator with a cushion orifice which has been used successfully in a Low Pressure Water Hydraulic on/off control system [7]. Accumulators and pressure relief valves have some disadvantages and accordingly, this paper concentrates on the alternative pressure peak minimization methods. The fundamental theory of the pressure peak phenomenon in digital hydraulics is studied and based on the theory, different solutions to prevent pressure peaks are introduced.

2. PRESSURE PEAKS IN DIGITAL HYDRAULICS

2.1. Fundamental theory of pressure peak phenomenon in PCM control

PCM control system generates always a force pulsation when the load is needed to accelerate or decelerate to the new required velocity level. This is due to fact that the effective valve opening is changed stepwise. The magnitude of these force pulses depends on the load mass, system dynamics and the magnitude of velocity change [4]. However, these minor force pulses are not a problem in normal circumstances but harmful pressure peaks are mainly caused by the inexact switching times of the valves. Switching times of the on/off valves vary always more or less, and in the worst case some valves close before the next ones open (or vice versa) when DFCU state (see table 1) is changed. Uncertainties of the DFCU states are shown in the figure 3 where the grey bars illustrate the theoretical opening range of the DFCU implemented with extremely fast operating valves. It is important to note that the uncertainties of the effective openings shown in Figure 3 are valid only in the case when the state of the DFCU is changed linearly one by one. This is not the only or often the best way to control DFCU but states can be changed arbitrarily.

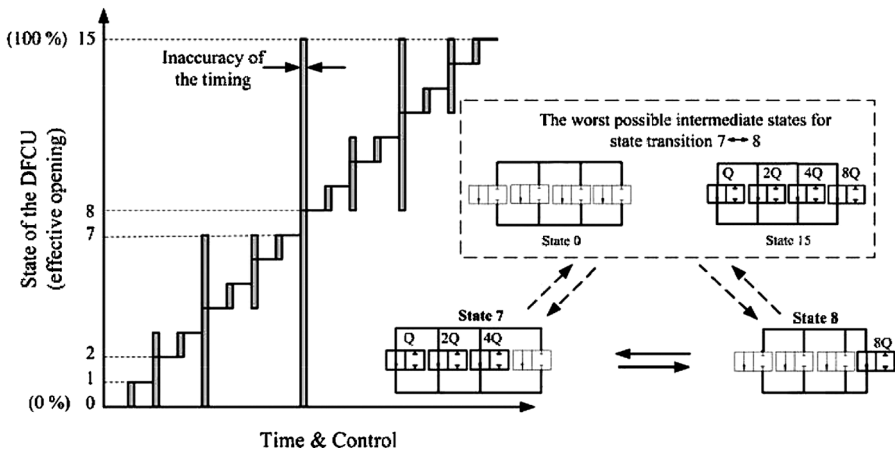


Figure 3. Uncertainties of the DFCU opening caused by the inaccurate switching of the valves. Control is changed linearly and then, the maximum error may occur in the state transition 7↔8.

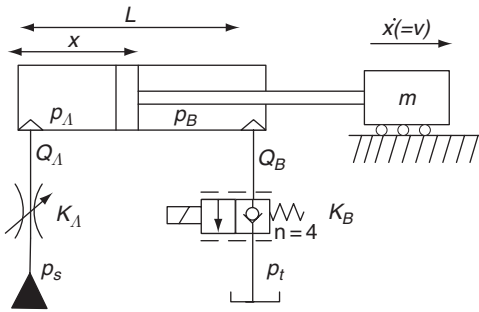
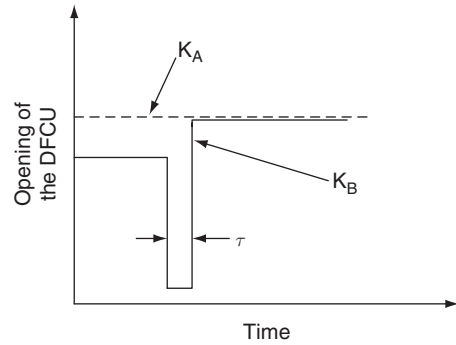
It can be noticed from Figure 3 that the transition from state 7 to state 8 is the most critical. This problem is faced up always when the state is changed from $2^{n-1}-1$ to state 2^{n-1} where n is the number of parallel connected valves. In this critical state transition, effective opening of the DFCU can be zero or maximum during a short term, if the worst possible intermediate state occurs.

From the viewpoint of pressure peaks, it is significant which DFCU fails to change state correctly in a SMISMO controlled cylinder application. Two different situations for the undesired pressure transients can be defined in the both control sides as shown in table 2.

Table 2. State transition failures of the DFCUs in SMISMO controlled cylinder application.

Effective opening	Forward side DFCU	Return side DFCU
Temporarily too low	pressure decreases, cavitation may occur	pressure may exceed supply pressure
Temporarily too high	pressure may increase up to supply pressure	pressure decreases, no cavitation

In practice, state transition failures occur separately but openings can fail also in both sides at the same time. All the different combinations are not reasonable to study and hence, this study concentrates only on the worst case: the most harmful pressure peaks occur when flow is restricted too much in the tank side due to failed state transition. This is studied in a simplified system shown in figure 4. There is only one DFCU in the return side and in the other side flow is restricted with an orifice. Supply pressure is p_s , tank pressure is p_t , load mass is m , the stroke of the cylinder is L and piston position is x . Figure 5 introduces a detail of a partly failed state transition in the system studied. τ is the error of the switching times and K_B shows the opening of the DFCU.


Figure 4. A simplified cylinder application.

Figure 5. A partial state transition failure, where some of the closing valves close before the next valves reach to open.

2.2. Calculation methods for pressure peaks

Pressure rate in a volume can be calculated if there is a difference in incoming and outgoing volumetric flow rates. The rate of pressure can be written as:

$$\frac{dp}{dt} = \frac{\beta_{eff}}{V} \left[Q - \frac{dV}{dt} \right] \quad (1)$$

where β_{eff} is the effective bulk modulus of the pressurized volume [Pa]
 V is the pressurized volume [m^3]
 Q is the net flow rate into the volume [m^3/s]

In the system of figure 4 with the given symbols, this equation can be applied as:

$$\dot{p}_A = \frac{\beta_{eff}}{V_A} \left[K_A \sqrt{p_s - p_A} - A_A \dot{x} \right] \quad (2)$$

$$\dot{p}_B = \frac{\beta_{eff}}{V_B} \left[K_B \sqrt{p_B} + A_B \dot{x} \right] \quad (3)$$

where p_A, p_B are chamber pressures
 A_A, A_B are piston areas

Load mass m can be assumed to be infinite in the cylinder applications where pressure peak duration τ is short compared to the natural frequency of the system ($\tau \ll 1/f_n$). Hence, the velocity of the load \dot{x} is unchangeable because acceleration \ddot{x} is according to force equation:

$$\ddot{x} = \frac{p_A A_A - p_B A_B}{\infty} \rightarrow 0 \quad (4)$$

In spite of the assumptions, pressures $p_A(t)$ and $p_B(t)$ are difficult to solve explicitly from the above differential equations (equations 2 & 3) which forces to use numerical methods in the solution. This may cause some problems if these equations are used in the cost function based controller [4-6] where a large number of different valve states must be compared in advance in order to find the optimal valve combination.

The above equations are universal in cylinder applications and they are valid in all different state transition failures. However, pressure peaks can be calculated also with the other methods in some specific state transitions. One interesting target is to approximate pressure peaks when the outlet flow is temporarily (τ) blocked ($K_B=0$) which is the worst possible state transition failure. In this case, the equation 3 can be simplified to:

$$\dot{p}_B = \frac{\beta_{eff}}{V_B} A_B \cdot \dot{x} \quad (5)$$

Velocity (see equation 4) and volume V_B are assumed to be constant during the state transition failure and then, approximation of the pressure rise is:

$$p_B(t) \approx \int_0^t \frac{\beta_{eff}}{V_B} A_B \cdot v \cdot dt = \frac{\beta_{eff}}{V_B} A_B \cdot v \cdot t \quad (6)$$

Equation 4 ($\ddot{x} = 0$) does not come true always and then, pressure rise calculation can be based on the equation of the motion which takes into account the load mass. When the piston of the cylinder is moving at a certain velocity and then flow is suddenly stopped, load tries to continue motion. It can be assumed that kinetic energy is stored in the fluid

spring as potential energy and subsequently, the system can be expressed as a second order harmonic oscillator:

$$m \cdot \Delta \ddot{x} + K_h \cdot \Delta x = 0 \quad (7)$$

$$\Delta x = \frac{v_0}{\omega} \cdot \sin \omega t \quad (8)$$

where $\omega = \sqrt{\frac{K_h}{m}}$ is natural frequency

K_h is hydraulic fluid spring constant [N/m]
 x is piston position [m]
 v_0 is initial velocity [m/s]

Based on these equations, pressure rise in chamber B is:

$$\Delta p_B = \frac{\beta_{eff} \cdot A_B}{V_B} \cdot \frac{v_0}{\omega} \cdot \sin \omega t \quad (9)$$

Merritt [8] studied the pressure peak phenomenon in a cylinder application where both flows were blocked. In this case, pressures vary equal but opposite amounts until forward chamber pressure becomes zero if the volumes and the areas of the actuator are equal in the both sides. Due to this phenomenon, pressure is defined piecewise in two intervals where the first one assumes two hydraulic fluid springs:

$$K_h = \frac{\beta_{eff} \cdot A_A^2}{V_A} + \frac{\beta_{eff} \cdot A_B^2}{V_B} \quad (10)$$

In the system studied, the flow is blocked only in the return side and then, it can be assumed that forward pressure p_A is constant until return pressure p_B has caused the velocity change. Therefore, fluid spring in the return chamber is dominant and hence, hydraulic fluid spring can be considered as:

$$K_h = \frac{\beta_{eff} \cdot A_B^2}{V_B} \quad (11)$$

2.3. Simulation of the pressure peaks in a cylinder application

The target of the simulations is to visualize the effect of different parameters on pressure peaks and to compare different pressure calculation methods to simulation model. The simulations are based on the low pressure water hydraulic (LPWH) cylinder application shown in figure 4. It consists of a cylinder ($\phi 32/16 \times 500$), one DFCU in the return side, load, and constant pressure source ($p_s=3\text{MPa}$). Only viscous friction ($b=150\text{ Ns/m}$) is included in the simulation model. The load is 200 kg and the effective bulk modulus is 900 MPa. The valves are direct acting poppet type on/off valves and their flow capacities are

according to binary series, i.e. 0.2, 0.4, 0.8 and 1.6 l/min at 0.1 MPa pressure differential. The switching time delays of the valves are 10/10 ms and time constant is 1 ms. Flow coefficient of the forward side orifice (K_A) is fixed and it is 2.0 l/min (at $\Delta p=0.1$ MPa).

Figure 6 introduces the effect of the switching time error on the chamber pressures in a system which was introduced in figure 4. In the simulations the biggest valve is opened too slowly and then, in the state transition $7 \rightarrow 8$ all the small valves are closed before the biggest valve opens. When this happens, pressures in both chambers change into same direction, but pressure transient is bigger in the side where switching has failed. In the other side, minor pressure transient is caused by the velocity change. Together with switching time error, piston position has also a significant role in pressure peak phenomenon. When the return chamber has low volume at the near of cylinder end, pressure peaks are highest as shown in figure 7.

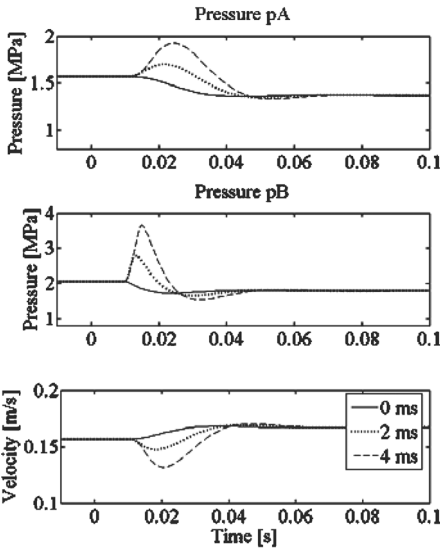


Figure 6. Effect of the opening time error of the biggest valve in the system studied (see figure 4). Control command for the state transition $7 \rightarrow 8$ is given at 0 s and piston position is 0.2 m.

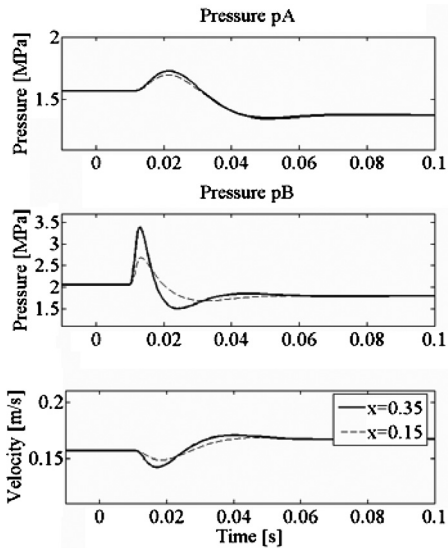


Figure 7. Effect of the piston position. Switching time error of the biggest valve is 2 ms.

Pressure peaks are studied with the certain switching time errors in the simulation model and these results are compared to different pressure peak calculation methods (see section 2.2) in the figure 8. The differences in the pressure values are distinguished significantly not until switching time error is more than 5 ms. In most systems, switching time errors are short in the relation to natural frequency and hence, all these equations can be used to approximate pressure rise caused by the worst possible state transition failures.

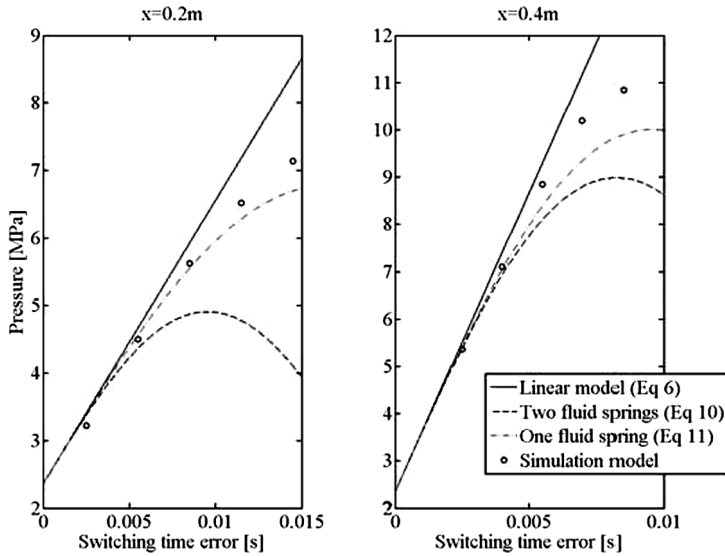


Figure 8. Comparison of the different equations (eq 6, 10 & 11) and simulation model.

3. MINIMIZATION OF THE PRESSURE PEAKS IN DIGITAL HYDRAULICS

Pressure peaks do not belong to modern hydraulic motion control systems and therefore, it is reasonable to try to minimize them. One alternative is to prevent the formation of the pressure peaks and the other, but not the primary solution is to take care of the pressure peak symptoms. These different solutions are discussed in this section.

3.1 Components

3.1.1 Valves

The basic reasons for pressure peaks in digital hydraulics are on/off valves and the control method. Valves should change their state simultaneously but in practise, switching times vary more or less which means that timing fails some times. This inaccuracy causes a short-term error to the flow rate and as a result, a pressure peak may occur. Hence, PCM control systems do not require extremely fast valves, but minor variation in delays is a requested quality.

Experimental measurements [9, 10] have shown that the main reasons for switching time variation of the poppet type oil hydraulic 2-way valves are changes in pressure difference over the valve and in viscosity. Varying concerns especially closing times, and opening times are more constant. Variation of the switching times is almost negligible in fixed circumstances and therefore, a challenge of the pressure peak minimization is how to define switching times in a reliable way in changing circumstances. One basic approach is to define valve delays in the certain operating points, but switching times can be defined also continuously during the system operation.

3.1.2 Control electronics

On/off valves have a certain delay due to their dynamics, but control electronics has also an important role in the formation of delays. It is difficult to improve significantly valve dynamics afterwards but delays caused by the control electronics are possible to minimize. This has been established in the experimental tests where the switching times of commercial water hydraulic valves have been enhanced. Measured opening delays of a simple direct acting 2-way poppet valve varied between 20 and 32 ms and closing delays between 7 and 12 ms when the valve was controlled with a basic control electronics [11]. After replacing the control electronics with more sophisticated control electronics, switching time delays were decreased considerably and they were varying between 8 and 14 ms. The improved control electronics is described more closely in [6].

3.1.3 Accumulators and pressure relief valves

A traditional way to minimize pressure peaks is implemented for example by using accumulators or low-hysteresis pressure relief valves. However, these are not the primary solution for pressure peak problem in digital hydraulics because they are “healing” the symptoms and not preventing the occurrence of pressure peaks. In addition, disadvantage of the accumulators is that they increase the costs, they are bulky and in addition, stiffness of the system is reduced. [8]

3.2 Coding methods

Lack of good and suitable valves will remain also in near future and therefore, it is reasonable to try to solve the pressure peak problem in the other ways. One solution is alternative coding method. PCM control is traditionally based on the binary coding which has advantages (e.g. high resolution), but also some disadvantages, such as the high risk of pressure peaks. Hence, if pressure peaks are wanted to minimize, the other coding methods are worth taken into account. One alternative is a system where parallel connected valves have equal flow capacities. This control method is known as Pulse Number Modulation (PNM). It has no risk for pressure peaks because valves are either opened or closed but not both simultaneously. Disadvantage of the PNM control is that in order to get good resolution, a large number of valves are required. For example, same resolution as in PCM control with four valves requires 15 valves in PNM system. In most cases a large number of valves are not accepted because of the physical size problem and therefore, the other more suitable options are worth thinking.

One of the alternative coding methods is based on Fibonacci coding [12]. The basic system is same as in the normal PCM control method, but the flow capacities of the valves are not in the ratios of binary series but according to Fibonacci numbers. The ideal Fibonacci sequence is 0, 1, 1, 2, 3, 5, 8... F_n , where F_n is the sum of the two preceding elements.

The advantage of the Fibonacci coding compared to the traditional binary coding is that it is possible to compose nearly all individual flow rates at least with two combinations of the open valves (see table 3).

Table 3. Same flow rates can be achieved with different valve combinations in Fibonacci coded system. Flow capacities of the valves are Q, Q, 2Q, 3Q and 5Q.

Option 1							Option 2						Option 3					Option 4						
Net flow	Valve 1, Q	Valve 2, Q	Valve 3, 2Q	Valve 4, 3Q	Valve 5, 5Q	State	Valve 1, Q	Valve 2, Q	Valve 3, 2Q	Valve 4, 3Q	Valve 5, 5Q	State	Valve 1, Q	Valve 2, Q	Valve 3, 2Q	Valve 4, 3Q	Valve 5, 5Q	State	Valve 1, Q	Valve 2, Q	Valve 3, 2Q	Valve 4, 3Q	Valve 5, 5Q	State
0	0	0	0	0	0	0	-	-	-	-	-	-	-	-	-	-	-	-	-	-	-	-	-	-
1xQ	1	0	0	0	0	1	0	1	0	0	0	2	-	-	-	-	-	-	-	-	-	-	-	-
2xQ	0	0	1	0	0	4	1	1	0	0	0	3	-	-	-	-	-	-	-	-	-	-	-	-
3xQ	0	0	0	1	0	8	0	1	1	0	0	6	1	0	1	0	0	5	-	-	-	-	-	-
4xQ	0	1	0	1	0	10	1	1	1	0	0	7	1	0	0	1	0	9	-	-	-	-	-	-
5xQ	0	0	0	0	1	16	1	1	0	1	0	11	0	0	1	1	0	12	-	-	-	-	-	-
6xQ	0	1	0	0	1	18	0	1	1	1	0	14	1	0	0	0	1	17	1	0	1	1	0	13
7xQ	0	0	1	0	1	20	1	1	1	1	0	15	1	1	0	0	1	19	-	-	-	-	-	-
8xQ	0	0	0	1	1	24	0	1	1	0	1	22	1	0	1	0	1	21	-	-	-	-	-	-
9xQ	0	1	0	1	1	26	1	1	1	0	1	23	1	0	0	1	1	25	-	-	-	-	-	-
10xQ	0	0	1	1	1	28	1	1	0	1	1	27	-	-	-	-	-	-	-	-	-	-	-	-
11xQ	0	1	1	1	1	30	1	0	1	1	1	29	-	-	-	-	-	-	-	-	-	-	-	-
12xQ	1	1	1	1	1	31	-	-	-	-	-	-	-	-	-	-	-	-	-	-	-	-	-	-

Fibonacci coding enables to avoid state transitions where exist a risk that all valves are closed during a short term due to failed state transition. This requires that the controller tries to keep as many valves open during the state transitions as possible (figure 9, control A). As a comparison, control B (figure 9) does not take into account the risk of pressure peaks.

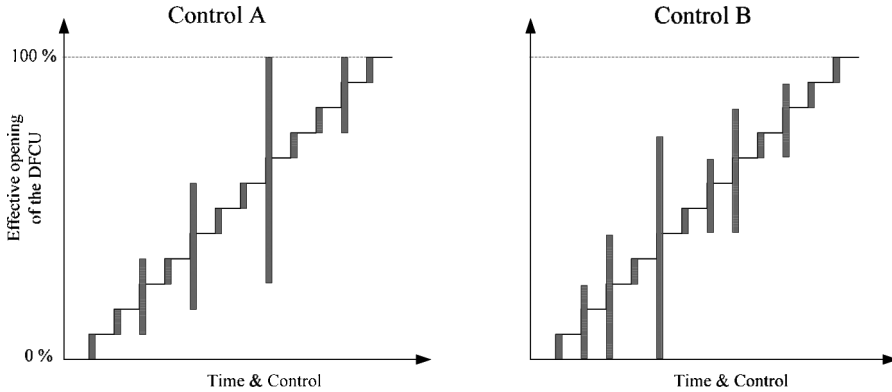


Figure 9. Opening uncertainties of the Fibonacci coded DFCU with two different control strategies. Control is changed linearly one by one state in both cases.

3.3 Controller

Controllers based on the cost functions have been developed and used successfully in digital hydraulic applications by Linjama et al. [4-6]. These controllers have shown their capabilities and therefore, pressure peak minimization can be also based on the cost function method.

In PCM control system, the size of the pressure peaks depends on the flow capacity of the valves. For example, unsuccessful timing of the biggest valve causes several times higher

pressure peak than the smallest valve. Therefore, it is reasonable to concentrate on the operation of the biggest valves. In addition, if the equations of the section 2.2 are studied more closely, it can be noticed that e.g. piston position and velocity have also influence on pressure peaks size. Accordingly, these variables should be included in the cost function.

Cost function method has been used earlier only with binary coded DFCUs, but Fibonacci coding can increase the potentiality of the cost function. This originates from the characteristic that different flow rates can be achieved with a number of valve combinations. This enables that the state transitions of the valves can be minimized even without velocity error. Some simulation results of the system studied (see figure 4) are shown in figures 10-12. Flow capacities of the valves in the Fibonacci coded system are 0.2, 0.2, 0.4, 0.6 and 1.0 l/min (at $\Delta p=0.1$ MPa). Binary coded DFCU has same flow capacities as in section 2.3 and accordingly, the smallest valve has same flow capacity in both systems. It is important to note that in this case, the maximum flow capacity of the Fibonacci coded DFCU is lower than in binary coded DFCU. There would have been also other options to choose flow capacities of the Fibonacci system, i.e. to choose same flow capacity for the biggest valve as in binary coded system or to size flow capacities in a way which offers the same total flow capacity in both DFCUs.

Switching times of the biggest valve are delayed 3 ms in the simulations in order to cause pressure peaks. Piston position is approximately 0.25 m during the state transitions. Flow coefficient of K_A is 1.6 l/min (at $\Delta p=0.1$ MPa) and the reference flow rate is $6Q \rightarrow 9Q \rightarrow 7Q$.

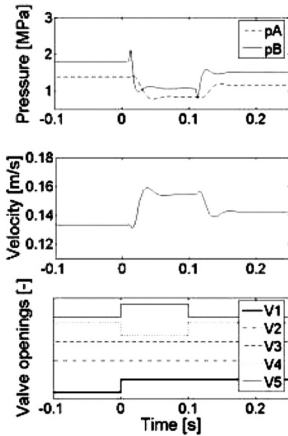


Figure 10. State transitions $14 \rightarrow 23 \rightarrow 15$ ($=6Q \rightarrow 9Q \rightarrow 7Q$) in the Fibonacci coded DFCU

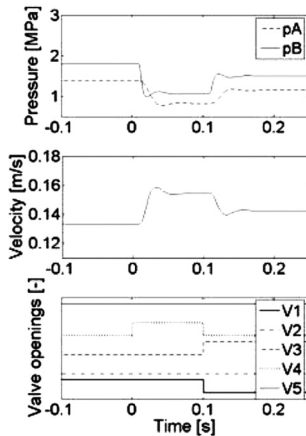


Figure 11. State transitions $17 \rightarrow 25 \rightarrow 20$ ($=6Q \rightarrow 9Q \rightarrow 7Q$) in the Fibonacci coded DFCU

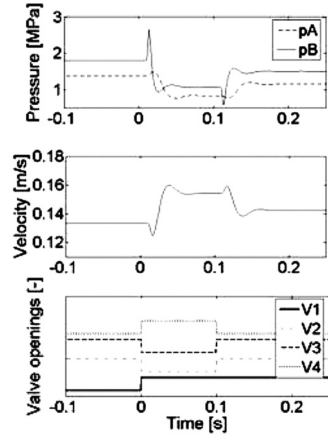


Figure 12. State transitions $6 \rightarrow 9 \rightarrow 7$ ($=6Q \rightarrow 9Q \rightarrow 7Q$) in the binary coded DFCU.

Depending on the original state, Fibonacci system has different options to achieve the required flow rates ($6Q \rightarrow 9Q \rightarrow 7Q$). In the figure 10, states of the DFCU are 14, 23 and 15 (see table 3) and then, a slight pressure peak occurs. If the initial state is 17, same step responses can be made for example by using states 25 and 20 (figure 11), and no pressure

peak is observed. As a comparison, binary coded DFCU (figure 12) has a higher pressure peak than Fibonacci coded DFCU in the worst case.

5. DISCUSSION AND CONCLUSIONS

Pressure peak phenomenon is closely related to switching times of the valves in digital hydraulics and especially, to switching time variation. Together with switching time variation, it is significant which DFCU fails to change state. The most severe pressure peaks are caused by the return side DFCU which supports the use of meter-in control. However, meter-in control is not suitable in some applications (e.g. overrunning loads) and in addition, it does not offer as good controllability as SMISMO control.

According to the earlier experimental studies, pressure peaks can be limited to the acceptable level also in SMISMO controlled systems. This requires careful tuning of the controller and in addition, circumstances (pressures, viscosity etc.) should stay constant. This problem can be fixed by adjusting switching times adaptively based on the system behavior. Switching times can be defined also in different operating points, and the controller uses these tabulated switching time values. Pressure decrease or in the worst case cavitation, are often less harmful than pressure peak and then, valves can be controlled with the intention that worst possible pressure peak does not occur in any circumstances. This is possible to implement by delaying either opening or closing times of the valves in a suitable way.

Together with switching time tuning, the most promising pressure peak minimization methods are cost function based controllers and the alternative coding methods (e.g. Fibonacci coding), and these methods together. The target of the future research is to develop a controller which limits efficiently pressure peaks. Development of the cost function based controller will be grounded on the theory which was introduced in this paper. However, there are some challenges. For example, the number of tuning parameters spread out easily in cost functions which may lead to complex controllers. Fibonacci coded DFCU has also disadvantages, such as lower resolution than binary coded DFCU, but this can be solved by using one or more extra valves in the Fibonacci coded DFCU.

ACKNOWLEDGMENTS

The research was supported by the Academy of Finland (Grant No. 80411).

REFERENCES

1. Bower, J. 1961. Digital fluid control system. US Patent No. 2999482.
2. Murphy, R. E. 1962. Hydraulic control system. US Patent No. 3038449.
3. Laamanen, A., Linjama, M., Tammisto, J., Koskinen, K.T. & Vilenius, M. 2002. Velocity control of water hydraulic motor. Proceedings of the 5th JFPS International Symposium on Fluid Power, Nara 2002, November 13, 2002. Japan. pp. 167-172.

4. Linjama, M., Koskinen, K. T. & Vilenius, M. 2003. Accurate trajectory tracking control of water hydraulic cylinder with non-ideal on/off valves. *International Journal of Fluid Power*, Vol. 4, No. 1. pp. 7–16.
5. Linjama, M. & Vilenius, M. 2004. Digital hydraulic control of a mobile machine joint actuator mockup. *Bath Workshop on Power Transmission and Motion Control (PTMC 2004)*. Suffolk, UK. Burrows, C.R., Edge, K.A. & Johnston, D.N. pp. 145-158.
6. Linjama, M., Koskinen, K. T. & Vilenius, M. 2005. Improved digital hydraulic tracking control of water hydraulic cylinder drive. *International Journal of Fluid Power*, Vol. 6, No. 1. pp. 29-39.
7. Linjama, M., Koskinen, K. & Vilenius, M. 2000. Suppression of pressure transients in on/off control of low-pressure water hydraulic cylinder. In: Burrows, C.R. & Edge, K.A. (eds.). *Bath Workshop on Power Transmission and Motion Control (PTMC 2000)*. pp. 199-212.
8. Merritt, H. E. 1967. *Hydraulic control systems*. John Wiley & Sons, Inc. New York. 358 p.
9. Laamanen, A., Linjama, M. & Vilenius, M. 2003. Characteristics of a Digital Flow Control Unit with PCM control. *7th Triennial International Symposium on Fluid Control, Measurement and Visualization, Sorrento, Italy, August 25-28, 2003*. Edinburgh, UK. Optimage Ltd., Edinburgh, UK, EH10 5PJ. pp. 1-16.
10. Laamanen, A., Siivonen, L., Linjama, M. & Vilenius, M. 2004. Digital Flow Control Unit - an alternative for a proportional valve? *Bath Workshop on Power Transmission and Motion Control (PTMC 2004)*. Suffolk, UK. Burrows, C.R., Edge, K.A. & Johnston, D.N. pp. 297-308.
11. Linjama, M., Koskinen, K., Tammisto, J. & Vilenius, M. 2000. Two-way solenoid valves in low-pressure water hydraulics. In: McLain, T. & Kim, D. *Fluid Power Systems and Technology 2000. The 2000 ASME International Mechanical Engineering Congress and Exposition, November 5-10, 2000, Orlando, Florida, USA*. pp. 55-60.
12. Laamanen, A., Nurmia, M., Linjama, M., Koskinen, K. T. & Vilenius, M. 2003. Two different control methods for Digital Flow Control Unit. *Proceedings of the Eight Scandinavian International Conference on Fluid Power, May 7–9 2003, Tampere, Finland*. pp. 887-898.

Water Hydraulic Systems

Control of Water Hydraulic Manipulator with Proportional Valves

Harri Sairiala, Kari T. Koskinen and Matti Vilenius

Tampere University of Technology, Institute of Hydraulics and Automation

ABSTRACT

Water hydraulics is an environmentally safe technology since the fluid is pure tap water. Water is also fire safe and cheap. Water hydraulic technology has been a subject to an intensive research in the last two decades. However the research of water hydraulics in manipulator control has been quite rare. This paper presents the basics of 2-degree of freedom manipulator control with water hydraulic proportional valves. The manipulator is a normal crane with water hydraulic actuators and control valves. The control system is used to realize manipulator tool-end coordinate control. Good results are achieved in final positioning accuracy of the tool-end. More research will be needed to improve the follow-up accuracy of the system.

NOMENCLATURE

x = x-coordinate of the tool-end [m]

y = y-coordinate of the tool-end [m]

θ_1 = Joint angle of lifting joint [deg]

θ_2 = Joint angle of tilting joint [deg]

L_1 = Distance between lifting and tilting joint [m]

T_x = Distance of tilting joint and tool-end in x-direction [m]

T_y = Distance of tilting joint and tool-end in y-direction [m]

S_x = Distance of station frame origin and lifting joint in x-direction [m]

S_y = Distance of station frame origin and lifting joint in y-direction [m]

1 INTRODUCTION

The interest for an environmentally friendly technology with controllability of water hydraulics but lower price level has encouraged the development low-pressure water hydraulics (LPWH). The original aim was to develop a fluid power technology with a price level of pneumatics and controllability of water hydraulics (1). In oil hydraulics proportional valves are widely used in controlling actuators but in LPWH the problem is the lack of suitable valves. Some valves exist on the market (2), (3). Also development of a low-cost proportional valve for LPWH has been going on (4), (5).

The most cost-effective solution for controlling a low-pressure water hydraulic system is the use of on/off valves. These valves are reliable, inexpensive and they already exist on the market. A lot of research has been carried out lately on this area and the results show that on/off control gives quite good results in LPWH (6). However, smooth movements or accurate path following are often needed. These can be quite difficult to realize with on/off technology and therefore proportional valves are needed.

The control of manipulators or cranes is a traditional area in oil hydraulics but there is very little published information about control of water hydraulic manipulators. In (7) some results of water hydraulic manipulator control was presented. This paper presents water hydraulic 2-degree of freedom manipulator control with proportional 4/3-way control valves.

2 MANIPULATOR POSITION CONTROL

The purpose in the coordinate control of the manipulator is to control the joint angles to achieve a desired position for the tool-end of the manipulator. Figure 1 shows a block diagram of the coordinate control system. Reference tool-end coordinates are given to the system as an input. Trajectory generation calculates the reference trajectory from the starting point to the given coordinates in a given time. From the reference trajectory the needed joint angles and actuator positions are calculated with inverse kinematics. Position controller controls the actuator positions with the feedback signal from the pulse encoders. In this paper the position controllers are proportional controllers.

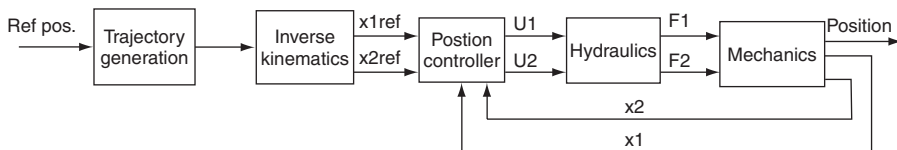


Figure 1. Block diagram of the manipulator coordinate control.

2.1 Inverse kinematics

The inverse kinematics is calculated from the geometry of the manipulator. The aim is to calculate the needed actuator positions to achieve a needed tool-end position in the XY-plane. Since the manipulator has only 2 degrees of freedom, for each tool-end coordinate

there is only one possible set of actuator positions. Hence further optimization for choosing the actuator positions is not needed as it would be if there were more degrees of freedom. Figure 2 shows the geometry of the manipulator and a table containing the manipulator dimensions.

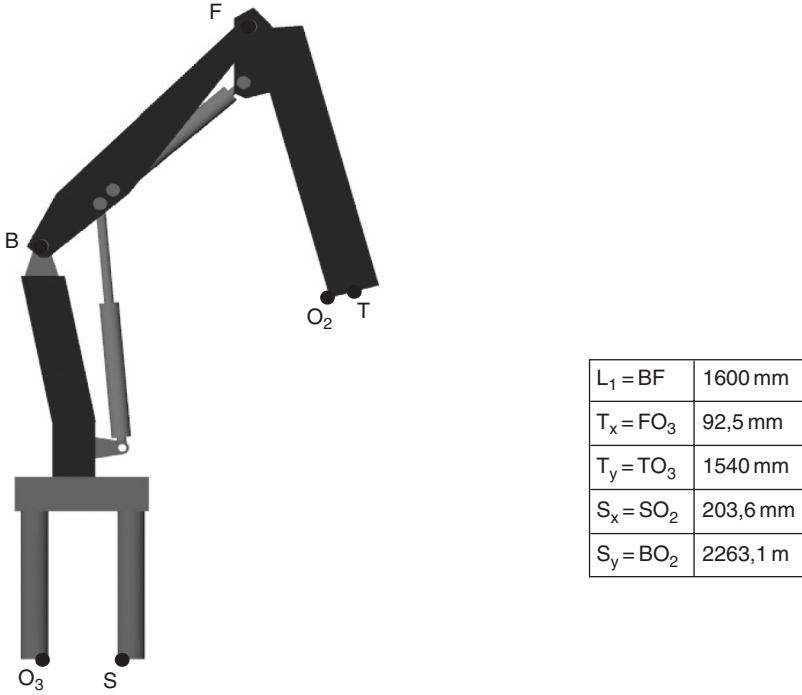


Figure 2. The geometry of the manipulator and dimension table.

Needed joint angles can be calculated from the tool-end reference coordinates with equations 1 (lifting joint) and 2 (tilting joint).

$$\theta_1 = a \cos \frac{L_1^2 - T_x^2 - T_y^2 + (S_x + x)^2 + (S_y - y)^2}{2 \cdot L_1 \sqrt{(S_x + x)^2 + (S_y - y)^2}} + a \tan \left(\frac{S_x + x}{S_y - y} \right) - 90^\circ \quad (1)$$

$$\theta_2 = a \cos \frac{L_1^2 + T_x^2 + T_y^2 - (S_x + x)^2 - (S_y - y)^2}{2 \cdot L_1 \sqrt{T_x^2 + T_y^2}} - a \tan \left(\frac{T_x}{T_y} \right) + 180^\circ \quad (2)$$

3 TEST SYSTEM

The test system is a HIAB 031 crane with pure tap water hydraulic circuit. The hydraulic circuit of the test system is shown in figure 3. The test system consists of a water hydraulic power pack, 2 4/3-way proportional control valves and two water hydraulic cylinders. The supply pressure of the hydraulic circuit is 50 bar. The cylinder piston positions are measured with pulse encoders and joint angles are calculated from the actuator positions.

The control valves are water hydraulic 4/3-way proportional control valves originally designed for water. The structure and characteristics of the valves are published in [3]. The valves are high quality proportional valves with spool position feed back and PI-controller. The static flow curve of the valves is not linear which causes nonlinearities in the system. These nonlinearities can be compensated in the control systems as Mäkinen et al. presented [8]. Nonlinearity compensation can be used effectively to improve the position accuracy of the control system [9] [10]. In this paper however the nonlinearity compensation has not been used.

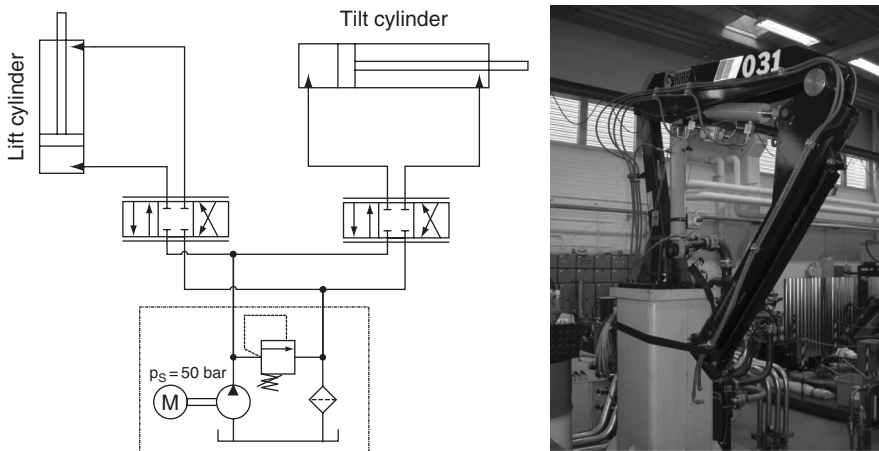


Figure 3. The hydraulic circuit and a photograph of the test system.

Figure 4 show the working area of the manipulator. Originally the oil hydraulic version of the manipulator had a larger working area but only lifting and tilting cylinders are used with water hydraulics and the telescope is not working. The maximum height of the tool-end of the manipulator is 3,18m.

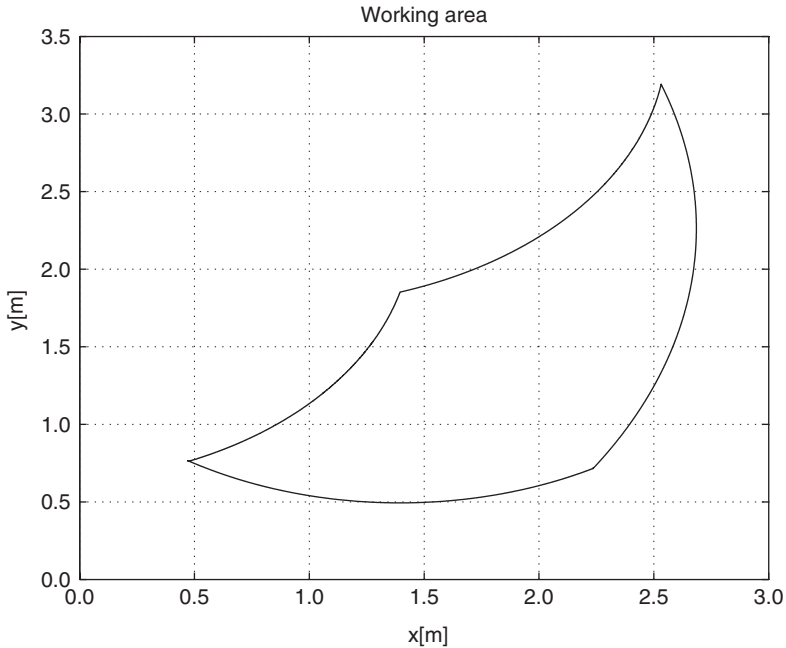


Figure 4. Working area of the manipulator.

4 EXPERIMENTAL RESULTS

The supply pressure in the tests was 50 bar. The reference trajectory is a square with corner points (2m; 1,5m), (2m; 1m), (1,5m; 1m), and (1,5m; 1,5m). The reference signal of the movement between the corner points is a trapezoid, which is calculated for each tool-end movement with 2,5s movement time. From this reference trajectory a position reference for each actuator is calculated with inverse kinematics.

Figure 5 shows a measured square response. In the left hand side figure the tool-end position and reference position is presented. In the right hand side figure the tool-end position error during the measurement is presented. The tool-end position error in the x-direction is less than 10mm and in the y-direction less than 20mm during the whole trajectory. The final tool-end positioning accuracy in x-direction is better than 0,6mm and in y-direction better than 0,5mm in all the corner points.

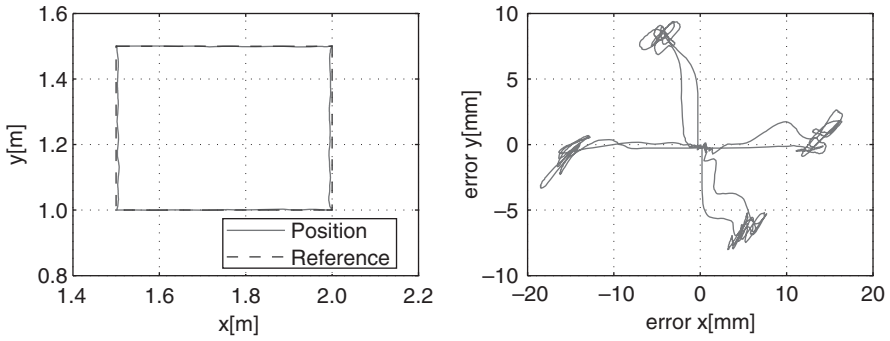


Figure 5. Tool-end position and position error.

Figure 6 shows the joint angles and angular errors during the same trajectory. The angular errors in both joints are less than 0,8 degrees during the movement. The steady state angular errors are less than 0,05 degrees.

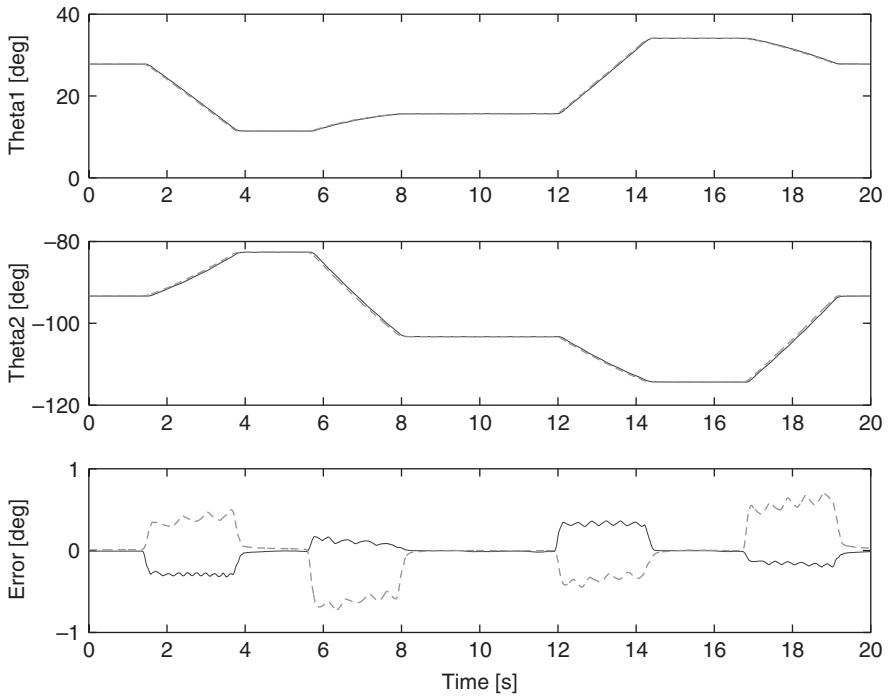


Figure 6. Joint angles and angular errors.

Figure 7 shows the actuator velocities in the measured movement. The maximum velocities of the lifting and tilting cylinders are 320 mm/s and 330 mm/s respectively.

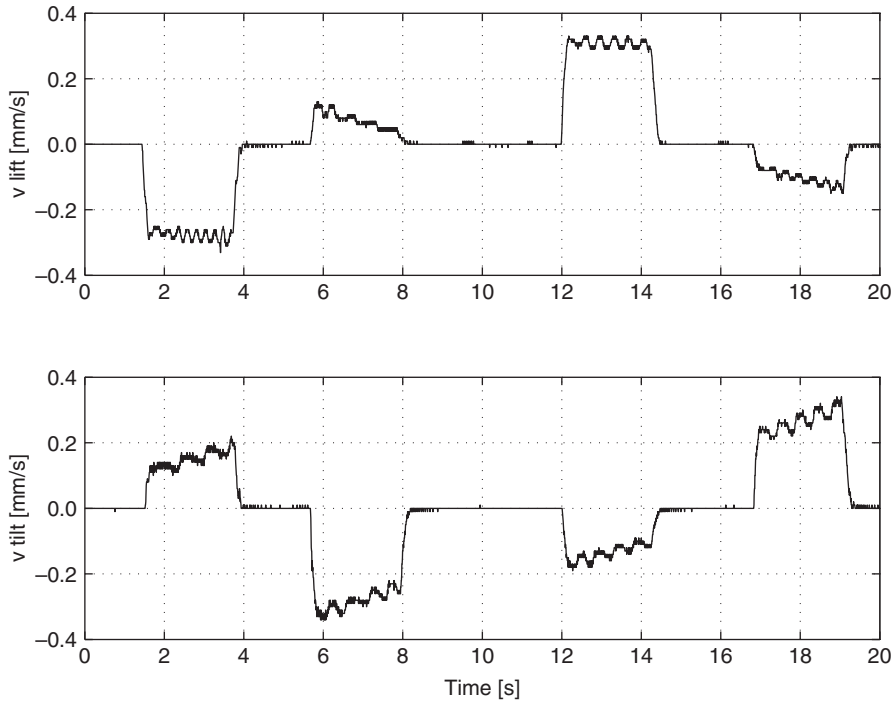


Figure 7. Actuator velocities.

5 CONCLUSIONS

Basics of 2-degree of freedom manipulator with water hydraulic actuation was presented. The manipulator was controlled with proportional 4/3-way proportional control valves. Coordinate control of manipulator tool-end was realized by calculating desired actuator positions from desired tool coordinates with inverse kinematics. The actuator positions were controlled with simple proportional controllers.

The achieved accuracy was quite good. The joint angle accuracies were well within 1 degree during the movement and within 0,05 degrees in final positioning. This leads to 20mm accuracy during movement and 0,6mm accuracy in final positioning in the tool-end of the manipulator.

Future research is needed to develop better controllers to improve the follow-up accuracy of the manipulator. Also the effect of loading conditions of the manipulator should be considered. Also comparison between proportional valve control and digital hydraulic control will be carried out in the near future.

6 REFERENCES

- (1) Kunttu, P., Koskinen, K.T. and Vilenius, M., 1999, Low-Pressure Water Hydraulics – State of the Art, In: Koskinen, K.T., Vilenius, M. & Tikka, K. (eds.), Proceedings of The Sixth Scandinavian International Conference on Fluid Power, SICFP'99, Tampere, Finland, pp.67-75.
- (2) Koskinen, K.T., Mäkinen, E., Vilenius, M. and Virvalo, T., 1996, Position control of a water hydraulic cylinder, Proceedings of The Third JHPS International Symposium on Fluid Power, Japan, pp. 43-48.
- (3) T. Takahashi, C. Yamashina, S. Miyakawa, Development of Water Hydraulic Proportional Control Valve, proceedings of the Fourth JHPS International Symposium on Fluid Power, Tokyo, Japan, 1999, pp.549-554.
- (4) Sairiala, H., Linjama, M., Koskinen, K.T. and Vilenius, M., 2001, Low-cost proportional valve for low-pressure water hydraulics. In: Burrows, C.R. & Edge, K.A. (eds.). Bath Workshop on Power Transmission and Motion Control, PTMC 2001, London, UK, pp. 134-145.
- (5) Sairiala H., Koskinen K.T., Vilenius M., Jauhola, L. Jauhola P. and Selkosmaa J., Control of a water hydraulic cylinder drive with new proportional valve, In: Koskinen, K.T. & Vilenius, M. (eds.) Proceedings of The Eight Scandinavian International Conference on Fluid Power, SICFP'03, Tampere, Finland, pp. 899-909.
- (6) Linjama, M., Koskinen, K.T. and Vilenius, M., 2003, Accurate trajectory tracking control of water hydraulic cylinder with non-ideal on/off valves, International Journal of Fluid Power 4, pp. 7-16.
- (7) Gawlik, A. & Sobczyk, A., Theoretical and experimental investigation of hydraulic manipulator position control. In: Codina Macia, E. et al. (Eds.). Proceedings of the 3rd FPNI-PhD Symposium on Fluid Power, Terrassa Spain, June 30-July 2, 2004. p. 195-203.
- (8) Mäkinen, E. & Virvalo, T. Improving the accuracy of the water hydraulic position servo by compensating servo-valve nonlinearities. In: Burrows, C.R. & Edge, K.A. (eds.). Bath Workshop on Power Transmission and Motion Control (PTMC 2000). pp. 283-295 (Professional Engineering publishing, London, UK, 2001).
- (9) Sairiala, H., Linjama, M., Koskinen, K.T. & Vilenius, M. 2002. Proportional Position Control of Low-Pressure Water Hydraulic Cylinder. SAE Technical Paper Series, SAE 2002-01-1379, NCFP I02-8.3 Warrendale, USA. 7 s.

- (10) Sairiala, H., Koskinen, K.T. & Vilenius, M. 2003. Trajectory Tracking Control of Low - Pressure Water Hydraulic Cylinder Drive with Proportional Valve. 7th Triennial International Symposium on Fluid Control, Measurement and Visualization, Sorrento, Italy, August 25-28, 2003. Edinburgh, UK. Optimage Ltd., Edinburgh, UK, EH10 5PJ. 8 p.

Development of a novel water hydraulic vane actuator applied for control of a two-links test manipulator

Finn Conrad and Francesco Roli

Department of Mechanical Engineering

Technical University of Denmark, Kgs. Lyngby, Denmark

ABSTRACT

The paper presents research results using IT-Tools for CAD and dynamic modeling, simulation, analysis, and design of water hydraulic actuators for motion control of machines, lifts, cranes and robots. Matlab/Simulink and CATIA are used as IT-Tools. The contributions include results from on-going research projects on fluid power and mechatronics based on tap water hydraulic servovalves and linear servo actuators and rotary vane actuators for motion control and power transmission. Development and design a novel water hydraulic rotary vane actuator for robot manipulators. Proposed mathematical modeling, control and simulation of a water hydraulic rotary vane actuator applied to power and control a two-links manipulator and evaluate performance. The results include engineering design and test of the proposed simulation models compared with IHA Tampere University's presentation of research measurements from a similar robot manipulator driven by tap water hydraulic components. Experimental and simulation results are compared for evaluation and verification of developed mathematical models of the motion control of the manipulator. Furthermore, this paper presents the selected experimental results and performance results.

NOMENCLATURE

K	Turbulent flow coefficient	$[\text{m}^3/(\text{s Pa}^{1/2})]$
x_v	Spool displacement	$[\text{m}]$
ρ	Water density	$[\text{Kg}/\text{m}^3]$
q	Specific volume	$[\text{m}^3/\text{rad}]$

K_l	Total leakage coefficient	[m ³ /(s Pa)]
K_{im}	Valve leakage coefficient	[m ³ /(s Pa)]
K_{act}	Actuator leakage coefficient	[m ³ /(s Pa)]
K_{ce}	Effective leakage coefficient	[m ³ /(s Pa)]
K_c	Flow – pressure coefficient	[m ³ /(s Pa)]
J_t	Total moment of inertia	[Kg m ²]
b_v	Viscous friction coefficient	[N m s/rad]
T_e	Total external load	[N m]
P_S	Supply pressure	[Pa]
P_T	Return pressure	[Pa]
P_A, P_B	Pressure in chambers A, B	[Pa]
P_{tr}	Laminar – turbulent transition pressure	[Pa]
u	Servo valve input voltage	[V]
K_{sv}	Spool displacement coefficient	
ω	Servo valve natural frequency	[rad/s]
δ	Servo valve damping ratio	
β_e	Water effective bulk modulus	[Pa]
V_t	Total actuator volume	[m ³]
V_0	Dead volume in actuator chambers	[m ³]
$\theta_{min}, \theta_{max}$	Actuator angle limits	[rad]
ω_h	Hydraulic frequency	[rad/s]
δ_h	Hydraulic damping ratio	
K_p	Position gain	[1/rad]
K_v	Velocity gain	[1/rad ²]
K_t	Velocity feedback gain	
e_s	Steady state position error	[rad]
D	Inertia – acceleration matrix	[N m s ² /rad]
h	Coriolis – centrifugal vector	[N m s/rad]
c	Gravity vector	[N m /rad]
b	Viscous friction vector	[N m s/rad]

1 INTRODUCTION

The proposed tap water hydraulic vane actuator presented in this paper is developed for a second joint of a 2 DOF water hydraulic manipulator. Water as pressure medium is chosen to drive the actuator. Water is a non-contaminant, fireproof, radiation proof, and readily available. Many industrial applications (Conrad et al [3]) such as food processing, steel, mining, pharmaceutical and nuclear industry, require particular cautions that water can provide. On the other hand, tap water has a very low viscosity relative to hydraulic oil, and can not in general be recommended today at pressure higher than 160 bar.

The water hydraulic rotary vane actuator is a primary driver for motion control. The vane actuator is designed with two parts bolted on the shaft and the external cover is divided into five parts. The leakage and the lubrication are the most critical problems due to using water as fluid, but can be solved through the use of stainless steel or titanium and modern sealing polymer material as PEEK, and a particular attention in the bearing design.

2 SYSTEM DESCRIPTION OF DEVELOPED VANE ACTUATOR AND MANIPULATOR

The developed vane actuator has 270° of travel and can provide 1120 Nm as a theoretical maximum torque at the supply pressure 140 bars. The actuator is made of high quality stainless steel, weighs about 19 Kg and the overall dimensions are $\varnothing 150 \times 140$ mm. The servovalve chosen to drive the actuator is the Ultra Premier Range 4658 Series with 9.6 l/min rated flow at 70 bars. The valve is directly connected to the actuator to keep the bulk modulus around the water effective value.

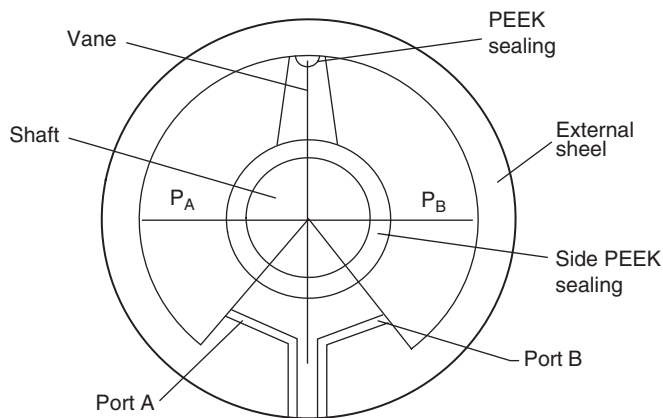


Figure 1 Schematic of a water hydraulic vane actuator

The two-links robot is driven by a double vane actuator as a first joint and the analyzed actuator in the single vane configuration as a second joint. The total manipulator length is 2 m and the all robot weight is around 60 Kg.

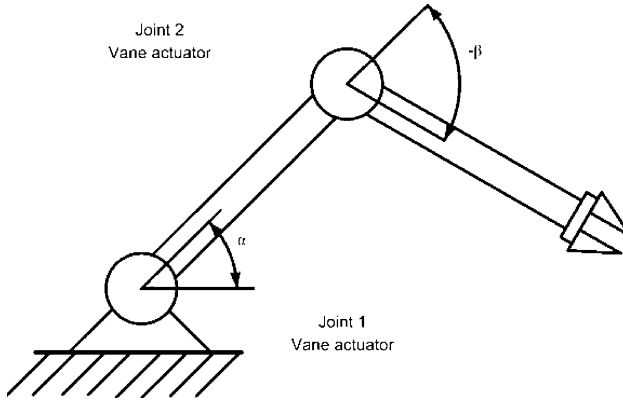


Figure 2 Schematic of water hydraulic robot manipulator driven by vane actuators

3 MATHEMATICAL MODELING AND CONTROL OF WATER HYDRAULIC VANE ACTUATOR

3.1 Fundamental equations

First, we present the fundamental equations used in the proposed model. For the servovalve, we use the turbulent law through the orifice.

$$\left. \begin{aligned} Q_{turb} &= K \cdot x_v \sqrt{\frac{1}{\rho} (P_S - P_A)} \\ Q_{turb} &= K \cdot x_v \sqrt{\frac{1}{\rho} (P_B - P_T)} \end{aligned} \right\} x_v \geq 0 \quad (1)$$

$$\left. \begin{aligned} Q_{turb} &= K \cdot x_v \sqrt{\frac{1}{\rho} (P_S - P_B)} \\ Q_{turb} &= K \cdot x_v \sqrt{\frac{1}{\rho} (P_A - P_T)} \end{aligned} \right\} x_v < 0 \quad (2)$$

Where K is the turbulent coefficient calculated from the servo valve datasheet. In the vane and arm model we use the continuity equation and the Newton's second law.

$$Q_L = q \cdot \frac{d\theta}{dt} + K_l \cdot (P_A - P_B) + \frac{V_l}{4\beta_e} \frac{d(P_A - P_B)}{dt} + \frac{q \cdot \theta}{2\beta_e} \left(\frac{dP_A}{dt} + \frac{dP_B}{dt} \right) \quad (3)$$

$$(P_A - P_B) \cdot q = b_v \cdot \dot{\theta} + J_l \cdot \ddot{\theta} + T_c \quad (4)$$

The leakage through the vane chambers and the servo valve is modelled as a laminar flow by the coefficient $K_l = K_{lm} + K_{act}$. Two simulation models, a linear and a non-linear model of the water hydraulic valve controlled rotary vane actuator are introduced in this section, respectively.

3.2 Linear model of water hydraulic vane actuator

The linear mathematical model is used for the theoretical analysis and simulation of the dynamic response of the vane actuator. Figure 3 show a block diagram presented in Simulink.

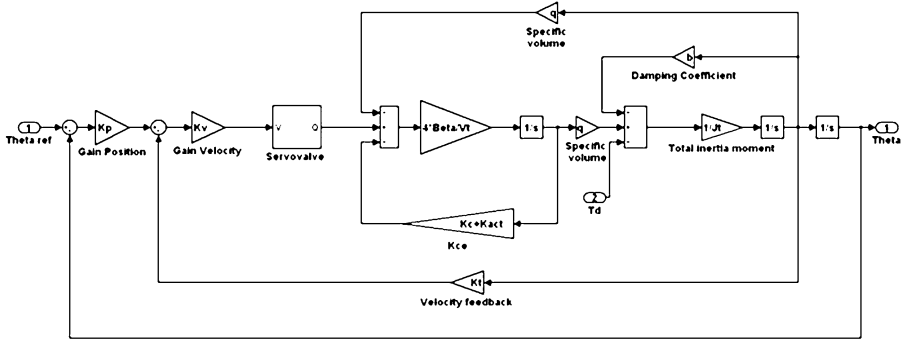


Figure 3 Linear Simulink model water hydraulic vane actuator

The servo valve dynamics from the voltage input signal to the spool displacement is modeled approximated by a second order transfer function.

$$\frac{\Delta x_v}{\Delta u} = \frac{K_{sv}}{\left(\frac{s^2}{\omega^2} + \frac{2\delta}{\omega}s + 1\right)} \quad (5)$$

Where $K_{sv} = K_{ii}/R_t$ is related to the servovalve's configuration, ω is the natural frequency and δ is the damping ratio of the servovalve. The equation that can describe the pressure-flow curve being linearized by using the Taylor's series

$$Q_L = K_q x_v - K_c P_L \quad (6)$$

Assuming a critical mach spool center valve operate in the most crucial situation to assure stability, $Q_{L,0} = P_{L,0} = x_{v,0} = 0$, we can assume $K_c = 0$. Also the non-linear term in the continuity equation be neglected, assuming $|q \cdot \theta| \ll V_0$. Using the described linearised equations above, we can figure out the transfer function below.

$$\theta = \frac{\frac{K_q}{q\left(\frac{s^2}{\omega^2} + \frac{2\delta}{\omega}s + 1\right)} u - \frac{K_{ce}}{q} \left(1 + \frac{V_t}{4bK_{ce}}s\right) T_e}{s\left(\frac{s^2}{\omega_h^2} + \frac{2\delta_h}{\omega_h}s + 1\right)} \quad (7)$$

Where ω_h and δ_h are the hydraulic frequency and damping ratio, respectively.

$$\omega_h = \sqrt{\frac{4\beta_e q^2}{V_t J_t}} \tag{8}$$

$$\delta_h = \frac{K_{ce}}{q} \sqrt{\frac{\beta_e J_t}{V_t}} + \frac{b_v}{4q} \sqrt{\frac{V_t}{\beta_e J_t}} \tag{9}$$

Since we consider $K_c = 0$ and the term $K_{ce} = K_c + K_{im} / 2 + K_{act}$ is associated only to the leakage and the damping is mostly related to the second term. If we consider the non linear equations, the first term became prevalent, so the system stability in the linear model is more critical because the damping is lowest. We chose a control system with position velocity feedback. So the transfer function for $T_e = 0$ became:

$$\frac{\theta}{r_{ref}} = \frac{K_p \cdot K_v \cdot K_q \cdot q}{\left(\frac{s^2}{\omega^2} + \frac{2\delta}{\omega} s + 1\right) \cdot \left[K_{ce} \cdot W \cdot s^3 \cdot J_t + (K_{ce} \cdot (W \cdot b + J_t)) \cdot s^2 + (K_{ce} \cdot b + q^2) \cdot s \right] + K_v \cdot K_t \cdot K_q \cdot q \cdot s + K_p \cdot K_v \cdot K_q \cdot q} \tag{10}$$

where W is defined as an auxiliary variable added to simplify the equation (10)

$$W = \frac{V_t}{4 \cdot B_e \cdot K_{ce}}$$

Analyzing the linear model, we can estimate the steady-state error for a step input and the stability range. The first is effect to the external load and can be reduced by decreasing the leakage and increasing both the position and the velocity gain. Position error

$$e_s = \frac{K_{ce} T_e}{K_p K_v K_q q} \tag{11}$$

Neglecting the valve dynamics, we work out an easy form for the stability, by applying the Routh-Hurwitz criterion. The system is stable for

$$(W + J_t)(q^2 + K_v K_t K_q q + K_{ce}) > W J_t K_p K_v K_q q \tag{12}$$

3.3 Non linear model of water hydraulic vane actuator

The non-linear model is used to validate a control scheme with position and velocity feedback, and to verify robot test trajectories in the free space. It consists of three subsystems: (1) a model of the servovalve, (2) a model of the vane actuator, and (3) a model of the manipulator arm. The *four ways servovalve* is illustrated in Figure 4.

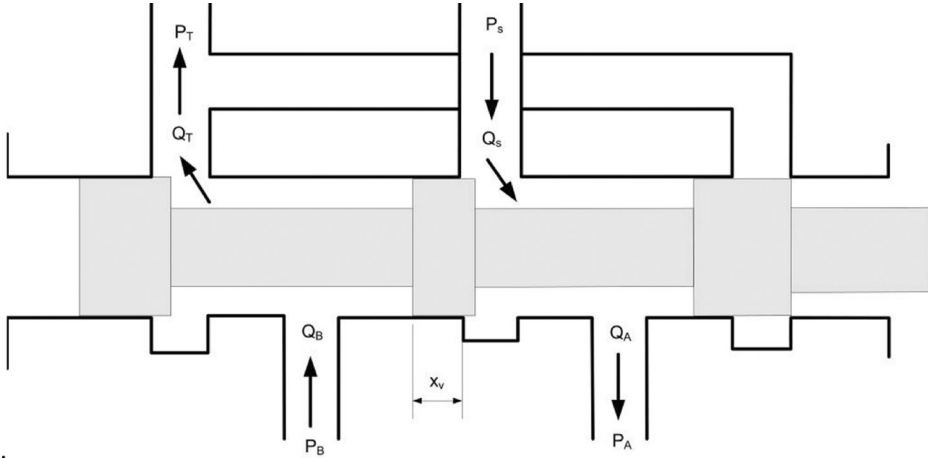


Figure 4 Four ways servovalve scheme

The spool dynamic is modelled approximately by the second order transfer function described before and the valve is simplified by defining four sub block, one for each orifice. The flow through the orifices is calculated switching from the laminar to the turbulent equation when the pressure difference became higher than the transition pressure P_{tr} . Instead of the laminar flow equation described before, we use a second order interpolation, worked out by using the Lagrange method to keep the continuity of the first derivate in the transition point.

$$Q = \frac{K(\Delta P - 3P_{tr})}{2P_{tr}^{3/2}} \quad (13)$$

In both case the flow is linear proportional to the spool displacement and the input voltage is limited to the maximum value of the servovalve.

The *vane actuator* is modeled considering both the chambers. From the continuity equation we figure out the equations to obtain the pressure in each chamber through the integration.

$$\dot{P}_A = \frac{(Q_A - q \cdot \dot{\theta})}{V_{0A} + q \cdot (\theta_{\min} + \theta)} \cdot \beta_e \quad (14)$$

$$\dot{P}_B = \frac{(Q_B + q \cdot \dot{\theta})}{V_{0B} + q \cdot (\theta_{\max} - \theta)} \cdot \beta_e \quad (15)$$

We consider also the flow through the two chambers, proportional to the leakage coefficient

$$Q_{leakage} = K_{ce}(P_A - P_B) \quad (16)$$

The *arms* motion equations proposed by Schiller [2] are expressed trough the direct application of the Lagrange-Euler formulation to non-conservative systems.

$$T_c = D(\theta)\ddot{\theta} + h(\theta, \dot{\theta}) + c(\theta) + b(\dot{\theta}) \tag{17}$$

Where D is the inertial acceleration matrix, and h , c , b are the Corioli's centrifugal, gravity and friction vector. Since the angular velocity is slow (< 5 rad/s), it makes sense here to assume to ignore the Corioli's impact and centrifugal terms.

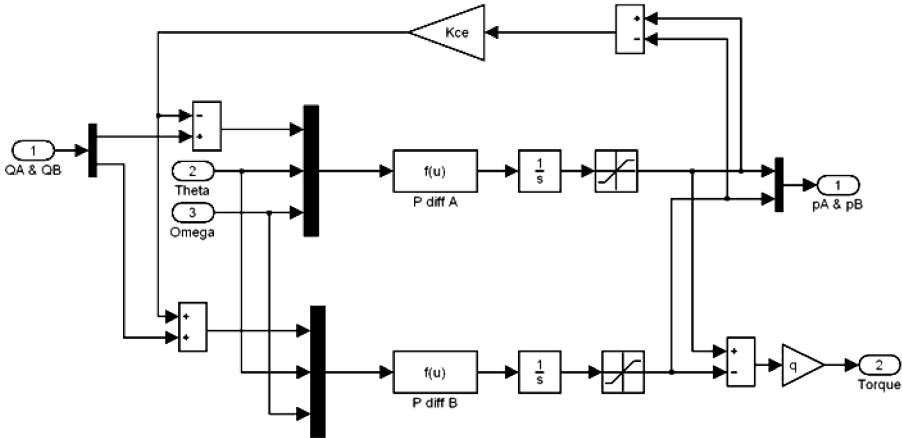


Figure 5 Simulink model of vane actuator modelled by non linear scheme

4 SIMULATION RESULTS AND DISCUSSION

4.1 Water vane actuator

The leakage flow rate is the most critical parameter in the water hydraulic vane actuator, because the viscosity is lower compared to mineral oil. The first simulation was checked a single vane actuator with only one arm connected and 60 Kg end mass. The input signal is a step, from the lower position (null gravity effect) to the horizontal position ($\pi / 2$ rad).

Two leakage coefficients are compared and the response is shown in the Figure 6. When $K_{ce} = 5e-12$ the response is slower and the steady state error is 2.8%, according to equation (11).

Table 1 shows the maximum torque and leakage flow rate obtained testing the previous model with an over range load mass.

K_{CE}	T_{MAX}	% $T_{NOMINAL}$	$Q_{LEAKAGE}$	% $Q_{NOMINAL}$
5,00E-13	1071Nm	95.63%	0.41 litre/min	4.27%
5,00E-12	820Nm	73.21%	3.08 litre/min	32.08%

Table 1

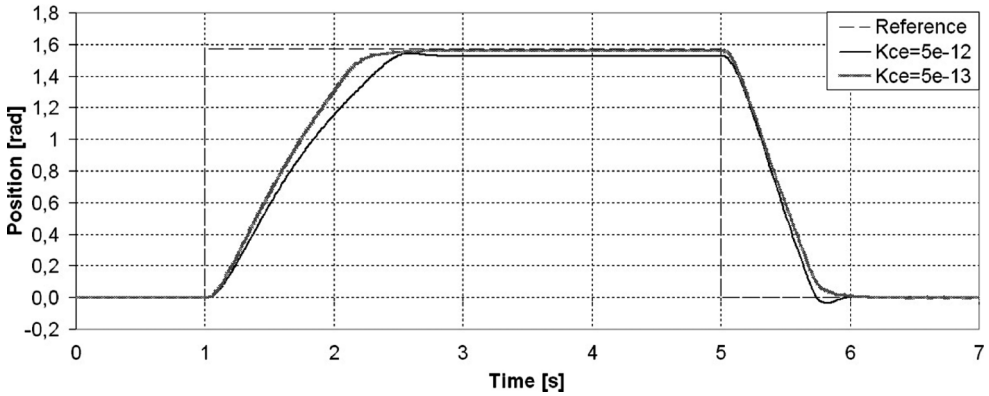


Figure 6 Step response for different leakage flow rates

The two tests above bear witness that the leakage flow rate does affect mostly the steady state error and the actuator maximum torque.

4.2 Robot manipulator test in free space

Finally we test how the two-link robot can follow simple shape paths: a square and a circle. The input signals comprise few ramps and the slope is opportunely set up, hence the robot can follow the trajectory according to the maximum actuator speed. The all test were running in 4 seconds.

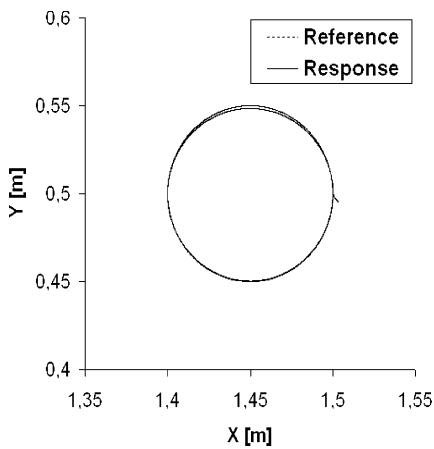


Figure 7 Circle path test

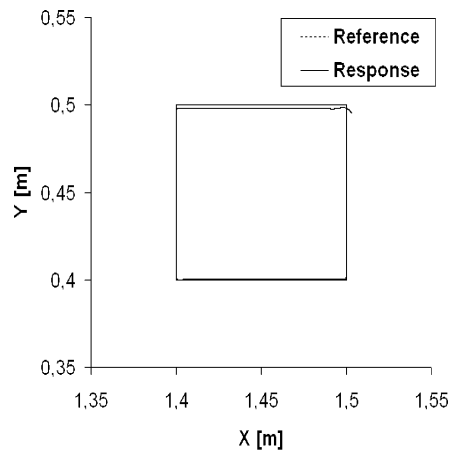


Figure 8 Square path test

Figure 9 and 10 show the position error for the two tests ran. The steady state error is the main root of the defect, and it cannot be correct slowing down the test's speed.

Since the leakage coefficient is set at $5e-13 \text{ m}^3/s \cdot Pa$, to improve the model, we can only adjust the gains securing the stability also for a null external load. During the all test, the slip range from 3 to 6 mm.

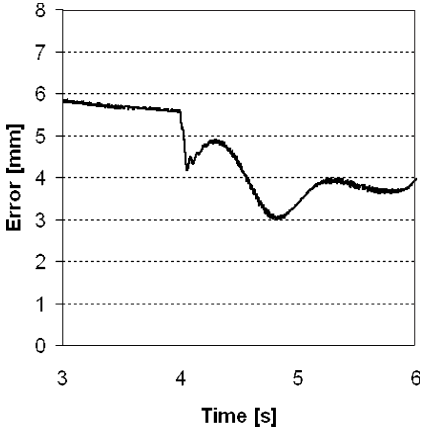


Figure 9 Position error circle path test

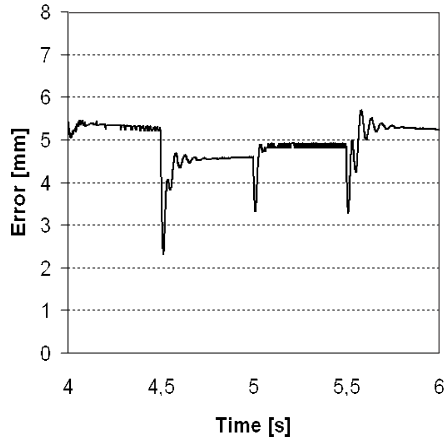


Figure 10 Position error square path test

5 EXPERIMENTAL RESULTS AND DISCUSSION

To evaluate and validate the proposed models we did compare our results with some experimental results earlier presented by IHA Tampere University’s research measurements from a similar robot manipulator driven by tap water hydraulic components [4].

In the next test the single arm models are ran in the open loop configuration from the vertical position, with zero gravity effect. The valve is kept open for one second. As shown in Figure 11, both the linear and the non-linear model match well with measurements position response performed the by a real vane actuator device by IHA, Tampere.

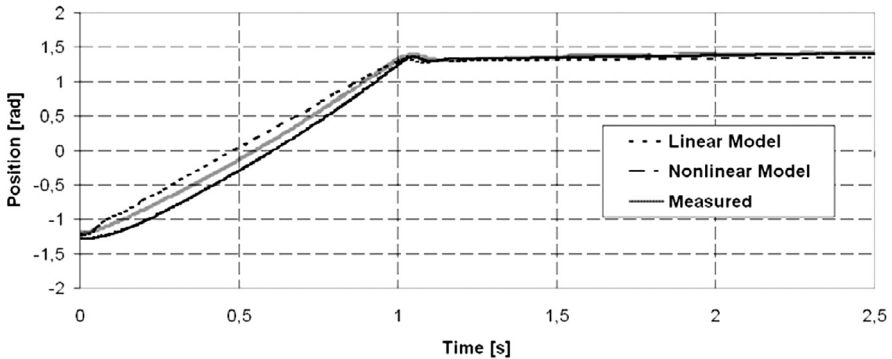


Figure 11 Open loop position response, simulated and experimental results.

Looking the velocity response in Figure 12, the linear model occurs some errors during the valve opening due to the large step input signal. In general, the simulated response with the linear model agrees well with the non-linear model and with measured response, and therefore the linear model can be used to simplify the controller design.

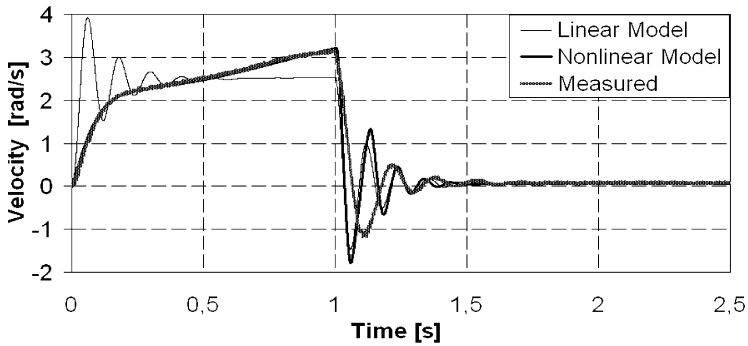


Figure 12 Open loop velocity response, simulated and experimental results

6 USING 3D CAD/CAE MODELLING AND DESIGN OF WATER HYDRAULIC ACTUATOR AND ROBOT

Figure 13 shows the proposed novel design of the water hydraulic rotary vane actuator by using CATIA for the development and design.

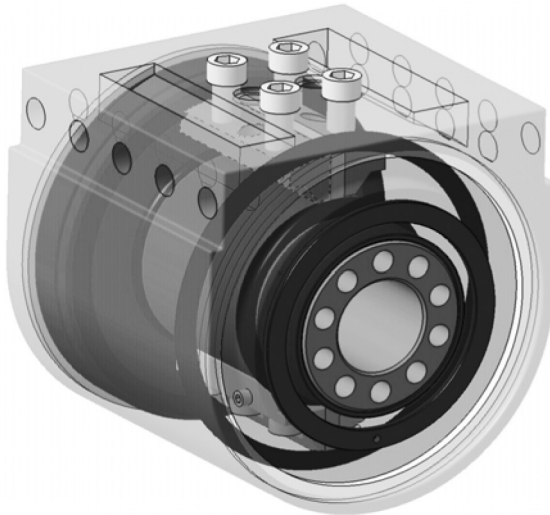


Figure 13 A novel CAD model of the water hydraulic vane actuator

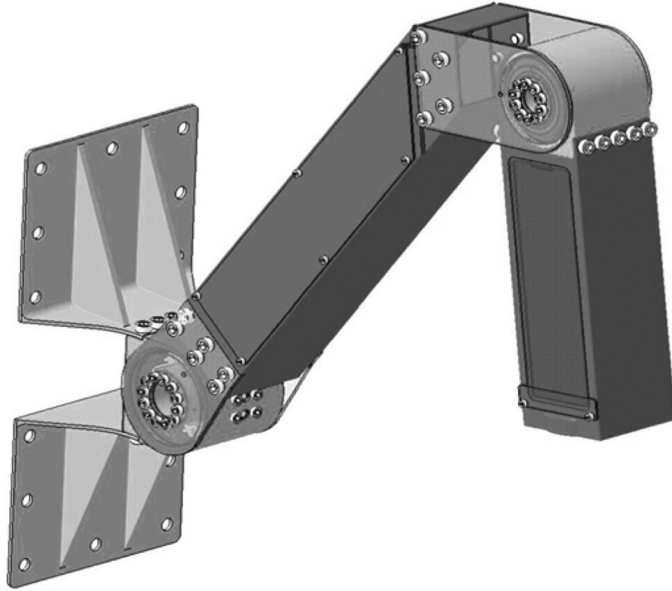


Figure 14 A view of the 3D CAD model of the novel two-link robot manipulator

The housing is separate in five cylindrical parts and both the vane are connected by screw to the stator and the rotor. The bearings are lubricated by water and protected with seals on the shaft. All the dynamic seals are made in PEEK material that can perform good performance versus the stainless steel.

The designed vane actuator driven robot has two links and is illustrated in figure 15. The water hydraulic vane actuators equipped by the servovalves and the electronic control devices drive the robot arm manipulator. The robot arm manipulator is undertaken for the design to be improved for a 6 DOF robot arm manipulator.

7 CONCLUSION AND OUTLOOK

The contributions presents research results using IT-Tools for CAD and dynamic modelling, simulation, analysis and design of water hydraulic actuators for motion control of machines, lifts, cranes and robots. Matlab/Simulink and CATIA were used as IT-Tools for the development and design a novel water hydraulic rotary vane actuator for robot manipulators. Furthermore, presents proposed mathematical modelling, control and simulation of water hydraulic rotary vane actuator applied to power and control a two links manipulator and evaluate the performance. The obtained results shows that even with a simple control system as a position feedback and an internal velocity feedback, the robot manipulator performance a good accuracy following trajectory at slow speed. In general, the simulated response with the linear model agrees well with the non-linear model and with the presented measured response, and therefore the linear model can be used to simplify the controller design.

The applied mass located at the TPC of the robot arm decrease the hydraulic frequency benefits the system stability. On the other hand, the position error is approximately proportional to the external load. The control gains cannot be optimized for all the load range and therefore a compromise have to be made. All the control parameters have to be optimized.

The non-linear model can be used instead the experimental design, at least for primary set up and provide good possibility to improve the control system. The robot manipulator was developed driven by the electronic control devices, and the robot arm manipulator is undertaken for the further design to be improved for a 6 DOF robot arm manipulator.

REFERENCES

- [1] H.E. Merrit: *Hydraulic Control Systems*, John Wiley & Sons Inc., New York, 1967.
- [2] R. J. Shilling: *Fundamentals of Robotics Analysis and Control*, Prentice Hall, New Jersey, USA, 1990.
- [3] F. Conrad, B. Hilbretch and H. Jepsen: *Design of Low-Pressure and High-Pressure Tap Water Hydraulic Systems for Various Industrial Applications*, SAE Transaction, USA, 2000.
- [4] A. Raneda: Impedance Control of a Water Hydraulic Manipulator for Teleoperation Applications, Doctoral Thesis, IHA, Tampere University of Technology, Finland, 2004.
- [5] R. C. Dorf, R. H. Bishop: *Modern Control Systems*, 10th Edition, Pearson Prentice Hall International, USA, 2005.

Fault Analysis and Diagnosis

Analysis of Fault Tolerance of Digital Hydraulic Valve System

Lauri Siivonen, Matti Linjama and Matti Vilenius

Tampere University of Technology, Institute of Hydraulics and Automation

ABSTRACT

The interest for fault monitoring and prevention of failures in mobile valves has increased lately. Most modern mobile valves monitor their state continuously and in case of a failure, the actions are usually limited only into fail-safe functions. Pulse Code Modulation based digital hydraulic valve system has some good features concerning fault-tolerant control. The programmability of the valve system allows re-configuration of the controller with only a small reduction in performance. This feature is analyzed and tested with hydraulic boom mockup. The results show that if the fault is detected, the valve system is capable for operating even if some valves are out of order.

KEYWORDS: Digital hydraulics, fault-tolerant mobile valve, Pulse Code Modulation

1. INTRODUCTION

Fault tolerance has been researched a lot lately. Especially the areas of fault-detection, condition monitoring and fault-diagnosis have been studied in many different areas of technology [1, 2]. Monitoring and condition diagnosis of hydraulic valves in industrial applications has been researched by Rininen et al. [3] and Lurette et al. [4]. Although the area of fault tolerance has developed lately, no commercial proportional or servo valve is actually fault-tolerant. The system can be made fault-tolerant e.g. by doubling some components or even the whole system as is often done e.g. in aerospace hydraulics [5].

Fault-tolerance is an important aspect especially in the area of mobile hydraulics where faults may stop the whole machine and create financial losses and significant time delays. Mobile hydraulic proportional valves are used to control actuators in different mobile applications. The requirements for such valves are robust design, fail-safe features, fairly accurate control, relatively small size and low price. The valves that are commonly used nowadays have troubles fulfilling all these expectations and therefore new, better valves are needed. One possibility for better flow control is to use digital hydraulics where the basic idea is to move the intelligence into controller and use simple on/off valves that are connected in parallel into PCM (Pulse Code Modulation) based series [6, 7]. Such system is called a digital flow control unit (DFCU) [7]. A complete digital hydraulic valve system

consists of four DFCUs, one for each land. The drawing symbol of a DFCU with n on/off valves and a digital hydraulic valve system with four DFCUs are presented in Figure 1.

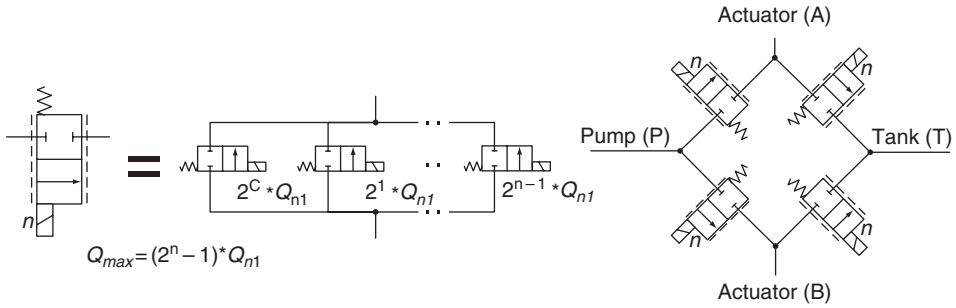


Figure 1. Hydraulic drawing symbol and maximum flow rate of a single DFCU (left) and Digital Hydraulic valve system with four DFCUs (right)

The digital hydraulic valve system has potential for replacing commonly used proportional or even servo valves in applications that require good controllability as Linjama et al. have shown [8, 9]. Laamanen et al. [10] published the first experimental comparison between DFCU and a commercial proportional valve and the results showed that both systems have their own good features and also some drawbacks. In normal conditions, the measurements showed that the DFCU is practically leak free, the response times are fast and the linearity is good.

1.1 Common faults in mobile applications

Common faults in hydraulic systems mainly include problems with pumps, hydraulic motors, cylinders, valves, filters, accumulators and hoses [11]. Also problems with seals are known to exist [12]. Thorstenson and Lövroth [13] studied the failures in hydraulic circuits with four different machines for three years. They found out that the failure rate of hydraulic valves is 69 faults in 10^6 hours. Same numbers for pumps, hydraulic motors, cylinders, filters, accumulators and hoses are 34, 237, 318, 14, 43 and 90. The problems for valves were usually jamming of the spool and leaks. The failures were caused by contamination, wearing, external damages, manufacturing or material error, maintenance error or excess load.

The common failures of forest harvesters have been researched by Hänninen et al. [12]. The studied harvester had 32 mechatronic failures during the reference period and 15 of them were faults with sensors, 10 were related to power and data transmission and included electric cable breakages and problems with connectors. The other 7 faults were related to mainframe and control systems. The same research also studied the faults of a mobile hammer drill and it had 31 mechatronic faults that included 12 sensor faults, 10 were related to power and data transmission, 5 control system failures and 4 failures with hydraulic valves and actuators.

It is typical for multi-functional machines, such as harvesters, that a single error halts the whole system. The harvester stopped completely 22 times and all of them were because of problems with sensors, electric cables, connectors and valves. The hammer drill was stopped 2 times because of sealing problem and jamming of spool valve caused one stop.

One stop was caused by control system of the valve. Six percent of all failures with actuators in systems were related to proportional valves. Jamming of the valve was the main reason at 45% of the cases, driver transistor at 45% and 10% were caused by a fuse. [12]

1.2 Common faults with spool and poppet valves

Most errors in valves are caused by either control electronics or jamming of the spool. The jamming is usually caused by contamination or bad assembly. The main problems with poppet valves are increased internal leaks caused by contamination and fracture of chilled armature [11]. The return spring can be a problem for both poppet and spool valves although the breakage of the spring is not usual. The congestion of pilot stage can also be a problem in some valves [11].

1.3 Faults defined by safety standard

The SFS-EN ISO 13849-2: *Safety of Machinery. Safety-related parts of control systems. Part 2: Validation* –standard [14] defines several safety categories and demands for them. One part of the standard is hydraulic valves and some of the defined faults are: change of switching times, non-switching (sticking at an end or zero-position), incomplete switching (sticking at a random intermediate position) and leakage.

2 FAULT TOLERANCE OF DIGITAL HYDRAULIC VALVE SYSTEM

Fault-tolerance in a system is a wide concept and it can be defined in many ways. One extensive definition can be found from the area of control systems [15].

- Fail-operational: The system is able to operate with no change in performance despite any single point failure.
- Fault-tolerant: A system is able to continue operation and degradation of performance may be accepted.
- Fail-safe: The system fails to a state that is considered as safe in either general or specific application.
- Passive Fault Accommodation: Robust design of the system covers certain faults.
- Active Fault Accommodation: Detection and isolation of a fault leads to a change in the system to accommodate a fault. May include re-configuration but is not limited into it.

Modern mobile hydraulic directional flow control valves are commonly considered as fail-safe and also some passive fault accommodation can be found. Usually mobile valves are driven into centre (neutral) position when a fault occurs. Also some error signal is usually transmitted to user with led or e.g. via CAN bus.

Digital hydraulic valve system can also be made fail safe since all the on/off –valves have a return spring. On/off valves are also generally considered as robust and therefore the passive fault accommodation exists. The big advantage with digital hydraulic valve system is that in case of a valve fault it might be possible to achieve fault-tolerant system if the controller is intelligent enough and the feedback signals are adequate. The basic idea of fault-tolerant control of the valve system is the re-configuration of the controller.

The key to the fault-tolerant control is fault-detection. A faulty acting valve can be detected in several ways, e.g. from coil current, voltage, resistance or inductance, pressure signals, flow rate or position sensor (spool/armature or position/speed of the actuator). The fault-detection is not studied in this paper.

2.1 Fault tolerance of digital flow control unit

If one or more on/off valves in a DFCU are acting faulty and the fault is detected and located, the effect of fault can be minimized by re-configuring the controller. If the faulty acting valve is for example closed, the controller disables all faulty acting opening combinations and calculates the next best combination from this reduced search space. The re-configuration is relatively simple to apply but on the other hand the controllability weakens since the search space is smaller. The re-configuration also reduces the maximum flow rate of the DFCU.

Figure 2 presents a DFCU with a faulty acting valve that remains closed regardless of the control signal. If the fault is not detected, the effect is the biggest with the biggest valve. The controllability suffers greatly and the valve system may even cause actual damage when controlling the actuator with half of the maximum flow rate and increasing slightly causing a total stop. Even if nothing breaks, the resulting pressure peaks and possible oscillation can make the actuator unusable. In this case the fault-detection is vitally important. If the fault is detected, the re-configuration of the valve controller can be done and the system can continue even without any significant degradation in performance. The smallest help from the re-configuration is for faults that are detected in the second biggest valve, where controllability suffers especially in the middle section of the valve opening range. This kind of fault only affects the system when the DFCU is actually used. For example if the fault is in $DFCU_{P \rightarrow A}$ and the controller passes flow from pump to B-port ($DFCU_{P \rightarrow B}$), the fault does not affect the behavior of the system at all.

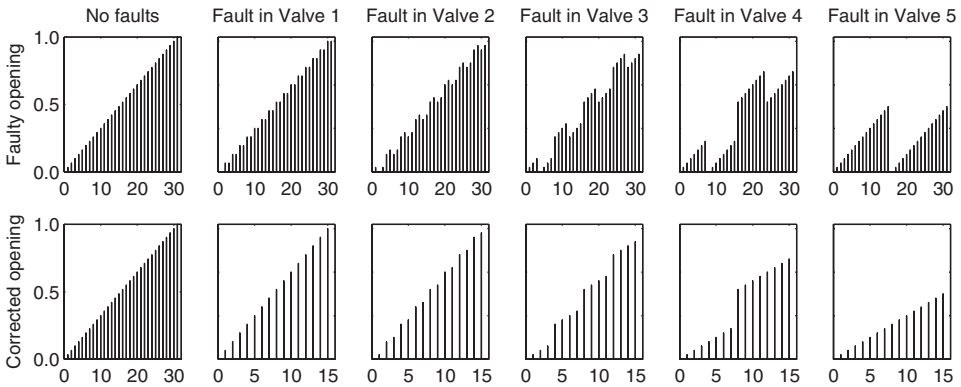


Figure 2. The effect of a faulty acting valve to DFCU performance (Opening vs. DFCU opening combination)

If the faulty acting valve is e.g. jammed into open position, the effect of the re-configuration is smaller. The extra leakage through the DFCU limits the minimum flow rate and reduces the controllability.

2.2 Fault tolerance of digital hydraulic valve system

When the digital hydraulic valve system is made with four DFCUs it is possible to compensate the error in one DFCU with correct control of another DFCU. The re-configuration can be done even without significant degradation in performance. If the on/off –valve is closed all the times, it is easier to compensate. The re-configuration of one DFCU is done as presented in section 2.1. Since the re-configuration of one DFCU decreases the controllability of the DFCU, it is improved with the other DFCU that is connected to the same actuator port.

If an on/off valve in e.g. pump side DFCU is jammed into open or middle position, it causes an extra flow to actuator. This can be compensated by passing the extra flow directly into tank. This is presented in Figure 3. The effect of the fault is Q_F , which is an extra flow through the valve to the actuator. In this case the correction would be Q_C that is passed directly into the tank. The correction creates an extra leakage through the valve system but the actuator is still usable.

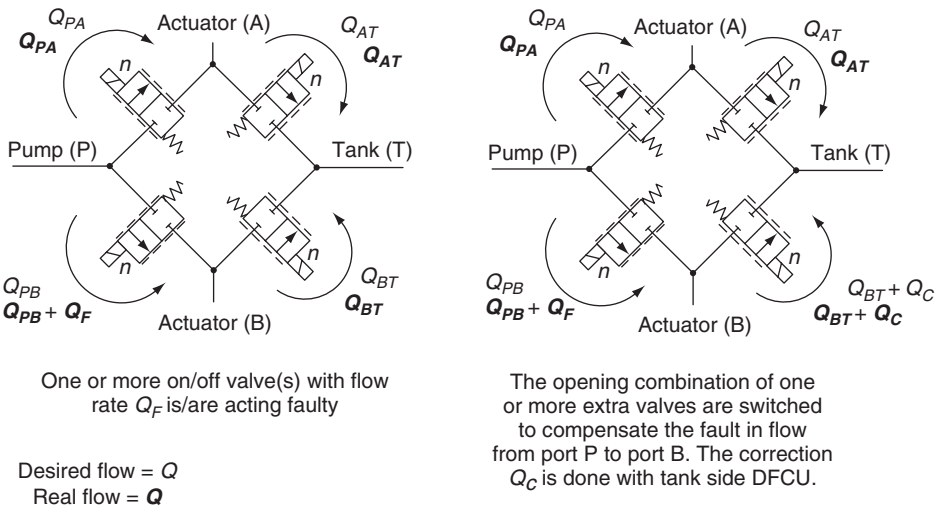


Figure 3. Faulty acting valve passes extra flow to the actuator (P→B) (left) Re-configuration eliminates the fault by passing the extra flow into the tank (right)

An estimate of the flow rate to the actuator's B-port is presented in Equation 1. The $Q_{N,PB}$ and $Q_{N,BT}$ are the flow coefficients that depend on opening combinations u_{PB} and u_{BT} , p_B is port pressure, p_S is supply pressure and p_T is tank pressure.

$$Q_B = Q_{N,PB}(u_{PB})\sqrt{p_S - p_B} - Q_{N,BT}(u_{BT})\sqrt{p_B - p_T} \quad (1)$$

Figure 4 presents the effect of a faulty acting valve that is jammed into fully open position. The presented valve system is on the pump side and the pressure difference of both DFCUs is assumed to be the same. The correction is made with the tank side DFCU.

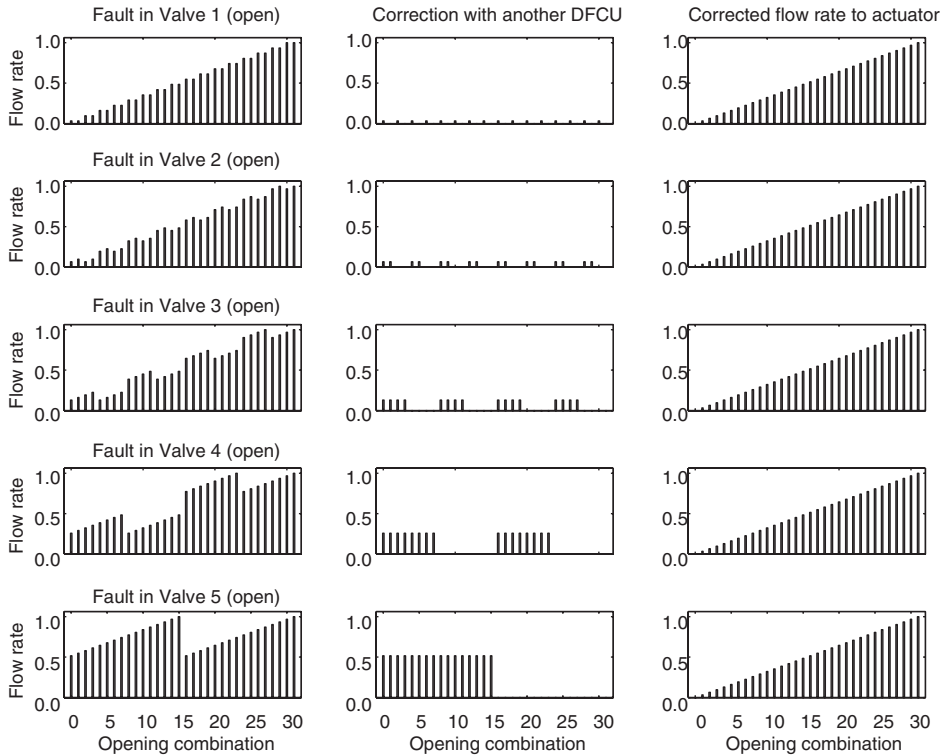


Figure 4. The effect of a faulty acting valve to DFCU performance, ideal case ($p_S - p_B = p_B - p_T$)

If the valve, that is jammed, is located on the tank side DFCU, the effect is bigger and harder to compensate. The fault will reduce the maximum flow rate and possibly even prevent the valve system from working. The problem is emphasized by the bigger pressure difference that creates a bigger flow. Figure 5 presents a typical connection of the half of the digital hydraulic valve system to B-port of a double acting cylinder. The pressure difference of the pressure side DFCU ($p_P - p_B$) can be even 10 times smaller than the pressure difference on the tank side DFCU ($p_B - p_T$). A big on/off valve that is jammed to open position can leak so much extra oil through the DFCU that it is not possible to operate the device without severe energy losses and reduced controllability. In such cases not even re-configuration helps. For example with the biggest valve, the extra flow from actuator to tank can be even over 100 l/min with typical port and supply pressures in mobile applications. On the other hand if the broken valve is small enough, it is still possible to compensate the fault and also gain fairly good controllability. The limit between controllable and uncontrollable system is a little bit fuzzy since it depends on the application. Even if the system can be controlled, the power loss caused by the correction can be too big to handle.

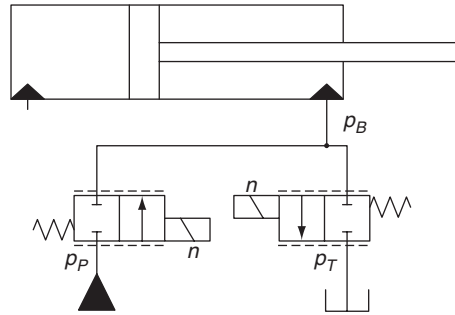


Figure 5. Typical connection between the digital hydraulic valve system and the B-port of a double acting hydraulic cylinder

If the valve is jammed into open position, the extra flow must be somehow estimated or measured. If the characteristics of the faulty acting valve are well known, the flow can be calculated from the pressure difference. Since the flow depends on more than just one parameter the calculation is not always correct. For example the temperature of the fluid can cause big changes in static and dynamic characteristics of the on/off valve [16]. If the application demands more accurate control, the flow must be either measured or calculated e.g. from actuator movement.

3 TEST SETUP

The effects of some different faults described in ISO 10770-1 -standard are tested in real conditions by using a hydraulic boom mockup.

3.1 The digital hydraulic valve system

The studied digital hydraulic valve system consists of four DFCUs which are in PCM based binary series. The binary series is done with orifice disks mounted on the bottom of the cavity between the valve block and the valve. Each DFCU has four Sterling Hydraulics GS02 05 pilot operated cartridge type screw-in on/off valves and one Sterling Hydraulics GS 02 70 directly controlled on/off valve. The PCM-based binary series is created with external orifices by using the same orifice diameters as was used by Linjama et al. [8]. The valves are controlled with 20 channel control box and each channel is controlled with International Rectifier IPS0151 SmartFET. The valve system is controlled with PowerPC – based dSPACE DS1005 microcontroller board and SmartFETs are controlled via DS4001 I/O card.

3.2 The hydraulic boom

The valve system is tested with a hydraulic boom that has similar dynamics as with a boom used in middle sized mobile machines. The same boom has also been used by Linjama et al. [8, 9]. The boom is four meters long and it is pivoted from the centre. The transmission ratio between boom tip and cylinder piston is about 10. The test system is presented in Figure 6.

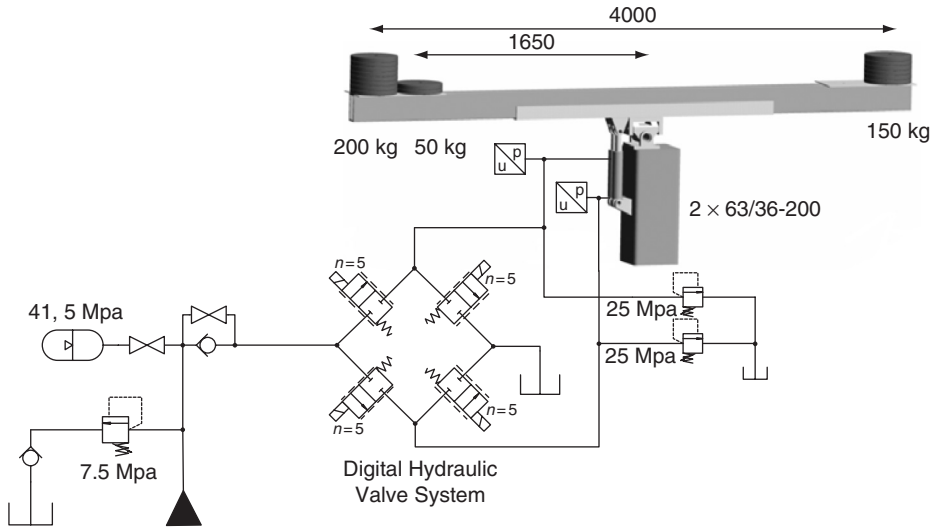


Figure 6. Hydraulic circuit of the test system

3.3 Controller parameters

The open loop controller is basically the same as was used by Linjama et al. [9] with slight modifications. The original valve system had only two DFCUs and one 4/2 valve to change flow direction. Since the studied system has four DFCUs, the controller now commands them all. Although the “four-block” –structure allows independent controlling of all lands, only two of them are controlled at the same time. The trajectory used in all measurements is basically the same as was used by Linjama et al. [9]. The sampling time is reduced from 60 ms to 40 ms due to faster control electronics. The delays of individual valves vary depending on valve types and orifices and therefore some of them need to be delayed. These delay compensations are the same as was used by Linjama et al. [8]. The open loop controller needs some parameters in order to control the system correctly. The load force estimate is 9 kN and the supply pressure estimate is 7 MPa.

3.4 Measured faults

The measurements include individual valve faults where valve does not open. These faults can be caused e.g. by bad electrical connection, faulty acting control electronics or jammed valve. The faults are created with software by disabling certain valves in certain DFCUs. The measurements include tests where the controller knows that the fault exists and tests where the controller does not know that the fault exists. The measurements also include tests with reduced supply voltage. The measured faults are also part of ISO 10770-1 *Test methods for four-way directional flow control valves* –standard [17].

4 EXPERIMENTAL RESULTS

The measured signals include piston position, supply and port pressures. The opening combination of each DFCU, or the valve state, is also presented. The maximum state is 31 for all DFCUs ($2^5 - 1 = 31$).

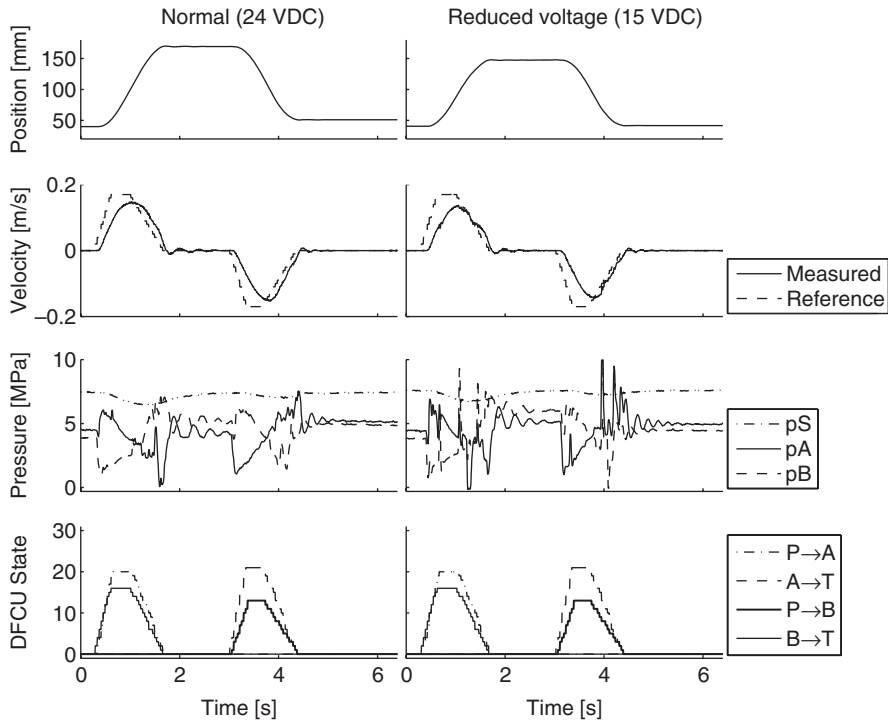


Figure 7. Digital hydraulic valve system with no faults (left) and with reduced supply voltage (right)

The system with no faults and the behavior of the valve system with reduced supply voltage is presented in Figure 7. The 15 VDC voltage increases pressure peaks and causes jerky motion. This is caused by increased valve opening delays. The behavior with 10 VDC supply voltage was also measured but then the piston did not move at all. With 20 VDC no significant disturbances were noticed.

Figures 8 and 9 present the system with two faulty acting valves, one for each direction. The fault on $DFCU_{P \rightarrow A}$ is effective in positive cylinder movement (increasing piston position) and the fault on $DFCU_{P \rightarrow B}$ can be seen in negative cylinder movement (decreasing piston position). The faults do not effect on each other. The effect of one faulty acting small valve can be seen only in pressure curves. The piston velocity follows the reference velocity quite accurately when comparing to the system with no faults. Figure 8 presents the behavior of the system with second smallest valve acting faulty. The measured position is still good in both cases. When the third biggest valve is acting faulty, the system cavitates heavily and the piston velocity has a notch in both acceleration and deceleration sector. If the controller knows that the fault exists, the curve is fixed and the cavitation reduces. The notches in piston velocity disappear when fault is known and corrected. The same kind of phenomena exists also on the tank side DFCUs.

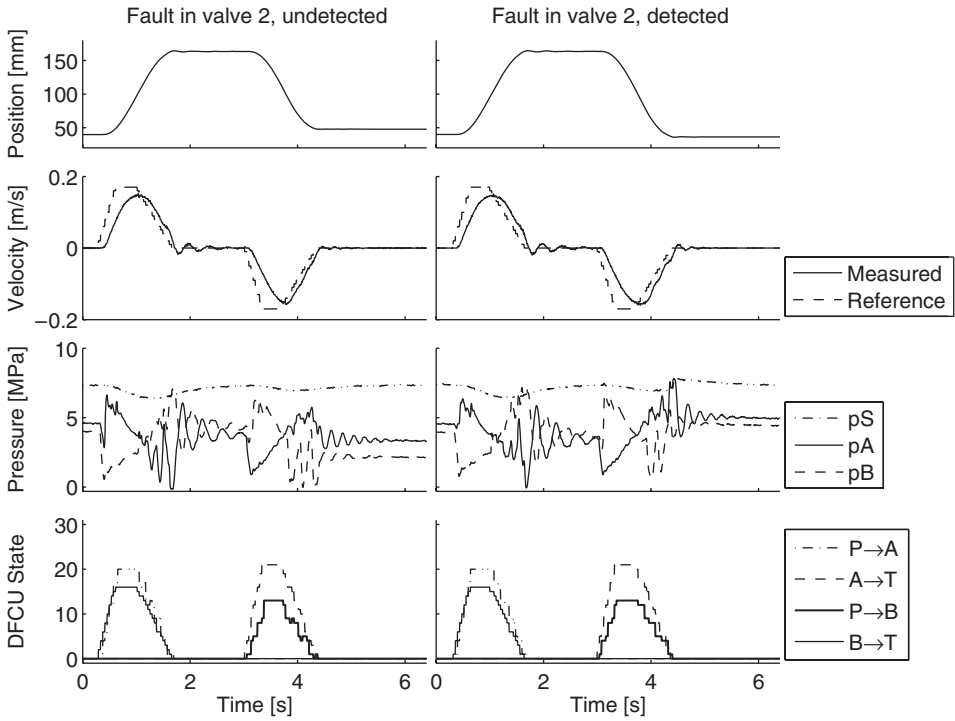


Figure 8. Digital hydraulic valve system with valve 2 on pressure side acting faulty

Figure 9 presents the behavior of the system when the second biggest valve is acting faulty. The piston velocity has big notches if the fault is not known. The system also cavitates heavily and the maximum velocity is significantly reduced. The fault can also be seen in control signals, where the state is not rising and falling smoothly. When the fault is known, the cavitation and jerky motion are almost completely gone. The fault can still be seen in pressure curves but the system is quite operational. The fault on the tank side causes similar effects.

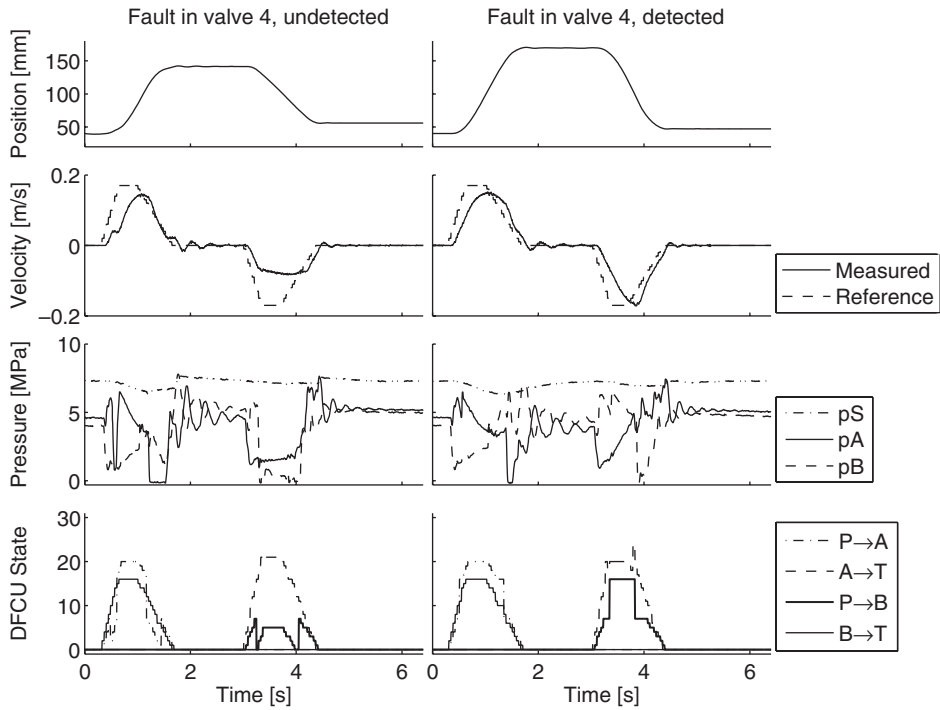


Figure 9. Digital hydraulic valve system with valve 4 on pressure side acting faulty

The Figure 10 presents the system behavior when the biggest valve on both tank side DFCUs are acting faulty. The faults don't effect on each other. The effects are big especially in piston velocity and piston displacement. When the fault is known, the system works well without any significant reduce in performance although the maximum velocity is now limited. If the fault occurs on the pump side DFCU, the fault only effects when the cylinder is moving into positive direction. There the effect is similar to tank side fault except that the pressure peaks are lower and system cavitates heavily. On the other direction, the desired flow rate never reaches an opening combination where fault could affect the performance of the system.

The improvement between the system with undetected fault and the system with correct re-configuration is the biggest when the fault is in the biggest valve on the tank side DFCU. The re-configuration has smallest help on the system behavior when the faulty acting valve is the second biggest.

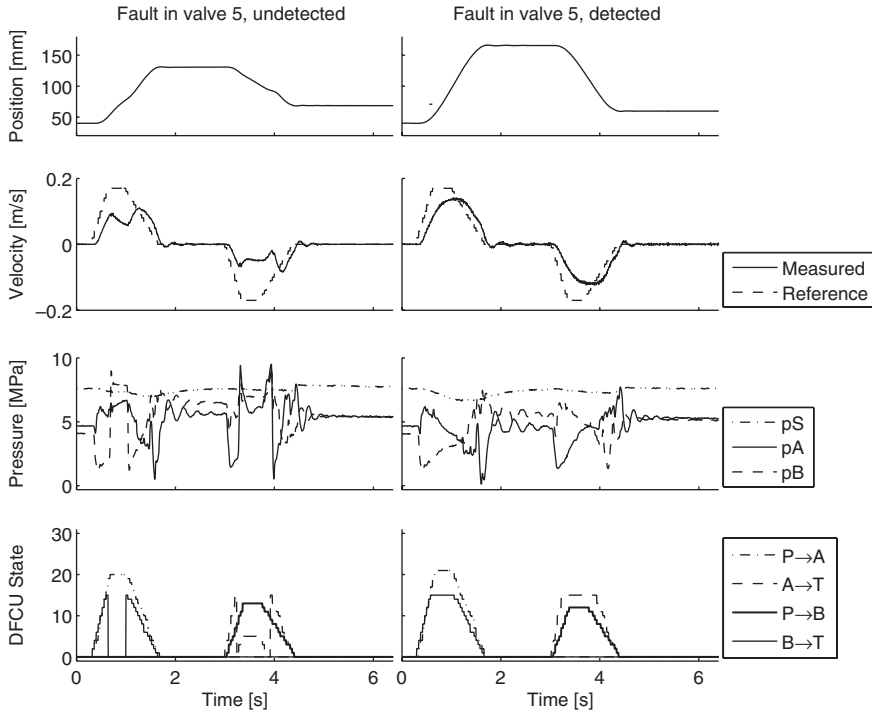


Figure 10. Digital hydraulic valve system with valve 5 on tank side acting faulty

5 SUMMARY

The study focuses on analyzing possible ways to improve the fault tolerance of digital hydraulic valve system. The analysis shows that a fault in some of the smaller valves has only a little effect on performance of the system. The bigger valves are more critical since they have bigger flow rates. If the valve jams to open position, the fault can be corrected with re-configuration if the amount of flow that passes through the DFCU is known. Although the correction might cause internal leakage that reduces the efficiency or reduced performance of the system when comparing to fully functional system, the result is almost fully functional system capable for operating long before actual maintenance is required. This increases the flexibility and possibly productivity of the system.

The experimental tests cover some valve faults, where on/off valve sticks into closed position and also some electrical faults where supply voltage decreases. The experimental results show that the valve system where fault is not detected might create high pressure peaks, sticky motion or even total loss of controllability depending the valve and DFCU where the fault is. The bigger valves are the worst and especially the valves on tank side DFCUs. If the fault is in smaller valve, the effect is rather small and does not necessarily be even corrected if the system does not require highly precise control. If the fault is detected and the re-configuration of the controller is done, the system is capable for relatively high accuracy with significantly smaller pressure peaks.

The key point in fault-tolerant control is to detect the fault. If the fault is not detected the system is not fault-tolerant. On the other hand, if the fault is detected, the system, e.g. mobile machine, is capable for continuing work without any significant degradation in performance.

ACKNOWLEDGEMENTS

This research was supported by the Academy of Finland (Grant No. 80411).

REFERENCES

1. **Hindman, J., Burton, R. and Schoenau, G.** 2002. Condition Monitoring of Fluid Power Systems: A Survey. *Proceedings of the 49th National Conference on Fluid Power* (NFPA'02), March 19-21, 2002, Las Vegas, USA.
2. **Isermann, R.** 1997. Supervision, Fault-Detection and Fault-Diagnosis Methods - An Introduction. *Control Eng. Practice*, Vol. 5, No. 5, UK, Elsevier Science Ltd, pp. 639-652.
3. **Rinkinen, J., Laukka, J. and Ahola, E.** 1997. Condition Diagnosis of Servo Valve in Oil Hydraulic Servo System of Hot Strip Mill. *Proceedings of the 5th Scandinavian International Conference on Fluid Power, SICFP '97*, 1997, pp. 429-444.
4. **Lurette, C. and Lecoecuche, S.** 2003. Unsupervised and auto-adaptive neural architecture for on-line monitoring. Application to a hydraulic process. *Engineering Applications of Artificial Intelligence*, Vol 16, 2003, pp. 441-451.
5. **Persson, U. and Fritz, K.** 2001. 728JET Primary Flight Control System. *Proceedings of the Seventh Scandinavian International Conference on Fluid Power, SICFP'01*, May 30 – June 1 2001, Tampere, Finland, pp. 237-251.
6. **Bower, J.L.** 1961. Digital Fluid Control System. US patent no. 2999482.
7. **Linjama, M., Laamanen, A. and Vilenius, M.** 2003. Is it Time for Digital Hydraulics? *Proceedings of the Eighth Scandinavian International Conference on Fluid Power*, May 7-9 2003, Tampere, Finland, pp. 347-366.
8. **Linjama, M. and Vilenius, M.** 2005. Digital Hydraulic Tracking Control of Mobile Machine Joint Actuator Mockup. To be published in the *Ninth Scandinavian International Conference on Fluid Power, SICFP'05*, Linköping, Sweden.
9. **Linjama, M. and Vilenius, M.** 2004. Digital hydraulic control of a mobile machine joint actuator mockup. *Proceedings of the Bath Workshop on Fluid Power Transmission & Motion Control*, September 1-4 2004 (PTMC'04), Bath, UK, pp. 145-158, ISBN 1 86058 466 7.
10. **Laamanen, A., Siivonen, L., Linjama, M. and Vilenius, M.** 2004. Digital Flow Control Unit - An Alternative for Proportional Valve? *Proceedings of the Bath Workshop on Fluid Power Transmission & Motion Control*, September 1-4 2004 (PTMC'04), Bath, UK, pp. 297-308, ISBN 1 86058 466 7.
11. **Lehmusto, M.** 1982. Hydraulijärjestelmän luotettavuus ja vikaantuminen. VTT, Espoo, Finland, ISBN 951-38-1447-5. (In Finnish)
12. **Hänninen, S., Järvenpää, J., Reunanen, M. and Suominen, J.** 1990. Mekatronisten komponenttien ja laitteiden vikaantuminen. Tekninen tiedotus 15/90, Suomen Metalli-, Kone- ja Sähköteknisen Teollisuuden Keskusliitto, MET ry, Helsinki, Finland. (In Finnish)

13. **Thorstensson, L. and Lövroth, C.** 1977. Tillförlitlighets- och fältstudier av hydrauliksystem, Del 1 – Slutrapport från projektet. Sveriges Mekanförbund, Stockholm, Sweden. (In Swedish)
14. **Anon.** 2004. SFS-EN ISO 13849-2: Safety of Machinery. Safety-related parts of control systems. Part 2: Validation, SFS ISO, Helsinki, Finland.
15. **Blanke, M.** 1999. Fault-tolerant Control Systems. *Advances in Control. Highlights of ECC'99*, Duisburg, Germany, Springer-Verlag London Limited, pp. 171-196.
16. **Siivonen, L., Linjama, M. and Vilenius, M.** 2005. The effect of Fluid Viscosity on Performance of Proportional Directional Valve and Digital Flow Control Unit. To be published in *The Ninth Scandinavian Conference on Fluid Power, SICFP'05*, Linköping, Sweden.
17. **Anon.** 1998. ISO 10770-1, Hydraulic Fluid Power - Electrically Modulated Hydraulic Control Valves - Part 1: Test Methods for Four-way Directional Flow Control Valves. ISO.

Experiences on Combining Fault Tree Analysis and Failure Mode, Effects and Criticality Analysis for Fault Diagnosis of Hydrostatic Transmission

Heikki Rusanen, Timo Koivula and Jari Rinkinen

Institute of Hydraulics and Automation

Tampere University of Technology

P.O.Box 589, FIN-33101 Tampere, Finland

Phone +358 3 3115 4437 Fax +358 3115 2240

e-mail: heikki.rusanen@tut.fi

ABSTRACT

Detecting the failed component from an unhealthy hydrostatic transmission system is usually not a straightforward task. Failure in either main component (pump or motor) can cause similar effects to the whole system. Unnecessary component replacements can play remarkable role in costs. In addition, diagnosing time can be significant cause of downtime costs. Analytical analysis methods shorten the diagnosing time and prevent needless replacement of healthy components. The paper is concerned with combination of two different kinds of analysis methods.

The most vulnerable components of the hydrostatic transmission are determined with the aid of Failure Mode, Effects and Criticality Analysis (FMECA). The FMECA analysis form is tailored to suit especially to the condition monitoring purposes. A disadvantage of the FMECA is that each component is analyzed individually and combinations of failures are not typically taken into account.

The Fault Tree Analysis (FTA) is used for representing the interaction between failures and basic events of top failures. FTA can handle combination of failures, but it is not ideal when dealing with symptoms of failures in individual components.

The combination of FMECA and FTA is used for creating troubleshooting charts for locating the failed component in the system. The charts are composed so that diagnosing is started from the failure that is the easiest to detect. The analyzing level of the related system is designed so that it reveals the smallest component or part of it that is replaceable in field conditions. The analysis methods can also be used for detecting the root cause for the malfunction and so to prevent future failures to occur.

Finally, experiences from field of using troubleshooting charts based on FTA and FMECA are presented.

KEYWORDS: Fluid power, diagnosis, troubleshooting, FMECA, FTA

ABBREVIATIONS

FMECA	Failure mode-, effects- and criticality analysis
FTA	Fault tree analysis
HST	Hydrostatic transmission

1 INTRODUCTION

The hydrostatic transmission system is in principle very simple system, including only two main components, pump and motor. However, recognizing the exact fault and locating the failed component is usually not a straightforward task. Failures in either of the main components can cause similar undesired effects for the whole mobile machine.

Locating the failure is often more time-consuming task than replacing or repairing the failed component. Decreasing the time used for troubleshooting leads to decreased downtime and hence decreased repairing costs. Using different analyzing methods for finding failures may speed up repairing tasks. Different kinds of analyses could also be used for training of maintenance personnel. When troubleshooting is done systematically by a certain procedure, every possible failure will most probably be taken into account.

In this paper, two commonly used analysis methods Failure Mode, Effects and Criticality Analysis (FMECA) and Fault Tree Analysis (FTA) are presented. FMECA is used for systematic study of each component in the system. It is tailored to suit especially in to condition monitoring purposes, but can also be used to analytically study the system. FTA is a TOP-DOWN construction method where a failure seen by the operator is selected as the starting point of the analysis.

Troubleshooting charts for maintenance personnel are presented in the end part of the paper. In addition to maintenance personnel, the troubleshooting charts can also be used by the machine operators for early investigation of failed machine.

1.1 The system under study

The studied system is a hydrostatic transmission of a mobile machine. The simplified hydraulic circuit of the system is presented in Figure 1.

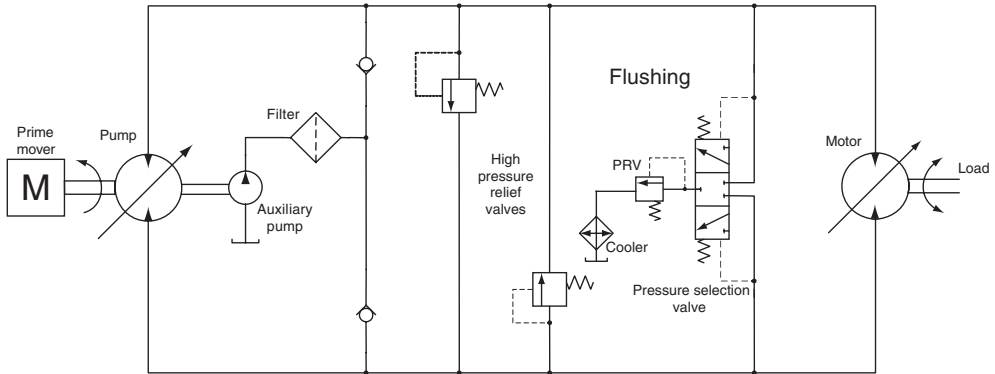


Figure 1. Simplified hydraulic circuit of the hydrostatic transmission system under study.

The diesel engine drives hydraulic pump, which is in this case a variable displacement axial piston pump. The pump provides flow for the hydraulic motor, which is a variable displacement axial piston unit. In addition, there are several auxiliary components such as boost pump (to keep adequate pressure in the return line) and flushing valves (to cool and clean the medium). The pressure in the power lines can be up to 450 bar. The used pressure medium is usually mineral oil but also vegetable oils can be used. [3]

2 ANALYSIS METHODS OF HYDRAULIC SYSTEMS

To analysed hydraulic systems effectively and productively thorough understanding of the system is needed. Drawings, operation descriptions, hydraulic diagrams, wiring diagrams, component specifications, and cross-sectional drawings are in good assistance during the course of the analysis. Quick and efficient troubleshooting requires that certain logical steps are followed to locate malfunctions in the shortest possible time. [1, 2, 6]

In the following sections, two commonly used analysis methods; failure mode-, effects-, and criticality analysis (FMECA) and fault tree analysis (FTA) are shortly presented.

2.1 Failure mode-, effects-, and criticality analysis

The Failure Mode, Effects and Criticality Analysis (FMECA) is an engineering quality method developed primarily for military purposes in USA in the mid of the past century. It is the first and the most common method used in reliability engineering. The need for FMECA was arisen when systems were getting more and more complicated and electrical control systems became more common. There are also various software tools for creating FMECA. [7, 4]

FMECA is a systematic procedure by which each potential failure of system is analysed. Each failure mode is classified according to its severity. [7]

FMECA is effective especially when it is applied to components which faults causes the failure to the whole system. Disadvantage of the FMECA is that each component is

analysed individually and combinations of failures are not taken into account. In addition, FMECA is carried out to each failure regardless of how significant or insignificant the failure mode is. This causes unnecessary documentation work and significant results can be snowed under the data. [7]

2.1.1 FMECA –form for condition monitoring purposes

The conventional FMECA –form made for the maintenance point of view has some restrictions. For example, it is not possible to evaluate how easy or difficult each faults are recognizable. Therefore, a new analysis form (with that feature) was tailored to suit especially for condition monitoring purposes. An example of proposed FMECA –form is presented in Table 1. [3]

Table 1. Proposed FMECA –form. [3]

Component name	Failure effect	S	Possible failures	Failure detection	Df	Cause of failure	O	SO	BestDf	Cause detection	Dc	BestDc	no.
Hydraulic Pump	Reduced output flow	1	Leak out of case	Pressure measurement	3	Faulty seals	2	2	3	Visual detection	0	0	1
				Visual detection	0	Broken case	0	0	3	Case pressure measurement	3	3	2
			Internal leak (to drain)	Pressure measurement	3	Wear of pistons, Wear of valve plate, Piston shoe failure	1	1	3	Visual detection	0	3	3
				Flow measurement	1		Temperature measurement			3			
				Angle measurement	2		Audible detection			0			
						Faulty seals	2	2	2	3	Visual detection	0	0

The component in the example is the hydraulic pump of the hydrostatic transmission system. There are four characteristic indexes in the form: severity (S), occurrence (O), detectivity of the cause of the failure (Dc) and the detectivity of the failure (Df). Severity index tells how serious the failure is. Occurrence number tells how often the failure will occur and detectivity numbers represent how well the failure or the cause of the failure is detectable, which is especially interesting when considering diagnosing or automated condition monitoring. The product of severity and occurrence numbers is called SO number. SO number depicts how much attention should be paid to each failure. In addition, there are two numbers to help presentation of the results, BestDf and BestDc. These numbers tell the highest detectivity number for current component. [3]

Table 2. Proposed FMECA –form, field explanations.[3]

Field	Description
Component name	Name of component under analysis.
Failure effect	Effect of the failure. What kind of effect failure has on component?
S	Severity number. Describes the severity of the failure.
Possible failures	Possible failures for the component in question. One or more failure for each component.
Failure Detection	Detection methods for possible failures. One or more method for each failure.
Df	Detectivity of the failure.
Cause of failure	Refers to Possible failures –field. One or more cause for each failure.
O	Occurrence number of cause of failure.
SO	Severity multiplied by occurrence. The greater value the more attention should be paid to.
BestDF	Highest failure detectivity number for current component. Refers to Df field.
Cause detection	One or more methods to detect the cause of failure.
Dc	Detectivity number for cause of failure.
BestDc	Highest cause detectivity number for current component. Refers to Dc field.
Fault ID	Number of target

2.1.2 Discussion --- FMECA

The proposed form of FMECA gives additional information about signals that are reasonable to monitor online or when diagnosing failed machine. This is important when determining targets to be checked in troubleshooting procedures. In addition, it can give information about how much attention should be paid to each failure mode in future development processes. From diagnosis or troubleshooting point of view the FMECA is not very effective. Analysis is carried out from the component point of view instead of the failure point of view.

2.2 Fault Tree Analysis

The Fault Tree Analysis (FTA) may be described as a logical representation of the relationships of primary events that leads to unwanted failure event called as the “top event”. It is widely used in industrial development processes. Especially, FTA is widely used from safety perspective. FTA was first presented at the 1960’s by Bell telephone laboratories. [1]

FTA represents TOP-DOWN -construction where analysing is started from the undesirable event (tree root) and logical combinations of sub-events are employed to map out the tree until reaching the initiating fault. In figure 2 the basic symbols of failure tree analysis is presented.[1]

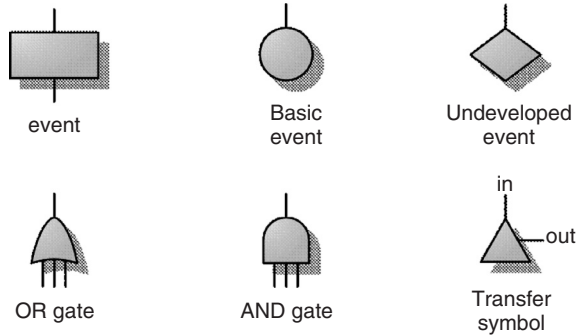


Figure 2. Symbols of fault tree analysis.

Table 3 explains the symbols shown in figure 1.

Table 3. Descriptions of fault tree symbols. [1]

Event	Fault event. Result of logical combination.
Basic Event	A basic fault event or failure of elementary part.
Undeveloped event	A fault whose causes are not been fully developed.
OR gate	Output fault occurs if one or more of the input faults occur.
AND gate	Output fault occurs if all of the input faults occur.
Transfer symbol	Symbol is used to avoid repeating segments of fault tree or if the fault tree is too big to one page.

With the help of FTA the critical parts of the system can be identified. The combinations of faults are also taken into account. FTA includes procedures to calculate probabilities of the certain failure events. Estimation of probabilities is carried out by using calculation rules of Boolean algebra. FTA helps also to understand systems ability to tolerate certain failures. [5]

Top faults of the previously described hydrostatic transmission can be for example like “Machine will not move”, “Speed control inoperative”, “Inadequate pulling power” or “Abnormal noise”. Determining the top fault is not necessarily very straightforward. For example, it may be difficult to say if the problem is “Reduced power” or “Reduced

maximum speed”. Recognizing the correct top fault requires knowledge and experiences of the encountered problems in the past. Interviews of maintenance and service personnel are of great help in this.

An example of usage of fault tree analysis is seen in the figure 3. In the example the top fault is identified as “The machine will not move”.

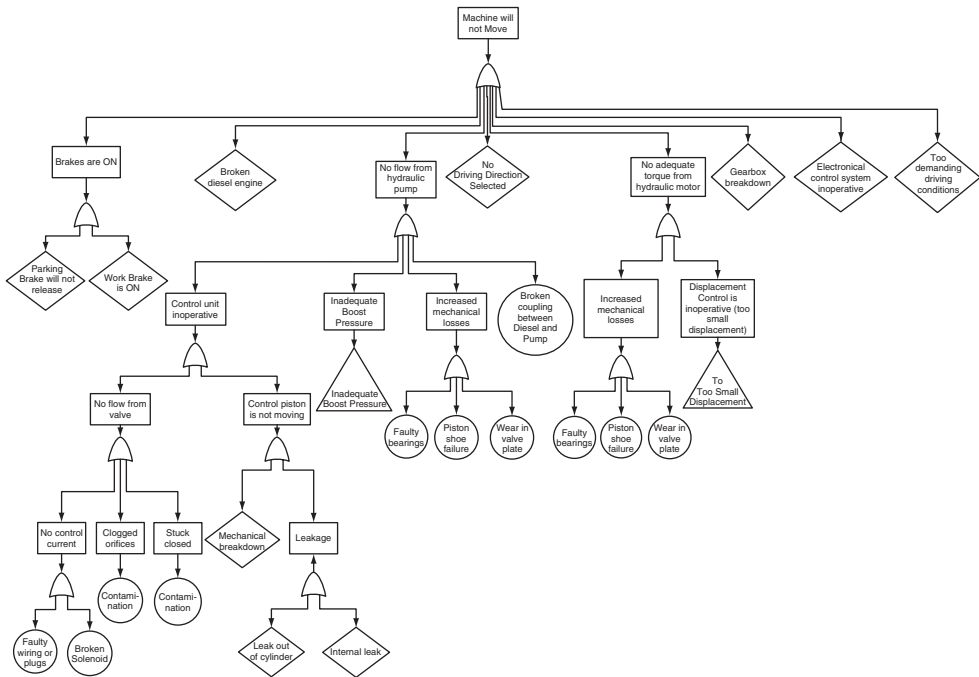


Figure 3. An example of FTA “Machine will not move”.

In the example, the top fault “Machine will not move” can be caused from eight different “high-level” reasons. Top fault is connected to sub faults with OR-gate. There are 5 diamonds to represents faults whose cases are not developed further. This is due to the fact that analysis in this case focuses on faults especially in hydraulics of the machine. Anyway, these are written in the analysis form that reader of the analysis form remembers other possible failures. Other causes for top fault could be faults such as “Broken diesel engine” or “Gearbox breakdown”.

Hydraulic related faults are located either in pump or in motor. In these cases the analysis is developed into quite a deep level. Basic faults are very detailed or they are not possible to be checked or repaired in field conditions. These are like “piston shoe failure” or “contamination in orifice of the pump controller”.

2.2.2 Discussion --- Fault Tree Analysis

The process of the fault tree analysis is started from the undesirable event. This is also the situation from which maintenance personnel starts to locate the failure. FTA takes also the combinations of faults into account. FTA does not define the troubleshooting order. Analysis is typically carried out too deep for troubleshooting point of view. Anyway, the results of the fault tree analysis is a very effective starting point for composing more practical troubleshooting charts. The FTA shows not only the critical failures but tells system ability to tolerate certain failures.

3 TROUBLESHOOTING CHARTS

Logical troubleshooting charts are written to shorten the time used for locating the failures in hydraulic systems. Just like the fault tree analysis, the troubleshooting charts presents TOP-DOWN –construction. Locating the failure is started from the symptom noticed by the operator e.g. “Machine will not move”. The troubleshooting chart is made keeping in mind the reasonable in practice changeable or repairable assemblies or sub-assemblies. Very small parts of components of mobile machine are not possible to be changed in the field conditions. Even dismantling a component in harsh environmental circumstances may lead to contamination of oil and hence to other problems. [2]

Charts are based on the results of both, the fault tree analysis and the failure mode-, effects- and criticality analysis. Construction of the charts is adopted mainly from fault tree analysis. The idea of TOP-DOWN thinking is present in both. In principle the difference between these two types of methods is the analysis order and the analysis level. The results acquired from FMECA are used for deciding the checking order and to give additional information how to check the suspected component or specific fault.

The charts are composed so that diagnosing is started from the failure that is the easiest to detect. There are a number of things which the operator can check even without leaving the drivers seat. Usually the first thing to check is whether there are active alarms in the cabin. Next targets are visual checks like external leaks, mechanical breakdowns etc.

There are many different initial failures which may cause symptoms seen in one top failure. This may lead to the need for carrying out tests when locating the cause of the top failure. The results from FMECA are of great aid when planning tests and reasonable targets to be monitored to reveal the initial causes of the failures. For example, which would be the signal which would reveal the failure in bearing seen in top fault “Speed control is working improperly”?

The troubleshooting charts are confined to the detection of the failure in the field. So, further analysis of already replaced components can be made with the help of FMECA or FTA. The troubleshooting charts are divided into top faults equally with the fault tree analysis. In figures 4a and 4b is an example of the troubleshooting chart.

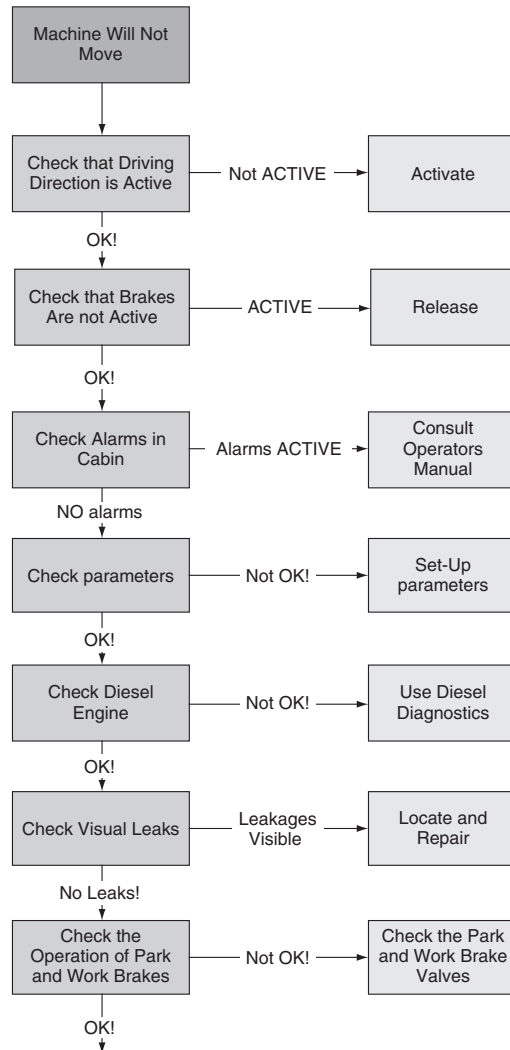


Figure 4a. Example of troubleshooting chart “Machine will not move”.

In the example the top failure is “Machine will not move”. Locating the failure is started from the cabin of the mobile machine. The first thing to do is to check if there are active alarms and make sure that there is no misuse in the machine operation. After that if fault is still active, troubleshooting is started by visual inspection for oil leaks and carried out further following the arrows and ruling out the possible faults.

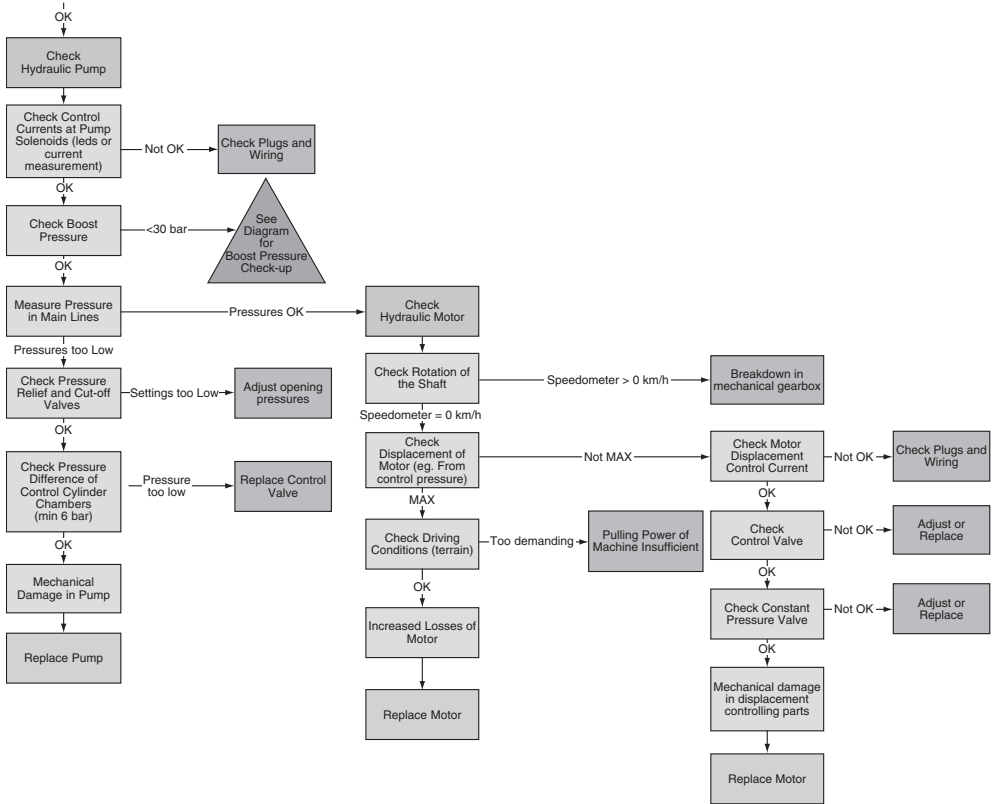


Figure 4b. Example of troubleshooting chart “Machine will not move”.

If the fault is not detected after visual checks, control system parameters are correct and others (diesel etc.) are diagnosed healthy, the fault needs to be searched in the hydraulic system itself. At first, a simple check is carried out to ensure that the control solenoids can get control current. Some systems have led lights for that in the control solenoid plugs. However, measuring the control current to solenoids is more thorough way to check the current in case of “control currents not ok”.

In order to correctly operate the pump and motor displacement control system need the correct control pressure. In the pump, this pressure is produced by the boost pump. To check the correct level of the boost pressure additional transducer is typically needed.

When going further in troubleshooting chart, more additional sensors are needed. For example both line pressures need to be measured. This in conjunction with blocking the power lines would reveal whether the failure is in the pump or in the motor. The troubleshooting is continued depending on the level of main pressures.

In field conditions, the smallest replaceable component is the controllers of the pump or the motor. After couple of measurements, it should be clear if the fault is in the controllers of either main unit or in other parts of them. In latter case, the whole component needs to be replaced.

3.1 Experiences of using troubleshooting charts

In the following, experiences in using troubleshooting charts are dealt with. The diagnosed top fault is “Machine will not move”. Troubleshooting is started with the chart seen in figure 4a. After adding a pressure sensor in boost pressure line it was noticed that it was not adequate enough. In figure 4b the troubleshooting is transferred to chart “Inadequate boost pressure”. This chart is partly illustrated in figure 5.

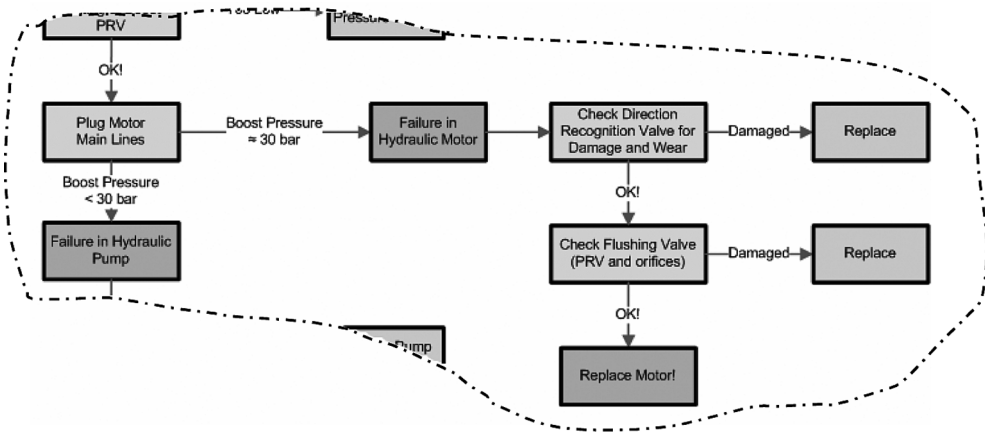


Figure 5. Part of troubleshooting chart “Inadequate boost pressure”.

Following the “Inadequate boost pressure” chart leads to diverge point where it is determined whether the problem is located in the pump or in the motor. This is carried out by blocking the lines from the pump to the motor. If the boost pressure is still decreased the problem is located in the pump. Otherwise it is associated with the motor. In this case the problem was found to be in the motor. After visual inspection of “Direction recognition valve” and “Flushing valve” the pressure relief valve of flushing valve was found to be stuck open and pressure from the return line was escaping through that. Flow from the boost pressure pump was not adequate enough to compensate the extra leakage and so the boost pressure was sunk. The controller of the pump uses the boost pressure for turning the swashplate and without the control pressure pump remains at zero displacement. At zero displacement the pump naturally produces no flow.

Instead of replacing the pump or/and the motor, replacing only the flushing valve solved the problem with minor costs. Usually problems with the boost pressure are assumed to be related with the pump but due to construction of the hydrostatic transmission system pressure can escape also from the motor. This is a problem that is not usually diagnosable

without blocking the lines to the motor. In the worst case the first component to be replaced could have been the pump and because this would have not led to desirable result also the motor would have been replaced.

For further analysis of the problem flushing valve the FMECA can be used (Table 4).

Table 4: FMECA of flushing valve package.

Component name	Failure effect	S	Possible failures	Failure detection	Df	Cause of failure	O	SO	BestDf	Cause detection	Dc	BestDc	no.
Flushing valve	Inadequate flushing	2	PRV stucked closed	Pressure measurement	2	Contaminated oil	2	4	2	Oil particle measurement	1	1	1
			Pressure selection valve stucked closed	Pressure measurement	2	Contaminated oil	2	4	2	Oil particle measurement	1	1	2
	Execccive flushing	3	PRV stucked open	Spool position measurement	1	Contaminated oil	2	6	2	Oil particle measurement	1	1	3
			Pressure selection valve in wrong position	Pressure measurement	2	Contaminated oil	2	6	2	Oil particle measurement	1	1	4

From table 4 it can be seen that problems in the flushing valve are typically caused by contaminated oil. Sticking of the pressure relief valve or pressure selection valve may be noticed by pressure measurement. If this kind of fault occurs the condition of oil should also be checked.

4 SUMMARY AND CONCLUSIONS

In this paper two analysis methods were presented. Failure mode-, effects and criticality analysis –form was tailored to suit especially condition monitoring purposes. Fault tree analysis was shortly presented and applied to a hydrostatic transmission system as an example. Troubleshooting charts based on these two types of analysis were introduced. Both FTA and troubleshooting charts represents TOP-DOWN construction where analysing is started from a high level failure. The level of analysis in the charts is chosen so that they reveal smallest replaceable component in field conditions. This helps to keep the charts as simple as possible. Due to detectivity estimation, proposed FMECA –form gives great value when deciding diagnosing order in troubleshooting charts. In addition, it is an effective tool for further analysing of failed components along with FTA.

According to experiences from the field, it was noticed that with the help of troubleshooting charts it is possible to locate failures quickly and they can prevent needless component replacements.

REFERENCES

- [1] Dhillon B S. 1999. Design Reliability: Fundamentals and Applications. CRC Press. ISBN: 0849314658. 416 p.
- [2] Mitchell J M, Pippenger J J. 1997. Fluid Power Maintenance Basics and Troubleshooting. Marcel Decker, ICN 270 Madison Avenue, New York. ISBN 0-8247-9833-3. 383 p.
- [3] Rusanen H, Rinkinen J. 2004. Model Oriented Condition Monitoring in Hydrostatic Transmission. Proceedings of the 3rd FPNI-PhD Symposium on Fluid Power, Terrassa Spain, June 30-July 2, 2004.
- [4] Stecki J S. 2003. Failure Analysis Using Energy Disturbance and AI Techniques. In the Eighth Scandinavian International Conference on Fluid Power, SICFP'03. Tampere, Finland. May 2003. ISBN 952-15-0972-4. Vol 1 pp 669- 682.
- [5] Vesely W E, Goldberg F F, Roberts N H, Haasl D F. 1981. Fault Tree Handbook. Systems and Reliability Research Office of Nuclear Regulatory Commission. Washington D.C.
- [6] Vickers. 1984. Logical Troubleshooting in Hydraulic Systems. Vickers, General Product Support. GB-B-9003. 37 p.
- [7] Väälisalo T. 1999. Vika-, vaikutus- ja kriittisyysanalyysi tuotekehitysprosessissa: Suoritusohjeet luotettavuuden analysointiin laite-/komponenttitasolla vvk:lla. Tampere, VTT Automaatio/AUT6. RISB006. 19 p. (in finnish).

System Modelling and Simulation

Model Identification of the Electrohydraulic Actuator for small signal inputs

Eric Sampson †, Saeid Habibi ‡, Richard Burton ‡, and Yuvin Chinniah §

† The MathWorks, Inc.

‡ Department of Mechanical Engineering, University of Saskatchewan

§ Research Institute for Occupational Health and Safety (IRSST)

ABSTRACT

A prototype of a high-precision hydrostatic actuation system, referred to as the ElectroHydraulic Actuator (EHA), has demonstrated an unprecedented level of accuracy for large load manipulation. This prototype has been able to move an inertial load of 20 Kg with an accuracy of 1 micron, and is currently being modified for sub-micron precision operation. The aim of this paper is to characterize the EHA using an empirical model for operation in the micron and sub-micron range. Previous experimental studies on the EHA have indicated that the system is nonlinear, but can be characterized as piecewise linear. The natural frequency and damping ratio of the EHA varies in a piecewise manner depending on its operating range, which is largely determined by the magnitude of the input signal. System characterization at input levels corresponding to micro-precision movements of the load has not been previously reported and is investigated in this paper. Piecewise linear empirical models are identified in view of implementing a nonlinear fuzzy control strategy.

NOMENCLATURE

$A1 = A2 = A$	Actuator pressure area	$5.05 \times 10^{-4} \text{ m}^2$
B	Coefficient of friction	$*760 \text{ N/m/s}$
$C1, C2, C3$	Actuator chambers	
D_p	Pump volumetric displacement	$1.6925 \times 10^{-7} \text{ m}^3/\text{rad}$
$E(s)$	Error signal	V
E_{ss}	Steady-state positional error	m
$F_{dis}(s)$	External force displacement	N
$G_{OL}(s)$	Outer loop controller	
$G_V(s)$	Motor/Pump subsystem transfer function	
$G_H(s)$	Hydraulic transfer function	
K_p, K_i	Controller gains	
L	Leakage coefficient	$*2 \times 10^{-15} \text{ m}^3/\text{s/Pa}$
M	Load mass	20 kg
$O1, O2, O3, O4, O5$	Actuator ports	
P_1, P_2	Actuator chamber pressure	Pa
Q_1, Q_2	Actuator chamber flow	m^3/s

$Q_{dis}(s)$	Disturbance flow	m^3/s
$Q_p(s)$	Pump flow	m^3/s
$U(s)$	Motor input voltage	V
V_o	Pipe plus mean actuator chamber volumes	$6.1 \times 10^{-5} \text{ m}^3$
$X(s)$	Position of actuator	m
$X_d(s)$	Demanded position of actuator	m
β_e	Effective bulk modulus of hydraulic oil	$*2.1 \times 10^8 \text{ Pa}$
κ_h	Hydraulic gain	
κ_v	Motor gain	40.55 rad/s/V
ω_{nh}	Hydraulic undamped natural freq.	
$\omega_p(s)$	Pump angular velocity	rad/s
ξ	Pump cross-port leakage coefficient	$*1.5 \times 10^{-13} \text{ m}^3/\text{s/Pa}$
ζ_h	Hydraulic damping ratio	
* Values obtained from (1)		

1. INTRODUCTION

A novel hydraulic actuation system referred to as the ElectroHydraulic Actuator (EHA) has been developed to overcome the drawbacks of conventional hydrostatic systems while providing high positional accuracy, as presented by Habibi and Goldenberg (2,3). The EHA uses a bi-directional fixed-displacement pump powered by a variable-speed servomotor (4,5,6,7,8). The actuator is directly connected to the pump as shown in Figure 1. The pump's speed and direction determine the fluid flow to and from the actuator and its resulting displacement. A prototype of the EHA has demonstrated an excellent level of performance. Using a nonlinear control approach, it has proved capable of moving a 20 kg load with an accuracy of 1 micron and a critically damped rise time of 0.3 s. Earlier work has demonstrated that the behavior of the EHA is both nonlinear and dependant on its input voltage. In this paper the EHA system will be modeled for input voltages less than 1.0V, a region where nonlinearities dominate and where precision operational control is most influenced. Previous work (9) has modeled the system for input voltages greater than 1.0V.

2. EHA SYSTEM

A brief introduction to the EHA system is beneficial at this point. The EHA system consists of the following components: Controller, Electric Motor, Bi-Directional Gear Pump, Accumulator, Sensors (Pressure, Position and Speed), Crossover Relief Valve, Symmetrical Actuator, and Load. A simplified schematic of the system is shown in Figure 1.

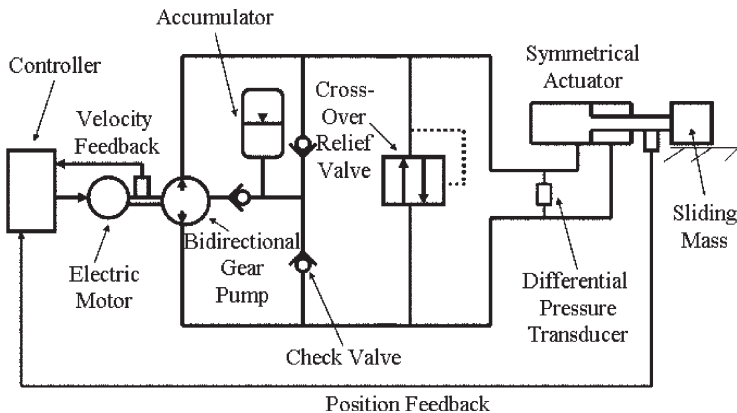


Figure 1: Schematic of ElectroHydraulic Actuator system

The three-phase brushless AC electric motor directly drives the pump. The pump in turn controls the flow of hydraulic oil to the two active chambers of the actuator. The pressure differential between the actuator chambers, which is a result of the resistance of the external load to motion, applies a net force on the load. In this case, the load is a 20 kg steel block mounted on two linear rails which is displaced horizontally by the force exerted on it by the actuator.

The symmetrical linear actuator used in the prototype has a single rod and has been designed expressly for the system, as described in (2,3). The actuator has two working chambers $C1$ and $C2$, illustrated in Figure 2. Chamber $C1$ is inside the hollow rod while chamber $C2$ is between the outside of the rod and the inside of the cylinder. Hydraulic fluid enters the two chambers of the actuator through ports $O1$ and $O2$. The working areas of the chambers $A1$ and $A2$ are made equal in area. This results in symmetrical flow, if leakage L is neglected. There also exists a third working chamber $C3$, which can be pressurized via port $O5$ to provide a bias to counteract a constant external force. Finally, ports $O3$ and $O4$ are provided to drain any actuator fluid leakage.

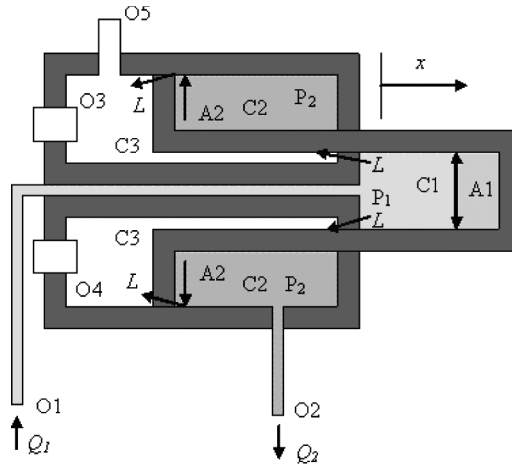


Figure 2: Cross-section of the actuator

An accumulator is connected to the low-pressure case drain of the gear pump. It prevents cavitation, and replaces fluid lost due to external leakage. The accumulator sets the minimum system pressure and can be adjusted from 2.76-6.9 Bar (40-100 psi). The crossover relief valve increases the safety of the system by preventing excessive pressure build-up if the actuator reaches the end of its travel, or if a fault were to occur. Finally, a position sensor measures the displacement of the load. The sensor, an optical linear encoder, has a resolution of 1 micron.

3. EHA MODEL

A mathematical model of the EHA system was developed in (10). This model was expanded by the author (11) to include the ability to simulate the effects of arbitrary time-varying force disturbances and flow disturbances on the EHA system. Figure 3 shows a simplified block diagram for the system showing the outer-loop position controller $G_{OL}(s)$, the inner-loop electrical subsystem $G_V(s)$, and the hydraulic subsystem $G_H(s)$.

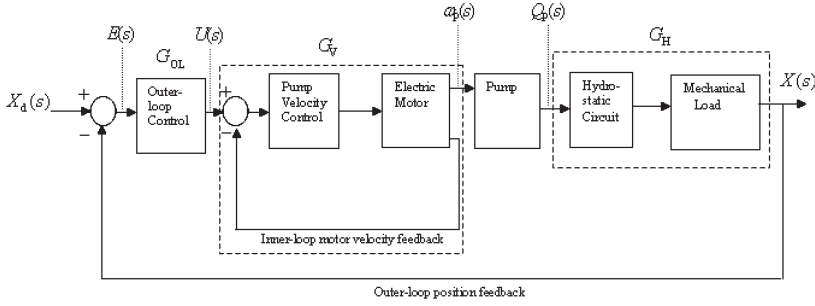


Figure 3: Simplified EHA block diagram

In (9), the transfer function of the electrical subsystem, $G_V(s)$, was identified using a constrained quadratic optimization technique. For a 5V sinusoidal input, the subsystem was found to be second-order with a zero:

$$\frac{\omega_p(s)}{U(s)} = \frac{2.779 \times 10^{-1} s + 40.55}{5.780 \times 10^{-5} s^2 + 1.061 \times 10^{-2} s + 1} \quad (1)$$

The analytical transfer function of the hydraulic subsystem, $G_H(s)$, presented in (10) is second-order Type 1:

$$\frac{X(s)}{\omega_p(s)} = \frac{\frac{2\beta_e A}{MV_o} D_p}{s^3 + s^2 \frac{B}{M} + \frac{(2\xi + L)\beta_e}{V_o} + s \frac{2\beta_e A^2}{MV_o} + \frac{(2\xi + L)\beta_e B}{MV_o}} \quad (2)$$

Substituting known system parameters into this theoretical transfer function results in the following hydraulic transfer function:

$$\frac{X(s)}{\omega_p(s)} = \frac{29.42}{s^3 + 39.04s^2 + 8.783 \times 10^4 s} \quad (3)$$

Combining Equations 1 and 3, the theoretical open-loop EHA transfer function for a 5V input is as follows, in pole-zero form:

$$\frac{X(s)}{U(s)} = \frac{141400 (s+145.9)}{s (s^2 + 183.6s + 1.73 \times 10^4) (s^2 + 39.04s + 8.783 \times 10^4)} \quad (4)$$

4. EXPERIMENT SPECIFICATION

In order to obtain the dynamic characteristics of the system for inputs less than 1.0V, a PC running MATLAB[®] Simulink and containing a 12-bit DAQ system was employed. The PC was used to both generate the input signal to the external controller and record the position of the load mass. The sampling time of the system was 0.001s.

The input signal was chosen to be a constant-magnitude discretely-swept sine wave. The frequency content was 1Hz to 500Hz in steps of 1 Hz. Each frequency was repeated for two full cycles to allow for settling time. A total of 18 inputs with magnitudes of 1.0V RMS to 0.1V RMS in steps of 0.05V were used as inputs for the open-loop system identification process.

The position signal was measured using a digital-output optical encoder with 1 micron resolution. Recorded signals from a typical test with a 0.45V RMS input signal and corresponding output position are shown in Figure 4. To eliminate the drift present in the output position data, the recorded position was numerically differentiated to obtain the output velocity, as shown in Figure 5. The output velocity was then used as the system output for the identification process. Due to the resolution of the position sensor and the sample time, the resolution of the velocity signal was 0.001m/s. Identification for input voltages less than 0.1V was not feasible using the current position sensor, since the differentiated velocity signal began to approach the resolution of the sensor.

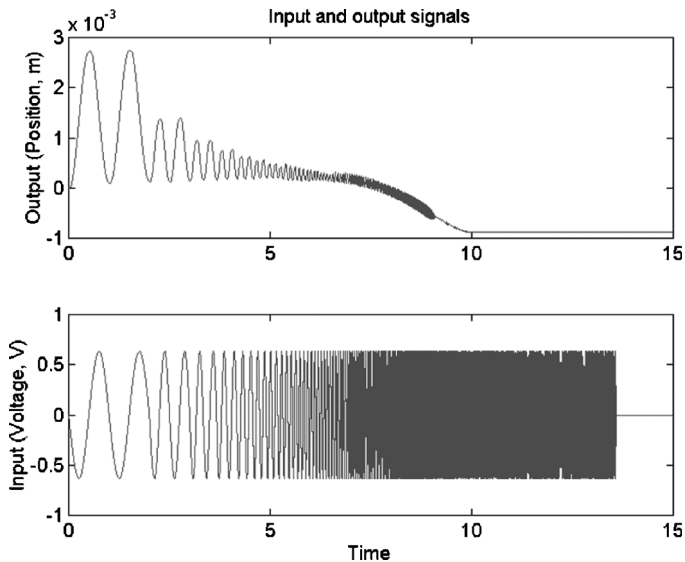


Figure 4: Output position and input voltage

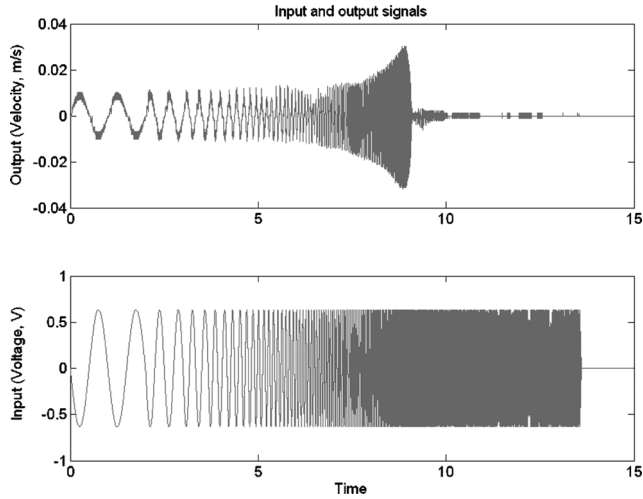


Figure 5: Output velocity and input voltage

5. INITIAL TESTS

The open-loop DC gain of the EHA system was determined for the input range -1.0V to 1.0V by setting the input to be a constant voltage, calculating the resulting load velocity and then determining the ratio of velocity/voltage. It can be seen in Figure 6 that the gain remains fixed at 0.0136m/s/V for the majority of the range tested, only changing as the input approached 0V. This demonstrates that the gain of the system was not significantly operating-point dependant over the range of interest.

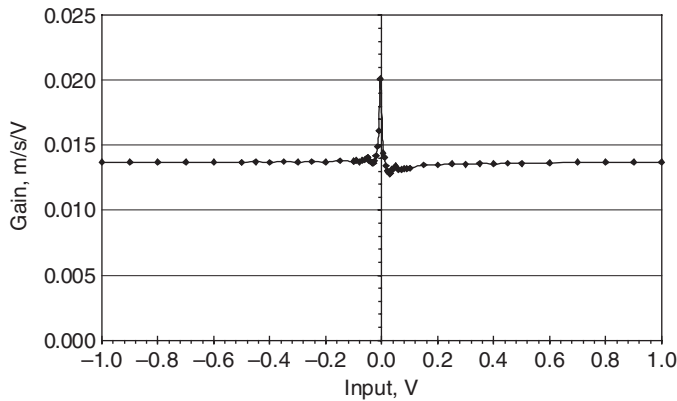


Figure 6: DC gain as a function of input voltage

To obtain the impulse response from the velocity data, a 100th order Finite Impulse Response (FIR) model was estimated using the Auto-Regression (AR) model structure (12). This produced the impulse response shown in Figure 7:

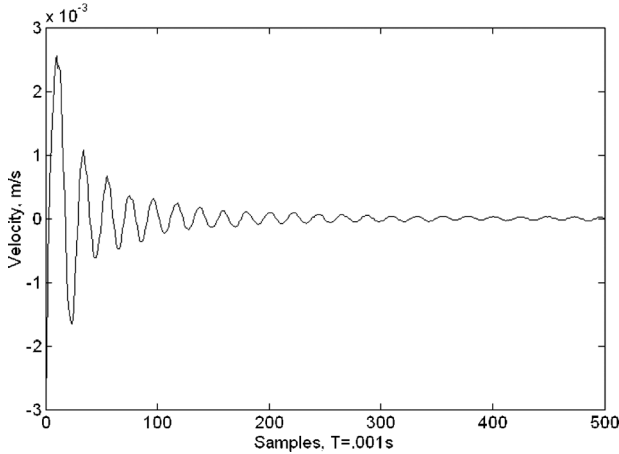


Figure 7: Computed velocity impulse response (from AR model)

The first forty coefficients of the Auto-Regression (AR) model “B” polynomial were used to construct a 20x20 Hankel matrix of Markov parameters. The singular values of the Markov parameters were then determined and plotted, as shown below in Figure 8. From inspection of this figure, it appears that the system is predominantly second order due to the prominence of the first two singular values. However, the system also appears to have some fourth order characteristics, as shown by the next two singular values being within a factor of 100 of the dominant singular values.

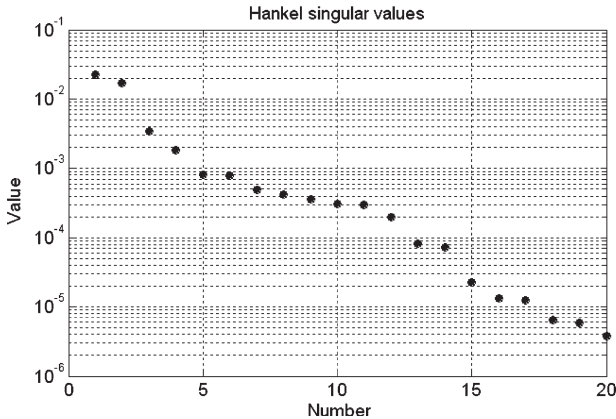


Figure 8: Hankel singular values of Markov parameters

6. DATA & PROCESSING

Once the form of the input signals was chosen and the initial tests completed, the working and validation data was obtained from the system. The working data was that used in the estimation process, while the validation data was reserved for verification of the performance of the models. The input and output signals were recorded with the input

voltage ranging from 0.1V RMS to 1.0V RMS in steps of 0.05V. The output velocity response was obtained by differentiating the recorded position data.

Figure 10 shows the working data set in a frequency-domain form. The transfer function magnitude as a function of frequency data was obtained using the Empirical Transfer Function Estimation (ETFE) technique at 512 points from 0-500Hz with a Hamming window of lag size 100 (12). Figure 10 shows the resulting Bode gain plot as a function of input voltage. Noticeable is the consistent underdamped response in the region 0.35V to 1.0V, with a bandwidth of approximately 55 Hz. Below this voltage, the system becomes overdamped and the bandwidth decreases significantly to approximately 8 Hz at 0.1V. The gain of the system is consistent at -37 dB for the majority of the input range, decreasing to -40 dB for the 0.1V input.

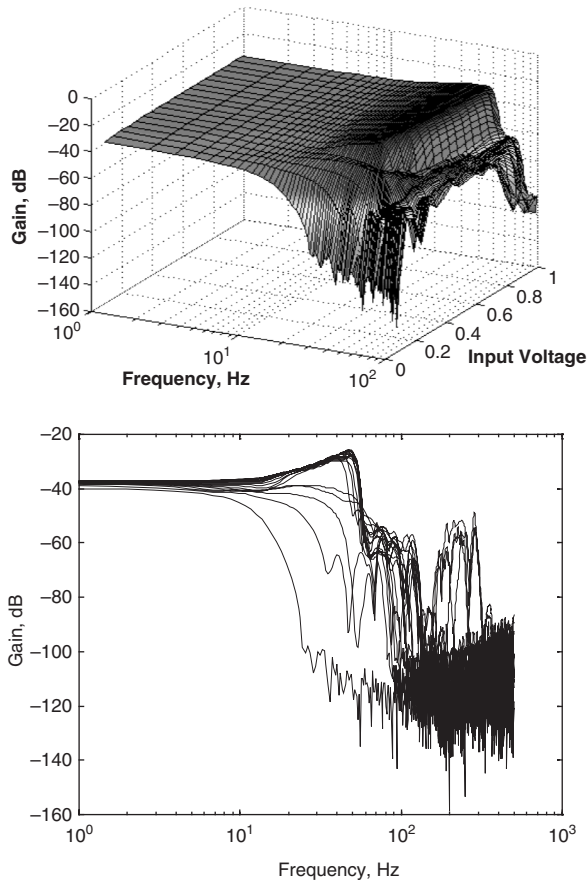


Figure 10: Experimental Bode gain plot as function of input voltage

7. MODEL IDENTIFICATION

The model identification process was performed using a frequency-domain identification methodology employing the working data shown in Figure 10. Specifically, the MATLAB® FREQID toolbox developed by de Callafon (13) was used to fit a linear time-invariant model to the frequency data recorded for the input voltage range 0.1V to 1.0V. This toolbox employs a least-squares curve fit attempting to minimize an arbitrarily weighted 2-norm between the data and the frequency response of the model. The weighting function for each of the inputs was specified in the frequency domain using the GUI tools available in the toolbox.

The model order was chosen to be fourth-order with one zero, to match the order of the theoretical system given in Eq. 4. After a model was predicted for each voltage input, dynamically insignificant poles and zeroes were manually removed. This gave the transfer functions shown in Table 1, listed in pole-zero form.

Table 1: Identified transfer functions

Input Voltage	Transfer Function $\frac{\dot{X}(s)}{U(s)}$
1.0-0.35	$\frac{187200(s+262.3)}{(s^2+192.2s+3.815 \times 10^4)(s^2+70.04s+9.532 \times 10^4)}$
0.30	$\frac{242.0(s+87.55)}{(s+51.77)(s^2+117.6s+3.364 \times 10^4)}$
0.25	$93760/[(s+141.3)(s^2+136.5s+5.815 \times 10^4)]$
0.20	$\frac{240.1(s+55.22)}{(s+38.61)(s^2+207.7s+3.009 \times 10^4)}$
0.15	$0.3948(s+374)/[(s+177.4)(s+78.55)]$
0.10	$0.4064(s+7)/[(s+37.91)(s+9.237)]$

Figure 11 shows the computed Bode gain plot for the identified models over the range of interest. In comparison with the experimental plot in Figure 10, it can be seen that the 0.35V to 1.0V range is matched quite well. Inspecting the experimental Bode plot shown in Figure 10, it appears that the system's output decreases, or rolls off, at approximately 80 dB/decade. As the input voltage decreases below the 0.35V level, the ability of the identification method to match the roll off characteristic of the system becomes impaired. This is likely due to an increase in the noise content of the data associated with the lower input levels.

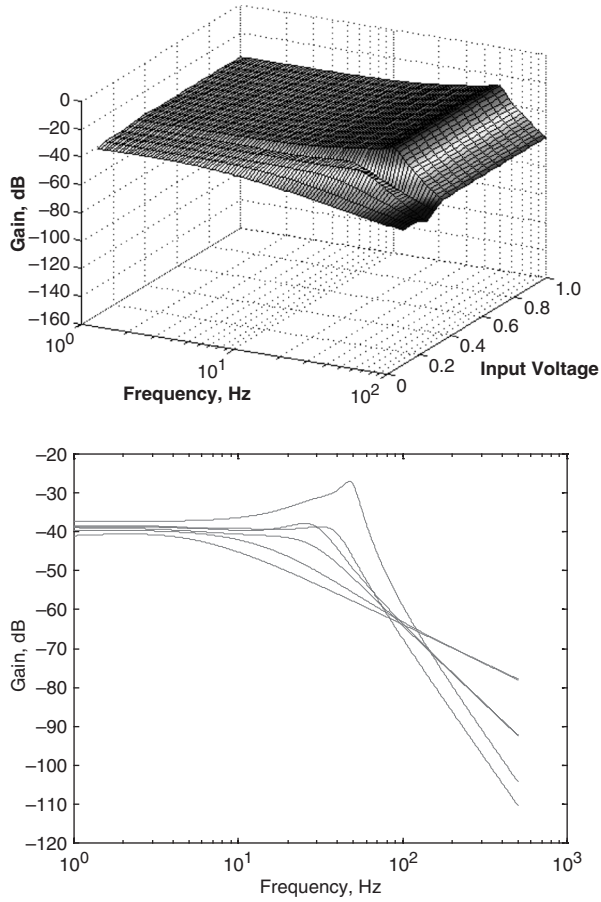


Figure 11: Identified Bode gain plot as a function of input voltage

8. VALIDATION

Once models were identified for each input voltage, the response of the model to the input data was simulated for validation purposes. The validation data set mentioned in the Data & Processing section was plotted on the same graphs as the simulated response in order to visually verify the validity of the models. Figures 12-15 show the simulated and experimental response to the discrete swept sine wave from 1-500Hz. The 'envelope' of the simulated response is overlaid on the experimental response as a black line in order to facilitate comparison between the simulation and the experimental responses. The agreement is generally very good up to a minimum of 10 Hz (in the 0.10V case) and to a maximum of 50 Hz (in the 0.60V case). It can be seen in all cases that the fit is not exact at

low frequencies. This is due to the optimization method employed in the FREQID toolbox, which gives an equal weight to each data point. Alternatively, decreasing the weights logarithmically as the frequency increases would compensate for the increasing number of data points per decade, as is discussed in (12). Furthermore, the accuracy of the identified models decreases noticeably as the input voltage decreases towards 0.1V. This may be due to the resolution of the velocity signal, which is obtained by differentiating the position signal. For example, the peak magnitude of the velocity signal for the 0.1V input is approximately 0.002 m/s, which is comparable to the sensor resolution of 0.001 m/s.

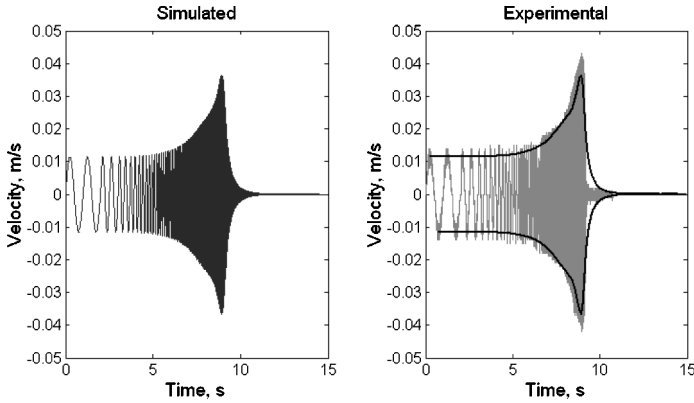


Figure 12: Comparison of simulated and experimental response for 0.60V input (typical of 1.0V-0.35V range)

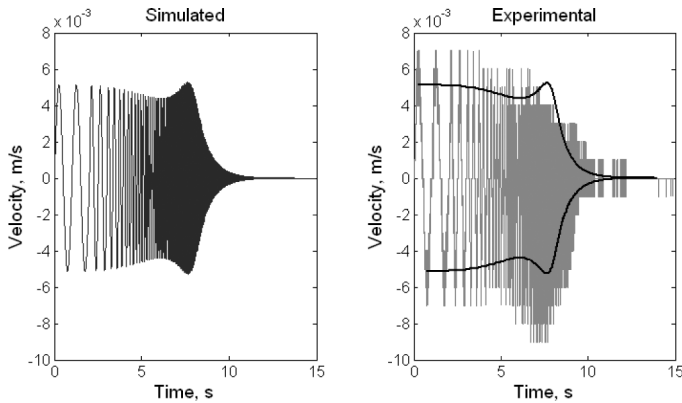


Figure 13: Comparison of simulated and experimental response for 0.30V input

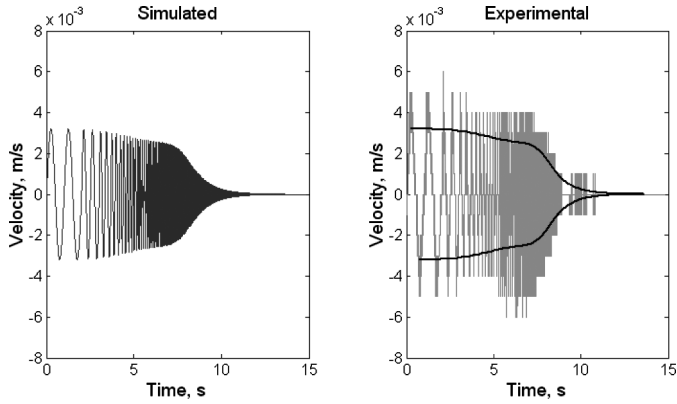


Figure 14: Comparison of simulated and experimental response for 0.20V input

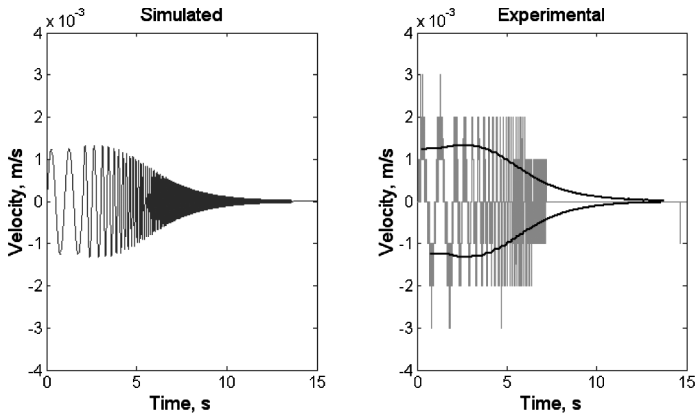


Figure 15: Comparison of simulated and experimental response for 0.10V input

Finally, Figure 16 shows the closed-loop experimental and simulated response to a 0.01m step input. The model simulated in this case was the one identified for the 0.35V to 1.0V range. In both cases, a proportional controller $G_{ol} = K_p = 585$ as employed in (10) was used. Excellent agreement between the simulated and experimental response is demonstrated, neglecting the time delay of 0.04 seconds that was not included in the system models.

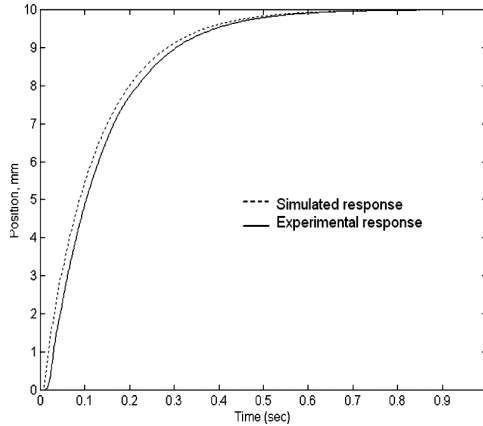


Figure 16: Simulated and experimental closed-loop step response

9. CONCLUDING STATEMENTS

The ElectroHydraulic Actuator (EHA) is a high-performance positioning system that employs a novel symmetrical linear actuator. As such, it has unique characteristics which were investigated in this paper for the input voltage range of 0.1V to 1.0V RMS. It has been found that the system exhibits consistent performance in the 0.35V to 1.0V RMS input range, with an underdamped response having a bandwidth of 55 Hz and a gain of -37 dB. As the input voltage decreases, the bandwidth becomes significantly lower and system becomes overdamped. At a 0.1V RMS input, the bandwidth has decreased to 8 Hz and the gain to -40dB. As such, a linear controller will not be able to achieve optimal control over the tested range, since the performance characteristics vary appreciably with the input voltage. A control scheme which can reflect the nonlinear damping ratio, gain, and natural frequency in the region of less than 1V input and can allow a smooth transition between the identified regions is necessary for nanometer precision control. For this reason, nonlinear control of the EHA system using a Fuzzy controller and other nonlinear controllers are now being investigated.

REFERENCES

- (1) Chinniah, Y. 2004. *Fault Detection in the Electrohydraulic Actuator Using Extended Kalman Filter*. PhD thesis. University of Saskatchewan.
- (2) Habibi, S. and Goldenberg, A. 1999. Design and Analysis of a Symmetrical Linear Actuator for Hydraulic Systems. *Transactions of the CSME*, Vol. 23, No. 3 & 4, pp. 377-397.

- (3) Habibi, S. and Goldenburg, A. 2000. Design of a New High Performance Electrohydraulic Actuator. *IEEE/ASME Transactions on Mechatronics*, Vol. 5, No. 2.
- (4) Arnautovic, S. 1993. *Electrohydraulic Actuator*. Technical Report. University of Toronto
- (5) Desai, J. and Bobrow, J. 1989. Modelling and Analysis of a High Torque Hydrostatic Actuator for Robotic Applications, *Exp. Robotics*
- (6) Manring, N. and Lueke, G. 1998. Modelling and Designing a Hydrostatic Transmission with a Fixed-Displacement Motor, *Journal of Dyn. Sys. Meas. & Cont.* Vol 120, pp. 45-50.
- (7) Merritt, H. 1967. *Hydraulic Control Systems*. John Wiley & Sons.
- (8) Watton, J. 1989. *Fluid Power Systems*. Prentice Hall.
- (9) Habibi, S., Pastrakuljic, V. and Goldenburg, A. 2000. Model Identification and Analysis of a High Performance Hydrostatic Actuation System, *SAE paper 2000-01-2619, 2000 SAE International Off-Highway & Powerplant Congress and Exposition*.
- (10) Habibi, S. and Singh, G. 2000. Derivation of Design Requirements for Optimization of a High Performance Hydrostatic Actuation System, *International Journal of Fluid Power*, Vol.1, No. 2.
- (11) Sampson, E., Habibi, S., Burton, R. and Chinniah, Y. 2004. Effect of Controller in Reducing Steady-State Error due to Flow and Force Disturbances in the ElectroHydraulic Actuator System, *International Journal of Fluid Power*, Vol. 5, No. 2
- (12) Ljung, L. 1999. *System Identification – Theory for the User, 2nd Ed.* Prentice Hall PTR.
- (13) de Callafon, R. A. and Van de Hof, P. M. J. "Frequid -- frequency domain identification toolbox for use with Matlab," *Sel. Top. Identification and Modeling. Control.*, Vol. 9, pp. 129--134, 1996.

ACKNOWLEDGMENTS

The authors acknowledge the financial support of the National Science and Engineering Research Council of Canada and the Department of Mechanical Engineering, University of Saskatchewan during this study.

An efficient numerical method for solving the dynamic equations of complex fluid power systems

S Esqué* and A Ellman**

* Institute of Hydraulics and Automation, Tampere University of Technology, Finland

** Institute of Machine Design, Tampere University of Technology, Finland

ABSTRACT

The numerical solution of fluid power circuit models, formulated as a set of ordinary differential equations, requires a numerical integrator able to deal with non-linearities, stiffness and discontinuities. In this paper a single-step second-order two-stage Rosenbrock formula that shows good stability properties (L -stability) is presented. Despite the reduced linear algebra of the formula itself, the numerical efficiency of the integrator (number of operations to advance through the integration) is further improved by reducing the computational costs required to determine the Jacobian matrix of the system: Rather than deriving numerically the Jacobian matrix for every integration step, the code generates the Jacobian matrix analytically (as a function of the state variables). Thus, only a few function evaluations are required to determine the Jacobian at every time step of the integration. Finally, the paper illustrates the advantages of using the analytical expression of the Jacobian in the integration formula and evaluates its costs.

1 INTRODUCTION

There is no rule of thumb when choosing a numerical integrator intended for solving a system of ODEs. Among the dozens of available codes targeted for solving systems of ODEs, the user must take into account the characteristics of the system to be simulated. The set of ordinary differential equations (ODEs) describing the dynamics of a fluid power circuit is commonly characterized for its:

- **Stiffness:** Different sizes of compressible fluid volumes make the eigenvalues of the Jacobian to be of greatly different magnitude. Large negative eigenvalues correspond to fast-decaying transients. The presence of these small time constants makes the integration of such systems difficult. As a consequence the length of the integration step is not dictated by accuracy requirements but by the boundary of the stability region.
- **Discontinuities:** Cushions, digital signals, sudden openings and closure of valves introduce discontinuities in the state equations and in their solution. This causes difficulties for achieving full accuracy of the solution and may also induce stability problems.

Hence, the numerical method for integrating the mathematical model of a fluid power circuit must guarantee at least two important properties in order to succeed with the solution: stability and accuracy. Another important property that the numerical method must retain is the *computational efficiency*, which can be quantified by the number of operations required by the formula in order to advance one step in the integration. Computationally efficient codes might be needed to run real-time simulations such as hardware-in-the-loop, teleoperation (man-in-the-loop) or in mobile-hydraulic simulators (forest machine simulator).

Numerical methods able to solve stiff systems of ODEs are *implicit*, meaning that the stages or variables of the formula are defined by coupled sets of equations. An iteration scheme is therefore needed, which requires the computation of the Jacobian of the system. Implicit methods are, by far, less computational efficient than explicit methods. Nonetheless, the main contribution of this paper is the reduction of computational expenses in the simulation of fluid power circuits. This is achieved by presenting:

- A simple (to implement) and efficient implicit numerical method with remarkably good stability properties (*L*-stable).
- A modelling scheme that allows the derivation of the analytical expression of the Jacobian matrix. The instantaneous Jacobian matrix at every integration step is then obtained by simply evaluating the stored analytical form.

2 MATHEMATICAL MODELLING OF COMMONLY USED FLUID POWER COMPONENTS

The first part of this section illustrates the formulation describing the dynamic behaviour of a few mostly used fluid power components and elements. Such models comprise: the pressure generation in a fixed-size volume, pressure generation and flow dynamics in a short pipe, dynamics of a cylinder actuator, a pressure relief valve, and an orifice flow formula. More detailed information of the formulation of these component models and a two-phase

fluid model can be found in Esqué & Ellman (1). Secondly, the section illustrates how a network of FP components can be built by interconnecting the individual models.

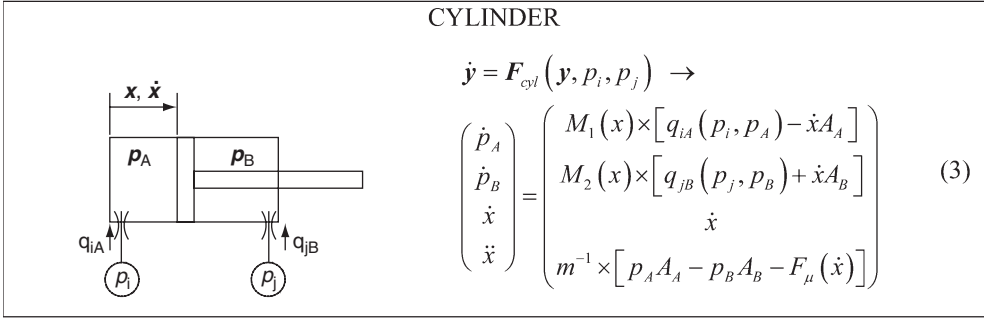
The components are modelled as independent object-oriented entities with connection ports. Each connection port transmits a two-way interaction (input and output variables) to the adjacent component. According to their interaction, the components can be sorted in two classes:

- Pressure generators
- Orifice-flow resistances (flow generators)

Pressure generators act as capacitances and include such elements of the hydraulics that contain a significant volume of compressible fluid, such as volumes, pipes, actuators, etc. Input variables of pressure generator models are the incoming and outgoing flows to and from the component. The output variable is then the pressure(s) in the volume(s) of the component. Table 1 shows schematics of the components and their mathematical formulation as a set of ODEs.

Table 1. Pressure generator components.

FIXED-SIZE VOLUME	
	$M_i \dot{p}_i = q(\mathbf{p}) \rightarrow$ $M_i \dot{p}_i = q_{ij}(p_i, p_j) - q_{il}(p_i, p_l) - q_{ik}(p_i, p_k) \quad (1)$
SHORT PIPELINE	
	$\dot{\mathbf{y}} = \mathbf{F}_{pipe}(\mathbf{y}, p_i, p_j) \rightarrow$ $\begin{pmatrix} \dot{p}_1 \\ \dot{p}_2 \\ \dot{q} \end{pmatrix} = \begin{pmatrix} \gamma_{M_1} \times [q_{i1}(p_i, p_1) - q] \\ \gamma_{M_2} \times [q_{j2}(p_j, p_2) + q] \\ [(p_1 - p_2) - (K_L q + K_T q q)] \times C \end{pmatrix} \quad (2)$ $K_L = \frac{p_b q_a^2 - p_a q_b^2}{(q_a - q_b) q_a q_b}; \quad K_T = \frac{p_a q_b - p_b q_a}{(q_a - q_b) q_a q_b}$ $C = A / (\rho L)$



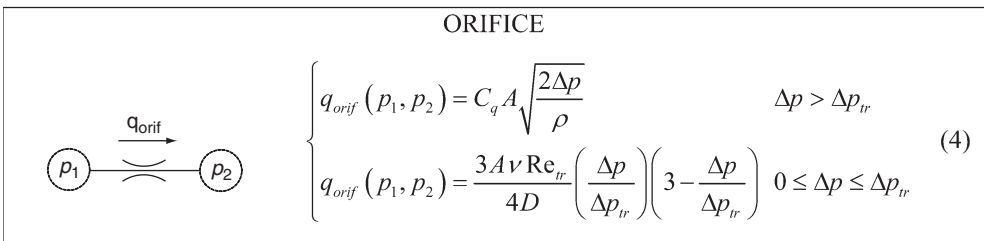
Formulation of the fixed-size volume and the hydraulic cylinder is well-known and it is written in equations (1) and (3). The pipeline model in equation (2) is modelled as two lumped volumes connected by a resistance, which takes into account the pressure losses due to laminar flow between the ports of the pipe (according to Hagen-Poiseuille law) and other energy losses caused by changes in the geometry of the pipe. Parameters K_L and K_T quantifying such losses can be determined semi-empirically in equation (2) by measuring a pair of pressure-flow points. Dynamics of the pipe are also accounted by considering the inertial load of the circulating fluid.

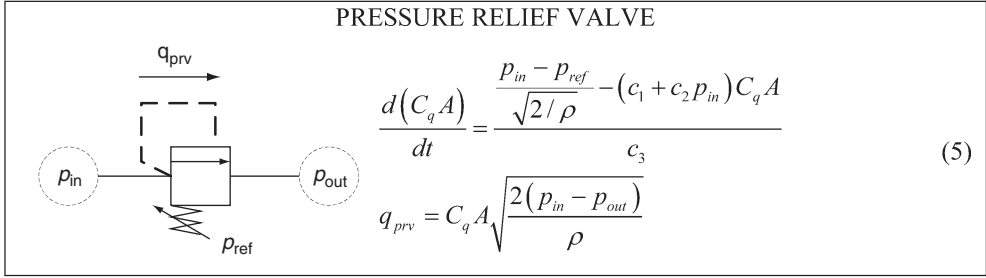
The second type of component (orifice-flow resistances) is based on the flow-through-orifice formula. Valves and restrictors are commonly modelled with this formula. Input variables of orifice-flow elements are pressures and the output variable is the flow through the orifice. Table 2 shows the schematic of the modelled elements (orifice and pressure relief valve) together with their formulation.

The formulation of the flow through an orifice takes into account the laminar and turbulent regimes of flow. The formula was derived by Ellman & Piché (2) and shows a smooth transition (continuous in q and in its first derivative) between laminar and turbulent regimes. The formula replaces the infinitive derivative of the Jacobian in the turbulent flow when pressure differences tend to zero.

The model of the pressure relief valve, Handroos & Vilenius (3), considers the dynamics of the spool as a first order model. Parameters c_1 and c_2 describe the steady-state of the valve and they are identified by means of pressure-flow pair measurements picked up at two different setting pressures. Parameter c_3 describes the dynamics of the valve.

Table 2. Orifice-flow resistance components.





A network of FP components can be therefore assembled in a modular way by connecting pressure generator models to orifice-flow resistance models, as Figure 1 shows. The state equation of the system $\dot{y} = F(y)$ is then formed by adding the individual state equations of the pressure generation components. The state equation of the system described in Figure 1 is given by the equation (6), with the vector of state variables $y = (p_1 \ p_2 \ p_3 \ x \ \dot{x})^T$.

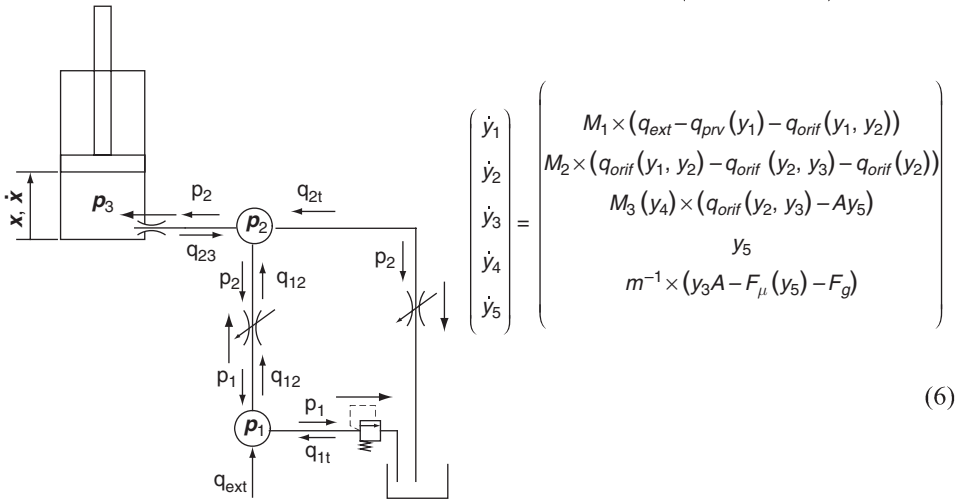


Figure 1. Schematic of a FP circuit built as a network of modular components.

3 NUMERICAL INTEGRATION FORMULA

In this section, a numerical method for the integration of fluid power circuits is presented. The autonomous system of ordinary differential equations describing the circuit may be written in matrix notation as

$$\dot{y} = F(y), \quad y(t_0) = y_0 \quad (7)$$

Multi-step algorithms (formulas using previous calculated solutions in order to evolve the solution) and single-step algorithms (only making use of the latest previous solution to cal-

culate the next one) have been used in the numerical integration of fluid power system equations. The advantages of single-step methods are their easy implementation, they show better stability properties, and the accuracy near discontinuities is better realized than in multi-step methods. The main disadvantage of single-step methods is, in general, that they require more computational time than multi-step methods of comparable accuracy. However, the latest disadvantage could be questioned when integrating fluid power circuits. The stiffness of its ODEs and the discontinuities present in fluid power circuits may weak the computational performance of the multi-step methods.

Runge-Kutta (RK) formulas are the most popular codes within the single-step methods. Most of the simpler algorithms that have been proposed belong to the family of semi-implicit RK formulas with A -stability properties. A -stable methods guarantee the numerical stability of the formula for any value of the step size. However, for very stiff systems A -stability is not sufficient. Piché & Ellman (4) analyse several two-stage semi-implicit RK formulas proposed for fluid power circuits and show that A -stable methods require excessively small time increment to avoid numerical oscillations in very stiff systems. A solution to the problem would be to set the small volumes as incompressible. The resulting system would be composed of algebraic differential equations, which would increase the complexity of the models: for example, when formulating elements of variable volume sizes (as actuators), where sometimes the fluid would be considered compressible and at other times incompressible. Another solution to avoid the problem of numerical oscillations is to implement an L -stable method, which can be defined as an A -stable method whose components of the response associated with the highly stiff modes are extinguished immediately. L -stable methods do not show the numerical oscillations observed in A -stable methods. A two-stage Rosenbrock formula (of the family of semi-implicit RK methods) with a reduced linear algebra is presented. The formula is L -stable and with second-order of accuracy.

A two-stage semi-implicit RK formula to integrate equation (7) from $\mathbf{y}_0 = \mathbf{y}(t_0)$ to $\mathbf{y}_1 = \mathbf{y}(t_0 + h)$ is given by equation (8). The term semi-implicit indicates that the implicit variables \mathbf{k}_i can be solved in order $i=1, 2, \dots, s$ (where s is the number of stages of the method). The implicitness of such equations requires that for each stage i , \mathbf{k}_i is obtained by solving r systems of non-linear equations sequentially by using some type of Newton iteration.

$$\begin{aligned} \mathbf{k}_1 &= h\mathbf{F}(\mathbf{y}_0 + a_{11}\mathbf{k}_1) \\ \mathbf{k}_2 &= h\mathbf{F}(\mathbf{y}_0 + a_{12}\mathbf{k}_1 + a_{22}\mathbf{k}_2) \\ \mathbf{y}_1 &= \mathbf{y}_0 + b_1\mathbf{k}_1 + b_2\mathbf{k}_2 \end{aligned} \quad (8)$$

Rosenbrock methods belong to a large class, which try to avoid non-linear systems and replace them by a sequence of linear systems (these formulas can be called also *linearly-implicit* RK formulas). They can be interpreted as the application of a single Newton iteration to each stage in the formula (8). The resulting Rosenbrock formulae are:

$$\begin{aligned}
 (\mathbf{I} - d_{11}h\mathbf{J})\mathbf{k}_1 &= h\mathbf{F}(\mathbf{y}_0) \\
 (\mathbf{I} - d_{22}h\mathbf{J})\mathbf{k}_2 &= h\mathbf{F}(\mathbf{y}_0 + a_{21}\mathbf{k}_1) \\
 \mathbf{y}_1 &= \mathbf{y}_0 + b_1\mathbf{k}_1 + b_2\mathbf{k}_2
 \end{aligned}
 \tag{9}$$

where \mathbf{J} is the Jacobian matrix, whose elements are defined as $J_{ij} = \left. \frac{\partial F_i}{\partial y_j} \right|_{\mathbf{y}=\mathbf{y}_0}$.

Wolfbrandt (5) formulated a class of Rosenbrock methods named ROW-methods or modified Rosenbrock methods. They are a generalization of the Rosenbrock method showed in (9). The s -stage modified Rosenbrock formula is given by

$$\begin{aligned}
 \mathbf{k}_i &= \mathbf{F} \left(\mathbf{y}_0 + h \sum_{j=1}^{i-1} a_{ij}\mathbf{k}_j \right) + h\mathbf{J} \sum_{j=1}^i d_{ij}\mathbf{k}_j \quad i = 1, \dots, s \\
 \mathbf{y}_1 &= \mathbf{y}_0 + h \sum_{i=1}^s b_i\mathbf{k}_i
 \end{aligned}
 \tag{10}$$

Esqué *et al* (6) presented a two-stage L -stable order-2 formula based on the modified Rosenbrock formula (11). A third-stage was added to the formula in order to obtain an error predictor of the solution and for implementing an adaptive step size controller. The formula was tested by integrating individual models (a double-acting hydraulic cylinder and a short pipeline) and showed excellent stability properties. It also proved to detect and handle discontinuities by adapting the step size of integration.

Due to its simplicity, this paper is going to focus in the Rosenbrock formula. The value of the five free-choice parameters $(a_{21}, d_{11}, d_{22}, b_1, b_2)$ in the formula (9) will determine the accuracy, stability and the computational efficiency of the formula. Conditions on the accuracy of the system are obtained from Taylor series. They can be found tabulated in Hairer 10.IV.7 (7). Conditions on the stability can be derived by means of the stability function $R(h\lambda)$, which can be interpreted as the numerical solution, $\mathbf{y}_1 = R(h\lambda)\mathbf{y}_0$, of the *Dahlquist* test equation $y' = \lambda y$, with $y_0 = 1$. A method is L -stable if the solution behaves maximally damped, i.e. $y_1/y_0 \rightarrow 0$, as $h\lambda \rightarrow \infty$. The latest condition is achieved when $R(\infty) = 0$. By imposing second-order accuracy and L -stability conditions to formula (9), four equations are obtained to determine the five free parameters. As a fifth equation, the equality $d_{11} = d_{22} = d$ is imposed. By assigning $d_{11} = d_{22}$ the matrices $(\mathbf{I} - d_{ii}h\mathbf{J})$ of formula (9) become identical. This allows solving the two linear systems by only using one LU-decomposition. The value of the five free parameters are then determined and showed in equation (11).

$$a_{21} = \frac{\sqrt{2}-1}{2}; \quad d_{11} = d_{22} = \frac{\sqrt{2}-1}{\sqrt{2}}; \quad b_1 = 0; \quad b_2 = 1 \tag{11}$$

This section concludes by summarizing the principal advantages of the presented Rosenbrock formula:

- A single Newton iteration is used to solve the implicitness of the formula. This reduces the linear algebra of the semi-implicit RK formula to the solution of two linear systems and two function evaluations.
- Only one LU decomposition is needed to solve the system of equations for each k_i .
- Rosenbrock methods need a full and accurate Jacobian to achieve the theoretical degree of stability. Although the determination of the Jacobian is computationally expensive, next section will show that the full Jacobian matrix can be obtained accurately in every integration step by just performing a few function evaluations.

4 GENERATION OF THE ANALYTICAL JACOBIAN MATRIX

This section describes how the simulator can provide, to the numerical integrator, an analytical expression of the full Jacobian matrix of the system. By storing the analytical form of the Jacobian, the integrator can calculate the Jacobian matrix at any integration point y_0 by simply evaluating its stored analytical expression. The next section will show the advantages of this strategy versus obtaining the Jacobian matrix numerically by means of iteration.

The fluid power circuit showed in Figure 1 is taken as an example in order to illustrate how the analytical Jacobian matrix can be generated by a subroutine. First, the user must provide a *formal* description of the fluid power system. An example of such description is given in the following lines:

```

volume(1).in = qp;
volume(1).out = 2, prv;
volume(2).in = 1;
volume(2).out = 3, tank;
cylinder_sa(1).in = 2;

```

(12)

where each pressure generator component (i.e. components contributing with state variables) has a structure assigned. From reading the provided description, the algorithm indexes the vector of state variables of the system ($y = [y_1 \ y_2 \ y_3 \ y_4 \ y_5]^T = [p_1 \ p_2 \ p_3 \ x \ \dot{x}]^T$). Next, the algorithm determines how the pressure generator components are interconnected. This is how the algorithm would interpret the description in (12):

- volume(1).in = qp;
Incoming flow to volume#1 by the external variable qp
- volume(1).out = 2, prv;
Outgoing flows from volume#1 are diverted to
 - a) volume associated to state variable y_2 (volume#2) via an orifice
 - b) a tank through a pressure relief valve
- volume(2).in = 1;
Incoming flow to volume#2 from volume associated to y_1 (volume#1) through an orifice

- `volume(2).out = 3, tank;`
 Outgoing flows from `volume#2` are diverted to
 - a) volume associated to state variable y_3 (cylinder pressure) via an orifice
 - b) a tank through an orifice
- `cylinder_sa(1).in = 2;`
 Incoming flow to cylinder from volume associated to y_2 (`volume#2`) through an orifice.

The algorithm writing the elements of the Jacobian matrix related to volume components is listed in Figure 2. The remaining part of the algorithm, which writes the elements of the Jacobian related to cylinder and pipe components, is analogous to the one presented. It only differs in that the code adds the partial derivatives of cylinder and pipe state equations with respect to their state variables.

```

for i=1 to n           % n=number of state variables
    if i_belongs_to_volume

% ===== writes the off-diagonal terms of J =====
        for j=1 to n
            if(volume(i).in == j) → write("J(i,j)=-vol(i).M*[dqdp_orif(j,i)]")
                                   → line_break
            if(volume(i).out == j) → write("J(i,j)=-vol(i).M*[dqdp_orif(i,j)]")
                                   → line_break
        end for

% ===== writes the diagonal terms of J =====
        for j=1 to n
            write("J(i,i)=vol(i).M*[")
            if (volume(i).in == j) → write("J(i,j)=dqdp_orif(j,i)")
            if (volume(i).out == j) → write("J(i,j)=dqdp_orif(i,j)")
            if (volume(i).out == tank) → write("J(i,j)=dqdp_orif(i,0)")
            if (volume(i).out == prv) → write("J(i,j)=dqdp_prv(i,0)")
            write("]")
            line_break
        end if
        if i_belongs_to_cylinder
        ...
        if i_belongs_to_pipe
        ...
    end for
    
```

Figure 2. Algorithm writing the Jacobian matrix elements related to volume components

Functions $dqdp_orif$ and $dqdp_prv$ are part of the orifice and the pressure relief valve model respectively. They contain the partial derivative of the flow equations (4) and (5) with respect to the pressure. When called, they evaluate the partial derivatives at port pressures.

$$dqdp_orif(i,j) = \left. \frac{\partial q_{orif}}{\partial p} \right|_{\substack{p_1=y_i \\ p_2=y_j}} ; \quad dqdp_prv(i,j) = \left. \frac{\partial q_{prv}}{\partial p} \right|_{\substack{p_1=y_i \\ p_2=y_j}} \quad (13)$$

Equation (14) shows the result of the algorithm after processing the description of the system: the analytical expressions of the non-zeros elements of the Jacobian matrix.

$$\begin{aligned}
 J(1,1) &= Vol(1).M \times [dqdp_{orif}(y_1, y_2) + dqdp_{prv}(y_1, 0)] \\
 J(1,2) &= Vol(1).M \times [-dqdp_{orif}(y_1, y_2)]; \quad J(2,1) = Vol(2).M \times [-dqdp_{orif}(y_1, y_2)] \\
 J(2,2) &= Vol(2).M \times [dqdp_{orif}(y_1, y_2) + dqdp_{orif}(y_2, y_3) + dqdp_{orif}(y_2, y_0)] \\
 J(2,3) &= Vol(2).M \times [-dqdp_{orif}(y_2, y_3)]; \quad J(3,2) = Cyl(1).M(y_4) \times [-dqdp_{orif}(y_2, y_3)] \\
 J(3,3) &= Cyl(1).M(y_4) \times [dqdp_{orif}(y_2, y_3)] \\
 J(3,4) &= \frac{\partial(Cyl(1).M(y_4))}{\partial y_4} \times [q_{orif}(y_2, y_3) - Cyl(1).A \times y_5] \\
 J(3,5) &= -Cyl(1).A \times Cyl(1).M(y_4); \quad J(4,5) = 1 \\
 J(5,3) &= Cyl(1).A / Cyl(1).m; \quad J(5,5) = -\frac{1}{Cyl(1).m} \times \frac{\partial F_\mu(y_5)}{\partial y_5}
 \end{aligned} \tag{14}$$

5 COMPUTATIONAL COSTS OF THE INTEGRATION

This section shows the advantages of using the analytical Jacobian in the integration formula. Computational costs involved in the integration will be measured and compared for two cases (integrator using analytical Jacobian and integrator using a numerically determined Jacobian). The second part of this section concerns the computational costs of the solution of the linear system $Wk_i = F$ and the function evaluation F .

Four models of different sizes are created in order to run simulation tests. The models are made of a network of volumes interconnected by orifices (in a random distribution). The sizes of the models (number of volumes or pressure generators) are 5, 10, 15 and 20. For every model the simulation is run twice. In the first test the integrator calculates the Jacobian matrix using the approach 1) and in the second test, the approach 2) is used:

- 1) Analytical Jacobian: the integration formula (9) access the stored analytical expression of the Jacobian matrix J and evaluates it at every time step as a function of the instantaneous values of the state variables y_0
- 2) Numerical Jacobian: the integration formula uses an iterative method in order to numerically determine the Jacobian matrix J . The Jacobian is approximated by finite differences using the code *ODENUMJAC*. *ODENUMJAC* is an implementation of a robust scheme due to Salane (8) for the approximation of partial derivatives when integrating systems of ODEs. *MATLAB/Simulink*[®] makes use of this code in all its stiff ODE solvers.

Table 3 lists the CPU time required to run the four fluid power circuits. The last row of the table corresponds to the simulation of hydraulic system composed of two double acting cylinders, two 4/3 proportional valves, four pressure relief valves and seven volumes. The table shows the relative CPU time required to solve 1000 integration steps in the two cases mentioned above: 1) when using an analytical Jacobian and 2) when the Jacobian is determined numerically.

Table 3. Comparison times of numerical integrations.

State variables (N)	Dimension of Jacobian	Density of Jacobian	CPU time ¹⁾ (Analyt. Jacob.)	CPU time ²⁾ (Num. Jacob.)	Ratio (Num/Analyt)
5	25	0.50	1.0	2.1	2.1
10	100	0.30	2.1	6.4	3.0
15	225	0.21	3.6	13.6	3.8
20	400	0.16	5.0	23.6	4.8
15	225	0.20	6.9	30.5	4.4

Concerning the simulations of volume-orifice network, the cost of integration, when using the analytical Jacobian, appears to be $O(N^\alpha)$, where $\alpha \approx 1.15$. This indicates that the cost of integration almost follows a linear relation with the size of the system N . The rightmost column of the table lists the ratio between both CPU times. It shows that the larger the system is the more advantageous the usage of the analytical Jacobian is. The last row of the table illustrates that computational costs cannot be always estimated only from the size of the system. More complex fluid power components, as hydraulic cylinders and pressure relief valves, require more computational time. However, the ratio measuring the advantage of the analytical Jacobian approach shows a ratio of 4.4, when the analogous (in size) orifice-network integration showed a ratio of 3.8.

It is important to comment on the robustness that the analytical Jacobian confers to the integrator: The integration of the model composed of with two cylinders and four pressure relief valves showed serious stability problems when the integrator was using the numerical Jacobian approach. In order to solve those stability problems, integration step sizes of the order of 0.1 ms had to be used. On the other hand, the simulation of the same system, when the integrator used the analytical Jacobian approach, showed exceptionally good stability properties even with step sizes of the order of 10 ms. This can be explained according to the nature of Rosenbrock integration formulas. Since the Rosenbrock method only makes use of a single Newton iteration to solve the implicit equations, a full and accurate Jacobian matrix is needed in order to guarantee the stability of the integration. The analytical form of the Jacobian matrix provides a fully accurate Jacobian.

When using the numerical approach to estimate the Jacobian, the integration required time steps h smaller than 0.1 ms to avoid stability problems. However, when performing the same integration but using the analytical Jacobian, the integration showed good stability for step sizes of the order of 10 ms. This can be explained according to the nature of Rosenbrock integration formulas. Since the Rosenbrock method only makes use of a single Newton iteration to solve the implicit equations, a full and accurate Jacobian matrix is needed in

order to guarantee the stability of the integration. The calculation of the Jacobian matrix by evaluating its analytical form makes it fully accurate.

As equation (15) shows, the numerical integration also requires the calculation of two function evaluations, $F(y_0)$ and $F(y_0 + a_{21}k_1)$, and the solution of two linear systems in order to determine the stage variables k_1 and k_2 .

$$\begin{aligned} Wk_1 &= hF(y_0); & \text{with } W &= (I - dhJ) \\ Wk_2 &= hF(y_0 + a_{21}k_1) \end{aligned} \quad (15)$$

For the relatively small linear systems found in the models of fluid power systems, the Gaussian elimination assisted by an LU-decomposition of the matrix W provides good results. Other methods for solving linear systems have been tested (codes for sparse matrices, banded matrices...) but the benefits were not significant, mainly due to high computational cost of the Jacobian matrix and function evaluations versus the cost of solving a linear system. Table 4 shows the relative cost of every task/operation involved in an integration step. The measured tasks are listed as follows:

1. Determination of the Jacobian matrix by evaluating its stored analytical form.
2. Two function evaluations (F).
3. Performing an LU-decomposition of W and solving two linear systems.
4. Other: This term accounts for the time consumed in performing other operations involved in the integration process, and it is calculated by subtracting the previous tasks (1,2,3) from the total integration time displayed in Table 3..

Table 4. Percentage of CPU time distributed in different tasks within the integration.

State variables (N)	Jacobian (Analyt.)	Function evaluations	Solving linear systems	Other
5	43.8	48.4	1.3	6.5
10	46.7	45.6	0.8	6.9
15	43.9	40.9	0.7	14.5
20	43.6	40.7	0.6	15.1
15	39.0	47.3	0.4	13.4

Table 4 shows that function evaluations require approximately the same computational time as the determination of the Jacobian. This fact emphasizes the cost reduction achieved in calculating the Jacobian matrix, which independently of the size of the model, it is comparable to the cost of the function evaluations.

CONCLUSIONS

The calculation of the Jacobian matrix, by using an iterative method, is the bottleneck in terms of computational costs of semi-implicit Runge-Kutta methods. In this paper it is presented a modelling scheme (for fluid power components) able to generate an analytical expression of the Jacobian matrix as a function of the state variables of the system. The calculation of the instantaneous Jacobian matrix can now be obtained by simply evaluating its analytical form. Using this approach, the time required to compute the Jacobian matrix is comparable to the time required to perform the two function evaluations involved in the integration formula. Yet another advantage of this approach is that the Jacobian matrix is determined fully accurately. Consequently the integration formula show better stability properties in highly stiff or discontinuous systems.

An *L*-stable Rosenbrock integration formula from the family of semi-implicit Runge-Kutta methods is also presented. The highlights of this formula are: easy implementation, good stability properties and the reduced linear algebra (two function evaluations, one Jacobian computation, one LU-decomposition and two linear systems), which guarantees highly computational efficient integrations.

REFERENCES

- (1) Esqué, S., Ellman, A., (2002), "Pressure Build-Up in Volumes". Bath Workshop on Power Transmission and Motion Control, PTMC 2002, September 11-13, 2002, Bath, UK. pp. 25-38
- (2) Ellman A., Piché R., (1996), "A modified orifice flow formula for numerical simulation". Fluid Power Systems and Technology 1996, Collected papers of 1996 ASME IMECE, Atlanta, November 17-22, 1996. pp. 59-63
- (3) Handroos, H., Vilenius, M., (1990), "The utilization of experimental data in modelling of hydraulic single stage pressure control valves". ASME journal of dynamic systems, measurements and control, Vol 112, number 3, September 1990.
- (4) Piché R., Ellman A., (1994), "Numerical Integration of Fluid Power Circuit Models using Semi-Implicit Two-Stage Runge-Kutta Methods", Proc. Instn. Mech. Engrs. part C, Journal of Mechanical Engineering Science, 208, pp. 167-175
- (5) Wolfbrandt, A., (1977), "A study of Rosenbrock Processes with Respect to order conditions and stiff stability" , Thesis, Chalmers Univ. of Technology, Goteborg, Sweden
- (6) Esqué, S., Ellman, A., Piché, R., (2002), "Numerical integration of pressure build-up volumes using an *L*-stable Rosenbrock method". Proceedings of the 2002 ASME International Mechanical Engineering Congress and Exposition, November 17-22, 2002, New Orleans, Louisiana, USA
- (7) Hairer, E., Wanner, G., (1996), "Solving ordinary differential equations II: Stiff and Differential-Algebraic Problems", Springer-Verlag
- (8) D.E. Salane, (1986), "Adaptive Routines for Forming Jacobians Numerically", SAND86-1319, Sandia National Laboratories.

Dynamic modelling of a pilot-operated pressure relief valve

Csaba Hős

Research Fellow, Department of Hydrodynamic Systems,
Budapest University of Technology and Economics (BUTE),
1521 Budapest, Pf. 91, Hungary¹
and

László Kullmann

Associate Professor, Department of Hydrodynamic Systems, BUTE

ABSTRACT

In this paper the dynamic behaviour of a commercial pilot operated pressure relief valve is studied. The mathematical model consists of four ordinary differential equations describing the motion of the main spool and the pilot poppet valve. Forces on the spool valve are estimated with the help of standard models described in the literature, while the fluid forces on the poppet valve are computed using a CFD-code. Special emphasis is put on realistic parameter identification. The performance of the model is then tested in the computer simulation of an existing experimental hydraulic linear actuator circuit, in the case of piston impingement against the cylinder end stop.

1. INTRODUCTION

The pressure relief valve is an essential part of every hydraulic system, whose function is to limit the maximum pressure in the system. According to the build-up of the valve, there are two main types: direct operated and pilot operated pressure relief valve. In sophisticated hydraulic systems, the pilot type is more frequently used due to its superior performance compared to direct acting ones. However, in the pilot valve, the motions of the pilot and main valve are coupled through the fluid and this makes the dynamic analysis highly nontrivial. Not only it is difficult to describe the complex fluid-structure interactions (e.g. the flow forces on a poppet valve) mathematically, but also parameter identification (e.g. orifice and damping coefficients) is a challenging task.

In this paper we present a nonlinear mathematical model of a commercial pilot-operated pressure relief valve, type Rexroth DB 10-1-10. The emphasis is not on giving general guidelines

¹Corresponding author, hoscsaba@vizgep.bme.hu

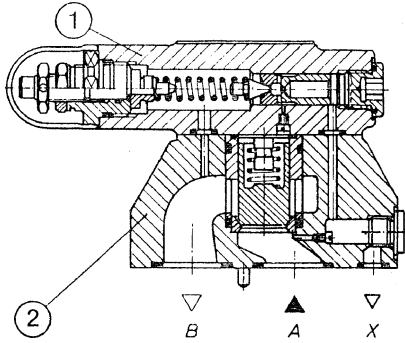


Figure 1: Rexroth DB pilot operated pressure relief valve.

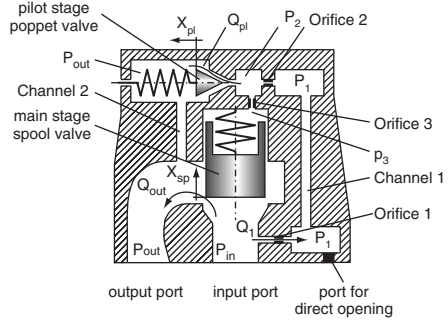


Figure 2: Simplified sketch of the valve for mathematical modelling.

for modelling pilot-operated relief valves but to develop modelling equations for this particular valve with the help of the CFD technique. Based on the corresponding literature (e.g. [5], [10] or [4]), the dynamic modelling of the main stage is a straightforward task. However, the description of the pilot stage is challenging due to the relatively long seat of the poppet valve. As pointed out by Urata [8] and Bergada & Watton [2], the pressure forces on the seat play a decisive role. Also, it is well-known that such valves have a strong tendency to oscillate and thus the damping forces are to be described carefully. In [2], the authors describe a new set of equations giving insight into the flow and pressure distribution across a poppet valve *at rest* with large cone-shaped seat. Based on their work, we present a relationship describing the effect of wall shear in the case of moving valve body, which results in a nonlinear damping force. The dynamic performance of the model is then tested in the computer simulation of a hydraulic linear actuator circuit, in the case of piston impingement against the cylinder end stop.

2. MATHEMATICAL MODELLING

The operation of the pilot operated pressure relief valve can be summarized as follows. Referring to **Fig.2**, the main stage of the valve consists of a spool valve and this main orifice is held closed by a light seating spring. If the pilot valve is closed, the pressure inside the pressure relief valve is balanced. Should the force due to the inlet pressure p_{in} exceed the force of the hard spring of the poppet valve, the pilot stage opens permitting flow to the return line and hence the pressure above the main spool drops and opens the main orifice. Flow is then bypassed to the return line in such a manner that the input pressure is kept at a value set by the pilot spring.

To be able to simulate the dynamic behaviour of the relief valve with high fidelity, the motion of the main spool and the pilot stage poppet valve is to be computed. This suggests the need of studying the relationship between the flow rates and pressures in different segments of the valve and the forces on the valve bodies simultaneously. In the case of the main stage spool valve, due to the simple geometry and the chamfered-type valve seat, the flow rate and the forces are easily calculated with the help of standard relationships given in the literature,

[5]. Contrary to this, there are several issues which make the study of the pilot poppet valve challenging;

- the valve seat and the valve body forms a cone-shaped channel with varying flow-through area and it is to be examined whether - in the operating range of the parameters - the flow inside is laminar or turbulent,
- there is a fixed orifice (Orifice 2 in **Fig.2**) before the poppet valve whose influence is to be studied and
- contrary to the main stage spool valve, where the fluid force acts mainly on the front of the valve body where the upstream pressure distribution can be considered as uniform, in the case of the poppet valve, the pressure distribution along the cone changes significantly. Hence, for a realistic force estimation, the pressure distribution along the cone should be computed.

2.1 Pressures and flow rates

Referring again to **Fig.2**, we consider the fluid to be incompressible everywhere inside the valve. The pressure losses are concentrated into the orifices as the cross-sectional areas of Channel 1 and 2 are large enough to neglect the pressure loss inside. Because of the large diameters, we also assume uniform pressure distribution in Channel 1 and 2.

The laminar or turbulent nature of the flow in an orifice influences the flow rate - pressure drop relationship fundamentally; if the flow is laminar, the dependence of the flow rate on the pressure difference is linear while if the flow is turbulent, we have $Q \propto \sqrt{\Delta p}$. Orifice 1, 2 and 3 are short, sharp-edged orifices, which suggests turbulent flow. Similarly, due to the sharp edges and the complex geometry, the flow through the main stage (spool valve) is also turbulent, (see e.g. [4]). These volume flow rates are calculated by using the orifice equation:

$$Q_1 = C_{d,1} A_1 \sqrt{\frac{2}{\rho}} \sqrt[p]{p_{in} - p_1} \stackrel{def.}{=} R_1 \sqrt[p]{p_{in} - p_1}, \quad (1)$$

$$Q_2 = C_{d,2} A_2 \sqrt{\frac{2}{\rho}} \sqrt[p]{p_1 - p_2} \stackrel{def.}{=} R_2 \sqrt[p]{p_1 - p_2}, \quad (2)$$

$$Q_3 = C_{d,3} A_3 \sqrt{\frac{2}{\rho}} \sqrt[p]{p_3 - p_2} \stackrel{def.}{=} R_3 \sqrt[p]{p_3 - p_2} \quad \text{and} \quad (3)$$

$$Q_{out} = C_{d,out} A_{out}(x_{sp}) \sqrt{\frac{2}{\rho}} \sqrt[p]{p_{in} - p_{out}} \stackrel{def.}{=} R_{out} \sqrt[p]{p_{in} - p_{out}}. \quad (4)$$

$C_{d,i}$ represents the discharge coefficient, A_i is the flow-through area and $\sqrt[p]{x}$ represents the signed square root function². Orifice 1 and 3 are identical restriction elements. The flow-through areas are fixed for Orifice 1-3, while for the main spool, we have

$$A_{out} = \pi x_{sp} \sin \alpha_{sp} \left(d_{sp} - \frac{x_{sp}}{2} \sin 2\alpha_{sp} \right), \quad (5)$$

where d_{sp} is the diameter of the spool, α_{sp} is the angle of the seat and x_{sp} is the spool displacement.

² $\sqrt[p]{x} = \text{sign}(x) \sqrt[p]{|x|}$

In general, the discharge coefficient is difficult to compute but solutions have been made for orifices with regular geometry and it was shown that for sharp-edged orifices with turbulent flow the theoretical value of $C_d = \pi/(\pi + 2) \approx 0.611$ can be used, see [5]. For other cases, C_d can be obtained by steady-state measurements as described in [7]. Orifice 1 and 3 are with regular sharp-edged geometry, thus the theoretical value will be used; $C_{d,1} = 0.61$. The geometry of the main stage is also regular and the standard value of $C_{d,out} = 0.61$ can be employed. It is not trivial how to estimate the discharge coefficient for Orifice 2 as the inflow side is a regular converging channel and the outflow is a sudden diameter step. The actual values are computed using CFD technique and the process is described further on in this section.

It has to be noted here that our aim is to model the flow in the valve under transient conditions, which means that during an unsteady process, the flow presumably passes in and out of laminar and turbulent regions. Thus, we need an orifice model which describes the laminar and the turbulent part simultaneously. Such a model for the discharge coefficient is described in [3] by Borutzky et al., where the equation

$$C_d = c_{turb} \frac{\sqrt{Re}}{\sqrt{Re} + \sqrt{Re_t}} \quad (6)$$

is proposed, with parameter values $c_{turb} = 0.61$ and $Re_t = 9.33$ (for sharp-edged orifices). The Reynolds number is defined as $Re = (Q/A)D_h/\nu$. (6) provides a linear flow rate - pressure drop relation for small velocities while for turbulent flows, it matches the conventional square root characteristics. The price for this is that the flow rate cannot be computed explicitly in (1) - (4) and iteration is needed at every time step.

Let us now turn to the orifice formed by the pilot valve and consider the narrow gap between the cone body and the housing. As the valve seat has a considerable length (it is not of chamfered type), laminar flow may occur even for large pressure differences. However, due to the motion of the pilot valve, the flow through this orifice can either be laminar (small openings or low upstream pressure) or turbulent (large valve displacement or large upstream pressure). To decide which case occurs in the operating range of the parameters (notably in terms of pressure differences and valve body displacements), a series of steady-state CFD computations of the pilot stage was performed with the commercial CFD code CFX 5.7. Valve displacements between 0.1mm and 0.5mm were set with pressure differences between 1bar and 40bar . The computational domain started at Channel 1 and ended at Channel 2, in both cases 10mm after entrance, in order to be able to prescribe stable uniform pressure field. The pressure at the inlet of Channel 1 was then systematically increased to 1bar , 2bar , 5bar , 10bar and so on up to 40bar . The symmetry of the geometry was exploited; only one half of the valve was built up and also the geometry was simplified: as under steady-state conditions the main spool is at rest, Orifice 3 was omitted in these computations. The SST Reynolds Stress model was used for turbulence modelling [1]. For a given pair of input pressure p_1 and output pressure p_{out} , the pressure before the pilot valve p_2 , the mass flow rate \dot{m} and the force components on the pilot poppet valve were extracted from the results. Plotting the flow rate versus $p_1 - p_2$ gives the $Q(\Delta p)$ relationship of fixed Orifice 2, while plotting $p_2 - p_{out}$ vs. the flow rate gives flow-through relationship of the pilot valve.

Although the primary aim of the CFD computations was to study the flow through the poppet

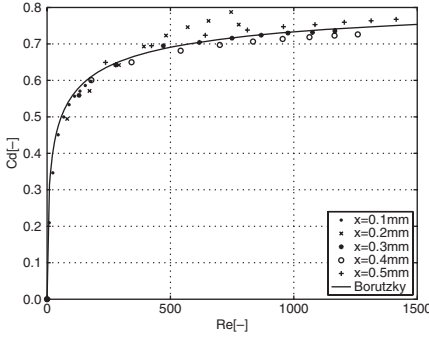


Figure 3: Discharge coefficient of Orifice 2 as a function of the Reynolds number and the fitted Borutzky approximation (6), with $c_{turb} = 0.86$ and $Re_t = 30$.

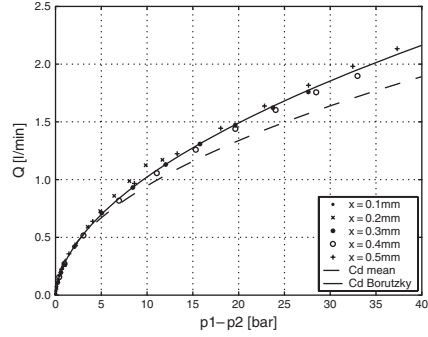


Figure 4: Volume flow rate vs. pressure difference for Orifice 2. Points denote CFD data, the dashed line represents (2) with an average C_d value while the solid line denotes (2) with (6).

valve, additional valuable information could be gained concerning to the behaviour of fixed Orifice 2. **Fig.3** depicts the discharge coefficient for Orifice 2 as a function of the Reynolds number. It is clearly seen that the discharge coefficient varies significantly and that - after c_{turb} and Re_t were identified - the Borutzky formula (6) gives a satisfactory approximation. The effect of constant and Re -dependent discharge coefficient is demonstrated in **Fig.4**, where the dashed curve indicates (2) with $C_d = 0.78$ (mean value of the CFD runs) and the solid line denotes Borutzky's formula. It is clearly shown that the dependence of the discharge coefficient on the Reynolds number should be taken into account in order to be able to compute the flow rate through the orifice.

We turn now to the analysis of the flow through the pilot cone body. Before plunging into the processing of the CFD results, let us consider some theoretical issues. For small poppet valve displacements, the flow in the channel between the valve body and the seat is supposed to be laminar. Thus, we can assume a Poiseuille velocity profile, and by integrating this along the gap, one can compute the volume flow rate as a function of the pressure gradient along the generatrix of the cone. By making use of the incompressibility, the flow rate can be explicitly computed (details of the calculation are given in [2]):

$$Q = \frac{\pi}{\mu} (p_2 - p_{out}) \frac{H^3}{6} \frac{\sin \alpha}{\ln \left(1 + \frac{l \sin \alpha}{r_{m,in}} \right)}, \quad (7)$$

where $H = x_{pl} \sin \alpha$ is the gap width and the mean inlet radius is $r_{m,in} = r_{2,in} - \frac{H}{2} \cos \alpha$, with half-cone angle α and $r_{2,in}$ inlet outer radius (for details, see **Fig.7**).

Obviously, (7) omits several issues, e.g. the effect of the fluid jet leaving Orifice 2, the effect of the contracting streamlines at the entrance of the conical channel or simply the deviation from the laminar velocity profile. However, (7) gives the basic relationship between the parameters, which can then be 'tuned' to give more accurate results. Neglecting the material properties and the geometric parameters (which are prescribed values) and keeping in mind

that laminar flow was assumed (which means that the dependence on the pressure difference has to be linear) we conclude that only the exponent of the valve displacement is a free parameter to be adjusted to the CFD results. As a first step, we expand (7) into Taylor series around $x_{pl} = 0$, and introduce a new, dimensionless parameter $e = x_{pl}/r_{2,in}$. This gives

$$Q \approx \frac{\pi}{\mu} (p_2 - p_{out}) \frac{\sin^4 \alpha}{6} \frac{r_{2,in}^3}{\ln \left(1 + \frac{l \sin \alpha}{r_{2,in}} \right)} e^3 + O(x_{pl}^4). \tag{8}$$

Next, we want to find a new exponent for e , denoted by β , which results in a better approximation of the CFD results. We define a new function $\Xi(e)$ containing only that part of (8) which depends on e , i.e.

$$\Xi(e) \stackrel{def.}{=} \frac{Q}{\frac{\pi}{\mu} (p_2 - p_{out}) \frac{\sin^4 \alpha}{6} \frac{r_{2,in}^3}{\ln \left(1 + \frac{l \sin \alpha}{r_{2,in}} \right)}} = e^\beta. \tag{9}$$

The unknown parameter β can be identified by computing $\log \Xi$ and $\log e$ and then employing linear regression, which gives $\beta = 2.8991$. Finally we conclude that the flow through the pilot valve can be computed as

$$Q_{pl}(x_{pl}, p_2, p_{out}) = \frac{\pi}{\mu} (p_2 - p_{out}) \frac{\sin^4 \alpha}{6} \frac{r_{2,in}^3}{\ln \left(1 + \frac{l \sin \alpha}{r_{2,in}} \right)} \left(\frac{x_{pl}}{r_{2,in}} \right)^{2.8991} \stackrel{def.}{=} R_{pl} (p_2 - p_{out}) \tag{10}$$

Fig.5 shows the actual values of $\log \Xi(\log e)$ computed from CFD results. Note that for every valve displacements e , ten independent points are depicted corresponding to the ten different pressure steps. It is clearly shown that the values are independent of the pressure. However, for $x_{pl} = 0.2mm$ ($e = 0.714$) we have a slight deviation in the data points, which is probably due to the insufficient error tolerance set in these CFD runs. In **Fig.6**, the volume flow rate vs. the pressure difference is depicted, for the five valve displacements. Note that the flow is clearly laminar. Again we see a deviation from the linear trend in the case of $x_{pl} = 0.2mm$ and also, for the $x_{pl} = 0.4mm$ case, where there is an error of up to approx. 25%. For the other three displacements, we observe a reasonable agreement between the theory and the CFD results.

Having defined the relationships between volume flow rates and pressures, we turn now to the actual computation issues. We have four unknown flow rates ($Q_{1..3}$ and Q_{pl}) and three unknown pressures $p_{1..3}$. Beside the three orifice equations (1)-(3) and the pilot valve restriction equation (10), we have the continuity equations due to the incompressibility $Q_1 = Q_2$ and $Q_2 = Q_{pl} + Q_3$, which means that one more equation is needed. This is simply $Q_3 = A_{sp} v_{sp}$, (where v_{sp} is the velocity of the spool body, obtained from the equation of motion) which is again a continuity equation for the chamber above the main spool body. If we consider the discharge coefficients to be constant, the system of equations can be explicitly solved, giving

$$Q = \frac{-1 + \sqrt{1 + 4R_{pl}\sigma (A_{sp}v_{sp} + R_{pl}(p_{in} - p_{out}))}}{2R_{pl}\sigma}, \quad \text{where} \quad \sigma = \frac{R_1^2 + R_2^2}{R_1^2 R_2^2}. \tag{11}$$

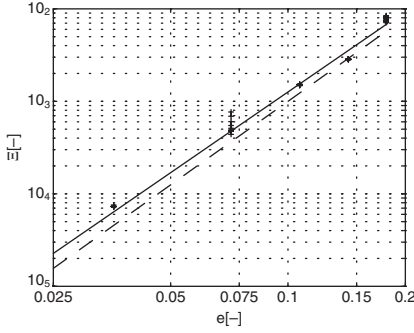


Figure 5: Function $\Xi(e)$ (defined by (9)) as a function of dimensionless pilot valve displacement e ; CFD data points are denoted by crosses, the dashed line represents the theoretical result e^3 and the solid line represents the tuned relationship e^β , with $\beta = 2.8991$.

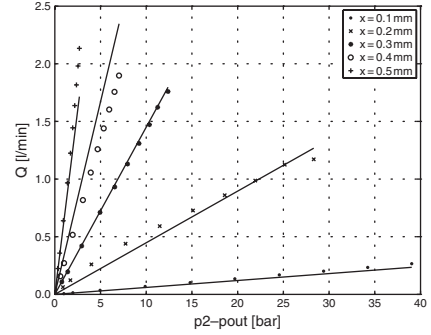


Figure 6: Volume flow rate through the pilot valve vs. pressure difference for several valve displacements. CFD data points are denoted by crosses, the lines represent (10).

The rest of the unknowns can then be easily computed. However, if we take into account the dependence of the discharge coefficients on the Reynolds number, the equations are cumbersome to solve analytically. Instead, we use the above formulae for function iteration, i.e. given an initial set of flow rates and pressures, we compute the discharge coefficients, employ the above equation, and compute new flow rates and pressures to start the process again. Numerical experiments show that for reasonably good initial conditions, 3 or 4 iterations steps are sufficient to achieve 0.1% accuracy in Q .

2.2 Fluid forces on the valve bodies In this section, we calculate the fluid forces needed for the equations of motions. In the case of the main spool valve, due to the simple geometry, the formulae available in the literature can directly be employed. In the case of the pilot stage, the fluid forces are computed by integrating an estimated pressure and wall shear distribution and the formulae obtained are compared to the CFD results.

The **steady flow force** acting on the main spool can be obtained with the help of the momentum equation. One obtains

$$F_{f,sp} = \rho v_{in}^2 A_{in} - \rho v_{out}^2 A_{out} \cos \theta + p_{in} A_{in} - p_{out} A_{out} \cos \theta, \quad (12)$$

where θ is the jet angle, and A_{out} is given by (5). For sharp-edged valve and housing pairs (typically in the case of servovalves), the jet angle depends strongly on the spool displacement. However, in our case, due to the chamfered valve seat, we have $\theta \approx \alpha_{sp}$. The pressure integral and the viscous forces along the chamfered part of the valve body can be neglected due to the shortness of the seat. Exploiting the continuity equation $v_{in} A_{in} = v_{out} A_{out}$ and (4),

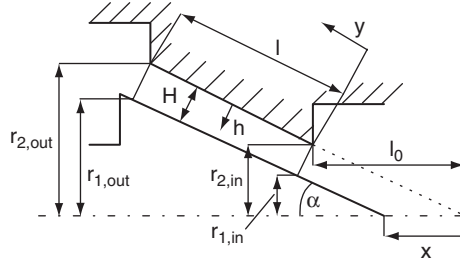


Figure 7: Geometry of the poppet valve. $\alpha = 21$ degrees, $L = 3.21\text{mm}$, $r_{2,in} = 2.8\text{mm}$, $r_{1,in} = r_{2,in} - H \cos \alpha$, $r_{2,out} = r_{2,in} + L \sin \alpha$, $r_{1,out} = r_{2,out} - H \cos \alpha$ and $H = x_{pl} \sin \alpha$.

we arrive at

$$\begin{aligned} F_{f,sp} &= p_{in}A_{in} - p_{out}A_{out} + \rho Q_{out}^2 \left(\frac{1}{A_{in}} - \frac{\cos \theta}{A_{out}} \right) \\ &= p_{in}A_{in} \left[1 + 2C_{d,out}^2 \frac{A_{out}}{A_{in}} \left(\frac{A_{out}}{A_{in}} - \cos \alpha \right) \right] - p_{out}A_{out} \left[1 + 2C_{d,out}^2 \left(\frac{A_{out}}{A_{in}} - \cos \alpha \right) \right]. \end{aligned} \quad (13)$$

In the corresponding literature, it is often assumed that the momentum force can be neglected. The terms in square brackets in the last row of (13) help us to decide whether this hold in our case or not. By exploiting (5), we have $A_{out}/A_{in} \approx 4x_{sp}/d_{sp} \sin \alpha$, which varies³ in the range of 0...0.435. It is easy to calculate that as x_{sp} varies from 0mm to 4mm, the factor of $p_{in}A_{in}$ varies from 1 to 0.907 and that of $p_{out}A_{out}$ from 0.472 to 0.797. Hence we conclude that the momentum forces in the case of the main spool have to be taken into account.

Let us now calculate the fluid force acting on the **pilot poppet valve**. As it was already stated in the previous section, the flow around the conical valve body is highly complex but a reasonably accurate estimation for the flow rate and pressure distribution can be given by assuming laminar velocity profile in the gap between the housing and the valve body. By exploiting again the steady momentum equation, we have

$$F_{f,pl} = \int_A (\mathbf{v}\rho)(\mathbf{v}d\mathbf{A}) + \int_A p d\mathbf{A} - \mathbf{S} = F_{f,pl,mom.} + F_{f,pl,pres.} - F_{f,pl,visc.} \quad (14)$$

The bold letters denote vector quantities. Taking a control volume which starts in front of the valve body and ends far behind it, we have

$$F_{f,pl,mom} = \int_A (\mathbf{v}\rho)(\mathbf{v}d\mathbf{A}) = \rho Q^2 \left(\frac{1}{A_{in}} - \frac{1}{A_{out}} \right), \quad (15)$$

where A_{in} and A_{out} are the cross-sectional areas of the chamber before and after the body and we assumed a uniform mean velocity distribution through these surfaces. Let us assume a large volume flow rate of 10l/min across the pilot stage. (The actual size of the relief valve is for 50l/min. Note that in the case of pilot operated pressure relief valves, the flow

³ $x_{sp,max} = 4\text{mm}$, $d_{sp} = 26\text{mm}$, $\alpha = 45^\circ$

through the main stage is dominant and the flow through the pilot stage is so small that it is usually neglected in analytical calculations.) Then, by taking into account that actual values are $A_{in} = 11.31\text{mm}^2$ and $A_{out} = 19.6\text{mm}^2$, the momentum force is $F_{f,pl,mom} = 2.456\text{N}$.

As the half-cone angle is small in our case ($\alpha = 21^\circ$), linear pressure distribution is assumed along the cone seat. The pressure distribution before and after the cone seat are assumed to be uniformly p_2 and p_{out} , respectively. Without performing here the actual computation, the pressure force is

$$F_{f,pl,pres.} = r_{1,in}^2 \pi p_2 - r_{1,out}^2 \pi p_{out} + 2\pi \sin \alpha \left[r_{1,in} l \left(p_2 - \frac{\Delta p}{2} \right) + \frac{l^2}{2} \left(p_2 - \frac{2}{3} \Delta p \right) \right], \quad (16)$$

where Δp is the pressure drop across the valve, $p_2 - p_{out}$. The viscous force can be computed as follows. Following [2] and assuming small valve opening (i.e. laminar flow), the Poiseuille velocity profile across the gap is

$$v(y, h) = -\frac{1}{2\mu} \frac{dp(y)}{dy} h(H-h) + v_{pl} \frac{h}{H}. \quad (17)$$

The wall shear is then

$$\tau(y) = \mu \left. \frac{\partial v(y, h)}{\partial h} \right|_{h=H} = -\frac{H}{2} \frac{dp(y)}{dy} + v_{pl} \frac{\mu}{H}. \quad (18)$$

Here we assume again linear pressure distribution, i.e. $dp/dy = p_{in} - \Delta p y/l$. With these assumptions, the axial component of the viscous force can be evaluated as

$$\cos \alpha \int_{\text{cone seat}} \tau d\mathbf{A} = \cos \alpha \int_{\text{cone seat}} \mu \left. \frac{dv(h)}{dh} \right|_{h=0} d\mathbf{A} = \Delta p H \pi r_{1,m} - v_{pl} 2\pi \mu \frac{l}{H} r_{1,m}, \quad (19)$$

where Δp is the pressure drop across the valve, $H = x_{pl} \sin \alpha$ is the gap width $r_{1,in}$ and $r_{1,out}$ are the inlet and outlet radii of the cone. The mean cone radius is $r_{1,m} = r_{1,in} + \frac{1}{2} \sin \alpha$ (l is the seat length and α denotes the half cone angle), see **Fig.7**.

Note that by assuming a linear pressure distribution along the seat violates the continuity along the diverging cone channel. Normally, one would integrate (17) across the gap and take into account that the volume flow rate is constant ($Q = \text{const} = \int_0^H v(y, h) 2\pi r_1(y) dh$). The resulting differential equation can then be solved for $p(y)$. Indeed, in [2] the authors compute the pressure distribution in a similar manner. However, numerical experiments with the resulting (cumbersome) equations show that for small cone angles, the error by assuming linear pressure distribution is reasonably small (the authors of this paper experienced a discrepancy below 8% for $\alpha = 21^\circ$).

Fig.8 depicts the pressure forces on the cone body obtained by CFD calculations and analytical calculations, (16). Note that the data is plotted versus $p_1 - p_{out}$ rather than $p_2 - p_{out}$, because the pressure force depends only slightly on the valve opening (at least for small openings). This result is in accordance with the findings of Bergada and Watton [2]. Note that the slightly negative value of the force for small pressure differences is due to the unbalanced area of the valve on the upstream and downstream side. It is shown that the pressure forces on

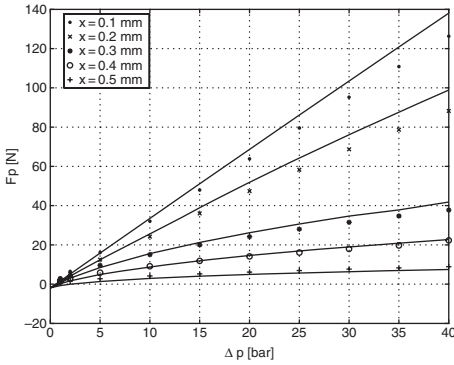


Figure 8: Pressure force on the cone body as a function of the overall pressure difference. CFD data points are denoted by crosses, solid lines represent the theoretical result given by (16).

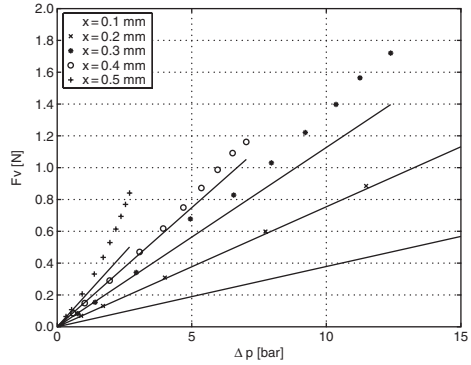


Figure 9: Viscous force on the valve body for several pressure differences. CFD data points are denoted by crosses, solid lines represent the theoretical result given by (19).

the seat play a decisive role and they have to taken into account in order to gain a reasonably accurate estimation. However, it is also shown that for small cone angles ($\alpha \approx 20^\circ$) a linear pressure drop can be assumed across the seat which simplifies the calculations significantly.

The force due to the viscous friction is depicted in **Fig.9**. For a meaningful comparison, the velocity of the valve body was set to zero in (19) as the body was also at rest in the CFD computations. In the CFD computations, a large number of cells are needed across the gap in order to have an accurate wall shear distribution, which could not be guaranteed in the case of $x_{pl} = 0.1\text{mm}$ displacement. Hence, these data points are not depicted in **Fig.9**. We experience an increasing deviation from the computed values with increasing pressure difference and gap width. This is probably due to that (a) for larger gap widths and pressure differences, the flow might become turbulent and (b) the presence of secondary effects, e.g. the contraction of streamlines at the inlet. However, note that the *initial slopes* of the CFD computations and the theoretical curves agree very well. Furthermore, theory reveals that the two components of the shear force behave counter wise as the gap width H changes (i.e. the valve body moves); the pressure term $\Delta p H \pi r_{1,m}$ is directly proportional to the gap width and disappears if the valve closes while the velocity term $v_{pl} 2\pi \mu \frac{l}{H} r_{1,m}$ increases quickly as the valve closes thus *the velocity term represents a highly nonlinear damping force, which tends (theoretically) to infinity as the valve body closes*. This second fact might have a significant influence on the dynamic behaviour of such valves.

2.3 Equations of motion By applying Newton's 2nd law to the main spool valve, we have

$$m_{sp} \ddot{x}_{sp} = F_{f,sp} + F_{d,sp} - p_3 A_{sp} - s_{sp} (x_{0,sp} + x_{sp}), \tag{20}$$

where x_{sp} is the displacement of the spool, m_{sp} is the mass of the spool, $F_{f,sp}$ represents the fluid forces defined by (13) apart from the pressure force on the upper part of the spool, i.e. $A_3 p_3$. F_d is the damping force (yet to de defined), s_{sp} is the spool spring constant and $x_{0,sp}$ is the precompression of the spring. Assuming a perfectly centred spool in a bore [5] the

damping force on the main spool reads

$$F_{d,sp} = \frac{\pi d_{sp} L_{sp} \mu}{C_r} \dot{x}_{sp} \stackrel{def.}{=} K_{sp} \dot{x}_{sp}, \quad (21)$$

where d_{sp} is the diameter of the spool, L_{sp} is the total spool length in contact with the bore and C_r is the clearance between the spool and the bore.

The equation of motion for the pilot cone is

$$m_{pl} \ddot{x}_{pl} = F_{p,pl} - F_{d,pl} - s_{pl} (x_{0,pl} + x_{pl}), \quad (22)$$

where $F_{p,pl}$ stands for the pressure forces $F_{d,pl}$ denotes the damping force, s_{pl} is the pilot spring constant and $x_{0,pl}$ is its precompression.

Equations (21) and (22) do not take into account that negative displacement is not possible due to the valve seats. In the numerical simulations, the valve seats are modelled as strong springs and dampers only acting in the case of negative valve displacements. In such cases, the flow rates are set to zero artificially.

In the numerical scheme, the input and output pressures p_{in} and p_{out} are boundary conditions. Once these values are given, knowing the valve displacements from the last step, the volume flow rate can be calculated (with iteration) with the help of (11). Internal pressures $p_{1..3}$ and fluid forces then can be easily computed. Finally, the ordinary differential equations (21) and (22) can be solved by any standard ODE solver algorithm.

3. EXPERIMENT AND SIMULATION

In order to verify the mathematical model developed in the previous sections, the dynamic behaviour of a simple hydraulic linear actuator apparatus was predicted. Before presenting the experimental results, the authors wish to note that only one representative measurement is given here due to the space limitations. In the experimental work, first steady-state performance curves were both measured and computed. Some parameters, which could not be identified directly (or only an estimated value was known), were tuned based on these steady-state measurements. Secondly, power spectra during steady-state operations were recorded to identify typical frequencies needed for poppet valve instability studies. In the third step, the valve model was built into a linear actuator circuit and several tests were performed. The authors are aware of the fact - and they also thank the reviewer for pointing it out - that by testing the valve in a hydraulic circuit rather than separately, it is not possible to differentiate between the adequacies and inadequacies of the circuit model and the valve model. Indeed, the transmission line model, the piston friction law, the pump model, etc. influences the results - notably the pressure histories - strongly.

A sketch of the test rig is shown in **Fig.10**. The pump was modelled as a constant flow source, delivering oil at $20.1[l/min]$. Transmission lines with indicated length were modelled as lumped elements, i.e. continuity and momentum equations are solved with a FEM technique similar to that described in [6]. It should be noted here that variable time stepping in the

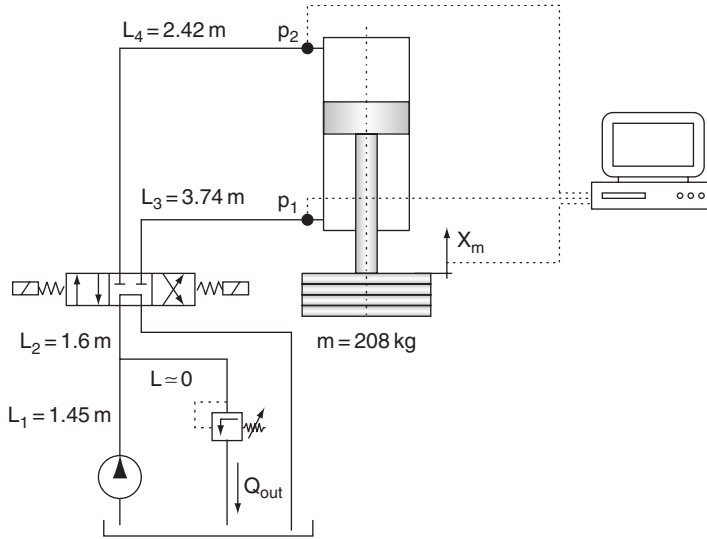


Figure 10: Experimental linear actuator circuit and data acquisition.

fluid transmission lines is essential in order to obtain compatibility with the small time steps required for ordinary differential equation (ODE) solvers used for solving the ODEs describing the dynamics of the piston and the pressure relief valve. The behaviour of the piston is described by the standard model given in e.g. [5]; i.e. a Newtonian equation of motion for the mass and two additional differential equations describing the pressure dynamics in the two chambers. Transmission lines without indicated length and additional elements (directional valves, filter, etc.) were modelled as concentrated losses.

Referring again to **Fig.10**, pressure histories close to the piston chambers and the displacement of the weight were recorded. The sampling frequency was 1000Hz. Unfortunately, there was no possibility to mount pressure transducers closer to the pressure relief valve. The set pressure of the relief valve was 65bar .

The test case was the impingement of the piston against the cylinder end stop. As it is shown in the topmost panel of **Fig.11**, initially the piston is at rest in some middle position. The total stroke of the piston was 0.246m and $x = 0$ corresponds to the lower extreme position. At $t \approx 0.26\text{s}$, the directional valve switches and the piston moves upwards until it hits the cylinder end stop at $t \approx 0.53\text{s}$. As after the impingement the directional valve remains in the same position, the pressure in the segment between the pump and the lower chamber of piston increases rapidly until it reaches the set pressure of the relief valve. After the relief valve opens, the flow is directed into the tank while the system pressure is kept constant.

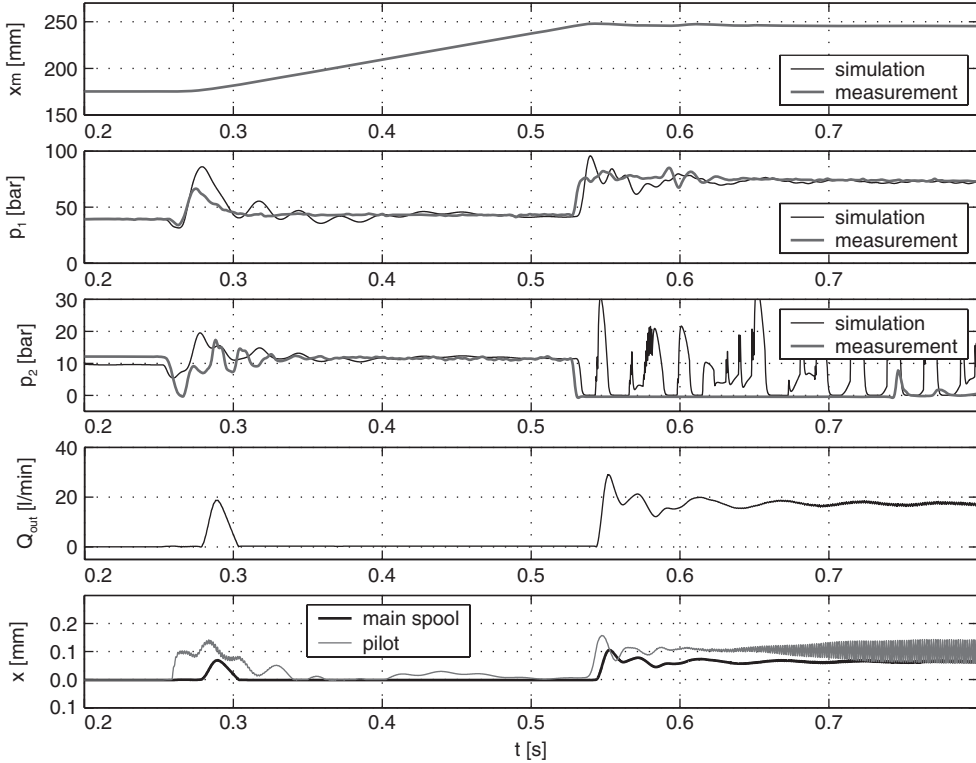


Figure 11: Results of experiment and simulation.

The first phenomena we observe is the insufficient damping in the transmission lines. Note that although Zielke's unsteady friction model [9] was employed, we experience significantly higher 'first' pressure peaks and several oscillations after that, although experiments show that these oscillations die away quickly.

After the piston impingement, a large depression occurs in the upper chamber and the connected transmission line. The simulation misses the reflection of this wave completely, which is probably due to the occurring unmodeled cavitation.

Simulations also suggest that the pilot valve oscillates heavily even under steady-state conditions with a frequency of 1350Hz , which is the eigenfrequency of the pilot valve (together with the pilot spring). This was experimentally verified by using accelerometers and it was found that there is indeed a peak in the spectra at approx. 1500Hz , which is present only if the relief valve operates. When varying the set pressure and the delivered volume flow rate (pump revolutionary speed), the location of this peak remained within a bound of $\pm 50\text{Hz}$. However, it is not clear at the moment that the mathematical model described previously is adequate at such high frequency, notably whether it is correct to neglect the fluid inertia effects.

4. CONCLUSIONS AND OUTLOOK

A nonlinear mathematical model for a particular commercial pilot-operated pressure relief valve was presented for hydraulic system simulation purposes. The key point of modelling was that theoretical relationships were developed and then 'fine-tuned' with CFD technique. It was concluded that the pilot stage is poorly damped, which results in oscillations even under steady-state operating conditions. At this stage, it is not clear whether these oscillations have a fundamental effect on the overall performance of the relief valve as the main spool is heavily damped. Nevertheless, efforts should be made to give guidelines to avoid this kind of instability. Finally, it was also observed that the damping inside the transmission lines was insufficient even in the case of employing the unsteady friction model of Zielke.

The authors wish to thank the valuable remarks and suggestions of the reviewer.

REFERENCES

- [1] ANSYS Inc. *CFX5.7 Users' Manual*, 2004.
- [2] J.M. Bergada and J. Watton. A direct solution for flowrate and force along a cone-seated poppet valve for laminar flow conditions. *Proc. Instn Mech. Engrs, Journal of Systems and Control Engineering*, 218:197–210, 2004.
- [3] W. Borutzky, B. barnard, and J. Thoma. An orifice model for laminar and turbulent conditions. *Simulation Practice and Theory*, 10:141–152, 2002.
- [4] K. Dasgupta and R. Karmakar. Dynamic analysis of pilot operated pressure relief valve. *Simulation Modelling Practice and Theory*, 10:35–49, 2002.
- [5] H.E. Merritt. *Hydraulic Control Systems*. John Wiley and Sons, 1967.
- [6] J.J. Shu. A finite element model and electronic analogue of pipeline pressure transients with frequency-dependent friction. *Transactions of the ASME, Journal of Fluids Engineering*, 125:194–199, 2003.
- [7] J.A. Stone. Discharge coefficients and steady state flow froces for hydraulic poppet valves. *ASME Journal of Basic Engineering*, 82:144–152, 1960.
- [8] E. Urata. Thrust of a poppet valve. *Bulletin of the JSME*, 12(53):1099–1109, 1969.
- [9] W. Zielke. Frequency-dependent friction in transient pipe flow. *IEEE Transactions on Journal of Basic Engineering*, March 1968.
- [10] P.S. Zung and M.H. Perng. Nonlinear dynamic model of a two-stage pressure relief valve for designers. *ASME Journal of Dynamic Systems, Measurement, Control*, 124:62–66, 2002.

Component Design and Analysis

A Computer Aided Conceptual Design Method for Hydraulic Components

B Steiner and **R Scheidl**

Institute of Machine Design and Hydraulic Drives, Johannes Kepler University, Linz, Austria

ABSTRACT

In this paper a method for supporting conceptual design work of hydraulic components is presented. It links together the graphical domain of sketches/drawings with the symbol domain for reflecting the physical effects and the domain of mathematical models for their quantification. The graphical domain is realised with a standard CAD program. The designer specifies his/her concepts by drawings. The functional roles of drawing entities are declared by predefined symbols associated to these entities. In this way, the designer declares his/her physical understanding and generates automatically a mathematical description. The mathematical model for each effect is stored in a database in a notation used by the symbolic manipulation program Maple. The geometrical and material design parameters of these individual effects can be linked to parameters given by some design entities. The models of each effect are combined to a set of equations describing the whole system.

Currently, the database symbols and the application are developed for hydraulic components. To exemplify the method and the capacity of the software the conceptual design of a fast hydraulic 2/2-way-switching valve with a positive feedback metering edge is modelled.

1 INTRODUCTION

Developing a technical product means to define a problem, to find a solution for the problem, to describe the solution, and to evaluate the solution with respect to the requirements. In reality, design is not a sequential but an iterative and sometimes a recursive process. This motivates computer support, because many iterations cost a lot of time and money. According to [1] the computer supported design process for technical products can be divided into 4 modelling levels which are shown in Figure 1.

- Specification modelling: Defines functional requirements and boundary conditions. The form of description is verbal in form of requirement lists.

- Functional modelling: Describes the functional interrelationships in the form of symbols in structure charts. G. Pahl and W. Beitz [2] define a function for a system as an interrelationship between Input and Output with the objective of fulfilling a requirement.
- Principle modelling: Describes the working interrelationship with physical effects in form of mathematical equations and material and geometrical parameters. Forms of description are symbolic pictures, line drawings and commonly non scaled sketches.
- Shape modelling: Defines the concrete geometric body structure of the technical product with the help of two or three dimensional single component drawings, assembly drawings, part lists, etc.

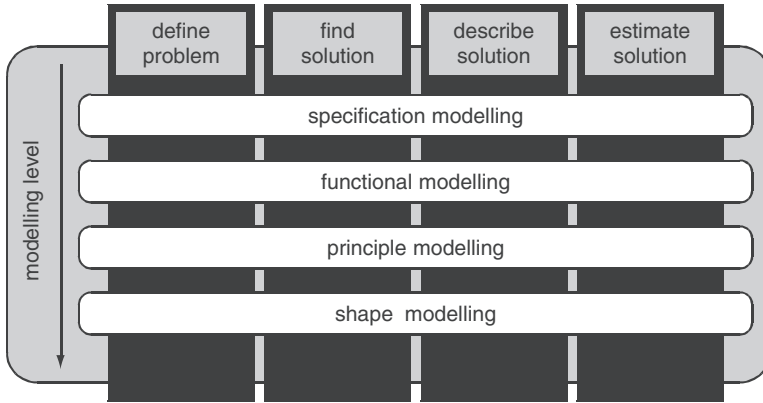


Figure 1 Design process with computer support [1]

Each modelling level of Figure 1 depends on its previous level. The high importance of a good conceptual design asks for an efficient computer aid by a software tool for functional and principle modelling. In the following, a computer based tool for principle modelling will be described. It is realised as a customisation software for a common CAD package in combination with a database. Functional modelling is not realised so far. Although it is targeting valve design in its current versions, the underlying concept is rather general. A fast 2/2 way switching valve with a positive feedback metering edge is used as a suitable example to explain the principle and the programming aspects.

The developed software is not intended for practical use but is a study object to obtain experiences for assessing the feasibility of the approach. It comprises a methodology for documenting and assisting conceptual design and its realisation as an addendum to some widespread CAD system.

2 COMPUTER ASSISTANCE IN CONCEPTUAL DESIGN

Computer assistance in conceptual design ideally should advise the design team to do its work in a systematic manner, to support the designer with existing know-how and references, to get an automatic documentation, to help in finding possible technical

realizations, and to assist further detailed design. The software environment to perform this assistance should fulfil the following demands:

- It should be easy to handle and should have a user friendly graphical interface.
- Standard and wide spread software packages should be used to the largest possible extent.
- Principle solutions should be described by an easy to understand symbolic language.
- For documenting and further processing, principle solutions should be saved on a server based database system.

Conceptual design finds solution principles, which are classes of technical solutions that share the same underlying physical principles [3]. There are different approaches to find and describe such principles if some inventive steps have to be taken. Work normally starts in an inductive manner by sketching some solution principles. In a second step a functional analysis of the problem might be carried out. This is normally a functional decomposition [2][4], by which the required functionality is subdivided into several elementary functional elements [3], which constitute elementary functional entities, and their interconnection – the so called structure of the system. The functional decomposition is an abstract way for describing solutions principles. It requires some physical insight because it breaks down the system functionality into basic physical effects. The human cognition and an effective and efficient design process need both, the sketching of ideas and the functional analysis. Computer support of such design activity should be able to handle these two types of design description. An algorithmic support for transferring one into the other would be of great benefit.

The graphical user interface can be provided best by a standard CAD software package. A graphical entity models a certain component geometrically. To attribute the physical or technical purpose of a certain component or subsystem to the graphical entity, a declaration must be made by the designer. In the sense of functional decomposition this purpose constitutes a functional element. When doing the design work by hand, sketches are typically made on a sheet of paper, whereas the functional meaning is stored in the designer's head. A different person, who uses a similar syntax to sketch such technical solution ideas, often can estimate the functional concepts from the sketches. But this might be ambiguous in details. The exact meaning of a certain functional element according to the designer's ideas can be declared best by mathematical models of the expected physical behaviour. The authors are aware that this is not always possible. In hydraulics however, well established models exist for most of the functionally essential physical effects. At this stage of work design is foremost a synthetic process, not yet an evaluative. Thus, it is most important to document the designer's ideas and not to have already a sound model of the real physical behaviour. Of course, it is desirable that the physical perception of the designer is correct. But it is the designer's responsibility to decide on modelling, no automatism is intended.

Experience and routine are important success factors. Models for certain functional elements are stored in the database. They can be used in later design work and are open to

improvement. Designers with little or no expertise in modelling can make use of such models. It is a matter of quality assurance in design to establish regulations which assure a proper use of such models by non-experts and the handling of their maintenance. This is an organisational problem and not discussed here, despite its importance for a successful use of such a tool in practice.

There might be different models for the same functional element, representing different levels of accuracy and complexity. Selecting the most appropriate is left to the designer. It would be desirable to document the experiences made with some model, for instance the comparison with experiments. But we don't see any other method but the skilful judgement by experts who document their decisions in a systematic manner.

2.1 Example 2/2-way-poppet valve with positive feedback metering edge – functional analysis

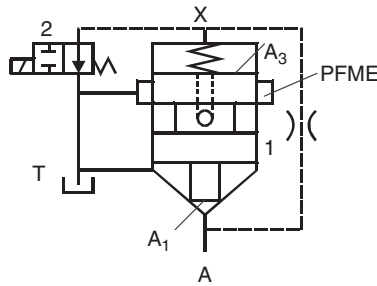


Figure 2 2/2-way-poppet-valve with positive feedback metering edge [5]

The functional principle of the valve, which is shown in Figure 2 is similar to a piloted 2/2-way-poppet-valve. A is the high pressure and T the tank pressure port. It consists of a main valve (1) for a high nominal flow rate and a solenoid actuated, normally open 2/2-way pilot valve (2), and is a modification of a 2/2-way-poppet-valve with an additional positive feedback metering edge (PFME). The latter should have a short opening time as possible, whereas the time for closing the valve is not reduced compared to the conventional design. The idea to use an additional metering edge was already utilised in the Valvistor-concept [6] and in a switching valve [7].

This valve exploits various elementary functional elements. The spool is a body that can move linearly in the axial direction and forms a seat valve. It has a rotational degree of freedom as well, but it is a dummy mode of motion which is not relevant. The seat valve consists of two elementary functions, a mechanical contact and a valve function, which is a variable flow passage area between the spool and the sleeve controlled by the axial motion of the spool. This motion couples mechanically with the seat valve function via the contact relation. The positive feedback metering function is composed of a conventional spool-valve metering edge and proper hydraulic connections as shown in Figure 2. The valve has several chambers with a hydraulic pressure which influence the motion of the spool like the obligatory spring to assure a well defined initial position. Figure 5 shows a screenshot of a CAD drawing of the valve supplemented with the symbols of the functional elements that are attributed to the drawing entities.

3 THE SOFTWARE TOOL FOR CONCEPTUAL DESIGN

3.1 The graphical user interface (GUI)

The GUI is provided by the common CAD package Pro/Engineer [8]. It offers a customisation toolkit [9], called “Pro/Toolkit”, to develop auxiliary applications in C++. The Pro/Engineer 2D Sketch environment is used to graphically define and represent the symbols for the functional purpose of a certain design entity which is identical to its property as a functional element. Some of these symbols and their meanings are shown in Figure 3.

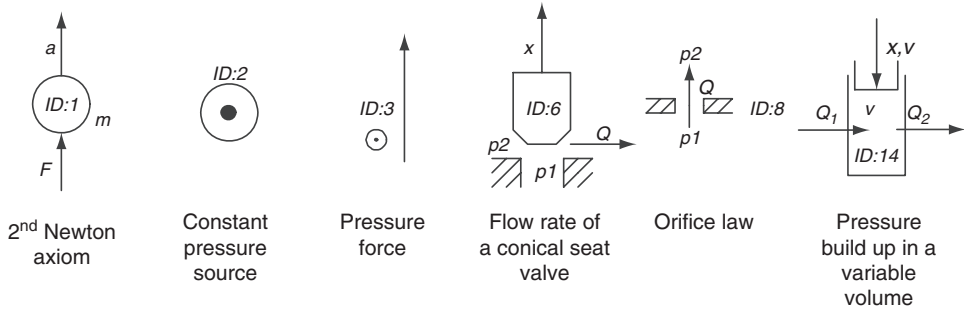


Figure 3 Some symbols for describing physical effects

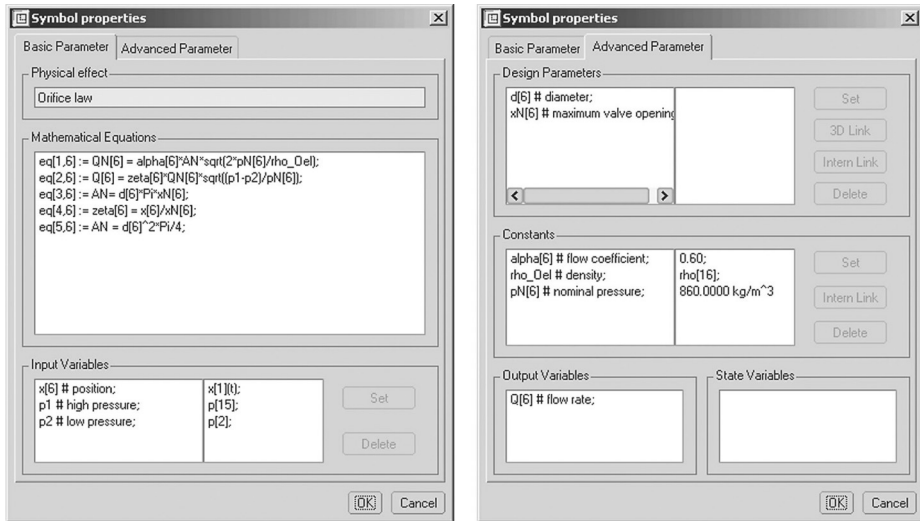


Figure 4 Screenshot of the symbol properties dialog box

Each graphical symbol is linked to a dataset in a database. A symbol properties dialog box allows defining, viewing, and altering all data from the database. Figure 4 shows the dialog box for a conical seat valve symbol. Typically, several of these functional elements are coupling functionally with other elements. This coupling is the so called structure of a certain solution principle [3] and corresponds to a network with quadripoles and nodes. The

different functional elements are linked at global nodes. In the current version of the software the user has to specify this structure by associating certain global names to certain symbol properties. Different kinds of data must be defined to specify a certain functional element:

- Input variables: they must be linked to output variables of another symbol. In Figure 4, for instance, the local pressure p_1 (it is one port of the functional element orifice) is linked to $p[15]$, which is a constant pressure source.
- Design parameters can be linked to a numerical value, to a feature value of a three dimensional object (typically geometric dimensions or inertia data) or to a design parameter of another functional element.
- The parameters in the constants box must be linked to a numeric value or to a constant parameter of another functional element.

3.1.1 Symbolic description of the 2/2-way-poppet valve

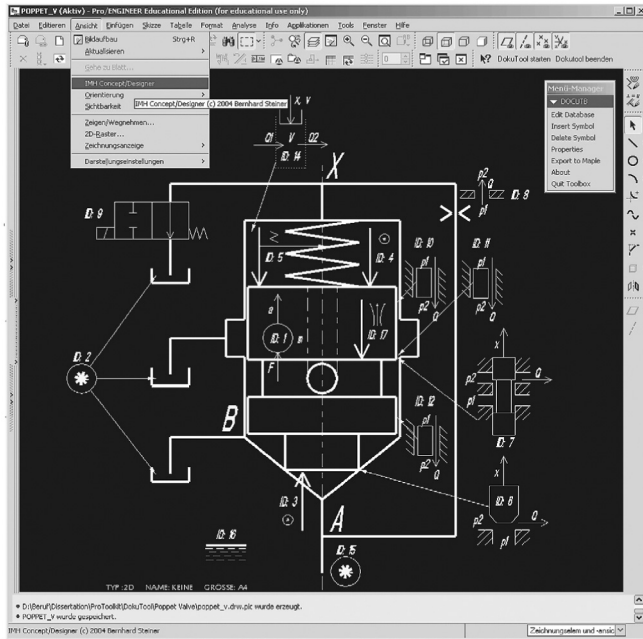


Figure 5 Pro/Engineer screenshot of the valve with symbolic description

Figure 5 shows the principle drawing of the 2/2-way poppet valve with positive feedback metering edge and the description of the essential physical effects by symbols. This way of description documents the designer’s physical understanding. For example, symbol, 10, 11 and 12 represent leakage across a sealing gap. If the designer considers that leakage might be an important problem he/she declares this by putting the corresponding symbol on the drawing. Each symbol is clearly defined by its ID. The used symbols with their mathematical equations for the mechanical motion are:

2nd Newton
axiom

$$m_1 \frac{d^2}{dt^2} x_1(t) = F_3 - F_4 - F_5 - F_{17} \quad (1)$$

Pressure force

$$F_3 = p_{15} \frac{d_6^2 \pi}{4}, F_4 = p_{14} \frac{d_7^2 \pi}{4} \quad (2)$$

Spring force

$$F_5 = F_0 + c_5 x_1(t) \quad (3)$$

Flow force

$$F_{17} = \frac{\rho_{16} Q_7^2}{d_7 \pi x_1(t)} \cos(\varepsilon_{17}) \quad (4)$$

The general equation for the flow rate of symbol 6, 7 and 8 is

$$QN_{ID} = \alpha_{ID} AN_{ID} \sqrt{\frac{2 p N_{ID}}{\rho_{16}}}, Q_{ID} = \zeta_{ID} QN_{ID} \sqrt{\frac{\Delta p_{ID}}{p N_{ID}}} \quad (5)$$

with the equations for the area AN_{ID} , ζ_{ID} and Δp_{ID} :

Conical seat
valve

$$AN_6 = d_6 \pi x N_6 = \frac{d_6^2 \pi}{4}, \zeta_6 = \frac{x_1(t)}{x N_6}, \Delta p_6 = p_{15} - p_2 \quad (6)$$

Slide valve

$$AN_7 = d_7 \pi x N_7, \zeta_7 = \frac{x_1(t)}{x N_7}, \Delta p_7 = p_{14} - p_2 \quad (7)$$

Orifice

$$AN_8 = \frac{d_8^2 \pi}{4}, \zeta_8 = 1, \Delta p_8 = p_{15} - p_2 \quad (8)$$

Normally closed
2/2-way valve

$$Q_9 = \zeta_9 QN_9 \sqrt{\frac{p_{14} - p_2}{p N_9}} \quad (9)$$

Laminar gap
flow for 10, 11
and 12

$$Q_{ID} = \frac{b_{ID} h_{ID}^3}{12 \eta_{16} l_{ID}} (p_{14} - p_2) \quad (10)$$

Pressure build-up
in a variable
volume

$$\frac{V_0 - x_1(t) A_{14}}{E_{16}} \frac{d}{dt} p_{14}(t) = Q_8 + \frac{d}{dt} x_1(t) A_{14} - Q_7 - Q_9 \quad (11)$$

$$A_{14} = \frac{d_7^2 \pi}{4}$$

Fluid viscosity

$$\eta_{16} = \nu_{16} \rho_{16} \quad (12)$$

3.2 Database environment

With the C++ interface MySQL++ [10] a MySQL database [11] can be linked to the graphical user interface. A database of functional elements for the purpose of valve design has been created. It consists of four table classes:

- The table of physical effects.
- Tables of elementary technical working principles: Uses one or several physical effects in combination with some geometry, kinematics, specific material properties to achieve an intended technical function.
- Table of sources: These are, e.g. pressure definitions, pressure sources, volume flow sources, etc. The structure is similar to the technical working principles table.
- Tables of derived technical functions: Describes principle models of technical products which are composed of elementary technical working principles.

Each table consists of Maple equations and parameter definitions, as shown in Table 1.

Table 1 Example of a physical effect

No	Name	Maple_Equation	Maple_Parameter
1	Pressure build up	$eq[1, ID] := V[ID] / E_{Oel} * Diff(p[ID](t), t) = Q_{In} - Q_{Out};$	V[ID] # volume; E_Oel # elasticity modulus; p[ID] # pressure; Q_In # inflow flow rate; Q_Out # outflow flow rate;

Elementary technical working principles and the source table are the heart of the database. The designer uses these datasets for describing technical products in form of mathematical equations in combination with graphical symbols. An example of an elementary technical working principle is given in Table 2.

Table 2 Example of an elementary technical working principle

No	Name	Symbol_Filename	Description	Physical_Effect
1	Variable volume	variable_volume.sym	Pressure build up in a variable volume with motion	basic_principles_energy:1;

Maple_Equation	Maple_Parameter	Input	Output	State	Constant	Design
eq[2,ID]:=V[ID]=V0[ID]- x1*A[ID]; eq[3,ID]:=Q_In=Q_In0[ID] +v1*A[ID]; eq[4,ID]:=A[ID]=d[ID]^2* Pi/4;	V0[ID] # volume; x1 # position; A[ID] # area; Q_In0[ID] # inflow rate; v1 # velocity; d[ID] # diameter;	0:2; 0:5; 0:4; 1:5;	1:3;	1:3;	1:2;	0:1; 0:6;

In the datasets the name and a short description for the elementary technical working principle and a link to a drawing symbol for visualisation are stored in columns one to three. A link to a physical effect is given in the fourth column. In the next two columns the mathematical equations of the underlying physical effect are described. In the last five columns the input, output, state, constant and design variables and parameters respectively are defined. This is done by referencing to the corresponding variable and parameter names in Maple_Parameter column of the physical effects and technical working principles tables. The user does not type these data, he/she even can't see these last five columns, but establishes these relations by a click onto symbols in the symbol property window.

Table 3 The description of the derived technical function of the 2/2 way valve

No	Children	Input Connection	Constant Connection	Design Connection
1	1:active_principles_mechanic,1; 2:sources,1; 3:sources,3; 4:sources,3; 5:active_principles_mechanic,3; ...	1:1->3:1; 1:1->5:1; 1:1->4:1; 8:2->14:1; 6:1->1:1; ...	8:1->0.60; 7:1->0.60; 5:1->10.00; 9:2->5.00; 11:1->16:2; ...	1:1->0.05; 10:2->7:2; 11:2->7:2; 12:2->7:2; 11:3->10:3; ...

The result of a definition of a system is a derived technical function. It is described by a table as shown for the example valve in Table 3. The first part of the table equals Table 2. In the last part links to elementary technical working principles and some connections to other elements or values of input, constants and design parameters are stored.

3.3 Maple interface

From the description of the system in the database a Maple input file can be generated automatically. All identification numbers in the equations (called [ID]) and parameters will be replaced by the global ID numbers of the specific functional element (this corresponds to the symbol ID). All local parameter names will be replaced by linked parameters or numerical values according to the declarations of the designer in the design phase. A fragmented listing of the example from Figure 5 is shown below.

```
# - - - - -
# Equation of motion for one degree of freedom
eq[1,1] := v[1](t) = Diff(x[1](t),t);
eq[2,1] := m[1]*Diff(v[1](t),t) = (F[3]-F[5]-F[4]-F[17]);
. . .
```

From such equations, in principle the system can be investigated qualitatively and quantitatively. According to [4] an important part of such investigations are the relations between the design parameters and the functional requirements. This is an upcoming subject in systematic design theory (e. g. [12]) and is not discussed here. Symbolic manipulation programs such as Maple [13] offer powerful methods to assist or even automate such investigations.

4 DESIGN EVALUATION OF THE 2/2-WAY-POPPET VALVE

The valve has to fulfil two main requirements: achievement of certain nominal flow rate and opening time. The nominal flow rate is explicitly given by the respective orifice equation (5, 6) which constitutes a simple design rule for the main diameter d_6 and the opening stroke xN_6 . For the latter a reasonable limit is $d_6/4$ because for larger strokes the cylindrical flow passage exceeds the cross section of the intake bore. Based on the specifications of Table 4 the results are: $d_6 = 12$ mm; $xN_6 = 3$ mm. With these two parameters a first design of the poppet as shown in Figure 6 can be made. An other important parameter of the valve is the diameter ratio $\beta=d_7/d_6$. A larger β increases the nominal flow rate of the positive feedback metering edge, which speeds up the valve, but enlarges also the mass of the spool and the volume V_{014} , which make the valve slower.

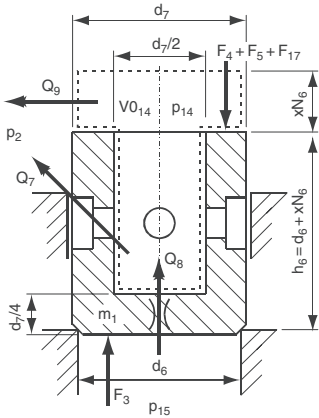


Figure 6 Mechanical model with main dimensions of the valve

The mass of the spool and the volume V_{014} can be estimated by the geometric dimensions shown in Figure 6. To evaluate the opening time of the valve the equation of motion and the pressure build-up equation according to equation (1) – (12) in nondimensional form are used.

$$\begin{aligned}
 \frac{d\xi_1(\tau)}{d\tau} &= \xi_2(\tau) \\
 \frac{d\xi_2(\tau)}{d\tau} &= f_0 - c_\omega \psi(\tau) - \xi_1(\tau) - \xi_1(\tau)\psi(\tau)f_\omega \\
 \frac{d\psi(\tau)}{d\tau} &= \frac{\xi_1(\tau)a_{\omega,7}\sqrt{\psi(\tau)} + \zeta a_{\omega,9}\sqrt{\psi(\tau)} - a_{\omega,8}\sqrt{1-\psi(\tau)} - \xi_2(\tau)b}{\varepsilon(b\xi_1(\tau)-1)}
 \end{aligned}
 \tag{13}$$

The nondimensional parameters are:

$$\begin{aligned}
 \xi_1 &= \frac{x_1}{xN_6}, f_0 = \frac{c_\omega}{\beta^2} - \frac{F0_5}{m_1 xN_6 \omega^2}, c_\omega = \frac{p_{15} A_7}{m_1 xN_6 \omega^2}, \omega^2 = \frac{c_3}{m_1} \\
 \tau = \omega t, \psi &= \frac{p_{14}}{p_{15}}, b = \frac{d^2 \pi xN_6}{4 V0_{14}}, \varepsilon = \frac{p_{15}}{E_{16}}, f_\omega = \frac{\rho_{16} QN_7^2 \frac{p_{15}}{pN_7} \cos(\varepsilon_{17})}{m_1 xN_6^2 \omega^2 d_7 \pi} \\
 a_{\omega,8} &= \frac{QN_8}{\omega V0_{14}} \sqrt{\frac{p_{15}}{pN_8}}, a_{\omega,9} = \frac{QN_9}{\omega V0_{14}} \sqrt{\frac{p_{15}}{pN_9}}, a_{\omega,7} = \frac{QN_7}{\omega V0_{14}} \sqrt{\frac{p_{15}}{pN_7}}
 \end{aligned}
 \tag{14}$$

Dimensionless equations mostly reduce the number of parameters in the equations which gives a better view on their role for the system performance. Their derivation can be supported by a symbolic manipulation language. To clarify the role of the diameter ratio β its influence on the opening time, that is the time τ needed for $\xi_1 : 0 \rightarrow 1$, is computed. Results obtained by a numerical integration of (13) for the parameter set according to Table 4 are shown in Figure 7.

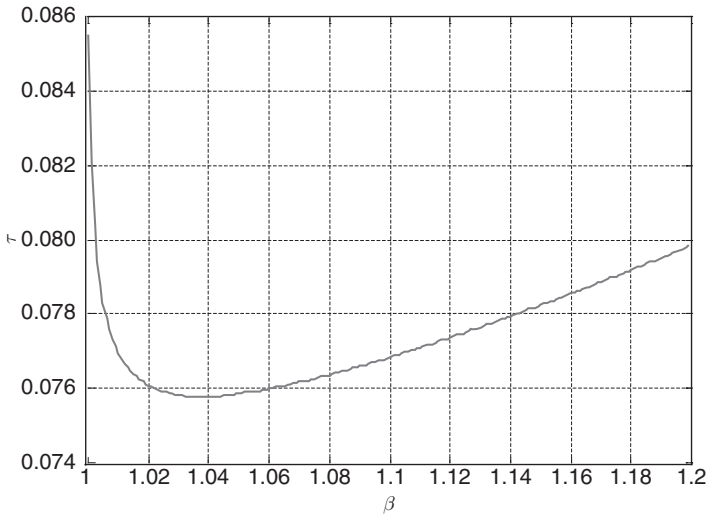


Figure 7 Nondimensional opening time versus diameter ratio β

Table 4 Parameter set

Parameter	Symbol	value	unit
pressure at high pressure port	p_{15}	200	[bar]
pressure at tank port	p_2	0	[bar]
nominal flow rate over main edge	QN_6	150	[l/min]
nominal flow rate over orifice	QN_8	0.5	[l/min]
nominal flow rate over pre valve	QN_9	2	[l/min]
nominal differential pressure	pN_6, pN_7, pN_8, pN_9	5	[bar]
effective bulk modulus of compressibility	E_{16}	16000	[bar]
oil density	ρ_{16}	860	[kg/m ³]
steel density	ρ_{Fe}	7850	[kg/m ³]
spring preload force	F_{05}	10	[N]
spring rate	c_5	2	[N/mm]
discharge coefficient	α_6, α_7	0.6	-

5 CONCLUSION AND OUTLOOK

A substantial computer support in the conceptual design phase in form of an auxiliary software add-on to common CAD programs is a promising approach. The two objectives, i) a clear documentation of the designer's ideas and physical understanding of his/her concept and ii) a support of the evaluation by some automatic generation of mathematical models have been achieved. Underlying physical effects and technical working principles are stored in a mathematical notation in a database and can be combined to form new, more complex systems. They are represented by graphical symbols in the drawings. The symbolic notation enables an immediate treatment of the mathematical models in a symbolic manipulation language for qualitative investigations, closed form solutions, where possible, or for transfer to a numerical simulation package. The computer supported evaluation of the design parameter functional requirement relation will be a next step in the research.

ACKNOWLEDGEMENT

The authors gratefully acknowledge the sponsoring of this work by the 'Linz Center of Competence in Mechatronics' in the framework of the Kplus program of the Austrian government. This program is funded by the Austrian government, the province Upper Austria and the Johannes Kepler University Linz.

REFERENCES

- [1] VDI RICHTLINIE 2249: CAD-Benutzungsfunktionen. April 1999.

- [2] Pahl G. and Beitz W., *Konstruktionslehre*. 2. Auflage. Berlin Heidelberg New York: Springer-Verlag, 1986.
- [3] Scheidl R., Dierneder S., Computerunterstütztes Konzipieren auf Basis einer „Funktionalen Zergliederung“. *Konstruktion* 7/8, 2000, pp. 51-55.
- [4] Suh Nam P., *The Principles of Design*, Oxford University Press, 1990.
- [5] Steiner B., Scheidl R. and Hametner G., Development of an ultra fast emergency stop valve. In *Proceedings of the 18th International Conference on Hydraulics and Pneumatics*, Prague, Czech Republic, 2003.
- [6] Anderson Bo R., On the Valvistor, a Proportionally Controlled Seat Valve. *PhD thesis*, Linköping, Schweden: Department of Mechanical Engineering, 1984, 192 p.
- [7] Achten, P. A. J., Van den Oever, J. P. J., Potma, J., Vael, G. E. M., Horsepower With Brains: the Design of the Chiron Free Piston Engine. In *SAE Technical Papers 2000-01-2545*, In *Proceedings of the International Off-Highway & Powerplant Congress & Exposition*, Milwaukee, WI, USA, September 2000.
- [8] Parametric Technology Corporation, Pro Engineer Wildfire M210, Parametric 3D-CAD Software.
- [9] Parametric Technology Corporation, Pro/Toolkit User's Guide, 2002.
- [10] Atkinson K., MySQL++ A C++ API for MySQL ver 1.7.9, May 2001.
- [11] MySQL AB., MySQL database server, Version 4.0.18.
- [12] Summers J. D., Bettig B., Shah J. J., The Design Exemplar: A New Data Structure for Embodiment Design Automation. In *Journal of Mechanical Design*, Vol. 126(2004), pp. 775-787.
- [13] Waterloo Maple Inc., Maple 9.01, Computer Algebra System.

Determining the Steady State Flow Forces in a Rim Spool Valve using CFD Analysis

NORENSE OKUNGBOWA, DON BERGSTROM, RICHARD BURTON

Department of Mechanical Engineering, University of Saskatchewan

Saskatoon, Saskatchewan, Canada

Contact: noo008@mail.usask.ca

ABSTRACT

Hydraulic spool valves are found in most hydraulic circuits in which flow is to be modulated. Therefore their dynamic performance is critical to the overall performance of the circuit. Fundamental to this performance is the presence of flow reaction forces which act on the spool. These forces can result in the necessity of using two stage devices to drive the spool and in some cases have been directly linked to valve and circuit instabilities. As such, a great deal of research and design has concentrated on ways to reduce or compensate for flow forces. In one particular series of studies conducted on flow divider valves, it was established that a rim machined into the land of the spool reduced the flow dividing error by approximately 70-80%, and it was deduced that the main contribution to this error was flow forces. Direct verification of the claim regarding flow force reduction was not achieved and hence was the motivation for this particular study.

This paper will consider the reaction (flow) associated with a conventional spool land and one with a rim machined into it. Computational Fluid Dynamics (CFD) analysis was used to elucidate the fluid mechanics associated with the steady state flow forces as it provided a detailed structure of the flow through the valve. The prediction of the steady state flow force on the rim spool was investigated and the results from the CFD analysis indicated a reduction by approximately 70% in a flow divider valve configuration.

1. NOMENCLATURE:

- u'_i fluctuating velocity component in the x_i direction (m/s)
- θ_i discharge angle at port i ($^\circ$)
- u'_j fluctuating velocity component in the x_j direction (m/s)
- δ_{ij} Kronecker delta
- a_1 a constant
- η a switching function (1 or 0)

ρ	fluid density (Kg/m ³)
\bar{P}	mean pressure (Pa)
\bar{U}_i	mean velocity component in the x_i direction; (m/s)
ΔP	pressure drop across the orifice (CFD model) (Pa)
Ω	the absolute value of the vorticity
ω	the inverse of the turbulence time scale, (s ⁻¹)
$k = (1/2)\overline{u'_i u'_i}$	the turbulence kinetic energy (m ² /s ²)
$\frac{\partial V_x}{\partial y}$	velocity gradient of V_x in the y direction (s ⁻¹)
$\overline{\rho u'_i u'_j}$	Reynolds stress tensor (kg/m.s ²)
μ_t	turbulent viscosity (Pa.s)
μ	viscosity of the fluid; (Pa.s)
A	area of the sleeve (m ²)
A_{pi}	the spool area of surface i (m ²)
A_{vi}	flow divider variable orifice i (m ²)
A_0	area of the orifice (CFD model) (m ²)
B	flow divider spool damping coefficient. (N.s/m)
Cd	discharge coefficient (assume constant in this study)
F_{spool}	steady state reaction force on the spool (N)
F_{fi}	the flow reaction force on flow divider surface i (N)
F_f	the frictional force (N)
K_i	the flow divider orifice i valve coefficient (m ³ /kg) ^{1/2}
m	the mass of the flow divider spool (kg)
P_{ii}	the pressure acting on flow divider land surface i (Pa)
P_{li}	the load port pressure at port i for the flow divider valve (Pa)
P_s	the supply pressure (constant) (Pa)
Q_i	the flow through orifice i on the flow divider valve. (m ³ /s)
t	the rim thickness
d	the rim depth
w	the area gradient for the flow divider valve (width of flow domain) (m)
x	the spool displacement from centre for the flow dividing valve (m)
x_{vi}	the opening displacement of orifice i for the flow divider valve (m)
l	the length of valve chamber (i.e. control volume) (m)
l_c	the length within the chamber in which flow is significant (m)
F_e	the flow divider error (%)
\dot{x}	the velocity of the spool (m/s)
\ddot{x}	the acceleration of the spool (m/s ²)

2. INTRODUCTION

Hydraulic valves are a major component of hydraulic systems. The primary functions of these valves are to control the rate of flow, the direction of flow and the pressure in hydraulic systems; further, their dynamic performance can directly affect the overall stability and transient response of the system in which they operate.

Fundamental to all valve operation are the flow forces. These forces can be described as the effect of momentum changes as oil flows through the valve. The flow force has both steady and transient components but the steady flow force is the most dominant. The transient flow force, although very important for stability, is not considered in this study. The inherent steady state flow forces act in a direction so as to close the valve and hence act as a nonlinear spring. The forces so produced can affect the metering accuracy of the valve. Since flow forces are a function of the product of pressure drop and orifice opening, the non-linearity can be a potential source of instability in the valve operation. In addition, for high bandwidth and flow rate applications, these forces become significant in which case a larger external force is needed to actuate the spool.

Many attempts have been made to compensate for flow forces by the use of one or more pilot stage valves or by using larger solenoids. The problem with these approaches is that higher order dynamics are introduced into the valve operation (which makes control design more challenging); in addition, larger solenoid actuators are usually expensive and have distinct force limitations and can limit single stage electro-hydraulic servo-valves to low performance applications, Merritt (1).

There have been some interesting approaches forwarded to reduce flow reaction forces. Merritt (1) prescribed the placement of many small holes symmetrically around the valve sleeve so that the angle at which the fluid leaves the metering orifice reaches 90° when the hole is completely uncovered. He also proposed a method of compensation to increase the shank diameter at both ends. Borghi et al (2), Bao et al (3), and very recently, Jyh et al (4) have compensated for the flow forces by modifying the spool geometry. Finke et al, (5) compensated for flow forces by adding a compensation cone to the spool and a full angular scallop to the body. In Finke's design study, the flow forces were reduced from 25 N to 9 N at a pressure drop of 320 bar.

Chan et al (6) and Burton et al (7 and 8) utilized a spool with a rim machined into the lands to reduce the flow division error in a flow divider valve. Chan surmised that since friction and flow forces were the major contributor to the flow division error, any reduction was primarily a consequence of reduced flow forces; thus they concluded that the rimmed configuration did contribute to this reduction. The authors were not able to directly measure flow forces on the particular spool arrangement that was used in their study. Thus their conclusions were based solely on indirect information such as the observed reduction in flow dividing error in the valve using the rim.

The challenge of verifying that flow reaction forces were, indeed, reduced was part of the motivation for this research. In addition, since Chan had demonstrated the difficulties in experimentally verifying their claim, it was decided that another approach using Computational Fluid Dynamics (CFD) could be a viable alternative to address the problem.

In the past decade significant advances to CFD and Particle Image Velocimetry (PIV) approaches have been made and applied to numerous fluid dynamics problems and more recently, hydraulic components. Wang et al (9) used Particle Image Velocimetry (PIV) to acquire data in simplified valve geometry. They measured the velocity and pressure fields in a spool valve based on two-dimensional PIV. Their results showed PIV to be an effective method to map the flow field in spool valve. Similarly, Gao (10) investigated the flow structure inside a spool valve by numerical simulation based on the Finite Element Method (FEM) and tried to validate his results by PIV experiments. Both visualization results indicated a similar flow structure but the data acquired from both methods did not agree well. Since valve geometry is extremely complex, Borghi et al (2) showed how the flow characteristics of complex geometry can be dramatically simplified using axis-symmetric approaches. This allowed for a reduction in the time needed to solve the governing equations.

Bao (3) investigated the flow behavior inside a hydraulic spool valve using CFD methods. He analyzed the relationship between flow rate, geometry and pressure losses by comparing the computed pressure loss for different flow rate and chamber structures. His results show that the changes in flow rate and in geometry decreased the pressure drop significantly in the valve, but modifications to the valve's spool geometry resulted in little improvement. Linda et al (11) utilized CFD as a tool to improve a valve design. With CFD, the authors predicted the primary source of pressure losses in the existing valve and then modified the valve features to minimize those losses. Vescovo and Lipolis (12, 13) provided a detailed study of flow forces in traditional and proportional directional valves using a CFD commercial code. In particular, a complete three dimensional analysis of both types of valves was demonstrated and the dependence of flow forces on pressure drop and on the spool opening analyzed.

Another school of thought proposed utilizing flow forces advantageously instead of eliminating them. Yuan et al (14 and 15) used fundamental momentum analysis, CFD analysis and experimental studies to examine how transient and steady flow forces can be manipulated to improve spool agility (dynamic response) in a single stage valve. The authors proposed that spool agility can be improved by inducing unstable transient flow forces, that is, by configuring the valve to have a negative damping length, and the unstable valves could be stabilized via closed-loop feedback. Also in this work, it was found that two previously ignored components, i.e. viscosity effects and non – orifice momentum fluxes, have strong influence on steady flow forces.

Based on the success that these researchers (and many others) have had in using CFD to analyze flow forces and to assist in flow visualization in valves and other hydraulic components, it was decided to use CFD as a means of establishing that the rim effect of Chan's design was indeed able to reduce the flow reaction forces. The rim effect was most interesting in that the fabrication was very straight forward compared to the valve contouring that alternate approaches utilized. Thus the objective of this study was to apply CFD to a basic 2D spool configuration to establish that flow forces using a rimmed spool were indeed reduced. A schematic of the basic spool with and without the rim machined into the land is illustrated in Figure 1. In section 3, the basic equations for force forces are presented. In section 4, the implementation of the CFD code and the boundary conditions are listed. In section 5, the results of the numerical simulation for various valve

configurations are presented. In section 6, the CFD approach is combined with a dynamic simulation of Chan’s flow divider valve utilizing an iterative approach. In section 7, the results are discussed and conclusions presented.

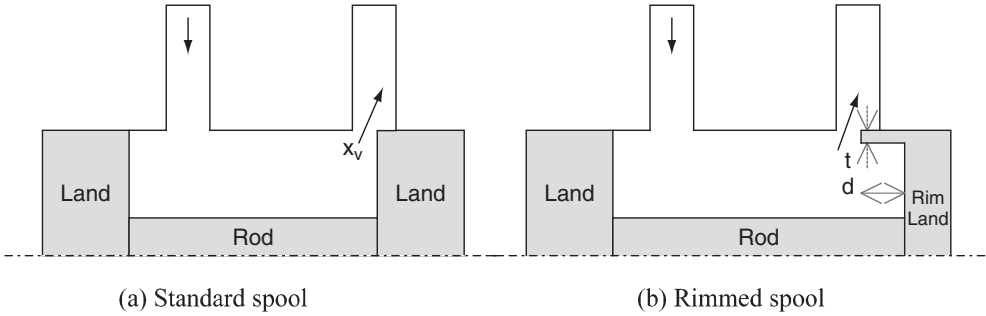


Figure 1: Standard spool and land arrangement with and without rim.

3. STEADY STATE FLOW FORCES EQUATIONS

The focus of this section is to present models for steady state flow forces. The effect of viscosity and the inlet momentum flux (non - orifice inlet) on steady state flow forces was studied by Yuan and Li, (15). Yuan expressed the momentum flux at the inlet to be proportional to the square of the flow rate and used the assumption of a laminar and Newtonian fluid to model the shearing forces that act on the spool rod and valve sleeve. In this work however, only the viscous contribution to steady state flow forces is examined.

In the first model, the classical flow reaction forces, Merritt (1) are considered. The valve configuration and nomenclature are provided in Figure 2. The development of the classical model of flow reaction forces is relatively straight forward and will not be repeated here. Applying appropriate assumptions (1), and using the nomenclature of Figure 1, it can be shown that:

$$F_{spool} = - \left(2C_D A_o \Delta P \cos \vartheta + \eta \iint_{A(sleeve)} \mu \frac{\partial V_x}{\partial y} dA \right) \quad (1)$$

When viscous effects are neglected, $\eta = 0$, Merritt (1) ; if they are included, then $\eta = 1$, Yuan and Li (15).

The second model was that used for CFD analysis, and was based on the Reynolds – Averaged Navier – Stokes (RANS) equations. A CFD software package called CFX-5.6 (ANSYS) was used to solve the RANS equations. For steady flow with constant fluid properties, the transport equations representing conservation of mass and momentum take the following form:

$$\rho \overline{u'_i u'_j} = -\mu_t \left(\frac{\partial \overline{U}_i}{\partial x_j} + \frac{\partial \overline{U}_j}{\partial x_i} \right) + \frac{2}{3} \rho k \delta_{ij} . \tag{4}$$

$k = (1/2) \overline{u'_i u'_i}$ is the turbulence kinetic energy associated with the fluctuations of the velocity field. Note that unlike the dynamic viscosity, the turbulent viscosity is not a fluid property but a function of the local flow field. In this case, it is solved using the so called Shear Stress Transport (SST) turbulence model available in the code CFX-5. The local value of μ_t is calculated using the following relation:

$$\mu_t = \frac{\rho a_1 k}{\max(a_1 \omega \Omega)} \tag{5}$$

In order to calculate μ_t , two additional transport equations are solved for k and ω . The specific form of the transport equations is described in the documentation for CFX-5, and their derivation is given in Menter F. R (16). One important aspect of this two-equation closure is that it is a low Reynolds number formulation that remains valid in the immediate vicinity of the wall, where typically the turbulence is strongly damped and viscous forces are dominant. It requires a sufficiently fine grid near the wall, but when correctly implemented can accurately resolve the local wall shear stress, τ_w , which can then be used to calculate the viscous friction force acting on the surface.

The flow forces are then evaluated by integrating the pressure profiles along surfaces of the two lands and integrating the shear stresses on the rod and piston face.

4. GEOMETRY AND BOUNDARY CONDITIONS

For this initial study, only a two dimensional model was examined. This was considered to be important because it would allow a more visual classical representation of flow through the valve which facilitates a physical explanation of flow force reduction. In reality, the CFD package used in this study used a 3 D model of the valve but with a width of 1 mesh unit. The meshes used are hexahedral in shape.

The computational model of the valve is shown in Figure 3 and includes the valve chamber and the entry and exit port. The width of the domains are taken as πD , where D is the diameter of the spool. In Figure 3, a label is used to represent each boundary. The spool comprises of boundary j , k and l ; the sleeve, a and e ; and the inlet and outlet, c and g , respectively. Because the model is actually 3D, the “front” and “back” surfaces are separated by 1 mesh unit. The front and back boundaries which cap the computational volume are considered as symmetry boundaries. Apart from the inlet (c), outlet (g), and the symmetry boundaries, all other surfaces are classified as no – slip boundaries. The no – slip boundary condition implies that the tangential velocity on each wall is zero due to friction. The inlet and outlet are strictly one way flow boundary conditions. For the inlet, the flow is directed into the flow domain, and at an outlet boundary, it is directed out of the domain.

The symmetry boundary condition implies that there is no change in the flow variables in that direction. The inflow boundary for the model shown in Figure 3 was a pressure boundary equal to 21.4 bar. The outflow was also a pressure boundary equal to 3.4 bar. All walls were considered to be thermally inactive and hydraulically smoothed.

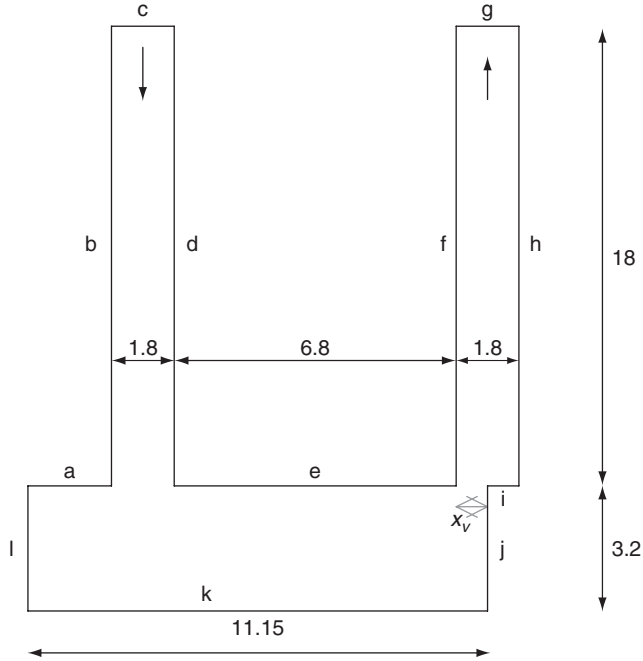


Figure 3: Computational model of the valve geometry

The 2D geometries were created and meshed using CFX 5.6 numerical software. The exit ports were extended adequately in order to achieve a fully developed flow at the outlet. The entire mesh elements used were hexahedral and fit the geometry of the problems. The exit ports and the flow restriction region were meshed more finely than at the entry port as flow variables were considered to vary more in these regions. The mesh was proven to yield solutions which were insensitive to further refinement. The inlet and outlet mesh are illustrated in Figure 4.

The physical property of the fluid was set as 871kg/m^3 for the fluid density and $0.0375\text{kg/m}\cdot\text{s}$ (40°C) for the dynamic viscosity. This corresponded to a kinematic viscosity of 43 centistokes.

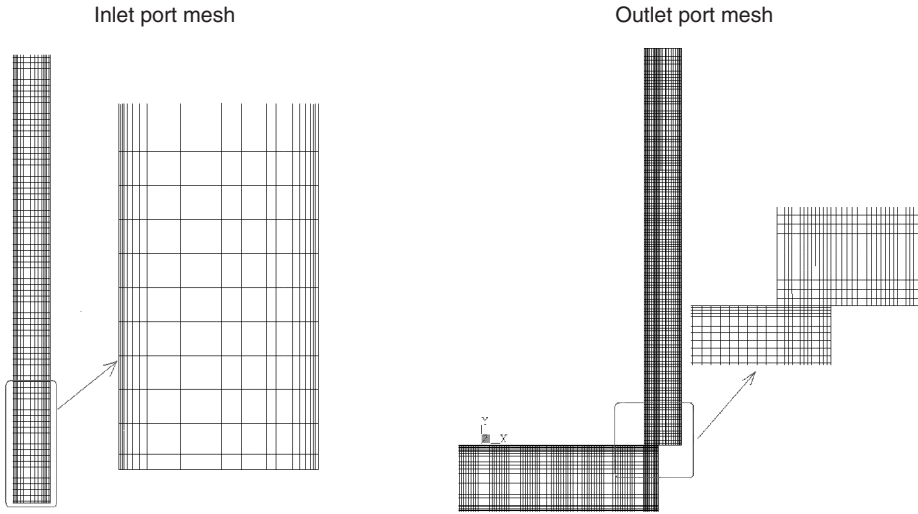


Figure 4: Inlet port mesh and Outlet port mesh at the orifice

5. SIMULATION RESULTS

Simulations were performed for different openings of the spool. The flow was modeled in CFX 5.6 (17) as Newtonian, turbulent, steady and incompressible. The CFX 5.6 code uses the finite-volume method to discretise the RANS equations. A second order differencing scheme was used to model the convective-diffusive transport. The SIMPLE algorithm was used for solving the mean pressure field. The approximations associated with the turbulence model represent an additional source of error. However, as mentioned in section 2, the Shear Stress Transport (SST) turbulence model which was adopted has been validated for a wide variety of flows. Grid refinement was used to ensure that the numerical errors were sufficiently small on the final mesh to enable meaningful conclusions to be drawn from the simulation results. For a given problem, the solver typically ran for 2 1/2 hours, and convergence of the solution was achieved after approximately 1000 iterations. The final values of the residuals for the continuity (pressure) and the two momentum equations (u and v) were below 1×10^{-6} .

Figures 5 and 6 show the CFD results in terms of the velocity vector plots for the standard reference and the rim spool valve configurations. The angle of the jet of fluid exiting the orifice is evident. A control volume analysis indicated that the steeper the angle, the lower the steady state flow force, and this was substantiated using the rim geometry

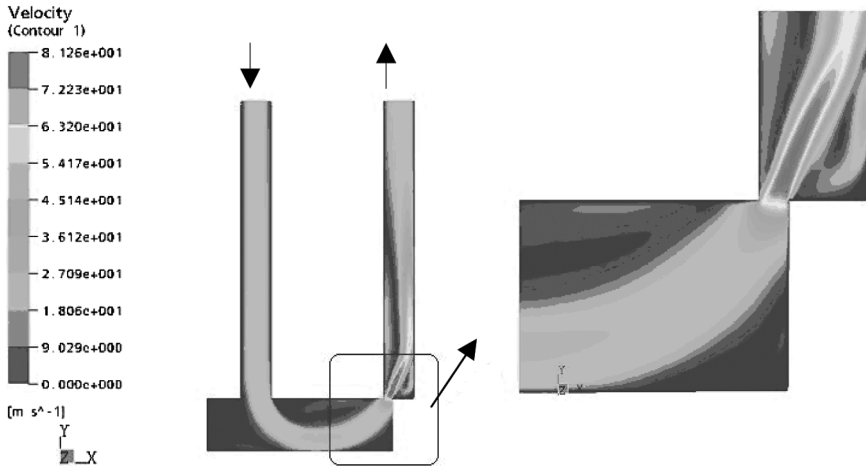


Figure 5 (a): Velocity vector plot for the conventional (non-rimmed) spool configuration ($x_v = 0.5\text{mm}$).

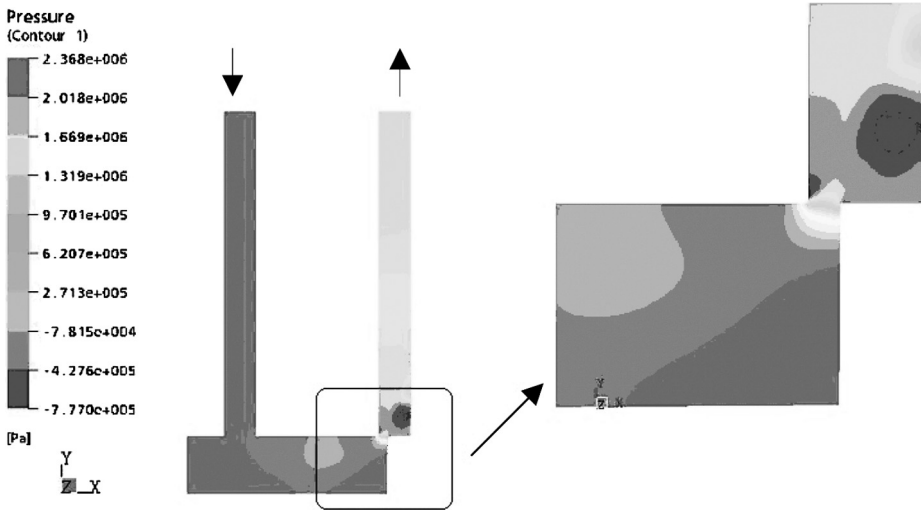


Figure 5 (b): Pressure plot for the conventional (non-rimmed) spool configuration ($x_v = 0.5\text{ mm}$). The estimated jet angle and steady state flow forces from the CFD analysis are 65.54° and 6.31 N .

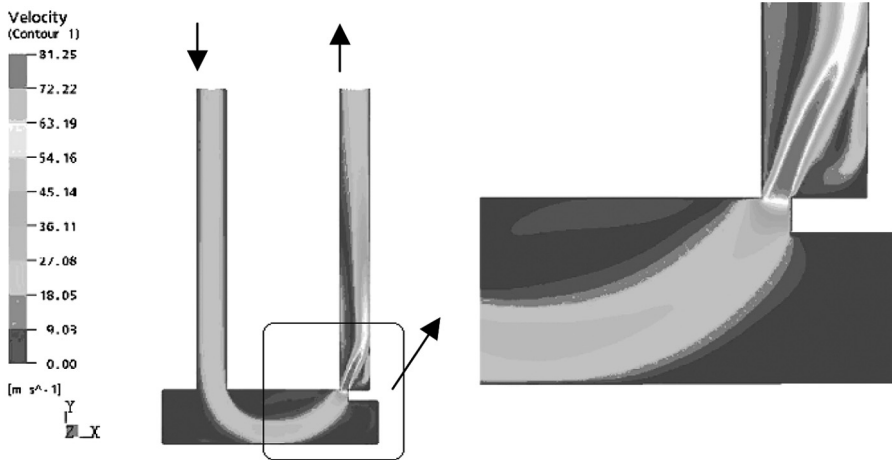


Figure 6 (a): Velocity vector plot for the rim spool valve configuration ($t = 0.8 \text{ mm}$ and $x_v = 0.5\text{mm}$)

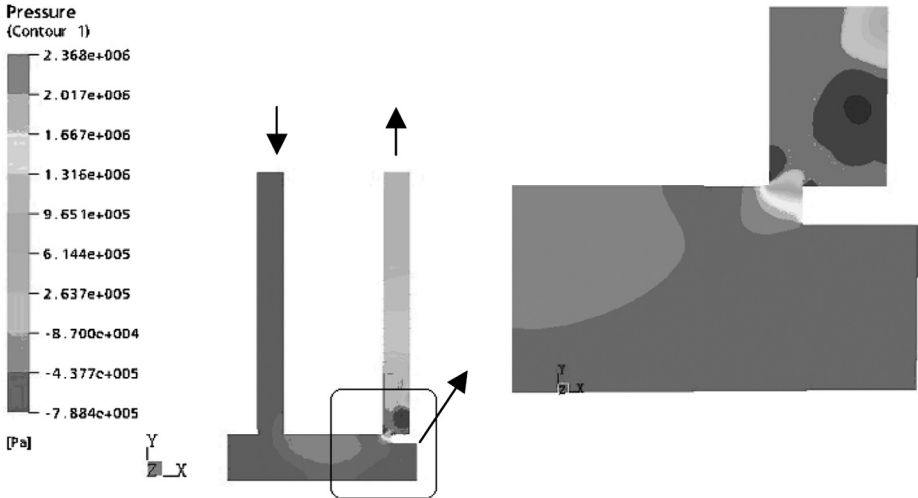


Figure 6 (b): Pressure plot for the rim spool valve configuration ($t = 0.8 \text{ mm}$ and $x_v = 0.5\text{mm}$). The estimated jet angle and steady state flow forces from the CFD analysis are 66.46° and 4.82N , respectively.

These simulations were repeated for various valve opening and the results summarized in Table 1.

Table 1: The estimated jet angle and steady state flow forces from CFD analysis for standard spool land and rimmed land (rim thickness $t = 0.8\text{mm}$)

x_v (mm)	Steady Flow Force(N)		% reduction	Jet Angles (degrees)	
	Standard	Rim		Standard	Rim
0	0	0		0	0
0.375	4.68	4.46	4.7	65.34	65.85
0.5	6.31	4.82	23.6	65.54	66.46
0.75	9.76	7.06	27.7	66.21	71.62
1.05	13.67	9.64	29.5	69.25	73.49

For a constant rim thickness, the flow forces are reduced by approximately 25% for spool positions greater than 0.5 mm. The jet stream angle also increases for the rimmed land. For very small displacements, the pressure gradient is localized around the opening and rim area whereas for larger openings, the pressure distribution is more distributed.

A comparison of the steady state flow force for the standard spool land using a CFD approach versus the standard classical flow reaction force calculation of equation (1) is demonstrated in Table 2. It should be noted that the classical force equation uses an assumed angle of 69 degrees, in order to provide a common basis for comparison. It is clear that the flow reaction forces for the outflow condition were under-estimated using the classical steady state equations. This is primarily because the frictional effects have been ignored in the classical equation. The opposite is true for the inflow conditions because viscous effects are subtractive.

Table 2: A comparison of steady state flow reaction forces using CFD versus that obtained from equation (1)

Spool opening x_v (mm)	CFD		Classical	
	Standard spool		Standard spool	
	SSFF (N)	θ ($^\circ$)	SSFF (N)	θ ($^\circ$)
0.375	4.68	65.34	2.95	69
0.5	6.31	65.54	3.93	69
0.75	9.76	66.21	5.30	69
1.05	13.67	69.25	8.25	69

It was of interest to demonstrate how the rimmed lands performed when the thickness was increased. The results are summarized in Table 3 and it is evident that there is very little flow force reduction at this thickness and the result is consistent with that predicted by Chan et al (6).

Table3: The estimated flow forces using the CFD approach for a rimmed land at a thickness of (t = 1.0mm).

Spool opening $x_v (mm)$	CFD			
	Standard spool		Rim spool	
	SSFF (N)	$\theta(^{\circ})$	SSFF (N)	$\theta(^{\circ})$
0.375	4.68	65.34	4.64	65.85
0.5	6.31	65.54	6.26	66.46
0.75	9.76	66.21	9.29	71.62
1.05	13.67	69.25	12.28	73.49

6. APPLICATION TO THE RIMMED FLOW DIVIDER

It was of interest to apply the CFD approach to the actual valve configuration of Chan’s rimmed flow divider valve. This required an iterative approach because the actual spool displacement in the valve depended on the calculated flow reaction forces, which in turn depended on the spool position. The model of the flow divider valve and the describing equations are presented in Appendix A for completeness. The dynamic equations were solved using Matlab/Simulink® (18). For an initial spool displacement from the centre, the flow reaction forces were estimated using the classical steady state flow force equation. Using the dynamic simulation a new steady state spool position was determined. CFX was applied to the new spool position model and a new flow force estimated. This value was then substituted back into the dynamic simulation and a new position calculated. This procedure was repeated until the spool position reached a steady state point at which the process was stopped.

Figures 7 and 8 shows typical velocity and pressure profiles for the rimmed and non-rimmed lands. The flow forces for the two cases are compared in Table 4. The results are presented for a pressure drop of 12 bar across the load ports. At steady state conditions, the percentage reduction in flow reaction forces are calculated to be approximately 80%. These results are consistent with the trends obtained experimentally with Chan’s work (6).

Table 4: Flow forces and jet stream angle for the flow divider valve (Pressure differential across the ports of 12 bars and a rim thickness of .16mm)

$x(cm)^*$	$x_{v1}(cm)$	$x_{v2}(cm)$	$\theta_1(^{\circ})$	$\theta_2(^{\circ})$	$F_f(N)$	Condition
0.06	0.14	0.26	88.1	87.3	3.925	Without Rim
0.01	0.19	0.21	89.2	87.9	0.747	With Rim

*In this table, x is the actual displacement of the divider spool and x_{v1} and x_{v2} are the relative displacement of the spool with respect to the initial centre position.

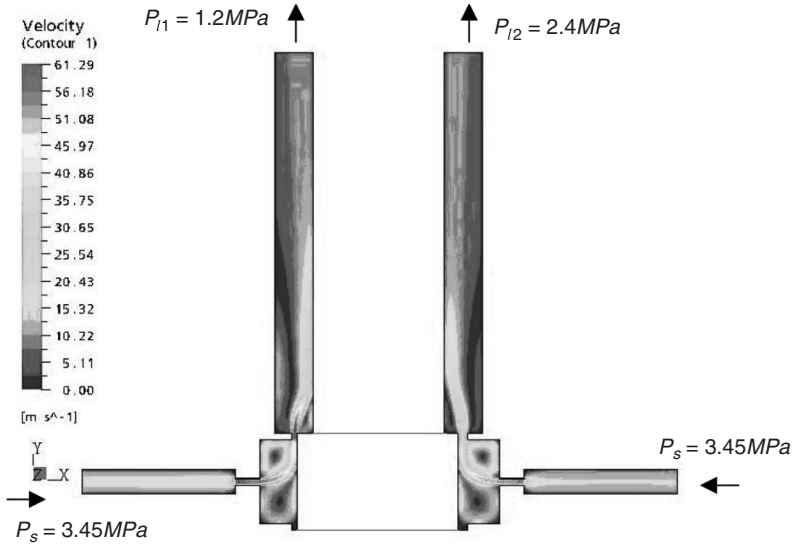


Figure 7 (a) Velocity plot ($x_{v1} = 0.14\text{ cm}$; $x_{v2} = 0.26\text{ cm}$)

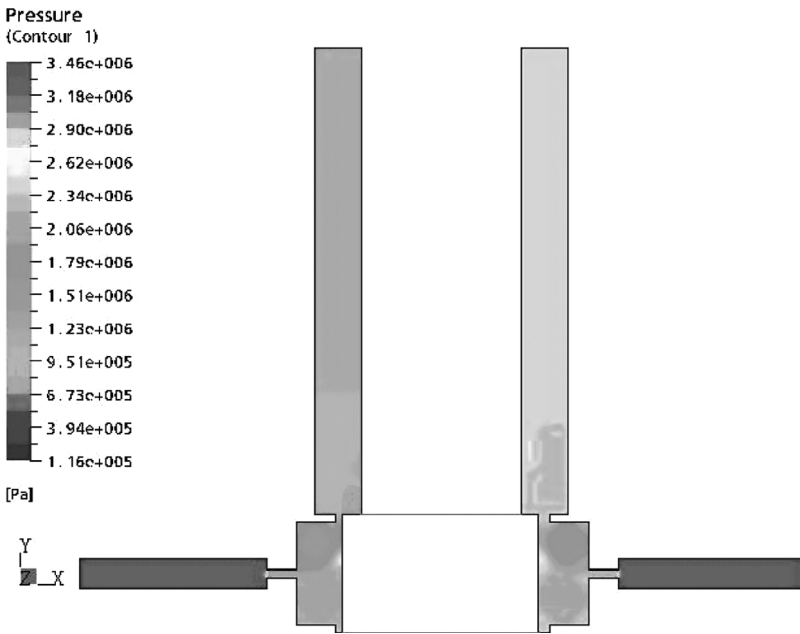


Figure 7(b) Pressure plot ($x_{v1} = 0.14\text{ cm}$; $x_{v2} = 0.26\text{ cm}$)

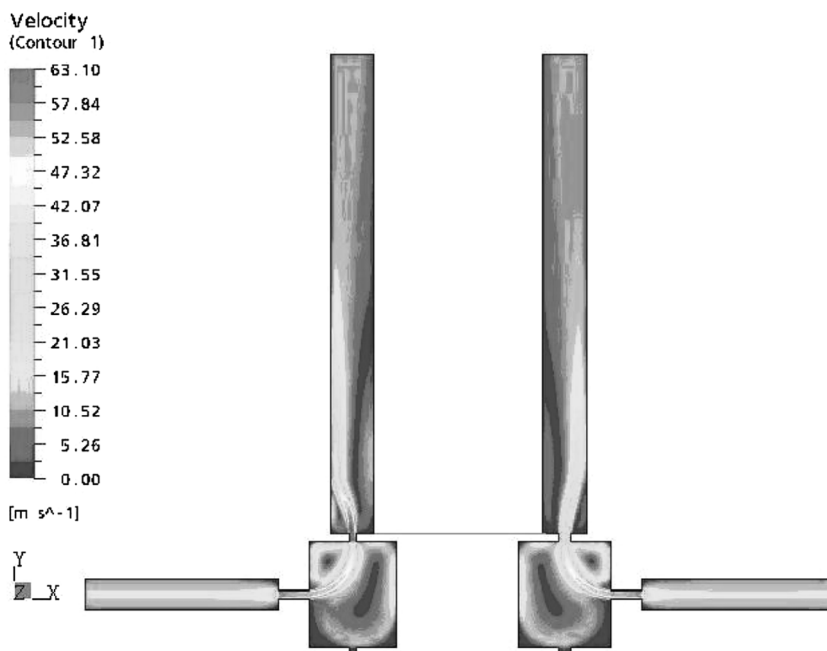


Figure 8(a) Velocity plot ($x_{v1} = 0.19$ cm; $x_{v2} = 0.21$ cm)

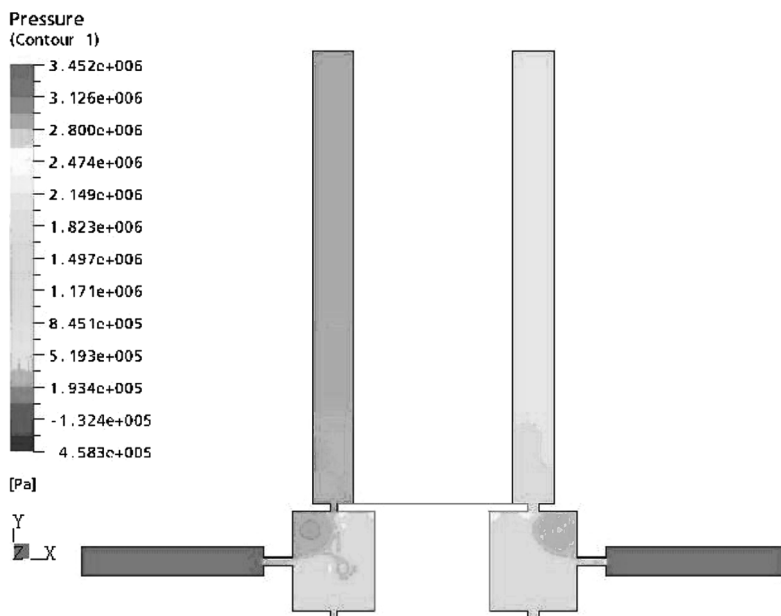


Figure 8(b) Pressure plot ($x_{v1} = 0.19$ cm; $x_{v2} = 0.21$ cm)

7. DISCUSSION AND CONCLUSIONS

The object of this paper was to present the results of a CFD study on flow reaction forces on a conventional and rimmed spool valve. The same CFD approach was then applied to the flow divider valve configuration of Chan et. al. and the same trends were observed. In all cases, the rim resulted in the jet efflux angle increasing as the reaction forces decreased. It is clear that the rim does indeed, reduce the reaction forces both for the conventional spool configuration of Figure 1 and the special flow divider spool arrangement of Figure A1 and is consistent with the results of Chan.. However, the percentage reduction in the conventional valve shown in Figure 1 was in the order of 30% whilst the reduction for Chan's valve was in the order of 80%. This is a bit deceiving because the flow reaction forces in Chan's device were based on the difference between two ports and hence the reduction reflects the total reduction of the difference.

It was concluded that that the rim proposed by Chan did result in a reduction of the flow reaction forces and that the presence of a rim in any valve, standard or otherwise, can be a simple and effective way to reduce flow reaction forces. It should be noted that this study has been extended to a new configuration in which the flow reaction forces are further reduced for a single land to approximately 70% of the conventional land. This configuration is now being considered for a patent and hence details cannot be presented here. It is however, important to note that the CFD approach can be extremely useful as a simulation and design tool for hydraulic systems.

REFERENCES

- (1) Merritt, H. E. *Hydraulic Control Systems*. John Wiley and Sons, New York, 1967.
- (2) Borghi M., Milani M., and Paoluzzi, R., 2002. Stationary Axial Flow Forces Analysis on Compensated Spool Valves. *International Journal of Fluid Power*, Vol. 1, No.1, pp. 13-22
- (3) Bao, M. Fu, X., and Chen, Y., 2001. Computational Fluid Dynamic Approach to Pressure Loss Analysis of Hydraulic Spool Valve. *Proceedings of the 5th International Conference on Fluid Power, Transmission and Control*, Hangzhou, China.
- (4) Jyh-Chyang Renn and Tien-Chis Kao., 2003. Application of CFD to Designing a Power-Saving Hydraulic Directional Two-Land-Four-Way Valve, *Proceedings of the First International Conference on Computational Methods in Fluid Power Technology*, Monash, Australia, Paper No. 08.
- (5) Finke, M., and Becher, D., 2004. Product Design and Testing at Moog: Turning High Performance into Reality. www.moog.com
- (6) Chan R, Schoenau G, and Burton R., 1981. A Simple Design Modification for Improved Accuracy of Piston Type Flow Divider Valves. *Proceedings of the 35th Conference on Fluid Power*, October, Chicago.
- (7) Burton R.T., Chan R.K. and. Schoenau, G.J, 1979. Mathematical Model for Predicting

the Steady State Flow Dividing Error of a Piston-Type Flow-Divider Valve. *Proceedings of the 35th National Conference on Fluid Power*, November, Chicago, Illinois.

(8) Burton, R.T. Schoenau, G.J. and Chan, R.J., 1980. A Single Stage Precision Flow Divider Valve. *Proceedings of the 36th National Conference on Fluid Power*, October, Cleveland, Ohio, pp 61-65.

(9) Wang, L., Shao, X., Ruan, X., Song, X., Yamamoto, F. 1997 PIV Measurement of Flow Field in Spool Valve Chamber, *Proceedings of the 4th International Conference on Fluid Power Transmission and Control (ICFP)*, p 42-45.

(10) Gao, D., 2004, Investigation of Flow Structure inside Spool Valve with FEM and PIV Methods, *International Journal of Fluid Power*, Vol. 5, No 1, pp 51-66

(11) Linda, T. and Glen, W. 2002. Application of Computational Fluid Dynamics (CFD) Anlysis in improving Valve Design, Transactions of the SAE, International Off-Highway & Powerplant Congress, March 2002, Las Vegas, NV, USA, Paper Series. 2002-01-1397,

(12) Vescovo, G. and Lipolis, A., 2003(a). CFD Analysis of Flow Forces on Spool Valves, *Proceedings of the First International Conference on Computational Methods in Fluid Power Technology*, Paper no 29 Nov., Monash, Australia.

(13) Vescovo, G. and Lipolis, A., 2003(b). Three – Dimensional Analysis of Flow Forces on Directional Control Valves. *International Journal of Fluid Power*, Vol 4, No 2, July 2003.

(14) Yuan, Q., and Li., P., 2002(a). An experimental Study on the use of Unstable Electrohydraulic Valves for Control, *Proceedings of the American Control Conference Anchorage, Alaska*. Vol. 6, pp 4843-4848

(15) Yuan, Q., and Li., P., 2002(b). Modelling and Experimental Study of Flow Forces for Unstable Valve Design, *America Society of Mechanical Engineering, Fluid Systems Technology Division Publication FPST*. Vol 10. pp 29-38

(16) Menter F. R., 1994. Two – equation eddy – viscosity turbulence models for engineering applications. *AIAA – Journal*, 32(8), pp.269-289.

(17) AEA Technology, 2001. CFX – 5 Documentation.

(18) Matlab/Simulink. Matlab Help. The Mathworks, Natick, MA. 2002.

(19) Okungbowa, N., 2005. CFD Analysis of Flow Forces in a Rimmed Spool Valve, *M.Sc. thesis*, University of Saskatchewan.

ACKNOWLEDGMENTS

The authors would like to acknowledge the financial support from the National Science and Engineering Research Council (NSERC) of Canada during this project.

APPENDIX 1

Using the flow dividing system illustrated in Figure A.1, the describing equations are given as:

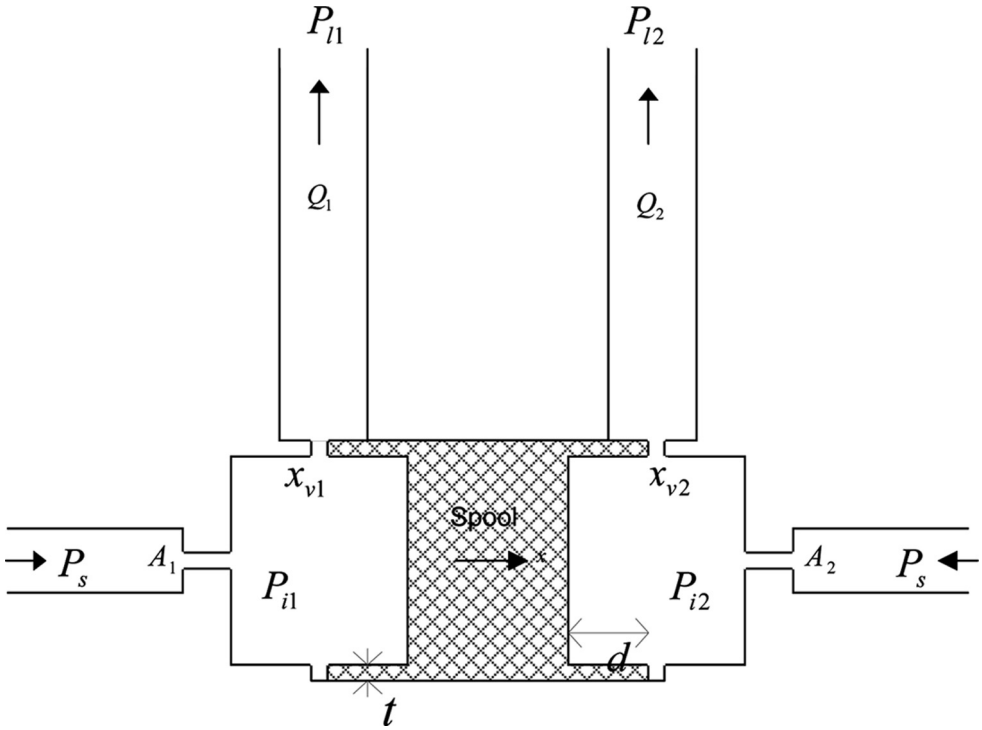


Figure A.1: Schematic of a Flow Divider Valve with the rim (Chan et al)

The following equations describe the operation of a flow divider valve. These equations were implemented on Matlab/Simulink® (18). Details of this material can be found in Okungbowa (19).

$$P_{i1}A_{p1} + F_{f1} - P_{i2}A_{p2} - F_{f2} = m\ddot{x} + B\dot{x} + F_f \tag{A.1}$$

$$F_{f1} = 2C_d A_{v1} (P_{i1} - P_{l1}) \cos \theta_1 \tag{A.2}$$

$$F_{f2} = 2C_d A_{v2} (P_{i2} - P_{l2}) \cos \theta_2 \tag{A.3}$$

$$A_{v1} = x_{v1}w \quad ; \quad A_{v2} = x_{v2}w \tag{A.4}$$

$$x_{v1} = x + 0.002 \quad ; \quad x_{v2} = 0.002 - x \quad ; \quad x_{v1} + x_{v2} = 0.004 \quad (\text{A.5})$$

$$Q_1 = A_1 K_1 \sqrt{(P_s - P_{i1})} \quad (\text{A.6})$$

$$Q_1 = A_{v1} K_1 \sqrt{(P_{i1} - P_{L1})} \quad (\text{A.7})$$

$$Q_2 = A_2 K_2 \sqrt{(P_s - P_{i2})} \quad (\text{A.8})$$

$$Q_2 = A_{v2} K_2 \sqrt{(P_{i2} - P_{L2})} \quad (\text{A.9})$$

$$K_1 = K_2 = C_d \sqrt{\frac{2}{\rho}} \quad (\text{A.10})$$

$$F_e = \frac{Q_1 - Q_2}{Q_1 + Q_2} \times 100\% \quad (\text{A.11})$$

Design of valve solenoids using the method of finite elements

Author: **Albert Schultz**

Institute for Fluid Power Drives and Controls, RWTH Aachen, FRG

ABSTRACT

The Method of Finite Elements (FE) is used in the design of valve solenoids to simulate the stationary as well as the transient magnetic field behaviour and predict the static and dynamic properties of the actuator. The intended paper shows how to apply FE simulation properly in the cases of non-rotational geometries, proportional solenoids and high excitations with possible eddy currents.

Many switching valves in pneumatics are driven by low-cost solenoids with a non-rotational bracket instead of a cylindrical housing. A bracket solenoid is modelled with both 3D- and 2D-software and the simulation results are compared in precision and effort.

Proportional solenoids mostly show rotational design and hence can be simulated with 2D tools. The challenge lies in the FE modelling of their cone and airgap, responsible for the linear force characteristics. Former observations have shown that the perfect match of simulation results with measurements is difficult [1]. Manual rectangular meshing in the solenoid's airgap is crucial. A detailed FE-analysis of the electromagnetic field in the airgap brings better understanding of the regional flux densities and the resulting solenoid forces.

Transient FEM allows to determine the dynamic behaviour of solenoids. Eddy currents play an important role in case of high excitations. The influencing parameters (specific electric resistance and magnetic permeability) are considered in transient simulation and their impact on the solenoid dynamics is visualised.

NOMENCLATURE

Latin Symbols

A	Surface
B	Magnetic flux density
F	Force
H	Magnetic field strength
I	Current
J	Current density
M	Material magnetization
N	Turns of the coil
p	Maxwell's surface tension
P	Vector potential
R	Resistance

U	Voltage
V	Volume
x	Armature position

Greek Symbols

$\mu_0 = 4\pi E-7Vs A^{-1}m^{-1}$	Magnetic field constant
μ_r	Relative magnetic permeability
θ	Ampère-turns
ρ	Specific electric resistance

Subscripts

ind	induced
-------	---------

1. INTRODUCTION

In former publications, the general possibilities of stationary as well as transient simulation to predict the static and dynamic solenoid behaviour for valve operation have been shown [1]. There are limitations though, that demand deeper insight into the application of the method of finite elements.

After a brief summary about correct FE modelling of solenoid geometries, a detailed look into three special cases is given.

2. FE MODELLING OF SOLENOIDS

The solenoid geometry is imported through a CAD interface. The meshing has to be done manually in critical areas like air gaps and cones in order to obtain homogeneous elements. The meshing between static (core) and moving part (armature) must adapt itself to the movement without losing its homogeneity.

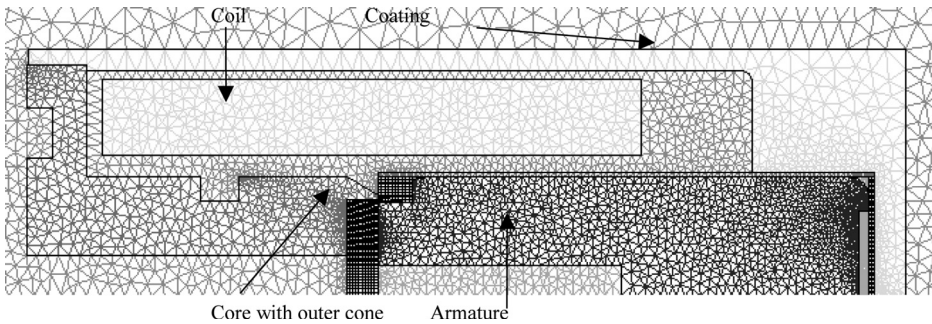


Figure 1: Proportional solenoid meshed with finite elements

Former observations have shown that rectangular meshing inside the air gap between armature and core is crucial for best force calculation [1], [2]. This is due to the higher potential approximation on rectangles [3].

$$P_x = P_y = 0 \quad \text{2D} \quad (1)$$

$$P_z \sim p_0 + p_1x + p_2y + p_3xy \quad \text{rectangles} \quad (2)$$

$$P_z \sim p_0 + p_1x + p_2y \quad \text{triangles} \quad (3)$$

$$\vec{B} = \text{rot} \vec{P} = \left(\frac{\partial P_z}{\partial y}; -\frac{\partial P_z}{\partial x}; 0 \right) \quad (4)$$

$$B \sim (p_2 + p_3x; -p_1 - p_3y; 0) \quad \text{rectangles} \quad (5)$$

$$B \sim (p_2; -p_1; 0) \quad \text{triangles} \quad (6)$$

The linear approximation of the magnetic flux density B on rectangles (Eq.5) corresponds better to reality than constant values on triangles (Eq.6). This positively affects the precision in force calculation (Eq.7).

$$F = \frac{B^2}{2\mu_0} A = \frac{\mu_0 H^2 \mu_r^2}{2} A \tag{7}$$

Once the meshing of the geometry is finished, material properties of the specific soft iron used have to be assigned in the form of B/H curves. They represent the correlation between the magnetic flux density B and the magnetic field strength H . Soft iron, commonly used for solenoids, typically shows a small magnetic hysteresis and therefore low energy losses when the magnetisation is changed (**Figure 2a**) [4].

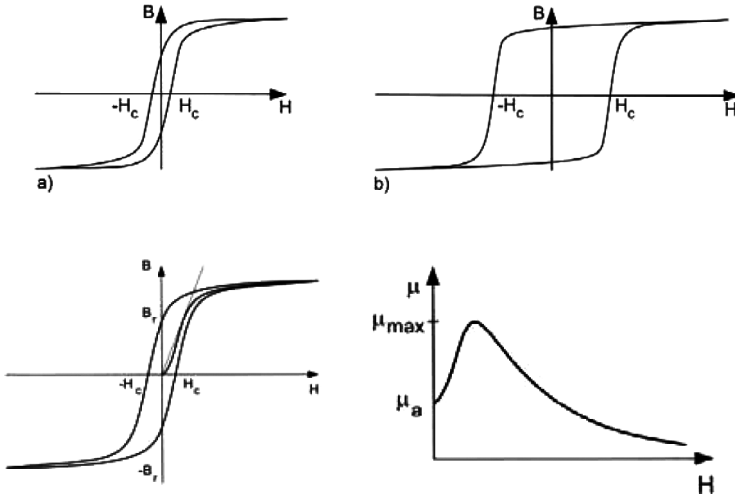


Figure 2: Hysteresis of magnetically soft (a) and hard (b) material, virgin curve (c) and permeability (d)

With the first magnetisation of the virgin material, the flux density B rises proportionally to H from the origin (**Figure 2c**). The relative magnetic permeability μ_r describes the slope of the curve (μ_0 : magnetic field constant) (Eq.8), [4].

$$\vec{B} = \mu_0 \mu_r \vec{H} = \mu_0 \vec{H} + \vec{M} \tag{8}$$

As can be seen in **Figure 2d**, the relative permeability first increases to a maximum (typically 6000 to 10000), then the material reaches saturation. The increase of B with H is flattened and the permeability decreases again. The slope of μ_r is characteristic for the chosen material and can be influenced by thermal treatment (annealing). The magnetic field strength H depends on the ampère turns put into the coil, following Maxwell's first equation about magnetic penetration (Eq.9).

$$\oint_{\partial A} \vec{H} \circ d\vec{s} = N \cdot I = \theta \Leftrightarrow \text{rot} \vec{H} = \vec{J} \tag{9}$$

If the ampère turns are reduced, the flux density follows the upper branch of the hysteresis loop back to the remanence B_R at field strength equal to zero (**Figure 2c**). The material keeps a remaining magnetisation that only can be neutralised with the coercive field strength of opposite polarity $-H_C$. Simulation tools normally use the virgin curve of the material and hence don't consider magnetic hysteresis.

As the final step, the electric activation of the coil ($N \cdot U/R$, high excitation, sinusoidal), the physical parameters (Newton's equation of movement) as well as mathematical boundaries (Dirichlet's boundary condition) and the simulation parameters (range of armature stroke, time discretization) have to be defined. Calculation of a stationary force vs. stroke characteristic takes a few minutes, of a transient-dynamic shifting operation up to 45 minutes in 2D (PC Win2000 Pro, 512MB RAM, 2.4GHz).

3. NON-ROTATIONAL GEOMETRIES

Many on/off-valves in pneumatics are driven by solenoids in bracket design with a partly non-rotational geometry. They basically demand 3D modelling and simulation. A standard on/off solenoid from pneumatic applications was chosen to compare the possibilities of 2D and 3D.

The 3D model has to be created step by step. First the iron parts (armature, core and bracket) are meshed. Then the coil is added (**Figure 3**). The most challenging part is the meshing of the surrounding air, the primary air gap between armature and core and the secondary airgaps in the junctions to the bracket. Automated algorithms tend to mesh complex parts of the geometry with large numbers of elements disregarding their shape (hexahedrons best choice for potential approximations, analogous to 2D rectangles). This unnecessarily increases the simulation time and does not assure the best possible results. Thus all meshing is done better manually in order to enable a coherent mesh and limit the size of the model and calculation time.

The material properties, electric activation, boundaries and simulation parameters are assigned like in the 2D case. A professional user of the software needs about two days to create a suitable 3D model of the regarded solenoid. The calculation time of one armature position and a constant coil activation takes six to eight hours.

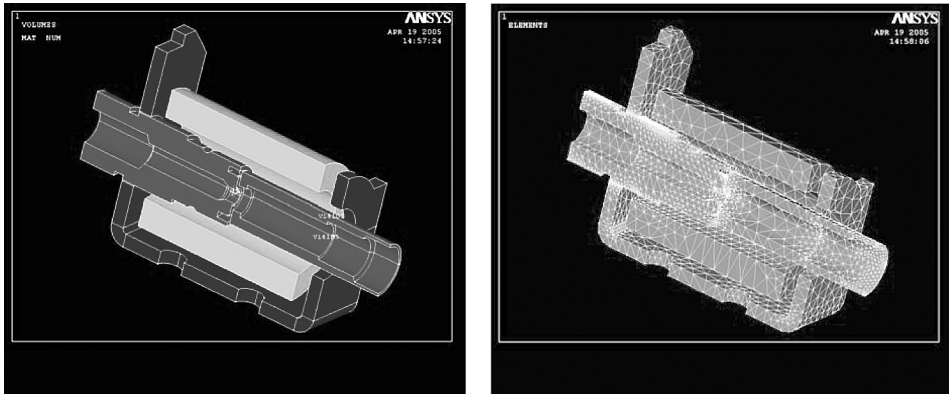


Figure 3: 3D model of a bracket solenoid

The static (core) and moving part (armature) of the solenoid are cylindrical, the bracket can be approximated as a cylinder with smaller profile. Ideal air gap meshing with rectangles easily is possible in 2D (**Figure 4** right), the calculation error in stationary force calculation remains below 10% (**Figure 6**).

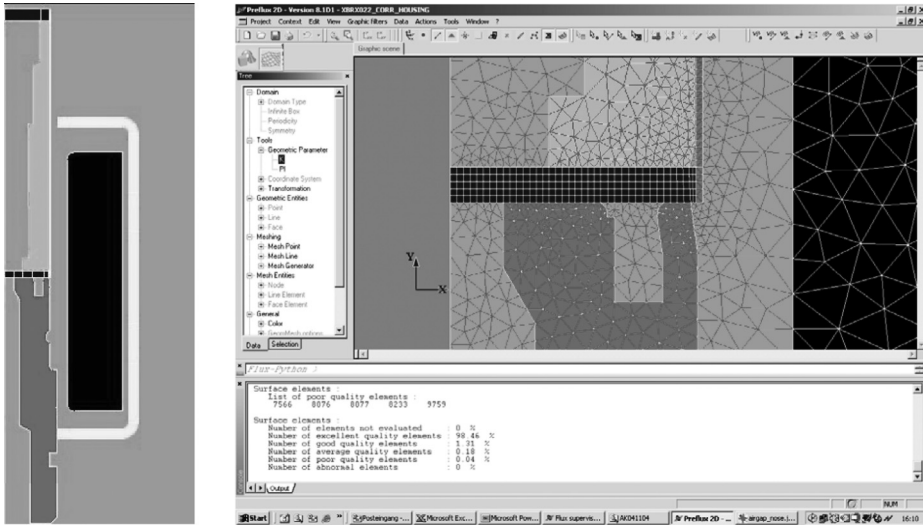


Figure 4: Approximated 2D model of the bracket solenoid

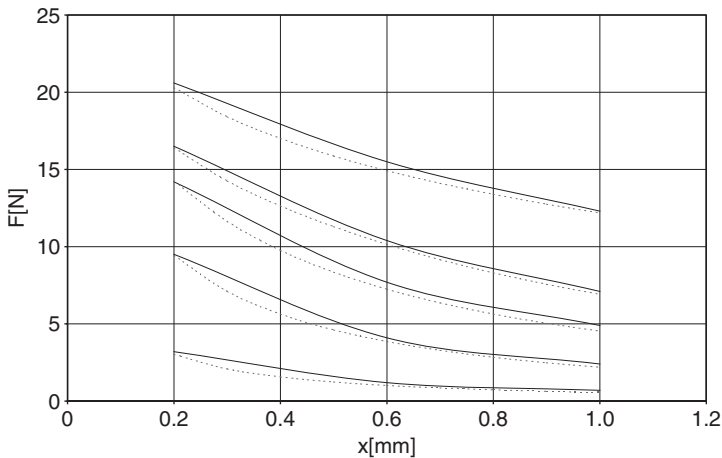


Figure 5: Measured (solid) and simulated (dotted) stationary force vs. stroke and current

The dynamic behaviour of the solenoid can also be determined precisely in 2D simulation (**Figure 6**). Thus, a 2D simulation delivers comprehensive results after a total of two to three hours including modelling and parameter variation. 3D does not deliver better precision.

During operation the armature will be torn towards the bracket and leave the axially symmetric trace assumed in 2D. This effect only can be considered in 3D simulation. Another advantage of the third dimension is the visualisation of the spacial field propagation (Figure 7).

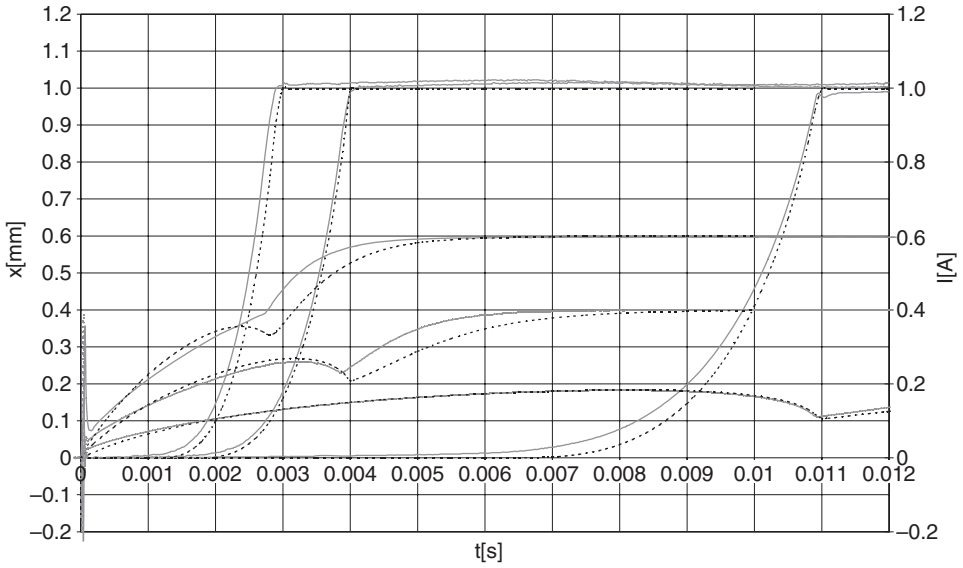


Figure 6: Measured (solid) and simulated (dotted) armature stroke and current vs. time

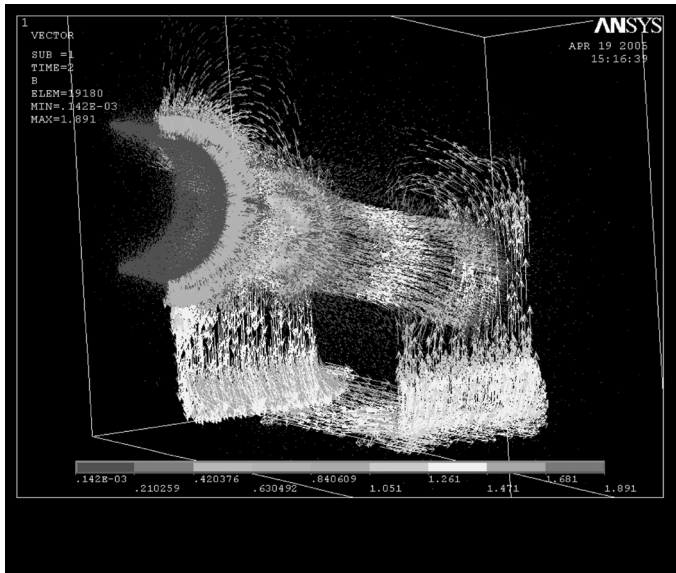
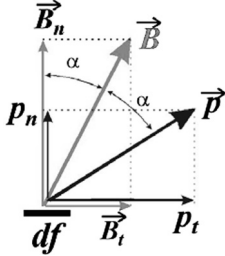


Figure 7: Vector graphic of 3D magnetic flux

4. PROPORTIONAL SOLENOIDS

The outer cone responsible for the proportional solenoid force and its resulting air gap are difficult to model with finite elements. The forces at the cone can be separated into an axial and a radial component, depending on the normal and tangential components of the magnetic flux density B . The magnetic force as described in Equation 7 can be analytically calculated on limited surfaces by integrating Maxwell's tension across the regarded surface (Eq.10) [5].



$$\vec{F} = \bar{p}d\vec{A} \tag{10}$$

$$p_n = \frac{1}{2\mu}(B_n^2 - B_t^2) \tag{11}$$

$$p_t = \frac{1}{\mu}B_nB_t \tag{12}$$

We now have to carefully distinguish between the normal tension component (Eq.11) and the tangential tension component (Eq.12) on both axial and radial iron surfaces for different air gaps.

In small air gaps, most flux lines (and hence flux densities) are normal to the surrounding surfaces (**Figure 8**). This results in normal components (Eq.11) of Maxwell's tension on axial (the measurable solenoid's force) and radial surfaces (force neutralised by radial symmetry). There are almost no tangential components (Eq.12) of tension and force due to the minimum of diagonal flux lines.

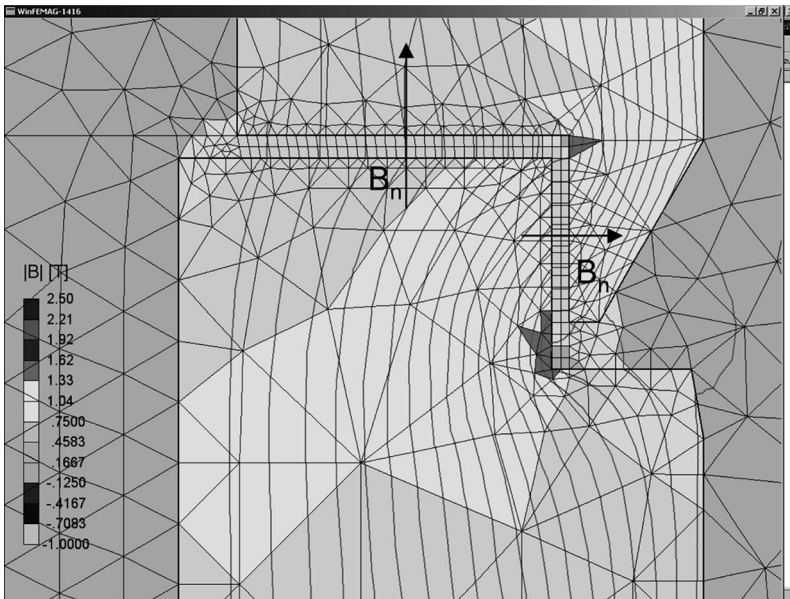


Figure 8: Flux lines and saturation at a proportional solenoid's cone with 0.2 mm air gap

In mid-sized air gaps, the number of diagonal flux lines (and hence B_t) in the radial air gap increases (**Figure 9**). The tension component normal (Eq.11) to the axial surfaces shrinks and is replaced by the increasing tension component tangential (Eq.12) to the radial surfaces. The components tangential to axial and normal to radial surfaces are again neutralised by radial symmetry.

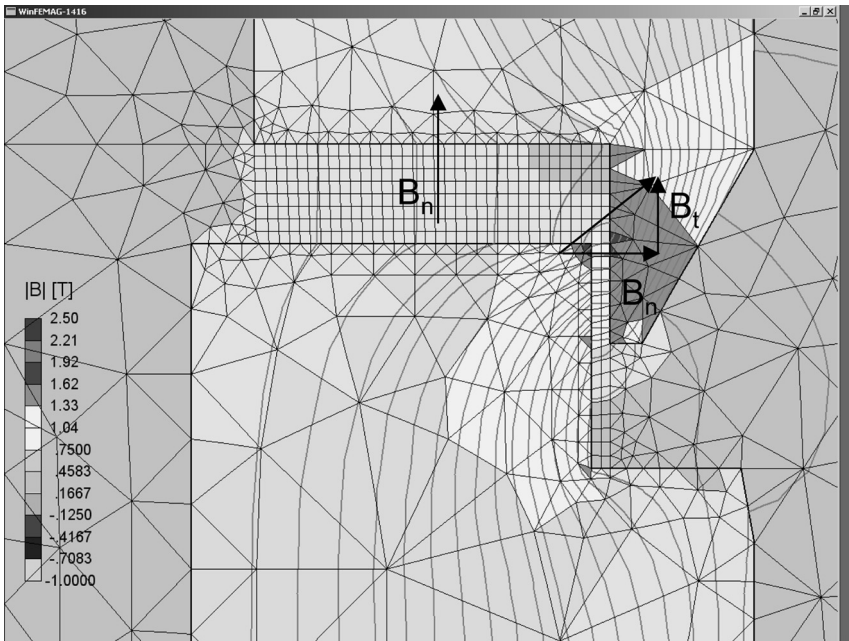


Figure 9: Flux lines and saturation at a proportional solenoid's cone with 0.9 mm air gap

In large air gaps (**Figure 10**), there are many flux lines with components tangential to radial surfaces and hence a strong tangential tension component (Eq.12). Together with the remaining component normal (Eq.11) to the axial surfaces, it assures a quasi constant solenoid force as long as the armature is overlapped by the cone's nose.

Certain FE tools allow the definition of local and open integration paths for the force calculation. The solenoid force resulting from axial and radial surfaces at the cone can be split up and quantified (**Figure 11**).

As shown before, only the normal tension component p_n on axial surfaces and the tangential component p_t on radial surfaces contribute to the effective solenoid force. With increasing air gap, the normal component of the flux density B_n on axial surfaces shrinks and so does the normal surface tension p_n (Eq.11) as a consequence. The tangential component on radial surfaces p_t (Eq.12) rises with the tangential flux density B_t increasing faster than its normal component B_n decreases. The latter can be assumed because of the higher total density of flux lines along the cone in larger air gaps and their diagonal orientation.

So, for small air gaps the force mainly is generated in the axial air gap between armature pole face and the core. For large air gaps, the force mainly is generated in the radial air gap between the armature's periphery and the core's outer cone (*Figure 11*).

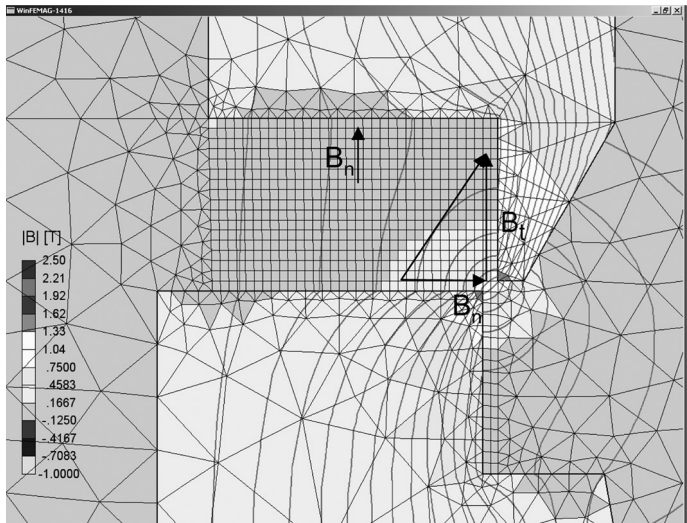


Figure 10: Flux lines and saturation at a proportional solenoid's cone with 1.6 mm air gap

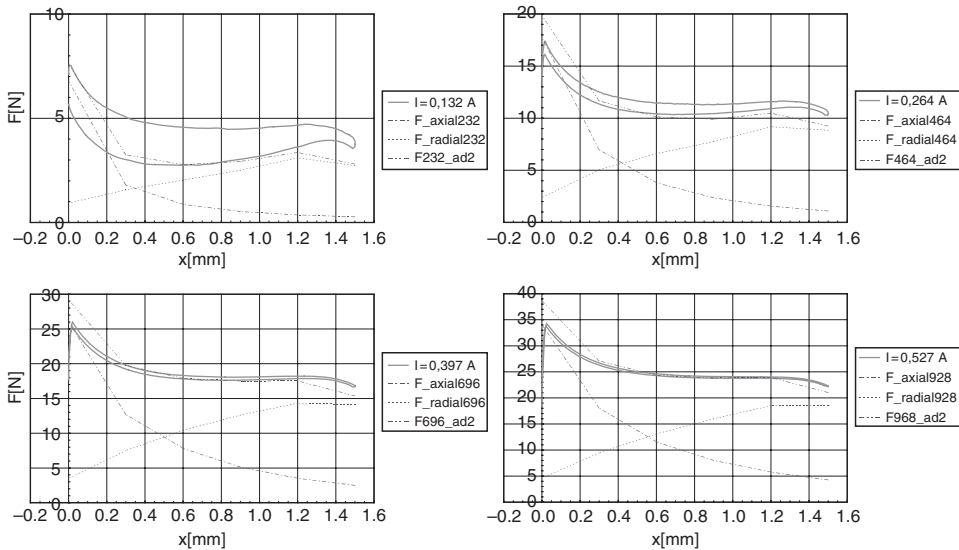


Figure 11: Simulated solenoid forces split up into axial and radial component

The magnetic material curves have a strong influence on the results of the simulation. Precision is low for the force calculation in small and large air gaps, the results generally are too high for high ampère-turns. This indicates too high flux densities assumed in simulation. A manual adaption of the material curve resulting in earlier

saturation (Figure 12 left) leads to a good match of the real force in the range of the working stroke (Figure 12 right).

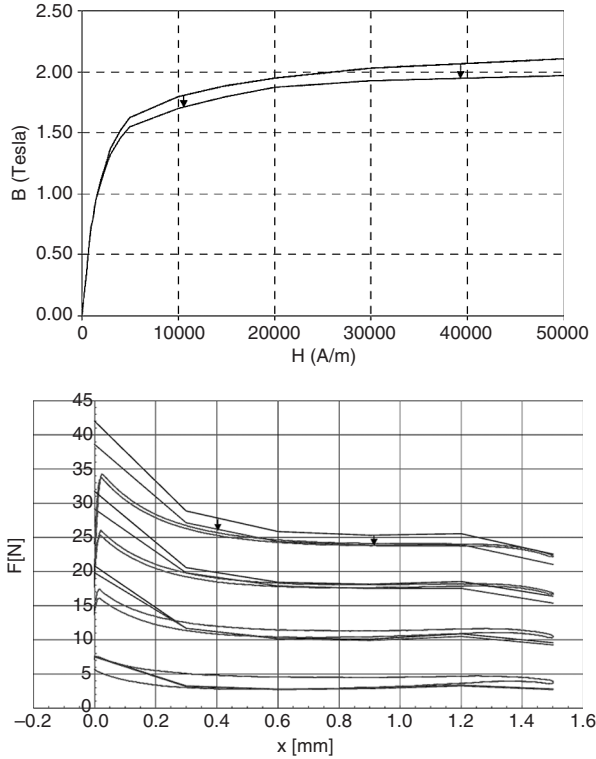


Figure 12: Magnetic curves and their impact on stationary force calculation

5. EDDY CURRENTS

The transient magnetic field induces a current into the electrically conducting iron armature (specific electric resistance $\rho_{\text{Copper}} = 1.7\text{E-}8 \text{ }\Omega\text{m}$, $\rho_{\text{Iron}} = 1\text{E-}7 \text{ }\Omega\text{m}$) during the shifting process of the solenoid. These so called eddy currents are swirling around the primary magnetic field and create a secondary magnetic field themselves that counteract the original field and its intrusion into the material following the rule of Lenz. The intrusion velocity depends on the specific electric resistance of the material and its magnetic permeability.

$$\frac{\partial^2 B}{\partial x^2} = \frac{\rho}{\mu} \frac{\partial B}{\partial t} \quad v^2 \sim \frac{\rho}{\mu} \tag{13}$$

With higher resistance lower eddy currents are induced with less counteraction against the original field, it then can intrude the material faster and vice versa.

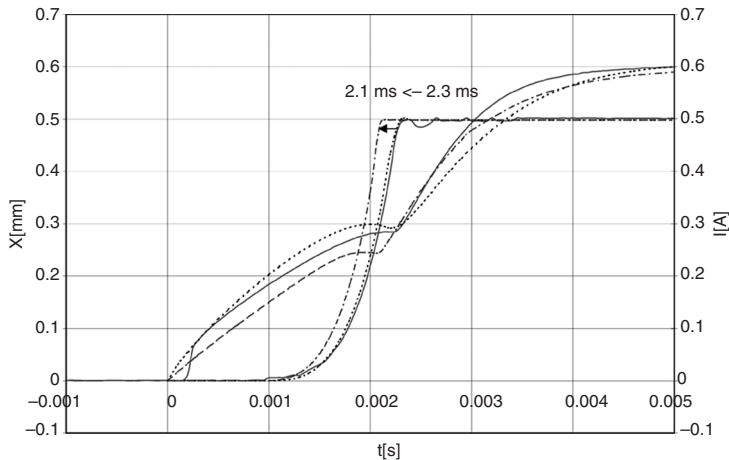


Figure 13: Dynamics of a bracket solenoid with and without eddy currents considered

Eddy currents play an important role in highly dynamic applications. A high specific resistance and low permeability speeds up the field intrusion, but the later also reduces the possible magnetic force (Eq.7). The specific electric resistance is considered as another material parameter in the FE model. It can be “switched off”, eddy currents then are not taken into account in transient simulation.

As an example, the bracket solenoid from chapter 3 (*Figure 3 to 7*) is regarded. In the case of over-excitation with 0.6A stationary in the coil, the measured shifting time of 2.4ms is well matched by simulation with eddy currents. When they are “switched off”, the calculated shifting time decreases to 2.1ms (12.5% error).

Thus FE simulation allows to visualize the influence of eddy currents on solenoid dynamics. The effect of geometric, material and other changes on eddy currents and solenoid dynamics can quickly be evaluated. This is comparable to the adaption of the solenoid parameters to optimize the stationary force characteristics.

6. CONCLUSION

The method of finite elements is a suitable tool to speed up the design process of valve solenoids.

The additional effort in modelling and calculation time of three-dimensional FE models can be avoided for on/off-solenoids in bracket design. Their stationary force characteristics as well as dynamic properties can be simulated in quick 2D models with an axially symmetric approximation of the bracket frame. 3D simulation does not deliver better precision but enables to show the influence of possible eccentric armature movement and to visualize spacial expansion of the magnetic field.

The force of proportional solenoids depends on the size of the air gap. For small strokes, the force mainly is generated in the axial air gap between armature and core pole faces. With increasing stroke, the tangential components of the magnetic flux inside the radial air gap contribute stronger to the force generation and mainly assure it at maximum strokes. FE

simulation can visualise the contribution of the different air gaps and geometric regions to the propagation and saturation of the electromagnetic field and hence the generation of the solenoid force. The impact of the magnetisation curves used is strong in case of proportional solenoids. The precise determination of magnetic material behaviour in machined solenoid parts is difficult. The interest of future works lies in the measurement methods of magnetic flux densities and their limitations.

The specific electric resistance of iron material has to be considered if the effect of eddy currents on the solenoid dynamics wants to be visualised in fast applications. Again material and geometric changes can be evaluated in simulation already.

REFERENCE LIST

- [1] Transient simulation of pneumatic valve solenoids with the method of finite elements, A.Schultz, 3rd FPNI-PhD Symposium on Fluid Power 2004, Terrassa/Spain
- [2] Integral equation formulations for the solution of magnetic field problems, S.Robertson, H.Karmaker, University of Toronto
- [3] Beitrag zur Lösung des Fehler-und Genauigkeitsproblems der Methode der finiten Elemente für elektromagnetische Felder, T.Tärnhuvud, Dissertaion ETH Zürich 1990
- [4] Elektromagnete: Grundlagen, Berechnung, Konstruktion, Anwendung, E.Kallenbach, L.Eick, P.Quendt, B.G.Teubner Stuttgart, 1994
- [5] Elektrische Maschinen und Antriebe – Numerische Verfahren für die Auslegung und Simulation, K.Reichert, VDE 2001

Virtual design of high dynamic pneumatic valves

M Fiedler, S Helduser, F Rüdiger

Institute of Fluid Power, Technische Universität Dresden, Germany

ABSTRACT

The paper deals with modelling and simulation of pneumatic servo valves. Main objective of the project is to obtain a methodology to design control valves without preceding experimental analysis at prototypes. A fundamental step to develop a virtual valve model is to define the required parameters only by analysing geometrical and material data. The simulation model consists of the mechanical subsystem, the pneumatic pilot and main stage as well as the solenoid. For validation the simulated subsystems will be compared to experimental results.

1 NOMENCLATURE

A	mm^2	cross section
b	-	critical pressure ratio
B	T	magnetic flux density
C	$\text{dm}^3/(\text{s} \cdot \text{bar})$	pneumatic conductance
H	A/m	magnetic field intensity
F	N	force
g	m/s^2	acceleration of gravity
I	A	current
m	kg	mass
p	bar	pressure
T	K	temperature
U	V	voltage
\dot{V}	m^3/s	flow rate
x	mm	position
Φ	Wb	magnetic flux
μ	-	permeability

2 INTRODUCTION

High performance applications in industrial pneumatic systems require high dynamic drives (e.g. testing machines). To control such drive systems high dynamic servo valves are essential to reach the required performance. The design of pneumatic valves is to a large extent still based on the experience of the involved staff as well as on a time- and cost-intensive development work that often produces a good solution only if iterations are performed.

The application of geometry based simulation models provides a lot of advantages that allow to reduce development time as well as the number of prototypes. Due to such an accurate simulation model the first prototype is changed from a physical to a virtual version. This simulation model allows first performance studies in conjunction with other systems (e.g. pneumatic cylinder) and optimizations of the complete system behaviour already in the development process. To get a very detailed simulation model the mechatronic system “servo pneumatic valve” is divided into subsystems like mechanics, pneumatics, electronics and electromechanical actuator. These different systems are simulated with the help of a multi domain simulator which allows to combine all subsystems in one integrated simulation model with lumped parameters [1–3]. The advantage of such a multi domain model is the calculation of interactions between the several subsystems. The parameterisation of the entire simulation model is only done by design data. Additional results of the Finite Element Method (FEM) and the Computational Fluid Dynamic (CFD) are used to get parameters for the solenoid model or to include special physical effects like transient flow forces [4].

The topic of this paper deals with the development of a new method for designing servo pneumatic valves with nominal flow rates up to 2000 l/min at 120 Hz cut-off frequency without preceding experimental tests. According to the presentation of the used pneumatic valve the classification in mechatronic subsystems will be shown and some of those subsystems are explained in detail. To validate the simulation results of the subsystems a test rig will be presented and in conclusion the results of the simulation and measurement will be compared.

3 PNEUMATIC SERVO-SOLENOID VALVE

The method for modelling a pneumatic valve will be developed on the specific valve of type FESTO MPES-3-1/8-10-010. In particular this is a proportional pressure control valve. **Fig. 1** shows the most important technical parameters.

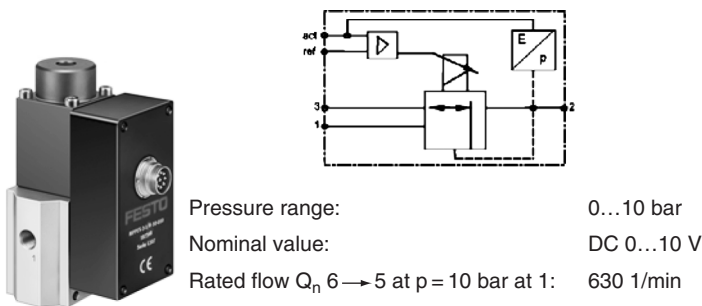


Fig. 1 Technical specifications of the MPES-3-1/8-10-010 pneumatic valve

The armature and the spool represent the moving parts of the mechanical system (see **Fig. 2**). Depending on the reference pressure value w_p the pressure at the working air connection (p_2) will be proportionally adjusted by the balance of power at armature and spool. There are two application areas one to aerate and another to bleed at connection 2.

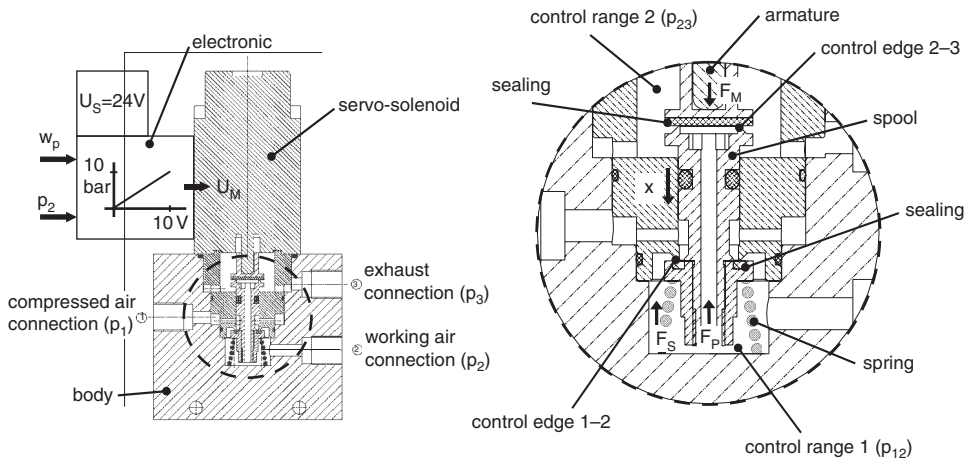


Fig. 2 Section of the MPPEs-3-1/8-10-010 pneumatic servo-solenoid valve

To aerate

To increase the pressure at connection 2 the pressure reference value had to be advanced and so the current at the solenoid changes. As a result of increasing the current at the solenoid the magnetic force F_M is higher than the sum of the pressure F_P and spring force F_S . The mechanical system is not in balance and the armature moves the spool down (positive x -direction). The control edge 1-2 opens and a flow rate adjusts from connection 1 to connection 2. The pressure at connection 2 increases. By reaching the reference value the pressure and the spring force are higher than the magnetic force. Therefore the spool and the armature are moving up and the control edge 1-2 closes.

To bleed

If the magnetic force drops down the pressure force, the armature will move up and the control edge 2-3 opens. The desired pressure at connection 2 adjusts with the help of the flow rate by connection 3.

4 MODELLING OF THE SERVO-SOLENOID VALVE

4.1 SUBSYSTEM OVERVIEW

The mechatronic system consists of the following subsystems: mechanics, pneumatic (valve, solenoid), magnetic, electric supply and control. The block diagram shown in **Fig. 3** describes the relationship between the subsystems by exchanging variables.

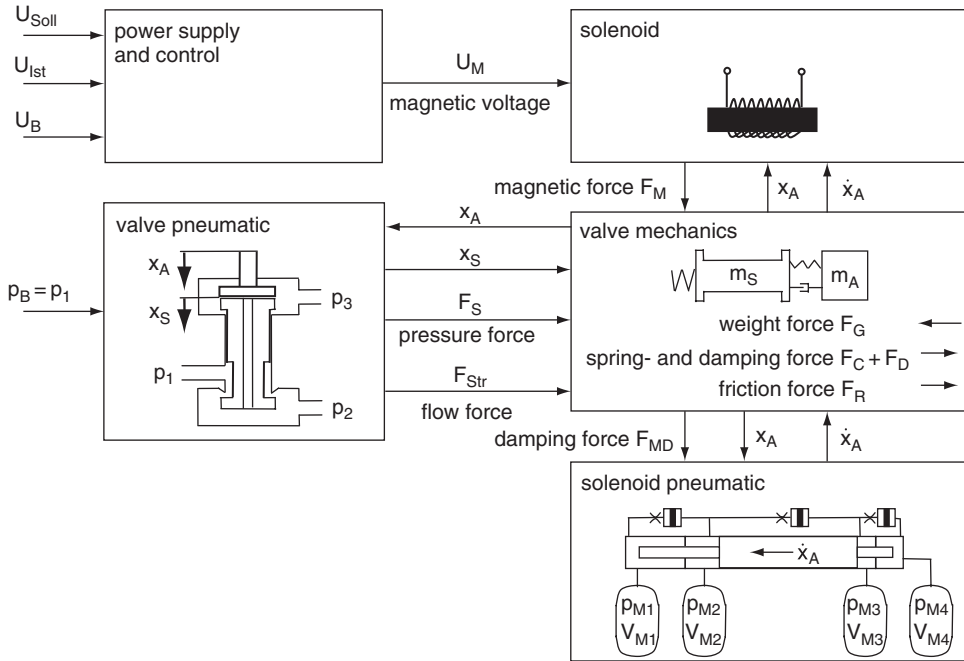


Fig. 3 Mechatronic System of the pneumatic servo-solenoid valve

The mechanical, the pneumatic and the solenoid subsystem will be more described below.

4.2 MECHANICAL SUBSYSTEM

The mechanical frequency response system consists of spring, damper (sealing, friction) and the masses armature and spool. The parameterisation is realised with technical graphs and material properties. **Fig. 4** demonstrates the simulated mechanical equilibrium.

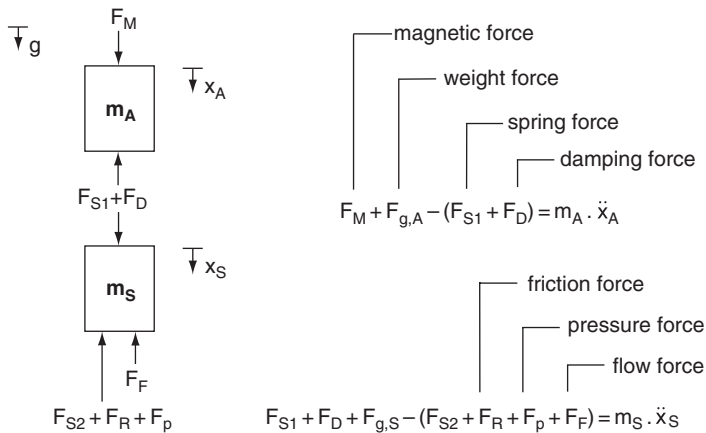


Fig. 4 Equilibrium of a two mass oscillating system (w/o end strokes contact force)

Because of the vertical oriented spool and armature the weight force F_g is included. For this first basic simulation the friction in the solenoid is regarded by an absolute attenuation.

By integrating the acceleration terms, the spool (x_s) and armature (x_A) motion can be calculated. At this point it is important to know the relative motion between these masses to describe the flow characteristic and the actual state (to increase or to decrease the pressure at connection 2) of the valve.

4.3 PNEUMATIC SUBSYSTEM

The pneumatic subsystem is simulated by one dimensional flow description. The valve geometry is described with throttles and volumes arranged in flow direction (see Fig. 5). Thereby the shape of the cross section (constriction or extension) determines the characterisation of the different throttles. The parameters volume V and pneumatic conductance C are extracted from engineering drawings, parameter variation with precedent appointing of target values or calculation. The critical pressure ratio b can be calculated by equations or estimated by empirical experience. The most important target values are the maximum cross section of control edge 1–2 (index h) and of control edge 2–3 (index l) which are directly related to the maximum flow rate in the corresponding flow direction.

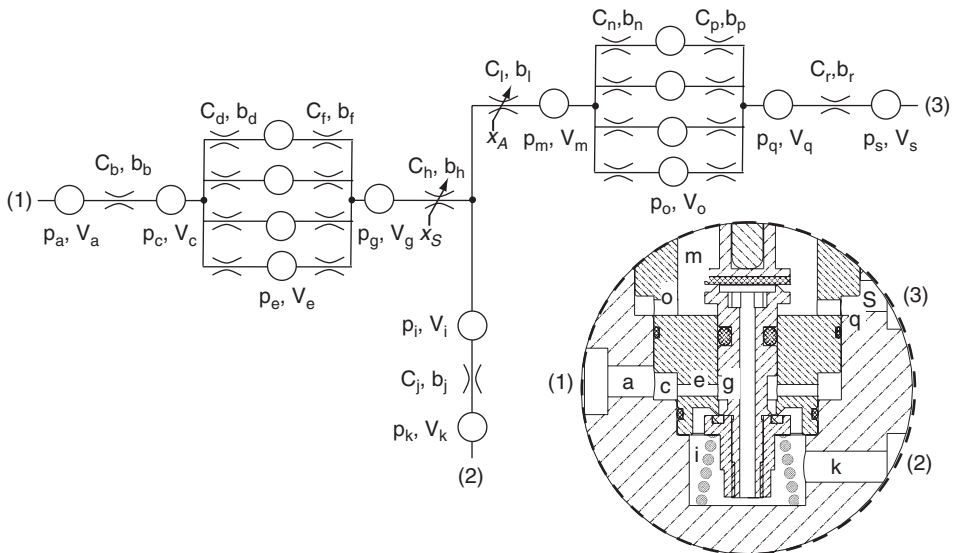


Fig. 5 Flow chart of the pneumatic model

The gateway to the mechanical system is the adjustment of the variable throttle that depends on the motion of the spool x_s or armature x_A . That means that the flow characteristic directly depends on the position of the masses.

4.4 MAGNETIC SUBSYSTEM

A mathematical description of the solenoid is realised with the help of a simplified solenoid model. There the magnetic force will be calculated depending on air gap, current and voltage.

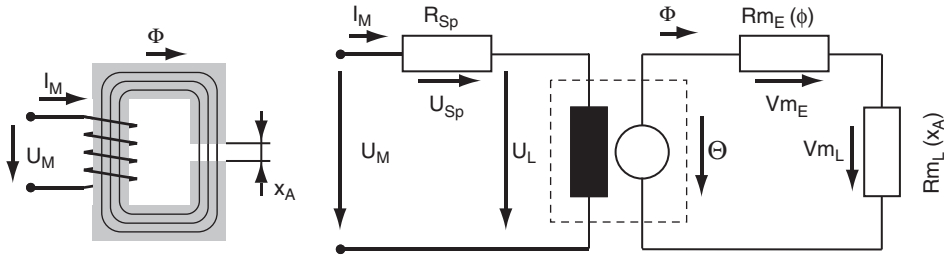


Fig. 6 Idealised solenoid model

Fig. 6 illustrates the substituted electric and magnetic system of the solenoid. The electric system consists of ohmic R_{Sp} and inductive resistance in series and the magnetic voltage U_M is separated at them (Kirchhoff's voltage law)

$$U_M = R_{Sp} \cdot J_M + U_L \tag{1}$$

The magnetic current I_M generates a magnetomotive force Θ which is the connection to the substituted magnetic system consisting of ferrous Rm_E and air gap resistance Rm_L .

$$\Theta = n \cdot J_M \tag{2}$$

The reaction from magnetic to electric circuit is calculated with the law of induction.

$$U_L = -\frac{d\Phi}{dt} \cdot n \tag{3}$$

In the magnetic circuit the sum of the magnetic voltage drops Vm at the magnetic resistances is identical to the magnetomotive force Θ

$$\Theta = Vm_E + Vm_L \tag{4}$$

To appoint the magnetic voltage drop the magnetic resistance Rm had to be calculated.

To reduce the size of the simulated model and to minimize calculating time the behaviour of the solenoid will be described within a reluctance model. That means that areas with constant magnetic flux are merged to a magnetic reluctance, the so-called “flux tube” (see **Fig. 7**). The flux tube describes the correlation between magnetic flux Φ and magnetic voltage Vm with constant cross sectional area A and length L .

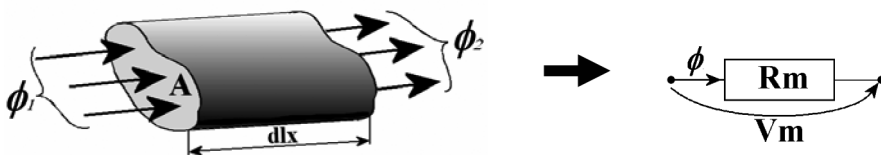


Fig. 7 Flux tube with constant cross section

Because of the continuity of the magnetic flux there are no flux losses and the magnetic resistance R_m of this flux tube is

$$R_m = \frac{V_m}{\Phi}. \quad (5)$$

The magnetic voltage V_m is the product of magnetic field intensity H and Length L of the flux tube.

$$V_m = H \cdot L \quad (6)$$

With equation 5, 6 and the magnetic flux density B

$$B = \mu \cdot H = \frac{\Phi}{A} \quad (7)$$

the magnetic resistance in the iron circuit is calculated to

$$R_{m_E} = \frac{L}{\mu_0 \cdot \mu_r \cdot A}. \quad (8)$$

Because of the constant relative permeability and the length which depends linearly on the distance between armature and core the magnetic resistance in the air gap can be calculated to

$$R_{m_L} = \frac{x_A}{\mu_0 \cdot A}. \quad (9)$$

The rapid changing of the relative permeability at the interface iron-air causes the magnet force in the solenoid. That is why the highest magnetic energy density W_m is in the air gap.

$$w_m = \frac{B \cdot H}{2} \quad (10)$$

The magnet force F_m in the ideal air gap can be calculated with the Maxwell formula

$$F_m = \frac{\Phi^2}{2 \cdot \mu_0 \cdot A}. \quad (11)$$

By using this equation two facts are to consider:

1. the relative permeability of iron is greater than the air ones
2. the field lines leave the iron perpendicular by low saturation

The simplified signal flow chart of the solenoid is shown in **Fig. 8**. The most important parameters for this model are:

- the characteristic of flux density and flux intensity
- the resistance and turns of the coil
- the flux cross section area and length

The difference ($U_S - U_R$) is equivalent to the alternation of the magnetic flux. With the help of this value the characteristic of the iron and the air gap can be specified and the magnetic force will be calculated.

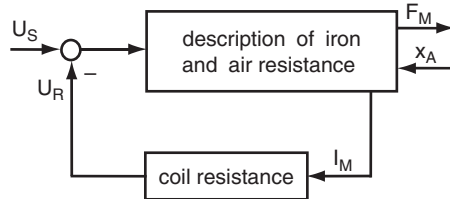


Fig. 8 Signal flow chart of the solenoid model

The appointment of the parameters crossing section area and length take place with engineering drawings and FEM-Simulation. An example for the allocation of the magnetic field lines is sketched in **Fig. 9**. This simulation was used to check the further found parameters.

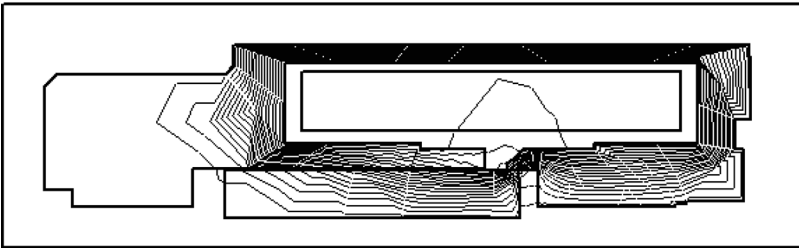


Fig. 9 Magnetic field lines at the solenoid

Special effects like eddy currents, transient magnetic effects (leakage flux) and hysteresis are neglected in this phase of modelling.

5 EXPERIMENTAL INVESTIGATION AND RESULTS

At the experimental investigation the signals shown in **Fig. 10** have been detected. The current I_M in the magnetic circuit is detected through a shunt resistor with resistance $R_S = 0,75 \Omega$ and the displacement of the spool (x_S) is detected by a laserinterferometric vibrometer. To minimize the impact of the flow the pressure in control range 1 would be measured with a subminiature pressure transducer. The data acquisition is realised with the National Instruments Software DasyLab.

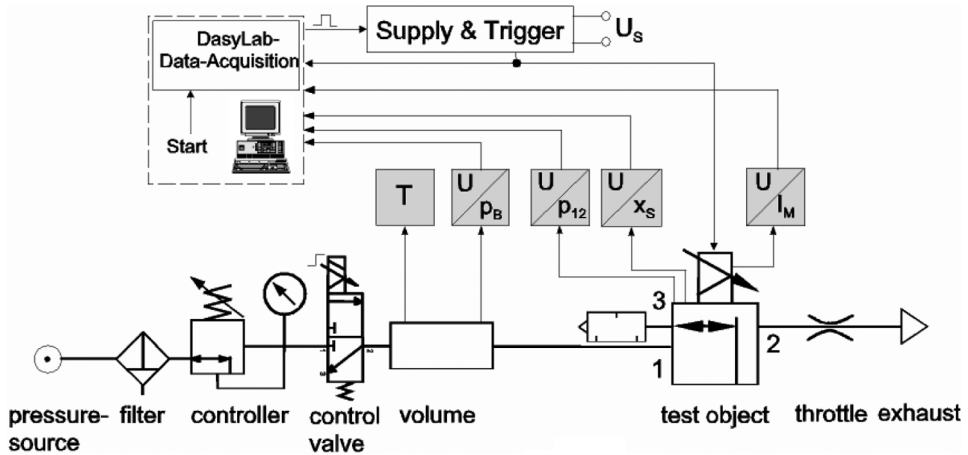


Fig. 10 Layout of the test rig

The results of measurement are compared with the results of the simulated subsystems mechanics and pneumatic. The operating conditions for this measurement are

Pressure at connection 1:	$p_1 = 8 \text{ bar}$
Pressure at connection 2 and 3:	$p_2 = p_3 = 1 \text{ bar}$
Operational voltage:	$U_S = 24 \text{ V.}$

The initial condition in the volume at connection 1 is constant on a pressure level of 8 bar. The control valve and the proportional pressure control valve (test object) are closed. After the direct activation of the solenoid at $t = 0,01 \text{ s}$ (bypass the valve electronic), the magnetic force increases and the armature and the spool move in positive x -direction till $x_s \approx 0,85 \text{ mm}$ (see Fig. 11).

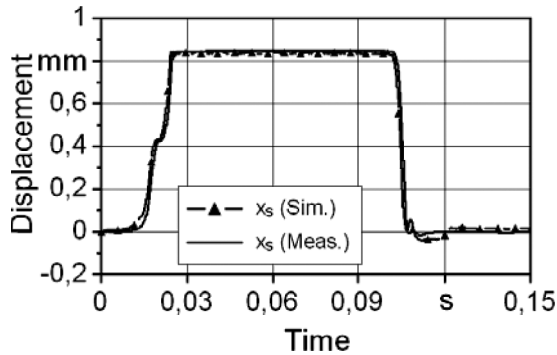


Fig. 11 Spool position (x_s)

A volume flow adjusts from connection 1 to connection 2. By the time the pressure in the volume (p_B) falls and the pressure in the valve (p_{12}) accumulates at $p_{12} \approx 7 \text{ bar}$ (see Fig. 12). At time $t = 0,1 \text{ s}$ the current at the solenoid will be turned off and the magnetic force drops down. The control edge 1–2 closes and the volume flow decreases. Furthermore the pressure in the valve falls and the total pressure in the volume arise in consequence of the decreasing dynamic pressure.

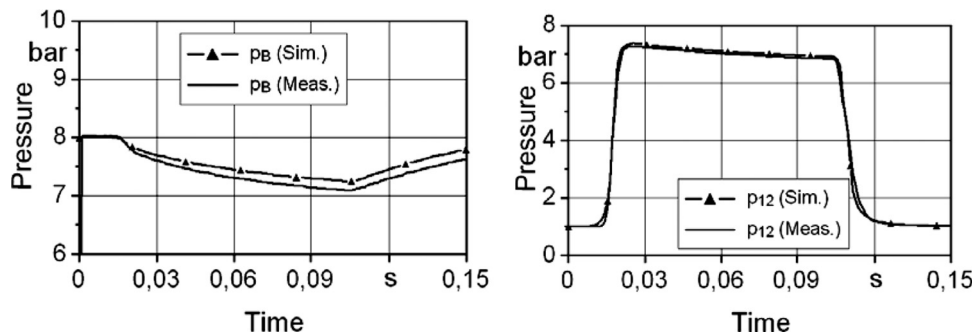


Fig. 12 a) pressure in volume (p_B) b) pressure in control range 1 (p_{12})

The comparison of the results shows a good compliance although small deviations are to register. The deviation in the spool position between measurement and simulation comes from the damping elements at control edge 1–2 respectively control edge 2–3 (see **Fig. 2**). The characterisation of the element sealing is actual incomplete in the simulation model.

The initial condition of the spool position in the simulation is not directly comparable with that in the measurement because of the deformation of the sealing. The boundary conditions in the pneumatic model differ from the real measuring conditions. Consequently the simulated pressure in the volume declines less than the measured pressure.

6 CONCLUSIONS

The first simulation results of the proposed procedure to simulate a mechatronic system with lumped parameters in a system simulator without preceding experimental analysis are promising. For good results it is essential to find accurate parameters for the separate simulation subsystems. These take place with geometrical and material data and additional with FEM simulation. So the mechanical and pneumatic subsystems are parameterised and the motion and flow behaviour of the servo pneumatic valve can be reproduced. To analyse the entire system behaviour the complete simulation model had to be built and validated in consideration of all subsystems (see **Fig.3**).

Eminently special effects like eddy currents, material hysteresis and transient magnetic effects in the proportional solenoid as well as transient flow effects in the pneumatic valve have to be considered in the model. To improve the motion behaviour a co-simulation with CFD would be used to assign the dynamic flow force. Also the influence of the resulting pressure force by changing the volume in the solenoid in succession of moving the armature had to be considered in the mechanic equilibrium.

REFERENCES

- /1/ Helduser S., Beyer O., Lausch H. Development and Optimization of Industrial Proportional Pressure-Relief Valves. Proc. 7th Scandinavian Int. Conf. On Fluid Power SICFP'01, Linköping, May 30 – June 1, 2001, pp. 191–203

- /2/ Figliolini G.,
Almondo A.,
Sorli M. Modelling and experimental validation of a pneumatic
servo-solenoid valve.
Power Transmission and Motion Control 2004, Bath,
September 1 – 3, 2004, pp. 85–98
- /3/ Beyer O.,
Kamusella A. Simulation und Optimierung schnellschaltender Magnete.
Simulation im Maschinenbau, Dresden, 2000
- /4/ Habr K. Gekoppelte Simulation hydraulischer Gesamtsysteme
unter Einbeziehung von CFD.
Dissertation, TU Darmstadt, 2002

Smart fluids

A Micro Artificial Muscle Actuator using Electro-conjugate Fluid

Kenjiro Takemura*, Shinichi Yokota* and Kazuya Edamura**

* Precision and Intelligence Laboratory, Tokyo Institute of Technology
4259-R2-41 Nagatsuta-cho, Midori-ku, Yokohama, 226-8503 Japan

** New Technology Management, Ltd.

2-9-1-306 Higashi-Shinkoiwa, Katsushika-ku, Tokyo, 124-0023 Japan

ABSTRACT

A *Soft Robot* inspired from natural systems is one of the main topics in robotic field. Accordingly, artificial muscles were widely investigated due to their potentials in soft robots. We propose here a novel micro artificial muscle actuator ($< 1 \text{ cm}^3$) utilizing the electro-conjugate fluid (ECF) generating powerful jet flow when subjected to a high voltage ($< 10 \text{ kV}$). The actuator mainly consists of a fiber-reinforced silicone rubber tube and a micro pressure source using ECF. The tube contracts along the actuator axis with increasing pressure by ECF jet. The experimental results confirm the effectiveness of the proposed actuation technology.

1. INTRODUCTION

As robots are becoming widely used in many fields, a soft robot inspired from natural systems becomes one of the main research topics in the field of robotics and mechatronics, especially in the application requiring closer and safer interactions between humans and machines. Hence, there have been reported many researches of soft structure, compliance control, and artificial muscles for robots. The authors think the muscle of natural systems which potentially has flexibility is worthy of note, and that to create a new type of artificial muscle actuator might be a great topic for robotics and mechatronics field. As artificial muscle actuators, for example, several types of actuators have been developed. The artificial muscle actuator which has the longest history is a pneumatic actuator such as McKibben type actuator. The constructions, numerical models, and applications of pneumatic actuators were widely studied (1)(2). It generates an extend-contract motion, however, there needs a bulky pressure source outside the actuator. Shape memory alloys are another example of artificial muscle (3)(4). They have great features as high power density, however, they suffer from slow response and heat problems. Polymer materials (5)(6) might be a recent research trend on artificial muscle actuator, however, they are still not suitable for robotic application because they must be used in particular environments. A most promising research of artificial muscle actuator in robotic field is electrically actuated

dielectric elastomer films (7). Although there reported several types of actuators as mentioned above, artificial muscle actuators are still being developed.

On the other hand, there is an interesting smart fluid or an electro-conjugate fluid (ECF) (8). The fluid generates a powerful jet flow when subjected to a high voltage (\sim kV). This kind of phenomenon is known as an EHD (electrohydrodynamics) effect (9). In our previous studies, the authors clarified the necessary condition for showing the effect, and the fluids meeting the condition are called ECFs. Although the mechanism of the effect has not been clarified yet, the ECFs are attractive for constructing new actuators. Hence, the authors applied the ECF effect on micro motors (10-12) and micro manipulators (13). According to our previous studies on the ECF, the jet flow becomes more powerful with smaller electrode pair, which means, the ECF effect is much suitable for micro actuation. Therefore, we propose a new type of micro artificial muscle actuator using the ECF in this study.

2. CONCEPT

Our previous studies proved the ECF effect is suitable for micro actuation (10-13). Because the powerful jet flow is generated by a tiny electrode pair, it is easy to construct a micro pressure source using the ECF. Therefore, a new type of micro artificial muscle actuator can be realized as shown in Fig. 1. As the inner pressure of a fiber-reinforced flexible tube increases by a jet flow, which is generated at the pressure source using ECF, the tube contracts along the actuator axis because the fiber cannot extend.

One of the main accomplishments of this research is the incorporation of the pump (pressure source) in the actuator. This results in a very compact actuation system and therefore, we can place the actuator in an array just like natural muscles. This kind of design solution cannot be realized by pneumatic artificial muscle actuators previously developed because they need bulky pressure sources outside the actuator.

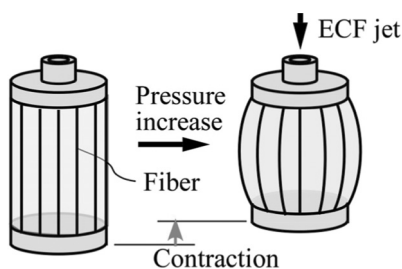


Figure 1 Concept of ECF micro artificial muscle

3. DESIGN AND MANUFACTURING

3.1 Fiber-reinforced silicone rubber tube

In the first step of our design procedure, we designed a fiber-reinforced flexible tube. In order to realize the micro artificial muscle actuator smaller than 1 cm^3 , we designed the fiber-reinforced flexible tube with 5 mm in diameter and with 10 mm in length. We used the silicone rubber and fiber listed on Table 1 to produce the fiber-reinforced silicone rubber tube. According to the number of fibers (4, 8 and 12 fibers) and the thickness of silicone rubber tube ($35 \mu\text{m}$ and $45 \mu\text{m}$), six types of tubes were produced. Fig. 2 shows the produced silicone rubber tube reinforced by 8 aramid fibers. The reference frame in the

Table 1 Materials used in this study

	Manufacturer	Product
Silicone rubber	Shin-etsu Chemical Co.,Ltd.	KE1316
Silicone solution	Shin-etsu Chemical Co.,Ltd.	CAT1316
Diluent	Shin-etsu Chemical Co.,Ltd.	RTV thinner
Reinforce fiber	Teijin Ltd.	Technora GNT220T

figure is common throughout the paper. Fig. 3 shows the relationship between the inner pressure and contraction of each tube measured using the hydro-column. Following conclusions were derived from Fig. 3 and observations during the experiments;

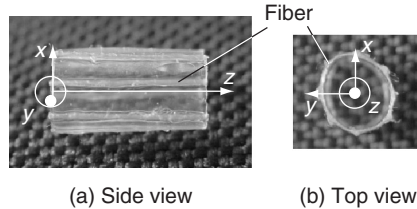


Figure 2 Silicone tube with 8 aramid fibers

(1) The displacement in the z -direction became smaller with fewer fibers in case of the tube with $35\ \mu\text{m}$ in thickness, because the silicone rubber tube extremely deformed like a bunch,

(2) The displacement in the z -direction also became smaller with too many fibers in case of the tube with $45\ \mu\text{m}$ in thickness, because the relative stiffness of silicone rubber between the fibers increased,

(3) There is an optimal relation of fiber number and tube thickness for micro artificial muscle actuators.

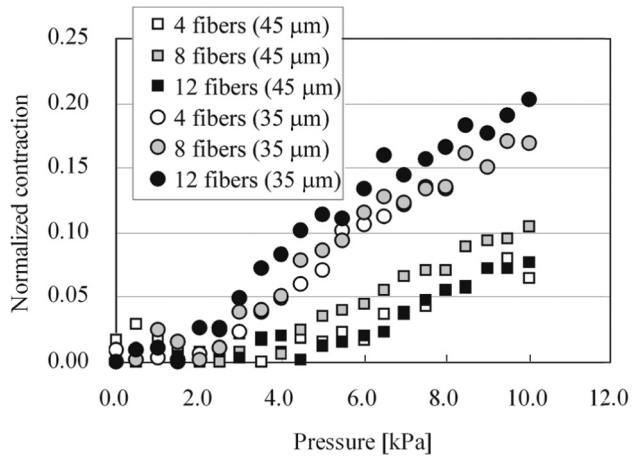


Figure 3 Contraction characteristics of fiber-reinforced tubes

As a result, the silicone rubber tube reinforced with 12 aramid fibers with thickness of $35\ \mu\text{m}$ was found to be the most suitable for the micro artificial muscle actuator among the tubes we produced. With inner pressure of 10 kPa, the silicone tube contracted around 20 % of its initial length. The relationship between the inner pressure and normal force generated was experimentally confirmed with the designed tube. Fig. 4 shows the experimental results. The fiber-reinforced silicone rubber tube linearly generated the normal force along the z -axis as the inner pressure increased. 0.17 N was obtained with the inner pressure of 8 kPa.

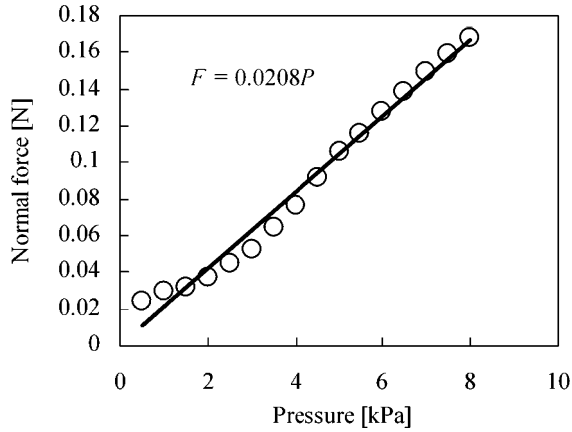


Figure 4 Experimental results for normal force of silicone tube with 12 fibers

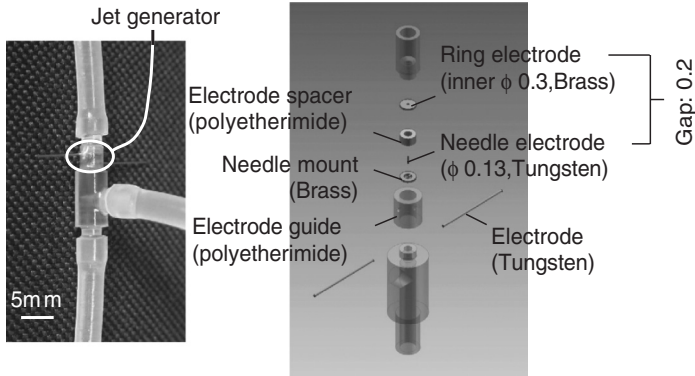


Figure 5 Micro pressure source (Jet generator)

3.2 Micro pressure source

In order to control the inner pressure of the designed tube, we designed and produced a micro pressure source using the ECF as shown in Fig. 5. The pressure source is basically composed of a pair of needle- and ring-type electrodes, and an electrode spacer. The needle-type electrode is made of tungsten. The mount for needle-type electrode and the ring-type electrode are of brass, and the spacer is of polyetherimide resin (engineering plastic). The diameter and length of needle-type electrode are 0.13 mm and 0.7 mm, respectively. The inner diameter and thickness of ring-type electrode are 0.3 mm and 0.2 mm, respectively. The electrode spacer keeps the gap between electrodes to be 0.2 mm. A powerful jet flow is generated from the needle- to the ring-type electrode with an applied voltage of several kV (“High” and “GND” are connected to the needle and the ring, respectively). For the fiber-reinforced silicone rubber tube is placed at the downstream of the jet flow, the inner pressure of tube can be increased. Using dibutyl decanedioate as ECF, about 10 kPa was obtained at applied voltage of 5 kV as shown in Fig. 6.

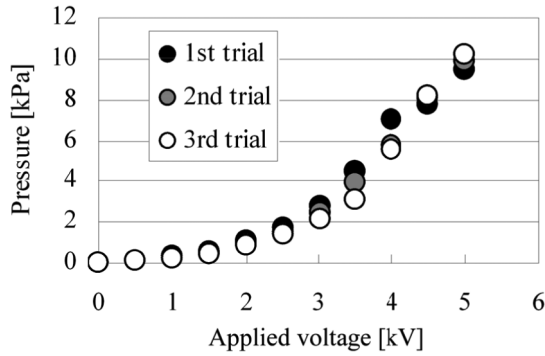


Figure 6 Generated pressure by jet generator

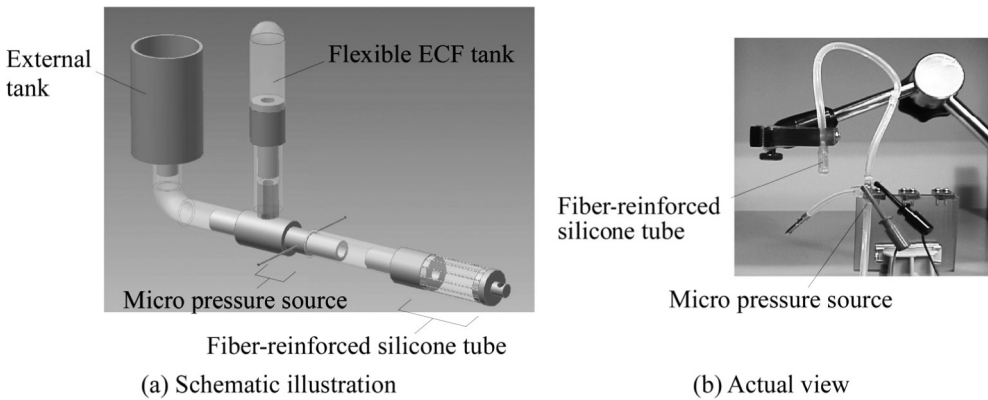


Figure 7 Prototype of micro artificial muscle actuator

3.3 Prototype

Here designs a prototype of novel micro artificial muscle actuator. Fig. 7 depicts the schematic illustration and actual view of the prototype. It mainly consists of the fiber-reinforced silicone rubber tube, the micro pressure source, and a flexible ECF tank. A bulky external ECF tank was connected to the micro pressure source so that we could easily regulate the pre-pressure of the tube. In case of practical use, the external ECF tank should be removed (the actuator only needs the flexible ECF tank for drive). We used dibutyl decanedioate as ECF.

4. EXPERIMENTS

4.1 Contraction characteristics

The contraction characteristics of the prototype were measured. Fig. 8 shows the experimental result of static contraction with input voltages up to 6 kV. The contraction rate showed a quadratic curve against the input voltage. The maximum contraction rate was

0.16 at the input voltage of 6 kV. From the maximum contraction rate, the inner pressure of the actuator is expected to be around 8 kPa (cf. Fig. 3).

Fig. 9 shows the experimental results of dynamic contraction when the step input of 5 kV was applied. No overshoot was observed and the rise time was around 7.9 s. The dead region of 2 s shown in Fig. 9 is caused by the following phenomenon: The initial shape of fiber-reinforced silicone rubber tube had a hyperbolic cross-section, which means, narrow in the middle, because of the surface tension. Consequently, the pressure increase at the early phase was used to deform the initial shape to be a straight column.

4.2 Force characteristics

The normal force generated by the prototype was measured. Fig. 10 shows the experimental result of static normal force. The static force measured here is that of so to say isometric contraction of natural muscle. The normal force showed a quadratic curve as the contraction rate did. This kind of characteristics is caused by the pressure characteristics shown in Fig. 6. The maximum normal force obtained was 0.18 N at the input voltage of 6 kV. The inner pressure of 9 kPa might generate the normal force of 0.18 N as shown in Fig. 4, although it is expected to be 8 kPa from the contraction characteristic. Due to

Fig. 6, the pressure generated by the micro pressure source fluctuates a bit in each trial. This may cause the difference of estimated inner pressures. The generative force of the actuator may seem to be small, however, note that the actuator with pressure source is extremely small. This means that higher actuation forces can easily be obtained by arranging several artificial muscle actuators in parallel.

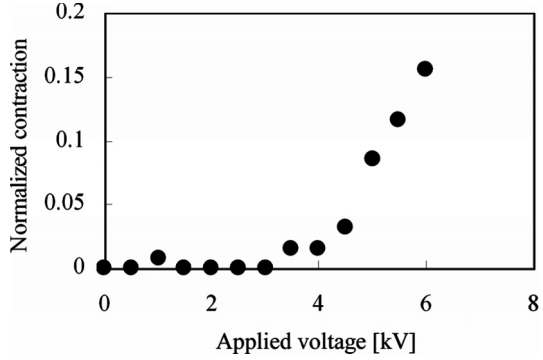


Figure 8 Static contraction

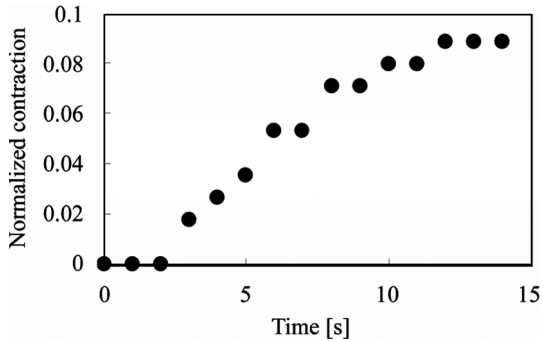


Figure 9 Step response of contraction

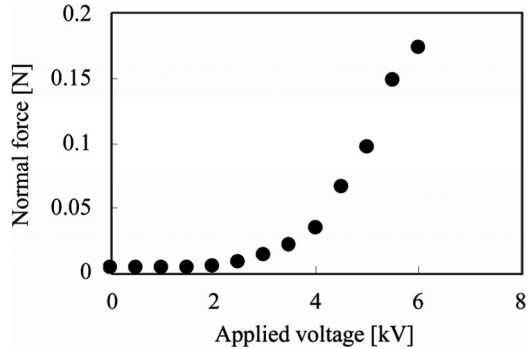


Figure 10 Static normal force

Fig. 11 shows the experimental result of dynamic normal force with the step input of 5 kV. No overshoot was observed and the rise time was around 7.5 s. The response of the micro artificial muscle actuator was not so high, however, it can be improved by placing several electrode pairs in series-parallel. Note that, the electrode pair required was extremely compact.

Finally, the normal force of so to say isotonic contraction of natural muscle was measured when the input voltage was 5 kV. Fig. 12 shows the experimental result. The relation between normal force and contraction rate showed non-linear characteristic as that of natural muscles do.

5. CONCLUSIONS

A new type of micro artificial muscle actuator using electro-conjugate fluid was developed in this study. The main contribution of this research is the incorporation of the pressure source in the actuator, utilizing the ECF. This enables us to construct a compact artificial muscle actuator, and then, it is easy to apply the actuator to autonomous systems or to micro systems. Furthermore, we can arrange the artificial muscle actuators in an array just as natural systems do.

Our future study focuses on controlling the micro artificial muscle actuator and compact the design solution for practical use. Also, we will be focusing on applications.

ACKNOWLEDGMENT

This study was supported in part by Grant-in-Aid for Exploratory Research #16656055, Grant-in-Aid for Scientific Research in Priority Areas #16078205 (“Next-Generation Actuators Leading Breakthroughs,” Term of Project:2004-2008) and Grant-in-Aid for Encouragement of Young Scientists (A) #17686013 of the Ministry of Education, Culture, Sports, Science and Technology of Japan.

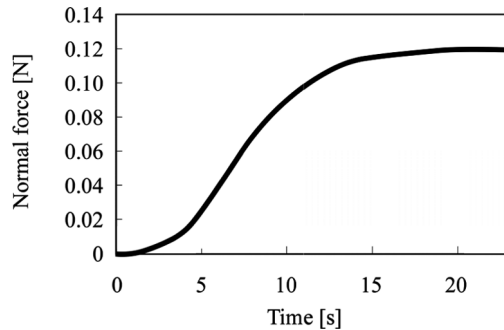


Figure 11 Step response of normal force

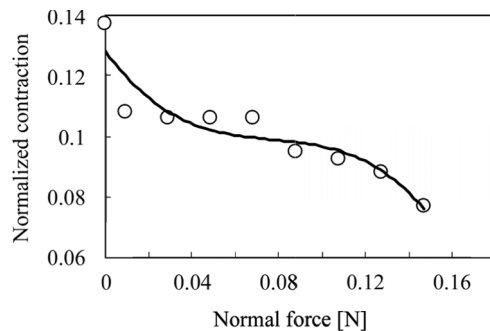


Figure 12 Isotonic normal force

REFERENCE

- (1) D. Sasaki, T. Noritsugu and M. Takaiwa, Development of Pneumatic Soft Robot Hand for Human Friendly Robot, *J. Robotics and Mechatronics*, Vol. 15, No. 3, pp. 164-171, 2003.
- (2) <http://www.shadow.org.uk/index.shtml>
- (3) H. Meier, L. Oelschlaeger, Numerical Thermomechanical Modelling of Shape Memory Alloy Wires, *Materials Science and Engineering A*, Vol. 378, pp. 484-489, 2004.
- (4) S. B. Choi, Y. M. Han, J. H. Kim, C. C. Cheong, Force Tracking Control of a Flexible Gripper Featuring Shape Memory Alloy Actuators, *Mechatronics*, Vol. 11, pp. 677-690, 2001.
- (5) <http://ndeaa.jpl.nasa.gov/nasa-nde/lommas/eap/WW-EAP-Newsletter.html>
- (6) Mihoko Otake, Yoshiharu Kagami, Yasuo Kuniyoshi, Masayuki Inaba, Hirochika Inoue, Inverse Kinematics of Gel Robots made of Electro-Active Polymer Gel, *Proc. 2002 IEEE Int. Conf. Robotics and Automation*, pp. 3224-3229, 2002.
- (7) Ron Pelrine, Roy Kornbluh, Qibing Pei, and Jose Joseph, High-Speed Electrically Actuated Elastomers with Strain Greater Than 100%, *Science*, Vol. 287, pp. 836-839, 2000.
- (8) Yasufumi Otsubo and Kazuya Edamura, Dielectric Fluid Motors, *Applied Physics Letters*, vol. 71, no. 3, pp. 318-320, 1997.
- (9) Seong-II Jeong, Jamal Seyed-Yagoobi, and Pierre Atten, Theoretical/Numerical Study of Electrohydrodynamic Pumping Through Conduction Phenomenon, *IEEE Trans. Industry Applications*, Vol. 39, No. 2, pp. 355-361, 2003.
- (10) Shinichi Yokota, Masakazu Hirata, Yutaka Kondoh, Koichi Suzumori, Atsushi Sadamoto, Yasufumi Otsubo, Kazuya Edamura, Micromotor Using Electroconjugate Fluid (Fabrication of Inner Diameter 2mm RE type ECF Motor), *J. Robotics and Mechatronics*, Vol. 13, No. 2, pp. 140-145, 2001.
- (11) Shinichi Yokota, Atsushi Sadamoto, Yutaka Kondoh, Yasufumi Otsubo, Kazuya Edamura, A Micro Motor Using Electro-conjugate Fluids (ECFs) (Proposition of Stator Electrode Type (SE-type) Micro ECF motors), *Int. J. JSME, Ser. C*, Vol. 44, No. 3, pp. 756-762, 2001.
- (12) Shinichi Yokota, A 2mm ECF micromotor, *Proc. 7th Int. Conf. Mechatronics Technology (ICMT'03)*, pp. 361-366, 2003.
- (13) Ryutaroh Abe and Shinichi Yokota, A Micro Actuator using ECF-Jet with Needle-type Electrode, *Proc. FLUCOME'03, CD-ROM*, 2003.

A Magneto-Rheological Valve-Integrated Cylinder and Its Application

Kazuhiro Yoshida^{*1}, Tsutomu Soga^{*2}, Shinichi Yokota^{*1}, Masashi Kawachi^{*3}
and Kazuya Edamura^{*4}

*1 Precision and Intelligence Laboratory, Tokyo Institute of Technology

*2 Graduate School, Tokyo Institute of Technology

*3 Neos Co., Ltd.

*4 New Technology Management Co., Ltd.

ABSTRACT

The paper presents a novel magneto-rheological (MR) valve-integrated cylinder and its application to manipulators. The proposed MR cylinder has an electromagnet-mounted piston whose differential pressure due to MR fluid flow and driving force can be controlled by the applied current. Also, to reduce the pressure loss in pipelines, a novel low base viscosity MR fluid using lightweight ferrite particles was developed. Based on experimental results of an MR cylinder fabricated with a one-link manipulator, improved MR cylinders were fabricated with a two-link manipulator and a part of the characteristics and the feasibility were experimentally clarified.

1. INTRODUCTION

An MR fluid has micrometer-sized magnetizable particles dispersed in an oily fluid. With applying magnetic field, the dispersed particles in the MR fluid form clusters and the apparent viscosity increases. The flow characteristics are those of the Bingham fluid whose yield stress increases with applied magnetic field. The controllable range of the yield stress is larger than electro-rheological (ER) fluids⁽¹⁾. The MR fluids have been applied to dampers, brakes⁽²⁾⁽³⁾, seals⁽⁴⁾⁽⁵⁾, actuators⁽⁶⁾, and control valves⁽⁷⁾⁻⁽⁹⁾. The MR dampers have been used in practical automobiles⁽²⁾.

We have proposed and fabricated a control valve using the MR fluid called MR valve⁽⁷⁾ and applied it to manipulators⁽⁸⁾⁽⁹⁾. The hydraulic actuators controlled by the MR valve were bellows actuators that have no sliding parts damaged by the dispersed particles in the MR fluids. However, bellows actuators have a large diameter and a small stroke restricted by the elastic limit.

In this paper, we propose and develop a novel MR valve-integrated cylinder called the MR cylinder and apply it to manipulators. First, the MR cylinder is proposed. Second, a novel low base viscosity MR fluid using lightweight ferrite particles is developed. Four samples

are fabricated and evaluated experimentally. Third, a one-link manipulator using the MR cylinder is fabricated and the characteristics are experimentally investigated. Finally, based on the results, improved MR cylinders are fabricated and applied to a two-link manipulator.

2. PROPOSITION OF THE MR CYLINDER

Figure 1 shows the proposed MR cylinder. The MR cylinder has a piston that has an electromagnet inside and a gap around it. An MR fluid flows through the gap being applied magnetic field by the electromagnet, that is, an MR valve forms on the pair of piston and cylinder. A restriction is attached to the inlet and constant pressure is supplied. With applying current to the electromagnet, due to increase of the apparent viscosity of MR fluid, the differential pressure ΔP between the upstream and downstream sides of the piston and the extending force increase. For the retraction, an external return force source such as return spring, counter MR cylinder, and so on is required. A rubber bellows is attached to the output shaft to prevent the dispersed particles in the MR fluid from entering the linear bearing. As the pressure around the rubber bellows is low, a flexible rubber bellows can be used. The MR cylinder features simple and compact structure, long stroke, and robustness against contamination, and so on. Furthermore, designing viscous term in differential pressure ΔP to be small (see equation (1) in section 3.2), the extending force can be controlled by the applied current. Hence, a fluid power system can be realized only by the MR cylinders and hydraulic pump and the output force can be easily controlled.

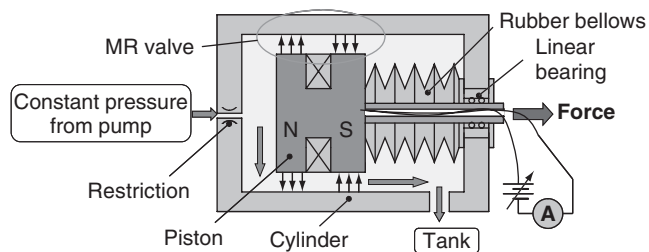


Figure 1 Proposed MR cylinder

3. NOVEL MR FLUID USING FERRITE PARTICLES

3.1 Proposition and fabrication of MR fluids using ferrite particles

Most of conventional MR fluids use heavy soft iron particles and the base viscosities without magnetic field are set to be high to decrease the sedimentation rates, which results in high fluid power losses in pipelines. The typical base viscosities are $0.2\sim 1.0\text{Pa}\cdot\text{s}^{(1)}$.

To decrease the base viscosity, in this study, a novel MR fluid using lightweight ferrite particles was proposed, fabricated and tested. The densities of ferrite are $3.2\sim 3.5\times 10^3\text{kg/m}^3$ and are lower than $7.8\times 10^3\text{kg/m}^3$ of soft iron.

By adjusting the viscosity of base fluid and the amount and composition of surfactants, four stable MR fluids were fabricated. Table 1 shows the properties of the fabricated MR fluids.

Table 1 Properties of fabricated MR fluids

MR fluids	Densities [$\times 10^3$ kg/m ³]	Particle materials	Particle diameters [μm]	Weight percents of solids
MRF-AS7	1.9	Mn-Zn	2.7	70
MRF-AS8	2.5	Mn-Zn	2.7	80
MRF-BL7	1.8	Mn-Mg-Zn	4.1	70
MRF-BS7	1.8	Mn-Mg-Zn	2.8	70
MRF-132LD	3.1	Soft-iron alloy	~5	81

3.2 Experimental apparatus

Performances of MR fluids were measured and evaluated. The measured MR fluids were the fabricated MR fluids shown in Table 1 and MRF-132LD that is a product of Lord Co., Ltd., USA and has dispersed particles made of soft iron alloy and the base viscosity 0.33Pa·s at a shear rate 80s⁻¹.

To evaluate the performances, a two-port MR valve shown in Fig. 2 was fabricated. The electromagnet applies magnetic field to the MR fluid perpendicularly to the flow direction. The flow control gap has width $w=6.4\text{mm}$, height $h=3.0\text{mm}$ and length $l=9.6\text{mm}$. The materials are silicon steel for the yokes and brass for the non-magnetic parts. The number of turns of electromagnet is $N=450$ and electric resistance is 0.95 Ω .

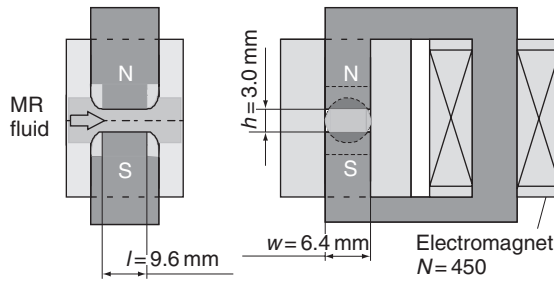


Figure 2 Fabricated two-port MR valve

The differential pressure ΔP of the two-port MR valve with magnetic flux density B and flow rate Q can be modeled as follows⁽³⁾:

$$\Delta P = \frac{2l}{h} \tau_y(B) + \frac{12\mu l}{wh^3} Q \tag{1}$$

where, $\tau_y(B)=kB$ is a shear stress due to magnetic field, k is an MR effect coefficient and μ is a base viscosity of the MR fluid.

As a fluid power source, a closed tank pressurized by an air compressor was used instead of a hydraulic pump because of the small amount of fabricated MR fluids. Pressures were measured by semiconductor type pressure transducers (Nagano Keiki Co., Ltd., KH-15)

and the values were fetched by a personal computer through A-D converter with sampling frequency 10kHz. For dynamic characteristics, an electric resistance was attached to reduce the time constant of the electric circuit which is a ratio of inductance of the electromagnet coil to resistance. The measured time constant of the magnetic flux density without MR fluids was less than 4ms.

The base viscosities were measured using cylindrical chokes with 1mm in diameter and 7.0~18mm in lengths. Based on the relation between differential pressure and flow rate of the cylindrical choke, the base viscosities were calculated.

3.3 Experimental results of MR fluids

The measured base viscosities are shown in Table 2. The values of the fabricated MR fluids are far smaller than the conventional MR fluid MRF-132LD.

Table 2 Measured parameters of the MR fluids

MR fluids	Base viscosities μ [mPa·s] (5000-10000s ⁻¹)	MR effect coefficients k [kPa/T]	Performance index (μ/k^2) [$\times 10^{-12}T^2\cdot s/Pa$]
MRF-AS7	40	32	39
MRF-AS8	60	41	36
MRF-BL7	42	16	160
MRF-BS7	43	12	300
MRF-132LD	280	110	23

Figure 3 shows the measured static characteristics of the two-port MR valve. The viscous term in equation (1) is estimated to be less than 1kPa and is negligible small, which means that the valve has low dependency on temperature because the magnetic force term in equation (1) is thought to have low dependency on temperature in the actual temperature condition. MRF-BL7 often choked due to the large particle diameter. Figure 4 shows the measured relation between magnetic flux density and applied current. Based on the results in Figs. 3 and 4, the MR effect coefficients k were calculated and shown in Table 2.

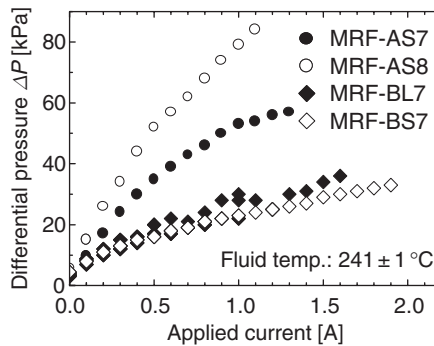


Figure 3 Measured static characteristics of the two-port MR valve using fabricated MR fluids

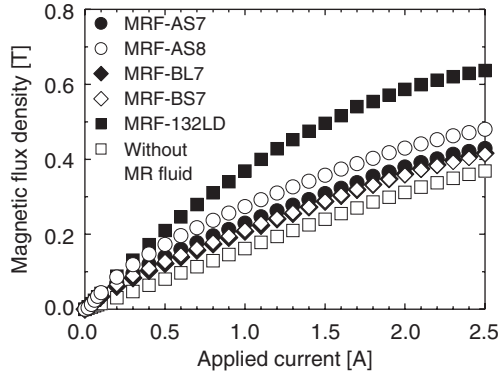


Figure 4 Relation between magnetic flux density and applied current of the two-port MR valve

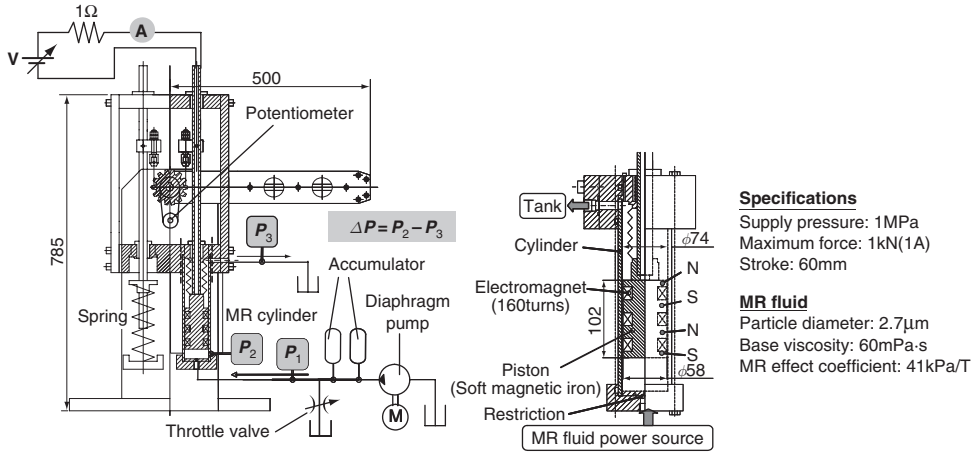
The required volume between magnetic poles is in proportion to a value of $(\mu/\tau_y^2)^{(1)}$. With the small volume, the cross sectional area or the gap length of the magnetic poles is small. The former makes the cross sectional area of the magnet small, the latter makes magnetomotive force of the magnet small and both make the MR device small. Hence, in this study, a parameter (μ/k^2) that is corresponding to the above-mentioned parameter was calculated as a performance index and shown in Table 2.

Based on Table 2, the following trends are found: 1) MR effect coefficient k with Mn-Zn ferrite is higher than that with Mn-Mg-Zn ferrite, 2) with large weight percent of solid, both the MR effect coefficient k and base viscosity are large, and 3) with large particle diameter, the MR effect coefficient k is large. As for the performance index (μ/k^2) , MRF-AS8 has the smallest value. Hence, in this study, MRF-AS8 is selected as a useful MR fluid.

4. FABRICATION OF ONE-LINK MANIPULATOR USING THE MR CYLINDER

4.1 Fabrication of one-link manipulator

An MR cylinder was fabricated and applied to a one-link manipulator with the arm length 0.5m and the joint angle range 60° as shown in Fig. 5. The specifications are the supply pressure 1MPa, the maximum differential pressure $\Delta P_{\max}=0.6\text{MPa}$ and the maximum extending force 1.6kN at the maximum applied current 1.5A. The piston made of soft magnetic iron has 58mm in outer diameter and 136.5mm in length. The cylinder made of low carbon steel has 60mm in inner diameter and 259mm in length. The gap between the piston and cylinder is $h=1\text{mm}$. The pressure loss due to the base viscosity in the MR valve is designed to be sufficiently low to control the differential pressure ΔP irrespective of the flow rate and temperature. To increase the magnetic flux under magnetic saturation in the yokes, three electromagnets with 160turns coils locate in face to face. The chain and sprocket transform linear motion of the MR cylinder with a counter spring (spring constant 65.1kN/m) to the arm rotation. The counter spring is also used to add a tension to the chain.



(a) One-link manipulator using the MR cylinder (b) MR cylinder

Figure 5 Fabricated one-link manipulator using the MR cylinder

4.2 Static characteristics of one-link manipulator

Static characteristics of the fabricated one-link manipulator were measured. The experimental apparatus shown in Fig. 5(a) has a diaphragm pump (Nikuni Co., Ltd. 25HYS-V, rated pressure 6.9MPa, rated flow rate 300cm³/s) without affection of the dispersed particles in the MR fluid and two accumulators (bladder type 1000cm³ and in-line type 30cm³). Applying sinusoidal waveform current of 0.01Hz to the MR cylinder, the differential pressure ΔP and the joint angle were measured and fetched by a personal computer through A-D conversion with the sampling frequency 1Hz. The joint angle was measured counterclockwise from horizontal.

Figure 6 shows the measured results. The reproducibility of the differential pressure ΔP is confirmed with some hystereses. However, the value of the differential pressure ΔP is 40% of the designed value.

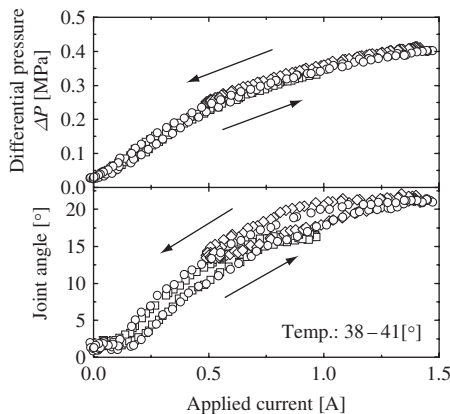


Figure 6 Static characteristics of MR valve in the MR cylinder

To investigate the reason, the characteristics of the MR fluid were measured before and after use. Figure 7 shows the results. Difference of the magnetization characteristics is small as shown in Fig. 7(a), however, the MR effect reduces after 2h due to the diameter reduction of the dispersed particles as shown in Fig. 7(b). However, the MR effect after 6h is in the same level for the one for 2h. Hence, the MR effect coefficient k should be modified after 2h use.

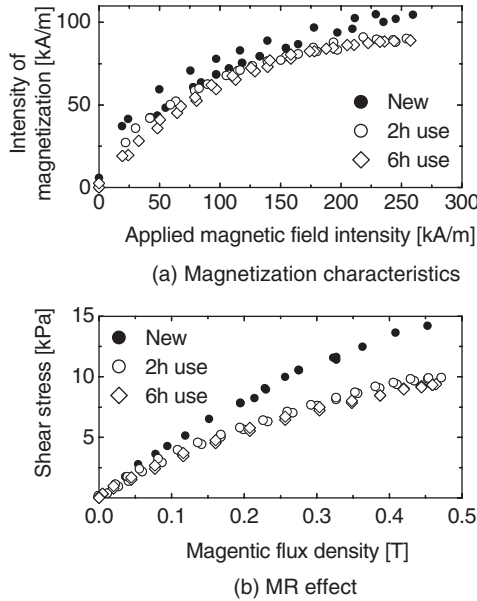


Figure 7 Static characteristics of MR valve in the MR cylinder

With considering the reduction of the MR effect coefficient k and the slanted output shaft, the differential pressure ΔP is still lower than the designed value. It is thought to be due to eccentric and slant of the piston.

As for the joint angle, there are hystereses as shown in Fig. 6 due to friction. The joint angle is unchanged with the applied current smaller than 0.15A due to a mechanical stopper.

4.3 Dynamic characteristics of one-link manipulator

Step responses of the fabricated one-link manipulator were measured with the experimental apparatus shown in Fig. 5(a). The sampling frequency was 500Hz.

Figure 8 shows the step responses of the MR valve in the MR cylinder with fixed arm. The rise times T_r are the same as the previous results⁽⁸⁾⁽⁹⁾.

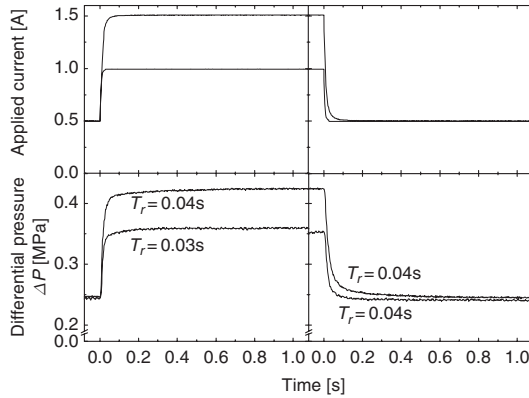


Figure 8 Step responses of MR valve in the MR cylinder

Figure 9 shows step responses of the joint angle without load. The response for step up is far lower than the one for step down because of the difference of the driving mechanism; for step up, the arm is pushed up by the MR cylinder with the supplied flow rate, for step down on the other hand, the arm is fallen down with unlocked MR cylinder, the counter spring and gravity. For step up, at the first stage, the joint does not rotate due to inertia and friction and the differential pressure ΔP rises like the MR valve shown in Fig. 8. After starting joint rotation, the differential pressure ΔP once decreases then increases. The joint rotational velocities are saturated.

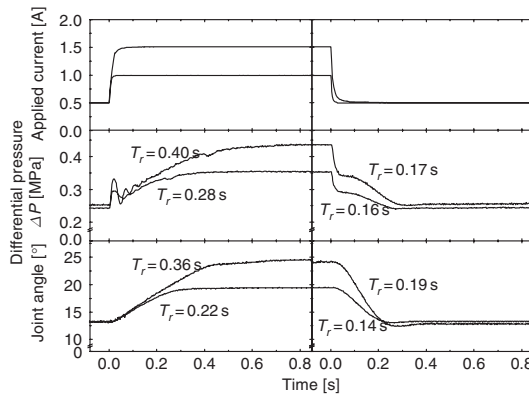


Figure 9 Step responses of the one-link manipulator

Figure 10 shows step responses of the joint angle with different supply pressures or supply flow rates. The higher the supply flow rate is with higher supply pressure, the higher the saturated joint rotational velocity is. The dotted lines in the figures show the values estimated by the maximum flow rates at the upstream restriction. At the first stage, the estimated rotational velocities agree well with the measured values. The upstream restriction determines the saturation of the joint rotational velocities. Trade-off between the response and the supply flow rate is required.

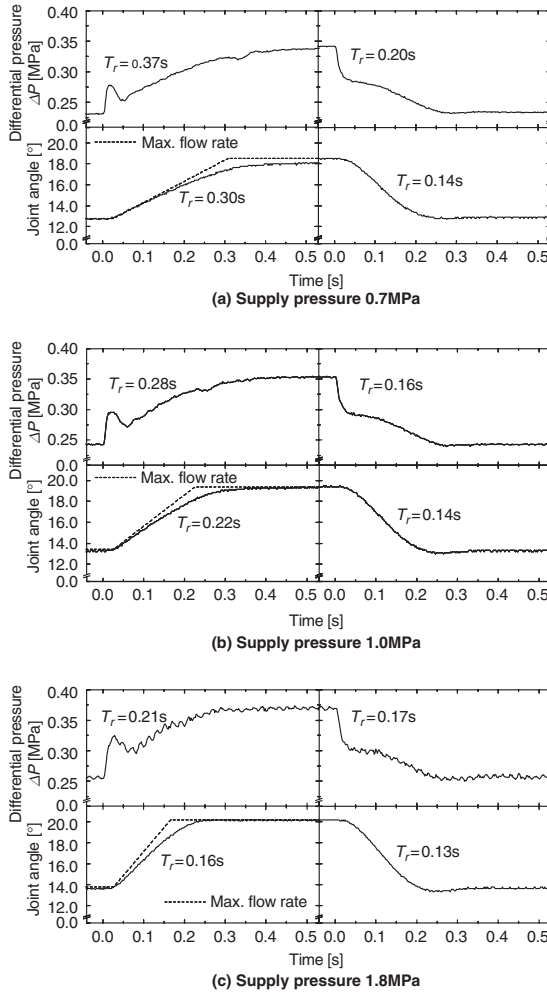
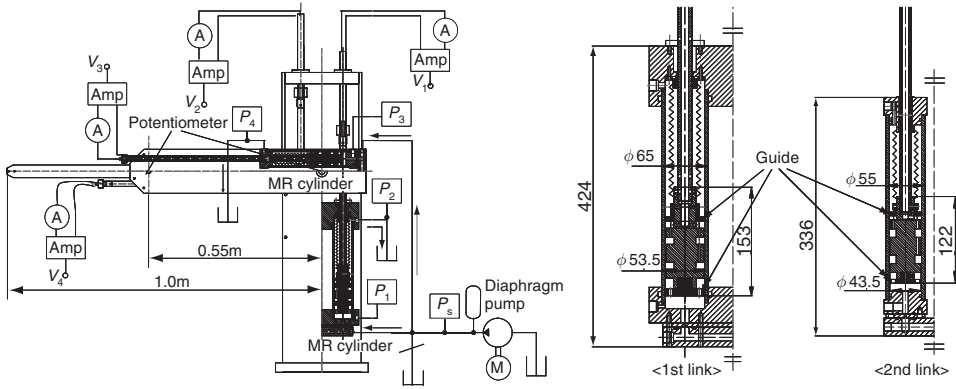


Figure 10 Step responses of the one-link manipulator with different supply pressures

5. FABRICATION OF TWO-LINK MANIPULATOR USING IMPROVED MR CYLINDER

5.1 Fabrication of two-link manipulator

Based on the afore-mentioned results, improved MR cylinders were designed, fabricated and applied to a two-link manipulator as shown in Figs. 11 and 12. The specifications of the two-link manipulator are the total arm length 1m, the payload 10kg, the supply pressure 1MPa, the joint angle range 100° for the first link, 110° for the second link. Each link has two MR cylinders with gap between the piston and cylinder $h=0.75\text{mm}$ and the push-pull linear motions are transformed to the joint rotation.



(a) Two-link manipulator using the MR cylinders (b) Improved MR cylinders

Figure 11 Fabricated two-link manipulator using improved MR cylinders

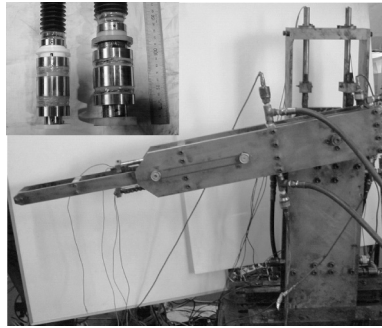


Figure 12 Photocopy of the two-link manipulator using the MR cylinders (top left: electromagnet-mounted pistons for the MR cylinders)

The design procedure of the MR cylinders is as follows: First, the maximum generated torque is derived from the specifications. Assuming the diameter of piston D and the number of electromagnets n , the sizes of the pistons and the maximum extending force are derived based on magnetic saturation of the yokes and the diameters of the sprockets are determined, where the pressure loss due to the base viscosity is designed to be sufficiently small. Then the strokes and length of the MR cylinders are determined from the maximum joint angle range. As a result, the sizes and masses of the MR cylinders are determined. By using the mass as the performance index to be minimized, D and n are determined. In the procedure, the measured MR effect coefficient $k=25\text{kPa/T}$ and the gap $h=0.95\text{mm}$ in consideration of the eccentric are used.

Figure 11(b) shows the improved MR cylinders. The designed maximum extending force, stroke, and mass are 2.0kN, 120mm, and 10kg for the first link, and 1.3kN, 75mm and 3.7kg for the second link. The pistons are made of soft magnetic iron and the eccentrics are less than 0.05mm with guides made of Teflon. The cylinders are made of carbon steel. The number of electromagnets of each MR cylinder is $n=2$ and all the electromagnets have

160turns coils. The total electric resistances are 2.0Ω for the first link and 1.7Ω for the second link.

5.2 Characteristics of MR valve in the MR cylinder

Characteristics of the MR valve in the improved MR cylinder were measured with the arm fixed. Figure 11(a) shows the experimental apparatus. The pump, accumulators and so on were the same as the ones in the previous chapter. The MR valve was driven by a voice coil motor driver (Servotechno Co., Ltd. VCM3AT) that produces output current in proportion to the applied voltage. As the first link was damaged, characteristics of the MR valve for the second link were investigated.

Figure 13 shows the measured static characteristics of the differential pressure ΔP_2 with the sinusoidal waveform current of 0.01Hz and the sampling frequency 1Hz. The theoretical value with $h=0.8\text{mm}$ is also shown by the dotted line in the figure. It is ascertained that though there are hystereses and saturations, the value with applied current smaller than 0.6A agrees well with the theoretical value. The saturation occurs in the yokes.

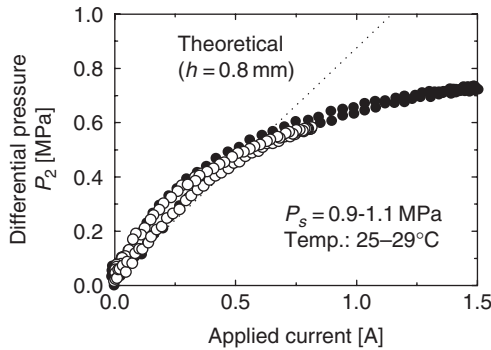


Figure 13 Static characteristics of MR valve in the MR cylinder for the second link

Figure 14 shows the step responses of the MR valve with the sampling frequency 500Hz. The rise times T_r for step up are the same value as in Fig. 8. However, for step down, the value is degraded. It is thought that the mechanisms are different for step up and down and it may be affected by the saturation and residual magnetism of the yokes.

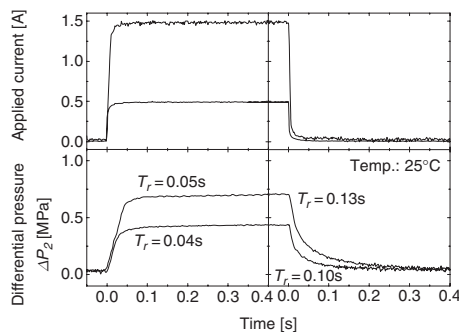


Figure 14 Step responses of MR valve in the MR cylinder for the second link

5.3 Characteristics of two-link manipulator

A PI control system was constructed as shown in Fig. 15. The output signal u of the PI control element with the input controlled deviation e is applied to the MR cylinders 1 and 2 for the second link with bias current $I_0=0.075A$ to maintain positive tension of the chain. The PI control system was constructed by software and the sampling frequency was 200Hz.

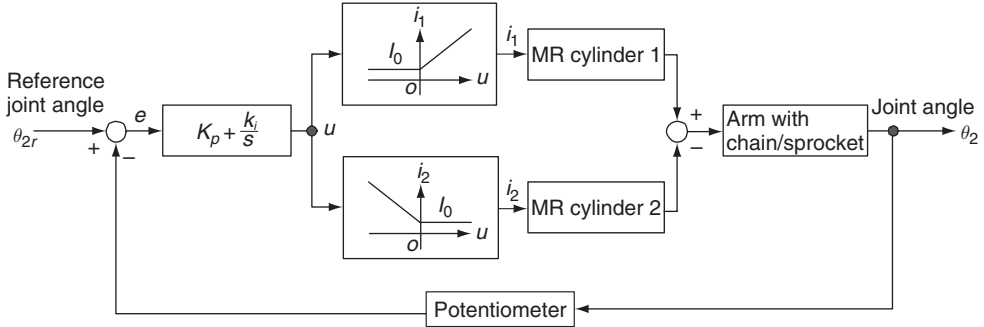


Figure 15 Block diagram of the PI control system for the second link

Figure 16 shows the step responses of the joint angle θ_2 for the second link without load under P control, whose gains are $K_p=2.9A/rad$ for proportional and $K_i=0$ for integral. The transient responses are practical, though the joint rotational velocities are constant due to saturation of the flow rate. The steady-state deviation is also a problem.

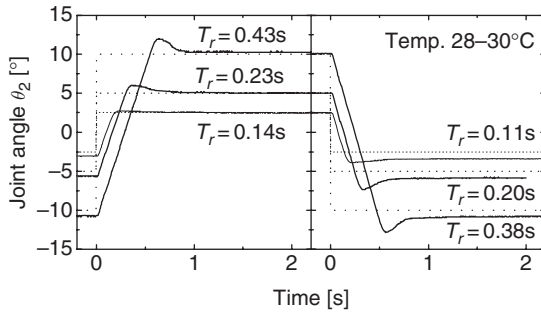


Figure 16 Step responses of the second link using P control

Figure 17 shows the measured step responses of the joint angle θ_2 for the second link without load under PI control. The proportional and integral gains of $K_p=1.7A/rad$ and $K_i=4.0A/(rad \cdot s)$ were determined with the measured step responses. With saturation of the flow rate, the joint rotational velocities are constant at the first stage. With increasing the step amplitudes, the rise times T_r increase and the overshoots increase with wind up. The response for step down is higher than the ones for step up due to the affection of gravity.

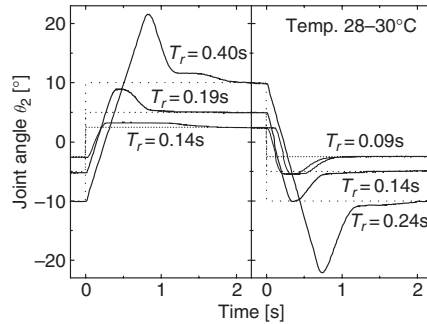


Figure 17 Step responses of the second link using PI control

6. CONCLUSIONS

The paper proposed and developed a novel MR cylinder using newly developed low base viscosity MR fluid using ferrite particles and applied it to manipulators. The basic characteristics of the MR cylinder were experimentally clarified with a one-link manipulator. Also, a two-link manipulator with improved MR cylinders was fabricated and a part of the characteristics and the feasibility were experimentally clarified.

REFERENCES

- (1) Carlson, J. D. and Spencer Jr., B. F., Magneto-Rheological Fluid Dampers for Semi-Active Seismic Control, Proc. of 3rd Int. Conf. on Motion and Vibration Control, III (1996-9), 35-40.
- (2) Carlson, J. D., Electro-Rheological and Magneto-Rheological Fluids: A State-of-the-Art Report, Proc. of 9th Int. Conf. on New Actuators (ACTUATOR 2004), (2004-6), 283-288.
- (3) Ashour, O., Rogers, C. A. and Kordonsky, W., Magnetorheological Fluids: Materials, Characterization, and Devices, J. of Intelligent Material Systems and Structures, 7 (1996), 123-130.
- (4) Kordonski, W. I. and Gorodkin, S. R., Magnetorheological Fluid-Based Seal, J. of Intelligent Material Systems and Structures, 7 (1996), 569-572.
- (5) Yoshida, K., Jung, Y.-O. and Yokota, S., A Microvalve Using MR Fluid Valve-Body, Proc. 6th Int. Conf. Mechatronics Technology (ICMT 2002), (2002), pp.423-428.
- (6) Takesue, N., Furusho, J. and Kiyota, Y., Fast Response MR-Fluid Actuator, JSME Int. J. Ser. C, 47-3 (2004), pp.783-791.
- (7) Yokota, S., Yoshida, K. and Kondoh, Y., A Pressure Control Valve Using MR Fluid, Proc. 4th JHPS Int. Symp. on Fluid Power, (1999), pp.377-380.
- (8) Yoshida, K., Takahashi, H., Yokota, S., Kawachi, M., and Edamura, K., A Bellows-Driven Motion Control System Using a Magneto-Rheological Fluid, Proc. 5th JFPS Int. Symp. on Fluid Power, (2002), pp.403-408.
- (9) Yoshida, K., Park, J.-H., Yokota, S., Kawachi, M., and Edamura, K., A Bellows-Driven Manipulator Using a New Magneto-Rheological Fluid, Proc. 4th Int. Symp. on Fluid Power Transmission and Control (ISFP2003), (2003), pp.542-547.

Systematic Experimental studies and Computational Perspectives of the non-linear squeeze Mode behaviour of Magneto-Rheological Fluids

Norbert Gstöttenbauer¹, Alexander Kainz², Bernhard Manhartsgruber³, Rudolf Scheidl⁴

^{1,3,4} Institute for Machine Design and Hydraulic Drives, Johannes Kepler University, Altenbergerstr. 69, A-4040 Linz, Austria

² Institute for Computer-Aided Methods in Mechanical Engineering, Johannes Kepler University, Altenbergerstr. 69, A-4040 Linz, Austria

ABSTRACT

Magneto-rheological (MR) fluids are suspensions of micron-sized ferromagnetic particles in a non-magnetic carrier fluid. The essential characteristic behaviour is the rapid and reversible transition from the state of a Newtonian-like fluid to the behaviour of a stiff semi-solid by applying a magnetic field of about 0.1-0.4 Tesla. This feature can be understood from the fact that the particles form chain-like structures aligned in field direction. The MR-fluid offers three modes of operation, namely the direct shear mode, the valve mode and the squeeze mode. The latter is of particular interest due to its highly non-linear behaviour, which is still not fully understood and therefore expected to give rise to new industrial applications. A test rig for the exploration of the MR-fluid behaviour was designed for experimental purposes. The present paper describes the results of measurements under sinusoidal loading modes. Special emphasis was put on the dependence of the MR-fluid response with respect to parameter variations of the applied static magnetic field, the cyclic loading amplitude and frequency values. Cavitation effects have been investigated and partially suppressed by pre-pressurising the MR-fluid, which enables a more thorough insight into particle chain disruption and segregation effects. Well pronounced hysteresis loops are observed and exhibit characteristic kinks, which cannot be understood within the frame of elementary constitutive laws such as for Bingham fluids. Therefore, highly sophisticated continuum mechanical theories or particle dynamics simulations seem to be essential to recover the measurement curves in full detail.

1 MR-FLUID CHARACTERISTICS

The essential characteristic of a Magneto-rheological (MR)-Fluid consisting of a suspension of micron-sized ferromagnetic particles in a non-magnetic carrier fluid (e.g. oil including special additives and antiwear agents) is the rapid and reversible transition from the state of a Newtonian-like fluid to the behaviour of a stiff semi-solid by applying a magnetic field of the order of about 0.1-0.4 Tesla. This feature, called the magneto-rheological (MR)-effect, cf. Refs.(1)-(3) can be understood from the fact that, in the presence of a magnetic field, the particles form chain-like structures aligned in field direction. Therefore, the columnar microstructure drastically increases its resistance to an applied shear strain. This behaviour has inspired the development and design of new products and applications, such as semi-active vibration dampers, brakes and clutches.

2 MODES OF OPERATION OF MR-FLUID DEVICES

The MR-fluid offers three modes of operation, as depicted in Fig. 1, whereby only two of them are used at present in the vast majority of commercial applications. The direct shear mode is characterized by the relative motion of two magnetic poles separated by the MR-fluid generating shear forces. In the valve-mode (or flow mode), the magneto-rheological effect is used to throttle the flow through passages. The resulting pressure difference is used for hydrostatic force generation. In the third mode of operation, the so called squeeze mode, the MR-fluid is squeezed out of a narrowing gap, thereby building up high pressures, which can be used to develop small devices capable of carrying high loads. However, particularly due to a lack of understanding of the highly non-linear material behaviour, commercial applications of the squeeze mode are up to now restricted to small amplitude vibration damping.

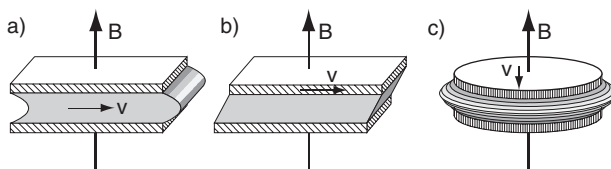


Figure 1: MR-Modes of operation, Ref (1): a) Valve (Flow) Mode, b) Direct Shear Mode, c) Squeeze-Mode

3 A TEST RIG FOR THE ANALYSIS OF THE SQUEEZE MODE BEHAVIOUR

To obtain a thorough understanding of the underlying material behaviour of the MR-fluid in the squeeze mode, which is expected to give rise to a great variety of new and innovative applications, a test rig for the exploration of the MR-fluid behaviour was developed, as depicted in Fig. 2, Refs.(1), (2).

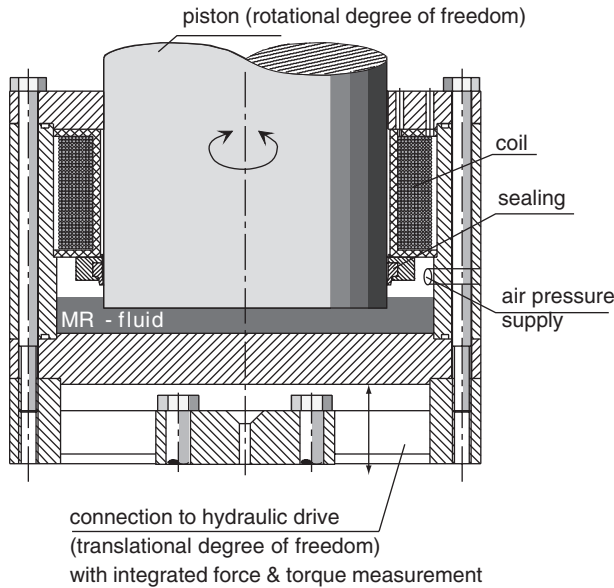


Figure 2: Experimental test-rig for the analysis of the squeeze mode

The design and optimization of the mechanical as well as the electromagnetic properties of the test rig were performed by utilizing finite element analysis (Abaqus Ref. (5), Maxwell 2D Ref. (4)). The purpose of the test rig is the acquisition of measurement data from experiments. While the basic task of squeezing the MR-fluid out of a narrowing gap can easily be accomplished, the measurement of the distributions of the hydrostatic pressure and of the shear stresses at the boundary of the MR-fluid turns out to be challenging. To keep the geometry of the gap filled by the MR-fluid as simple as possible, a cylindrical container is equipped with a coil for the generation of the magnetic field. The axis-symmetric squeezing gap filled by the MR-fluid is formed by the bottom of the container and a piston that dives into the MR-fluid. The container is attached to a servo-hydraulic drive with an integrated absolute path measurement resolving $2\ \mu\text{m}$, which enables a controlled translatory motion in the vertical direction using a state control, while the piston is attached to a shaft driven by an electrical servo motor for controlled rotary motion. Due to the high degree of symmetry of the set-up, both the evaluation and interpretation of integral measurement quantities, such as the reaction forces and torques (e.g. integrated normal pressure on the gap boundary) are simplified. The measurement is performed by a system of strain gauges, which also allows for the detection of the point of attack of the equivalent vertical force corresponding to a potentially asymmetric behaviour of the MR-fluid filled gap, e.g. due to an inhomogeneous distribution of magnetic particles in the carrier fluid. A seal is used to close the annulus above the MR-Fluid so an air pressure can be set up through the pressure supply for changing the pre-pressurising and thus the cavitation boundaries of the MR-Fluid.

4 EXPERIMENTAL PARAMETRIC STUDIES

To obtain a deeper insight into the MR-Fluid properties a systematic parametric study has been performed to explore the behaviour and trends under certain operational conditions. The load case used for the experimental parametric squeeze study was a gap of initial thickness of 5 mm, varied sinusoidally with predefined amplitude, frequency, magnetic field and air pressure (pre-pressurising) values. The parameter range for the amplitude values was 0.025 mm up to 2 mm in adequate steps, the frequency values were varied from 0.2 to 1 Hz in 0.2 Hz steps, the magnetic field was varied from 0 mT to 400 mT in steps of 50 mT and the air pressure was modified in three steps from atmospheric pressure up to about 2 bars. This led to more than 620 measurements. The essential results are presented in selected diagrams of test series in this paper.

Considering the first test case, Fig. 3 demonstrates the sequence used for each measurement of the parametric studies. Preceding each measurement a thorough mixing and demagnetisation process has to be carried out to ensure well defined initial conditions. The measurement starts with an initial gap thickness of 5 mm and an applied pre-pressurising (in this case atmospheric pressure). First the magnetic field (here 300mT) was applied by keeping the gap thickness constant (see Graphs A and C), resulting in a drag corresponding to a negative force (see Graphs B and D). After a settling time of 3 sec. for the set up of the target value for the magnetic flux density, the sinusoidal movement with predefined amplitude and frequency values (in this case 0.2 mm and 0.2 Hz) started, as depicted in Graph A. Thus the MR-Fluid is squeezed out of the narrowing gap, leading to the initial curve in Graph D. Note the counter clockwise orientation of the hysteresis loop. At the upper reversal point of the sinusoidal movement the maximum squeeze force (in this load case of about 2000 N) is attained. Exceeding this point the dragging period follows, extending the gap to its maximum value, resulting in tensile (i.e. negative) forces. The subsequent squeezing part then completes the first load cycle, whereby the force in the MR-Fluid increases again. In total 10 periods are recorded resulting into a steady state hysteresis curve, as represented in Graph D (note that only the first three periods are depicted).

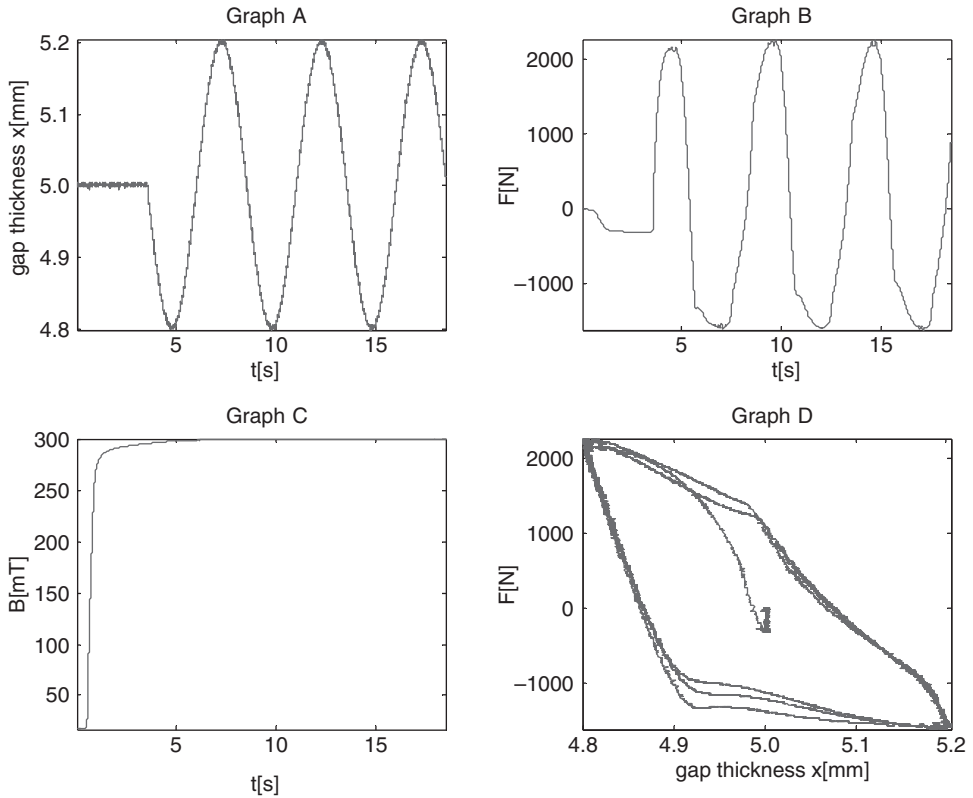


Figure 3: Measurement sequence. Initial gap thickness 5 mm, Amplitude 0.2 mm, Magnetic Field $B = 300$ mT, Frequency $f = 0.2$ Hz. Graph A: Gap thickness vs. Time, Graph B: Force vs. Time, Graph C: Magnetic Field vs. Time, Graph D: Force vs. Gap thickness.

The hysteresis curve in Fig. 3, Graph D exhibits the complex material behaviour of an MR-Fluid with pronounced kinks in slope while squeezing and dragging. A variation of the control parameters, namely amplitude, frequency, magnetic field and air pressure, leads to modifications in the hysteresis behaviour, which will be discussed in the subsequent sections. Fig. 4 shows the hysteresis curve of the MR-Fluid without applied magnetic field. One obtains the shape of a typical viscoplastic material, as expected.

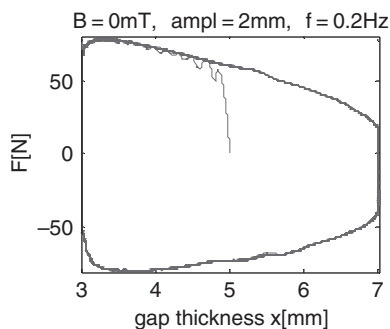


Figure 4: Hysteresis curve of an MR-Fluid without a magnetic field. Initial gap thickness 5 mm, Amplitude 0.2 mm, Frequency $f = 0.2$ Hz.

4.1 Amplitude and Magnetic Field Dependence

A selection of measured hysteresis curves, as obtained by a systematic variation of the amplitude and magnetic field values is depicted in Fig. 5. The resulting force values (in Newton) are plotted as functions of the gap thickness (in millimetres). In each column of the graph matrix same constant magnetic induction is applied with values of 200 mT, 300 mT and 400 mT, respectively. Every single row of the graph matrix represents a particular amplitude value of the sinusoidal movement, starting with 2 mm down to 0.025 mm. For reasons of clarity the corresponding values are also given in each diagram. The frequency of 0.2 Hz and a pre-pressurising with atmospheric pressure were kept constant throughout the measurement series presented here.

For tiny amplitudes of 0.025 mm, pure elastic material effects are observed for magnetic flux values beyond about 250 mT. Below this value increasing visco-elastoplastic hysteresis effects up to pure viscoplastic behaviour in the limiting non-magnetic case occur. With increasing amplitude and magnetic field values the initially increasing symmetric hysteresis curves are become more and more distorted. This might be explained by the occurrence of cavitation inside the MR-fluid. Fig. 6 exhibits the schematic simplified normal pressure distributions acting inside the MR-fluid during the dragging period. The maximum pressure drop is located near the centre of the piston and the normal pressure increases in radial direction up to the pre-pressurising value prevailing in the annulus above the MR-fluid filling level. Approaching the cavitation boundary of zero pressure will cause cavitation inside the MR-fluid, starting spatially in the centre and extending to the boundary regions.

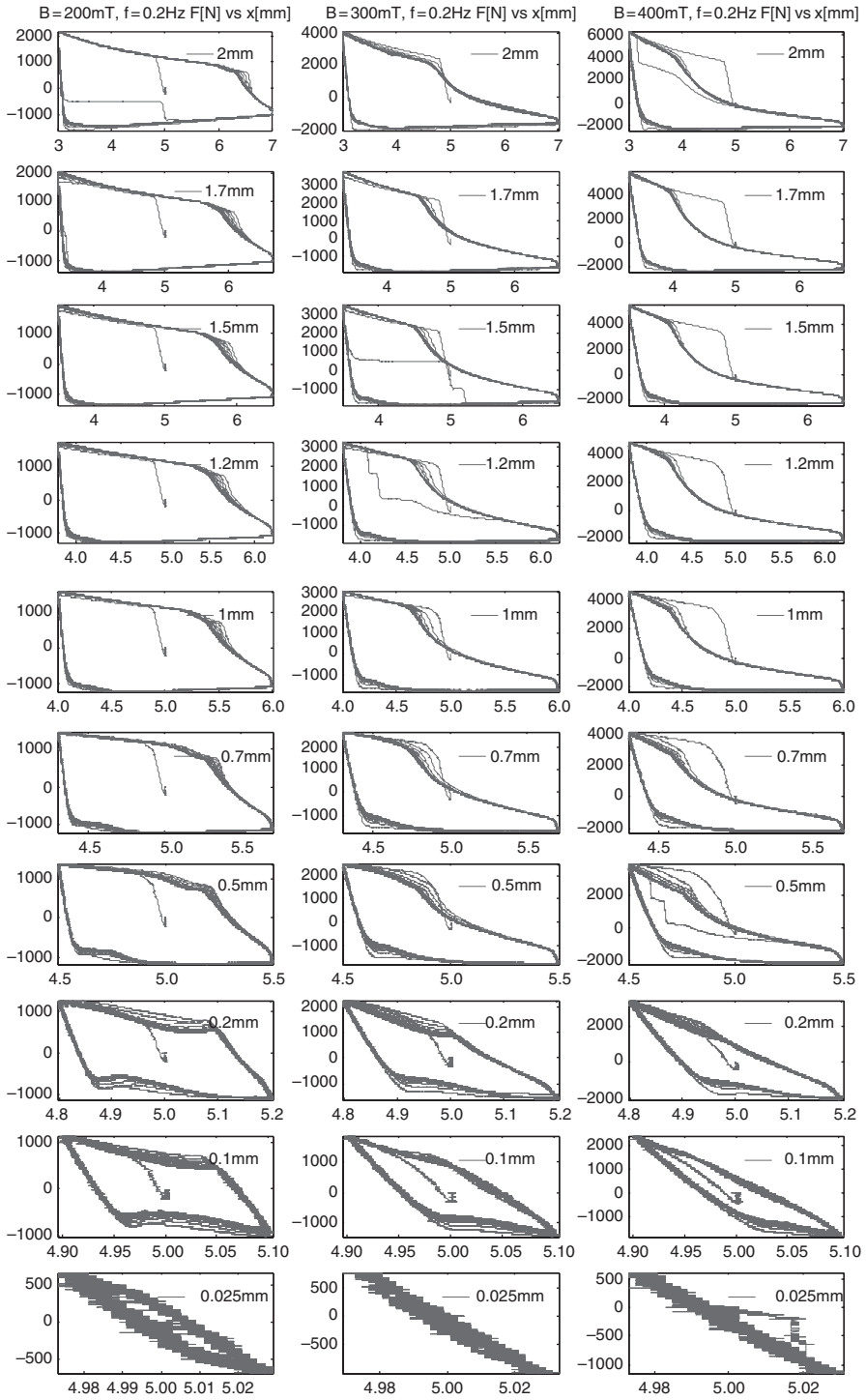


Figure 5: Measured hysteresis curves of the amplitude and magnetic field parameter study

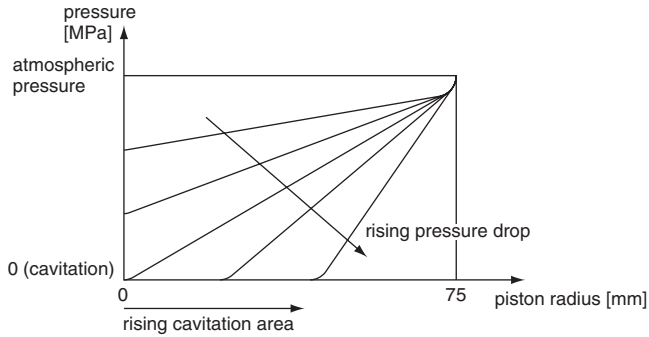


Figure 6: Schematic simplified normal pressure distributions acting inside the MR-fluid while dragging, showing cavitation area.

In the case of full cavitation the calculated dragging force can not exceed 1770 N for our test rig. However, the maximum dragging (tensile) force in all cases considered is cut off at about 2200 N. The difference of about 400 N results from the dragging force built up by the magnetic field of 400 mT and has to be subtracted, which indicates that the MR-fluid is in a pronounced cavitation mode.

In areas of cavitation a disruption of the chain like ferromagnetic particles takes place. This may cause a serious segregation of the carrier fluid and the particles, due to the tendency that the cavitation voids are filled successively with inflowing carrier fluid. This segregation changes the material behaviour of the MR-fluid until a homogeneous suspension is re-established in the ensuing squeeze cycle. This might explain the phenomenon of the increasing force rising delay while squeezing. The larger the amplitude and magnetic field values (and therefore, the cavitation area and time), the longer the time period until the MR-fluid is homogeneous and recovering its original load carrying capacity. This phenomenon is clearly visible in Fig. 5 whereas the initial curve immediately builds up a significant squeeze force due to the initial mixing process.

4.2 Investigation of the Cavitation Effect

To analyse the cavitation effect, as described in the preceding section, in more detail, the pressure in the annulus above the MR-fluid filling level was increased for pre-pressurising the MR-fluid. Fig. 7 gives an overview of the measurement results. All graphs are recorded with a magnetic induction of 400 mT. For all measurements in the left column of the graph matrix an amplitude value of 0.2 mm was prescribed whereas the graphs in the right column correspond to an amplitude value of 2 mm. Each row was recorded with different pressure values spanning from atmospheric pressure (AP) up to AP+2 bars, as specified in the figures.

Considering the hysteresis curves with 0.2 mm amplitude, the unsymmetrical curve recorded at atmospheric pressure level tends to a fully symmetrical hysteresis curve due to high pre-pressurising values. This shows that due to the pre-pressurising of the MR-fluid the cavitation level is lowered and therefore the cavitation area located near the centre of the MR-fluid decreases until cavitation is fully suppressed. At an amplitude value of 2 mm the same effect can be observed in principle. However, the area of cavitation becomes smaller with rising pressure, and therefore the disruption and segregation effects inside the MR-fluid are less pronounced. This leads to an earlier build-up of the force during the

squeezing period. In case of even higher pre-pressurising levels until no more cavitation occurs, the hysteresis loop would also be symmetrical for this high amplitude case.

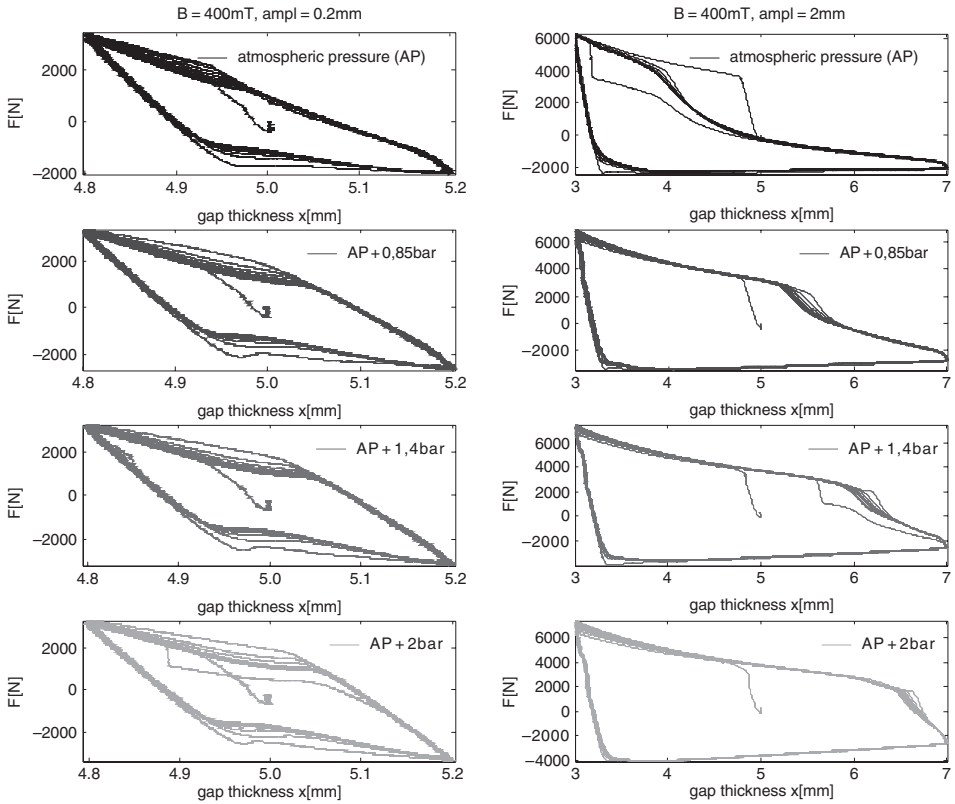


Figure 7: Investigation of the cavitation effects by rising the pressure.

4.3 Frequency Dependence

The experimental results of the frequency parameter study of the sinusoidal movement, reaching from 0.2 to 1 Hz in steps of 0.2 Hz, are summarised in Fig. 8. Here a magnetic field of 300 mT was applied. Selected hysteresis curves with amplitude values of both 1.5 mm and 0.1 mm are depicted. In the left column of the graph matrix the initial loops are depicted, whereas the right column represents one steady state cycle for each frequency.

These measurements show that the material behaviour of an MR-fluid is only slightly frequency dependent, respectively rate dependent, and the effect becomes more pronounced with higher amplitude values. Concerning the initial curve it is obvious that the slope decreases at the beginning of the movement at higher frequencies. Moreover, the maximum load carrying capacity reduces marginally.

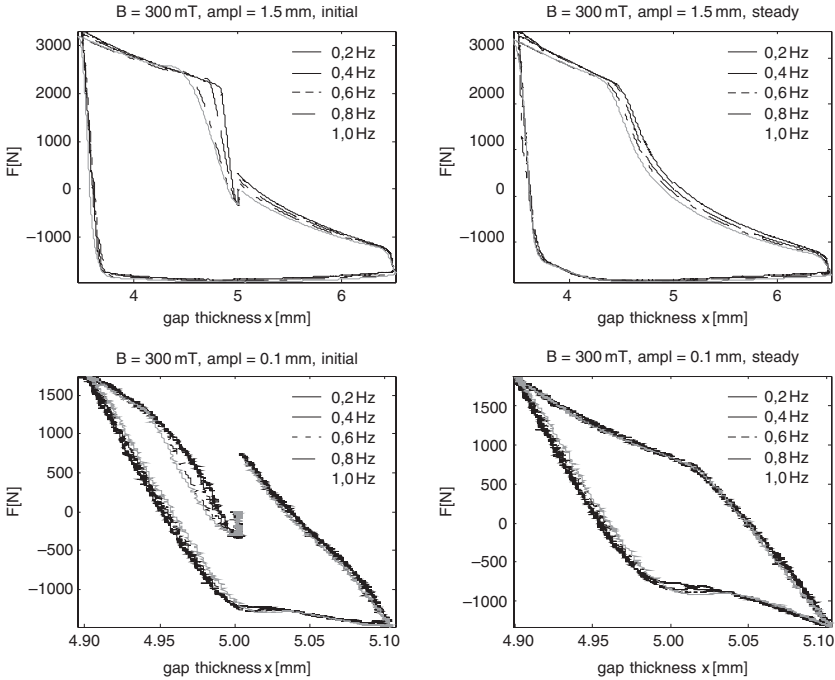


Figure 8: Frequency parameter study of the sinusoidal movement from 0.2 to 1 Hz in steps of 0.2 Hz, showing initial curves and steady state curves.

5 OVERVIEW OF THEORETICAL MODELLING CONCEPTS AND NUMERICAL INVESTIGATIONS

The most commonly used and simplest modelling approach is the assumption of a *Bingham medium*. It behaves elastic up to the yield stress, which depends on the magnetic flux density (called the “MR-effect”). Above the yield stress level the shear stress rises linearly with the shear rate. The occurrence of a well pronounced shear yield stress, which can be controlled by the applied magnetic field, can be understood by looking at the mesoscopic structure of such MR-fluids. The iron particles form chains along the applied field and interact between each other via the long-range two-particle magnetic dipole-dipole interaction potential (3), which reads for point dipoles with magnetic dipole moment m

$$V_{12} \cong \frac{(\epsilon^2 - 2)m^2}{4\pi\mu_\ell\mu_0r_0^3(\epsilon^2 + 1)^{5/2}} \rightarrow U_D \cong \frac{\Phi}{V_p}V_{12} \rightarrow \tau_f(\epsilon) = \frac{\delta U_D(\epsilon)}{\delta \epsilon},$$

where μ_ℓ denotes the relative permeability of the liquid part, r_0 is the undisturbed distance between two iron particles, and ϵ designates the “effective” shear strain between two adjacent iron particles of the chain (i.e. for one-dimensional shear with deflection in x -direction $\epsilon = x/r_0$). The interaction energy density U_D is obtained by multiplication with

the particle number density, given as the ratio of the particle volume fraction Φ with the particle volume V_p . Note that the mean magnetic polarisation per particle is given by $J_p = m/V_p$. The induced shear stress is determined by the variation of the interaction energy density U_D with respect to the shear strain \mathcal{E} . The corresponding shear yield stress can be identified as the maximum shear stress value. However, such single chain modelling approaches based on the magnetic dipole-dipole interaction merely give a very rough upper bound estimate of the actual yield stress values. Therefore, more sophisticated models also take into account the higher multipole contributions and the interactions between adjacent iron particle chains (cf. reports about MR-fluid particle dynamics simulation approaches (e.g. 12)).

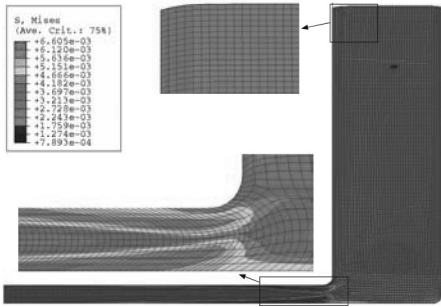


Figure 9: von Mises stress distribution in the MR-fluid at a step time of 0.45 sec. of the numerical simulation model in Abaqus, Ref. (5).

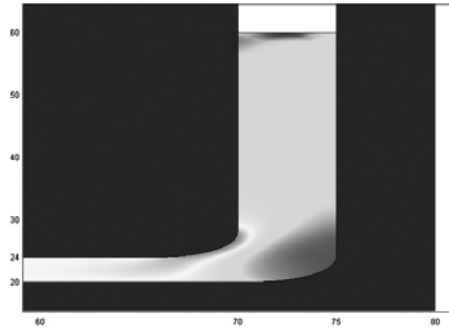


Figure 10: An adequate Femlab simulation model with an applied pressure of 10 bar to suppress cavitation.

The data obtained by the test-rig (cf. section 4) serve as valuable input for the development and analysis of more adequate macroscopic material models for the squeeze mode behaviour of MR-fluids. Previous numerical studies of single squeezing as well as cyclic loading periods were performed by utilizing the commercial finite element packages Deform (6), Abaqus (5) and Femlab (7). The underlying constitutive models were based on elasto-viscoplastic assumptions with a Young's modulus of $E = 1600 \text{ MPa}$ and an effective yield stress of $\bar{\sigma} = 2.7 \text{ kPa}$, ascertained as a result of the previous Deform calculations (1). Concerning strain-rate dependency, an overstress power law was employed. On the contact surface between the MR-fluid and the repository a classical isotropic Coulomb friction law with a friction coefficient of $\mu = 0.2$ was applied modelling the contact shear forces. While elastic effects occur merely for tiny displacements, plasticity and friction play the dominant role for the appearance of the well pronounced hysteresis loops.

To obtain a more detailed insight into the underlying constitutive laws of the MR-fluid behaviour in the squeeze-mode, including the electromagnetic coupling effects, leading to the formation of iron-particle chains along the magnetic field lines, highly sophisticated continuum models have to be applied in principle. Of particular interest is the influence of the hydrostatic pressure on the yield strength and flow behaviour of the MR-fluid. From a theoretical point of view, the rather complex and highly non-linear rheological behaviour of MR-fluids in the squeeze mode can be treated to some extent by taking into account

concepts developed originally for *porous media* (9-11), i.e. fluid-saturated or porous solid materials. Many efforts have been made during the last decades to develop reliable and praxis-relevant theories for such media models fulfilling the requirements of both their theoretical accuracy and their applicability in engineering practice. The basis of the description of porous media is the derivation of constitutive models for two-phase systems on the basis of the fundamental equations of the mixture theory including the concept of volume fractions. An extension of classical continuum mechanics toward the description of multi-phase media is given by the theory of mixtures with both solids and (or) liquids as constituents. For multi-phase continua, one additionally has to take care of structural parameters such as volume fractions. Note that such macroscopic approaches are based on the concept of constituents that are statistically distributed over the control space, i.e. smeared over the total control space. Therefore, neither a geometrical interpretation of detailed structure properties nor the exact localisation of the individual components is taken into consideration. Within the framework of the porous media theory, beside the balance equations of mass, momentum and energy and the concept of volume fractions, adequate constitutive relations describing the frictional stress-strain (rate) relations have to be postulated, which of course have to fulfil thermodynamic restrictions resulting from the entropy inequality. The fundamental restrictions of mechanics and thermodynamics principles can be summarised as follows: Determinism, equipresence (response functions depend on a common set of variables), local action, material frame indifference (objectivity) and dissipation (second law of thermodynamics). Therefore, the set of independent constitutive equations can be interpreted as functions of a common set of time dependent process variable field functions, e.g. partial densities, density gradients and deformation gradients of the constituents. For the case of compressible constituents, both the volume fractions and gradients cannot directly be determined by the partial densities and have to be considered as additional variables of the deformation process.

Of utmost importance is the formulation of relatively simple and consistent constitutive equations that predict the non-linear material response especially in the plastic range sufficiently accurate and are still numerically tractable. It turned out that many aspects of the non-linear MR-fluid behaviour in the squeeze-mode can already be understood to some extent by utilizing much simpler “*effective single-continuum*” model approximations (5, 11), which were originally developed for the description of porous metal plasticity (metal containing a dilute concentration of voids) and models for granular and polymer behaviour. All these constitutive models are essentially pressure-dependent plasticity models, which are very popular and widespread especially in the geotechnical field. Some of these models are extensions of the classical Drucker-Prager (1952) model (12) and comprise curved yield surfaces in the meridional plane (p - q plane with p denoting the hydrostatic pressure $p = -tr(\bar{\sigma})/3$ and q designating the von Mises stress $q = \bar{\sigma} = \sqrt{(3/2)tr(\bar{\sigma}':\bar{\sigma}')}$), non-circular yield curves in the deviatoric stress plane.

Moreover, some model variants employ non-associated flow rules and can be extended to include rate-dependency, hardening and creep effects. The main assumption for dealing with metal porosity is the postulation of a curved yield surface in the meridional p - q plane, which depends on the volume fraction of the voids in the material. In compression the material hardens due to closing of the voids, and in tension it softens due to growth and nucleation of the voids, where the nucleation rate of the voids is usually assumed to be proportional to the plastic strain rate. It has to be emphasized that the adaptation of such simplified single continuum approximations to MR-fluids leads to sophisticated parameter

identification procedures, especially with respect to the dependence of some adaptation parameters with respect to the magnetic flux density (B - field).

These modelling concepts, as outlined above, can (at least to some extent) be applied to MR-fluid simulations, as our latest experimental investigations clearly pointed out. A systematic variation of pre-pressurising values conjectures that especially for high metal volume fractions and for low till moderate magnetic flux densities a non-negligible dependence of the deviatoric stress from the hydrostatic pressure might occur, i.e. the Mises-stress values increase with increasing pressure values. The accurate functional dependence (linear, hyperbolic or exponential) including parameter adaptation is currently under investigation. It is obvious that for too low pre-pressurising values cavitation effects play a dominant role in the dragging part of the cyclic loading process. The lower the absolute pressure, the more dominant cavitation will be, leading to a significant amplification of material disruption and segregation effects, therefore delaying the building up of shear stresses and associated normal contact pressures, as can be observed in the experimental hysteresis loops. As for most practical applications cavitation should be avoided, pre-pressurising turned out to be essential especially for cyclic loading scenarios with high amplitudes.

It should be pointed out that “single-continuum approaches”, as mentioned above, are spatially averaged and smoothed theories, and therefore not suited for the prediction of mesoscopic structures, such as the dynamics of chain formation and disruption of single iron particles. If one is interested in the microstructure evolution in MR-fluids, explicit *particle dynamics* simulations have to be performed (13). The motion of the particles is governed by magnetic, hydrodynamic and repulsive interactions. As is well known, the fluid-particle interactions are accounted for by Stokes’ drag with suitable (B -field dependent) phenomenological expressions for the drag coefficient, expressing the viscous force per unit volume due to a relative motion between the fluid and the solid phase. The inter-particle repulsions have to be modelled by applying hard sphere repelling forces. Further essential results attainable by such particle dynamics simulations comprise effective magnetic permeabilities and estimates of response time-scales, which are often of crucial importance in the design of MR fluids.

6 CONCLUSIONS AND OUTLOOK

To obtain a more thorough insight into the underlying process details, including the formation of iron particle chains along the magnetic field lines, highly sophisticated continuum mechanical theories or particle dynamics simulations have to be applied in principle. To recover the measured hysteresis loops for cyclic loading periods at least in the non-cavitating case (i.e. for sufficiently high pre-pressurising values), single continuum mechanical concepts, which were originally developed for the description of porous metal plasticity and for granular and polymer behaviour, seem to be promising. Systematic rheological system identification procedures, incorporating the effects of the applied magnetic field, as well as the elastic and cyclic hardening MR-fluid properties, based on both measured and calculated data and enhanced numerical simulation concepts, are currently under investigation and will lead to valuable information about the phenomenological material and interaction parameters occurring in the underlying constitutive laws and boundary conditions.

ACKNOWLEDGMENTS

The financial support of the main part of this work by the “Linz Center of Competence in Mechatronics” within the framework of the *Kplus* program of the Austrian government is gratefully honoured.

REFERENCES

- (1) Manhartgruber, B., Kainz, A., Scheidl, R., Computer Aided Design and Optimization of a Test Rig for Magneto-Rheological Fluid Behaviour, *Conference Proceedings for the First International Conference on Computational Methods, in Fluid Power Technology*, Stecki, Jacek S (Editor), Fluid Power Net Publications, ISBN 0-9578574-1-1, November 26-28, 2003, Melbourne, Australia.
- (2) Winkler, B., Manhartgruber, B., Scheidl, R., A Visco-Elasto-Plastic Material Law for Magneto-Rheological Liquids, *2nd International Workshop on Computer Software for Design, Analysis and Control of Fluid Power Systems*, September 5-7, 2001, Ostrava-Malenovice, Czech Republic, pp. 175-182.
- (3) Rosensweig, R.E., Ferrohydrodynamics, *Cambridge University Press*, Cambridge, London, New York, 1985.
- (4) Maxwell 2D V9.0, Ansoft Corporation, 4 Station Square, Pittsburgh, Pennsylvania, USA.
- (5) Abaqus Standard, Explicit, CAE / V6.4, Hibbit, Karlsson & Sorensen, Inc., 1080 Main Street, Pawtucket, Rhode Island, USA.
- (6) Deform 2D V8.0, Deform 3D V5.0, Deform Tools V4.1, Trademark of SFTC (Scientific Forming Technologies Corporation), 5038 Reed Road, Columbus, Ohio, USA.
- (7) Femlab 3.0, COMSOL, Inc., 8 New England Executive Park Suite 310 Burlington, MA 01803, United Kingdom.
- (8) Zienkiewicz, O.C., Taylor, R.L., The Finite Element Method, Vol. 1-3, Butterworth, Heinemann, 5th edition, 2000. USA.
- (9) Boer, R. de, Ehlers, W., Kowalski, S., Plischka, J., Porous Media (a survey of different approaches), *Forschungsbericht aus dem Fachbereich Bauwesen, Universität Essen*, Juli 1991.
- (10) Boer, R. de, Lade, P.V., Towards a general plasticity theory for empty and saturated porous solids, *Forschungsbericht aus dem Fachbereich Bauwesen, Universität Essen*, Juli 1991.
- (11) Boer, R. de, *Theory of Porous Media, Highlights in the historical development and current state*, Springer, Berlin, 2000.
- (12) Drucker, D.C., Prager, W., Soil Mechanics and Plastic Analysis of Limit Design, *Quart. Applied Mathematics*, Vol. 10, No.2, pp.157-165, 1952.
- (13) Subia, S.R., Ingber, M.S., Mondy, L.A., Altobelli, S.A., Graham, A.L., Modelling of concentrated suspensions using a continuum constitutive equation, *J. Fluid Mech.*, Vol. 373, pp. 193-219, 1998.
- (14) Gstoettenbauer, N, Kainz, A, Manhartgruber, B, Scheidl, R, Experimental and Numerical Investigation of the Squeeze Mode of Magneto-Rheological Fluids, *Third European Conference on Structural Control, 3ECSC*, 12-15 July 2004, Vienna University of Technology, Vienna, Austria

Vehicle systems

An adaptable hydraulic system for tractors

T FEDDE, T LANG and H-H HARMS

Institute of Agricultural Machinery and Fluid Power, Technical University of Brunswick, Germany

ABSTRACT

Hydraulic systems of modern tractors have to provide the energy supply of several functions regarding comfort, general operation and working applications. Due to the increasing variety of accessory equipment, the supplying hydraulic system of the tractor has to fulfil several ambitious requirements.

Current tractor hydraulic systems are mostly implemented as Load Sensing systems. The permanent increase in functional demands amplifies the conflict of the objectives dynamic behaviour and efficiency of the Load Sensing system.

A new research project at the Institute of Agricultural Machinery and Fluid Power, supported by the DFG (Deutsche Forschungsgemeinschaft), deals with the development and investigation of an adaptable hydraulic system for tractors. The new system is based on an electronically controlled variable displacement pump in combination with an electronically activated proportional valve group. The system allows several strategies to adapt to the special characteristics of the actuators and the demands of the process.

1. INTRODUCTION

The hydraulic system of tractors permits a wide variety of functions regarding comfort, general operation and working applications, as shown in figure 1. The actual technical standard of tractor hydraulics has been based on the propulsion system of the three-point-hitch and the appropriate control system for over 70 years. Today a lot of additional functions are introduced into agricultural machinery. Actual developments are mainly enabled by the use of electronically activated valves.

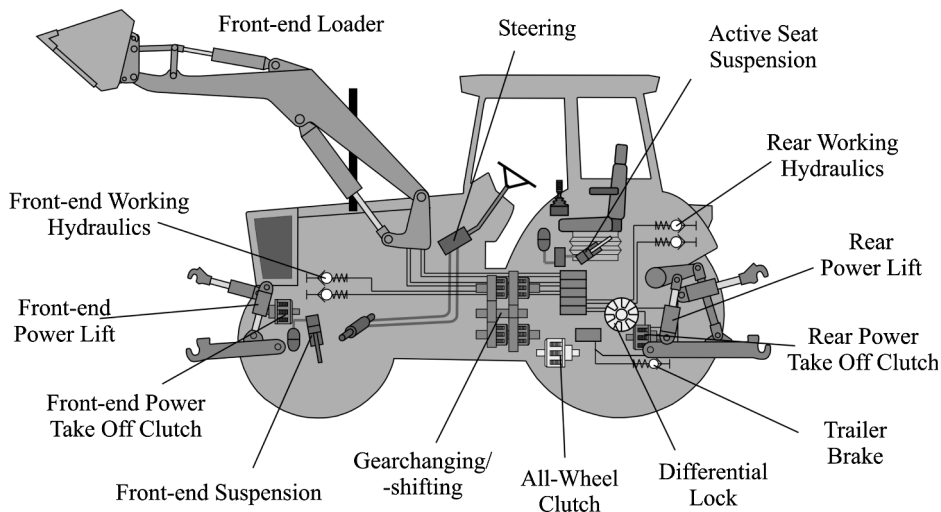


Figure 1: Functionality of a typical hydraulic system for tractors

The possibilities to control a drive system by electronically activated valves are the key for the implementation of automated functions, e.g. a closed loop speed control for pneumatic conveyors or other closed loop control systems. Load Sensing systems prevail as the tractor's hydraulic system. By realising automation with the aid of state-of-the-art electro-hydraulic valve technology two main problems occur:

- When movements have to be fulfilled with high accelerations, the Load Sensing system limits this due to the sensitivity of oscillations. It is possible to give the conventional Load Sensing more speed, but by doing that a loss of damping has to be accepted. As a consequence the system can become unstable, particularly when the inertias of driven masses are large.
- The Load Sensing principle relies on the control of the pressure drop at the metering orifice, which is dedicated to the actuated consumer under highest load. Typical pressure drops are in the range of 2 MPa. In relation to the nominal pressure of 20 MPa the system efficiency can not achieve more than 90 %. The pressure drop at the normally used quick couplings decreases the efficiency again. This can cause temperature problems when high duty cycles occur, e.g. at continuously activated drives.

2. CLASSIFICATION OF TYPICAL HYDRAULIC CONSUMERS

In order to solve the present problems and to extend the functionality a systematic consideration of the actual and future tasks of the working hydraulics of tractors has to be made. The actual situation and consequential trends concerning the working hydraulic of the tractor can be described as follows:

- Simple, manual controlled functions and partially switch on/off functions, e.g. dumping or swinging out implements, are actually the most common hydraulic functions. This will probably be one of the most common use in the future.
- Manually controlled accessory equipment for handling, e.g. front-end loaders for forage and other material, are the most ambitious hydraulic consumers at present. When joystick controlled actuators are used, the operator expects a high quality of the drive system if fast as well as sensitive motions have to be carried out.
- The functionality of sensors and micro controllers, suitable for mobile hydraulics, gets higher whereas prices are falling. This leads to an expanding use of automated functions. For example, within the last few years GPS based automated steering systems for agricultural vehicles captured the market. [1, 2].
- Tractors with multi-dimensionally handling systems for the accessory equipment have been developed and investigated in the field of research. In particular the dynamic behaviour of the Load Sensing system limits the performance of the systems [3, 4].
- Productivity and size of agricultural machinery are increasing. A better adaptation of the processes to the process conditions, e.g. by speed regulations, can be useful [2]. For this electronically activated proportional valves are predestined, but the efficiency of the Load Sensing is insufficient. Typical tractor hydraulic systems don't have enough capacity to ensure cooling for the total energy losses at continuous operation.

To realise an adaptable hydraulic system, a classification of the prospective hydraulic consumers and their main requirements has to be carried out. Figure 2 shows a classification of the hydraulic consumers and some typical examples. The main requirements and the estimated power conditions are shown in the figure. Due to the properties of the working process and the characteristic of the consumer (actuator) several requirements are important.

It is evident, that different hydrostatic consumers introduce different demands on the tractor hydraulic system.




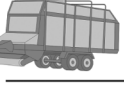

Consumer characteristics	Main requirements	Power conditions
 <p>Closed loop controlled intermittently used actuators <small>Source: John-Deere</small></p>	<ul style="list-style-type: none"> • High dynamics • Proportional behaviour 	<ul style="list-style-type: none"> • Three point hitch: light up to high power, up to 60 cycles per hour
 <p>Manual controlled intermittently used actuators</p>	<ul style="list-style-type: none"> • Proportional behaviour • Sensitivity • Smoothness 	<ul style="list-style-type: none"> • Front-end Loader: medium up to high power, about 45 cycles per hour
 <p>Simple manual controlled intermittently used actuators</p>	<ul style="list-style-type: none"> • Robustness 	<ul style="list-style-type: none"> • Tipping: Light up to high power, seldom in use (about 15 cycles per hour)
 <p>Ordered pressure or flow input</p>	<ul style="list-style-type: none"> • Configuration as: constant flow, constant pressure or Load-Sensing 	<ul style="list-style-type: none"> • Medium up to high power, continuous at work, partly stand-by on ride
 <p>Open or closed loop controlled steadily used actuators <small>Source: Bosch Rexroth</small></p>	<ul style="list-style-type: none"> • Strictly no flow fluctuations, e.g. influence of hydraulic steering 	<ul style="list-style-type: none"> • Medium up to high power, continuous at work, partly stand-by on ride

Figure 2: Simple classification and estimated power conditions of the hydraulic consumers

3. ADAPTIVE HYDRAULIC SYSTEM

The desired functionalities of the adaptation are the availability of high dynamics for automated multi-dimensional handling systems and an optimal efficiency at continuous driven consumers. The basic devices of the new system are an electro-proportional adjustable variable displacement pump and electronically activated proportional valves. These components allow the regulation of the pump corresponding to the summated flow demanded by the opening of the proportional valves. Several publications have been published on this topic already, e.g. [5, 6 and 7].

The adaptive hydraulic system for tractors consists of four main parts:

- Variable displacement pump with a regulator for the electro-proportional adjustment of the swash-plate angle and a pressure regulator, limiting the pump pressure up to 20 MPa. A conventionally flow controller is mounted additionally to the pump.
- Electronically actuated proportional valve group with primary arranged pressure compensators.
- Open-Center pressure compensator, acting as a bypass and regulating the pump pressure according to the Load Sensing principle.
- Consumers as single or double acting rotational and translational actuators

Figure 3 shows a schematic hydraulic circuit of the system, equipped with two proportional valves. The control strategy works with the flow commands of the operator (given by joystick or software) and needs information on the pump speed, the pump pressure and the temperature of the oil. The pump speed is required to calculate the swash plate angle for a flow summation system. With the information of the pump pressure, a power- or torque-limitation of the system is realised. This is useful for the integration into a tractor's management system. In one direction the hydraulic system can ask for a higher pump speed or enable a lower pump speed and in the other direction it is possible to give the hydraulic system a limitation of the maximum power or the maximum pump torque. The oil temperature control affects the system strategy and can also limit the maximum output power of the hydraulic system in case of overheating. A load-independent behaviour is fulfilled by individual pressure compensators. If the pump shows saturation, the valve control can accordingly decrease the opening of the activated valves, similarly for each valve or by a pre-defined priority of the consumer.

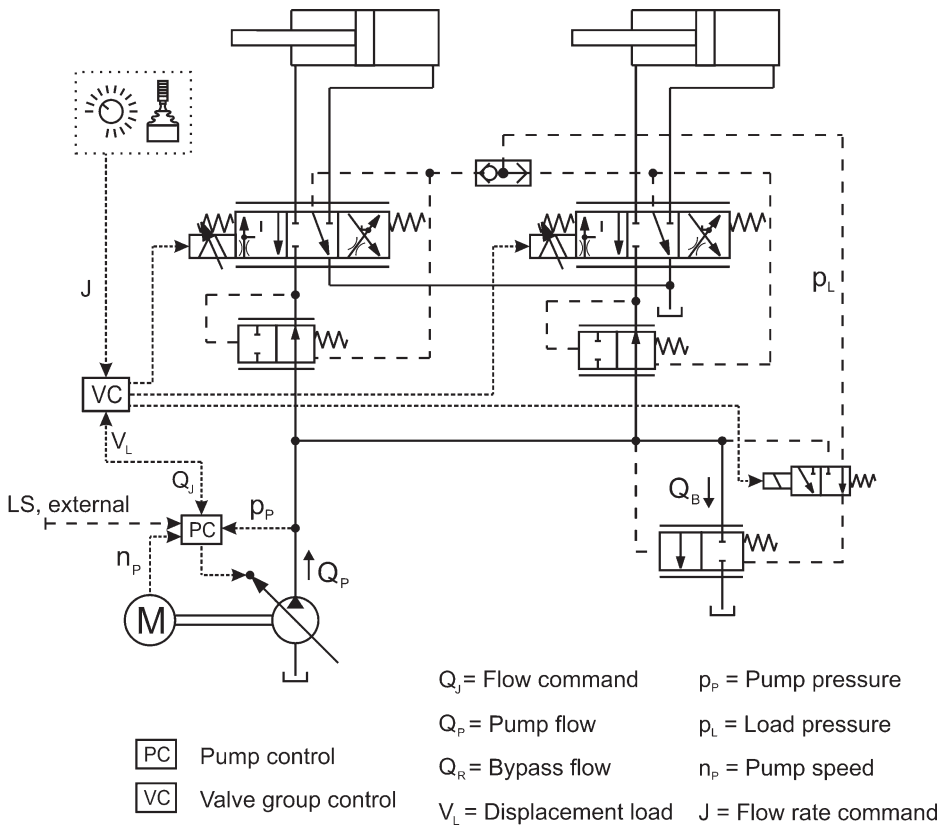


Figure 3: Hydraulic circuit of the adaptive hydraulic system

The system can be set up with the following strategies:

Table 1: System strategies of the adaptive tractor hydraulic system

System strategy	Valve Group Control	Pump Control	Bypass
Constant pressure	Direct actuation of single valves	hydraulic-mechanical pressure control device	Deactivated
Constant flow	Direct actuation of single valves	Pump at maximum displacement	Pressure control
Flow summation	Summation of flow rate commands plus dynamic overhead on demand	Pump flow rate by valve group control	Pressure control
Load Sensing	Deactivated	Hydraulic-mechanical flow rate control device	Deactivated

In flow summation mode it is possible to adjust an additional flow overhead. This overhead is required for the bypass to control the pump pressure. If a valve is shutting down faster than the pump displacement decreases, the bypass makes way for the temporary surplus pump flow. The flow overhead also ensures the balancing of flow fluctuations, caused by inner leakages and the valve actuations. Figure 4 shows a measured step response of the flow summation system with a stand-by flow of 20 l/min and a flow overhead of about 10 l/min. The cylinder velocity is increasing very straight to the desired value within a time 300 ms after activation.

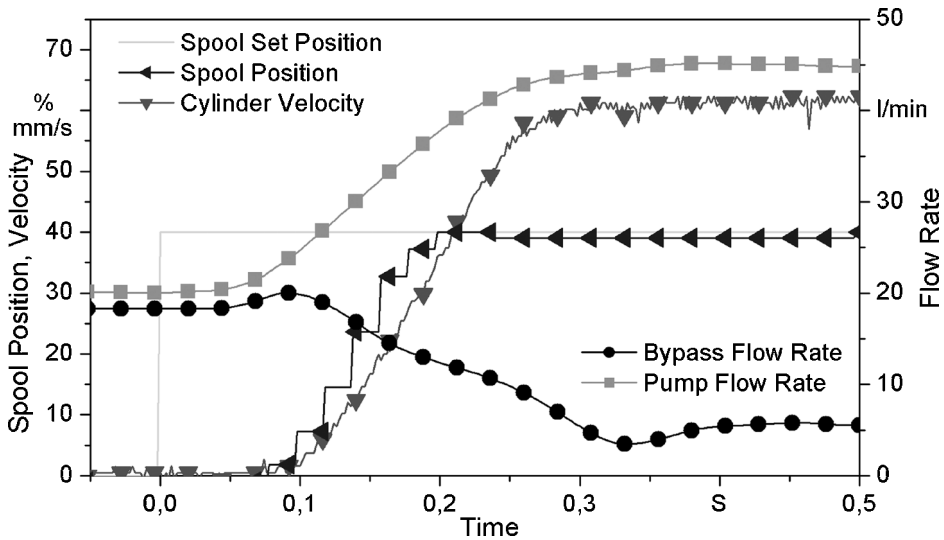


Figure 4: Measured step response of the flow summation system

If the flow overhead is set below zero, the effect of undersupplying the valve group can be used for an increase of system efficiency. In this case the bypass closes because the pump pressure decreases to the highest load pressure. This introduces a lower pressure drop at the valve with the highest loaded consumer. If a single valve is activated, a significant increase in the system efficiency is possible.

If a consumer is blocked, the pressure of the consumer increases. The bypass flow raises the pump pressure until the pressure control device of the pump cuts the delivery flow of the pump by reducing the swash plate angle. As a result the system changes to a constant pressure system.

A conventional Load Sensing mode is also important because there are several implements with closed-center Load Sensing valve groups on the market. It is essential that a new tractor hydraulic system can deal with such machines.

4. EXPERIMENTAL PLANT

Table 2 shows the technical data of the stationary experimental plant.

Component	Technical data
Electrical drive	45 kW asynchronous motor, driven by frequency converter
Variable displacement pump	Brueninghaus A10 VNO45EK, Variable displacement pump, 45 cm ³ , equipped with sensors for pump speed and torque
Valve group	<ul style="list-style-type: none"> • Sauer-Danfoss PVG 32, 100 l/min spools, electronically activated • Open-Center bypass with pressure compensator
Consumer	<ul style="list-style-type: none"> • Stoll HD 40 front-end loader, Ø 80/56 mm lifting and Ø 80/50 mm tilting cylinders with integrated MTS position and velocity sensors (magnetostrictive principle) • 63 cm³ fixed displacement motor with mechanical load
Control	dSPACE measurement and development package

5. SIMULATION

The control strategies have been developed and investigated by simulations. Models of the systems have been developed and investigated with the hydraulic simulation tool AMESim. The components have been modelled with the following characteristics:

Variable displacement pump

- Swash plate adjusting piston with reduced swash plate inertia mass
- Reduced activation spring forces and internal reaction forces at swash plate
- Hydraulic-mechanical and volumetric pump efficiency
- Electro proportional swash plate control device
- Pressure control device
- Flow control device

Valve group

- Electronically activated proportional valves (mechanical PT_2 -element and linearised flow equation)
- Individual pressure compensators for every valve
- Open-Center bypass

Connections

- Pipes with compressibility and resistance

Load

- Translational and rotational hydraulic consumers

The simulations show problems with the system behaviour in relation to the individual pressure compensators, which are optimally adjusted to the Load Sensing system. Especially in constant pressure mode problems occur and the following section gives more information about this. The investigations lead to the conclusion that an adaptation of the valve parameters has to be made with consideration of the actual hydraulic system strategy.

6. RESULTS

Practical results of the system have been determined using a stationary test rig. Figure 5 shows the measured step response of the four systems and allows a direct comparison of the various systems. The focus is on the dynamic behaviour of the systems. The measured spool position of the activated proportional valve shows a switchover of the main spool 50 ms

after the step is initiated at around 100 ms. The shown spool position is in constant pressure mode. The delay of the CAN-Bus transmitted spool position is 20 ms. Obviously the system is able to achieve the highest accelerations in constant pressure mode. But high oscillations follow the phase of high acceleration, probably caused by the dynamic behaviour of the pump and the pressure compensator. During the opening phase of the main spool, the firstly opened pressure compensator is not able to close simultaneously and thus the flow rate and the cylinder speed rises. This leads to a temporary decrease of the pump pressure. The simulation confirms the interaction of the pump and the compensator.

The Load Sensing shows a lower dynamic behaviour, but here the typical oscillations of the Load Sensing have to be recognized. By throttling the load pressure feedback the damping of the system is increased, but this slows down the system behaviour as well.

In comparison the constant flow system and also the flow summation system show the best system behaviour. The flow rate of the constant flow system is 60 l/min. The flow summation system works with a minimum flow rate of about 15 l/min and a flow rate overhead of 10 l/min.

The losses of the adjusted flow summation system are above the losses of the Load Sensing but much lower than the losses of the simple constant flow system. In both systems (CF and FS) the cylinder gets to the desired velocity with an harmonic characteristic.

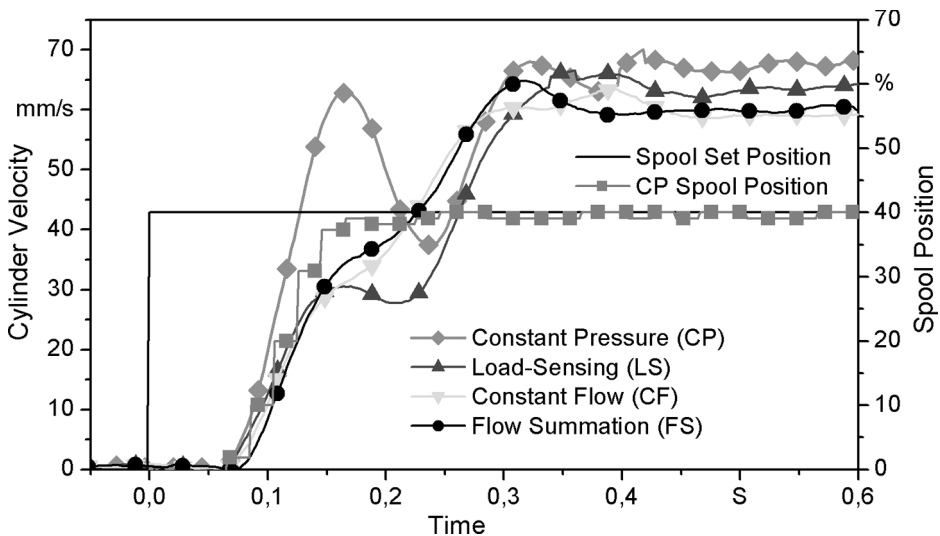


Figure 5: Measured step response of constant pressure, Load Sensing, constant flow and flow summation system

Measurements with a zero flow overhead show lower dynamics. The bypass is adjusted to regulate a pressure drop of 1,4 MPa between the load pressure and pump pressure. In comparison to the Load Sensing system the system efficiency is increased by 30%, if a Load Sensing pressure difference of 2 MPa is assumed. If the flow summation system is working

with a negative flow overhead, the pressure drop at the valve decreases and an additional increase of the system efficiency is achieved.

7. CONCLUSIONS AND OUTLOOK

The realised adaptable hydraulic system shows a significant improved dynamic behaviour in comparison to conventional Load Sensing systems. It is also possible to increase the system efficiency by the direct adjustment of the delivered pump flow. The system is configurable towards high dynamics or towards low energy losses.

One approach is to develop an automatic control for the optimal adjustment for the several hydraulic consumers. With the aid of intelligent electronics, the system makes the decision on how the system has to be configured in an optimal way. Another challenge is to realise the transitions of the system strategies. A context-sensitive help facility should allow the system to be configured to the different applications and consumers.

The next stage is to transfer the system to a real tractor. Here the practicability of the system and a user-friendly handling for the adaptable hydraulic system can be investigated.

REFERENCES

- [1] N N: 16 Parallelfahrssysteme im Überblick.
dlz agrarmagazin 56, february 2005, Deutscher Landwirtschaftsverlag GmbH
munich
- [2] G. Keuper: Zusatznutzen hydraulischer Antriebe für die kontrollierte
Ausbringung von Mineraldünger.
O + P – Öldruck und Pneumatik 45, No. 2, p. 92 - 97
- [3] T. Lang: Mechatronik für mobile Arbeitsmaschinen am
Beispiel eines Dreipunktkrafthebers.
Dissertation, TU Braunschweig, Shaker Verlag, Aachen 2002.
- [4] S. Fedotov, G. Bernhard and R. Rudnik: Prototype and Control of a New
Implement Interface with Six Degrees of Freedom. In Conference
Agricultural Engineering 2002 Halle/Saale, p. 99-104.
- [5] B. Zähe: Energiesparende Schaltungen hydraulischer Antriebe mit
veränderlichem Versorgungsdruck und ihre Regelung.
Dissertation, RWTH Aachen, Aachen 1993.
- [6] H. Joengebloed, D. van Büren, U. Völkel and C. Jabs: Energy-Saving Valve
System for Mobile Hydraulic Applications – Load Control System (LCS).
4th International Fluid Power Conference, Dresden 2004, p. 117 – 128.
- [7] M. Djurovic and S. Helduser: New control strategies for electrohydraulic
Load Sensing.
In proceedings of the Bath Workshop on Power Transmission and Motion
Control (PTMC 2004), Bath, p. 201 – 210.

Design of a Hybrid Vehicle Powertrain using an Inverse Methodology

E. Bideaux^{1,*}, J. Laffite¹, A. Derkaoui¹, W. Marquis-Favre¹, S. Scavarda¹, and F. Guillemard²

¹Laboratoire d'Automatique Industrielle, INSA de Lyon, France

*INSA de Lyon, 25 av. J. Capelle, F-69621 Villeurbanne Cedex email: eric.bideaux@insa-lyon.fr, web: <http://www-lai.insa-lyon.fr>

²Mechatronic Team, DRIA (Division of Research and Automobile Innovation), PSA Peugeot Citroën, France

ABSTRACT

The development of hybrid vehicles is nowadays a new challenge for the automotive industry since it appears a relevant solution to reach the next ten years pollution standards. However several commercialized vehicles are yet available, the new advantages which could be achieved by hybrid architectures of powertrains are generally difficult to study. The purpose of this paper is to introduce an inverse approach that allows to define in a first step the admissible architecture of the powertrain according to the objectives of the design, and in a second step to compare different solutions using the same references in a multi-objective context. The proposed approach is here detailed considering the study of the requirements for the powertrain architecture of a hybrid vehicle in order to achieve some consumption criteria on a standard road cycle.

Keywords: Hybrid vehicles, Bond Graph, Inverse method, Design, Power transmission, Powertrain.

1 INTRODUCTION

Hybrid vehicle concepts allow completely new powertrain architectures to be imagined and evaluated. Conventional powertrains have been extensively studied (1–5), and their performances have been improved in many ways using new technologies and control principles. However, these conventional architectures are limited due to the use of a single energy source and motor. Each technology presents some advantages over the other ones, but the requirements of the next generation vehicles such as autonomy, dynamic performance, polluting particle emission, etc., seem difficult to reach using a single

technology. Combining several energy sources and motors provides an interesting approach for solving the complex compromise imposed to the automotive industry (6). In this context, the global control strategy is obviously an essential aspect to be considered. Furthermore, because of the number of possible hybrid architectures and their complexity, it seems important to propose tools for rapidly analyzing, sizing and comparing the different designs.

Since the initial data of a new design are the specifications and not a specific architecture of the system, we develop here a set of tools based on inverse approaches for analyzing, sizing and comparing the different solutions being given a set of design specifications. Contrary to other methods such as simulation and optimization, for which an iterative procedure is required in order to reach results approaching the design specifications, inverse methods enable the final results to be obtained from a single computation or simulation.

In a first step, the proposed approach applies, at a functional system level, the concept of power lines introduced by Wu and Youcef-Toumi (7) in a bond graph model (8). Since each specifications expressing the different objectives on the system to design can be related to energetic degrees of freedom in a elementary structure, it is possible to determine an architecture for the powertrain, which should allow all the objectives to be achieved, by defining a set of independent power lines. To reach this condition, we propose here to modify the architecture by adding power modulating components or drives, or by enabling the control of some components in the system. As the consistency of the objectives can also be checked during the procedure, it constitutes a straightforward approach for new design projects.

In a second step, when the architecture of the powertrain has been chosen, the bicausality concept introduced by Gawthrop (9, 10) can be used to determine the inverse model and the regularity required for the specifications. The inverse model is usually used to verify the adequacy of a designed system to the desired objectives, to obtain new specifications for some components in the system, and also to determine the open loop inputs (11, 12). Another useful application of inverse approaches consists in quickly comparing different potential solutions. The advantage over other techniques such as optimization is that the comparison references stay the same for all the potential solutions since the design specifications, used as the inputs in the inverse model, are verified by definition. Here, using the previously determined powertrain architecture, different control strategies for the powertrain of an hybrid vehicle are compared in terms the required size for the engine and an additional electrical drive (13).

Although the approach is here developed in the context of hybrid vehicles, the choice of the right architecture and the comparison of different designs considering simultaneously several objectives are common problems in power transmission and mechatronic systems. Therefore, the inverse methodology proposed in this paper can be extended to many other design problems.

2 POWER LINES AND THEIR USES IN DESIGN PROBLEM

Power lines are not especially a bond graph concept, as it defines the existence of a path to provide energy from a power source to an output, but the bond graph representation is interesting because these lines appear graphically on the model representation, where they

are a set of consecutive power bonds between a source (or an energy storage element) and an output. A system output being a function of the model independent state variables, the previous definition can be expressed as the existence of a path to provide energy from a power source to an independent energy variable related to the considered output. Obviously, for changing the state of the system, it is necessary to change its energy state, and consequently to modify the energy stored in at least one energy storage. Furthermore, a necessary condition that enables the control of the power transfer from the source to the storage element is the existence of modulated element in a sub-system connected to the considered power line. These previous remarks lead to define a two types of power lines : power supply lines and power modulation lines.

Definition 1 *A power supply line is a set of successive power bonds between a energy source or an energy storage element and an energy storage element port corresponding to the energy variable associated to an output*

Definition 2 *A power modulation line is a set of successive power bonds between a modulated element and an energy storage element port corresponding to the energy variable associated to an output*

Proposition 1 *A necessary condition for controlling an output is the existence of a power supply line and of a power modulation line converging towards the same energy storage element port corresponding to the energy variable associated to the output.*

Proposition 2 *A necessary condition for controlling a set of outputs is the existence of a set of independent power modulation lines between the inputs and the outputs of the system, each of them being associated to at least one power supply line.*

Proof 1 *R. Ngwompo et al. (14) have shown that a necessary condition for structural model inversion is the existence of a set of independent input/output power lines. This means that this condition is necessary to express the inputs as a functions of some states and of the outputs and their derivatives. Obviously, this is the same as determining the open loop control for given specifications on the outputs.*

In the case of a multi-objective problem, it is now possible to extract structural rules in order to achieve a design problem. Firstly, for each independent specification imposed by the new system design, a power supply line and an associated power modulation line has to be determined on the model. Secondly, the power modulation line has to be independent from the other power modulation lines associated to the other specifications. At the first design stage, it is then possible to use this condition as a design procedure and also, to keep in mind this condition when the consistency of the final architecture of the system is checked. Therefore, we propose here a procedure that aims at modifying the architecture by adding power modulation components or by enabling the control of the transmitted power in some components in order to define the power supply lines and of power modulation lines required to verify the necessary inversion condition.

The procedure can be summarized by the following steps:

- associate each design specification to an energy variable in the system and identify the corresponding ports of the energy storage element,

- add power modulation elements or enable some components to be controlled in order to define one power modulation line for each specification,
- check the association of each power modulation line with at least one power supply line,
- check the existence of a set of independent power modulation line in the designed system.

Obviously, using the previous procedure, several system architectures can be determined from the same design criteria. Each of them constitutes a potential solution structurally in adequation with the design criteria. Then, in the next step, the sizing of each component in the system, the designer is quite sure to study only the admissible architectures.

3 FUNCTIONPROACH OF A HYBRID VEHICLE DESIGN

The previous procedure is now applied to the design of a vehicle powertrain. For this example, we assume that initial considerations have imposed the use of an engine, and have defined the load to be driven, that is to say the vehicle. Let us apply the proposed procedure to the design of a vehicle for which the design criteria is the following: the average fuel consumption for the engine is fixed to x_{ECE} (or x_{EUDC}) for the ECE¹ road cycle (or the EUDC² road cycle). Firstly, since the criteria relies on a specific road cycle, the trajectory of the vehicle is perfectly defined and consequently, the output corresponding to the longitudinal velocity V_{veh} of the vehicle is imposed. Secondly, in a first approach, it can be assumed that the fuel consumption of the engine is a function of its speed W_{eng} and of the delivered torque T_{eng} according to equation (1).

$$x_{eng} = f_{csn}(\omega_{eng}, T_{eng}) \quad (1)$$

If the average fuel consumption is fixed, this equation shows that the criteria introduces a constraint between the speed and the delivered torque. It means that if the trajectory to be followed by one of these variables is fixed, the other one will be a consequence of equation (1). Then, it can be concluded that either the engine speed or the engine supplied torque trajectory has to be defined in order to satisfy the consumption criteria. This first analysis of the design criteria leads to the conclusion that three outputs have to be considered in the system, each of them being associated to a trajectory imposed by the design criteria. These outputs are the longitudinal velocity, which is associated to the road cycle trajectory, both the speed and the supplied torque of the engine, which are associated to trajectories whose definition requires additional information. These two last trajectories can be deduced from a global control strategy of the powertrain for example.

It is interesting to remark that fractions of power lines can be defined locally at the component level. A fraction of power line is a set of successive power bond inside the component connecting a power or control input bond and an output power bond, defining therefore a fraction of a power supply line or a fraction of a power modulation line. Furthermore, at a functional level, it is still possible to identify fractions of power lines in a

¹ Economic Commission for Europe

² Extra-Urban Driving Cycle

component without the complete knowledge of the structure of the component. For example, if we consider a gearbox (Fig. 1), it can be naturally assumed that this component presents at least a fraction of a power supply line and a fraction of a power modulation line. The power bonds linking the input and the output power bonds define a fraction of a power supply line, and the power bonds linking the modulated transformer and the output power bond or the input power bond define two distinct fraction of two distinct power modulation lines.

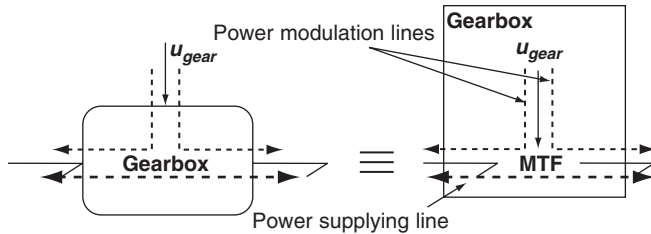


Figure 1: Power lines in a gearbox

In order to define a correct architecture, it is then essential to identify the fraction of power lines in the known parts of the system. Considering an elementary modelling approach, the bond graph models of the components known in the system, that is to say the engine and the vehicle, can be represented as shown on figure 2 and 3. The engine is represented by a modulated source corresponding to the maximum delivered torque $T_{max}(u_d)$ for a given control input u_d , a non linear dissipative element that characterizes the loss of torque $T_{loss}(w_{eng})$ according to the engine speed, and a kinetic energy storage representing the motor inertia J_{eng} . Since only a longitudinal displacements are considered in this case, the vehicle is only represented here by its mass M_{veh} and a dissipative phenomenon, representing the aerodynamic and rolling drag. The outputs of interest in the problem are represented by detectors. Figure 4 shows the word bond graph model, which is sufficient at the first design stage.

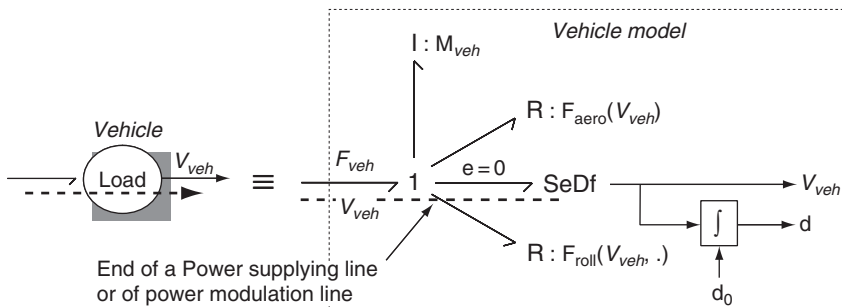


Figure 2: Power lines inside system load (vehicle) and elementary bond graph model

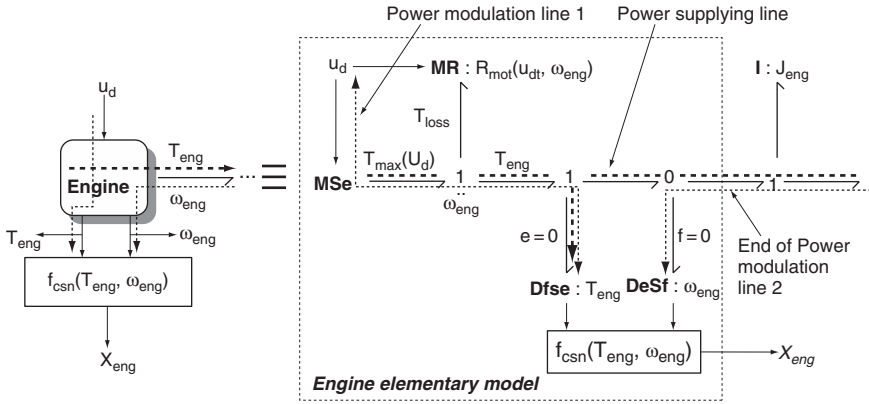


Figure 3: Power lines inside engine and elementary bond graph model

The balance between inputs and outputs in the known parts of the system shows that there are three specified outputs (V_{veh} , w_{eng} , T_{eng}) for only one control input (u_d), and one power supply line. According to proposition 2, a structural condition to achieve the design criteria is the existence, in this case, of a set of three independent power modulation lines in the system. The solution consists yet to add at least two components that enable the power modulation and define two additional power modulation lines. If we consider the model of the engine, it appears that one of the power line has necessarily to be considered inside this component in order to verify the independency of the power lines (Fig.3). The two other power lines have to be defined from the engine and the vehicle models towards the part of the system to be designed as shown on figure 4.

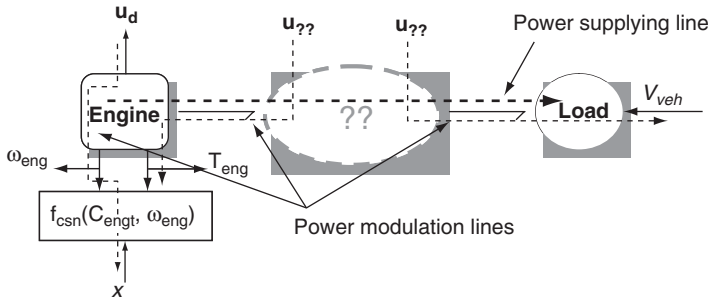


Figure 4: Initially known parts of the system and introduction of the design criteria

Several solutions are then possible. For example, an hydraulic transmission including a controlled displacement pump and a controlled displacement motor constitutes an admissible solution (figure 5); an other solution may be the use of a gearbox and of an electrical motor (figure 6). In both cases, due to the two additional control inputs, two additional power lines are defined on the model.

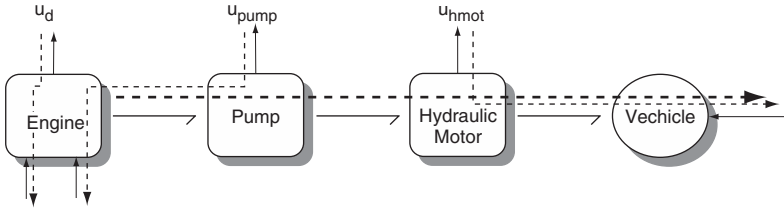


Figure 5: Solution to the design problem using an hydraulic transmission

In order to verify the structural conditions (Proposition 2), the independency of the three power lines have now to be checked. Although parts of power lines can be defined in each new components, this property can only be verified if the connection between the different components is known, that is to say the architecture of the system. For example, several architectures of the final system can be considered when a gearbox and an electrical motor are added. Firstly, the gearbox can be placed up or down the connection of the electrical motor on the powertrain (figure 6 and 7), but not between the junction J and the electrical motor because the two power lines are dependent in this case. Secondly, the type of connection (junction J) between the electrical motor and the powertrain can be essential in order to verify the independency of the power lines. Indeed, two cases can be suggested: a single axle hybrid vehicle (15) where the connection can be represented by a 1-junction (common flow), and a double axle hybrid vehicle with a differential, that is to say a 0-junction (common effort), connecting the electrical motor, the engine and the rest of the powertrain. Although both solutions are acceptable for the studied problem, in some cases this choice will directly allow to cancel the further study of one of the architecture.

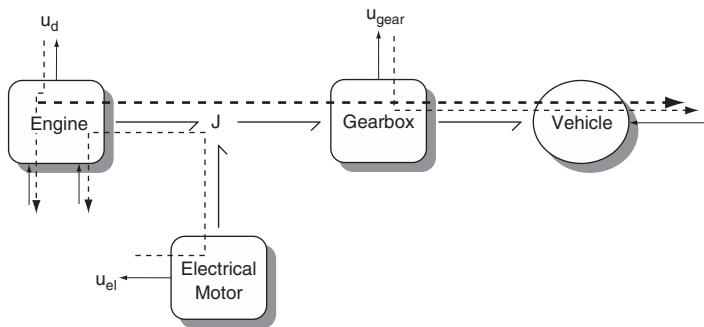


Figure 6: Solution to the design problem using an electrical motor and a gearbox

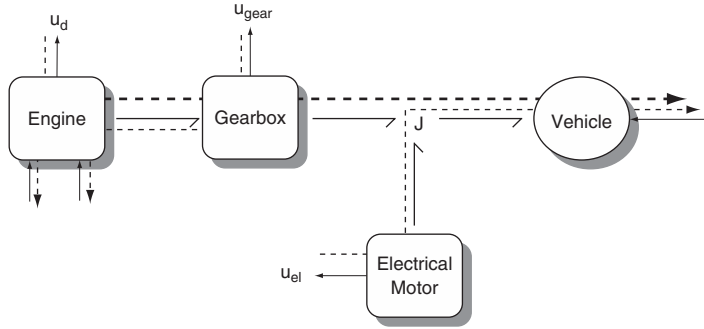


Figure 7: Potential architectures of the solution to the design problem

This first part shows that, at the first design stage, the use of acausal properties such as power lines presents advantages since it enables the architecture and the necessary components to be selected according to the design criteria. Complex multi-objective criteria may be applied, and only an elementary knowledge of the system model is required. This procedure constitutes therefore a pertinent approach, which can help the engineer in the early stages of any design project.

4 SIZING USING AN INVERSE MODEL

Following this first step, a second procedure that is still based on an inverse approach may complete the proposed method in order to determine the correct sizing of the new components in the designed system. An important part of the inversion problem has already been achieved as Proposition 2 is directly derived from the necessary condition for the existence of a structural inverse for a system modelled by bond graph. Indeed, using acausal and causal considerations, the sufficient conditions for the structural inversion of a system has been shown by Ngwompo et al. (11, 12, 14):

Proposition 3 *The inverse of a system exists if there is a single set of independent inputs/outputs power lines in the system.*

However, if several sets of independent inputs/outputs power lines can be determined in the system, a second condition is required:

Proposition 4 *If several sets of independent inputs/outputs power lines can be determined in the system, the inverse of a system exists if there is at least a set of disjoint inputs/outputs causal paths.*

In this last case, the set of shortest length has to be considered in order to obtain the maximum order inverse model. Thus, the sizing problem will simply depends on the knowledge of the data required for the simulation of the inverse model.

According to equation (2), a "direct" formulation requires the knowledge of the inputs and of the initial conditions for system simulation. However, in an "inverse" formulation (eq.3), it is necessary to provide the specifications associated to outputs, the initial conditions on the remaining state variables in the model, and the imposed inputs. The successive derivatives of the specifications, respectively of the remaining inputs, may also be needed until order p , respectively r .

$$\begin{cases} \frac{d}{dt}x = f(x, u) \\ y = g(x, u) \end{cases} \quad (2)$$

$$\begin{cases} \frac{d}{dt}x_{int} = f_{inv}(x_{int}, u_{spec}, \dots, u_{spec}^{(r)}, y_{spec}, \dots, y_{spec}^{(p)}) \\ [y_{dir}, u_{inv}]^T = g_{inv}(x_{int}, u_{spec}, \dots, u_{spec}^{(r)}, y_{spec}, \dots, y_{spec}^{(p)}) \end{cases} \quad (3)$$

The inverse approach is a natural procedure in system design and sizing, but usually its use is limited to a single objective criteria and to steady state considerations. It seems that there are mainly two reasons to this: first, a problem related to the numerical aspect of inversion since it introduces differentiations; second, a difficulty to manipulate the design criteria since they are usually not given in a right format for an inverse approach or are more well-suited for "direct" problems or optimization. The bond graph approach is here an interesting tool as it allows the considerations about the design specifications and their correct formulation to be taken into account without writing an equation. Furthermore, using causality and structural properties of the bond graph, the symbolic manipulation of the model equations is easier and leads to a minimum number of differentiations normally related to the outputs in a design context. Therefore, the step following the functional design of the system (section 2 and 3) consists in analyzing the design criteria in order to introduce the right specifications on the bond graph model according to the analysis the structural properties of the inverse model (model order, number of output differentiations, number of initial conditions, etc.)

Due to the fuzziness of the design criteria or the lack of some information, the design criteria usually have to be discussed, clarified, and completed. Several solutions are available to complete the design criteria in order to obtain the adequate data for the simulation of the inverse model:

- adding new criteria (but this might require to modify the system architecture),
- deducing new specifications from the design criteria,
- choosing specifications and control inputs corresponding to critical behavior.
- defining a control strategy in the system.

This is a very important step as the remaining inputs, the output specifications and the remaining initial conditions have to be consistent. It can be noticed that this can constitutes a problem by itself, especially for non linear model. It is essential to be careful when choosing or deducing the missing specifications in order to keep the consistency of the design problem. Finally, defining a control strategy in the system can appear a good solution since the control law will couple the known specifications to the missing ones; this is corresponding to integrate some part of the system global control in the design problem.

If the consistency of the design specifications with the remaining inputs and initial conditions has been achieved, the final inverse model of the system to be designed can be deduced from bicausality and causality assignments as described in Ngwompo et al. (11, 12, 14). Then, the simulation of the inverse model enables the designer to determine the missing open loop control variables and/or new specifications for the missing parts of the system (power sources, actuators, power modulating devices, etc.), to make a validation of the component choices taking into account the influence of the system dynamics and the energetic aspects, or to compare straightforwardly design options such as control strategies, component technologies, etc. An advantage of the inverse approach over other methods is that the design specifications are here directly verified since they are the inputs of the inverse model, therefore simplifying the comparison of the solutions, the choice and the validation of the system components.

5 COMPARING CONTROL STRATEGY IN HYBRID VEHICLE

The design criteria of the example have already been analyzed, and it has been shown that the formulation of the specifications presents some fuzzy points like the evolution of the engine power variables (W_{eng} , T_{eng}). According to the previous section, one of these variables can be specified considering for example the engine efficiency or a critical case, but it can also be determined by using a control strategy that defines an assistance degree (or hybridization degree) with regard to the additional actuator, that is to say the electrical motor.

The assistance degree (eq. 4) is usually defined as the ratio α_{assel} of the torque T_{el} supplied by the additional actuator and the torque T_{veh} applied to the load (the vehicle in this case), then a complementary function α_{assth} can be determined relating the torque T_{eng} supplied by the engine and the torque T_{veh} applied to the load, as expressed by equation (5).

$$\alpha_{ass_d} = T_{el} / T_{veh} \quad (4)$$

$$\alpha_{ass_{eng}} = T_{eng} / T_{veh} \quad (5)$$

$$\alpha_{ass_{eng}} = \frac{T_{eng}}{T_{veh}} = f_{ass}(V_{veh}) \Rightarrow T_{eng} = f_{ass}(V_{veh}) \cdot T_{veh} \quad (6)$$

In a global control strategy of a hybrid vehicle, it seems interesting to control this ratio according to the vehicle velocity (eq.6) and acceleration in order to improve the vehicle performances and polluting particle emission. Consequently, the engine torque T_{eng} can be deduced (eq. 6) at any time from the computation of the torque T_{veh} supplied to the vehicle and the specification on the assistance ratio $\alpha_{ass_{eng}}$ according to the vehicle velocity V_{veh} .

$$T_{eng} = f_{eng}(u_d, \omega_{veh}) \Rightarrow u_d = f_{eng}^{-1}(T_{eng}, \omega_{veh}) \quad (7)$$

$$x_{eng} = f_{csn}(\omega_{veh}, T_{eng}) \Rightarrow \omega_{eng} = f_{csn}^{-1}(x_{eng}, T_{eng}) \quad (8)$$

Assuming that the engine has been chosen and using its characteristics, it is possible in a "direct" formulation to determine firstly the engine torque T_{eng} as a function f_{eng} of the engine speed W_{eng} and of the control input U_d (eq. 7), and secondly, the fuel x_{eng}

consumption as a function of the engine torque T_{eng} and the engine speed W_{eng} (eq. 8). Then, if the reciprocal function for f_{csn} exists, the engine speed W_{eng} may be deduced from the engine torque T_{eng} and the specified consumption x_{eng} (eq. 8), and similarly, the engine control from the engine speed W_{eng} and torque T_{eng} (eq. 7).

The design problem has now a complete formulation, two specifications being imposed from the design criteria and the third one being deduced from the other ones and from a power variable in the system. Since the functional design of the design (section 3) has defined three power lines linking the inputs to the outputs and since it can be observed that they are corresponding to the only set of independent power lines, the structural inversion is verified. Considering for the model an ideal global transmission ratio including all the movement transformations due to gears, differentials, wheels in the powertrain, it is possible to associate this phenomena to the controlled gearbox and to represent the whole transformation ratio by a modulated transformer. Because a manual or automatic gearbox would introduce a discrete control law, it is necessary to consider here a CVT (Continuously Variable Transmission).

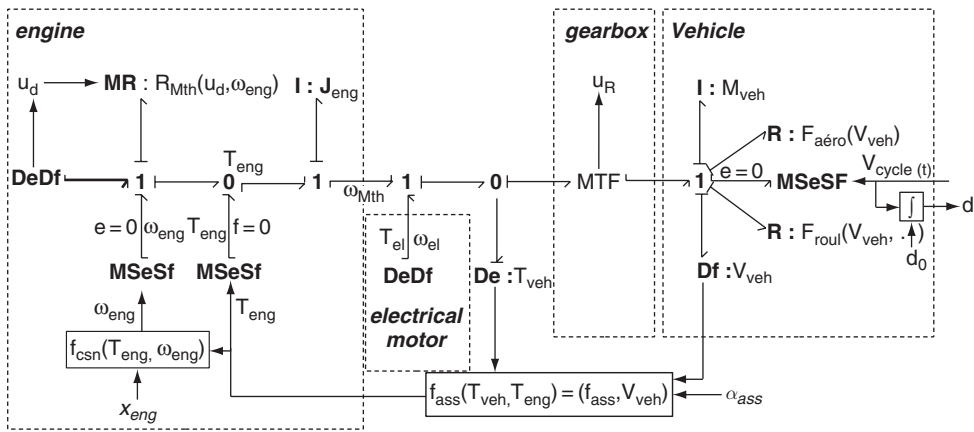


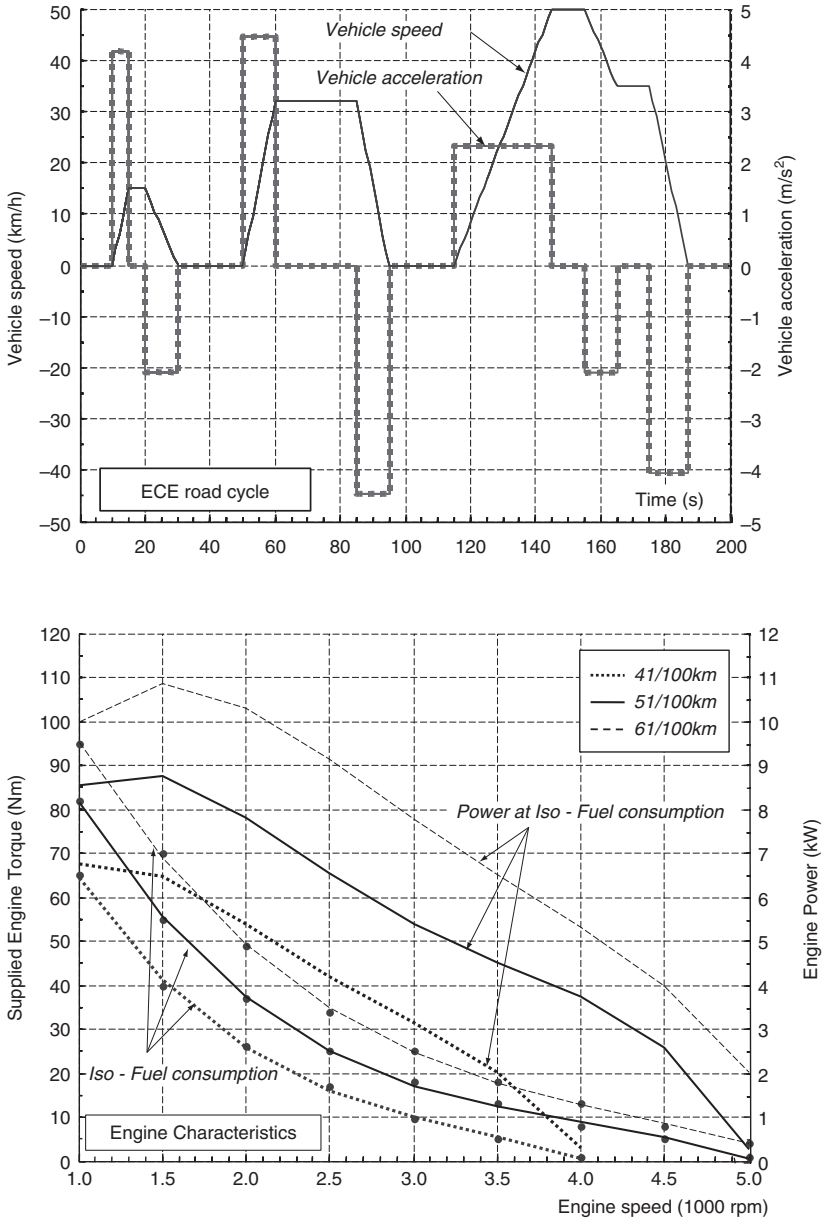
Figure 8: Inverse bond graph model for the proposed design criteria

The inverse bond graph model (Fig. 8) is finally determined by substituting the detectors by double sources and the sources by double detectors, assigning the bicausality along the power lines from outputs to inputs, and finally completing the causal assignment by a preferential integral causality. From this causal assignment and from the study of the causal loops in the inverse model, several properties can be deduced:

- all the storage elements are in derivative causality, and accordingly, the inputs are functions of the outputs and their successive derivative (this property is corresponding to the flatness of the model),
- the orders of the causal paths are one and zero, and consequently the specifications have to be at least once differentiable,

- the inverse model presents an algebraic loop (implicit form), which has been introduced by the control strategy,
- the inverse model is then a set of two algebraic and one implicit equations.

Using the ECE road cycle and fixing the fuel consumption to $x_{eng} = 5l/100 \text{ km}$, it is now possible to compare different control strategies (Fig. 9).



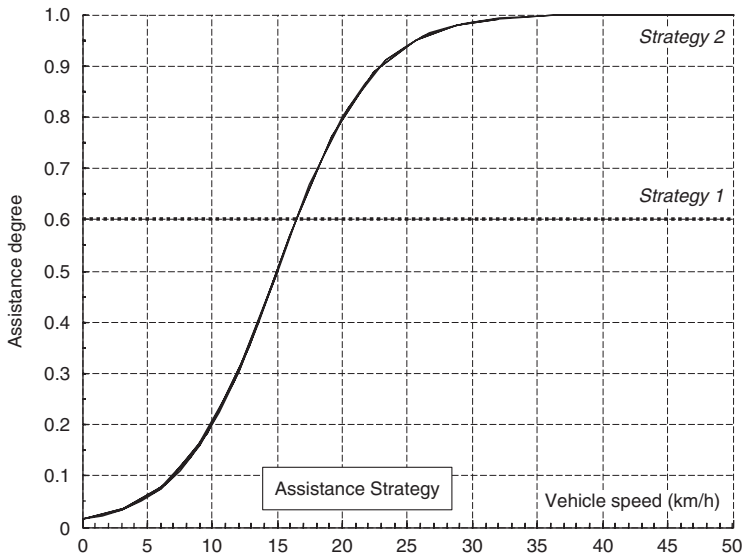


Figure 9: Design specifications: ECE road cycle, Engine characteristics and Control strategies

Figure 10 shows some results of the inverse model simulation. Firstly, the power which has to be supplied respectively by the engine and by the electrical motor are computed in both cases. It can be noticed that negative power are corresponding here to slowing down phases, and can be considered as potentially retrievable energy. Therefore, if a reversible electrical motor is used, the control strategy can be adjusted in order to balance the electrical motor energy consumption on the studied road cycle. The power requirement for the electrical motor is near to be twice for strategy 1 than the one for strategy 2. While strategy 1 is corresponding to a constant assistance, strategy 2 tries to express that, for pollution reason, it is more efficient at low vehicle speed to use the electrical motor than the engine. This implies naturally a smaller sizing of the electrical drive (Stop & Go strategy).

The open loop control of the engine and of the CVT are also obtained from the simulation. Here the global transmission ratio is given in an user friendly unit, which is the equivalent vehicle speed for an engine speed of 1000 rpm³. By this way, the computed global transmission ratio can be compared to any other vehicle transmission and especially to manual gearbox (1st, 2nd and 3rd gears in this case). In both cases, the simulation of the inverse model shows if the computed input variables are in physical limits. These results can be used to check for example if the engine is not undersized for the design criteria. In the case of strategy 2, it appears clearly that the maximum power (and torque) is reached for the specified fuel consumption.

Although the considered model is corresponding to an elementary approach, the obtained results are relevant in the early stages of the powertrain design. From a single simulation, the minimum power of the electrical drive is determined whatever its control is (new specifications for the electrical drive), the validation of the engine choice is realized, and the open loop control laws for the engine and the CVT are obtained. Furthermore, if the assistance strategy is changed, the comparison criteria (engine consumption and ECE road cycle) are still exactly verified, which is generally not achievable with "direct" approaches or optimization. The comparison is then very consistent.

³ 1 kmh⁻¹/1000 rpm is 2.652 10⁻³ ms⁻¹/rads⁻¹

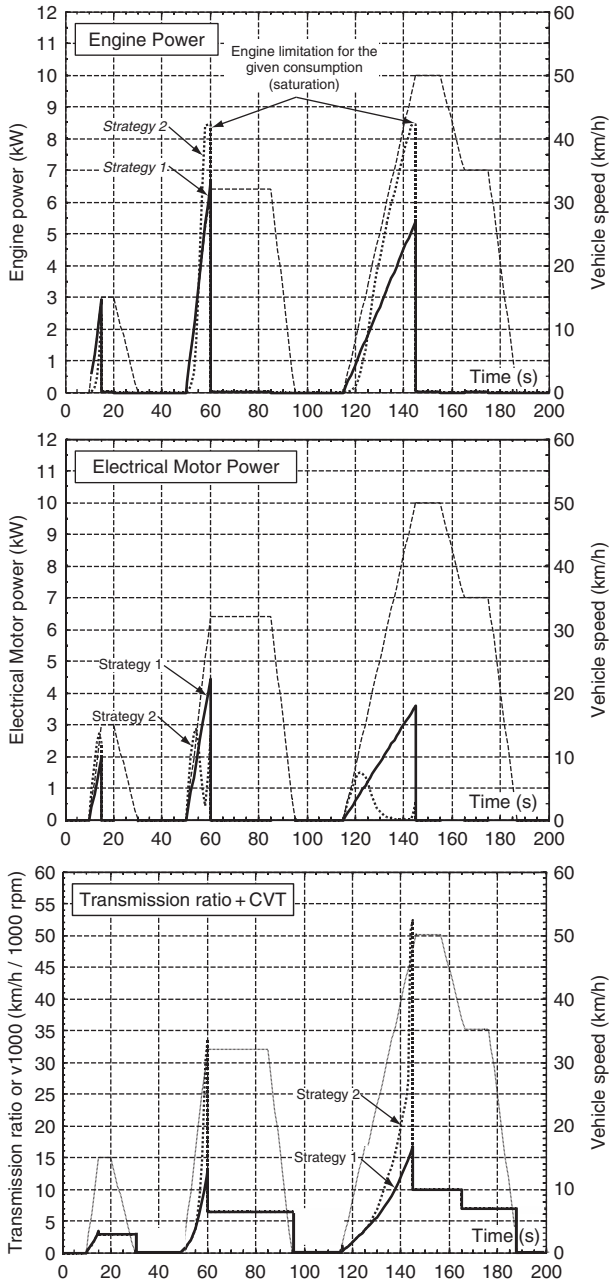


Figure 10: Engine and Electrical motor power requirements and global transmission ratio for each control strategy

6 CONCLUSION

The proposed inverse approach gives another point of view and help concerning the technical aspect of the design, however other aspects such as cost and reliability are evidently essential in the new product design. It is primordial to note that the actual development of the simulation tools are in agreement with the requirement of inverse methodology since it aims at introducing robust numerical algebraic-differential solvers and algorithms allowing symbolic manipulations of a model equations before the simulation.

In the paper, it has been shown in a first step how the inverse approach can be applied to determine the correct architecture of a system according to the design criteria. A procedure for the system architecture design has been proposed and illustrated in an example. In a second step, the sizing of the designed system has been achieved still using the inverse methodology. The advantages of this approach for the validation and the choice of components, the specification of additional components, and the comparison of the different solutions have been pointed out especially for multi-objective design problems. The complete design of the powertrain for a hybrid vehicle has shown the potentiality of the proposed approach in industrial applications, even if there are non linearity in the system.

In conclusion, it is essential to point out that the proposed inverse methodology constitutes a complementary approach to "direct" model simulation and optimization at least in the early stage of the system design, which can be efficiently applied to structure the design thought process.

REFERENCES

- (1) Karnopp, D.C., and Rosenberg, R.C.: Application of Bond Graph Techniques to the study of vehicle drive line dynamics: *Journal of Basic Engineering Transaction, ASME*, 1970, Vol. 92 n°2, 1991, pp. 355-362.
- (2) Hrovat, D., Tobler, W.E., and Tsangarides, M.C.: Bond graph modeling of dominant dynamics of automotive powertrains: *ASME Winter Annual Meeting*, Miami, USA, nov. 1985, pp. 293-301.
- (3) Hrovat, D. and Tobler, W.E.: Bond graph modeling of automotive powertrains: *Journal of the Franklin Institute*, Vol. 328 n°5/6, 1991, pp. 623-662.
- (4) Gillespie, T.D.: Fundamentals of vehicle dynamics: *Society of Automotive Engineering, Inc.*: 1992, 495p.
- (5) Eriksson, L.: Simulation of vehicle in longitudinal motion with clutch lock and clutch release: *IFAC Workshop Advances in Automotive Control*: 2001, pp. 75-80.
- (6) Roverta, G., and Ravello, V.: Scenario and trends on hybrid propulsion technologies: *International Conference "Spart Ignition Engine: CO² Challenge"*: Venice, 2002, pp. 78-89.

- (7) Wu, S.-T., and Youcef-Toumi, K.: On relative degrees and zero dynamics from physical system modeling: *Journal of Dynamic Systems, Measurement, and control*, Vol. 117, june 1995, pp. 205-217.
- (8) Karnopp, D.C., Margolis, D.L., and Rosenberg, R.C.: *System Dynamics: A Unified Approach*: New York, John Wiley, 1990.
- (9) Gawthrop P.J.: Bicausal bond graphs: International Conference on Bond Graph Modeling and Simulation (ICBGM'95), Las Vegas, USA, jan. 95, pp. 83-88.
- (10) Gawthrop, P.J.: Physical Interpretation of Inverse Dynamics Using Bicausal Bond Graphs: *Journal of The Franklin Institute*, Vol. 337, 2000, pp. 743-769.
- (11) Fotsu-Ngwompo, R., Scavarda, S., Thomasset, D.: Physical Model-based Inversion in Control Systems Design Using Bond Graph Representation. Part 1: Theory: *Proceedings of the IMECHE Part 1, Journal of Systems and Control Engineering*, Vol. 215, n°2, 2001, pp. 95-103.
- (12) Fotsu-Ngwompo, R., Scavarda, S., Thomasset, D.: Physical Model-based Inversion in Control Systems Design Using Bond Graph Representation. Part 2: Applications: *Proceedings of the IMECHE Part 1, Journal of Systems and Control Engineering*, Vol. 215, n°2, 2001, pp. 105-112.
- (13) Laffite, J., Bideaux, E., Scavarda, S., and Guillemard, F.: Electric motor sizing for an automotive power train to reach thermal engine powered vehicles performance using an inverse bond graph-based method: *International Conference on Bond Graph Modeling and Simulation (ICBGM'03)*: Orlando, USA, jan. 2003, pp. 283-289.
- (14) Ngwompo, R.F., Bideaux, E., Scavarda: On the Role of Power Lines and Causal Paths in Bond Graph based Model Inversion: *International Conference on Bond Graph Modeling and Simulation (ICBGM'05)*: New Orleans, USA, jan. 2005, pp. 5-10.
- (15) Beretta, J.: New classification on electric-thermal hybrid vehicles, EVS15, Bruxelles, Belgium, oct. 98, 12 p.

CPS Hybrid Vehicle with Flywheel for Energy Storage

S.Lee¹, K.Ichiryu¹, K. Kawamura¹, S.Ikeo², K.Ito², H.Shimoyama³ and E.Koyabu²

1 Tokyo University of Technology

2 Sophia University

3 NISSAN MOTOR CO., LTD.

ABSTRACT

In the last two decades, we are facing air pollution problem and the green house effects which are successive results of increase in CO₂, Particulate Matter and so on. This leads to the development of the hybrid vehicle and the fuel saving has been realized.

In this research, the hybrid vehicle using Constant Pressure System (CPS) is discussed. CPS keeps the line pressure constant by regulating the output flow rate from energy storage device according to the requirement of load. The vehicle is accelerated with energy fed from the high-pressure line to the drive pump/motor while the kinetic energy of the vehicle is stored in flywheel by working the drive pump/motor as a pump during the deceleration. In this paper, first the driving principle of the vehicle used in this study is explained, and the flywheel system is discussed. Then the vehicle speed control performance is examined on real machine and the method for improving the fuel economy is also discussed.

NOMENCLATURE

b	: Net specific fuel consumption 285 [g/kWh]	r_w	: Radius of wheel 0.28 [m]
D	: Displacement [m ³ /rad]	S	: Distance [m]
F_{dr}	: Driving force [N]	$T, \Delta T$: Rotating torque and torque loss of each P/M [Nm]
G_f	: Fuel Economy [km/l]	v	: Vehicle speed [m/s]
i_{dr}	: Final reduction gear ratio 4:1	V_h	: Volume of hydraulic pipe 0.05 [m ³]
J_{fw}	: Flywheel moment of inertia 2.02 [kgm ²]	W_{ep}	: Net power of engine [W]
K_e	: Bulk modulus of elasticity 1320 [MPa]	δ	: Nondimensional displacement of pump/motor
M	: Gross mass of vehicle 1860 [kg]	ΔT_1	: Torque loss due to viscosity
n	: Polytropic index	ΔT_2	: Torque loss due to leakage
P_h	: Hydraulic line pressure [MPa]	ΔT_3	: Torque loss due to compressibility
P_{loss}	: Gross loss of flywheel 250 [W]	ΔQ_1	: Flow rate loss due to leakage
$Q, \Delta Q$: Flow rate and loss flow rate of each P/M [m ³ /s]	ΔQ_2	: Flow rate loss due to compressibility
R	: Travel resistance including rotating,	ρ_f	: Fuel density [kg/ m ³]
ω	: Rotational speed [rad/s]		

Subscripts

<i>dr</i>	: Driving unit	<i>g</i>	: Gas in accumulator
<i>eg</i>	: Engine unit	<i>o</i>	: Default of accumulator gas
<i>fw</i>	: Flywheel unit		

1. INTRODUCTION

Nowadays, we are facing problems that include the green house effect by increase of CO₂ or the air pollution. To cope with these problems, Kyoto Protocol was adopted in 1997 and then more attention has been paid to the development of the hybrid vehicle, which is of characteristics of low gas emission and energy savings⁽¹⁾.

Even though the electrical hybrid vehicle has been developed and the fuel saving has been realized, the cost for producing the high-energy battery and treatment of the wasted battery still need to be reduced. On the other hand, the hydrostatic hybrid buses, which use the accumulator as the energy storage device, have been also studied and developed. However, the flywheel is more proper both in energy density and power density than the accumulator. With the development of high-strength steel which can be used for higher speed rotation, it became possible for a flywheel to be used as an energy storage device⁽²⁾.

Moreover, Constant Pressure System (CPS), which keeps the pressure in high-pressure-line constant by regulating the output flow rate from energy storage device according to the requirement of load, is proposed. This system has the merits such as energy savings, noise and shock reduction compared with the conventional hydraulic system. However, neither is there enough study on development of the system in which a flywheel is combined with a constant pressure system nor on development of its applications to the hybrid vehicle.

In this paper, we will focus on the application of the above mentioned system to a light motor-truck whose payload is 1500[kg]. As the first step of research and development, the flywheel for proper energy storage is discussed. Then the vehicle speed control performance and the method for the test of fuel economy at the JAPAN 10 MODE will be shown (in Japan, we usually adopt the JAPAN 10-15 MODE which is more complicated driving mode than that of the JAPAN 10 MODE for measurement of the fuel economy). As the first step of the test, the method for vehicle speed control is verified. The tested driving mode combines liner acceleration, constant speed, and liner deceleration driving, where the acceleration and the deceleration are the same absolute value as is used in JAPAN 10 MODE. Next we estimated the fuel economy with simulation at the same driving mode as the former experiment, and compared the results. After confirmation of the validity of the numerical simulation model, the fuel economy in the JAPAN 10 MODE is estimated by numerical simulations. Finally, three methods for improving the fuel economy are investigated by the simulation and the effectiveness of CPS hybrid vehicle is discussed.

2. CONSTANT PRESSURE SYSTEM

CPS is the system which has an almost constant pressure hydraulic line and controls the torque of hydraulic pump/motor by controlling displacement. Since the system pressure is held constant, the torque of each actuator in multi-actuator drive system can be controlled without coupling. The greatest advantage of the CPS is that it can recover and reuse the energy of

load⁽³⁾.

The method of energy recovery is as follows: In Fig.1, the arrow is the symbol of variable displacement of pump/motor. If it is directed to upbeat, this corresponds to positive displacement of pump/motor, and vice versa. In the case of (a), since the rotational direction is positive and the displacement is negative, the generated torque accelerates the inertial load. In the case of (b), since both rotational direction and displacement are positive, the pump/motor works as a pump, and it decelerates the inertial load. Therefore the energy beyond the setting pressure is recovered in energy storage device (in this study, it is flywheel).

3. DRIVINGPRINCIPLE

Fig.2 shows the hydraulic circuit of CPS hybrid vehicle. Mainly, this system consists of three units which are engine unit, flywheel unit and driving unit. Each unit has one or two pump/motor.

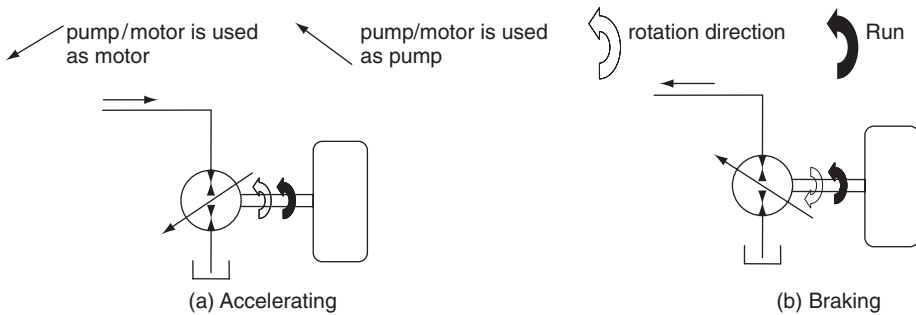


Fig.1 Vehicle kinetic energy recovery

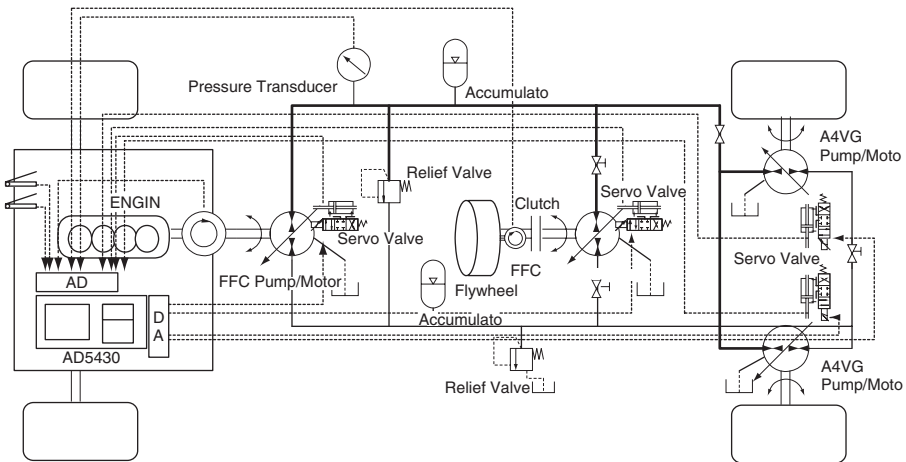


Fig.2 Schematic diagram of cps hybrid vehicle

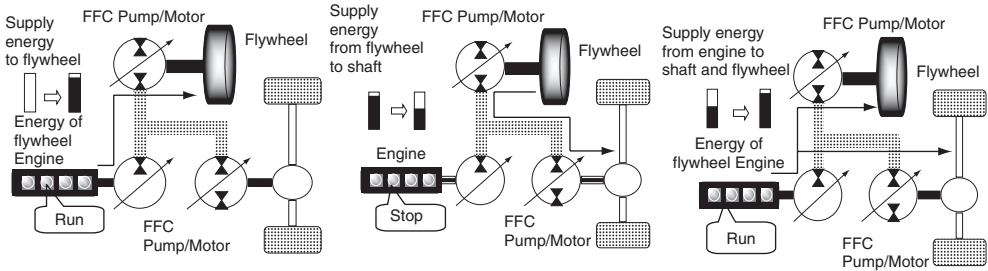


Fig.3 Driving principle

The driving principle of CPS hybrid vehicle is as follows: the Internal-Combustion Engine (ICE) starts up firstly, and when the line pressure reaches set value, flywheel as the energy storage starts to rotate. If the rotational speed reaches upper limit, ICE stops and the vehicle is driven only by hydraulic energy. The proportional controller maintains the hydraulic pressure to set value by controlling the displacement of pump/motor in flywheel unit.

Since the system of the hybrid vehicle has no mechanical transmission and the operation of ICE is independent on the driving condition, the ICE works at the optimal operating point all the time. Energy storage flywheel stores the vehicle kinetic energy during braking, and releases it during accelerating. If the flywheel rotational speed has decreased to the lower limit by consuming the energy of the hydraulic line, ICE is restarted automatically. These are shown in Fig.3. This implies that the ICE works intermittently.

4. FLYWHEELS FOR ENERGY STORAGE ^{(4),(5)}

Two kinds of flywheel device are examined: the normal type and the overdriven type. Both are able to accumulate equal energy. The normal type flywheel is designed to be layer-built and easy assemble; therefore, pump/motor is integrally constructed to be compact sized. The maximum speed of the flywheel is 419[rad/s] (4000[rpm]), and the maximum accumulation energy is 177[kJ], corresponds to the kinetic energy where the vehicle of 1800[kg] in mass runs 50[km/h] (14[m/s]).

The overdriven type flywheel is designed to be more compact and lighter, where planetary gear is adopted between pump/motor and flywheel to increase the speed of the pump/motor. In this research, the rotational speed of the overdriven type flywheel is designed to be 3-times of the speed of hydraulic pump/motor by designing the planetary gear ratio.

4.1 Rotational duration test

In order to realize lighter and more compact flywheel the planetary gears is used between the pump/motor and the flywheel for speed increasing in the overdriven type flywheel. These planetary gears cause mechanical loss. The windage loss also increases with the rotational speed. The performance of normal type and overdriven type flywheel are compared by measuring the duration time of rotation. To keep the initial stored energy equal, the rotational speed of the overdriven type flywheel is set to 9250[rpm] and that of the normal type flywheel to 3000[rpm].

For estimation of the efficiency, the reference point for normal type flywheel is set to 1000[rpm] and the overdriven type flywheel to 3177[rpm], because it is impossible to measure until 0[rpm] accurately for the performance of the rotational sensor. From this result, it can be observed that the efficiency of the overdriven type flywheel is decreased by 27.8[%] compared

Tab.1 Specification of flywheels

	Normal type flywheel	Onerdrive type flywheel
Flywheel diameter	500[mm]	280[mm]
Flywheel mass	55.03[kg]	21.6[kg]
Moment of inertia	2.02[kgm ²]	0.2[kgm ²]
Unit mass	100[kg]	70[kg]

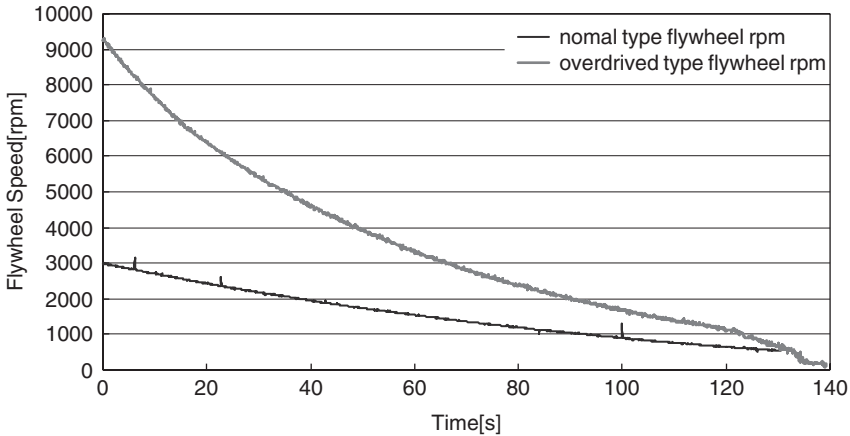


Fig. 4 Comparison of revolution duration

Tab.2 Flywheel revolution duration

	Rotation duration[s]
Normal type flywheel	90.7
Overdriven type flywheel	65.5

with normal type. Most of the loss is caused by pump/motor torque loss for the friction, and windage loss also decreases the efficiency.

4.2 Flywheel with clutch

In previous subsection, it was shown that the energy stored in flywheel had been wasted in only few minutes. This is caused by driving loss of pump/motor, friction of bearing and windage loss. To reduce these losses, the effectiveness of the clutch between flywheel and the pump/motor (see Fig.5) is examined by measuring the duration time of flywheel speed. Fig.6 shows the flywheel speed response where the initial speed is 2000[rpm]. It is obvious that the clutch system can keep the flywheel speed and this data shows the effectiveness of the clutch system.

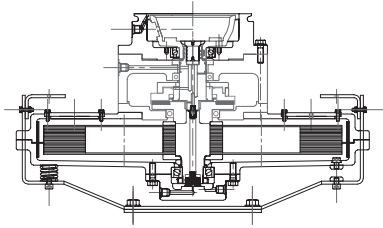


Fig.5 Cross section of flywheel with clutch

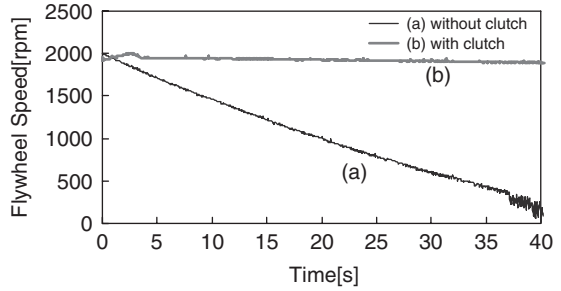


Fig. 6 Comparison of flywheel speed

4.3 Regenerative braking test

In this subsection, the recovery of the braking energy is discussed. The flywheel is used to drive the vehicle run and also to store the braking energy through the pump/motor. The ICE drives the pump/motor as a motor and let the flywheel rotates until it reaches the maximum speed of 3000[rpm] (9250[rpm]). If it once reached 3000[rpm] (9250[rpm]), then the ICE is stopped and the vehicle is driven only by the energy of the flywheel. If the speed decreases to 1000[rpm] (3177[rpm]), pump/motor of the driving unit is driven as a pump; therefore the braking torque can be stored as a rotational energy in the flywheel. In this paper, the energy recovery rate is defined by:

$$\text{Energy Recovery Rate} = \text{Recovery Energy} / \text{Vehicle Kinetic Energy} = \frac{1}{2} (J_{fw}^2 / \omega_{fw}^2)$$

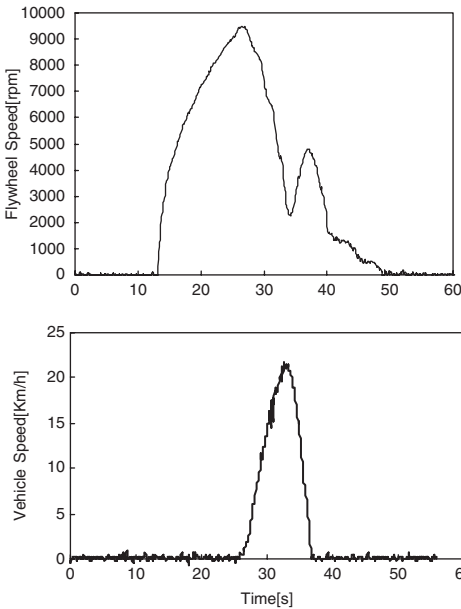


Fig. 7 Energy recovery test with normal type flywheel

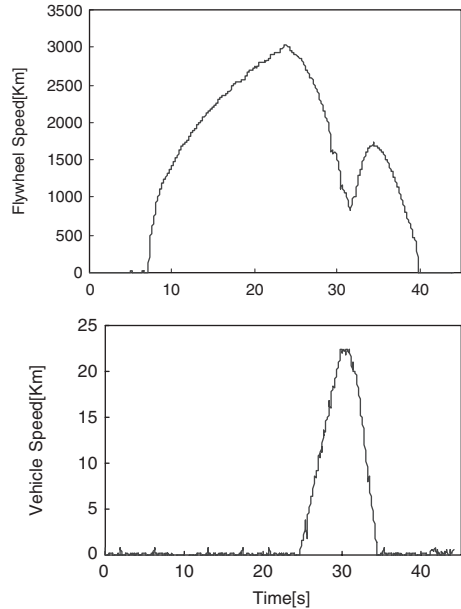


Fig. 8 Energy recovery test with overdriven type flywheel

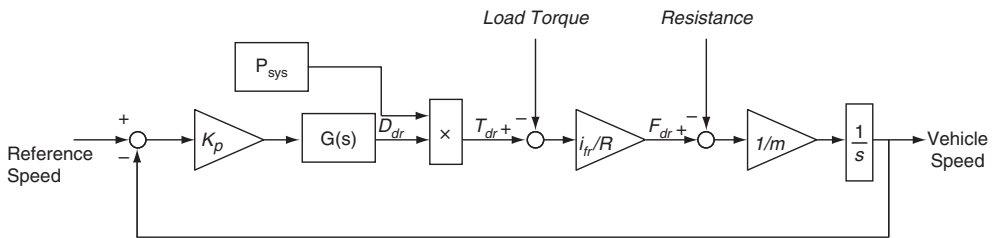
With this definition, 73[%] of recovery rate was obtained with the normal type flywheel, while 63[%] with the overdrived type flywheel. The recovery efficiency for a hybrid vehicle with an accumulator, used as energy storage device, is known to be 67[%]⁽⁶⁾. This implies that the flywheel is more satisfactory in energy recovery performance than that of the conventional accumulator system.

The efficiency of the overdrived type flywheel is lower than the normal type flywheel, because the mechanical loss of the overdrived type flywheel is large. Therefore, in the experiment, the normal type flywheel with clutch system is used to reduce the mechanical loss.

5. VEHICLE SPEED CONTROL

The block diagram of speed control method is shown in Fig.9. To control the vehicle speed, the displacement of pump/motor at driving side is controlled using proportional control, in other words, the torque of pump/motor is controlled.

In this section, the performance of the speed controller at constant speed driving test is examined. In this test, the motor truck is driven at linear acceleration, constant speed (20[km/h] and 40[km/h]) and in linear deceleration mode. The experimental results are shown in Fig.10.



K_p : Proportional gain for speed control, D_{dr} : Displacement of P/M, T_{dr} : Hydraulic torque, i_{fr} : Final reduction ratio, R : Radius of the tire, m : Mass of the vehicle

Fig.9 Block diagram of speed control

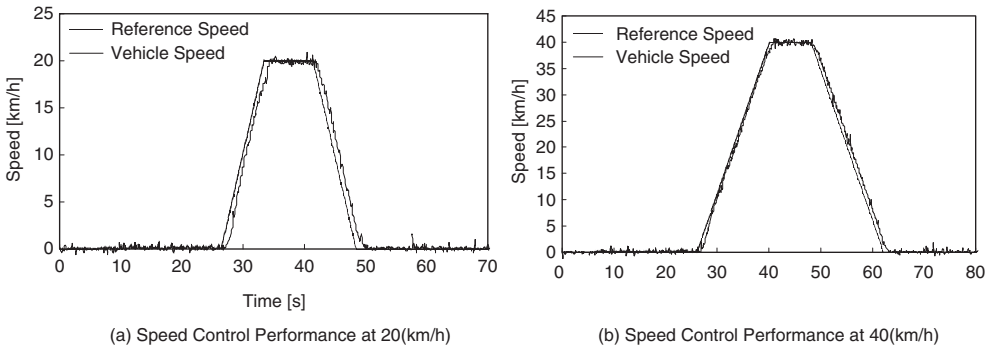


Fig.10 Result of speed control test

This shows that there is an error between the reference speed and the vehicle speed for simple proportional control. In order to reduce this error, the PI controller was also examined. However, this vehicle system was very sensitive to the integral gain and large integral wind-up occurred. The speed tracking error is within 2[km/h] and it is enough to evaluate the fuel economy.

6. NUMERICAL SIMULATION FOR ESTIMATING THE FUEL ECONOMY

For evaluating the fuel economy of the CPS hybrid vehicle, we simulated it using following models on simulation software (MATLAB/Simulink).

6.1 Simulation models^{(7), (8), (9)}

Flywheel Unit

$$J_{fw} \frac{d\omega_{fw}}{dt} = T_{fw} - \Delta T_{fw} - P_{loss} / \omega_{fw} \quad (1)$$

Hydraulic Line Pressure

$$Q_{eg} - \Delta Q_{eg} + Q_{fw} - \Delta Q_{fw} + (Q_{dr} - \Delta Q_{dr}) = \frac{V_h}{K_e} \cdot \frac{dP_h}{dt} \quad (2)$$

Driving Unit

$$M \frac{dv}{dt} = F_{dr} - R \quad (3)$$

$$F_{dr} = (T_{dr} - \Delta T_{dr}) i_{dr} / r_r \quad (4)$$

where, ΔT and ΔQ were obtained from following equations.

$$\Delta T = \Delta T_1 + \Delta T_2 + \Delta T_3$$

$$\Delta T_1 = 0.107(\omega / 2\pi)$$

$$\Delta T_2 = 0.19\delta(\omega / 2\pi) + 0.00102\delta^2(\omega / 2\pi)^2$$

$$\Delta T_3 = 1.86 \times 10^{-7} P_h$$

$$\Delta Q = \Delta Q_1 + \Delta Q_2$$

$$\Delta Q_1 = 1.68 \times 10^{-7} (\omega / 2\pi) + 1.72 \times 10^{-12} P_h$$

$$\Delta Q_2 = 0.119(\omega / 2\pi)q - 1.307 \times 10^{-6} \delta(\omega / 2\pi)$$

These equations are obtained from experiments. Fig.11 shows an example of the comparison between experimental data and calculated data.

Fuel Economy

$$G_f = S \rho_f l \left(\int b \cdot W_{ep} dt \right) \tag{5}$$

$$W_{ep} = \omega_{eg} D_{eg} P_h$$

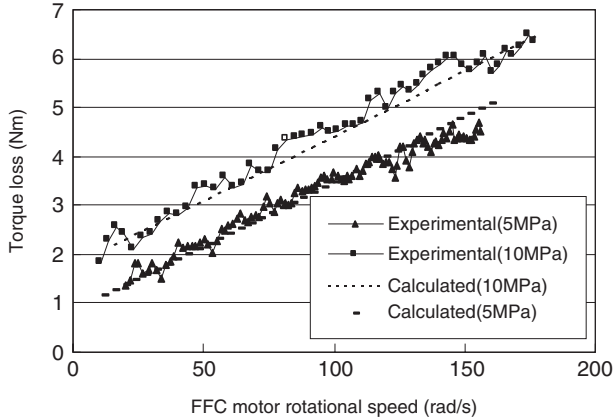


Fig.11 The comparison between experimental data and calculated data (Torque losses in different supply pressures)

where, S is driving distance. In this study, the displacement of engine pump/motor is fixed and the line pressure is held constant, that is the load torque to the drive shaft of engine are regarded as constant. Also the engine throttle is kept constant in the experiment. Therefore, the wet specific fuel consumption b is treated as constant in equation (5).

Accumulator (for pulsation absorption)

$$P_g V_g^n = P_0 V_0^n \tag{6}$$

$$V_g = \int_0 Q_g dt \tag{7}$$

$$P_g = P_h \tag{8}$$

6.2 Comparison between simulation and experimental results

For confirming the validity of simulation models, we compared the results of simulation and experiment. Fig.12 shows the comparison of line pressure, engine speed, flywheel speed and vehicle speed between the simulation and experimental results. Fig.13 shows the results for different constant speed. Each result of simulations almost fit for the experimental result. For the engine speed data shown in Fig.12, there are striking difference between simulation and

experimental data, marked with “A”. In the experiment, the load torque of engine is small at the instant of engine start due to the low line pressure. But the engine throttle is fixed. Therefore the engine speed exceeds the set value. To cope with this overspeed, the throttle control should be implemented. The simulation data on vehicle speed exhibited better results than the experiment. This is because we failed to consider the effects of friction, marked with “B”. Using line pressure, engine speed and vehicle speed data such as shown in Fig.12, we estimate the fuel economy from equation (5), and show the result in Tab.3. Although the driving distance is short, it can be seen from this result that the mathematical model is reasonable to estimate the fuel economy.

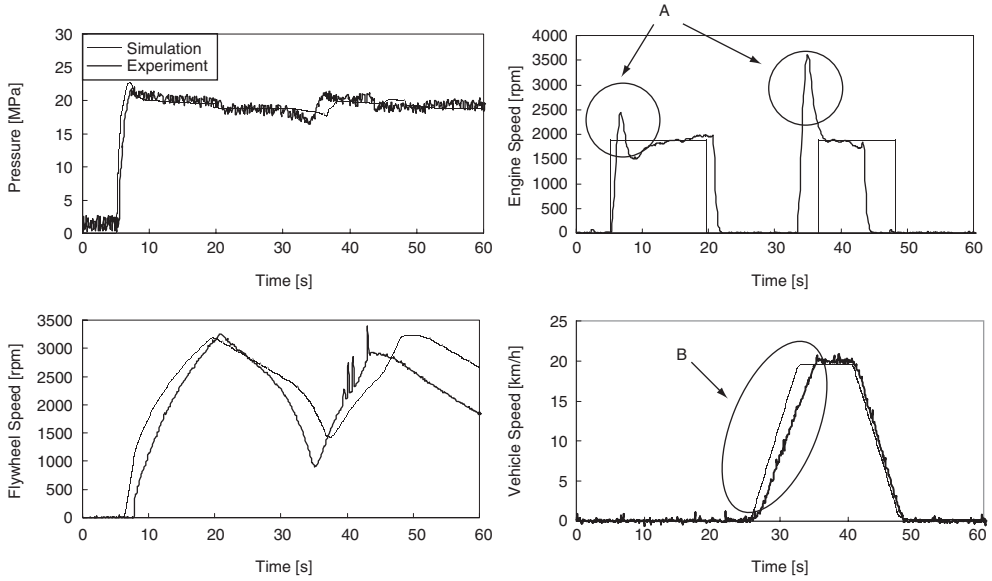


Fig.12 Comparison between simulation and experiment

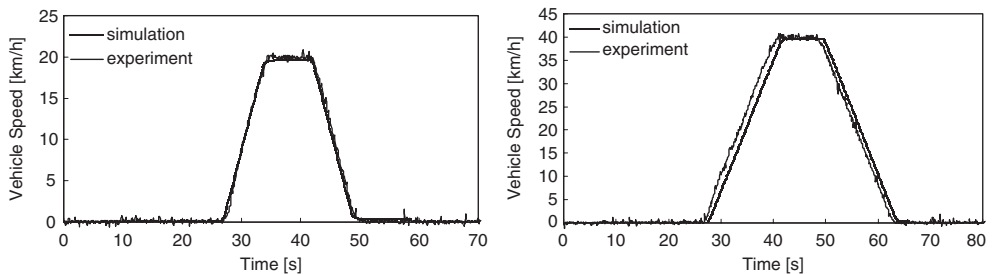


Fig.13 Comparison between simulation and experiment

Tab. 3 Comparison the fuel economy between simulation and experiment

	Fuel Economy [km/l]
Simulation	1.09
Experiment	1.01

6.3 Simulation at japan 10 mode

As we confirmed the validity of the simulation model, we simulated in JAPAN 10 MODE. The results are shown in Fig.14. In this simulation, the hydraulic line pressure is not constant precisely, because the relief valve for safety is not considered in the mathematical model. And then, we estimated the fuel economy using equation (5). The fuel economy obtained from simulation was 8.7[km/l] (the value of conventional vehicle is about 8~9 [km/l]).

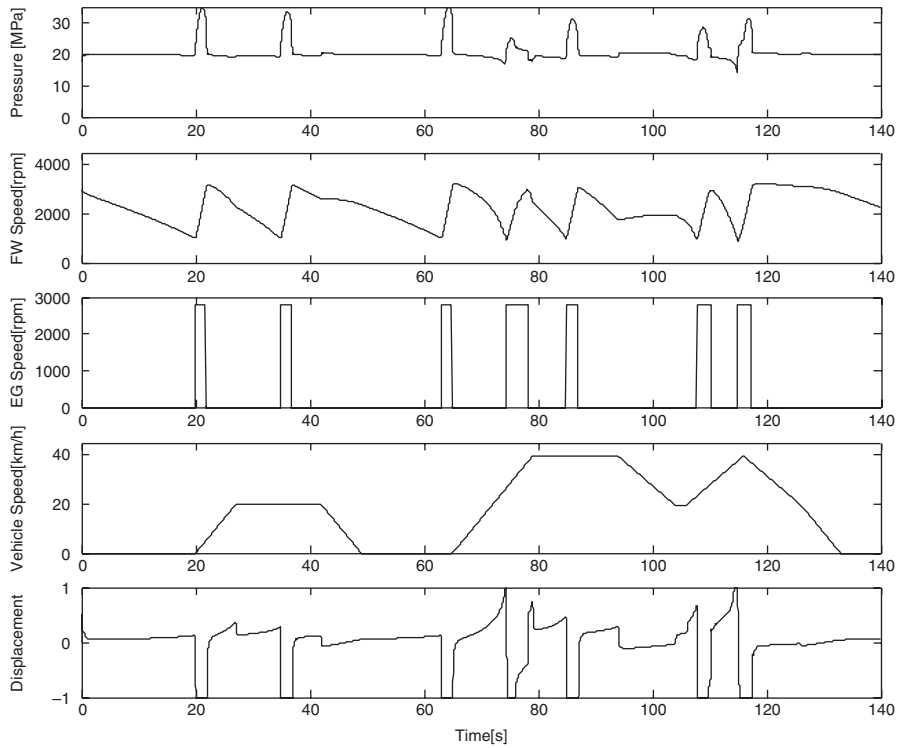


Fig.14 Simulation result at Japan 10 mode

6.4 Improvement of the fuel economy

Since this system is the series type hybrid vehicle, the efficiency of the system depends on the efficiency of variable displacement of the pump/motor, therefore it is the key how to control the pump/motor. We introduce the following methods:

- (1) ON-OFF Pressure Control
- (2) 2-Phased Pressure Control
- (3) ON-OFF Pressure Control with 2-Phased Pressure Control

Since the efficiency of pump/motor at higher displacement region is better than that of lower displacement region, we tried to control the pressure almost constantly only by controlling displacement of pump/motor around 100[%] or 0[%] in the method (1). During idling or constant-speed driving, it is not necessary to keep the line pressure higher and

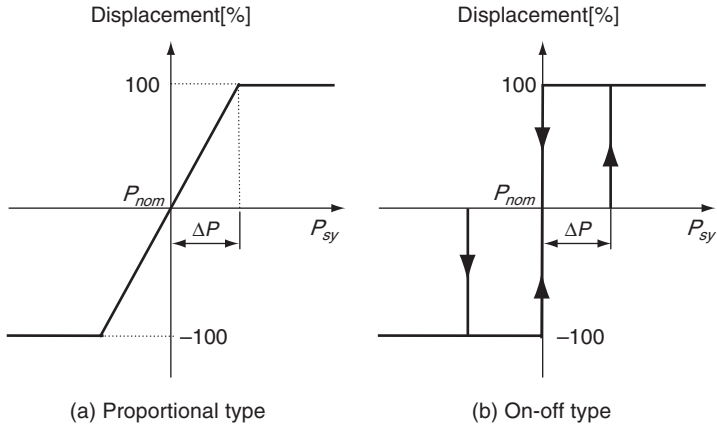


Fig.15 Control method of flywheel pump/motor displacement

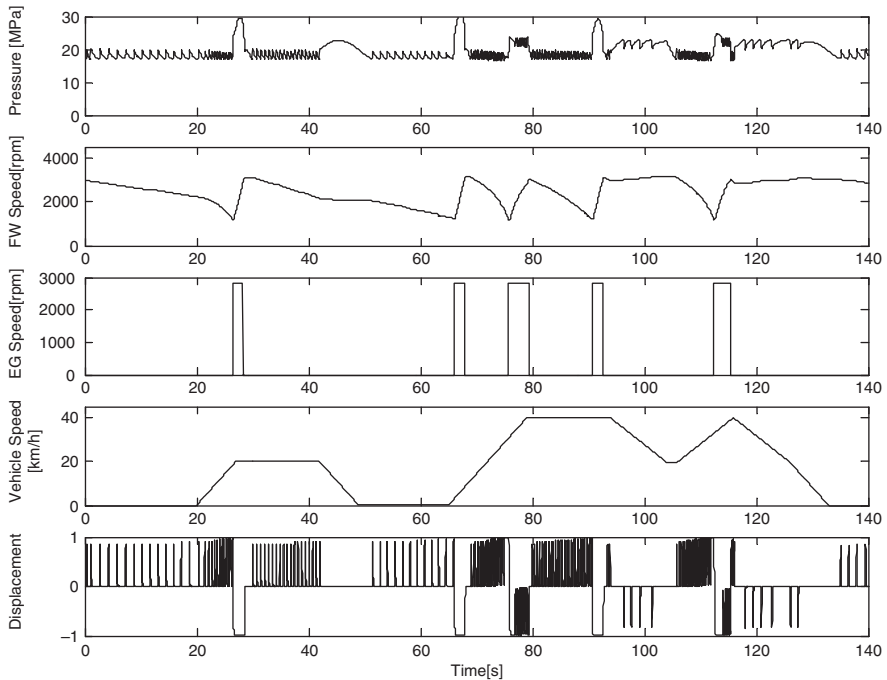


Fig.16 Simulation result at Japan 10 mode (method1)

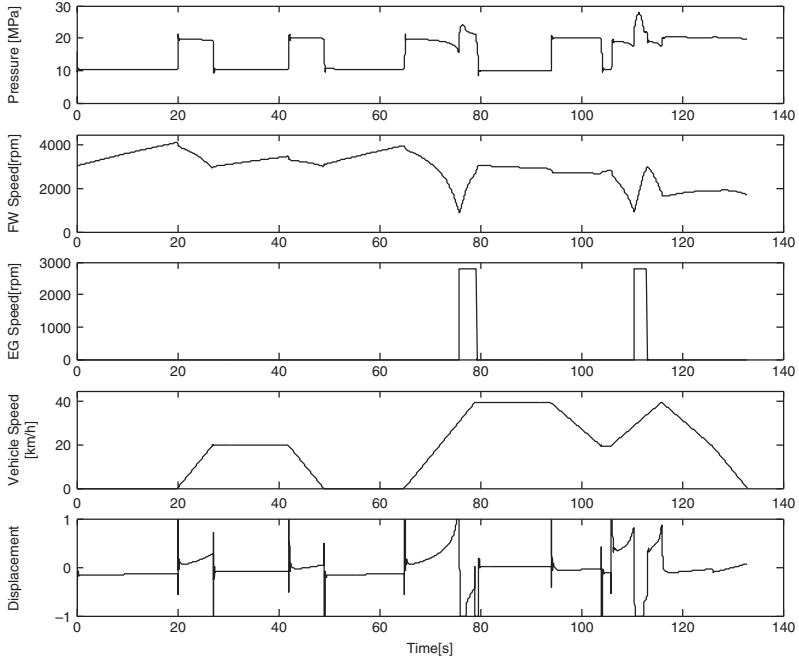


Fig.17 Simulation result at Japan 10 mode (method 2)

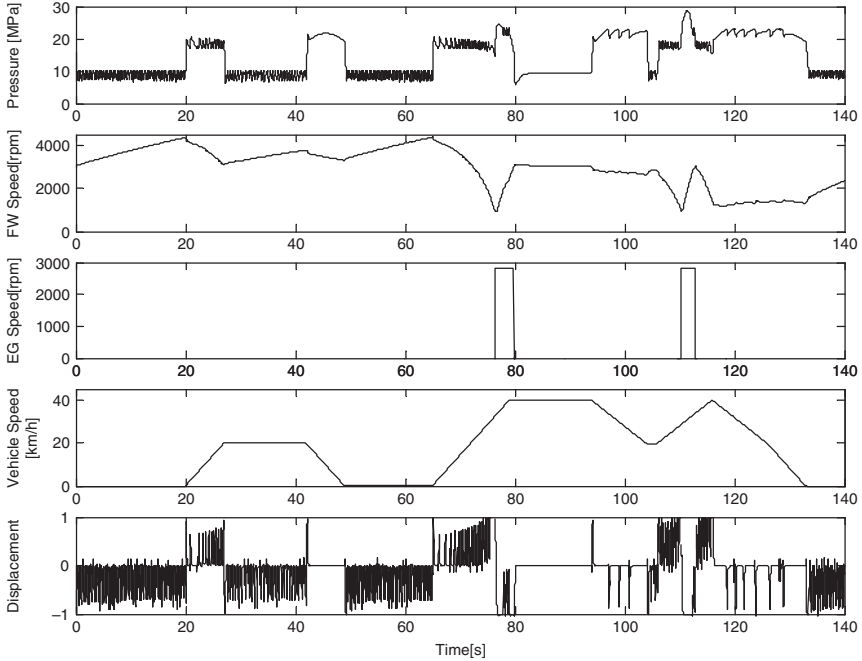


Fig.18 Simulation result at Japan 10 mode (method 3)

is the waste of the energy of flywheel. Therefore in the method (2), we invented reducing the set-pressure during idling or constant-speed driving. Method (3) is using the ON-OFF pressure control method (1) together with 2-phased pressure control method (2). Each simulated results are shown in Fig. 16~18.

The obtained fuel economies from above mentioned simulation are shown in Tab.4. We were able to achieve fuel economy almost identical to traditional vehicles by proportional control. Because the pump/motor is used in the most efficient range in method (3), the fuel economy is better than 3 times the proportional control.

In method (1) and (3), it is necessary to change the displacement of pump/motor so quickly and is seemed to be difficult to implement. However, by selecting the larger pressure deflection ΔP in Fig.15, these method will become realistic as shown by Yokota et al⁽¹⁰⁾.

Tab. 4 Comparison of the simulated fuel economy

	Fuel Economy[km/l]
Proportional Control	8.75
Method (1)	13.03
Method (2)	27.33
Method (3)	29.11
Conventional Vehicle	8~9

7. CONCLUSIONS

In this paper, we showed the principle of the CPS hybrid vehicle and investigated the effectiveness of the vehicle.

From regenerative braking test, 73[%] of recovery rate was achieved and the clutch for flywheel is effective to prevent energy loss, when the energy is not supplied in the flywheel. Although the overdriven type flywheel has lower efficiency, it has the merits of weight and space saving, if the efficiency is improved.

The vehicle speed controller was implemented and examined with full-scaled model. The fuel economy was also estimated numerically and the validity of the simulation model was also confirmed. Then we estimated the fuel economy at JAPAN 10 MODE by simulation, and discuss 3 methods to improve the fuel economy. The best fuel economy obtained from above mentioned simulations was 29.11[km/l] .

In the future, the full-scaled vehicle in JAPAN 10 MODE should be tested with and the implementation for fuel economy introducing new control strategy will be examined.

REFERENCES

- [1] K.Minato, "Conference of the Parties Nine Session and Future Subjects", JARI Research Journal Vol.26, pp.21-29, January, 2004 (in Japanese)
- [2] R.J.Hayes, J.P.Kajs, R.C.Thompson and J.H.Beno, "Design and Testing of a Flywheel Battery for a Transit Bus", SAE Special Public 1999-01-1159, pp.71-79, January, 1999

- [3] H.Shimoyama, S.Ikeo, K.Ichiryu, S.Lee, et al., “Study on Hybrid Vehicle using Constant Pressure Hydraulic System with Flywheel for Energy Storage”, Society of Automotive Engineering 2004 Powertrain & Fluid System Conference & Exhibition, October, 2004
- [4] K. Ichiryu, S. Ikeo, H.Sugawara, H.Kawamura, H.Shimoyama, “The Development of CPS Driven Flywheel Vehicle”, The 18th International Conference on Hydraulics and Pneumatics, pp.195-204, September 30-October 1, 2003
- [5] H. Kawamura, “The Development of Flywheel Hybrid Vehicle”, master dissertation of Tokyo University of Technology, pp.35-42, February, 2004 (in Japanese)
- [6] O. Umemoto, “Hybrid system with accumulator or battery for city bus”, JFPS of Autumn seminar 2002, pp.9-21, 2002 (in Japanese)
- [7] J.Hao, “Study on Energy Saving Effectiveness of Hybrid Vehicle Using Constant Pressure System”, doctoral dissertation of Sophia University, pp.52-89, November, 1998 (in Japanese)
- [8] H.Nakazawa, S.Yokota, Y.Kita, “A HYDRAULIC CONSTANT PRESSURE DRIVESYSTEM FOR ENGINE-FLYWHEEL HYBRID VEHICLES”, Proc. of the Third JHPS International Symposium on Fluid Power Yokohama’96, pp.513-518, November,1996
- [9] H. Shimoyama, S. Ikeo, K. Ichiryu, “Study on hybrid vehicle using Constant Pressure System”, Preprint of JSME Yamanashi Congress, pp.217-218, October, 2003 (in Japanese)
- [10] S. Yokota, T. Nishijima, Y. Kondoh,, Y. Kita, “A Flywheel Hybrid Vehicle Making Use of Constant Pressure System [Fabrication of Stationary Test Facility and Experiment of Urban Driving Schedule]”, Trans. of JSME C,68-671, pp.2127-2132, 2002 (in Japanese)

Pneumatics

Bilateral Control of Multi DOFs Forceps Using a Pneumatic Servo System

Kenji KAWASHIMA*, Kotaro TADANO** and Toshiharu KAGAWA*

*Precision and Intelligence Laboratory, Tokyo Institute of Technology,
4259 Nagatsuta-cho, Midori-ku, Yokohama, 226-8503 Japan

**Graduate student, Department of Mechano-Micro Engineering, Tokyo Institute of Technology

SYNOPSIS

Recently, the development of instruments for minimally invasive surgery has been required. In this paper, we proposed a master-slave system for laparoscopic surgery, which can provide force feedback to the surgeon without force sensors. First, we developed a forceps manipulator that has 4-DOFs at its tip. Pneumatic cylinders were used as the actuators for them and the force at its tip was estimated from the differential pressures of the cylinders. We designed a bilateral dynamic control system using a neural network for acquisition of the inverse dynamics. The obtained inverse dynamics was used for feedforward control and to estimate the external force. Experimental results showed that the developed system successfully display the contact force on the slave side to the operator on the master side.

1. INTRODUCTION

Recently, minimally invasive laparoscopic surgery has been widely performed. This surgical procedure, as compared with traditional open surgery, enables a smaller incision, and this result in less patient pain and shorter duration of hospital stays. While there are such advantages for patients in laparoscopic surgery, it requires increased skill on the part of the surgeon. This is because surgical instruments in laparoscopic surgery are restricted to the degrees of freedom (DOFs) motion due to trocars, and surgeons have to handle the instruments at the opposite end to the abdominal cavity with respect to the trocar point. This prevents surgeons operating intuitively.

To solve the above problems, robotic manipulators, which have multi-DOFs at their tip, have been reported as alternative to conventional instruments [1]. These manipulators can be divided into two approaches with regard to the operating method. One is the manipulator where some DOFs are added to the tip of the conventional forceps [2], [3]. A system of this type is comparatively small, and it is easy to introduce into surgery. However, the problem that the operation is not intuitive still remains. The other is a master-slave type in which the operating portion for the surgeon is separated as master from the forceps [4]. In this type, a surgeon is able to teleoperate the forceps at the master side, as if he/she handles the forceps at the slave side in the abdominal cavity. We, therefore, approve this master-slave type because of the intuitiveness. This system,

however, has the problem that the sense of force is lost. Some studies have been made on the force display in the master-slave surgery system [5], [6], in which the force sensor, that is almost strain gauge, is attached into the tip of forceps manipulator. However, the sensor at the end of manipulator makes sterilizing and downsizing difficult.

In this research, we propose a master-slave system with multi-DOF forceps manipulators that is able to provide a force display to surgeons without a force sensor. To achieve this, we use pneumatic cylinders as the actuator, because they are effective for a haptic device due to the facility in measurement and control of their driving force, and enable the estimation of the external force from the driving force and the impedance. This paper is organized as follows. In Section 2, we describe the mechanism of the newly developed manipulator and the configuration of the master-slave system using it. In Section 3, the bilateral control with neural network is designed. Experimental results of the system performance are shown in Section 4, and concluding remarks are given in Section 5.

2. 4-DOF MANIPULATOR WITH PNEUMATIC CYLINDERS

2.1 Structure of the Manipulator

Fig. 1 shows the developed forceps manipulator that has 4-DOFs, a roll, two bending joints and a holder. Each joint in the manipulator is actuated by a pneumatic cylinder, which generates torque using a rack and pinion. Fig.2 shows the tip part of the manipulator. The diameter of the manipulator is 10mm that is useful for laparoscope surgery. The power for two bending joints at the tip of the manipulator is transmitted by a wire rope as shown in Fig. 3.

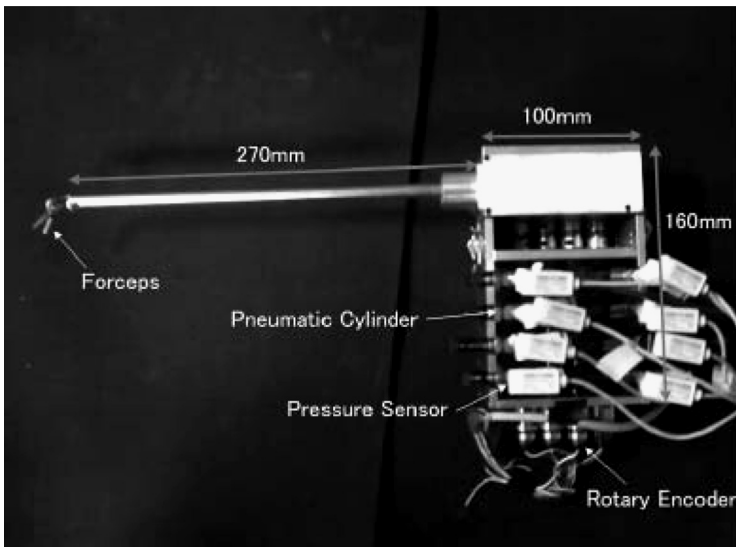


Fig. 1 Developed forceps manipulator

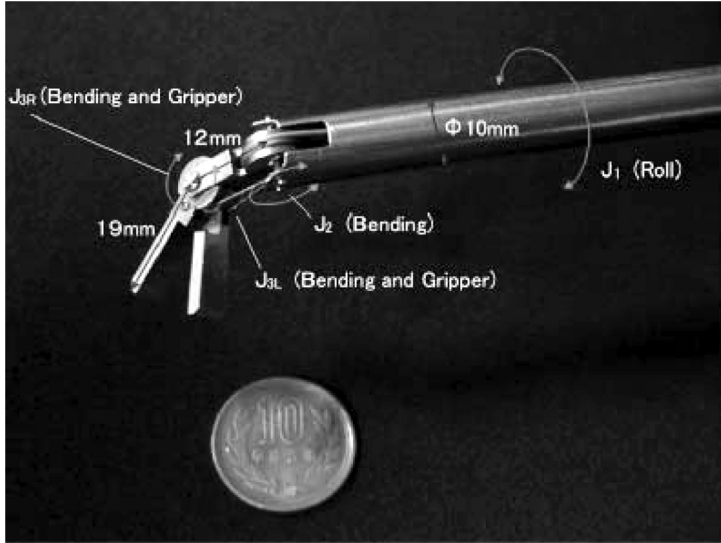


Fig. 2 Configuration of tip of the forceps

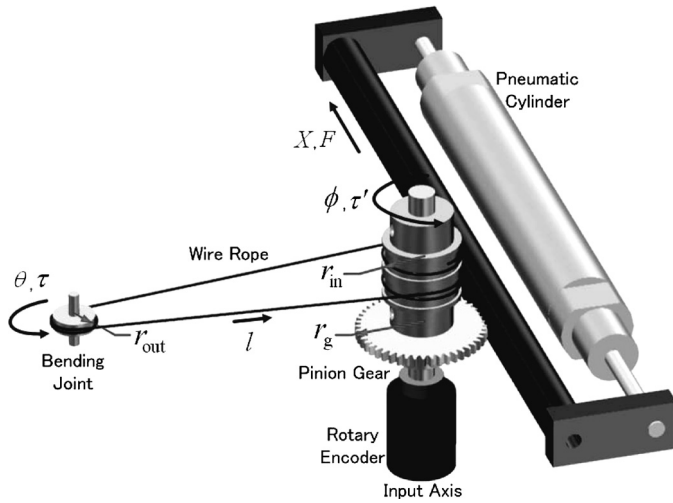


Fig. 3 Mechanism for power transmission

The cylinder made by Airpel was used because it uses a precision fit graphite piston which slides freely - without lubrication - inside a pyrex glass cylinder. Therefore, the friction force is negligible small. The size of the cylinder used is 9.3mm in diameter, 3.2mm in the piston rod diameter and 25mm for the full stroke. The driving force of the cylinder F_{dr} is given as

$$F_{dr} = A\Delta P \quad (1)$$

Where A and ΔP indicate the pressurized area and the differential pressure in the cylinder.

The supply pressure was set at 500kPa and a pressure sensor having a resolution of 20Pa was used. Since the pressurized area is 60mm², the maximum driving force becomes 30N which is considered to be enough for driving the manipulator.

The cylinder was controlled by a five ports servo valve made by FESTO. The servo valve receives the voltage signal and controls the flow rate to the cylinder. Pressures in the cylinder are measured with semiconductor type sensors and are used to control the driving force. Position is measured by an encoder having a resolution of 1000Pulse/Rev. We have confirmed in the preliminary experiment that the position error of the cylinder is not more than 0.1 mm using a PID controller. Also, we have confirmed that the force control could be achieved with 0.05N accuracy.

The displacement of the wire rope l shown in Fig. 3 is proportional to that of the cylinder X .

$$l = r_{in}\phi = \frac{r_{in}}{r_g}X \quad (2)$$

where ϕ is the rotation angle of the pinion gear and the pulley, r_g is the pitch circle radius of the pinion and r_{in} is the radius of the pulley. Then, the angle of bending θ is given as

$$\theta = \frac{l}{r_{out}} = \frac{r_{in}}{r_{out}r_g}X = \frac{X}{R} \quad (3)$$

where r_{out} is the radius of the small pulley at the bending joint. Thus, the angle of bending θ is linear to the displacement of corresponding cylinder. We designed that the wire rope for driving the bending joint J_3 passed through the center of the joint J_2 to prevent interference between the joints. Additionally, the relationship between the torque τ for bending and the driving force of the pneumatic cylinder F is also linear and is given by

$$\tau = RF \quad (4).$$

Where R is an equivalent value to reduction ratio. To improve the resolution of the rotation angle at the tip of the manipulator, R should be small. However, in contrast, to improve the force sensitivity R should be large. In this prototype manipulator, we adopted 8 [mm] as R

($r_{in} = 6.5 \text{ mm}$, $r_g = 13 \text{ mm}$, $r_{out} = 4 \text{ mm}$) to reasonably satisfy both of these conditions. As a result, the resolution of the bending angle is considered to be 0.7 degree.

Fig.4 shows the configuration of the master slave system with the manipulator described above. The manipulator whose structure is the same as that of the slave side is used as the master side for simplification of control. Measured position and pressure signals are sent to a computer for control, and the computed voltage signals are provided to the servo valves.

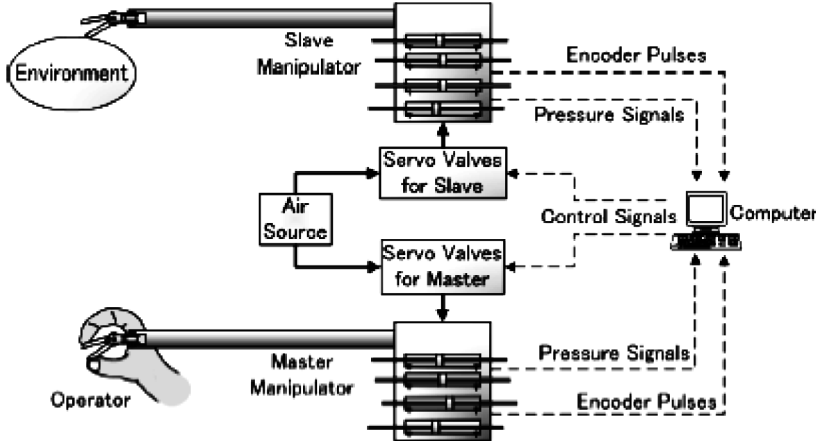


Fig.4 Configuration of master-slave system

3. BILATERAL CONTROL

3.1 Proposed control method

In this section, we describe the proposed method of bilateral control without force sensors in the master-slave system. Although a bilateral control method called symmetric position servo type needs no sensing of force, the performance is influenced by the dynamics of the manipulator. Therefore, the dynamic control using the impedance and the external force that are estimated by neural network as the driving force of the cylinders has been implemented. Since the linear coordinate system of the cylinders and that of the joint rotation can be linearly transformed to each other as shown in Eq. (2) and (3), the rotation angle θ is used in the following discussion.

The ideal response of the master-slave system is that both the position and force response in the master and slave side are identical with each other [7]. Consider a teleoperation system with two 4-DOF master and slave manipulator, whose dynamics described as

$$F_{dr}^s = Z^s(\theta^s, \dot{\theta}^s, \ddot{\theta}^s) + F_{en} \tag{5}$$

$$F_{dr}^m = Z^m(\theta^m, \dot{\theta}^m, \ddot{\theta}^m) - F_{op} \quad (6)$$

where F_{dr} , F_{op} , F_{en} , Z and θ are translational vectors of the driving force of the pneumatic cylinders, the force exerted by an operator on the master side, the force applied on the environment, the impedance function of the manipulator and the bending angle of the joint respectively, and subscript s and m denote slave and master side. The conditions of ideal response in this system can be written as

$$\theta^s = \theta^m \quad (7)$$

$$F_{op} = F_{en} \quad (8).$$

To satisfy Eq.(8), the driving forces of cylinders should be

$$F_{dr}^s = Z^s(\theta^s, \dot{\theta}^s, \ddot{\theta}^s) + F_{op} \quad (9)$$

$$F_{dr}^m = Z^m(\theta^m, \dot{\theta}^m, \ddot{\theta}^m) - F_{ex} \quad (10).$$

There are, however, disturbances due to the uncertainty of impedances, external forces and so on. Therefore, position and velocity feedback has been added to restrain them as follows:

$$F_{dr}^s = K_p^s(\theta^m - \theta^s) + K_d^s(\dot{\theta}^m - \dot{\theta}^s) + Z^s(\theta^s, \dot{\theta}^s, \ddot{\theta}^s) + F_{op} \quad (11)$$

$$F_{dr}^m = K_p^m(\theta^s - \theta^m) + K_d^m(\dot{\theta}^s - \dot{\theta}^m) + Z^m(\theta^m, \dot{\theta}^m, \ddot{\theta}^m) - F_{en} \quad (12)$$

where K_p and K_d are gain vectors. Substituting Eq. (11) and (12) to Eq. (5) and (6) yields

$$K_p^s e + K_d^s \dot{e} + F_{op} - F_{en} = 0 \quad (13)$$

$$-K_p^m e - K_d^m \dot{e} - F_{en} + F_{op} = 0 \quad (14)$$

where

$$e \equiv X^m - X^s \quad (15)$$

Combining Eq.(13) and (14) yields the error equation:

$$(K_p^s + K_p^m)e + (K_d^s + K_d^m)\dot{e} = 0 \quad (16)$$

Hence, e converges asymptotically to zero with appropriate gains, and then from Eq.(13) or (14), Eq.(8) is also satisfied. This means that the ideal response is realized. In practical control, the position, velocity and acceleration of the other side were used as the input of the impedance function as shown in Eq.(17) and (18) to improve the speed of response.

$$F_{dr}^s = K_p^s(\theta^m - \theta^s) + K_d^s(\dot{\theta}^m - \dot{\theta}^s) + Z^s(\theta^m, \dot{\theta}^m, \ddot{\theta}^m) + F_{op} \quad (17)$$

$$F_{dr}^m = K_p^m(\theta^s - \theta^m) + K_d^m(\dot{\theta}^s - \dot{\theta}^m) + Z^m(\theta^s, \dot{\theta}^s, \ddot{\theta}^s) - F_{en} \quad (18).$$

Here $Z^s(\theta^m, \dot{\theta}^m, \ddot{\theta}^m)$ and $Z^m(\theta^s, \dot{\theta}^s, \ddot{\theta}^s)$ behave as a feedforward controller having inverse dynamics. The controller symmetrically sends the values of displacement and external force to one another. This symmetrical system is able to change the roles of master and that of the slave side.

3.2 Acquisition of inverse dynamics using a neural network

To implement Eq.(17) and (18), it turns out that the impedance function and the external force must be given in addition to the position. Here, it should be noticed that the driving force of pneumatic cylinder can be obtained from the differential pressure as shown in Eq.(1). Therefore, if the values of the impedance are given, the external force F_{ext} is given by

$$F_{ext} = F_{dr} - Z(\theta, \dot{\theta}, \ddot{\theta}) \quad (19)$$

where F_{ext} denotes the vector of external force to the cylinder, which is F_{en} at the slave side and $-F_{op}$ at the master side. We can estimate the external force from Eq.(19) using a disturbance observer. Therefore, it is significant to obtain the impedance of the manipulator which is equivalent to the inverse dynamics problem. Thus, acquisition of the inverse dynamics enables both estimation of the external force and feedforward control.

Generally, the dynamics of a multi-DOF manipulator depends on its attitude, mainly because of the influences of inertia and gravity vary with the position. The tip of the forceps manipulator is small and light so that their effects are negligible. In the prototype manipulator, there is, however, the dependence of dynamics due to the position. This is because of the variation in friction caused by the wire rope. This friction characteristic seems to have strong nonlinearity and is very difficult to model mathematically. Although

friction model in a single pneumatic cylinder has been reported [8], the model is unable to represent the dependence on the position.

For the reason mentioned above, a neural network is used to obtain the inverse dynamics of the manipulator. We used a three-layered neural network in which there are twelve displacement inputs ($\theta_1, \dot{\theta}_1, \ddot{\theta}_1, \theta_2, \dot{\theta}_2, \ddot{\theta}_2, \theta_{3R}, \dot{\theta}_{3R}, \ddot{\theta}_{3R}, \theta_{3L}, \dot{\theta}_{3L}, \ddot{\theta}_{3L}$) and four outputs of impedance (Z_1, Z_2, Z_{3R}, Z_{3L}). Fig. 5 shows the architecture used for training to obtain the inverse dynamics of the manipulator. The network is trained offline with back-propagation using the data collected through a closed-loop experiment in which the manipulator is assigned random position trajectories and no external load. In no-load motion, the driving force corresponds to the impedance from Eq.(19). After the training is finished, the network can be used as a feedforward controller and disturbance observer. The detail of the master or slave controller is represented as Fig.6. The controller has a major loop for position and a minor loop for differential pressure which realize the desired driving force. The neural network is incorporated as feedforward and disturbance observer. The measured position and estimated external force are provided to the other side as an input.

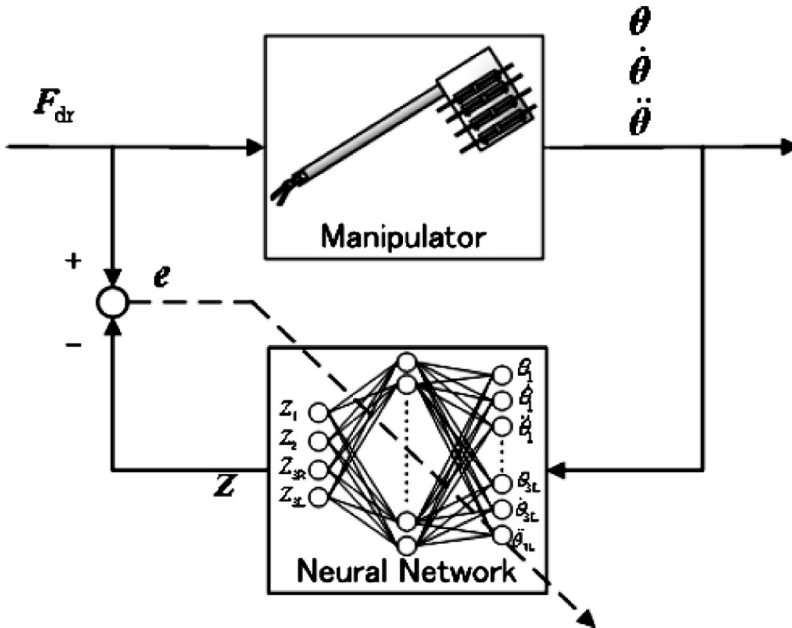


Fig. 5 Training diagram with neural network

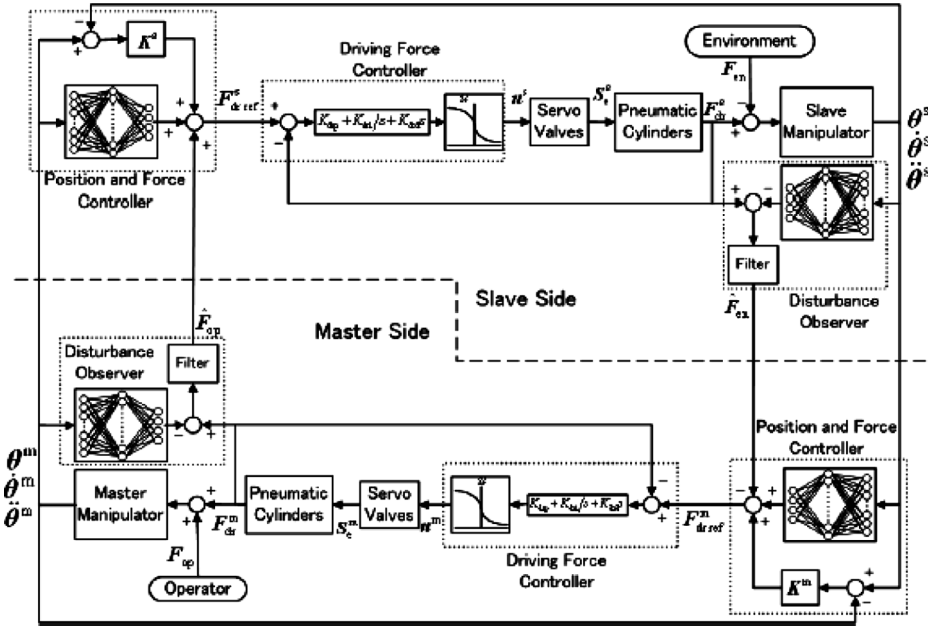


Fig. 6 Block diagram of bilateral control system

4. EXPERIMENTAL RESULTS

4.1 Evaluation of the impedance estimated by neural network

At first, we made an experiment to examine accuracy of the impedance estimated the by neural network. The number of neurons in the hidden layer was twenty which is considered to be sufficient to represent the inverse model of the manipulator. A sigmoid function was selected as the activation function for the hidden layer and a linear function was used for the output layer. A PD controller was used to generate the teaching position signals. The teaching signals are sinusoidal curves whose amplitudes and frequencies were obtained using random numbers. The teaching cycle was a thousand steps.

Fig. 7 shows the experimental results in the estimation of inverse dynamics. As shown in Fig. 7, the output of the neural network is in good agreement with the driving forces of the pneumatic cylinders in no-load motion; this is equivalent to the actual impedance. Therefore, this neural network is sufficiently effective to obtain the inverse model of the manipulator. This network was used in the following experiments.

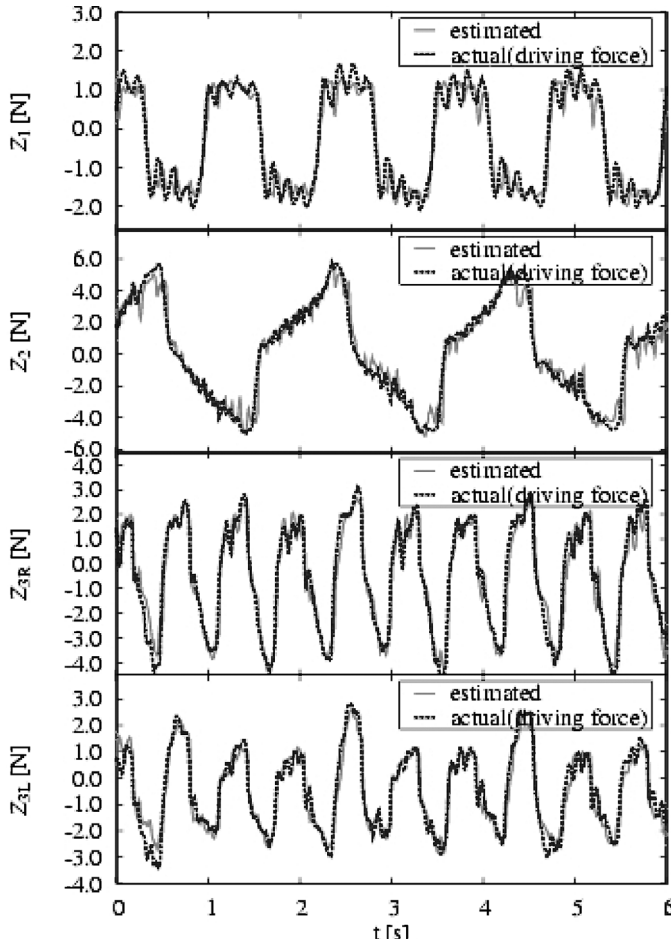


Fig. 7 Comparison between the output of neural network and actual impedance

4.2 Examination of Force Estimation

Some experiments were undertaken to verify the precision of the force estimation by the disturbance observer. We placed a single axis load cell that is a force sensor as an object on the slave side. Fig. 8 shows a photograph of the experimental apparatus. To compare the external forces estimated by Eq.(19) with the output of the force sensor, we transformed them into Cartesian coordinate system at the tip of the manipulator using a Jacobian matrix.

Fig. 9 shows the experimental results. It is clear from the results that the estimated force is slightly larger than the output of the load cell especially at the maximum value. This is because the force at the tip of the manipulator was not entirely transmitted to the cylinders due to mechanical flexure and the

friction caused by the load. This could be improved by modifying the structure of the manipulator. However, the estimated value corresponded well with the output of the load cell on the whole.

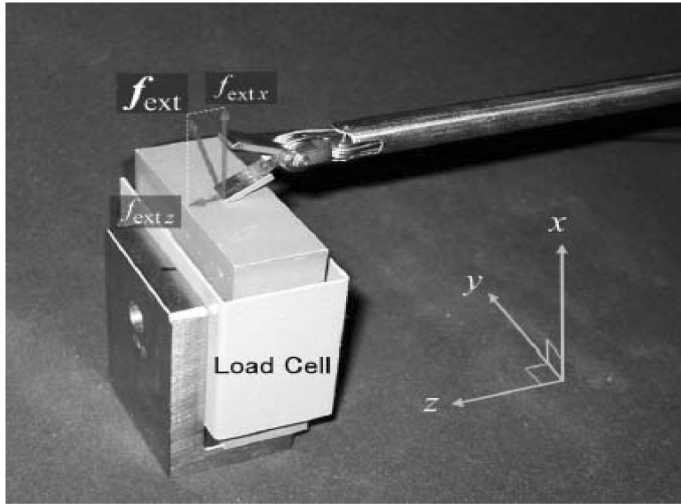


Fig. 8 Experimental view of force measurement

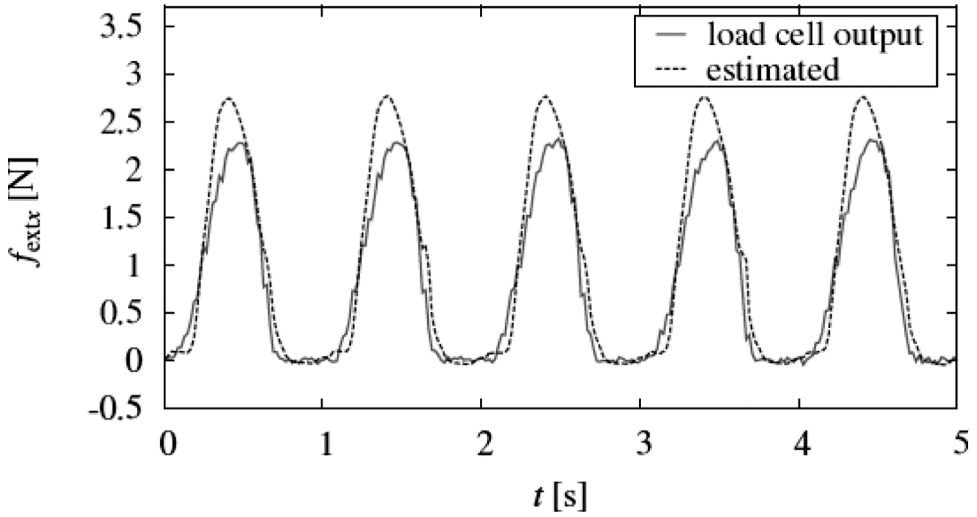


Fig. 9 Experimental results of force measurement

4.3 Bilateral Control Experiment

The performance of the master-slave system was examined with the proposed bilateral control by use of the estimated inverse dynamics and external force. The neural networks in the master and slave side were previously trained with the data in the no-load motion. The slave manipulator was brought into contact with an object by the operator handling the master manipulator.

The experimental results at joint J_1 and J_2 are shown in Fig. 11 and Fig. 12. The upper graphs indicate the position of the cylinder. The lower graphs show the external forces at the master and slave side. While there are some disagreement in the position, which is caused by the mechanical flexure and friction under load, it can be seen that the force exerted by the operator on the master side and the force applied on the environment correspond well. The effectiveness of the proposed bilateral control method was therefore demonstrated.

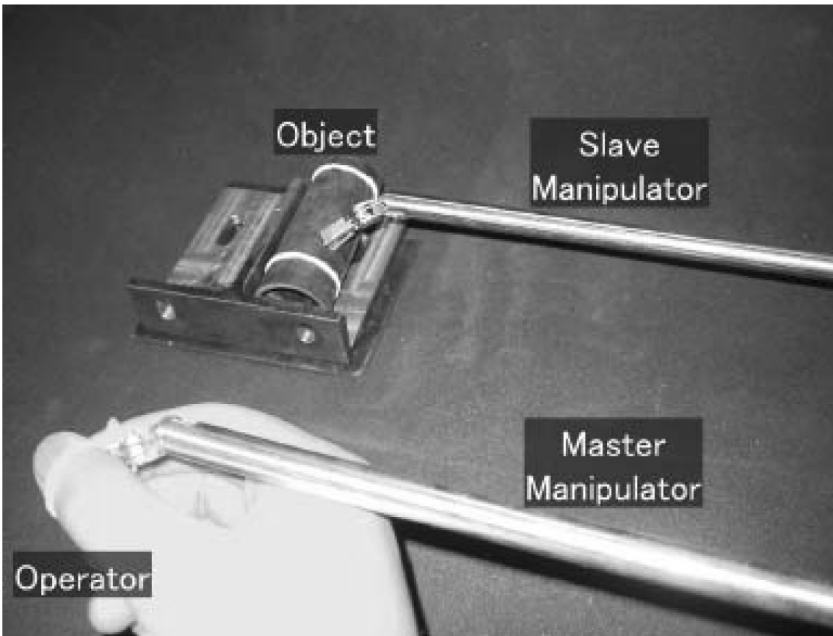


Fig. 10 Photograph during experiment

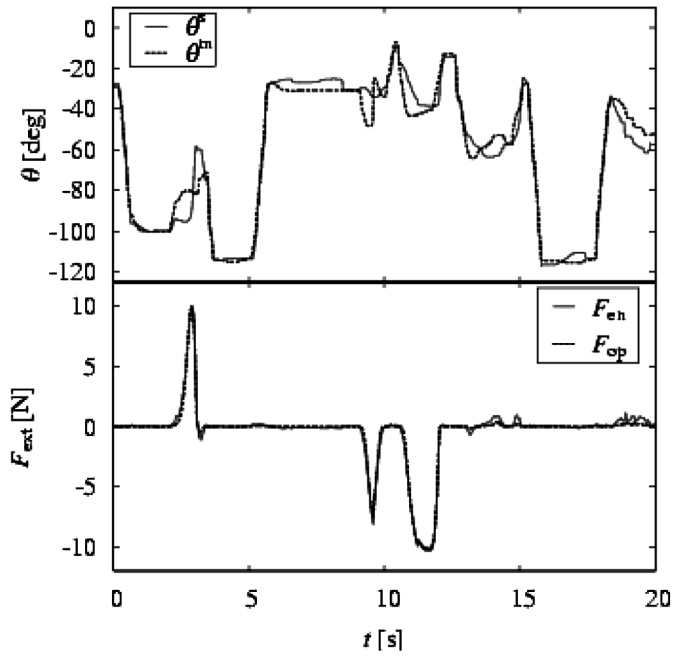


Fig. 11 Experimental results of bilateral control at Joint J_1

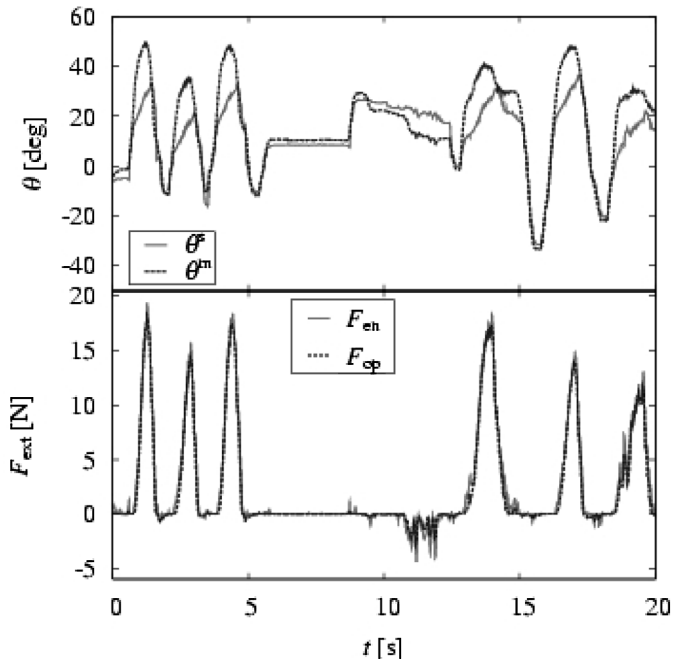


Fig. 12 Experimental results of bilateral control at Joint J_2

5. CONCLUSION

In this paper, a manipulator has been developed which has 4-DOFs actuated by pneumatic cylinders. A master-slave system has been established with the manipulator for laparoscopic surgery. Neural networks were applied to the controller for acquisition of the inverse dynamics and the external force without using force sensors. The experimental results indicated that the operator felt the force at the slave side to a satisfactory extent.

REFERENCES

- [1] Garth H. Ballantyne, Jacques Marescaux, and Pier Cristoforo Giulianotti, editors. *Primer of Robotic & Telerobotic Surgery*. LIPPINCOTT WILLIAMS & WILKINS, 2004
- [2] H. Yamashita, D. Kim, N. Hata, T. Dohi Multi-Slider Linkage Mechanism for Endoscopic Forceps Manipulator Conference on Intelligent Robots and System, pp2577-2582, 2003
- [3] N. Matsuhira, et al Development of a functional model for a masterslave combined manipulator for laparoscopic surgery *Advanced Robotics*, Vol. 17, No. 6, pp 523-539, 2003
- [4] K. Ikuta, M. Kawai, K. Fukuda and T. Hasegawa Hyper Finger for Remote Minimally Invasive Surgery in Deep Area Robotics society of Japan, CD-ROM, 2003
- [5] Carsten Preusche, Tobias Ortmaier, Gerd Hirzinger Teleoperation concepts in minimal invasive surgery *Control Engineering Practice* 10, pp1245-1250, 2002
- [6] M. Tavakoli, R.V. Patel and M. Moallem A Force Reflective Master-Slave System for Minimally Invasive Surgery, *IROS 2003* pp3077-3082, 2003
- [7] Y. Yokokohji and T. Yoshikawa, Bilateral Control of Master-Slave Manipulators for Ideal Kinesthetic Coupling, *IEEE Trans Robot Automat*, Vol. 10, No.5, pp605-620, 1994
- [8] Luis R. TOKASHIKI, Toshinori FUJITA, Toshiharu KAGAWA, Stick-Slip Motion in Pneumatic Cylinders Driven by Meter-out Circuit, *journal of the Japan Hydraulics and Pneumatics Society*, Vol.30, No.4, pp110-117, 1999

1 INTRODUCTION

Pneumatic servo-systems are used in industrial fields of process automation and manipulation, or robotics in general, in biomedical fields, and for actuation devices of road and rail vehicles. Typical applications including positioning servo-systems are reported in (1) and (2), where a food packaging machine and a parallel manipulator have been analyzed respectively. Other applications such as force control servo-actuators can be found, for example, in suspensions devices of road and rail vehicles (3-4), or in the cam mechanisms for high-speed engines (5). An example of the application of pneumatic servo-systems in active orthosis was proposed in (6). Pneumatic drives exhibit several non linear characteristics, which are mainly due to the compressibility of the air, the friction between piston and cylinder tube, and between rod and covers. Moreover, the proportional valves, which are used as operating device of the pneumatic servo-actuators, are characterized by other non linearities according to their mechatronic design, as shown in (7). This non linearity is more evident when the proportional valve is substituted by PWM modulated on/off digital valves, as analyzed in (8). Other examples on the design and test of positioning servo-systems are reported in (9-11), where the control strategy is also taken into account. An open-loop force control system by means of PWM modulated on/off digital valves was proposed in (12).

The present paper deals with the experimental identification and validation of a linearized model of a pneumatic positioning servo-system. A suitable test-bed has been built for the identification of the physical parameters of the model and for its experimental validation, which has been carried out in the frequency and time domains by analysing the open-loop and closed-loop frequency-responses. The linearized model of the positioning servo-system has been validated as a first approximation by neglecting the effects of the friction forces in the servo-actuator, which are more evident at low amplitudes of the sinusoidal input signal.

2 LAY-OUT OF BUILT TEST-BED

The lay-out of the built test-bed to carry out the experimental identification and validation of the pneumatic positioning servo-system is sketched in Fig. 1.

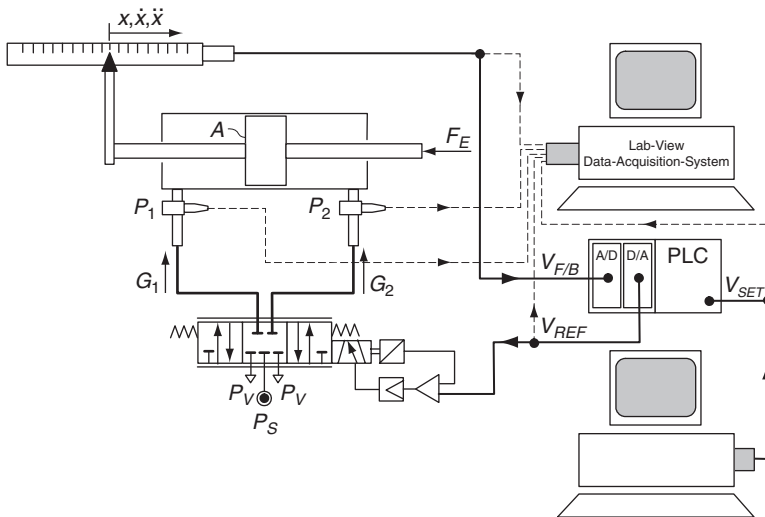


Fig. 1 Lay-out of built test-bed of the positioning servo-system

In particular, this test-bed consisting: a pneumatic double-acting cylinder with double piston rod of type Festo DNC-32-160-PPV-A-S2, a five-way flow proportional valve of type Festo MPYE-5-1/8-HF-010 B, a linear position transducer of type Festo MLO-P01-225-TLF, a PLC (Programmable-Logic-Controller) of type Allen-Bradley Compact Logix, which is provided with a suitable 12 bit A/D-D/A converter.

Moreover, two ISO pipes are connected to the ports of the cylinder in order to measure the pressures P_1 and P_2 through two suitable pressure transducers with signal conditioning. Thus, signals V_{SET} , $V_{F/B}$, V_{REF} , P_1 and P_2 are acquired through a Lab-View Data-Acquisition-System using the electronic board NI AT MIO 16E2.

3 THE EXPERIMENTAL RESULTS

The experimental frequency response of the pneumatic positioning servo-system shown in Fig. 1 has been detected using a Gain-Phase-Analyzer of type SI 1253, as shown in Figs. 2 and 3. In particular, the open-loop frequency response has been obtained between the voltage feed-back signal $V_{F/B}$, which comes from the signal conditioning of the position transducer, and the voltage signal V_{REF} , which is produced by the PLC and sent to the flow proportional valve.

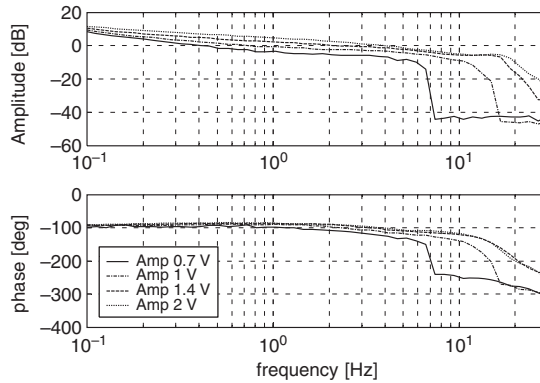


Fig. 2 Open-loop frequency response for different amplitudes of the V_{SET} signal

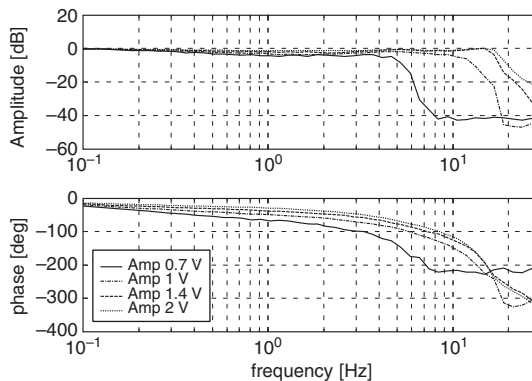


Fig. 3 Closed-loop frequency response for different amplitudes of the V_{SET} signal

Four diagrams of the open-loop frequency response are shown in Fig. 2 in continuous, dash-dotted, dashed and dotted lines, respectively. These diagrams have been obtained by imposing a sinusoidal voltage signal V_{SET} with a constant off-set value of 5 V and amplitudes of 0.7, 1, 1.4 and 2 V, respectively. The off-set value of 5 V corresponds to the half-stroke position of the piston, where the overall stroke of the cylinder is equal to 160 mm. The closed-loop frequency response has been obtained between $V_{F/B}$ and V_{SET} , which is imposed through the Gain-Phase-Analyzer and sent to the PLC controller.

The non linearity of the pneumatic positioning servo-system of Fig. 1 is evident in both frequency response diagrams of Figs. 2 and 3, because a simple changing of the amplitude of the sinusoidal voltage signal V_{SET} with a constant average value of 5 V, changes the band-width of the servo-system. This non linear behaviour is mainly due to the effects of the Coulomb friction between the piston and cylinder tube, and between the rod and covers, due to the seals. This behaviour can be also observed in the diagrams of Figs.4 to 7, where the signals V_{SET} , V_{REF} , $V_{F/B}$, P_1 and P_2 have been acquired versus time through the Lab-View Data-Acquisition-System, and represented through a continuous, dashed, dotted, dash-dotted and light continuous lines, respectively. In particular, observing the diagrams of the feed-back signal $V_{F/B}$ (dotted line) of Figs. 4 and 5, it is noteworthy that the oscillation of the piston disappears when the frequency of the V_{SET} input signal is measured from 6 Hz to 13 Hz at an amplitude of 0.7 V. However, this effect is more evident at low amplitudes because, as also shown in the diagrams of Figs. 6 and 7, the servo-actuator works at both frequencies of 6 Hz and 13 Hz for an amplitude of 1.4 V of the V_{SET} signal.

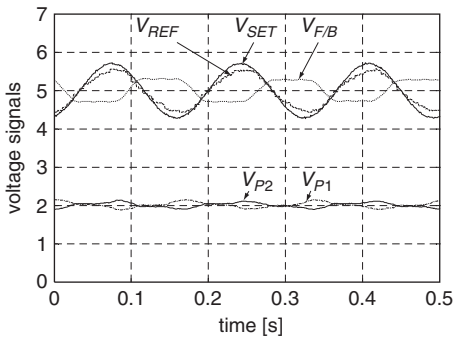


Fig. 4 Frequency response in the time domain ($f = 6$ Hz and $Amp. = 0.7$ V)

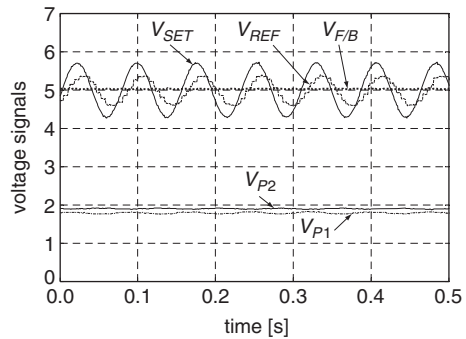


Fig. 5 Frequency response in the time domain ($f = 13$ Hz and $Amp. = 0.7$ V)

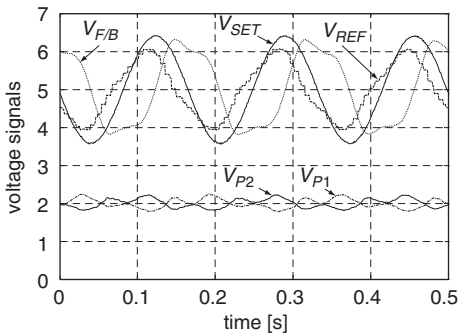


Fig. 6 Frequency response in the time domain ($f = 6$ Hz and $Amp. = 1.4$ V)

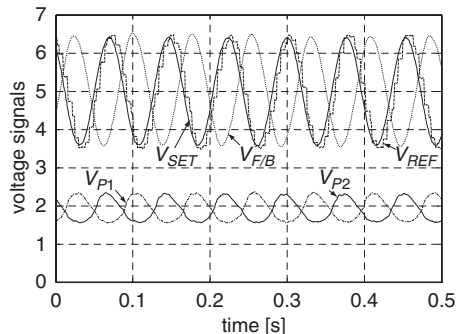


Fig. 7 Frequency response in the time domain ($f = 13$ Hz and $Amp. = 1.4$ V)

4 NON-LINEAR DYNAMIC MODEL

The lay-out of the positioning servo-system is shown in Fig. 8. The input signal of the servo-system is the reference signal X_{SET} , which corresponds to the time position law of the piston and is sent to the regulator as a voltage signal V_{SET} through the static gain K_{SET} . In the closed-loop regulator, the V_{SET} signal is compared with the feed-back signal $V_{F/B}$, which comes from the signal conditioning of the position transducer that is connected to the cylinder rod. Error e is compensated through the control law G_C . The output signal V_{REF} of the regulator is the command signal of the five-way flow proportional valve. The V_{REF} signal, which is related to the spool position of the valve, controls the opening of the internal ways of the valve among the supply port at pressure P_S , the discharge port at pressure P_V and the outlet ports at pressures P_1 and P_2 . Consequently, the mass flow-rates G_1 and G_2 are sent to both chambers of the double-acting cylinder with double piston rod through the pneumatic pipes. Neglecting the static and dynamic effects of the pipes, the outlet pressures P_1 and P_2 of the valve can be assumed to be equal to the pressures inside the chambers of the cylinder. The regulation of the mass flow-rates G_1 and G_2 allows the regulation of the pressures P_1 and P_2 because of the continuity of the fluid mass in the chambers of the cylinder and, consequently, the motion law of the piston is also regulated. The pneumatic positioning servo-system of Fig. 8 can be divided in four sub-systems, which are: the regulator, the five-way flow proportional valve, the double-acting cylinder with double piston rod and the position transducer. Moreover, the five-way valve can be thought as composed by two three-way valves, where each of them controls the pressures in the corresponding chambers of the cylinder. This is shown in Fig. 9, where the three-way flow proportional valves V_1 and V_2 are controlled through the reference signals V_{REF1} and V_{REF2} respectively, which are generated in the regulation block. Thus, the functional lay-out of the servo-system becomes that shown in Fig. 10, where the input and output signals of each block of the overall servo-system are shown in detail.

4.1 Regulation block

The command signal of the valve V_1 can be expressed as

$$V_{REF1} = G_C (V_{SET} - V_{F/B}) + V_{OFF1} \tag{1}$$

where V_{OFF1} is the offset that can be required to represent the valve static characteristic.

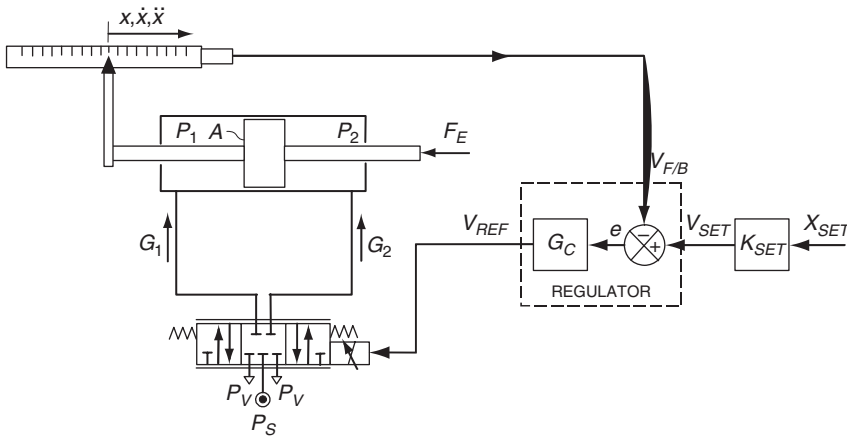


Fig. 8 Lay-out of the positioning servo-system

Likewise, for the valve V_2 , one has

$$V_{REF2} = \alpha G_C (V_{SET} - V_{F/B}) + V_{OFF2} \tag{2}$$

where the parameter α is assumed in relation to the condition of symmetry of the valve. The order of the Eqs.(1) and (2) depends by the transfer function G_C , which is assumed as compensator.

4.2 Flow proportional valve block

Referring to the valve V_1 of Fig. 9 and supposing a bipolar reference signal V_{REF1} , fluid flow from the supply port at pressure P_S to the outlet port at pressure P_1 can be assumed for $V_{REF1} > 0$, while fluid flow from the outlet port to the discharge port at pressure P_V can be assumed for $V_{REF1} < 0$.

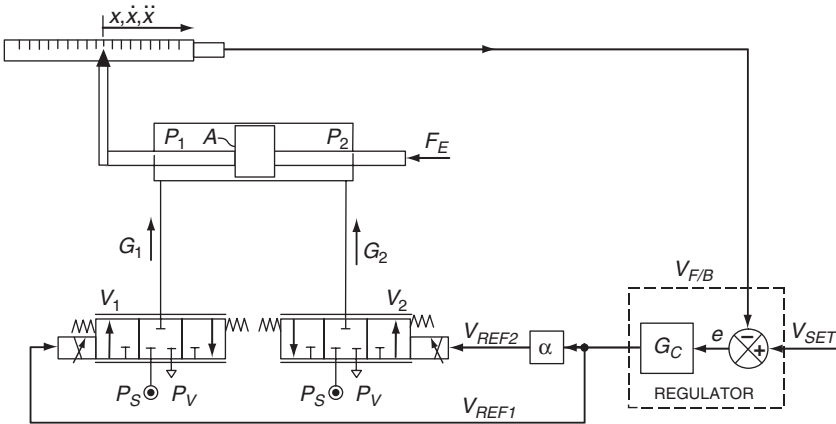


Fig. 9 Lay-out of the positioning servo-system with two three-way valves

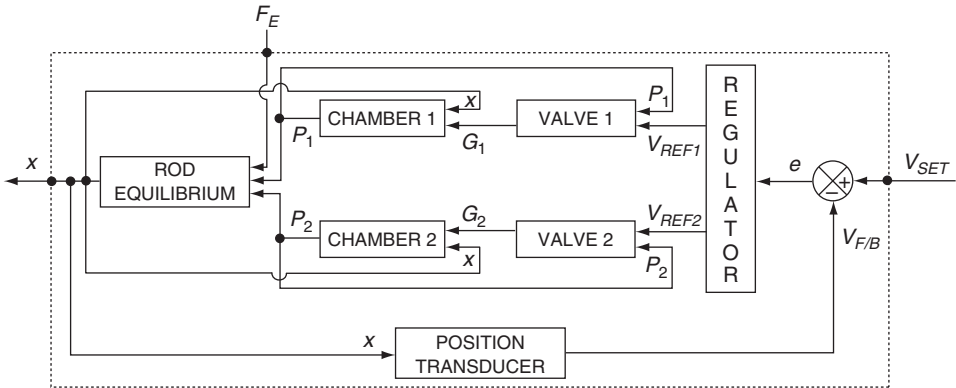


Fig. 10 Functional lay-out of the servo-system

Identifying the internal ways through the conductance C in agreement with the ISO 6358 and assuming a second order dynamic model, one has

$$\frac{d^2 C_1}{d^2 t} + 2 \xi_1 \sigma_{n1} \frac{d C_1}{d t} + \sigma_{n1}^2 C_1 = K_{V1} \sigma_{n1}^2 V_{REF1} \tag{3}$$

where $K_{V1} = C_{1max} / V_{REF1max}$ is the static gain of the valve, σ_{n1} and ξ_1 are the natural frequency and the damping ratio of the valve, respectively.

In the Eq.(3), the conductance is assumed with a sign, which is that of the V_{REF1} control signal. The mass flow-rate G_1 that is controlled by the valve V_1 with the hypothesis for which the supply and discharge pressures are constant, is a non linear function of the conductance C_1 and the downstream pressure P_1 . A typical diagram of the flow-rate $G_1 = G_1(C_1, P_1)$ is shown in Fig. 11, which can be expressed analytically through ISO 6358. Similar considerations can be done for the valve V_2 .

4.3 Cylinder block

The pneumatic actuator can be modeled through the continuity equations of the air mass flowing to the rear and front chambers, which expresses the dynamic relation between the input flow-rates and the pressures that are produced, and through the equation of the dynamic equilibrium of the piston. For each chamber, the continuity equation is given by

$$\sum G_{IN} - \sum G_{OUT} = \frac{d(\rho V)}{dt} = \rho \frac{dV}{dt} + V \frac{d\rho}{dt} \tag{4}$$

In the hypothesis the polytropic transformation of the air is represented by the exponent n , giving

$$G_1 = \frac{P_{li} A_1}{RT_{li}} \left(\frac{P_1}{P_{li}} \right)^{\frac{1}{n}} \frac{dx}{dt} + \frac{A_1 (x_0 + x_{m1} + x)}{nRT_{li}} \left(\frac{P_1}{P_{li}} \right)^{\frac{1-n}{n}} \frac{dP_1}{dt} \tag{5}$$

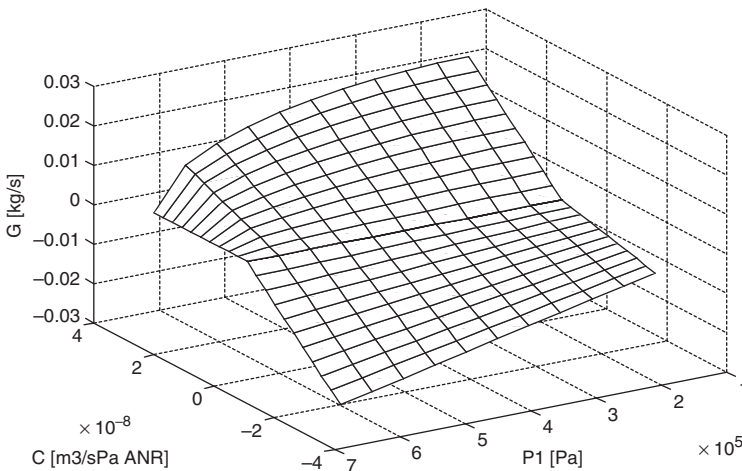


Fig. 11 Diagram of the mass flow-rate across a three-way proportional valve

$$G_2 = -\frac{P_{2i} A_2}{RT_{2i}} \left(\frac{P_2}{P_{2i}}\right)^{\frac{1}{n}} \frac{dx}{dt} + \frac{A_2(x_0 + x_{m2} - x)}{nRT_{2i}} \left(\frac{P_2}{P_{2i}}\right)^{\frac{1-n}{n}} \frac{dP_2}{dt} \tag{6}$$

for the rear and front chambers, respectively. Referring to Fig. 9, the dynamic equilibrium of the piston for each position within the cylinder stroke with $|x| \leq x_0$, is expressed by

$$\frac{d^2 x}{dt^2} = \frac{(P_1 - P_{amb})A_1 - (P_2 - P_{amb})A_2 - F_E - \gamma \frac{dx}{dt} - F_F}{M} \tag{7}$$

where the position $x = 0$ corresponds to half stroke of the piston.

4.4 Position transducer block

The position transducer can be assumed as a zero order system, which is characterized by the static gain K_{TP} between the position x and the normalized voltage signal $V_{F/B}$, through the expression

$$K_{TP} = \frac{V_{F/B \max}}{x_{\max}} \tag{8}$$

where the subscript “max” indicates the maximum value.

5 LINEAR DYNAMIC MODEL

The pneumatic positioning servo-system shown in Fig. 9 is modelled through the following 8-order system of non-linear equations

- a) $V_{REF1}(t) = f(G_C, V_{SET}, V_{F/B})$
- b) $V_{REF2}(t) = f(G_C, V_{SET}, V_{F/B}, \alpha)$
- c) $C_1(t) = f(V_{REF1})$
- d) $C_2(t) = f(V_{REF2})$
- e) $G_1(t) = f(C_1, P_1)$
- f) $G_2(t) = f(C_2, P_2)$
- g) $P_1(t) = f(G_1, \dot{x}, x)$
- h) $P_2(t) = f(G_2, \dot{x}, x)$
- i) $x(t) = f(P_1, P_2, F_E, F_F)$

In order to carry out a linear analysis with the aim to shown the static and dynamic performances of the servo-system for design purposes, a linearization of some of the equations (9) is necessary. In particular, Eqs.9a) and 9b) can be assumed linear when the signals are lower than the saturation values of the hardware controller. Equations 9c) and 9d) are linear already because the static gain K_V of the valves V_1 and V_2 has been expressed from a linear regression. Moreover, supposing as a first approximation that the Coulomb friction can be neglected ($F_F \approx 0$), the motion law 9i) can be considered linear.

The considerations reported below are carried out for the valve V_1 , but they are also valid for the valve V_2 . The linearization of the mass flow-rate G_1 requires that the surface shown in Fig. 11 is approximated through a plane. At this supply condition ($V_{REF1} > 0$), a subsonic flow from the supply port to the outlet port can be assumed, while in the discharge condition

($V_{REF1} < 0$), a sonic flow from the outlet port to the discharge port can be also assumed. These hypothesis limit the variation range of the downstream pressure P_1 , which can be defined by the following inequalities

$$b P_S \leq P_1 \leq P_S \quad (\text{subsonic flow in supply}) \quad (10)$$

$$P_v/b \leq P_1 < \infty \quad (\text{sonic flow in discharge}) \quad (11)$$

Thus, one has

$$\max(P_v/b, b P_S) \leq P_1 \leq P_S \quad (12)$$

In the subsonic configuration ($V_{REF} > 0$) with $b < b^* < 1$, linearization of the supply mass flow-rate can be carried out through a secant line joining the points $P_1 = P_S$, $G_1 = 0$ and $P_1 = b^* P_S$, $G_1 = G_{1\text{sonic}}$. Thus, it yields

$$G_{1S} = \frac{\rho_{ANR}}{1-b^*} (P_S - P_{1r}) C_1 - \frac{\rho_{ANR}}{1-b^*} C_{1r} P_1 + \frac{\rho_{ANR}}{1-b^*} C_{1r} P_r \quad (13)$$

where P_{1r} and C_{1r} are the outlet pressure and the conductance of the linearization, respectively. In the sonic configuration ($V_{REF1} < 0$), one has

$$G_{1D} = \rho_{ANR} P_r C_1 + \rho_{ANR} C_{1r} P_1 - \rho_{ANR} C_{1r} P_r \quad (14)$$

where the conductance C_1 and the corresponding linearized conductance C_{1r} are negative. An arithmetic mean (13) of the Eqs.(13) and (14) gives the following expression

$$G_1 = K_{GC1} C_1 + K_{GP1} P_1 + K_{GR1} \quad (15)$$

where

$$K_{GC1} = \rho_{ANR} \frac{P_S - b^* P_{12}}{r(1-b^*)} \quad (\text{flow gain}) \quad (16)$$

$$K_{GP1} = -\rho_{ANR} \frac{C_{12}(2-b^*)}{(1-b^*)} \quad (\text{flow/pressure gain}) \quad (17)$$

$$K_{GR1} = \rho_{ANR} \frac{\rho_{12} C_{12}(2-b^*)}{2(1-b^*)} \quad (\text{flow constant gain}) \quad (18)$$

When the linearization range of the conductance C_{1r} is equal to zero, which corresponds to the valve operating range of the central position of the valve V_1 , the Eq.(15) takes the form

$$G_1 = K_{GC1} C_1 = \rho_{ANR} \frac{P_s - b^* P_{1r}}{r(1-b^*)} C_1 \tag{19}$$

Similar considerations can be done for the valve V_2 and assuming that $C_{2r} = 0$, one has

$$G_2 = K_{GC2} C_2 = \rho_{ANR} \frac{P_s - b^* P_{2r}}{r(1-b^*)} C_2 \tag{20}$$

where P_{2r} is the pressure of linearization.

The linearization of the continuity Eqs.(5) and (6), which are indicated with g) and h) in the equations system (9), is carried out by choosing the linearization range : $P_1 = P_{1r}$, $P_2 = P_{2r}$, $x = x_r$, $\dot{x} = \dot{x}_r = 0$, $\dot{P}_1 = \dot{P}_{1r} = 0$, $\dot{P}_2 = \dot{P}_{2r} = 0$, where the volumes corresponding to the dead positions x_{m1} and x_{m2} of the piston, are neglected. According to these hypothesis, the Eqs.(5) and (6) take the form

$$G_1 = \frac{P_{1r} A_1}{RT} \dot{x} + A_1 \frac{x_0 + x_r}{nRT} \dot{P}_1 \tag{21}$$

$$G_2 = -\frac{P_{2r} A_2}{RT} \dot{x} + A_2 \frac{x_0 - x_r}{nRT} \dot{P}_2 \tag{22}$$

The equations system (9), which involves the Eqs.(15), (21) and (22), can be represented through the block diagram of Fig.12, where both inputs X_{SET} and F_E , and the output x of the piston position, are shown. In the hypothesis of identical valves V_1 and V_2 ($K_{V1} = K_{V2} = K_V$, $\sigma_{n1} = \sigma_{n2} = \sigma_n$, $\xi_1 = \xi_2 = \xi$, $\alpha = -1$), the block diagram of Fig. 13 can be obtained from that of Fig.12, in order to achieve the Laplace transfer function of the output displacement \bar{x} versus both inputs \bar{x}_{SET} and \bar{F}_E . Thus, it yields

$$\bar{x} = \frac{G_C K_{OLV} \sigma_n^2 \sigma_A^2 K_{SET}}{s(s^2 + 2\xi \sigma_n s + \sigma_n^2)(s^2 + 2\xi \sigma_A s + \sigma_A^2) + G_C K_{OLV} \sigma_n^2 \sigma_A^2 K_{TP}} \bar{x}_{SET} + \frac{s(s^2 + 2\xi \sigma_n s + \sigma_n^2) K_{OLF} \sigma_A^2}{s(s^2 + 2\xi \sigma_n s + \sigma_n^2)(s^2 + 2\xi \sigma_A s + \sigma_A^2) + G_C K_{OLV} \sigma_n^2 \sigma_A^2 K_{TP}} \bar{F}_E \tag{23}$$

According to the linearization hypothesis assumed above, the characteristic parameters of the servo-system are

$$K_{OLV} = \frac{\rho_{ANR} RT_i}{2(1-b^*)} \frac{K_V}{A_1} \left(\frac{2P_s - b^* P_{1r} (1 - x_r/x_0) - b^* P_{2r} (1 + x_r/x_0)}{P_{1r} (1 - x_r/x_0) + (A_2/A_1) P_{2r} (1 + x_r/x_0)} \right) \begin{matrix} \text{(uncompensated static} \\ \text{gain in open-loop} \\ \text{or speed gain)} \end{matrix} \tag{24}$$

$$k_0 = \frac{F_E}{\Delta x} = \frac{nA_1 P_r (1 - x_r/x_0) + (A_2/A_1) P_{2r} (1 + x_r/x_0)}{x_0 (1 - (x_r/x_0)^2)} \quad (\text{linear actuator stiffness}) \quad (25)$$

$$\sigma_A = \sqrt{\frac{k_0}{m}} = \sqrt{\frac{nA_1 P_r (1 - x_r/x_0) + (A_2/A_1) P_{2r} (1 + x_r/x_0)}{m x_0 (1 - (x_r/x_0)^2)}} \quad (\text{cylinder natural frequency}) \quad (26)$$

$$\xi_A = \frac{\gamma}{2\sqrt{k_0 m}} = \frac{\gamma}{2\sqrt{\frac{m n A_1 P_r (1 - x_r/x_0) + (A_2/A_1) P_{2r} (1 + x_r/x_0)}{x_0 (1 - (x_r/x_0)^2)}}} \quad (\text{cylinder damping ratio}) \quad (27)$$

$$K_{OLF} = \frac{1}{k_0} = \frac{x_0}{nA_1 P_r (1 - x_r/x_0) + (A_2/A_1) P_{2r} (1 + x_r/x_0)} \quad (\text{force constant}) \quad (28)$$

Referring to the experimental set-up of Fig.1, the constant values of the Eqs.(24-28) and the other parameters indicated above, are reported in Table 1.

Referring to the linearized block diagram of Fig.13 and to the Eq.(23), the diagrams of the frequency response of the transfer functions \bar{V}_{F1B}/\bar{e} and $\bar{V}_{F1B}/\bar{V}_{SET}$, in open-loop and closed-loop, respectively, are reported in Figs.14 and 15, along with the experimental results for a V_{SET} amplitude signal of 2 V (40% of the maximum V_{SET} value). For the open-loop frequency response of Fig.14, a good agreement between the theoretical results of the linearized model and the experimental results can be observed on the phase diagram and in the value of the natural frequency of the servo-actuator ($\sigma_A = 16.4$ Hz), while a relevant difference between the slopes of the amplitude curves is evident, mainly at low frequencies. At difference of the linearized model, which gives a slope of -20 dB/dec of the amplitude curve at frequencies lower than 5 Hz, the slope of the experimental curve is about the half of this theoretical value. This behavior is due to the significant Coulomb friction between piston and cylinder tube, and between rod and covers, as already shown in the time sinusoidal responses of Figs.4-7. The closed-loop frequency response confirms the good prediction of the band-width for an amplitude of 40% of the V_{SET} signal.

Table 1 Numerical values of the physical parameters of the servo-system

$A_1=A_2$	$6.91 \cdot 10^{-4} \text{ m}^2$	P_S	$6.5 \cdot 10^5 \text{ Pa}$
b^*	0.65	R	287.1 J/Kg K
G_C	0.55 V/V	T_i	293 K
k_0	$8.64 \cdot 10^3 \text{ N/m}$	n	1
K_{OLF}	$1.16 \cdot 10^{-4} \text{ m/N}$	x_0	80 mm
K_{OLV}	0.832 m/s V	x_r	0
K_{TP}	62.5 V/m	γ	50 N s/m
K_{SET}	62.5 V/m	ξ	0.6
K_V	$6.2 \cdot 10^{-9} \text{ m}^3/\text{s Pa V}$	ξ_A	0.3
m	0.8 Kg	σ_A	103 rad/s
P_{1r}	$5 \cdot 10^5 \text{ Pa}$	σ_n	600 rad/s
P_{2r}	$5 \cdot 10^5 \text{ Pa}$	ρ_{ANR}	1.188 Kg/m^3

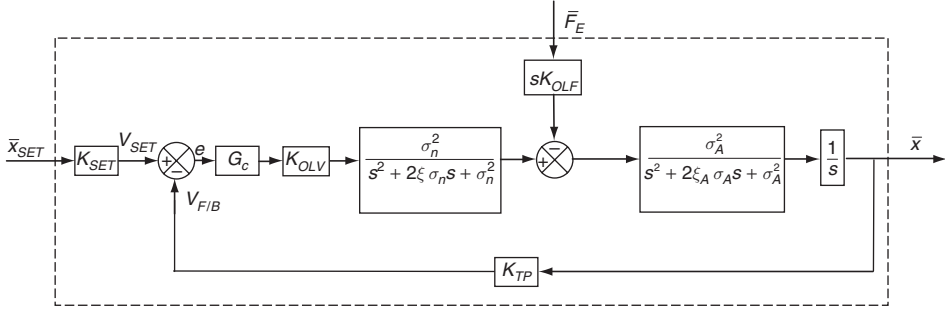


Fig. 13 Block diagram of the linearized model of the pneumatic servo-system

The linearized model is not able to give useful results in open-loop and closed-loop, when the amplitude of the sinusoidal V_{SET} signal is lower than 2 V, as shown by comparing the results of Figs. 14 and 15 with the experimental results of Figs. 2 and 3, respectively.

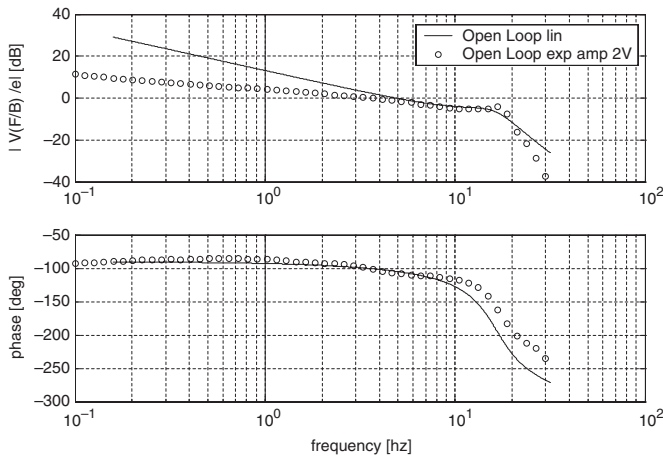


Fig. 14 Theoretical and experimental open-loop frequency responses

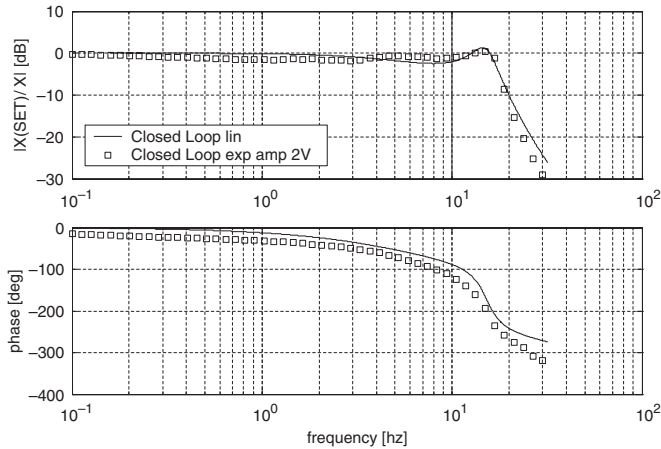


Fig. 15 Theoretical and experimental closed-loop frequency responses

6 CONCLUSIONS

The proposed analysis of a typical pneumatic positioning servo-actuator has allowed the validation of the linear model presented. This experimental validation is good in the case of high amplitudes of the input control signal, in order to overcome the significant effects of the Coulomb friction inside the cylinder, which is increased by the double rod piston. In this conditions, the proposed model allows the characteristic parameters of the servo-actuator to be shown by varying the pressures and position, which are chosen in the linearization range.

ACKNOWLEDGEMENTS

The Italian “Ministero dell’Istruzione, dell’Università e della Ricerca” is acknowledged for the financial support 2003-2005 of the project *Pneumatic and mechatronic systems for the growing and the harvesting of traditional and strictly related with the specific background agricultural products*.

REFERENCES

1. Wang J., Pu J., Moore P., Accurate position control of servo pneumatic actuator systems: an application to food packaging, *Control Engineering Practice*, 7, 1999, pp.699-706.
2. Pastorelli S., Sorli M., Design of the pneumatic servo-system of a 3 d.o.f. motion simulator, 3rd FPNI-PhD Symposium on Fluid Power, Terrassa, 2004, pp.433-440.
3. Quaglia G., Sorli M., Guala A., Air suspensions: non linear analysis and design considerations, 2nd Int.Fluidtechnisches Kolloquium IFK, Dresden, 16-17 mar 2000, pp.470-492
4. Sorli M., Franco W., Mauro S., Quaglia G., Giuzio R., Vernillo G.. Features of a lateral active pneumatic suspensions in the high speed train ETR470, *Mechatronics '98*, Elsevier Science Ltd, Oxford, 1998, pp.621-626, (Proc. 6th UK Mechatronics Forum Int. Conf., Skovde, Sweden, 9-11 sett. 1998)
5. Pastorelli S., Almondo A., Sorli M., Performances of cam-follower systems with pneumatic return spring, *PTCM 2005 - Bath Workshop on Power Transmission & Motion Control*
6. Belforte G., Gastaldi L., Pastorelli S., Sorli M., “Active Gait Orthosis with Pneumatic Proportional Control”, 4th Int. Conference on Climbing and Walking Robots CLAWAR 2001, Sept. 24-26 2001, pp.47-54
7. Figliolini G., Almondo A., Sorli M., Modelling and experimental validation of a pneumatic servo-solenoid valve, *Bath Workshop on Power Transmission and Motion Control*, Eds.C.R. Burrows, K.A. Edge and D.N. Johnston, Professional Engineering Publishing, London, 2004, pp.85-98.
8. Varseveld R.B., Bone G.M., Accurate position control of a pneumatic actuator using on/off solenoid valves, *IEEE/ASME Transactions on Mechatronics*, 2 (3), 1997, pp.195-204.
9. Brun X., Thomasset D., Bideaux E., Influence of the process design on the control strategy: application in electropneumatic field, *Control Engineering Practice*, 10, 2002, pp.727-735.
10. Lee H. K., Choi G. S., Choi G. H., A study on tracking position control of pneumatic actuators, *Mechatronics*, 12, 2002, pp.813-831.
11. Krivts I. L., New pneumatic cylinders for improving servo actuator positioning accuracy, *ASME Journal of Mechanical Design*, 126 (3), 2004, pp.744-747.
12. Figliolini G., Sorli M., Open-loop force control of a three-finger gripper through PWM modulated pneumatic digital valves, *Journal of Robotics and Mechatronics*, 2000, pp.480-493.
13. Sorli M., Pastorelli S., “Hydraulic and Pneumatic Actuation Systems”, Chapter 20.4 in *The Mechatronics Handbook*, ed. in chief R.H. Bishop, CRC Press, Boca Raton, 2002, pp.20-62 20-96.

Performances of cam-follower systems with pneumatic return spring

S. Pastorelli, A. Almondo and M. Sorli

Department of Mechanics, Politecnico di Torino, Italy

ABSTRACT

The paper deals with the dynamic analysis of a cam-follower transmission system with particular attention to the elastic return device, which is required to guarantee the maintenance of the contact between the cam and the follower. Traditional mechanical springs and innovative pneumatic springs are analysed and compared in terms of dynamic stiffness of the mechanism. A combined lumped-distributed parameters model, capable of predicting the effects of the higher harmonics of the cam lift profile on system performances, is presented. The advantages of the pneumatic spring solution are discussed and a pressure control circuit is proposed.

1. INTRODUCTION

The cam-follower mechanism is used by designers to obtain a particular output motion, with precise positioning and phase synchronization. This work is focused on the dynamic analysis of this transmission system, with particular attention to the elastic return device, which is required to guarantee the maintenance of the contact between the cam and the follower.

One factor of particular concern is the proper choice of stiffness and preload of the return spring. Inadequate amount of the latter results in follower jump at high rotation speeds. Excessive return spring force, on the other hand, is also undesirable due to increased contact forces between the cam and the follower, resulting in greater surface stresses and shorter life as well as increased power requirements. Other problems, such as collision between spring coils and vibrations can be caused by the undesirable response of the spring under displacement excitation.

An analytical model of a cam-follower system based on distributed parameters description of the spring was proposed by Pisano and Freudenstein [1] providing a comparison between model prediction and experimental results. The model was capable of accurately predicting both normal system response as well as pathological behaviour associated with the onset of toss, bounce and spring surge. Tümer and Ünlüsoy [2, 3] analysed the dynamic

stiffness of force-closed cam mechanism obtaining results about the time history of the contact force too. Their parametric approach highlighted that the operating limit conditions of the follower jump depend on the spectral power of the follower displacement, which is function of the cam profile and rotational speed, on the follower mass, on the resonances of the return spring and on the internal damping of the system.

In this work, the same approach will be applied to compare the dynamic behaviour of a traditional cam-follower system with the behaviour of an innovative system with pneumatic return spring. The presented analysis is based on a linear model for the simulation of the transmission system dynamics in frequency and time domain, assuming the follower to be a rigid body, with defined mass and displacement imposed by the cam profile, and adopting a continuous model of the return spring. The model proposed is valid within the hypothesis of continuous contact between cam, follower and spring and is able to evaluate the contact forces for different working conditions. The pneumatic spring will be analysed both as a closed volume and connected to a suitable pressure control device. Pneumatic springs are commonly applied in vehicular air suspension devices [4]; at present gas return spring solutions are earning great interest for those applications where high operation speeds of the cam-shaft require high dynamic performances of the system, i.e. for automotive racing engines.

The advantages of a pneumatic spring, compared with a mechanical one, will be discussed: the regulation of the internal pressure enables tuning of the preload, in order to suitably control the contact force between the cam and the follower when the speed of the camshaft changes; besides, higher values of spring resonances enable to avoid follower jump with high operating speeds or with severe acceleration cam profiles.

In conclusion, a design solutions of a pneumatic return spring and control circuit for a cam-follower mechanism is proposed and analysed.

2. CAM-FOLLOWER SYSTEM

Figure 1a shows a schematic drawing of the cam-follower system. It is assembled from a overhead cam, a direct-acting sliding inverted bucket follower and the return spring.

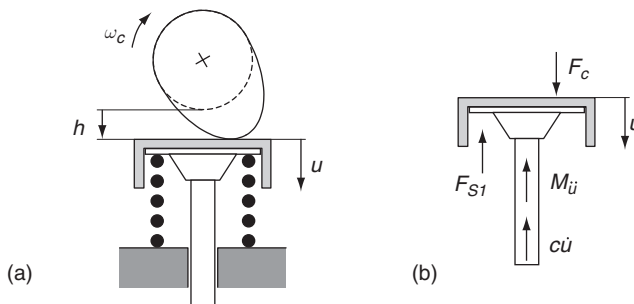


Figure 1 Cam-follower system

By considering the forces acting in axial direction on the follower (figure 1b), that are the contact force with the cam F_c , the elastic force of the spring F_{S1} , the inertia force proportional to the follower mass M and the damping force due to an equivalent viscous damping c , the equilibrium equation can be written:

$$F_c - F_{S1} - M\ddot{u} - c\dot{u} = 0 \tag{1}$$

The follower motion is related to the cam lift history. This can be described approximating the cam profile $h(\vartheta)$ with a finite Fourier series, writing:

$$h(\vartheta) = a_0 + \sum_{r=1}^N a_r \cos(r\vartheta + \varphi_r) \tag{2}$$

where a_r and φ_r are the amplitude and phase angle of each harmonic component of the profile. For a constant speed of rotation ω_c of the camshaft, $\vartheta = \omega_c t$ and the cam lift time history can be obtained as:

$$h(t) = a_0 + \sum_{r=1}^N a_r \cos(r\omega_c t + \varphi_r) \tag{3}$$

As an example, in figure 2a the profile of an automotive cam, that will serve as a basis for the study, is shown. In figure 2b the amplitudes of the first 50 Fourier profile components are diagrammed.

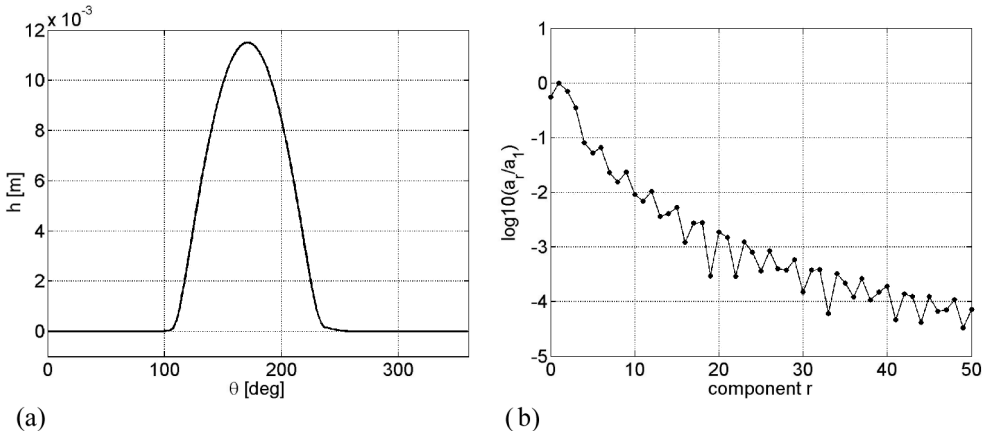


Figure 2 Cam profile (a) and Fourier components amplitudes (b)

With the contact hypothesis, the displacement imposed to the spring-follower system is coincident with the cam lift $h(t) = u(t)$; the force between the cam and the follower can be computed starting from the cam harmonic content and from the expression of the system

dynamic stiffness.

For the generic harmonic component $u(t) = \bar{u} \cos(\omega t)$, from equation (1), it is possible to express the dynamic stiffness of the spring-follower system as a function of the frequency ω :

$$k_{dyn}(\omega) = \frac{\bar{F}_c}{\bar{u}}(\omega) = \frac{\bar{F}_{S1}}{\bar{u}}(\omega) + j\omega \cdot c - M\omega^2 \tag{4}$$

Then the contact force can be computed, as a superposition of the effects of each Fourier component of the cam lift $h(t) = u(t)$:

$$F_c(t) = F_0 + k_S a_0 + \sum_{r=1}^N |k_{dyn}(r\omega_c)| \cdot a_r \cos(r\omega_c t + \varphi_r + \phi(r\omega_c)) \tag{5}$$

where $|k_{dyn}(r\omega_c)|$ and $\phi(r\omega_c)$ are the magnitude and phase of the dynamic stiffness function for $\omega = r\omega_c$, F_0 is the value of the preload on the spring and k_S is the spring static stiffness. The preload must be opportunely chosen to guarantee a positive value of the contact force F_c in each working condition. To efficiently set the preload value it is necessary to analyse the system stiffness function $k_{dyn}(\omega)$, that relates the displacement history to the contact force in each time instant. To analyse the system stiffness it is necessary to study the dependence of the spring stiffness $\frac{\bar{F}_{S1}}{\bar{u}}$ on the frequency of excitation. In the following part of the paper this stiffness is determined in the cases of mechanical and pneumatic spring.

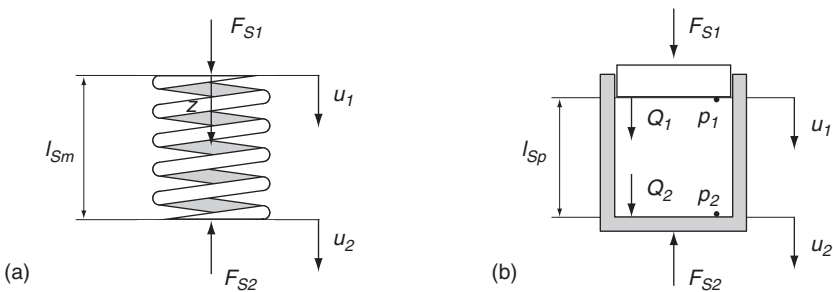


Figure 3 Mechanical (a) and pneumatic (b) spring

2.1 Mechanical spring

Considering a coil spring, schematically represented in figure 3a, described as a continuous system and subject to a sinusoidal axial stress with frequency ω , it is possible to write the translation equilibrium equation and the equation describing the longitudinal elastic

deformations:

$$\frac{d\bar{F}(z)}{dz} + \frac{m_{Sm}}{l_{Sm}} \omega^2 \bar{u}(z) = 0 \quad (6)$$

$$\bar{F}(z) = k_{Sm} l_{Sm} \frac{d\bar{u}(z)}{dz} \quad (7)$$

These equations form a system of differential equations, that relates the amplitude of time variation of force $\bar{F}(z)$ and displacement in axial direction $\bar{u}(z)$, as a function of the axial coordinate z , of spring mass m_{Sm} , length l_{Sm} and static stiffness k_{Sm} and of the vibration frequency ω .

From this system it is possible to obtain a wave propagation equation, from which a transfer matrix formulation can be write, relating force and axial displacement values at the ends of the spring, following the conventions shown in figure 3a:

$$\begin{bmatrix} \bar{u}_1 \\ \bar{F}_{S1} \end{bmatrix} = \begin{bmatrix} \cos(\omega / \omega_{Sm}) & 1/k_{Sm} \cdot (\omega_{Sm} / \omega) \cdot \sin(\omega / \omega_{Sm}) \\ -k_{Sm} \cdot (\omega / \omega_{Sm}) \cdot \sin(\omega / \omega_{Sm}) & \cos(\omega / \omega_{Sm}) \end{bmatrix} \cdot \begin{bmatrix} \bar{u}_2 \\ \bar{F}_{S2} \end{bmatrix} \quad (8)$$

being:

$$\omega_{Sm} = \sqrt{\frac{k_{Sm}}{m_{Sm}}} \quad (9)$$

By imposing the boundary conditions, i.e. the null displacement at the fixed end of the spring ($u_2 = 0$), the dynamic stiffness $\frac{\bar{F}_{S1}}{\bar{u}}$ can be found, as a function of the vibration frequency:

$$k_{Smd}(\omega) = \frac{\bar{F}_{S1}}{\bar{u}_1}(\omega) = k_{Sm} \frac{\omega}{\omega_{Sm}} \cdot \frac{1}{\tan(\omega / \omega_{Sm})} \quad (10)$$

Besides, in a mechanical spring the preload can be set by imposing a constant compression δ_0 , obtaining a preload force F_{0m} proportional to the static stiffness:

$$F_{0m} = k_{Sm} \delta_0 \quad (11)$$

2.2 Pneumatic spring

A schematic representation of a closed volume pneumatic spring is given in figure 3b. It can be considered as a closed cylinder with a piston, connected to the follower. The piston

displacement determines a compression or an expansion of the contained gas, varying its pressure and causing an elastic effect on the follower.

To evaluate its dynamic behaviour with a linear model, the pneumatic spring has been modeled as a short fluid transmission line. The relation between flow rate Q and pressure p can be expressed through the continuity and equilibrium equations:

$$\frac{d\bar{Q}(z)}{dz} = -\frac{1}{c \cdot Z_c} j\omega \cdot \bar{p}(z) \quad (12)$$

$$\frac{d\bar{p}(z)}{dz} = -\frac{Z_c}{c} j\omega \bar{Q}(z) \cdot N(j\omega) \quad (13)$$

where $N(j\omega)$ is the viscous friction factor, proportional to the dynamic viscosity μ_0 , c is the speed of sound, function of the polytropic exponent n and of the mean pressure p_0 and density ρ_0 :

$$c = \sqrt{\frac{np_0}{\rho_0}} \quad (14)$$

and Γ and Z_c are the wave propagation constant and the characteristic impedance for a line of length l_{Sp} and transverse area A_{Sp} :

$$\Gamma = \frac{j\omega \cdot l_{Sp}}{c} \sqrt{N(j\omega)}; \quad Z_c = \frac{\rho_0 c}{A_{Sp}} \sqrt{N(j\omega)} \quad (15)$$

Starting from equations (12) and (13), the four pole equation can be obtained [5] expressing the relationship among the upstream and downstream pressure and volume flow rate amplitudes:

$$\begin{bmatrix} \bar{Q}_1 \\ \bar{p}_1 \end{bmatrix} = \begin{bmatrix} \cosh \Gamma & 1/Z_c \sinh \Gamma \\ Z_c \sinh \Gamma & \cosh \Gamma \end{bmatrix} \begin{bmatrix} \bar{Q}_2 \\ \bar{p}_2 \end{bmatrix} \quad (16)$$

By imposing as a boundary condition a null value of flow at the fixed spring end ($Q_2 = 0$), the dynamic relation between pressure and flow rate at the spring piston can be written:

$$\frac{\bar{p}_1}{\bar{Q}_1}(\omega) = \frac{Z_c}{\tanh \Gamma} \quad (17)$$

and using the relations between the pressure and force and between flow rate and speed at the piston surface:

$$\bar{Q}_1 = A_{Sp} \bar{v}_1 = A_{Sp} j \omega \cdot \bar{u}_1 \quad (18)$$

$$\bar{p}_1 = \frac{\bar{F}_1}{A_{Sp}} \quad (19)$$

the dynamic stiffness $\frac{\bar{F}_{S1}}{\bar{u}}$ of the pneumatic spring can be found as a function of the vibration frequency:

$$k_{Spd}(\omega) = \frac{\bar{F}_{S1}}{\bar{u}}(\omega) = A_{Sp}^2 j \omega \frac{Z_c}{\tanh \Gamma} \quad (20)$$

The pneumatic spring static stiffness can be obtained by computing the limit for $\omega \rightarrow 0$ of equation (20), showing its relation with the gas compressibility, the spring transversal area and length:

$$k_{Sp} = \frac{np_0 A_{Sp}}{l_{Sp}} \quad (21)$$

Besides, in a pneumatic spring the preload is determined by the effect of the internal pressure on the piston surface:

$$F_{0p} = p_0 A_{Sp} \quad (22)$$

It can be observed that, while in a mechanical spring the preload F_{0m} and static stiffness k_{Sm} can be chosen independently, this can not be done in a pneumatic spring with given geometry, where the variation of internal pressure affects both the static stiffness k_{Sp} and preload value F_{0p} .

3. DYNAMIC STIFFNESS OF THE CAM-FOLLOWER SYSTEM

The comparison between the dynamic stiffness of mechanical and pneumatic spring has been done by choosing a particular mechanism. In this case a valve train of an automotive engine has been considered, with follower and mechanical spring data listed in Table 1. The related cam profile has been previously presented in figure 2. The characteristics of a pneumatic spring, with a geometry compatible with that of the mechanical one, are presented in the table too. A complex value has been used for the mechanical spring static stiffness, to take into account the effect of the internal damping. For the pneumatic spring, a mean pressure value $p_0 = 10^6 Pa$ has been chosen.

The absolute value of the spring-follower dynamic stiffness as a function of the vibration frequency in the range between 0 and 1500 Hz is shown in figure 4, both for mechanical and pneumatic spring systems. The stiffness is obtained from equation (4) in which expression (10) or (20) is introduced, assuming the contact between follower and spring ($\bar{u} = \bar{u}_1$).

Table 1

Follower	Mechanical spring	Pneumatic spring
$M = 0.140 \text{ kg}$ $c = 10 \text{ N} \cdot \text{s} / \text{m}$	$k_{Sm} = 5.5 \cdot 10^4 \cdot (1 + 0.02j) \text{ N} / \text{m}$ $l_{Sm} = 0.050 \text{ m}$ $m_{Sm} = 0.050 \text{ kg}$	$A_{Sp} = \pi \cdot 0.015^2 = 7.07 \cdot 10^{-4} \text{ m}^2$ $l_{Sp} = 0.025 \text{ m}$ $p_0 = 10^6 \text{ Pa}$ $\rho_0 = 12.7 \text{ kg} / \text{m}^3$ $\mu_0 = 1.82 \cdot 10^{-5} \text{ Pa} \cdot \text{s}$ $n = 1.2$ $k_{Sp} = np_0 A_{Sp} / l_{Sp} = 3.4 \cdot 10^4 \text{ N} / \text{m}$

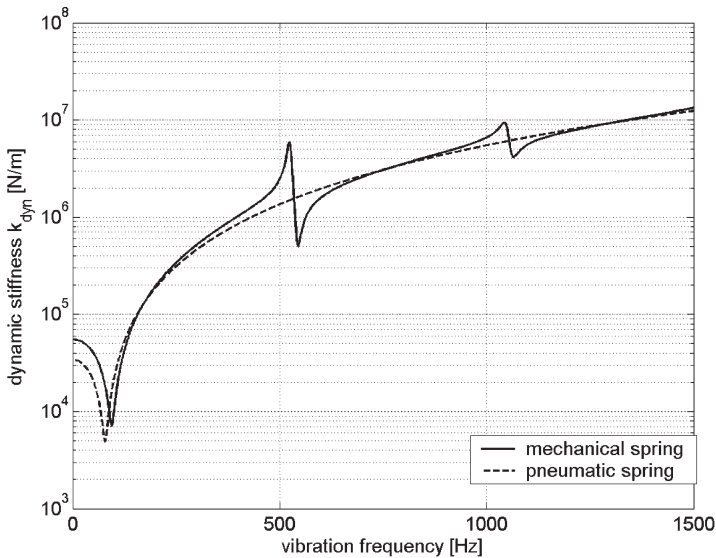


Figure 4 Variation of dynamic stiffness with vibration frequency for mechanical and pneumatic spring

In both cases a minimum stiffness can be observed around a frequency value equal to $1/2\pi \cdot \sqrt{k_{Sm} / M} = 100 \text{ Hz}$ and $1/2\pi \cdot \sqrt{k_{Sp} / M} = 78 \text{ Hz}$ respectively for mechanical and pneumatic spring systems. These values represent the first resonance of the spring-follower

system. The absolute stiffness values in this conditions are determined by the viscous damping coefficient c . For vibration frequencies lower than the first resonance the dynamic stiffness is mainly determined by the static stiffness k_{Sm} or k_{Sp} , on the other hand, for frequencies higher than the first resonance, the behaviour of both systems is determined by the follower inertial effect, proportional to $M\omega^2$. Moreover, in the case of mechanical spring, two dynamic stiffness peaks can be observed, for frequency values of about $i\omega_{Sm}/2$ ($i=1,2$), related to the period of the tangent function in equation (10). The physical meaning of these local stiffness maxima is the presence of internal resonances of the spring coils in axial movement. In the case of pneumatic spring model an analogous internal resonance can be observed only for frequencies higher than 5000 Hz, and its effect is small if compared with the predominant inertial term at that frequency.

The effect of the internal resonances can be seen analysing equation (5). If the follower displacement has a significant sinusoidal component with a frequency round the resonance frequency, the contact force F_c can have high oscillation amplitudes and so an higher preload must be imposed to prevent the cam follower separation.

4. CAM-FOLLOWER CONTACT FORCE EVALUATION AND PRELOAD DESIGN

Knowing the cam profile Fourier decomposition, the cam rotation speed and the system dynamic stiffness, from equation (5) the time variation of the contact force between the cam and the follower can be obtained.

For example, in figure 5 the follower displacement and the time history of the contact force for a cam rotation frequency $f_c = 50 \text{ Hz}$ ($\omega_c = 2\pi f_c$) are shown, obtained for the systems with mechanical and pneumatic spring, described in table 1. The force has been evaluated without preload effects. Both figures show two contact force peaks at the beginning and ending of the follower lift, caused by positive peak acceleration imposed by the cam profile. Different behaviour can be observed close to the maximum follower lift. For the mechanical spring system (figure 5a) the oscillations of the force due to the first internal resonance can be seen, with a frequency of about 500 Hz, related to the stiffening effect previously shown in figure 4. In the case of pneumatic spring (figure 5b), three different values of mean internal pressure have been considered. It can be observed that no resonance effects are present, while a sensible dependence of the contact force from the internal pressure is shown. The minimum negative value of the contact force decreases when internal pressure is reduced. In the force computation, the first 40 harmonic components of the cam profile have been considered; the neglected components have an amplitude four orders of magnitude lower than the first harmonic component, as can be seen in figure 2b. Some high frequency oscillations can be seen in both pneumatic and mechanic spring system simulations. These are due to the non uniform convergence in cam profile harmonic reconstruction, known as Gibbs phenomenon, but they do not influence the model capability of predicting the main behaviour of the contact force history, as observed by Tümer and Ünlüsoy in [2].

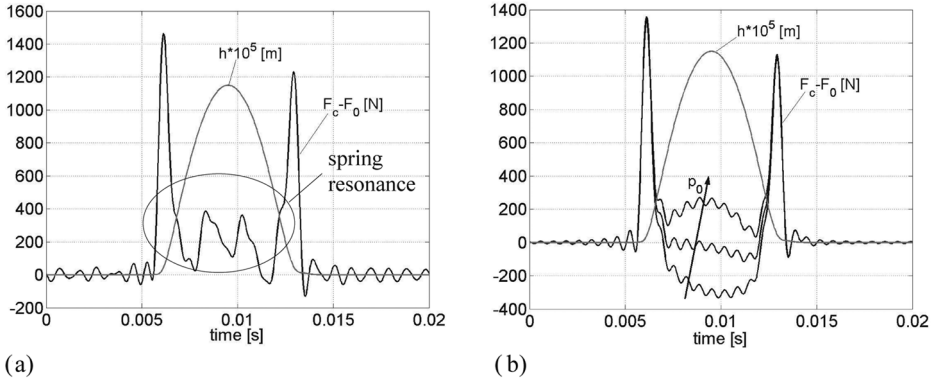


Figure 5 Contact force F_c profile for $f_c = 50\text{ Hz}$: **a)** mechanical spring system; **b)** pneumatic spring system with different values of mean air pressure ($p_{01} = 1 \times 10^5\text{ Pa}$, $p_{02} = 8 \times 10^5\text{ Pa}$, $p_{03} = 15 \times 10^5\text{ Pa}$)

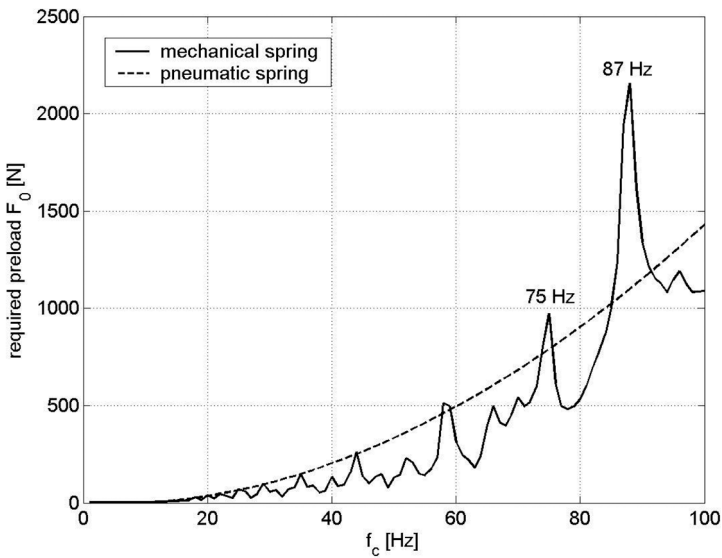


Figure 6 Minimum preload required to maintain the contact between the cam and the follower, for mechanical and pneumatic ($p_0 = 1 \times 10^5\text{ Pa}$) spring

A negative value of the contact force is not physically possible and indicates a violation of the contact hypothesis, i.e. a separation between the cam and the follower. So, to prevent this separation, a preload must be imposed to the spring, to compensate for the minimum negative force value obtained from the model. A different value of the required preload can

be found for each camshaft rotation speed. In figure 6 the preload force values obtained from the contact force simulation for cam rotation frequency varying between 0 and 100 Hz, are shown. This camshaft rotation speed range (0÷6000 rpm) corresponds, in a four-stroke engine, to a crankshaft speed from 0 up to 12000 rpm, thus considering the cam-follower behaviour of an high-speed engine. In pneumatic spring simulation, an internal pressure of $1 \times 10^5 \text{ Pa}$ has been used, obtaining the lower value of static stiffness and so overestimating the required preload.

As previously analysed in figure 4, at frequencies higher than the first resonance, the behaviour of the spring-follower system is mainly determined by the inertial effects. The simulation for cam rotation frequency range 0÷100 Hz, with 40 components of the cam profile considered, involves an harmonic contribute from 0 Hz up to 4000 Hz. Thus, having an important high frequency content, the time history of the contact force has an high inertia contribute, proportional to the acceleration of the follower. The spring preload has to be set in order to overcome the effect of the higher negative acceleration, that tends to separate the cam follower contact, and, with a given cam profile, is proportional to the square of the rotation speed.

The previous considerations are directly applicable to the pneumatic spring system, whose internal resonances occur for frequencies higher than 5000 Hz and thus are not significantly excited. In the case of the mechanical spring, the dynamic stiffness peaks effects are superimposed to the inertial behaviour of the system, as already described in figure 5a. When a component of the excitation is close to an internal resonance frequency of the spring, an increasing of the amplitude of the oscillation of the contact force is determined and higher values of the preload can be required.

For example, for a cam rotation frequency equal to 87 Hz, the 6th harmonic component of the profile excites the frequency $6 \times 87 = 522 \text{ Hz}$, which is close to the first internal resonance peak of the dynamic stiffness, with maximum at 523 Hz, as can be seen in figure 4. Analogously, the peak of the required preload in figure 6 at 75 Hz is the consequence of the 7th harmonic component.

Moreover, it can be observed as the required preload is lower for the mechanical spring than for the pneumatic spring system, except for the frequencies in which the mechanical spring presents the preload peaks. On the other hand it should be considered that the preload of the mechanical spring is fixed by its mounting condition, while the preload of the pneumatic spring can be changed varying the internal pressure. So, for the mechanical spring the preload is a consequence of the worst condition in the range of cam rotation and it is maintained for all rotation speeds, while the preload in a pneumatic spring can be changed as a function of the rotation speed, thus minimising in each condition the contact force between the cam and the follower.

As seen, in a pneumatic spring the variation of the internal pressure determines a variation of the preload, but also of the spring static stiffness. The diagram of figure 6, has been obtained with the static stiffness effect correspondent to a pressure $p_0 = 1 \times 10^5 \text{ Pa}$; actually, the preload increase can be given only increasing the internal pressure and so

changing the stiffness contribution.

To evaluate the effect of a pressure increase on the contact force history and so on the required preload and to better determine a pressure control strategy, a different approach can be proposed. The minimum value of the contact force for the pneumatic spring system is computed for the frequency range of interest, as in figure 6, for different internal pressure values. Thus a map of the minimum required preload can be obtained as a function of the frequency f_c and the mean pressure p_0 , as reported in figure 7 with the thin lines and the right axis. Successively, on the left axis the internal pressure $p_{0r} = F_{0p} / A_{Sp}$, necessary to provide each value of the required preload, is represented. At the end, the point in which each curve of the map with constant p_0 assumes a value $p_0 = p_{0r}$ represents a real working condition. In fact in that point the required internal pressure is equal to the pressure considered in evaluating the spring stiffness. Linking these points with a line, an evaluation of the strategy of variation of the internal pressure can be obtained. This method, taking into account the spring stiffness variation, permits to optimise the internal pressure at each rotation frequency and so to minimise the cam-follower contact force.

It can be observed that the preload demand obtained with this approach is lower than the one obtained with the hypothesis of ambient pressure in the spring ($p_0 = 1 \times 10^5 Pa$), with a preload saving, especially at high rotation frequencies.

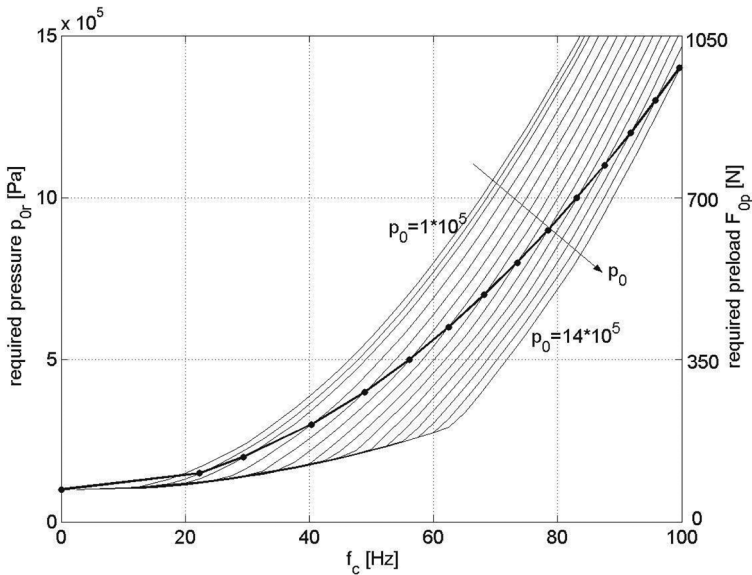


Figure 7 Pneumatic spring preload map as a function of the internal pressure (thin lines) and pressure control strategy (thick line)

5. PNEUMATIC SPRING PRESSURE CONTROL CIRCUIT

To control the internal pressure of the pneumatic spring, a pneumatic circuit can be developed. This circuit is composed by two modulated digital valves, a reservoir, a pneumatic line and an orifice connected to the spring chamber. A schematic representation of the system is given in figure 7. In particular, the pneumatic spring is a piston, provided with sliding seals, fixed to the follower. Seals between follower and spring case are adopted too. The volume is required in order to reduce the effects of gas loss through the seals and to improve the digital control performance. The pneumatic line is necessary to adapt the circuit geometry, and the orifice partially decouples the spring from the control system dynamic, as successively analysed.

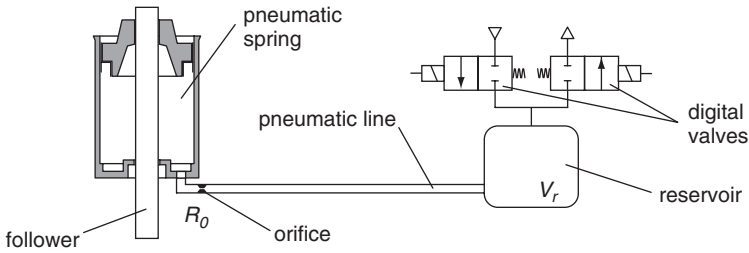


Figure 8 Pneumatic spring with pressure control circuit

The presence of the control circuit can vary the system dynamics and give results that are different from those obtained with the closed volume pneumatic spring. In order to analyse its dynamic behaviour, a dynamic model of the control circuit can be developed, introducing the dynamic effect of each component. In this study the control valves will be considered in their closed condition, analysing the system behaviour when a constant mean pressure has been imposed.

Representing the spring with the quadrupole model of equation (16), the orifice with a lumped resistance model, the pneumatic line with a distributed parameters transmission line model in form of equation (16) and the reservoir with a lumped capacitance, the transfer matrix model of the spring with control system can be obtained [6], relating the flow rate \bar{Q}_1 and the pressure \bar{p}_1 at the spring piston surface with the flow rate \bar{Q}_5 and the pressure \bar{p}_5 at the connection of the reservoir with the valves:

$$\begin{bmatrix} \bar{Q}_1 \\ \bar{p}_1 \end{bmatrix} = \begin{bmatrix} \cosh \Gamma_s & 1/Z_{c_s} \sinh \Gamma_s \\ Z_{c_s} \sinh \Gamma_s & \cosh \Gamma_s \end{bmatrix} \cdot \begin{bmatrix} 1 & 0 \\ R_o & 1 \end{bmatrix} \cdot \begin{bmatrix} \cosh \Gamma_l & 1/Z_{c_l} \sinh \Gamma_l \\ Z_{c_l} \sinh \Gamma_l & \cosh \Gamma_l \end{bmatrix} \cdot \begin{bmatrix} 1 & 0 \\ 0 & 1 \end{bmatrix} \cdot \begin{bmatrix} \bar{Q}_5 \\ \bar{p}_5 \end{bmatrix} \quad (23)$$

being C_r the capacity of a reservoir with volume V_r :

$$C_r = \frac{V_r}{np_0} \tag{24}$$

and R_o the orifice resistance, obtained from linearization of the equation expressing the volume flow rate in subsonic conditions (ISO 6358), as a function of the orifice conductance C , of the critical pressure ratio b and of ratios of the mean values and ambient condition values of fluid density and temperature:

$$R_s = \frac{1-b}{C} \frac{\rho_0}{\rho_{ANR}} \sqrt{\frac{T_0}{T_{ANR}}} \tag{25}$$

The dynamic stiffness k_{SpC} of the pneumatic spring with control circuit can be obtained in analogy with the stiffness of the simple closed volume pneumatic spring, by imposing in equation (23) as a boundary condition a null value of the flow rate through the control valves $Q_5 = 0$:

$$k_{SpC}(\omega) = A_{Sp}^2 j\omega \cdot \frac{\frac{T_{11}}{Z_L} + T_{12}}{\frac{T_{21}}{Z_L} + T_{22}} \tag{26}$$

It can be seen that the dynamic stiffness function depends on the geometry of the system, on the mean pressure p_0 , on the orifice resistance R_o and on the reservoir volume V_r .

In figure 9a the dependence of the absolute value of the spring-follower system dynamic

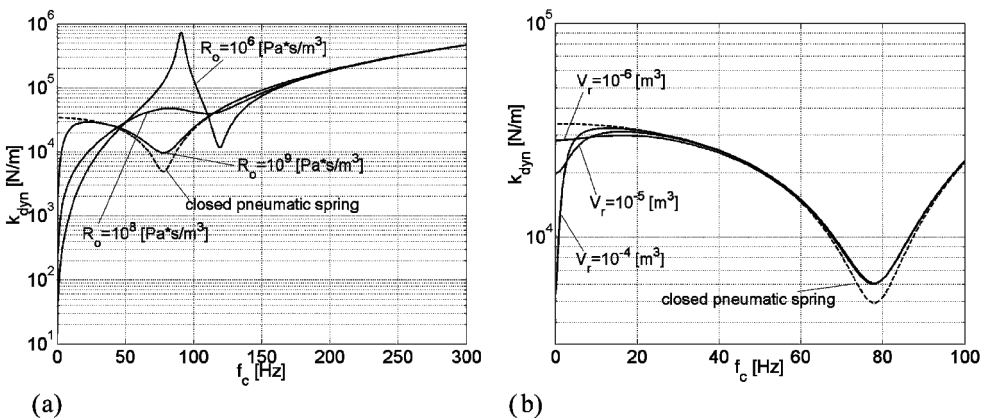


Figure 9 Spring-follower stiffness for pressure controlled pneumatic spring: a) influence of the orifice resistance; b) influence of the reservoir volume

stiffness from the orifice resistance is shown. A mean pressure $p_0 = 10^9 \text{ Pa}$, as in the analysis of the closed volume spring dynamics, has been assumed, with a reservoir volume of 10^{-4} m^3 . The effect of a 0.2 m long pipe with a 4 mm internal diameter has been introduced with the distributed parameters line model. In all the simulations an ambient temperature of $20 \text{ }^\circ\text{C}$ has been hypothesised. The dashed line represents the dynamic stiffness value obtained with the closed volume spring model, as in previous figure 4. It can be seen that for low values of the orifice resistance ($10^6 \text{ Pa}\cdot\text{s}/\text{m}^3$), of the same order of the pipe resistance, the system presents a local stiffness maximum. This is due to a resonance of the spring-line-reservoir system and it can have effects on the cam-follower contact force analogous to what has been seen for mechanical spring. Increasing the orifice resistance, this internal resonance can be avoided. The resistance in fact decouples the spring dynamics from the line-reservoir dynamics for frequency values inversely proportional to its value. For an infinite resistance, the spring would be fully decoupled from the control system and the dynamic stiffness would be coincident with the stiffness of the closed volume spring.

In the static condition ($f_c = 0$), a very low stiffness value can be observed, being inversely proportional to the fluid system capacitance, that includes the line and reservoir fluid volume. For high frequencies, the dynamic stiffness coincide with the values obtained for the closed volume spring, being the spring dynamics decoupled from the control circuit. The point of transition between the low stiffness to the high stiffness behaviour is determined by the orifice resistance value.

In figure 9b the influence of the reservoir volume on the spring-follower system stiffness is analysed. The mean pressure has been maintained equal to $p_0 = 10^6 \text{ Pa}$ and an orifice resistance $R_o = 4 \times 10^9 \text{ Pa}\cdot\text{s}/\text{m}^3$ has been assumed. This value corresponds in a first approximation to a 1 mm diameter orifice and gives a good decoupling between spring and control system fluid dynamics for frequencies higher than 10 Hz . So, the reservoir volume has an influence only in the low range of frequencies, varying the quasi-static spring stiffness. In figure 9b the effect of the volume variation on the static stiffness can be seen and the similitude with the closed volume spring behaviour for frequencies higher than 10 Hz is evidenced. Moreover, an added damping can be seen on the spring-follower resonance, due to the orifice-line dynamic effect and almost independent from the reservoir volume.

6. CONCLUSIONS

A model and an analytical methodology for the study of the dynamic behaviour of cam-follower system has been presented. In particular, a spring distributed model has been considered in predicting the cam follower contact force evaluating internal spring resonances. Working limits of the mechanical spring solution are imposed by the internal resonances which can be excited by high speed cam revolution. They induce wide oscillations of the contact force between the cam and the follower, which could bring to contact loss, unless an excessive preload is applied.

A comparison between mechanical and pneumatic return spring has revealed that the pneumatic design solution, although being characterised by a lower static stiffness when an equal preload is given, presents values of internal resonance frequencies an order of magnitude higher than mechanical one and avoid follower jump with high operating speeds or with severe acceleration profile of the cam. Moreover, the pneumatic spring has the advantage of preload tuning availability as a function of the cam rotation speed. This can be done setting the internal pressure by means of a suitable control circuit.

An optimisation methodology of the pressure control law has been proposed in the paper, as well as some design consideration are given analysing the influence of the control circuit parameters on the pneumatic spring dynamic behaviour. Further research activities will be devoted to the study of the effects of the circuit parameters on the dynamic performances of the pressure control.

ACKNOWLEDGMENTS

This research has been supported by the Italian “Ministero dell’Istruzione, dell’Università e della Ricerca” within the research project PRIN 2003 - Design and experimental validation of cam transmissions.

REFERENCES

- [1] Pisano, A.P., Freudenstein, F., (1983), “An Experimental and Analytical investigation of the Dynamic Response of a High-Speed Cam-Follower System” Parts 1 and 2, *J. of Mechanism, Transmission and Automation in Design*, vol. 105, Dec.1983, pp. 692-704.
- [2] Tümer S.T, Ünlüsoy, Y.S., (1991), “Nondimensional Analysis of Jump Phenomenon in Force-closed Cam Mechanism”, *Mech. Mach. Theory*, vol. 26, No. 4, pp. 421-432.
- [3] Ünlüsoy, Y.S., Tümer S.T, (1993), “Analytical Dynamic Response of Elastic Cam-Follower System with Distributed Parameter Return Spring”, *J. of Mechanical Design*, vol.115, Sept.1993, pp. 612-620.
- [4] Quaglia, G., Sorli, M., (2001), “Airsuspension dimensionless analysis and design procedure”, *Vehicle Systems Dynamics*, Vol. 35, n.6, pp.443-475.
- [5] Stecki J.S., Davis D. C., (1986), “Fluid Transmission Lines-Distributed Parameter Models, Part 1: A Review of the State of Art”, *Proc. Inst. Mech. Engrs. Part A*, Vol. 200, pp. 215-228, 1986.
- [6] Sorli M., Franco W., (2001), "Pneumatic line transients", 7th Scandinavian Int. Conf. On Fluid Power SICFP'01, Linköping, May 30 – June 1, 2001, pp.181-196.

Motion Simulator with 3 D.o.F. Pneumatically Actuated

G. Mattiazzo, S. Pastorelli, M. Sorli

Department of Mechanics, Politecnico di Torino, Italy

ABSTRACT

The paper presents the research activity on the design and realisation of a spatial motion simulator with 3 degrees of freedom. At first the complete motion simulator apparatus is described, in particular dealing with the geometry of the parallel architecture, the inverse kinematics algorithm and the related position control loops of the three servo-axes. Moreover, the practical solutions adopted during the construction of the device are described, as well as the control hardware and the control strategies to manage the simulator. Besides preliminary actuation tests carried out on the simulator both in time and frequency domain, with different motion amplitudes and payloads, are presented. The experimental results are compared with the performances evaluated by means of a numerical simulator of the device implemented in Matlab/Simulink environment. Finally future developments of the research are discussed.

1. INTRODUCTION

A motion simulator interacting with a person is a device which allows to reproduce the sensations developed by a vehicle movement on the driver, the passengers or generally on the carried components. Possible applications involve vehicles user training and test on physical systems or devices. When the simulation is finalised to create a virtual reality environment it must properly supply stimuli to all the perception organs involved: eyes, human vestibular system and human senses. Thus a simulator has to consist of a mechanical structure, able to move the user who experiences the simulated movement, and an environment which reproduces in a consistent manner visual feelings, re-creating the simulated scenery. Finally, when the driven situation of a specific vehicle has to be re-created, the driven position and the management and command devices are to be likely built in a real or virtual manner. Typical applications of the motion simulators interacting with the users are flight simulators, widely and efficaciously adopted both for training and tests of technical skills of professional pilots. Usually, for flight simulators the platform that drives the 6 degrees of freedom of the cockpit is conceived as a Stewart Platform parallel architecture actuated by linear hydraulic servo-actuators.

The platform forms the mechanical component which is the basis of a motion simulator system. It consists of three logical main blocks: *i*) the mechatronic hardware; *ii*) the motion control software, which is divided in the algorithms to evaluate the reference signals for the servo-actuators in order to realize a defined trajectory and in the local servo-axes controls; *iii*) the program module needed to plan the desired trajectory as a function of the dynamic behaviour of the simulated aircraft, of the motion detection capabilities of the pilot vestibular system and of the static and dynamic performances of the motion simulator, according to suitable washout filters and motion cueing algorithms.

The research whom this paper refers to concerns the design of parallel platforms for single user motion simulation in domestic or associative environment, for professional or sporting training or recreational entertainment. Key factor in designing these devices is the availability of low-cost virtual environment and actuations characterised by high degree of integration and flexibility. Previous studies has revealed that to reproduce the suitable motion sensation, filtered by the user by means of his human vestibular perceptive system, only 3 d.o.f. devices are sufficient, if low-frequency motions typical of commercial airliners are considered [1]. With reference to payloads and workspace requirements of these applications the motion simulator here presented has been built.

In previous researches, the authors analysed the performances of parallel architecture with several degrees of freedom with electrical actuation. Starting with [2] at the Department of Mechanics of the Politecnico of Turin, a research has been managed for several years dealing with the realization of parallel robot with 6 d.o.f. for industrial applications of robots co-operation as work pieces support during process operations, as deburring, milling and so forth. [3-5]. Moreover, new class of parallel structure, in particular as concerning the actuation devices realised by means of wire actuator, are under study in order to identify appropriate analysis and design criteria for the development of devices devoted to manipulation and sensed teleoperation [6].

In the research here presented a pneumatic actuation system has been foreseen in order to guarantee human compatibility in terms of structure compliance, in particular for wrong functioning conditions. In comparison with these advantages, typical of a pneumatic actuation system, usually it performs low bandwidth, as the pneumatic stiffness of the servo-actuators is small and the damping properties are reduced. In order to reach sufficient stability margins and acceptable static and dynamic accuracy required for the envisaged application, it is determinant to evaluate at first the effects of the sizes of the system components and of the working conditions [7], and successively to optimise the control loops of the servo-system [8, 9]. Supporting these analysis, the evaluation of the gains of the linear model of the pneumatic servo-system with position control loop could be necessary [10], as carried out in [11] for a preliminary study on the examined motion simulator.

2. GEOMETRY OF THE MOTION SIMULATOR ARCHITECTURE

The kinematic architecture assumed for the dynamic flight simulator is shown in figure 1.

This platform is identified with the notation HPR, from the degrees of freedom that it performs: translation along vertical axis (heave) and rotations about two horizontal axes (pitch and roll). With respect to the Stewart Platform with 6 d.o.f. this architecture doesn't allow degrees of movement of rotation about vertical axis (yaw) and translations along horizontal axes. The choice of this architecture has been defined in accordance with the results presented in [1], where the authors compared two different 3 d.o.f. parallel architecture (HPR and a spherical mechanism) with a Stewart Platform. They verified that the HPR architecture performed well enough in simulation realism and might be appropriate for low-cost procedure training simulators.

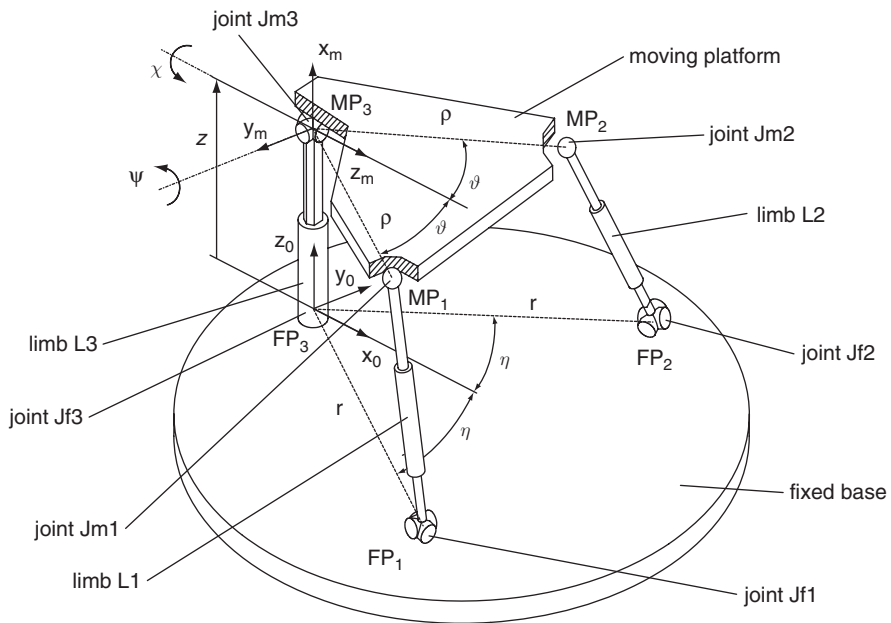


Figure 1 Scheme of the parallel architecture of the motion simulator

With reference to figure 1, the mechanics architecture consists of a moving platform connected to a fixed base by three extensible limbs $L1$, $L2$, $L3$. Limbs $L1$ and $L2$ are made up of linear servo-actuators provided with moving spherical joints $Jm1$, $Jm2$ and fixed universal joints $Jf1$, $Jf2$. Limb $L3$ is a linear servo-actuator mounted at the base with a fixed joint $Jf3$ and connected to the platform by a moving universal joint $Jm3$. Controlling the limbs' lengths the platform can be moved in the operational workspace with three degrees of freedom z , ψ and χ , respectively heave translation, pitch and roll rotations. The simulator working space guarantees a heave range equal to 300 mm and pitch and roll angles equals to $\pm 30^\circ$, with pneumatic cylinders having 50 mm bore diameter and strokes equals to 300 mm ($L3$) and 450 mm ($L1$ and $L2$) in length.

Assumed the reference values of the degrees of freedom of the platform in the operational

workspace $[z \ \psi \ \chi]$, the length of the limbs $L1, L2, L3$, defined as the distance between fixed joint and moving joint centres of each limb, corresponding to the reference input of the position control loop of each servo-actuator, can be evaluated by mean of the inverse kinematics algorithm. Referring to notations of figure 1, a fixed frame $x_0 y_0 z_0$ and a mobile frame $x_m y_m z_m$ linked to the platform are recognised; the homogeneous transformation matrix from moving to fixed co-ordinate axes is:

$${}^0 A_m = \begin{bmatrix} -\cos \chi \sin \psi & \sin \chi \sin \psi & \cos \psi & 0 \\ \sin \chi & -\cos \chi & 0 & 0 \\ \cos \chi \sin \psi & -\sin \chi \cos \psi & \sin \psi & z \\ 0 & 0 & 0 & 1 \end{bmatrix} \quad (1)$$

The position vectors of the points FPi ($i = 1 \div 3$), centres of the fixed joints Jfi ($i = 1 \div 3$), and of the points MPi ($i = 1 \div 3$), centres of the mobile joints Jmi ($i = 1 \div 3$), with respect to the fixed frame are:

$$\begin{aligned} FP1 &= [r \cos \eta \quad -r \sin \eta \quad 0 \quad 1]^T \\ FP2 &= [r \cos \eta \quad r \sin \eta \quad 0 \quad 1]^T \\ FP3 &= [0 \quad 0 \quad 0 \quad 1]^T \end{aligned} \quad (2)$$

$$\begin{aligned} MP1 &= {}^0 A_m [0 \quad \rho \sin \vartheta \quad \rho \cos \vartheta \quad 1]^T \\ MP2 &= {}^0 A_m [0 \quad -\rho \sin \vartheta \quad \rho \cos \vartheta \quad 1]^T \\ MP3 &= {}^0 A_m [0 \quad 0 \quad 0 \quad 1]^T \end{aligned} \quad (3)$$

Finally, the vectors Li ($i = 1 \div 3$), representing the length of each servo-actuator, can be obtained:

$$Li = MPi - FPi \quad (4)$$

3. ACTUATION DEVICES OF THE MOTION SIMULATOR

The layout of the circuits of the motion simulator actuation devices, with the control and sensorisation hardware included, is shown in figure 2. With reference to the demanded motion law of the platform $[z, \psi, \chi]_{SET}$, the reference lengths of the three limbs are calculated using inverse kinematics of the mechanism. Successively, considering the offset lengths corresponding to the “zero position” of the simulator, the displacement reference $x_{SET1}, x_{SET2}, x_{SET3}$ of each cylinder are generated.

A schematic representation of each servo-actuator operating in closed loop position control is shown in Figure 2. The pneumatic double acting single ended actuator is managed by flow-proportional 4-ways servo-valve which controls the air mass flows G_1 and G_2 entering

the thrust chambers 1 and 2, at pressures P_1 and P_2 . The position set x_{SET} , and in particular the corresponding voltage signal V_{SET} , is compared with the feedback signal $V_{F/B}$ of the actual position x_{FB} , measured by a position transducer, and the error is compensated in a control regulator and valve driver, which produces the voltage signal V_{REF1} . On the rod of the actuator the force disturbance F_E is exerted.

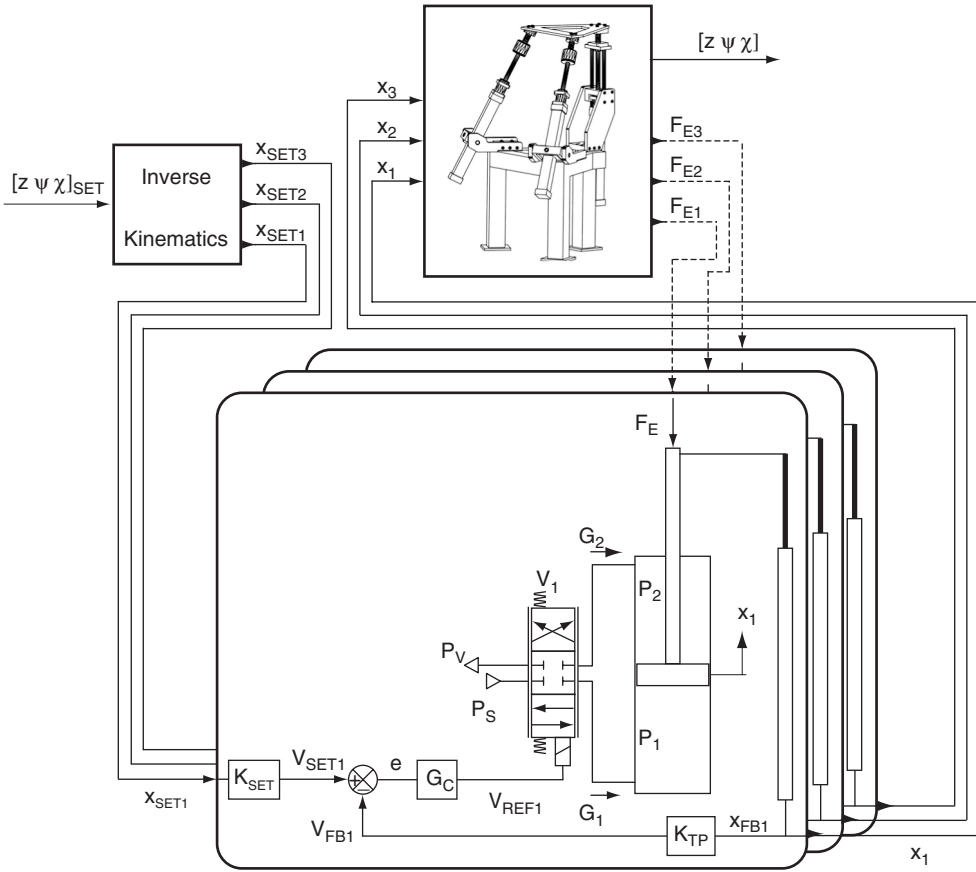


Figure 2 Working scheme of the motion simulator servo-system

The actual position x_1 is determined by the dynamic equilibrium of the mass moved with the rod actuator 1, on which forces due to pressures P_1 and P_2 , disturbance force F_{E1} and internal friction and damping actions are exerted. Pressures P_1 and P_2 are determined by the integration of the mass continuity of the air inside the cylinder chambers caused by the piston motion and by the air flows G_1 and G_2 introduced through valve $V1$ according to the command signal V_{REF1} , supply and exhaust pressures and P_1 and P_2 themselves. Similar considerations may be done to determine positions x_2 and x_3 . Then, the actual limbs lengths impose the real motion law of the platform $[z, \psi, \chi]$, according to the direct kinematics scheme that the parallel mechanism actually performs. At last, subsequently to the platform

movement which is subjected to the dynamic and static loads of the own weight and of the payload, the constrain reactions in each mobile joint, which represents the forces disturbance F_{E1}, F_{E2}, F_{E3} acting on each servo-actuator, are produced.

The devices adopted to realise the simulator are reported in Table 1. In Figure 3 three photographs of different configurations of the simulator displaced in its operational

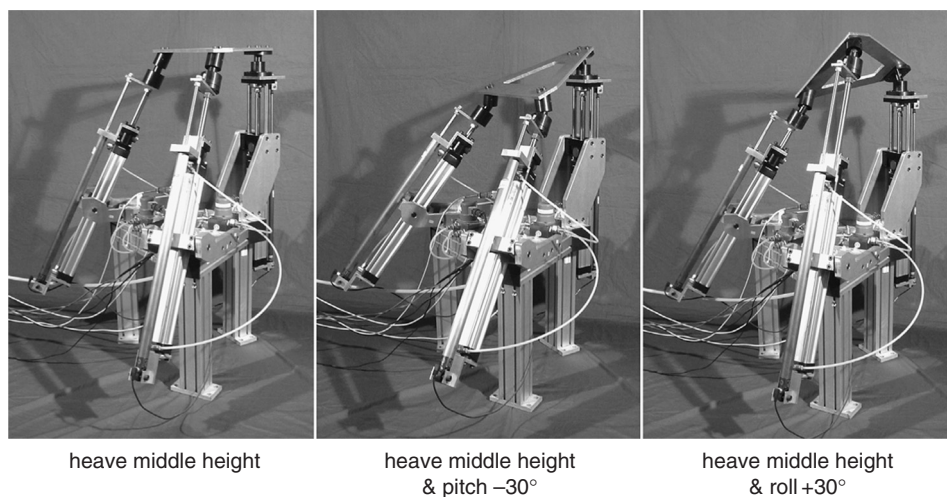


Figure 3 Examples of different position configurations of the motion simulator

Table 1

<i>Control</i>	HW:	PC Pentium III 650 MHz + boards National Instruments PCI-6052E and Lab-PC-1200
	SW:	MathWorks Simulink + Real-Time Windows Target
<i>Servo-actuator 1</i>	cylinder:	Metal Work CIL 124 050 0450 CP ISO 6431
	valve:	Schneider PVM 065-020-1111-0A
	transducer:	Penny & Giles SLS 190 stroke 325 mm
<i>Servo-actuator 2</i>	cylinder:	Metal Work CIL 124 050 0450 CP ISO 6431
	valve:	Schneider PVM 065-020-1191-0A
	transducer:	Penny & Giles SLS 320 stroke 500 mm
<i>Servo-actuator 3</i>	cylinder:	Metal Work CIL 124 050 0300 CP ISO 6431
	valve:	Schneider PVM 065-020-1141-0A
	transducer:	Penny & Giles SLS 320 stroke 500 mm

working space are presented, in particular middle height position and minimum pitch and maximum roll rotations respectively are shown. Platform rotation limits are imposed via software within the angular range of the moving spherical joints.

Details of the *Hardware-in-the-Loop Management System* of the motion simulator are depicted in figure 4. At the present, the parallel architecture is not yet integrated with the simulator virtual environment, thus it is managed as a slave robot controlled by means of a *Command Console* by an operator, without direct detection of the platform configuration in the workspace. The console consists of a joystick with 2 d.o.f. and a knob linked respectively to the platform rotations and heave motion, as well as digital selectors to reset platform position and to manage emergency. The *Control Hardware* performs the closed loop position control of each servo-actuator, as previously described, and the management

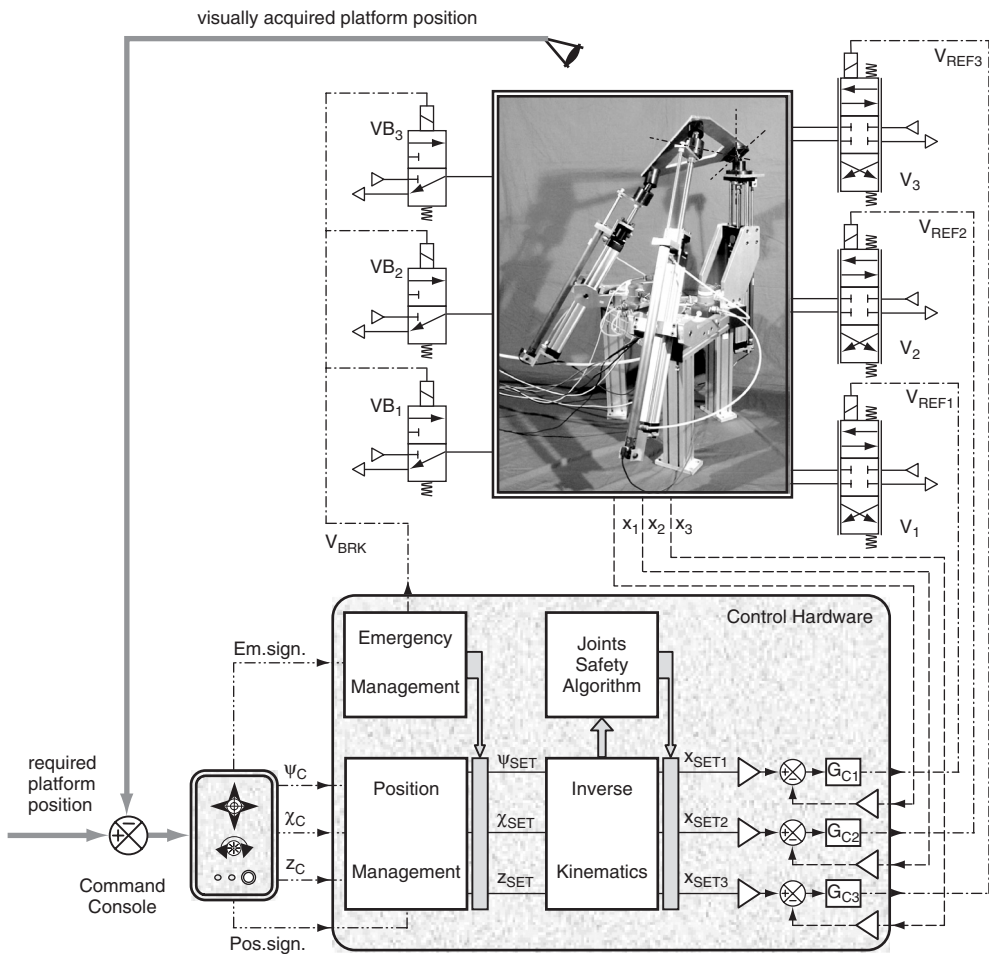


Figure 4 Hardware-in-the-Loop Management System of the motion simulator

of some auxiliary functions. At starting and ending phases of the motion, some predetermined movements of the platform are activated with the *Pos.sign.* signals in order to reach the “zero position”. Successively, the operator watches the platform movement and he adjusts the input commands to reach the required position. The reachable workspace of the platform is not previously mapped in terms of platform $[z, \psi, \chi]$ d.o.f., thus safety management is needed. Simultaneously with the *Inverse Kinematics* block the *Joints Safety Algorithm* evaluates the angles performed in each mechanism joints and set a suitable saturation threshold to the values of x_{SETi} ($i = 1+3$) in order to limits the angles to safety maximum values. Moreover, when a dangerous situation happens the operator can activate the *Emergency Management* block with the *Em.sign.* signal: as a consequence the console is disabled, the references $[z, \psi, \chi]_{SET}$ are frozen and the cylinder are blocked by means of three pneumatic brakes activated by the VB_i ($i = 1+3$) valves.

4. ACTUAL PERFORMANCES OF THE PNEUMATIC SERVO-ACTUATOR L3

Two different user location could be expected, hypothesising that a pilot seat is carried by the moving platform of the parallel structure shown in figure 1, taken into account the longitudinal symmetry about axis z_m , as depicted in figure 5. The front of the pilot could be turned toward the single vertical actuator (figure 5a) or, vice versa, toward the couple of inclined actuators (figure 5b). A study of the platform equilibrium for different displacement within the workspace has led to observe that the first configuration (5a) carried to an increasing of the load applied to the vertical limb and to a reduced loads on the inclined limbs, in comparison to the forces involved by the second configuration (5b) for each limb at equal platform displacements. Thus the first seat solution has been developed in order to limit the magnitude of force disturbances on rear limbs, allowing better dynamic performances of these servo-actuators, mainly involved in platform rotations, which are the fundamental movements to reproduce a motion sensation to the user.

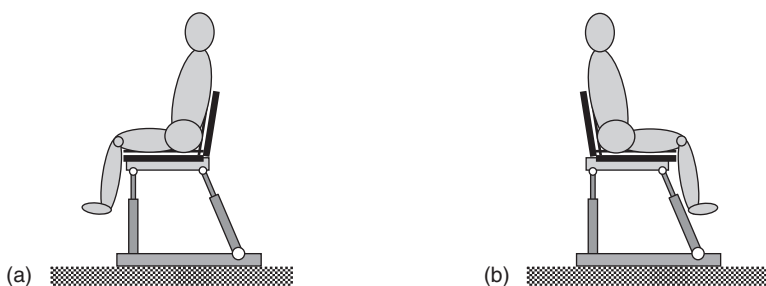


Figure 5 Pilot seat location on the motion simulator

For the seat configuration assumed the most loaded cylinder is the vertical L3, and thus on this servo-actuator the dynamic analysis afterwards presented has been carried out. The study is not only addressed to optimise the device performances, on this matter the research is in progress, but also to validate nonlinear and linear models of the parallel mechanism,

helpful to develop the whole motion simulator system. Characteristic parameters of the servo-actuator *L3* under test, as well as actuators *L1* and *L2* are reported in table 2.

Table 2

		<i>servo-actuator</i> <i>1</i>	<i>servo-actuator</i> <i>2</i>	<i>servo-actuator</i> <i>3</i>
<i>servo-valve</i> + <i>pipe</i>	input signal [V]	± 10	± 10	± 10
	conductance [$\text{m}^3/\text{sPa}_{\text{ANR}}$]	3.5×10^{-8}	3.5×10^{-8}	0.8×10^{-8}
	critical pressure ratio	0.4	0.4	0.4
	supply pressure [Pa_{abs}]	6.5×10^5	6.5×10^5	6.5×10^5
	natural frequency [rad/s]	200	200	200
	damping	0.8	0.8	0.8
<i>cylinder</i>	\varnothing bore [mm]	50	50	50
	\varnothing rod [mm]	20	20	20
	stroke [mm]	450	450	300
	mass [kg]	8 + load	8 + load	6 + load
	coulomb friction force [N]	30	30	30
	viscous damping [Ns/m]	100	100	100
<i>transducer</i>	gain [V/m]	18.0	18.0	26.5
<i>control</i>	proportional gain	5	5	3

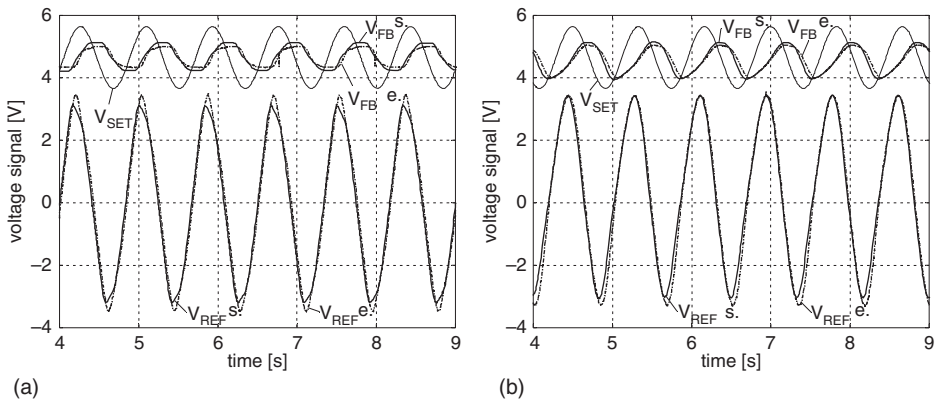


Figure 6 Responses to sinusoidal reference signals without load (a) and with load 30 kg (b)

Experimental tests have been carried out on the servo-actuator *L3*, disconnect from the moving platform, without external load or with 10 kg and 30 kg mass-load on the rod, with different input reference time laws. Results corresponding to sinusoidal reference signal with amplitude $\Delta V_{SET} = 1$ V around middle stroke ($V_{SET} = 5$ V) and frequency 1.2 Hz, without load and with 30 kg respectively, are shown in figure 6a and 6b.

Input signal V_{SET} , feedback V_{FB} , reference signal to the servo-valve V_{REF} , with proportional control gain $G_c = K_p = 3 \text{ V/V}$ are represented in figure 6. For the sake of comparison, experimental signals $V_{FB e.}$ and $V_{REF e.}$ are superimposed with simulated values $V_{FB s.}$ and $V_{REF s.}$, obtained with a numerical simulator implemented in Matlab/Simulink environment, whose block diagram is shown in figure 7.

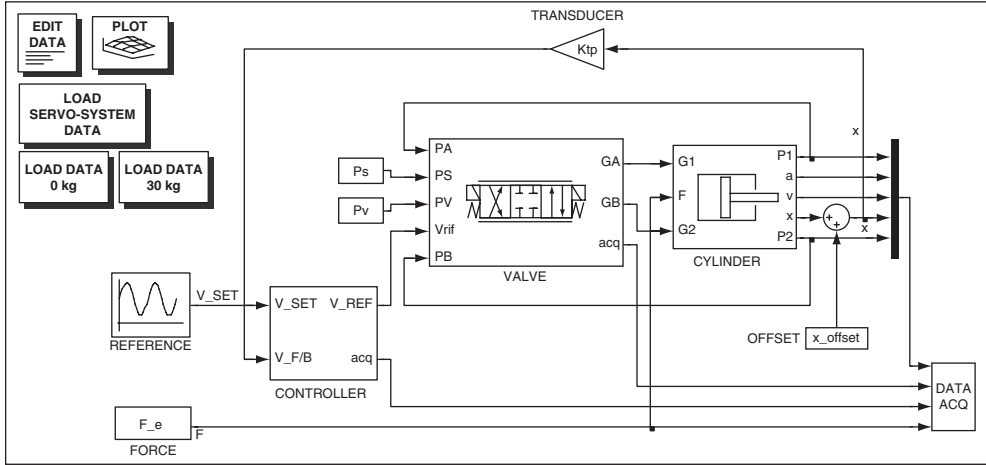


Figure 7 Simulink model of a single servomotor

A synthesis of the servo-actuator $L3$ performances is deduced from the Bode diagrams in figures 8 and 9. In figure 8 experimental results and numerical results of the nonlinear model for no-load tests are shown, respectively for the open loop frequency response V_{FB}/V_{REF} (figure 8a) and for the closed loop frequency response V_{FB}/V_{SET} (figure 8b). Analogous results are presented in figure 9 for tests with load equals to 30 kg.

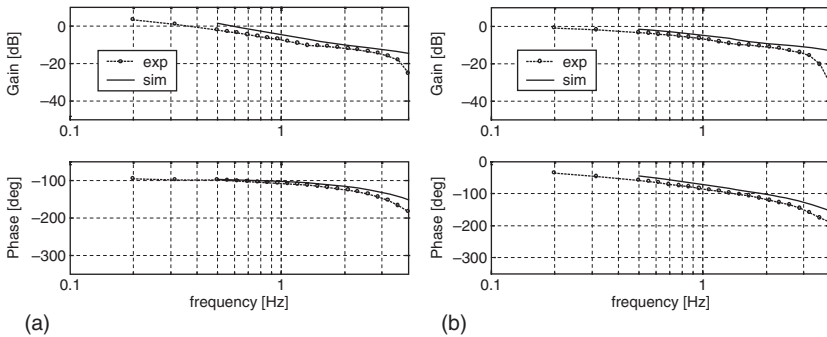


Figure 8 Open (a) and closed (b) loop frequency responses without load

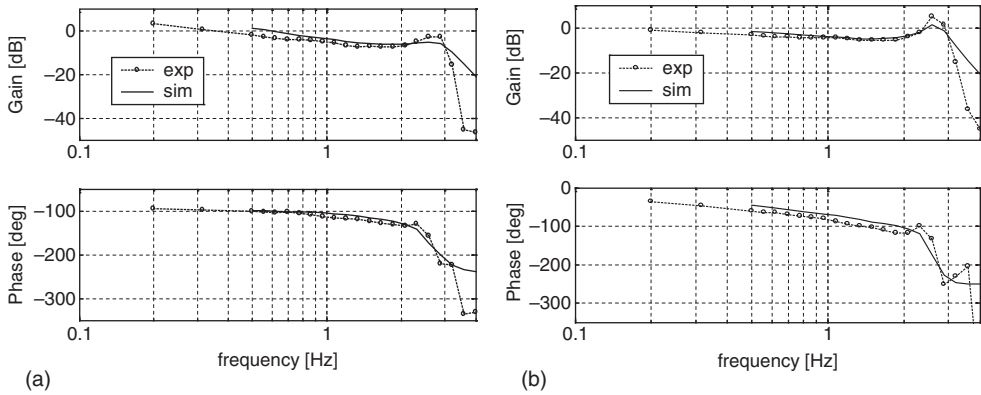


Figure 9 Open (a) and closed (b) loop frequency responses with load 30 kg

The performances of the servo-actuator are at present not very satisfactory in terms of bandwidth and gain margin and damping. Although, considering the numerous non-linearities of the system, and the quite wide frequency range analysed, the authors think that the model is validated and thus a software optimisation of the dynamic performances of the actuator could be expected and an effective hardware improvement will be achieved.

5. CONCLUSIONS

The research project on the design and realisation of a motion device of a flight simulator for domestic environment or professional applications in flight school has been presented.

The architecture of the simulator system has been described trying to define the main functional interactions between different sub-systems and relating the adopted solutions.

The experimental tests and the numerical simulations carried out on the most loaded servo-actuator has allowed to highlight the limits at the present and thus to define the developing trends for the future. In particular The damping properties of the servo-actuator have to be increased; at the present they are too small and they are not able to guarantee a sufficient gain margin, unless a modest bandwidth frequency is accepted.

At the same time of the activities described in the paper, authors are working on the interactions between the motion simulator, the flight control cockpit devices, the aircraft simulator, the motion cueing algorithms. The interaction between these parts will provide for the references of the degrees of freedom of the moving platform.

REFERENCES

- [1] Pouliot, N.A., Gosselin, C.M., (1998), "Motion simulation Capabilities of Three-Degree-of-Freedom Flight simulators", *J. of Aircraft*, Vol.35, No.1, pp.9-17.
- [2] Romiti A., Sorli M., (1992), "A parallel 6 d.o.f. manipulator for cooperative work between robots in deburring", 23rd Int. Symp. on Industrial Robot ISIR 92, Barcellona, Spain, pp.437-442.
- [3] Sorli M., Pastorelli S., (1995), "Practical construction of the 6 d.o.f. parallel robot Turin Platform", 1st ECPD Int. Conf. on Advanced Robotics and Intelligent Automation, Athens, Greece, pp.509-514.
- [4] Sorli M., Kolarski M., Ferraresi C., Borovac B., Vukobratovic M., (1997), "Mechanics of Turin parallel robot", *Mech. Mach. Theory*, 32(1), pp.51-77.
- [5] Sorli, M., Pastorelli, S., (1999), "The 6 d.o.f. parallel robot Turin Platform", *Int. Workshop on Parallel Kinematic Machines, PKM 99*, Milan, Italy, pp.137-145.
- [6] Ferraresi C., Paoloni M., Pastorelli S., Pescarmona F., (2004), "a new 6 dof parallel robotic structure actuated by wires: the WIRO-6.3", *J. of robotic systems*, 21(11), pp.581-595.
- [7] Uebing, M., Vaughan, N.D., Surgenor, B., (1997), "On Linear Dynamic Modelling of a Pneumatic Servo System", 5th Scandinavian Int. Conf. on Fluid Power, Linköping, Sweden, pp.363-378.
- [8] Pandian, S.R., Hayakawa, Y., Kanazawa, Y., Kamoyama, Y., Kawamura, S., (1997), "Practical Design of a Sliding Mode Controller for Pneumatic Actuator", *J. Dynamic Systems and Measurement Control*, Trans. ASME n. 119, pp.666-674.
- [9] Virvalo, T., (1996), "Comparing Different Controllers of Electropneumatic Position Servo", 3rd JHPS Int. Symp., Yokohama, Japan, pp.151-156.
- [10] Sorli, M., Pastorelli, S., (2002), "Hydraulic and Pneumatic Actuation Systems", in *The Mechatronics Handbook*, CRC Press, pp. 20.62–20.96.
- [11] Pastorelli S., Sorli M., (2004), "Design of the pneumatic servoactuators of a 3 d.o.f. motion simulator", 3rd FPNI Fluid Power Net International PhD Symposium, Terrassa, Spain, pp.433-440.

Fluid Dynamics and Noise

Elucidation of the Noise Generating Mechanism produced by a Hydrodynamic Source associated with Cavitation in an Oil Hydraulic Valve Orifice

E Kojima, T Yamazaki and A Terada

Department of Mechanical Engineering, Kanagawa University, Japan

KA Edge

Centre for Power Transmission and Motion Control, University of Bath, UK

ABSTRACT

This paper presents a semi-empirical analysis for elucidating the noise generation mechanism arising from cavitation in a system comprised of an oil hydraulic valve and downstream pipe. It is shown that the downstream pipe is excited principally at the natural frequencies of both the bending and pipe ring vibration modes in response to the broad band random pressure fluctuation that occurs during the collapse of cavitation bubbles. The airborne noise is radiated from the pipe wall predominantly at these natural frequencies. New knowledge obtained from this study arises from both a finite element method analysis and an experimental modal analysis of the valve downstream pipe structure, combined with measurements of narrow band frequency spectra of pressure fluctuation in the pipe, the vibration acceleration of the piping structure and the nearby sound pressure of a pipe wall.

Key words: Cavitation, Turbulence, Noise, Valve, Orifice, Cavitating jet, Turbulent jet, FEM

1. INTRODUCTION

Important noise generating mechanisms in pipeline systems are associated with cavitation and turbulence. Cavitation in valves, in particular, is a major noise source. A great deal of work has been performed on studying the effects of cavitation on valve performance and on understanding the cavitation noise emitted by the valve orifice in perspective [1]. The ability to predict structure borne and airborne noise is of great important to the users of such valves and hence practical noise prevention measures have been a goal in many of the fluid transportation industries. However, little work has been published on detailed investigations of transforming mechanism of vibration energy from the hydrodynamic sources associated with turbulence and/or cavitation within a valve to the air borne radiated

noise from the downstream pipe structure. Baumann and Kiesbauer [2] have devised a semi-empirical method to predict A-weighted sound levels by supposing that the sound measured external to a piping system is a product of the internal sound pressure (pressure fluctuation), occurring at or near the peak amplitude, and the transmission loss of the downstream pipe. In their work, however, the transmission loss at the pipe ring vibration mode frequency has only been considered. This is not appropriate for metal piping systems in which the length/diameter ratio and thickness/diameter ratio are relatively large. This is generally the case in oil hydraulic systems.

The ultimate goal of the research is to develop a numerical simulation technique capable of predicting, with sufficient accuracy for practical usage, the noise that is generated inside a valve and radiated from the adjacent piping, and thereby to find reasonable and practical noise control techniques. Of these, this paper aims at elucidation of the generation mechanism of the noise from a downstream pipe wall produced by hydrodynamic sources associated with cavitation within a valve orifice in oil hydraulic piping systems. Firstly, the characteristics and relationship between the narrow band frequency spectra of pressure fluctuation in a pipe, the vibration acceleration of the pipe and the nearby sound pressure are examined experimentally. Next, the vibration modes (mode shapes and natural frequencies) of the downstream piping structure are examined by FEM analysis and experimental modal analysis (EMA). Finally the contribution of each vibration mode of the downstream pipe structure (i.e., bending, breathing, longitudinal and ring vibration modes) to the frequency characteristics of pipe vibration during cavitation occurrence is investigated by a FEM forced vibration analysis.

2. EXPERIMENTAL SYSTEM AND MEASUREMENT PROCEDURES

A schematic diagram of the hydraulic test circuit, showing the location of the valve orifice (flow restriction), downstream pipe (steel pipe and flexible hose) and instrumentation is presented in Fig.1. The flow restriction is a simple cylindrical orifice (diameter: 2mm, length: 8mm) mounted within a steel block. Two straight steel pipes (length: 0.5m and 1.0m, inner diameter: 19.6mm, outer diameter: 27.3mm) and one straight flexible hose (length: 1.0m, inner diameter: 19.0mm, outer diameter: 29.4mm) were used in turn as the downstream pipe; in each case, the pipe was supported rigidly at both ends by a massive steel block. An oil hydraulic piston pump provided the necessary flow rate, with a pressure relief valve used to control the upstream mean pressure of the orifice, \bar{p}_u , and a needle valve used to control downstream pressure, \bar{p}_d . The upstream and downstream mean pressures were measured with accurately calibrated Bourdon pressure gauges.

Fluid borne-, structure borne- and airborne noise measurements were made using flush mounted piezo-electric pressure transducers at the inlet and outlet of the downstream pipe, a piezo-electric accelerometer bonded to the pipe wall and a condenser microphone positioned in close proximity to the pipe wall. The signals from the pressure transducers, accelerometer and microphone are naturally dependent on their mounted location. All acceleration and sound pressure measurements presented in this paper were carried out 100mm downstream from the leading edge (fixed end) of the downstream pipe, and the pressure fluctuation was measured 12.5mm downstream of the restriction.

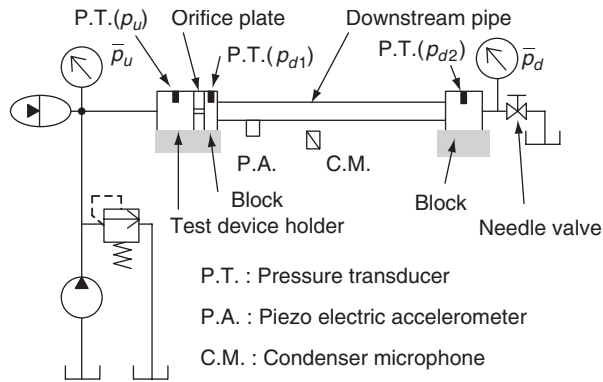


Fig.1 Schematic of hydraulic test circuit and instrumentation

The dissolved air content of the oil, which is a potentially important factor in investigations of this nature, was not precisely controlled during the test programme. However, because the main purpose of this study is not to predict the cavitation noise quantitatively, but to elucidate the generation mechanism of cavitation noise, the lack of control of air content is not considered to be an issue. In order to gain a general impression of the nature of cavitation in the test system photographic observations of the cavitation flow around the emerging jet were made (Fig.2) together with measurements of pressure distributions along the radial and axial directions in the cavitation region (Fig.3). For these initial investigations the steel block was replaced with a perspex block with 12 holes along the pipe axis for a static pressure measuring probe. It can be seen from the results of Fig.3 that the cavitation that occurs in the test circuit is gaseous rather than vaporous because the pressure inside the potential core of the emerging jet does not fall much below -0.07 MPa (gauge) which is close to the air separation pressure.

After the initial testing, the steel block was substituted for the perspex block. Fig.4 shows the narrow band frequency spectra of the pressure fluctuation downstream of the orifice, the vibration acceleration of the downstream pipe wall and the nearby sound pressure for frequencies up to 20kHz. It is noticeable that the pressure fluctuations occurring during the collapse of cavitation bubbles are a very broad-band random phenomenon whilst the spectra of the vibration acceleration and sound pressure are predominantly at a number of discrete frequencies. There is a high degree of correlation between vibration acceleration and sound pressure; the cavitation noise has a strong sound power up to the upper reaches of the audible frequency range (around 18kHz).

Fig.5 shows the pressure fluctuations at the inlet and outlet of the downstream pipe (a) with cavitation and (b) without cavitation, respectively. Pressure waves are greatly attenuated in the course of propagation once cavitation occurs and the harmonic components of pressure fluctuations over about 2kHz are barely transmitted to the downstream pipe. From these experimental results and the knowledge that cavitation-induced noise is a by-product of cavitation erosion, the impact forces (hydrodynamic sources) exciting the pipe solid surface

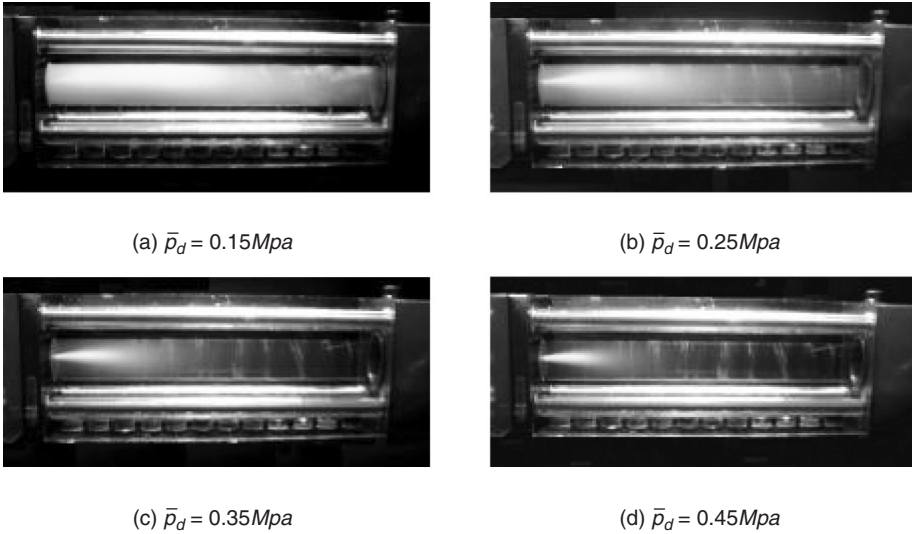


Fig.2 Photographic observations of cavitation flow around emerging jet ($p_u = 8\text{MPa}$)

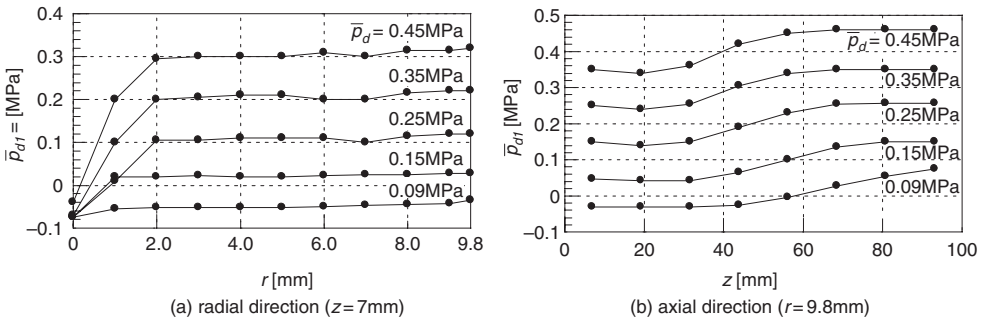


Fig.3 Measured pressure distributions for radial and axial

may be said to be concentrated in a narrow region around the emerging jet. The magnitude (harmonic amplitude) and application point of the impact forces cannot be identified correctly by the measurement of pressure fluctuations alone. It is inferred that in practice a rather stronger impact than that predicted from the pressure fluctuations detected by the pressure transducer is applied at some place locally (probably, at or near the position of cavitation erosion occurrence). Further investigation of the impact exciting force is not pursued here.

It has also been possible to establish through this study that the relation between the sound pressure levels and the cavitation index showed the same trends as described in the literature [1]. However, space constraints do not allow further discussion in this paper.

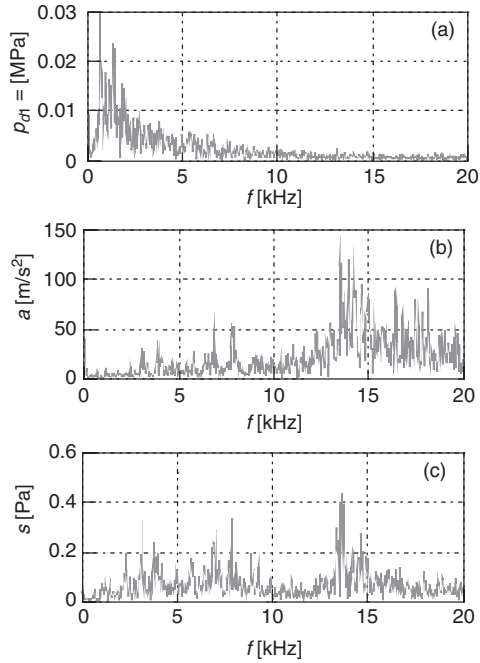


Fig.4 Measured narrow band frequency spectra of (a) orifice downstream pressure fluctuation, (b) vibration acceleration of downstream pipe and (c) nearby sound pressure (1.0m length of steel pipe $\bar{p}_u=8\text{MPa}$, $\bar{p}_d=0.15\text{MPa}$)

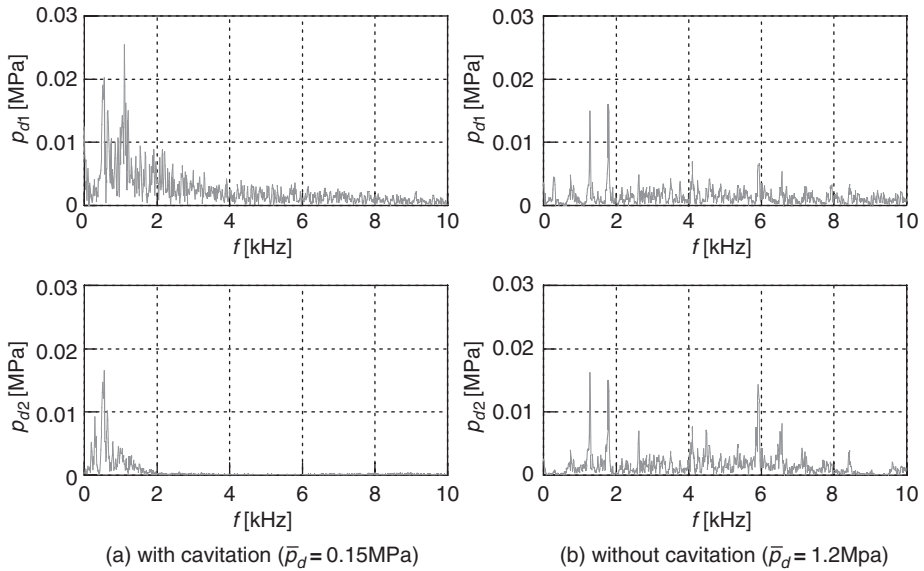


Fig.5 Measured pressure fluctuations at the inlet and outlet of a downstream pipe with and without cavitation ($\bar{p}_u = 8\text{MPa}$)

3. VIBRATION MODE ANALYSIS OF DOWNSTREAM PIPING STRUCTURE BY FEM AND EMA

From the preliminary noise test results (Fig.4) that demonstrate that the spectra of cavitation noise exhibit prominent components at several special discrete frequencies, it can be inferred that the cavitation noise is affected significantly by the dynamics of the downstream piping structure. Therefore, the vibration modes (natural frequencies and mode shapes) of the downstream piping structure were examined using both FEM analysis and EMA, with the mode shapes in the EMA only being analysed for the low-frequency modes. Here, we used ANSYS Release.8.0 for the FEM modal analysis and ME'scopeVES for the EMA. The FEM model assumed the downstream pipe was fixed at both ends and was built using an eight-node solid element, containing 6048 nodes and 3000 elements for the 0.5m length of steel pipe; 12048 nodes and 6000 elements for the 1.0m length of steel pipe; and 7760 nodes and 3860 elements for the 1.0m length of flexible hose. Fig.6 shows the FEM model of the downstream piping structure.

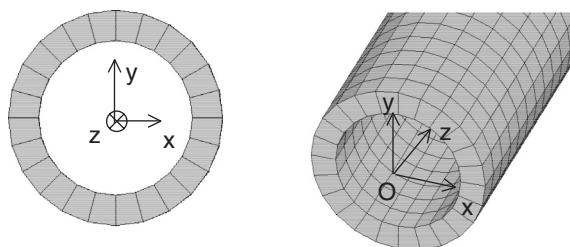
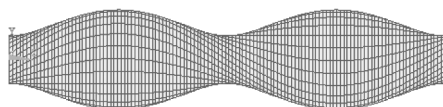


Fig.6 FEM model of a downstream pipe (solid model) and an orthogonal coordinate system



(a) Bending mode (B-3)



(b) Torsional mode (T-2)



(c) Longitudinal mode (L-2)

Fig.7 Examples of mode shapes (3rd bending mode, 2nd torsional mode and 2nd longitudinal mode) of a straight steel pipe obtained by FEM analysis

Table 1 Natural frequencies and mode shapes of downstream steel pipe obtained by EMA and FEM for $L_d=1.0\text{m}$ and $L_d=0.5\text{m}$

Mode No.	Mode Shape	Natural Frequency[Hz]			
		$L_d=1.0\text{m}$		$L_d=0.5\text{m}$	
		EMA	FEM	EMA	FEM
1	B-1	97	151	387	592
2	B-2	373	413	1222	1571
3	B-3	726	799	2492	2944
4	B-4	1356	1299	3895	4624
5	B-5	1748	1905	5560	6542
6	B-6	2445	2606	7525	8638
7	B-7	3182	3392	8653	10869
8	B-8	3903	4253		
9	B-9	4747	5180		
10	B-10	5767	6163		
11	B-11	6831	7196		
12	B-12	7904	8272		
13	B-13	9000	9384		
14	T-1	1642	1594	2200	3187
15	T-2	3096	3187	5600	6375
16	T-3	4982	4781	9512	9564
17	T-4	6930	6375		
18	T-5	8477	7969		
19	L-1	-	2562	-	5130
20	L-2	-	5124	-	10254
21	L-3	-	7684		

B: Bending vibration mode
T: Torsional vibration mode
L: Longitudinal vibration mode
-: unobservable by EMA

Table 1 presents the mode shapes and natural frequencies obtained by FEM and EMA for the straight steel pipes, for a frequency range up to around 10kHz. Here, 'B' relates to the bending vibration mode, 'T' the torsional vibration mode and 'L' the longitudinal vibration mode. A dash represents an unobservable mode in the EMA. Fig.7 shows examples of the mode shapes in the frequency range up to around 10kHz for the straight steel pipe (3rd bending mode, 2nd torsional mode and 2nd longitudinal mode). As can be seen from Fig.7 a radial deformation vibration mode is also induced, accompanying the occurrence of torsional vibration. It was also found in this study that the results using a four-node shell element agreed very closely with those using an eight-node solid element.

Table 1 shows that the natural frequencies and mode shapes predicted by the FEM correlate relatively well with the results of the EMA for almost all vibration modes up to around 10kHz except for the 1st bending mode. The differences between the FEM analysis and the EMA probably arise because the ideal boundary conditions in the model do not match those in the real piping system in which the downstream pipe is coupled to the block by a screw connection.

It was also found from FEM modal analysis that ring vibration modes occurred in the very high-frequency range above around 18kHz for the 1.0m length of steel pipe. These were extremely strongly coupled at narrow frequency intervals of around 10~20Hz. Fig.8 shows the mode shape and natural frequency of the 1st and 2nd pipe ring vibration. It can be inferred from these analyses that the broad band resonances appearing around 14kHz in Fig.4 are caused by these pipe ring vibration modes - although the natural frequencies obtained from FEM modal analysis (around 18kHz) are around 30% higher than the observed resonance frequencies. The differences between FEM analysis and the observed result are likely to be due to the assumption of ideal boundary conditions (perfectly fixed conditions) in the FEM model which do not match those in the real piping system. Indeed, if some elasticity is considered at the boundaries the natural frequencies of pipe ring vibration modes become considerably lower and approach the observed resonance frequencies.

Table 2 presents the mode shapes and natural frequencies for a frequency range up to around 4 kHz obtained by the FEM modal analysis for the straight flexible hose. Here, the flexible hose was simply treated as an orthotropic elastic pipe (although a real hose has an anisotropic visco-elastic wall). The elastic coefficients ($E_x = E_y = 10.1 \times 10^9$ Pa, $E_z = 2.6 \times 10^9$ Pa, $G_{xy} = 2.0 \times 10^9$ Pa and $G_{yz} = G_{xz} = 1.4 \times 10^9$ Pa) were determined experimentally using the approach described by Yu and Kojima [3]. It was found from the FEM modal

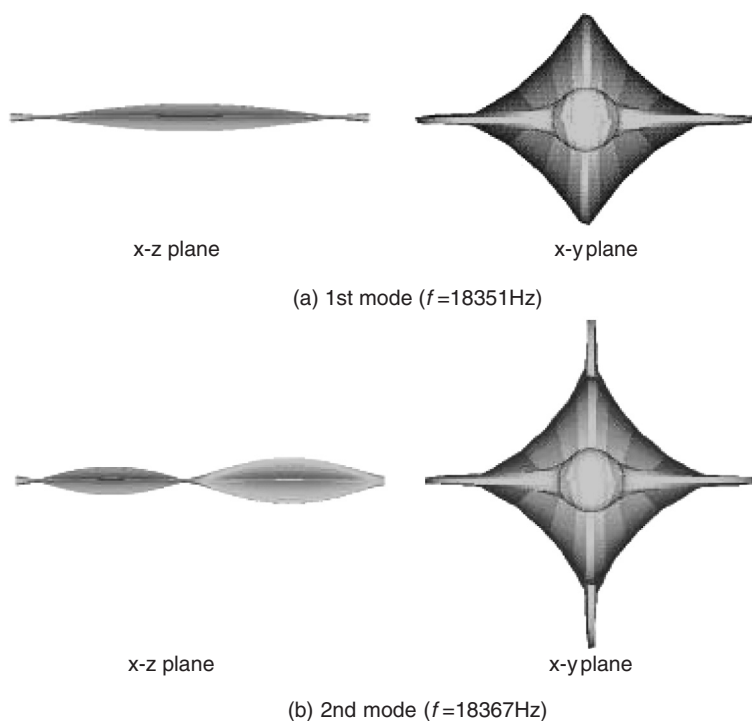


Fig.8 1st and 2nd pipe ring vibration modes for the 1.0m length of steel pipe

Table 2 Natural frequencies and mode shapes of downstream flexible hose estimated by FEM analysis

Mode No.	Mode Shape	Natural Frequency [Hz]	Mode No.	Mode Shape	Natural Frequency [Hz]
1	B-1	31	20	B-20	3831
2	B-2	85	21	B-21	4111
3	B-3	164	22	T-1	370
4	B-4	268	23	T-2	741
5	B-5	394	24	T-3	1112
6	B-6	540	25	T-4	1482
7	B-7	705	26	T-5	1853
8	B-8	886	27	T-6	2224
9	B-9	1082	28	T-7	2595
10	B-10	1291	29	T-8	2966
11	B-11	1512	30	T-9	3337
12	B-12	1743	31	T-10	3709
13	B-13	1983	32	L-1	505
14	B-14	2230	33	L-2	1010
15	B-15	2484	34	L-3	1515
16	B-16	2745	35	L-4	2020
17	B-17	3010	36	L-5	2525
18	B-18	3280	37	L-6	3031
19	B-19	3554	38	L-7	3536

B: Bending vibration mode
 T: Torsional vibration mode
 L: Longitudinal vibration mode

analysis that the flexible hose also had the same vibration modes as those of the steel pipe, including the ring vibration mode which appeared in the high-frequency range (above around 6kHz).

Next, in order to investigate, in outline, the contribution of each of the vibration modes on the cavitation noise, an FEM forced vibration analysis was carried out; from this the frequency response functions of the displacement of the nth vibration mode, η_n , to the reference force, F_0 , (the so called “receptance”, $H_n(\omega)$) were evaluated for each mode using the following equation [4,5]:

$$H(\omega) = \frac{\eta_n}{F_0} = \frac{\sum_{i=1}^I f_i \Phi_n(z_{f,i})}{(\omega_n^2 - \omega^2) + j2\zeta_n \omega_n \omega} \Phi_n(z_r) \text{-----(1)}$$

where $\phi_n(z)$ is the mass normalized eigenfunction (mode shape) of the nth vibration mode, z_r is the positional co-ordinate, in the z direction, of the displacement response; z_f is the

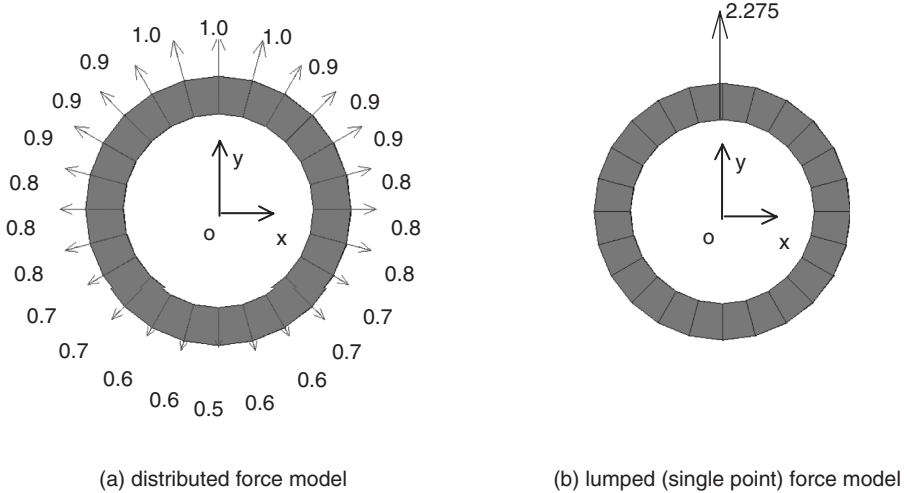


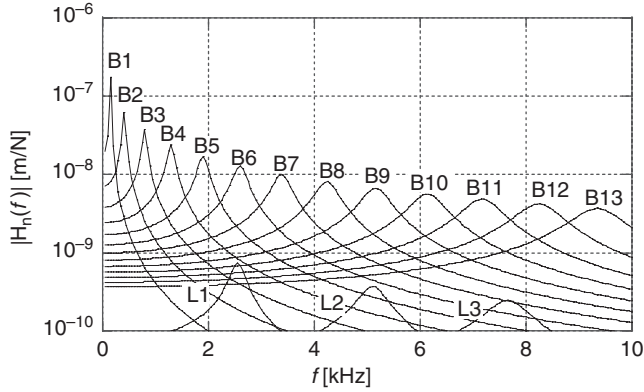
Fig.9 FEM model of the cavitation-induced non-dimensional exciting force f_i

positional co-ordinate, in the z direction, of the application of the distributed exciting force F_i ; f_i is the non-dimensional distributed exciting force; ω_n is the natural angular frequency of the n th mode; ω is the angular frequency of the exciting force; ζ_n is modal damping ratio; and I is the total number of terms considered.

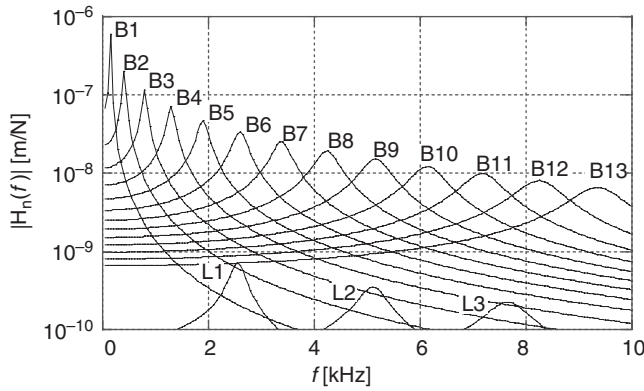
In this evaluation, the broad band random hydrodynamic sources associated with the collapse of the cavitation bubbles were assumed to be able to be replaced with a harmonic force $F_i e^{j\omega t} (= f_i F_0 e^{j\omega t})$. This force is applied at I grid points in the FEM model of the downstream pipe, as shown in Fig.9(a) ($I=24$ in this case) and accounts for the probable non-uniform distribution of the cavitation intensity on the inner circumference of the pipe that occurs in the real case.

Fig.10 shows an example of the receptance frequency response characteristics for each mode calculated from Eq.(1) for the 1.0m length of steel pipe, with (a) $z_f = 20\text{mm}$ and (b) $z_f = 40\text{mm}$, respectively. Here, the response position z_f was selected to be the position where each vibration mode takes the maximum harmonic amplitude (i.e., the antinode of the mode shape). Hence the vertical axis of Fig.10 represents the maximum harmonic displacement amplitude per unit reference force ($F_0=1\text{N}$) for each vibration mode under the force distribution conditions shown in Fig.9 (a). It is notable that the results of the simulation of the receptance frequency characteristics using the distributed exciting forces (shown by Fig.9 (a)) and an equivalent exciting force applied at a single grid point (shown by Fig.9 (b)) were in very close agreement, so far as the bending vibration modes were concerned.

It can be seen from these receptance analyses that the maximum harmonic displacement amplitude of the bending vibration mode is particularly large for all the harmonic components compared to those of the other vibration modes. It should be noted here that



(a) $z_f = 20\text{mm}$



(b) $z_f = 40\text{mm}$

Fig.10 Frequency response characteristics of the receptance for 1.0m length of steel pipe

the maximum harmonic displacement amplitude of the longitudinal vibration mode is around one fiftieth to one hundredth of that of the neighbouring-frequency bending vibration mode; moreover, the vibration amplitude (receptance) of this mode is in the direction of the pipe axis and hence scarcely influences the radiated sound pressure. It should also be noted that the torsional vibration cannot be induced, basically because a torsional moment is not applied in the case of Fig.9. However, if a torsional exciting moment is applied in addition to an exciting force in the y direction, as shown in Fig.11, then torsional vibration modes are induced and their harmonic displacement amplitude is, in this instance, around the same order of that of the neighbouring-frequency bending vibration mode, as shown by Fig.12.

From a comparison of Fig.10(a) and 10(b) it can be seen that, as would be expected in treating the pipe wall as a distributed parameter system, the closer the point of application

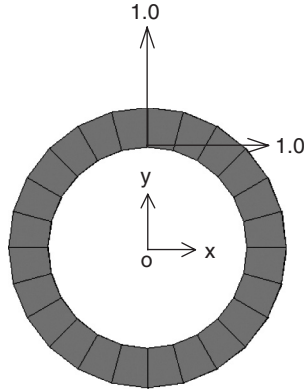


Fig.11 FEM model of the cavitation-induced exciting force for the case of a torsional moment being applied

of the exciting force, z_f , gets to the node point of each mode shape ($z = 0$), the smaller the receptance becomes (and vice versa). The flexible hose had the same tendency, qualitatively, as that of steel pipe in respect of the contribution of each vibration mode to sound pressure.

4. STRUCTURE BORNE NOISE AND AIRBORNE NOISE EXPERIMENTS

Fig.13 shows the experimental frequency spectra of the vibration acceleration of downstream pipe wall and nearby sound pressure up to 10kHz for the 1m length of steel pipe with (a) $\bar{p}_d = 0.1\text{MPa}$ and (b) $\bar{p}_d = 0.2\text{MPa}$, respectively. Acceleration was measured 100mm from pipe leading edge and sound pressure was measured 20mm from pipe wall (a

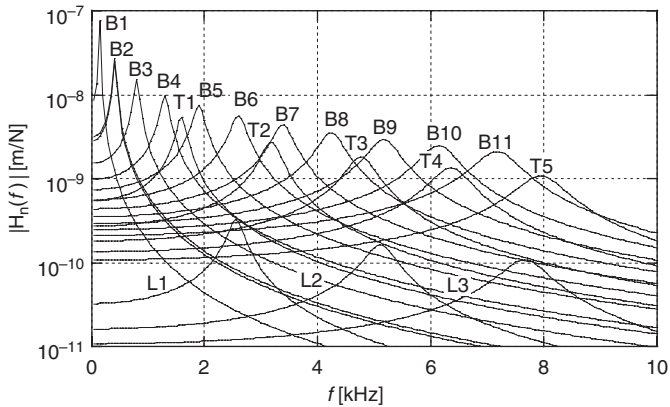


Fig.12 Frequency response characteristics of the receptance for 1.0m length of steel pipe ($z_f = 20\text{mm}$)

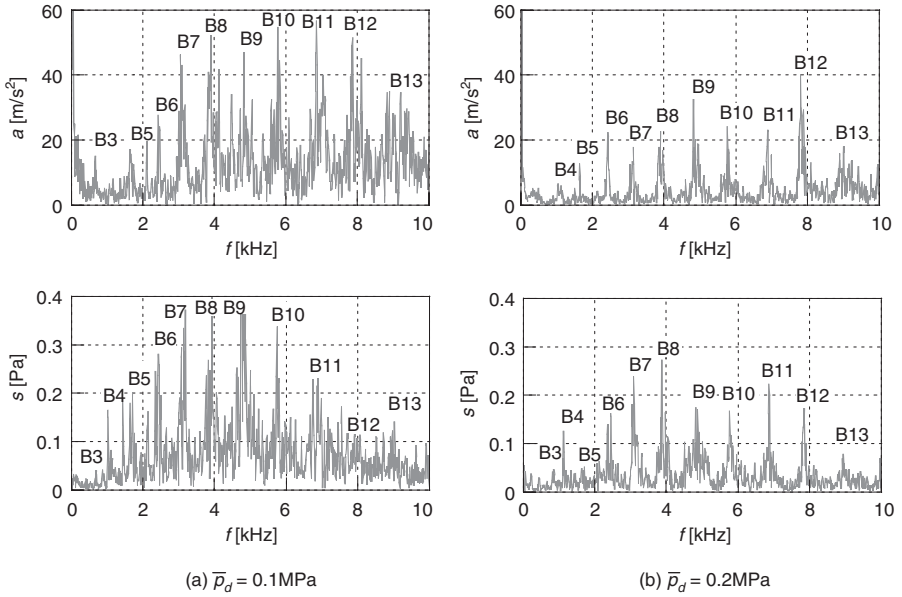


Fig.13 Measured narrow band frequency spectra of vibration acceleration of downstream pipe wall and nearby sound pressure for 1.0m length of steel pipe ($\bar{p}_u = 8 \text{ MPa}$)

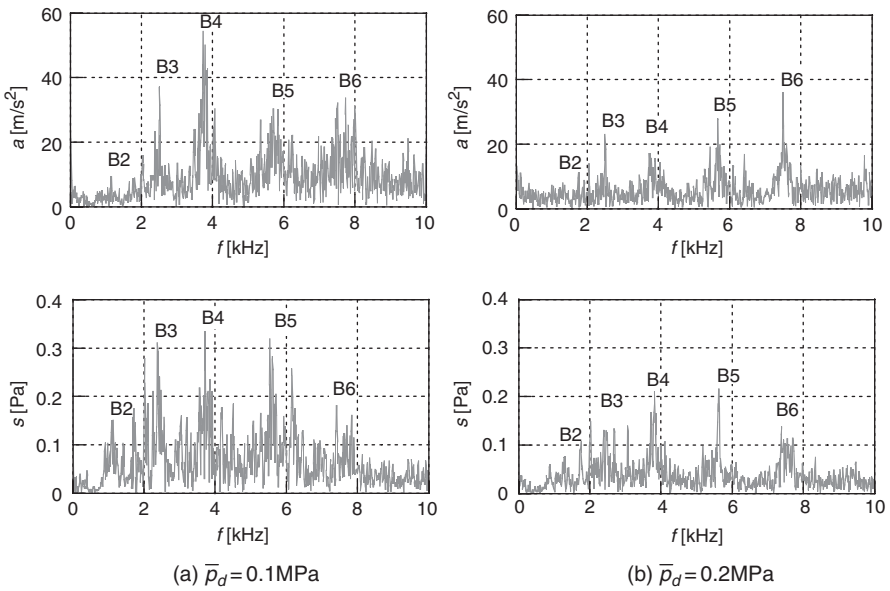


Fig.14 Measured narrow band frequency spectra of vibration acceleration of downstream pipe wall and nearby sound pressure for 0.5m length of steel pipe ($\bar{p}_u = 8 \text{ MPa}$)

distance of 100mm from pipe leading edge) with a mean pressure in the orifice upstream line of 8MPa and oil temperature being $40^{\circ}\text{C} \pm 2^{\circ}\text{C}$. Fig.14 shows the corresponding results for the 0.5m length of steel pipe.

It can be seen from these experimental results that, of the three vibration modes, the bending mode is exclusively excited by the broad band random pressure fluctuation created by the collapse of cavitation bubbles, and only the sounds associated with these natural frequencies are radiated predominantly from the pipe wall. Experimental results of pipe vibration agree qualitatively well with the analytical results obtained for the receptance in the previous section. These experimental facts agree with such results that the fundamental mechanism for the generation of pipe wall vibration and subsequent external acoustic radiation from pipes due to internal flow disturbances is the coincidence of internal higher order acoustic modes with resonant bending modes in pipe wall, which was demonstrated by Bull and Norton [6,7]. In addition, the following also can be seen: (i) the strong spectral frequencies agree well with those shown in Table 1 obtained by the EMA; (ii) as the mean pressure in the downstream pipe is reduced, the vibration acceleration (and hence sound pressure) correspondingly increases; (iii) as the application position of the exciting force moves closer to the antinode of the mode shape (in other words, as the pipe length becomes shorter in the case of exciting position being fixed), the amplitude of the associated vibration mode becomes larger (and vice versa).

Fig.15 shows the experimental results for the flexible hose. Mechanical vibration of the hose wall and radiated noise from it are strongly correlated in the same manner as for the steel pipe. But, because the resonance modes of a flexible hose are highly coupled, it is very difficult to establish quantitatively the correspondence between the resonance modes in Fig.15 and the vibration modes obtained by the FEM modal analysis shown in Table 2. However, there is reasonable correlation between the number of resonance frequencies of the bending vibration modes that appear in a certain frequency range. For example, in the frequency range 2kHz to 4kHz there are 8 ~9 resonances, as shown by the ‘●’ symbols in the acceleration spectra; 8 are predicted by FEM (modes 14 to 21). In addition, broad band vibration and noise due to the pipe ring vibration modes, which are heavily coupled, also occur in the high frequency range above around 6 kHz. Hence it may be concluded that the noise from the flexible hose is also generated by the same mechanism as that in a steel pipe.

Lastly, the harmonic amplitudes of the exciting force for the bending vibration during cavitation conditions were roughly estimated by comparing the calculated vibration amplitude from Eq.(1) with the experimental value measured at the middle of the pipe; the hydrodynamic sources were again assumed to act at a single grid point at the position of $z_f = 40\text{mm}$, as shown by Fig. 9(b). Fig.16 shows the experimental frequency spectra of vibration amplitude for the 1m length of steel pipe for the case of $\bar{P}_u = 8.0\text{MPa}$ and $\bar{P}_d = 0.10\text{Mpa}$. The normalized amplitude was obtained by dividing the measured acceleration amplitude by $(2\pi f)^2$. Table 3 presents the estimated harmonic amplitude of the exciting force of the odd orders of the bending vibration modes for the case of $\bar{P}_u = 8.0\text{MPa}$ with various downstream pressures, \bar{P}_d . The magnitudes of the virtual exciting forces for the respective bending modes are considered to be reasonable, considering the magnitude of pressure fluctuations around resonance frequencies in Fig.4.

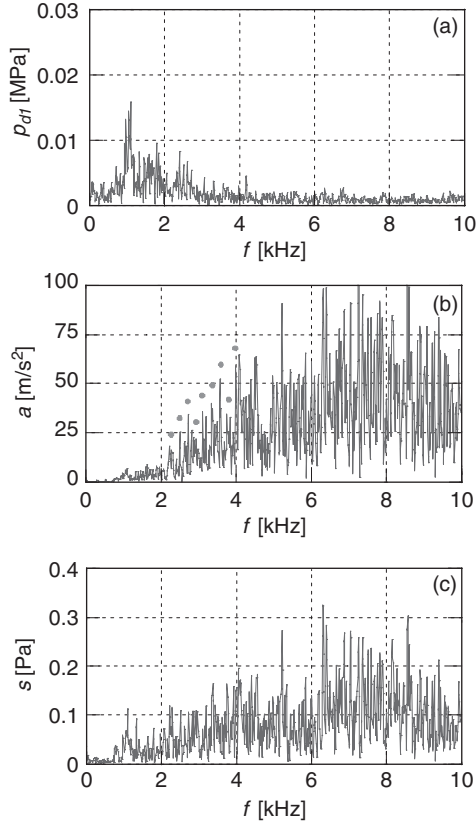


Fig.15 Measured narrow band frequency spectra of (a) orifice downstream pressure fluctuation, (b) vibration acceleration of downstream pipe and (c) nearby sound pressure [1.0m length of flexible hose ($\bar{p}_u=8\text{MPa}$, $\bar{p}_d=0.25\text{MPa}$)]

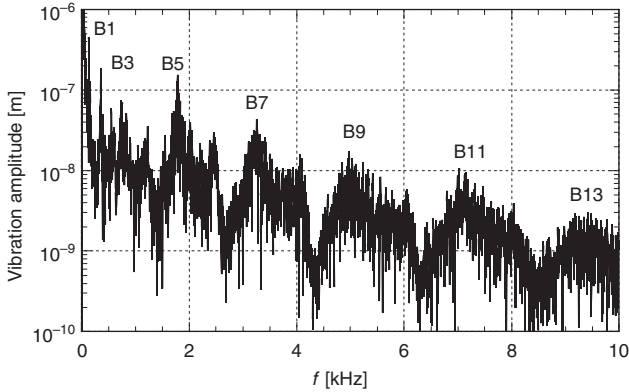


Fig.16 Measured narrow band frequency spectra of vibration amplitude at the middle of 1.0m steel pipe ($\bar{p}_u=8\text{MPa}$, $\bar{p}_d=0.1\text{MPa}$)

Table 3 Estimated harmonic amplitude of the exciting force of the odd order of bending vibration modes ($\bar{p}_u=8\text{MPa}$, $z_f=40\text{mm}$)

	$\bar{p}_d = 0.10 \text{ MPa}$		$\bar{p}_d = 0.20 \text{ MPa}$		$\bar{p}_d = 0.30 \text{ MPa}$		$\bar{p}_d = 0.40 \text{ MPa}$		$\bar{p}_d = 0.50 \text{ MPa}$	
	η_n [m]	F_i [N]	η_n [m]	F_i [N]	η_n [m]	F_i [N]	η_n [m]	F_i [N]	η_n [m]	F_i [N]
B-1	2.02E-08	0.1	1.83E-08	0.1	2.00E-08	0.1	1.68E-08	0.1	1.53E-08	0.1
B-3	3.77E-08	0.7	3.81E-08	0.8	3.26E-08	0.6	3.08E-08	0.6	3.01E-08	0.6
B-5	5.98E-08	2.9	1.80E-08	0.9	1.07E-08	0.5	4.12E-09	0.2	4.03E-09	0.2
B-7	3.08E-08	2.8	2.25E-08	2.1	9.96E-09	0.9	5.47E-09	0.5	5.15E-09	0.5
B-9	1.50E-08	2.3	8.30E-09	1.3	6.24E-09	0.9	5.82E-09	0.9	5.14E-09	0.8
B-11	8.51E-09	2.0	5.05E-09	1.2	3.52E-09	0.8	3.16E-09	0.7	2.02E-09	0.5
B-13	2.46E-09	0.9	2.92E-09	1.0	2.74E-09	1.0	2.81E-09	1.0	2.09E-09	0.7

5. CONCLUSIONS

A study has been undertaken to establish the noise generation mechanism from a downstream pipe produced by hydrodynamic sources associated with cavitation within an oil hydraulic valve orifice. The following conclusions are drawn:

- (1) A steel pipe mounted downstream of a valve is excited principally at the natural frequencies of both the bending vibration modes and pipe ring vibration modes by the broad band random pressure fluctuation that occurs during the collapse of cavitation bubbles. The airborne noise radiated from the pipe wall is generated predominantly at these natural frequencies. This means that the sound pressure level of cavitation noise is also significantly affected by the resonance of the bending and pipe-ring modes of the valve downstream pipe, as well as the intensity of the hydrodynamic source (i.e., cavitation intensity).
- (2) The ring vibration modes have substantial effects on the noise levels in the very high frequency regions, typically above around 15kHz for oil hydraulic steel piping systems.
- (3) Cavitation noise radiated from a flexible hose has the same trends as for the case of the steel pipe, although each mode is heavily coupled due to the soft elastic hose wall.
- (4) The torsional vibration mode accompanying the radial deformation vibration mode of the downstream pipe has practically no effect on the cavitation noise, because the torsional excitation of the pipe is very small.
- (5) The effects of the longitudinal vibration mode, which accompanies the bending vibration, on cavitation noise can be ignored.
- (6) The harmonic amplitude of the cavitation-induced exciting force can be roughly estimated by comparing the measured value of vibration amplitude with the simulated value from the FEM forced vibration analysis, so far as the bending vibration modes are concerned

These conclusions are generally applicable to the sound produced by the hydrodynamic sources associated with turbulence and/or cavitation within a valve in various kinds of pipeline systems. In order to use FEM to predict, with reasonable accuracy, cavitation-induced noise that is generated inside a valve orifice and radiated from the adjacent pipe, further detailed work should be undertaken. This should include an examination of the characteristics of the cavitation-induced exciting force (e.g. amplitude spectra, application

point, etc.) and the frequency response characteristics of the acoustic radiation efficiency of the pipe wall. Statistical energy analysis (SEA) may be appropriate for the prediction of the noise levels caused by the pipe ring vibration modes in the high frequency regions, where the modal densities are extremely high.

REFERENCES

- 1) A. E. Moore, "Oil hydraulic cavitation noise from simple flow restrictions", BHRA fluid engineering, CR1647 (December 1980).
- 2) H. D. Baumann and J. Kiesbauer, "A method to estimate hydrodynamic noise produced in valves by submerged turbulent and cavitating water jets", Noise Control Eng. J. 52(2), 49~55 (2004 Mar-Apr).
- 3) J. Yu and E. Kojima, "Wave propagation in Fluids contained in finite-length anisotropic viscoelastic pipes" J. Acoust. Soc. Am., 104(6), 3227~3235 (1998).
- 4) M. P. Norton, "Fundamental of noise and vibration analysis for engineers", Cambridge University Press.
- 5) I. M. Howard, M. P. Norton and B. J. Stone, "A coincidence damper for reducing pipe wall vibrations in piping systems with disturbed internal turbulent flow", Journal of Sound and Vibration, 113(2), 377~393 (1987).
- 6) M. P. Norton and M. K. Bull, "Mechanisms of the generation of external acoustic radiation from pipes due to internal flow disturbances", Journal of Sound and Vibration, 94, 105~146 (1984).
- 7) M. K. Bull and M. P. Norton, "The proximity of coincidence and acoustic cut-off frequencies in relation to acoustic radiation from pipes with disturbed internal turbulent flow", Journal of Sound and Vibration, 69, 1~11 (1980).

An Experimental Result on the Measurement of Concentrated Flow Resistances

B MANHARTSGRUBER

Institute of Machine Design and Hydraulic Drive Technology, Johannes Kepler University, Linz, Austria

ABSTRACT

Current developments in fuel injection, variable engine valve actuation systems, and related fields of technology result in an increasing demand for accurate and fast simulation methods for fluid flow in networks of small pipelines or bores within valve manifolds. Besides the description of the flow in straight pipes, the understanding of the influence of elbow fittings, branch connections, intersecting bores, and the like is crucial for an accurate prediction of the dynamic behaviour. While there is a vast literature on the steady state pressure drop of hydraulic components, the dynamic case is poorly understood even for pulsatile laminar flow. The paper gives experimental results on the input output behaviour of test case including a single pipeline with a concentrated flow resistance at the connection between the pipe and a cavity of comparatively large diameter as well as minor concentrated losses due to the mounting points of pressure sensor. Results are given in the form of frequency response functions up to 2 kHz for the test case with a pipe length in the order of one metre.

NOMENCLATURE

a	m/s^2	acceleration difference between piston and housing
c_0	m/s	speed of wave propagation
p_0, p_1, p_2	Pa, bar	pressure measurements
$p_{0,1}, p_{1,1}, p_{1,2}, p_{2,1}$	Pa, bar	entry and exit pressures of the two pipe sections
s	rad/s	Laplace variable
t	s	time
A	m^2	cross sectional area of the excitation piston
Dn	-	dissipation number
E_{fl}	N/m^2	modulus of compressibility of the hydraulic fluid
J_0, J_2	-	Bessel functions
L	m	transmission line length
Q_0, Q_1, Q_2	m^3/s	volumetric flow rates
R	m	transmission line internal radius
R_1, R_2	$\text{kg}/(\text{m}^4\text{s})$	concentrated flow resistance coefficients
V	m^3	volume of the excitation chamber
Z_0	$\text{kg}/(\text{m}^4\text{s})$	characteristic impedance of the transmission line
$Z(s)$	$\text{kg}/(\text{m}^4\text{s})$	frequency-dependent hydraulic impedance
α	-	geometry parameter

$\gamma(s)$	1/m	frequency dependent propagation coefficient
ρ	kg/m ³	mass density of the hydraulic fluid
ν	m ² /s	kinematic viscosity of the hydraulic fluid

1 INTRODUCTION

Wave propagation in pipelines and hoses has long been studied with respect to the dynamic characteristics of fluid power systems and for better understanding of the transmission of fluid-borne noise. In the case of moderate line diameters and typical viscosity values of mineral oil, the majority of connections between fluid power components are operated under laminar flow conditions for reasons of energy efficiency and noise mitigation. The geometric shape of these connections is almost always dominated by long straight segments with constant and circular cross section. This is why the well developed theory of laminar pipe flow of a compressible Newtonian fluid has widely been used in the fluid power community.

In order to keep the focus on the influence of concentrated flow resistances, the phenomenon of cavitation or column separation is omitted in this paper. Furthermore, the pipelines are assumed to be mounted rigidly to a supporting structure allowing only radial deflection of the elastic pipe wall. The influence of the radial deflection on the wave propagation in the fluid is assumed to be treatable by an effective bulk modulus of compressibility somewhat lower than the value suggested by the fluids properties. This restriction allows to treat the pipe flow problem without coupling to the structural dynamics of the pipework. In the case of internal connections within hydraulic manifolds this assumption holds quite generally. An important application area of such internal connection pipe networks arises in the technology of hydraulically operated variable valve train systems where a set of small bores within a cylinder head establishes the supply connections for the small hydraulic drives operating the engine valves.

The so-called 'frequency-dependent' friction theory of axisymmetric flow [1] describes the input-output behaviour of fluid power pipelines with rigid walls very well under the following assumptions:

1. The ratio between the operating pressure and the bulk modulus of compressibility is small compared to one. In this case a scaling of the equations using dimensionless variables for pressure, flow rate, and time shows that the convective terms are negligible.
2. Fluid properties can be regarded as independent of pressure and temperature
3. The geometry of the pipeline system is dominated by sections of cylindrical shape with a length much bigger than the diameter.
4. Any change of direction of the pipeline appears smoothly with a radius of curvature considerably larger than the radius of the circular cross section.
5. Steps in the pipeline diameter are small.
6. If three or more pipes join in a node, the nodal volume can be neglected and all pipelines face a pressure boundary condition computable from a Kirchhoff-type nodal equation.

The first assumption is normally met for both oil and water hydraulic systems because of the high modulus of compressibility. The second assumption may be violated if a pipeline operates in a wide pressure or temperature range. While this is a problem with respect to modal approximation methods, the resulting nonlinearities can be treated in simulation codes built on a spatial discretization of the pipeline like finite element methods.

A number of open questions exists about the necessary degree of fulfillment of the remaining assumptions. While there is abundant literature about pressure drops in stationary flow [5], the information about the instationary case is sparse. For a theoretical treatment of pipe wall discontinuities see, for instance [6]. The gap between highly sophisticated computational fluid dynamics approaches and the low order models needed for system design and control is large. While special applications have already been treated in the fluid mechanics literature [7], the fluid power community has long concentrated on transmission line modeling under ideal conditions. However, the effect of sharp pipe curvatures, T-joints and the like becomes more important due to the high operating frequencies and short pipe lengths involved in fuel injection, variable valve actuation, and other non-classical fluid power systems.

This paper describes the first experimental results of a project aimed towards the clarification of the influence of non-ideal geometries such as large steps in pipe diameter or sharp elbow bends on the dynamical behaviour of fluid transmission lines.

2 EXPERIMENTAL SETUP

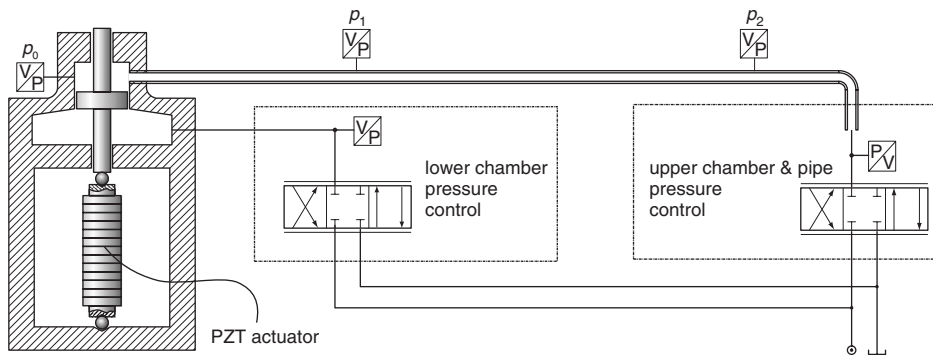


Figure 1: Experimental setup.

Because of the high eigenfrequencies of pipe networks with characteristic lengths in the order of one meter, both the excitation and the measurement devices need to be capable of dealing with frequencies up to several thousand Hertz. If fast hydraulic servo-valves are operated at small amplitudes like 1 to 5 % of full scale, frequencies up to 1000 Hz can be generated. However, this is still too low for the application at hand. Some authors have used fast cutoff devices and generated high frequency excitation by closing a valve so fast that the closing time is small against the inherent time constants of the pipe system. A classical experiment in this area was done by Holmboe and Rouleau [3] in 1967.

The approach presented in this paper uses a piezo-electric stack translator as excitation source.

Table 2: Experimental equipment.

PZT actuator	Physik Instrumente	P 245.70
piezo electric pressure gauges	Kistler	6005
piezo-resistive pressure gauges	GE Druck	PDCR 4060
accelerometers	Kistler	8202A10
lower chamber pressure control valve	Moog	D633
upper chamber & pipe pressure control valve	Moog	D760-995A

A simplified sketch of the excitation device is given in Fig. 1. The device features a piston loaded by a piezo-electric stack actuator and two cylinder chambers. The pressure in the lower chamber is maintained by a servo-hydraulic pressure control loop with an absolute pressure gauge and a directional control valve. The pressure at the end of the pipeline under test is again stabilized by a servo-hydraulic control loop. The voltage at the piezo-electric actuator is controlled by a power amplifier. The volumetric flow rate injected into the system by the movement of the excitation piston is captured by two accelerometers attached to the piston and the housing, respectively. This allows for the computation of the acceleration difference between piston and housing.

The pressure values for the control of the mean pressure levels both in the lower chamber and at the end of the pipe system under test are measured by piezo-resistive transducers giving absolute pressure values.

2 A FIRST TEST CASE

Table 3: Parameter values for the first test case.

pipe section length	L	1321 mm
inner pipe radius	R	4 mm
geometry parameter	α	1/3
mean pressure in the pipe section		60 bar
kinematic viscosity of the hydraulic fluid	ν	90 cSt @ 20°C
cross sectional are of the excitation piston	A	754 mm ²
excitation chamber volume	V	$A \cdot 25$ mm ³

The sketch of the experimental setup in Fig. 1 already contains the first test case. A straight pipe section is attached to the excitation device. A first piezo-electric pressure gauge measures the pressure in the upper chamber of the excitation device, a second one at a distance of $L/3$ and a third one at a distance L measured from the start of the pipe section at the inner wall of the upper cylinder chamber. The details of the pressure sensors mounted within the pipeline are given in Fig. 2.

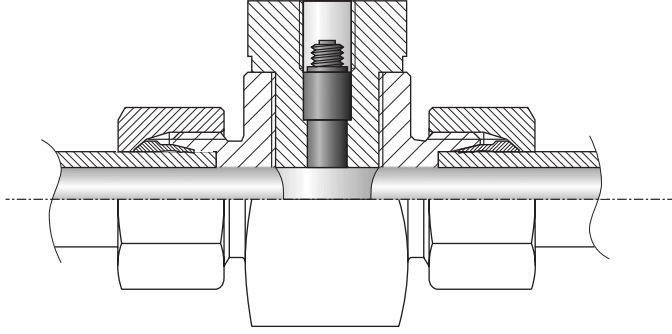


Figure 2: Kistler type 6005 sensor mounted in a steel pipe.

A simplified equivalent circuit diagram of the experimental setup is given in Fig. 3. Two sections of a straight pipeline with lengths αL and $(1 - \alpha) L$ are mathematically represented by their transfer function matrices

$$\begin{bmatrix} \hat{p}_{1,1}(s) \\ \hat{Q}_1(s) \end{bmatrix} = \begin{bmatrix} \cosh(\gamma\alpha L) & -Z \sinh(\gamma\alpha L) \\ -\frac{1}{Z} \sinh(\gamma\alpha L) & \cosh(\gamma\alpha L) \end{bmatrix} \begin{bmatrix} \hat{p}_{0,1}(s) \\ \hat{Q}_0(s) \end{bmatrix} \quad (1a)$$

$$\begin{bmatrix} \hat{p}_{2,1}(s) \\ \hat{Q}_2(s) \end{bmatrix} = \begin{bmatrix} \cosh(\gamma(1-\alpha)L) & -Z \sinh(\gamma(1-\alpha)L) \\ -\frac{1}{Z} \sinh(\gamma(1-\alpha)L) & \cosh(\gamma(1-\alpha)L) \end{bmatrix} \begin{bmatrix} \hat{p}_{1,2}(s) \\ \hat{Q}_1(s) \end{bmatrix} \quad (1b)$$

where the propagation coefficient γ and the hydraulic impedance Z are defined as

$$\gamma = \frac{s}{c_0} \sqrt{-\frac{J_0(\sqrt{-\frac{s}{\nu}}R)}{J_2(\sqrt{-\frac{s}{\nu}}R)}} \quad \text{and} \quad Z = Z_0 \sqrt{-\frac{J_0(\sqrt{-\frac{s}{\nu}}R)}{J_2(\sqrt{-\frac{s}{\nu}}R)}}$$

with the speed of wave propagation c_0 and the characteristic impedance Z_0 given by

$$c_0 = \sqrt{\frac{E_{fl}}{\rho}} \quad \text{and} \quad Z_0 = \frac{\sqrt{E_{fl}}}{R^2\pi}$$

Leakage flow over the gap between cylinder and piston in the excitation device is neglected and the differential acceleration measurement is assumed to be ideal, i.e. the integral of the acceleration with respect to time multiplied with the piston area is assumed to give the flow rate injected into the chamber connected to the first section of the pipeline. The pressure within this chamber will then obey the equation

$$\frac{V}{E_{fl}} s \hat{p}_0(s) = A \frac{\hat{a}(s)}{s} - \hat{Q}_0(s). \quad (2)$$

Concentrated flow resistances are supposed to be present at the attachment of the pipeline to the excitation chamber and at the points where the mounting of pressure sensors within the pipe disturbs the cylindrical geometry of the inner pipe wall. The resistances are modelled as linear relationships between flow rate and pressure drop resulting in

$$\hat{p}_0(s) - \hat{p}_{0,1}(s) = R_1 \hat{Q}_0(s), \tag{3a}$$

$$\hat{p}_{1,1}(s) - \hat{p}_1(s) = R_2 \hat{Q}_1(s), \tag{3b}$$

$$\hat{p}_1(s) - \hat{p}_{1,2}(s) = R_2 \hat{Q}_1(s), \tag{3c}$$

$$\hat{p}_{2,1}(s) - \hat{p}_2(s) = R_2 \hat{Q}_2(s). \tag{3d}$$

A number of assumptions have been made in order to arrive at the equivalent circuit diagram of Fig. 3 and the mathematical equation system (1-3):

- Nonlinear effects such as the convective terms in the Navier-Stokes equations describing the pipe flow and nonlinear material behaviour such as the variation of the bulk modulus of compressibility with pressure are neglected
- Wave propagation is modelled by the frequency-dependent friction model [1] in the two pipeline sections only. The pressure distribution within the excitation chamber is assumed to be uniform. This assumption relies upon the small geometric dimensions of the excitation chamber compared to the pipeline length.
- Mechanical vibration of the pipelines and their supporting structure are neglected. The influence of the radial deflection of the pipe wall is accounted for by an effective bulk modulus of compressibility which is somewhat lower than the value suggested by the fluid properties.

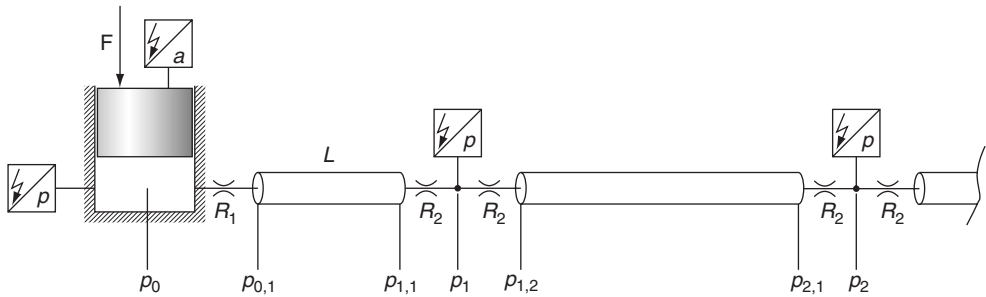


Figure 3: Equivalent circuit diagram for the first test case.

3 A SCALED MODEL FOR PARAMETER IDENTIFICATION

The basic idea of this paper is to study the influence of concentrated flow resistances within systems of hydraulic transmission lines by matching measurement results to theoretical transfer functions in the frequency domain. As this match involves the identification of unknown system parameters, the number of independent parameters has to be known. In the example given by eqs. (1-3), the physical parameters are the fluid properties ρ , ν , and E_{fl} , the pipeline dimensions R , L , and α , the volume of the excitation chamber V , and the values for

the concentrated flow resistances R_1 and R_2 . This gives a total of nine parameters. While the pipeline dimensions are exactly known, the information about the other parameters ranges from approximate values for the volume V and the density ρ to rough guesses for the effective bulk modulus E_{fl} and the resistance values R_1 and R_2 . A diagram for the viscosity of the hydraulic fluid used in the tests is available giving a value of $90 \cdot 10^{-6}$ m²/s at an oil temperature of 20°C. To this end, only three parameters can be regarded as known, the others have to be identified within reasonable lower and upper limits. In order to improve the numerical properties of the parameter identification problem, the model is reformulated by using a dimensionless time and frequency scale

$$\tau = \frac{c_0}{L} t, \quad \tilde{s} = \frac{L}{c_0} s, \quad (4)$$

the dimensionless dissipation number [2]

$$Dn = \frac{\nu L}{c_0 R^2}$$

and a scaling of all flow rates in the form

$$\tilde{Q}_i(\tau) = 8 Dn Z_0 Q_i(t), \quad i = 0, 1, 2.$$

The rescaled model reads

$$\begin{bmatrix} \hat{p}_{1,1} \\ \hat{Q}_1 \end{bmatrix} = \begin{bmatrix} \cosh(\tilde{\gamma}\alpha) & -\tilde{Z} \sinh(\tilde{\gamma}\alpha) \\ -\frac{1}{\tilde{Z}} \sinh(\tilde{\gamma}\alpha) & \cosh(\tilde{\gamma}\alpha) \end{bmatrix} \begin{bmatrix} \hat{p}_{0,1} \\ \hat{Q}_0 \end{bmatrix} \quad (5a)$$

$$\begin{bmatrix} \hat{p}_{2,1} \\ \hat{Q}_2 \end{bmatrix} = \begin{bmatrix} \cosh(\tilde{\gamma}(1-\alpha)) & -\tilde{Z} \sinh(\tilde{\gamma}(1-\alpha)) \\ -\frac{1}{\tilde{Z}} \sinh(\tilde{\gamma}(1-\alpha)) & \cosh(\tilde{\gamma}(1-\alpha)) \end{bmatrix} \begin{bmatrix} \hat{p}_{1,2} \\ \hat{Q}_1 \end{bmatrix} \quad (5b)$$

$$Dn c_1 \tilde{s} \hat{p}_0 = Dn c_2 \frac{\hat{a}(s)}{\tilde{s}} - \hat{Q}_0(s) \quad (5c)$$

$$\hat{p}_0 - \hat{p}_{0,1} = \tilde{R}_1 \hat{Q}_0 \quad (5d)$$

$$\hat{p}_{1,1} - \hat{p}_1 = \tilde{R}_2 \hat{Q}_1 \quad (5e)$$

$$\hat{p}_1 - \hat{p}_{1,2} = \tilde{R}_2 \hat{Q}_1 \quad (5f)$$

$$\hat{p}_{2,1} - \hat{p}_2 = \tilde{R}_2 \hat{Q}_2 \quad (5g)$$

with a scaled hydraulic impedance \tilde{Z} and a scaled propagation coefficient $\tilde{\gamma}$ defined as

$$\tilde{Z} = \sqrt{-\frac{J_0\left(\sqrt{-\frac{\tilde{s}}{Dn}}\right)}{J_2\left(\sqrt{-\frac{\tilde{s}}{Dn}}\right)}}, \quad \tilde{\gamma} = \tilde{s} \tilde{Z}$$

The remaining parameters are the known geometry parameter α , the dissipation number Dn and the new parameters

$$c_1 = \frac{8V}{R^2 \pi L}, \quad c_2 = 8\rho L \frac{A}{R^2 \pi}, \quad \tilde{R}_1 = \frac{R_1}{\frac{8\nu\rho L}{R^4 \pi}}, \quad \tilde{R}_2 = \frac{R_2}{\frac{8\nu\rho L}{R^4 \pi}} \quad (6)$$

resulting from the scaling process. The speed of wave propagation c_0 is needed in the time scaling of eq. (4) and therefore has to be included in the list of parameters to be identified.

The differential acceleration a and the pressure p_2 are regarded as system inputs, the remaining two measurements p_0 and p_1 are treated as outputs. The equation system (5) is solved for \hat{p}_0 , \hat{p}_1 , \hat{Q}_0 , \hat{Q}_1 , \hat{Q}_2 , $\hat{p}_{0,1}$, $\hat{p}_{1,1}$, $\hat{p}_{1,2}$, and $\hat{p}_{2,1}$. After measuring the input and output signals of the real system under appropriate excitation, the measured inputs can be substituted into the solution for the outputs \hat{p}_0 and \hat{p}_1 . These predicted outputs are then compared against the measured values. The match is optimised by variation of the unknown parameters using a nonlinear least squares algorithm from the Matlab optimization toolbox [4].

4 EXPERIMENTAL RESULTS

Experimental data is collected by using pulse excitation with the piezo-electric actuator. Measurements of the pressures p_0 , p_1 and p_2 and the differential acceleration a are collected at a sampling frequency of 100 kHz. The Fourier transforms of the signals are computed by the FFT algorithm with a number of 100000 samples. The parameter identification is performed by minimisation of the quadratic error between the Fourier transforms of the measured system outputs and the values predicted from the measured inputs by use of the model (5). The residual difference between measured and predicted values is shown in Fig. 4 in the form of spectral amplitude densities. The identified speed of wave propagation is $c_0 = 1382$ m/s and the dimensionless concentrated flow resistances parameters are $\tilde{R}_1 = 0.05193$ and $\tilde{R}_2 = 0.001682$. Due to the scaling defined in eq. (6), this translates directly to a fraction of the stationary pressure loss coefficient for the pipeline with length L . The pressure loss coefficient for the pipe inlet is 5.2 % of the Hagen-Poiseuille friction coefficient for the whole pipeline. The minor losses turn out to be negligible with a fraction of $1.7 \cdot 10^{-3}$ of the total stationary pressure loss along the pipeline for each of the resistors labeled R_2 in Fig. 3.

4 CONCLUSIONS AND OUTLOOK

An experimental procedure has been set up for the measurement of concentrated flow resistances within a fluid transmission line. A first test case has shown promising results. A number of further tests will now be performed to validate the method:

- The validity of the linear relationship between flow rate and pressure drop has to be tested by variation of the excitation amplitude.
- The pulse excitation will be replaced by sinusoidal excitation. This will allow the measurement of the system response frequency by frequency. Nonlinearities can be detected by higher order harmonics in the response signals.
- The assumption of rigid mounting of the pipeline was not fully met in the first experimental setup. New experiments will be performed with a stiffer support of the pipelines or with bores built into massive manifolds.

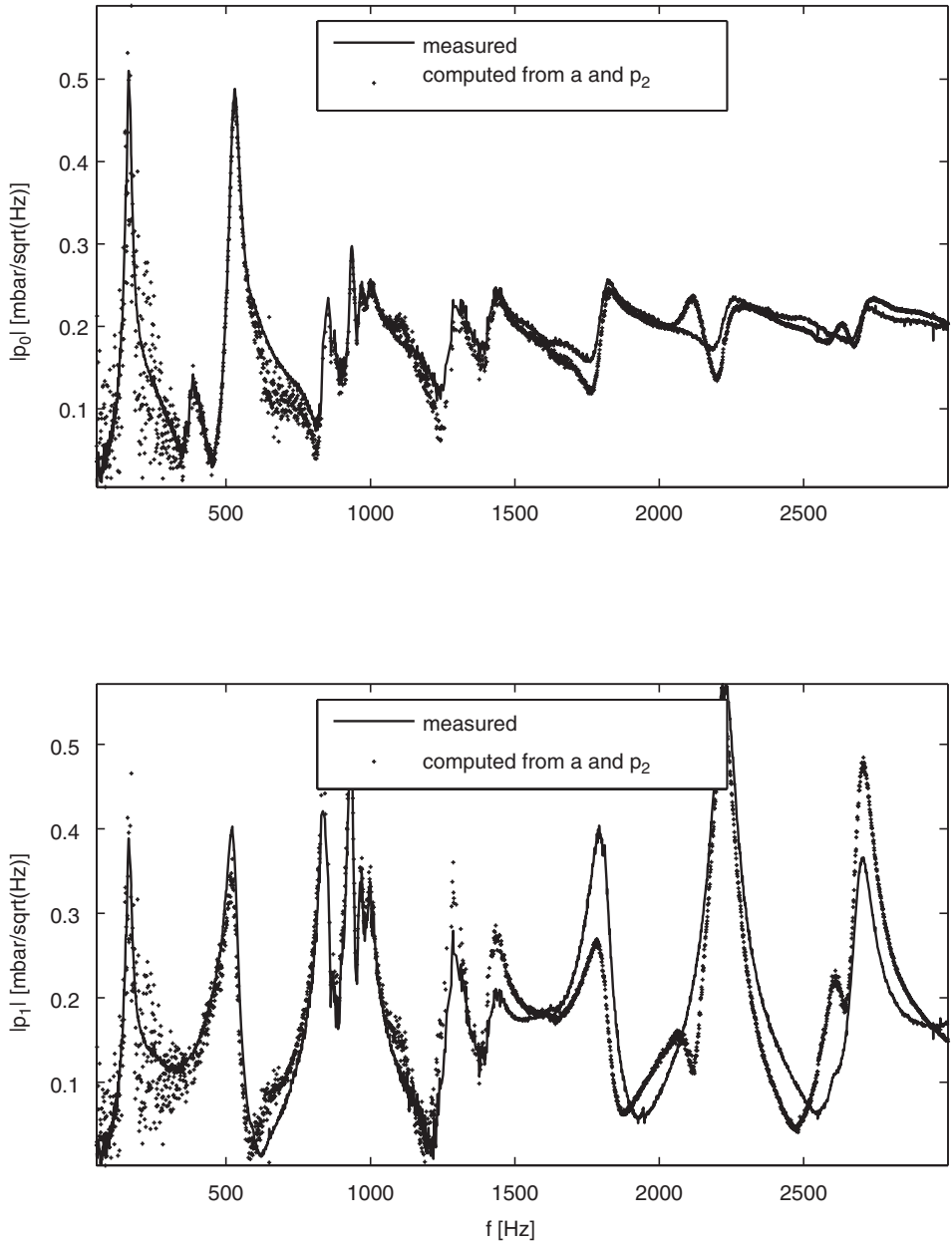


Figure 4: Comparison between measured and predicted outputs.

References

- [1] A.F. D'Souza and R. Oldenburger. Dynamic response of fluid lines. *Trans. ASME, J. Basic Engng*, 86:589–598, 1964.

- [2] R. E. Goodson and R. G. Leonard. A survey of modeling techniques for fluid transients. *Transactions of the ASME - Journal of Basic Engineering*, 94(2):474–482, 1972.
- [3] E.L. Holmboe and W.T. Rouleu. The effect of viscous shear on transients in liquid lines. *Journal of Basic Engineering - Trans. ASME*, 89(1):174–180, 1967.
- [4] The MathWorks, Inc., 3 Apple Hill Drive, Natick, MA. *Optimization Toolbox User's Guide*, fifth printing edition, June 2004.
- [5] D.S. Miller. *Internal flow systems*. BHRA Information Services, Cranfield, Bedford, UK, 2nd edition edition, 1990.
- [6] J.M. Muggleton and M.J. Brennan. Axisymmetric wave propagation in buried fluid-filled pipelines: effect of wall discontinuities. *Journal of Sound and Vibration*, 281:849–867, 2005.
- [7] H. Telib, M. Manhart, and A. Iollo. Analysis and low-order modeling of the inhomogeneous transitional flow inside a t-mixer. *Physics of Fluids*, 16(8):2717–2731, 2004.

The dynamics of hydraulic fluids – significance, differences and measuring

J-P Karjalainen, R Karjalainen, K Huhtala, M Vilenius

Tampere University of Technology, Institute of Hydraulics and Automation

ABSTRACT

In this paper the most important dynamical properties of hydraulic fluids and the significance of fluid dynamics on hydraulic systems control are introduced. The bulk modulus, density and sound velocity of five different types of commercial hydraulic fluids were measured at different temperatures and pressures up to over 600 bar. The measurements were based on defining the pressure wave propagation time at known length of rigid straight pipe. The conventional measuring system had to be modified due to aeration and reflection problems which were revealed at pressures over 300 bar. Finally the results are discussed and compared with each other. The results are also compared with recent, relatively easy-to-use mathematical models for possible correlation.

NOTATION

B_{eff}	Effective bulk modulus [Pa]
B_{sa}	Secant adiabatic bulk modulus [Pa]
B_{si}	Secant isothermal bulk modulus [Pa]
B_{ta}	Tangent adiabatic bulk modulus [Pa]
B_{ti}	Tangent isothermal bulk modulus [Pa]
c	Speed of sound in the fluid [m/s]
p	Pressure [Pa]
p_{atm}	Atmospheric pressure
T	Temperature [°C]
ρ_n	Density at measured pressure and temperature [kg/m^3]
$\rho_{\text{atm},T}$	Density at atmospheric pressure and at temperature T [kg/m^3]
$\nu_{\text{atm},20^\circ\text{C}}$	Kinematic viscosity at atmospheric pressure and temperature of 20 °C [cSt]

1. On the significance of hydraulic fluid dynamics

The dynamics of hydraulic fluid is an important factor when dealing with accurate control systems. The dynamic fluid parameters considered in this paper are the bulk modulus and density which are no doubt the most important ones – the sound velocity can be calculated from these values (12).

The bulk modulus is the most crucial fluid parameter considering the system dynamics. The effect of fluid bulk modulus on the control responses is demonstrated using a simple simulation model of a P-controlled hydraulic cylinder position servo (figure 1). The control signal of the servo valve is a typical trapezoid. The idea of the model is only to give an example rather than to mimic most accurately the real-life solutions. Nevertheless, the effect of fluid bulk modulus is similar to more accurate models.

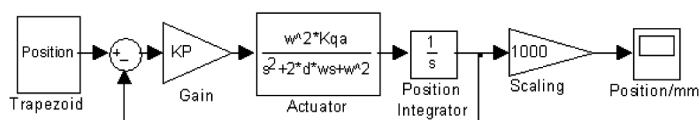


Figure 1 The simulation model.

The system is designed using the common belief that the fluid bulk modulus is 1500 MPa independent of the pressure, temperature or the fluid. The set value of 200 mm with the accuracy of 0.2 mm would be reached at 0.45 seconds and the maximum overshoot would be 0.2 mm (figure 2). However, the fluid bulk modulus was found out to vary from 1300 MPa up to 2200 MPa at temperatures 40-70 °C and pressures 50-600 bar with different types of commercial hydraulic fluids (9). Therefore the assumption of bulk modulus of 1500 MPa is not necessarily accurate enough.

Even in the simple simulation model the bulk modulus affects the natural frequency and the damping ratio. The bulk modulus used in the equations is naturally the effective value of the whole system, but especially in high-pressure systems the constructions have to be so stiff that the fluid has the decisive role. The simulations show that if the fluid bulk modulus is 1300 MPa the set value of 200 mm with the accuracy of 0.2 mm is reached only at 1.1 seconds and the maximum overshoot is nearly 0.4 mm (figure 2) due to lowered natural frequency. On the other hand, using the bulk modulus of 2000 MPa the set value with the same accuracy is reached at 0.7 seconds and the overshoot is nearly 0.3 mm due to lower damping. Both the too low and the too high value for the bulk modulus give poorer results – one can imagine the effect in the more critical and to the extreme tuned solutions.

If the fluid bulk modulus is over 2200 MPa the natural frequency increases more rapidly than the damping ratio decreases and thus the simulated response would seem to become better and the gain used might be even raised. On the other hand, if the actual bulk modulus is low enough compared to the estimated one the whole system becomes unstable due to exceeding the critical gain. Therefore it is most harmful to estimate the bulk modulus too

high without proper knowledge of the actual fluid behavior. However, estimating the bulk modulus too low can be harmful as well.

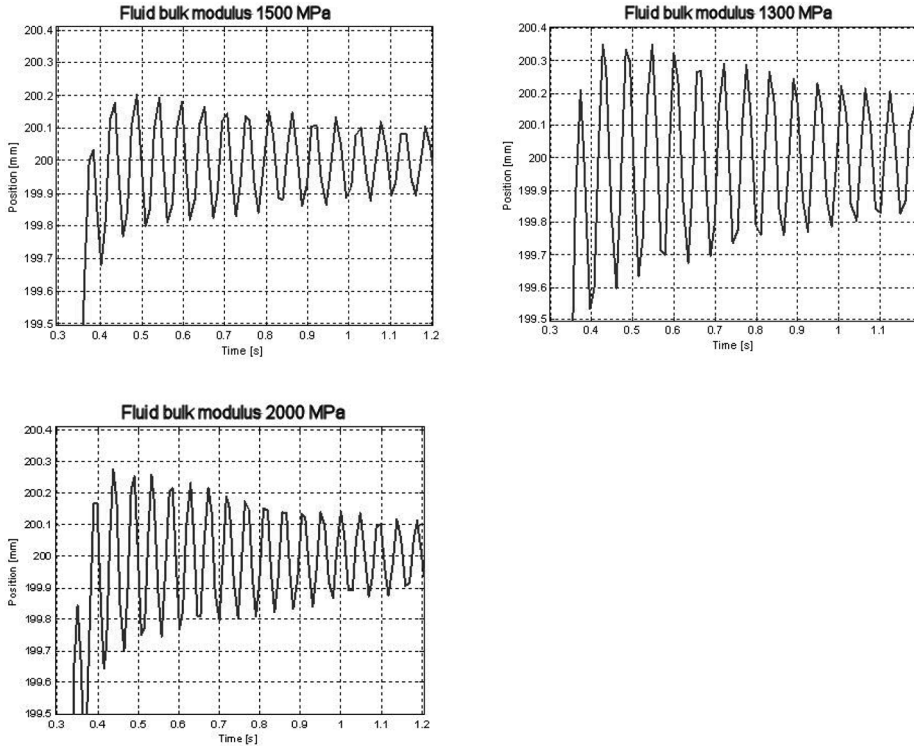


Figure 2 The simulated responses using different fluid bulk modulus.

The designer also has to take into account some other factors arising from the fluid dynamics. Although the high bulk modulus was desirable in the control sense it can cause difficulties in the form of pressure hammer effect. The less compressible the fluid the less it dampens the pressure peaks. Also, the density of fluid affects the pressure hammer in the same way. The density can also be important in very accurate control solutions where the mass of the fluid has to be taken into account when calculating the inertia of the system. Last but not least the sound velocity in the fluid determines the minimum response time of the system – the response cannot be faster than the speed of sound in the fluid. Furthermore the sound velocity determines the resonant conditions at certain fluid line length and pump output frequency (13).

2. Measuring the dynamic parameters of fluids

The common practice to measure the dynamic bulk modulus and density of a fluid is based on determining the sound velocity in the fluid. For example two or more pressure transducers are used to measure the pressure pulsation caused by the pump. When the

transducers are attached to a rigid straight pipe at known distance from each other the pressure wave propagation speed (equals the speed of sound) can be measured from the time shift of the wave. There are more than one published measuring systems based on the above principle having mostly calculative differences (6, 8, 11). However, probably the most “convenient” method in mathematical sense is known as the “cross correlation method” where the idea is to calculate the time delay of two waves with computational cross correlation algorithm (16). According to references (11, 16) the method had been found out to be accurate enough at pressures up to 300 bar and was therefore selected as the measuring method. Nevertheless, the measurements at pressures over 300 bar revealed some problems demanding modifications to the system.

In a nut shell the principle of finding out the bulk modulus and density of a fluid by measuring the speed of sound is based on two equations. On one hand the effective bulk modulus of the system and the density of the fluid are linked together by the speed of sound according to the equation (1) (12). On the other hand there is another connection between the effective tangent bulk modulus and the density of the fluid according to the equation (2) (3). Having only two unknown variables the density of the fluid and the effective bulk modulus can be now calculated with iteration. By estimating the bulk modulus of the system and removing its effect from the effective bulk modulus the fluid bulk modulus can also be found out – when the fluid is assumed air free.

$$c = \sqrt{\frac{B_{\text{eff}}}{\rho_n}} \tag{1}$$

$$\rho_n = \rho_{\text{atm},T} e^{\frac{p-p_{\text{atm}}}{B_{\text{eff}}}} \tag{2}$$

3. The modifications to the original measuring system

The schematic picture of the original measuring system is illustrated in figure 3. The main components are a radial piston pump, two piezoresistive pressure transducers sampled at 100 kHz, two temperature sensors and a flow control valve. The system was designed to operate at continuous pressures up to 700 bar.

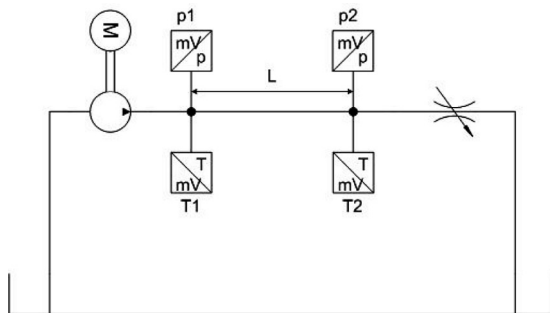


Figure 3 The original measuring system.

The system was tested using typical ISO VG 46 mineral hydraulic oil which has properties reasonably well known. To be able to measure the parameters at different temperatures and to maintain the desired temperature stable enough a relay-controlled water cooler was added in the system. The test measurements gave quite promising results at pressures up to 300 bar but at higher pressure levels the results became more and more mysterious. The measured densities were way too high and the bulk moduli were way too low. Something had to be wrong with the system.

The aeration problem was quite naturally the first concern and actually significant air formation was discovered at pressures over 300 bar – due too high a pressure difference over the flow control valve (10). Three minor flow control valves were added in the return line but it was discovered that probably with only one additional flow control valve there could have been adjusted just enough back pressure to prevent the air formation. Also a transparent “air separation tank” was built and added on top of the original tank to be able to monitor the condition of the returning fluid – no air was further detected. Although a major flaw was fixed the following measurements did not show any improvements.

The next step was to assume that the pipe and the fittings were not rigid enough. Those were replaced with high pressure components for pressures up to 3200 bar. The following measurements gave even poorer results which began to indicate that there might be some problems with wave reflections – becoming even worse due to less bending constructions.

The real-time monitoring of the pressure signals was added to the system and it was obvious that the pressure wave reflected from the flow control valve distorting the wave form observed by the transducers. The shape of the wave should not change in the rigid straight pipe (14) but as it can be seen from the figure 4 the waves were far from identical. Although reflections began to distort the results more clearly at pressures over 300 bar minor reflections were observed even at pressures under 300 bar also slightly affecting the results.

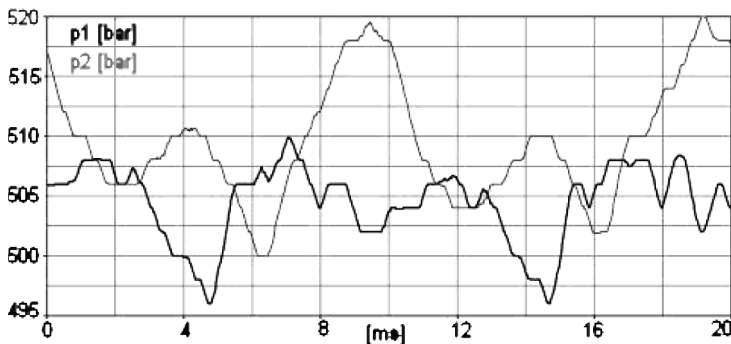


Figure 4 Pressure wave reflection at 500 bar.

The solution to the problem was to build a damping chamber (1, 4, 7) in the pressure line to remove the reflections. The orifice of the chamber inlet is adjusted to set the impedance of the chamber equal to the line impedance – the chamber acts like a very long straight pipe removing the reflections. A schematic picture of the chamber is shown in figure 6 and the effect of orifice opening on the pressure waves is illustrated in figure 5.

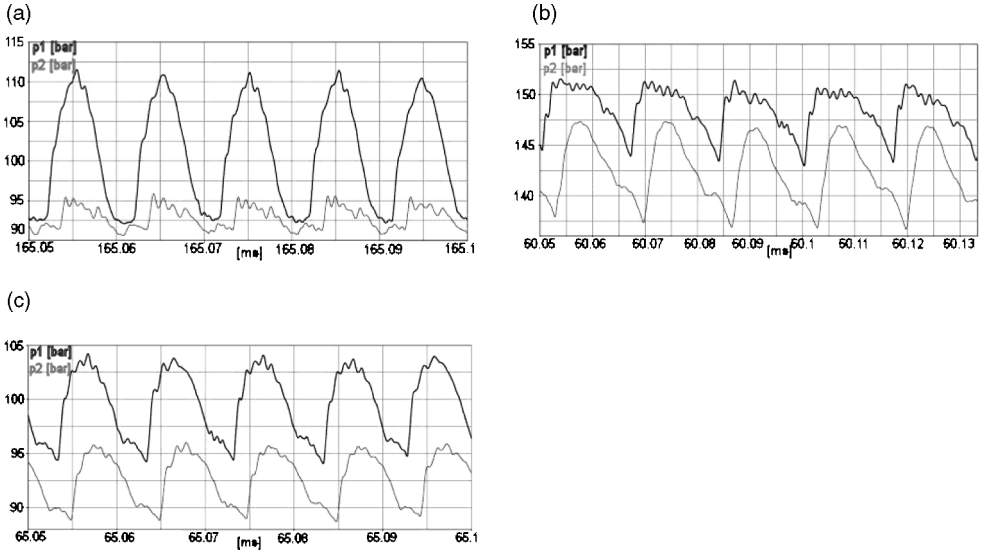


Figure 5 The pressure waves when the orifice opening is (a) too big, (b) too small and (c) reasonably well adjusted.

The damping chamber was adjusted before every measurement and the test measurements proved that the mystery was solved. The schematic diagram of the modified system is shown in figure 7. The need for similar modifications especially at elevated pressures to the other measuring systems introduced in (6, 8, 11) was not tested. Nevertheless, the basic concept of all the systems is quite similar and probably it would be wise to be at least prepared to confront such problems as well.

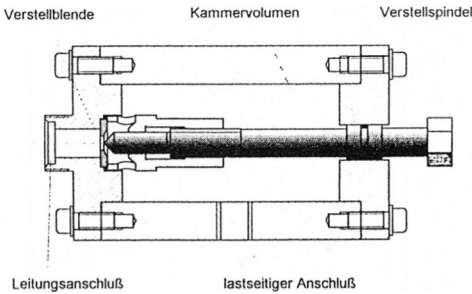


Figure 6 The damping chamber. (1)

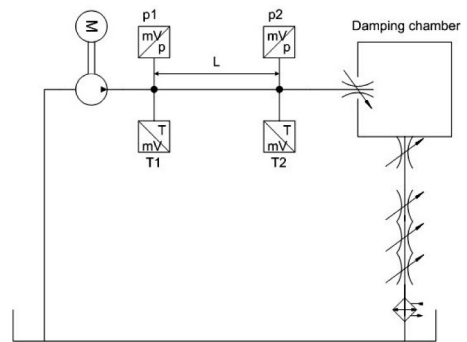


Figure 7 The modified system.

4. The measured dynamic parameters of various hydraulic fluids

The speed of sound, bulk modulus and density were measured with five different commercial hydraulic fluids at three temperatures (40 °C, 55 °C, 70 °C) and at pressures 60-

600 bar. The fluids and reported fluid characteristics used in later calculations are listed in table 1. The measurements were made at pump speed of 1000 rpm. In practice the pumping frequency should not affect the results (15, 16) but to make sure this was also proofed by doing some measurements at pump speed of 1500 rpm with similar results (9). The results are discussed and compared in the following.

Table 1 The measured fluids.

Hydraulic fluid	Density, atm.pressure, 15 °C temperature	Viscosity, 40 °C temperature	Viscosity, 100 °C temperature
ISO VG 46 Mineral oil	875 kg/m ³	46 cSt	6,9 cSt
ISO VG 46 Pine oil	928 kg/m ³	46 cSt	9,9 cSt
ISO VG 46 Synthetic HF-E fluid	928 kg/m ³	46 cSt	9,1 cSt
ISO VG 46 High-VI mineral oil	880 kg/m ³	46 cSt	8,4 cSt
SAE 10W-30 Diesel engine oil	880 kg/m ³	73 cSt	11,3 cSt

4.1 The measured speed of sound

Although the measurements were carried out at three different temperatures the results are presented here only at temperatures of 40 °C and 70 °C due to the fact that there was no unpredicted temperature behavior noted between these two temperatures (9). The results of measured speed of sound are presented in the figures 8 and 9.

The speed of sound seems to behave rather similarly at changing pressure and temperature regardless of the fluid. It can also be noticed that the magnitude of speed of sound does not have a great difference between the fluids – the values for all the fluids are well within 50 m/s. However, the speed of sound is highest in the pine oil but lowest in the HF-E fluid. The values for mineral oil based fluids fall between them.

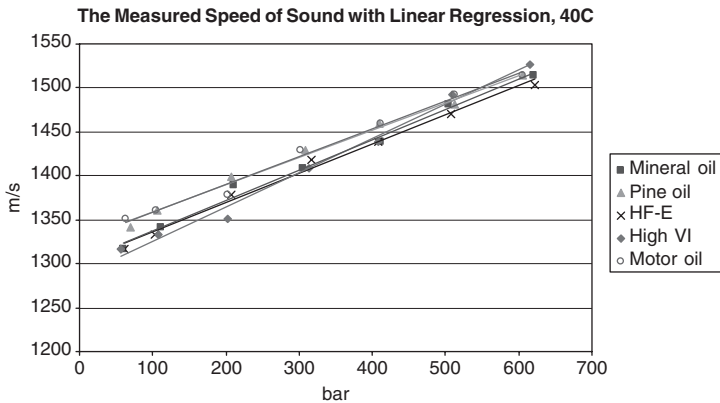


Figure 8 The measured speed of sound at 40 °C and pressures 60-600 bar.

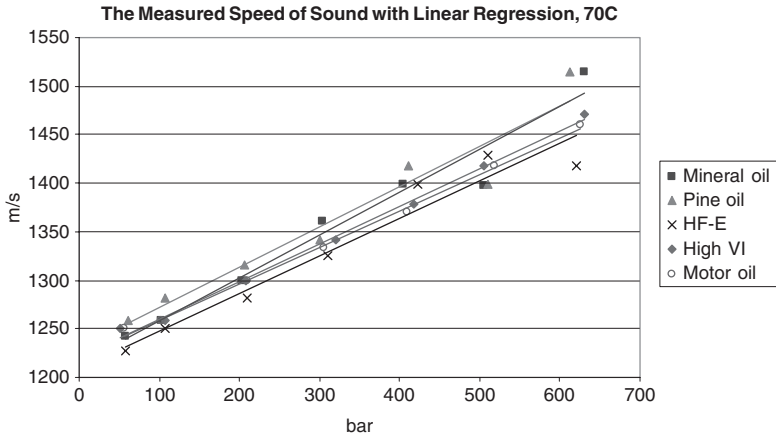


Figure 9 The measured speed of sound at 70 °C and pressures 60-600 bar.

4.2 The measured bulk modulus

The results of measured bulk modulus at temperatures of 40 °C and 70 °C are presented in the figures 10 and 11. In practice all the fluids seem to have similar compressibility behavior at changing temperature and pressure. However, there are quite remarkable differences between the absolute values depending on the fluid. The pine oil clearly has the highest bulk modulus being almost 200 MPa higher than for example the bulk modulus of the high VI oil. The synthetic HF-E fluid has the second highest values and so it can be pointed out that the mineral oil based fluids have the lowest bulk moduli. Therefore, in terms of control system response, the mineral based fluids seem to have poorer performance than the less commonly used alternatives.

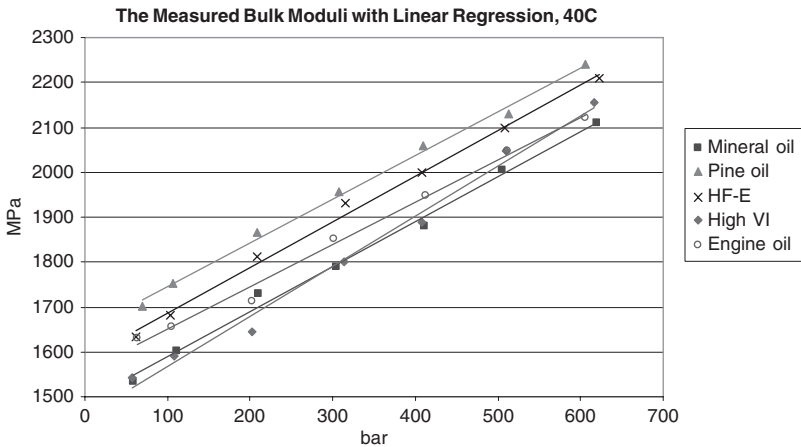


Figure 10 The measured bulk moduli at 40 °C and pressures 60-600 bar.

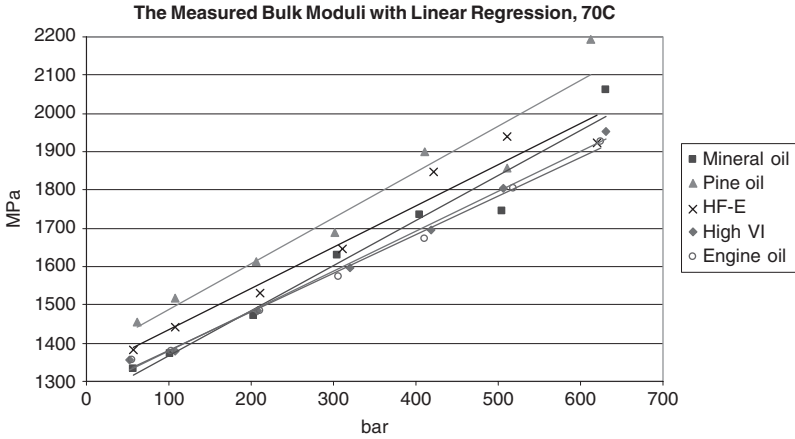


Figure 11 The measured bulk moduli at 70 °C and pressures 60-600 bar.

At first look one might say that the value of bulk modulus can be predicted by comparing the densities given in table 1 and partly it can be true. However, for example the pine oil and HF-E fluid have the same densities but still different bulk moduli. Therefore the actual values should preferably be measured. Furthermore, depending on the manufacturer there might be differences between fluids although classified under the same category and therefore one should be prepared to regard every fluid individually.

4.3 The measured density

The results of measured density at temperatures of 40 °C and 70 °C are presented in the figures 12 and 13. All the fluids seem to have entirely similar changes in density at changing temperature and pressure. The magnitude difference between the densities of fluids appears to be exactly the same as difference given in table 1, independent on pressure or temperature. Therefore, unlike the bulk modulus the density difference between certain fluids is not necessarily as difficult to predict.

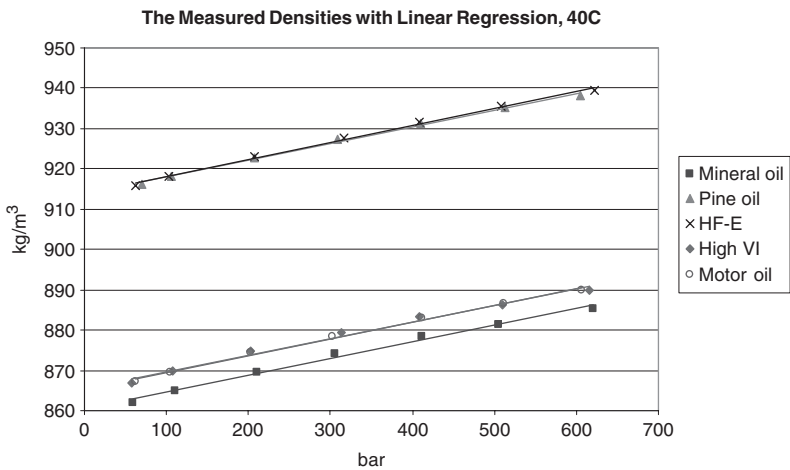


Figure 12 The measured densities at 40 °C and pressures 60-600 bar.

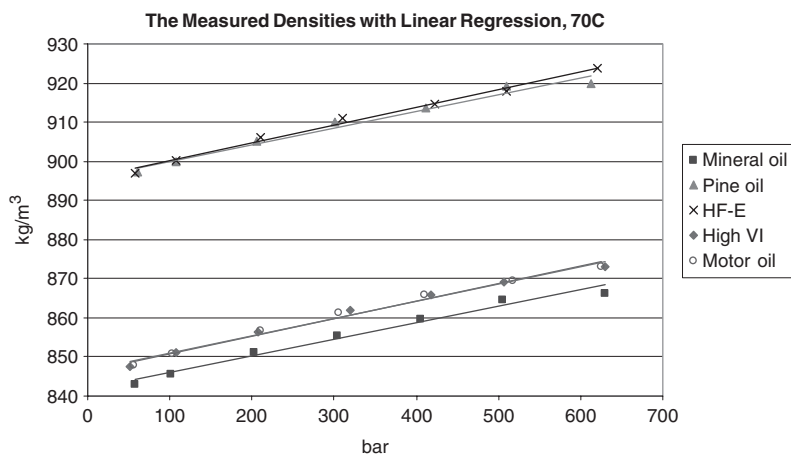


Figure 13 The measured densities at 70 °C and pressures 60-600 bar.

4.4 On the accuracy of the measurements

The relative error of the measured speed of sound depends on the sampling ratio used and on the pipe length (11). Using a pipe length of 2 meters and a sampling rate of 100 kHz will lead to an error under 1 %. The accuracy of bulk modulus and density is more difficult to define as precisely due to the iterative nature of the calculations and due to some uncertainty coming from the fluid density reported by the manufacturer. Otherwise the error of pressure values used in the calculations was well below 2 % and the temperature error was within 1 °C. In any case the measurements can be regarded as relatively accurate.

5. Comparing the measured results with mathematical models

Mathematical equations for modeling fluid parameters in changing pressure and temperature are presented in the reference (2). The equations do not use any experimental constants unique for some certain systems but all the information needed can be found from the fluid characteristics informed by the manufacturer like the ones in the table 1 – the viscosity at the temperature of 20 °C can be for example calculated with the Walther equation (5). Therefore such equations would be easy to use in any hydraulic simulations. The measured values of bulk moduli and densities were compared to the calculated ones and the results are discussed in the following.

At first there should be pointed out that the bulk modulus can be expressed in four ways. On one hand the bulk modulus can be either secant or tangent and on the other hand it can be isothermal (constant temperature) or adiabatic (constant enthalpy). Due to the rapid nature of hydraulic processes it is usually suggested that the adiabatic tangent bulk modulus should be scientifically correct value (5). The measuring concept used is also commonly linked to the adiabatic tangent bulk modulus.

The four different bulk moduli (isothermal secant, adiabatic secant, isothermal tangent, adiabatic tangent) were calculated using the equations (3)-(6) (2) respectively for every

fluid at every measuring temperature and pressure. Same way the density was calculated using the equation (7) (2).

$$B_{si}(p, T) = (1.3 + 0.15 \log v_{atm, 20^\circ C}) 10^{4 + \frac{20-T}{435}} + 5.6p \quad (3)$$

$$B_{sa}(p, T) = (1.57 + 0.15 \log v_{atm, 20^\circ C}) 10^{4 + \frac{20-T}{417}} + 5.6p \quad (4)$$

$$B_{ti}(p, T) = \left[(1.3 + 0.15 \log v_{atm, 20^\circ C}) 10^{4 + \frac{20-T}{435}} + 5.6p \right] \frac{(1.3 + 0.15 \log v_{atm, 20^\circ C}) 10^{4 + \frac{20-T}{435}} + 4.6p}{(1.3 + 0.15 \log v_{atm, 20^\circ C}) 10^{4 + \frac{20-T}{435}}} \quad (5)$$

$$B_{ta}(p, T) = \left[(1.57 + 0.15 \log v_{atm, 20^\circ C}) 10^{4 + \frac{20-T}{417}} + 5.6p \right] \frac{(1.57 + 0.15 \log v_{atm, 20^\circ C}) 10^{4 + \frac{20-T}{417}} + 4.6p}{(1.57 + 0.15 \log v_{atm, 20^\circ C}) 10^{4 + \frac{20-T}{417}}} \quad (6)$$

$$\rho_n(p) = \rho_{atm, T} \frac{C + 5.6p}{C + 4.6p} \frac{C + 4.6p_{atm}}{C + 5.6p_{atm}}, \quad C = (1.3 + 0.15 \log v_{atm, 20^\circ C}) 10^{4 + \frac{20-T}{435}} \quad (7)$$

The calculated results and the measured results were plotted in the same diagrams. In practice there did not seem to be drastic temperature dependent differences between the measured and calculated results (9) and therefore only the results at the temperature of 40 °C are shown here. Furthermore all the mineral oil based fluids seemed to have similar simulation results with respect to measured values (9) and therefore only the results for basic mineral oil are shown here in the figures 14 and 15. The results for pine oil and HF-E fluid are also presented in the figures 16-19.

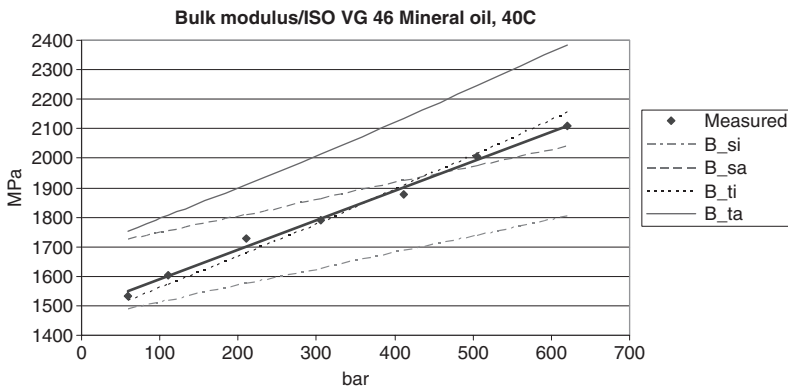


Figure 14 The measured and calculated bulk moduli of mineral oil.

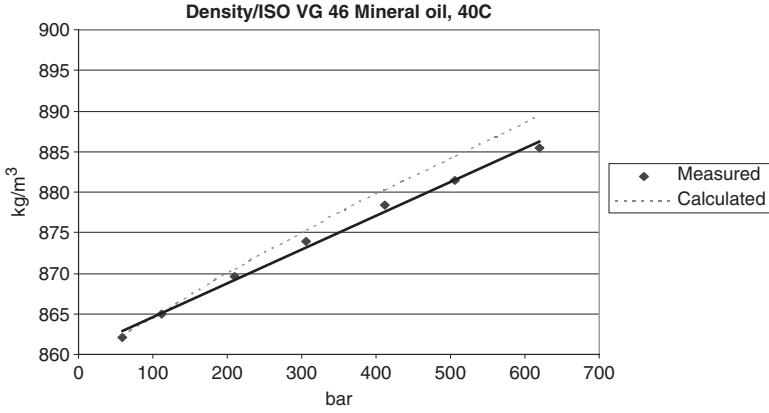


Figure 15 The measured and calculated densities of mineral oil.

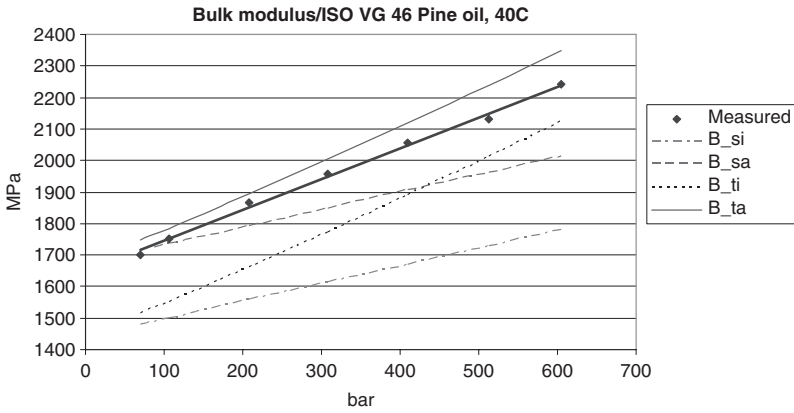


Figure 16 The measured and calculated bulk moduli of pine oil.

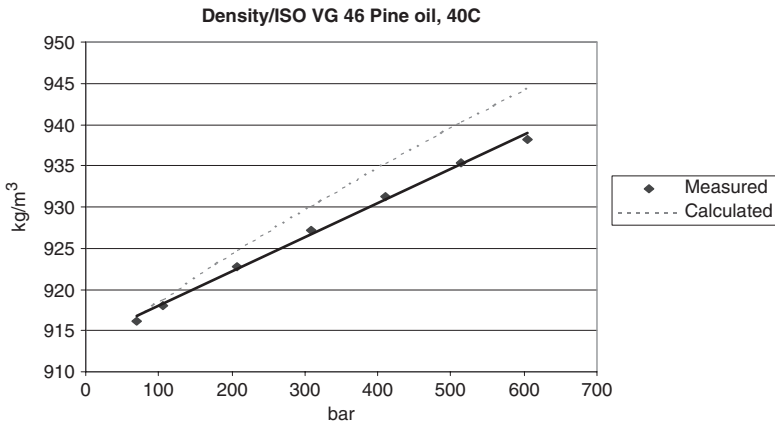


Figure 17 The measured and calculated densities of pine oil.

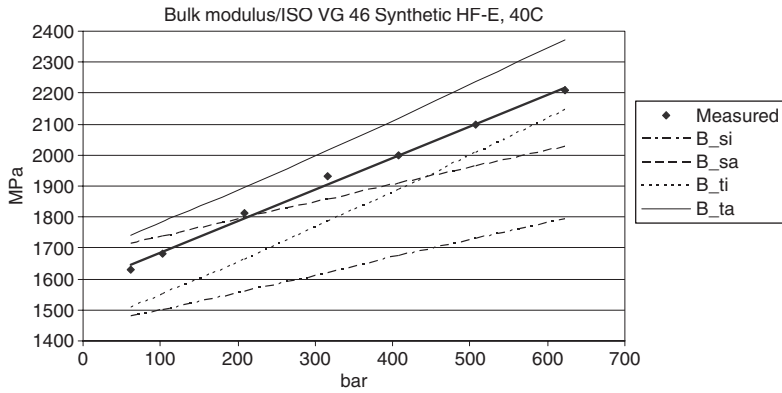


Figure 18 The measured and calculated bulk moduli of HF-E fluid.

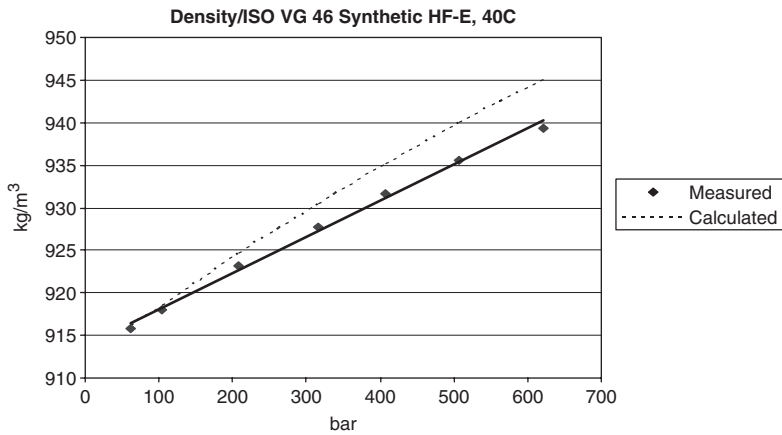


Figure 19 The measured and calculated densities of HF-E fluid.

As it can be noticed the measured and calculated densities are practically the same for every fluid the largest difference being about 5 kg/m³ and as mentioned earlier at higher temperatures the results were similar. Hence, it is probably appropriate to say that on one hand the measurements had to be quite successful and on the other hand the mathematical model for density is rather realistic.

Unlike densities the measured and calculated bulk moduli have some differences depending on the fluid. The measured values of mineral oil based fluids would seem to be exactly the same as the calculated isothermal tangent values. On the other hand the measured values of pine oil correlate well with calculated adiabatic tangent values – actually at higher temperatures even slightly better (9). The measured values of HF-E fluid lie in the middle of the above mentioned calculated lines. In any case the slopes of calculated tangent and measured lines are practically always the same and therefore it is quite safe to say that air has no effect on the results. Otherwise the measured slope should be steeper compared to the calculated one because air makes the fluid more compressible at lower pressures.

6. Conclusions

In this paper the dynamics of hydraulic fluids and its importance on hydraulic systems control was discussed. The common measuring system for fluid bulk modulus, density and speed of sound was modified for operating also at pressures over 300 bar. Five different types of commercial hydraulic fluids were measured at different pressures and temperatures. According to the results the dynamic parameters acted similarly at changing pressure and temperature independent on the fluid. However, significant differences were found in absolute values. The results were also compared to mathematical models for bulk modulus and density which raised the question of whether the measuring system actually will give the adiabatic tangent bulk modulus instead of the isothermal one. After all the mineral oil is usually considered as a reference fluid and the mathematical model was found out to be quite accurate at least in calculating densities. Furthermore, the pine oil and HF-E fluid are known to bond water easier while stored but would this have the effect of raising the bulk modulus of pure fluid enough? Further research is needed.

References

- (1) Bergemann, M. 1993. Systematische Untersuchung des Geräuschverhaltens von Kolbenp. mit gerader und ungerader Kolbenz. DSc thesis. RTWH, Aachen. (pp. 27-32)
- (2) Borghi, M., et al, 2003. A Numerical Approach to the Hydraulic Fluids Properties Prediction. Proc. 8th SICFP. Tampere University of Technology. (pp. 715-729)
- (3) Garbacik, A., Stecki, J.S. 2000. Developments in Fluid Power Control of Machinery and Manipulators. Fluid Power Net publication. (pp. 227-257)
- (4) Haarhaus, M. 1984. Geräuschestehung und Geräuschminderung bei Axialkolbenpumpen in Schrägscheibenbauweise. DSc thesis. RWTH, Aachen. (pp. 33-37)
- (5) Hodges, P. 1996. Hydraulic Fluids. London: Arnold. (167 p.)
- (6) ISO 15086-2:2000. 2000. Hydraulic Fluid Power – Determination of the Fluid-borne Noise Characteristics of Components and Systems – Part 2 (27 p.)
- (7) Jarchow, M. 1997. Massnahmen zur Minderung hochdruckseitiger Pulsationen hydrostatischer Schrägscheibeneinheiten. DSc thesis. RTWH, Aachen. (pp. 18-23, 29-31)
- (8) Johnston, D., Edge, K. 1991. In-situ Measurement of the Wavespeed and Bulk Modulus in Hydraulic Lines. Proc.I.Mech.E., Part 1, 205. (pp 191-197)
- (9) Karjalainen, J-P. 2004. Hydraulic Fluid and its Dynamics as a Part of Hydraulic Systems (in Finnish). MSc thesis. Tampere University of Technology. (102 p.)
- (10) Koivula, T., 2002. Cavitation in Hydraulic Valves – Aspects on the Effect of Oil Type, Erosion and Detection Methods. DSc thesis. Tampere Univ. of Technology. (130 p.)
- (11) Kojima, E., Yu, J. 2000. Methods for Measuring the Speed of Sound in the Fluid in Fluid Transmission Pipes. Society of Automotive Engineering, Inc. (10 p.)
- (12) Merritt, H.E. 1967. Hydraulic Control Systems. USA: John Wiley & Sons Inc. (358 p.)
- (13) Smith, jr. L.H., et al. 1960. Hydraulic Fluid Bulk Modulus – Its Effect on System Performance and Techniques for Physical Measurement. NFPA. (19 p.)
- (14) Viersma, T.J., 1980. Analysis, Synthesis and Design of Hydraulic Servosystems and Pipelines. Amsterdam: Elsevier. (279 p.)
- (15) Watton, J. 1989. Fluid Power Systems. Cambridge: Prentice Hall. (490 p.)
- (16) Yu, J., et al. 1994. The Variation of Oil Effective Bulk Modulus with Pressure in Hydraulic Systems. Jour.Dyn.Syst.,Meas.&Contr. vol.116. Trans.ASME. (pp.146-150)

Measurements of elastohydrodynamic pressure field in the gap between piston and cylinder

Monika IVANTYSNOVA, Changchun HUANG and Robert BEHR
College of Engineering ,Purdue University , USA

ABSTRACT

The paper presents the design of a new test device, which was developed to measure dynamic pressure fields and temperature distribution in the gap between the piston and cylinder of swash plate axial piston machines. For this purpose, a special pump has been developed and built. This pump allows the measurement of pressure and temperature in the gap between piston and cylinder on 1620 points using a special mechanism to readjust 9 piezoelectric pressure sensors and 9 thermocouples. The aim of these measurements is to investigate the elastohydrodynamic pressure generation in narrow gaps and to improve current mathematical models. Measurement results for two different operating parameters will be presented and compared with simulation results using the EHD version of CASPAR. The basic elastohydrodynamic model implemented in the EHD CASPAR version has been presented at Bath workshop 2003 [1].

INTRODUCTION

The achievable operating parameters, the loss behaviour and the reliability of displacement machines are mainly influenced by the design of the sealing and bearing gaps. Sealing and bearing gaps are presented in nearly all types of displacement machines. The problems associated with an optimal gap design are very similar for all machine types. The gap height varies usually in a range of a few micrometers where the other gap dimensions (length and breadth) lie in the range of some ten millimetres. The primary design goal is to achieve full lubrication in a wide range of operating parameters of the pump or motor. This requires sufficient load carrying ability of the lubricating gap. Despite extensive worldwide research investigating the influence of surface shape, material and surface roughness on gap flow condition, many questions about the physical behaviour in the sealing and bearing gaps of these machines have been left unanswered, refer e.g. [2-11]. The major

problem is to understand the interaction of physical the phenomena created by the fluid flow in the gap, especially the influence of micro motion, temperature and elasto-hydrodynamic effects on the resulting dynamic pressure field. The non-isothermal gap flow model which incorporates elasto-hydrodynamic effects and time dependent gap heights developed for the connected gaps of swash plate axial piston machines by Huang and Ivantysynova [1] tries to take all known effects into consideration. This model has been implemented in an updated version of the simulation tool CASPAR [12]. It allows for example the calculation of friction forces between the piston and cylinder. Lasaar and Ivantysynova [13] have compared these calculated piston friction forces with measurements using a special test rig. The piston friction forces obtained with the elasto-hydrodynamic model presented in [1] fit much better with measurements than the results of the rigid model, where elasto-hydrodynamic effects were neglected. Nevertheless there are deviations between measurement and simulation especially during the suction stroke of the piston which cannot be explained with the current model. Further investigations are required to understand the physical effects better and to improve current models. This lack on understanding was the main reason for developing a special measurement method for measurement of dynamic pressure fields between piston and cylinder of swash plate axial piston machines.

1 MEASUREMENT METHOD

The aim of the presented research is to develop a method for measuring dynamic pressure fields in narrow gaps under realistic operating conditions of an axial piston pump. The measurements should enhance the understanding of the physical effects taking place in these gaps better, which finally should allow to improve current simulation models. The measurements performed in this research study will be compared with simulation results obtained by the elasto-hydrodynamic model implemented in the EHD CASPAR version.

1.1 Requirements and boundary conditions

The generated pressure field in the lubricating gap balances external forces, which are exerted on the parts forming the gap. This requires a sufficient fluid film thickness, i.e. an appropriate gap height avoiding mixed friction. The investigations and measurements undertaken in the presented research work concentrate on the piston cylinder assembly of swash plate axial piston machines. The piston cylinder assembly in piston pumps and motors cannot be balanced hydrostatically. Therefore the hydrodynamic pressure generation is particularly important for the lubricating gap between piston and cylinder. Since the pressure and inertia force exerted on the piston change with rotating angle, i.e. the forces are time dependent, the forces generated by pressure field in the gap must also change with rotating angle of the cylinder block. The time dependent forces exerted on the piston lead to a micro motion of the piston causing a varying gap height over one shaft revolution, i.e., the position and shifting velocity of the piston changes periodically. The varying gap height leads finally to a dynamic pressure field in the gap, i.e. for each angular position of the rotating cylinder block a different pressure field is generated by the fluid film in the gap. Figure 1 shows the gap between piston and cylinder and a typical hydrodynamic pressure field, which was obtained using the EHD version of CASPAR. Figure 2 shows the calculated pressure fields for different angular positions ϕ of the rotating cylinder block. It is obvious that the hydrodynamic pressure field in the gap changes periodically. Figure 2

further shows that the measurement of the hydrodynamic pressure field requires an array of measurement points, because of very high pressure gradients appearing in relatively small areas. For the measurements of the reported research a pump speed up to 3000 rpm should be realizable. The boundary conditions for the measurement of dynamic pressure fields can be summarized as follows:

1. The time dependent change of the pressure field requires an appropriate bandwidth of pressure sensors depending on the maximal pump speed. Based on the calculated dynamic pressure fields, where the pressure rise of 420 bar within a time of $\Delta\tilde{t} = t_2 - t_1 = 8 \cdot 10^{-4}$ s has been calculated, the corresponding required bandwidth of the pressure sensor is $f_m = 1.25$ kHz. For realistic measurements of amplitudes as shown in Fig. 2 the time constant of the measurement system needs to be at least five times faster than the measured signal. This finally requires a signal bandwidth of the measurement systems of $f \geq 5 \cdot 1.25\text{kHz} \geq 6.25\text{kHz}$.
2. An array of pressure measurement points is necessary to measure the local pressure peaks, thus a method had to be found to realize this with available sensors or a complete new sensor had to be developed. For the measurements a standard piston cylinder assembly was chosen allowing comparison with friction force measurements, which were made on a 75 cc units. Thus the basic gap dimensions are given, see Fig.1.
3. Large hydrodynamic pressure peaks are often generated close to the ends of the piston guide length, i.e. on both ends of the gap. This requires the placement of sensors very close to the gap end.

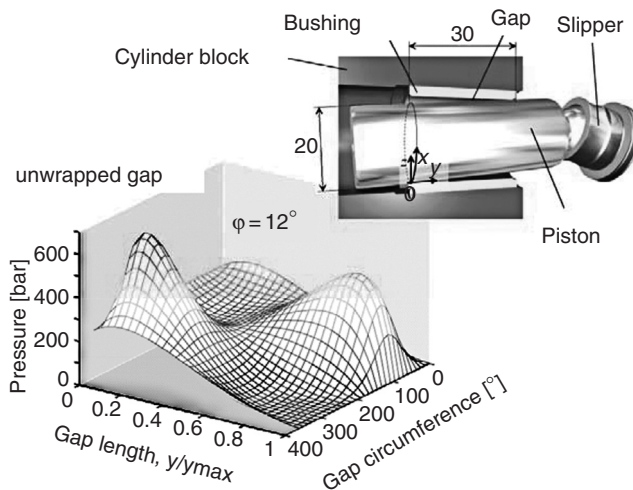


Figure 1: Gap between piston and cylinder and simulated pressure field using EHD

The fluid flow in the lubricating gap leads to energy dissipation heating the fluid and finally changing the viscosity of the fluid in the gap. The change of temperature and viscosity of the fluid influences the load carrying ability of the fluid film. Therefore the measurement of the temperature distribution in the gap is a second important task of the proposed experimental set up.

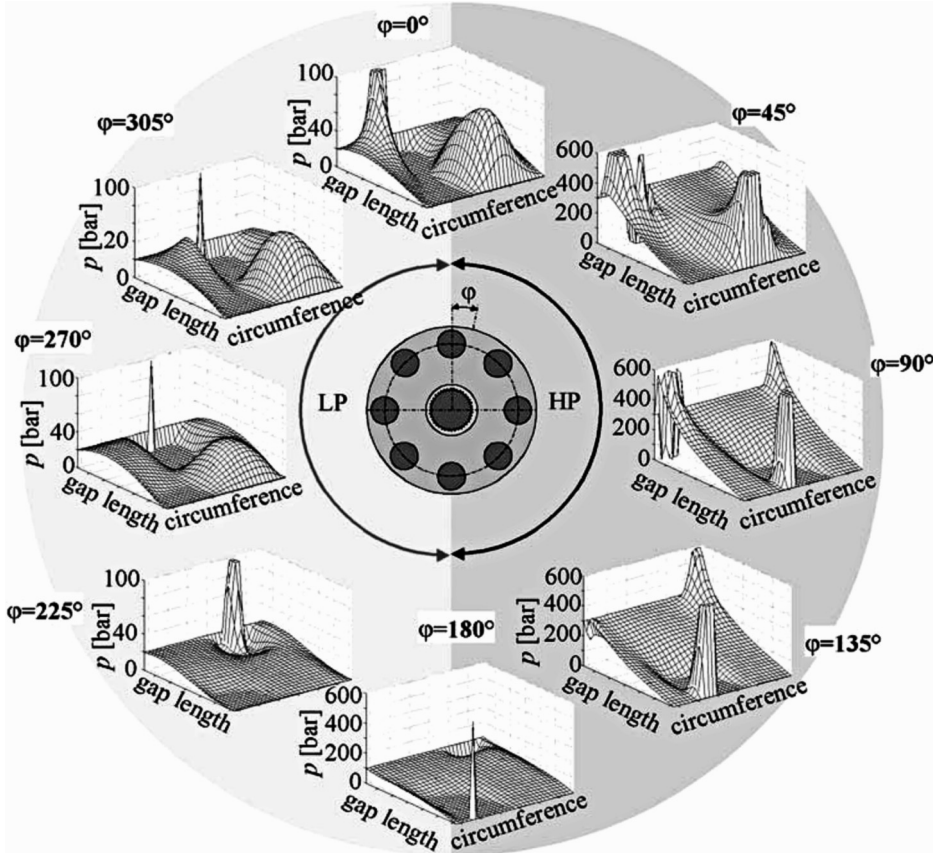


Figure 2: Calculated pressure fields between piston and cylinder using the EHD CASPAR simulation tool, $n = 3000$ rpm, $p_{HP} = 300$ bar

1.2 Measurement principle

The measurement of dynamic pressures requires the placement of the pressure sensor very close to the measurement point. Fig. 3 shows the chosen basic installation principle, where the pressure sensor is connected with the gap by a very thin and short bore. The piezoresistive pressure sensor 4065A from *Kistler* is currently the smallest pressure sensor currently available on the market, which fulfils the given requirement regarding measurement range (up to 1000 bar) and bandwidth. The measurements are made using a standard piston- cylinder assembly corresponding to a 75 cc unit, see Fig. 1. For the measurements, a single piston pump design with kinematic reversal of the standard swash

plate pump has been proposed, i.e. a rotating swash plate and a fixed cylinder block. This avoids a signal transfer from the rotating cylinder block. The developed measurement procedure is based on the idea of measuring the entire pressure field by repeating measurements after turning the entire cylinder block against piston. Fig. 4 explains that the size of the gap and the dimensions of the chosen sensor make it possible to measure the pressure and temperature at 1620 points of the gap by implementing 9 pressure sensors and turning the cylinder block around the piston 180 times, i.e. for every 2°.

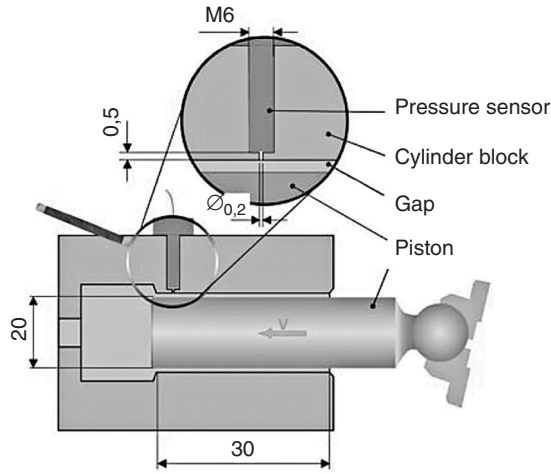


Figure 3: Basic installation principle of pressure sensors

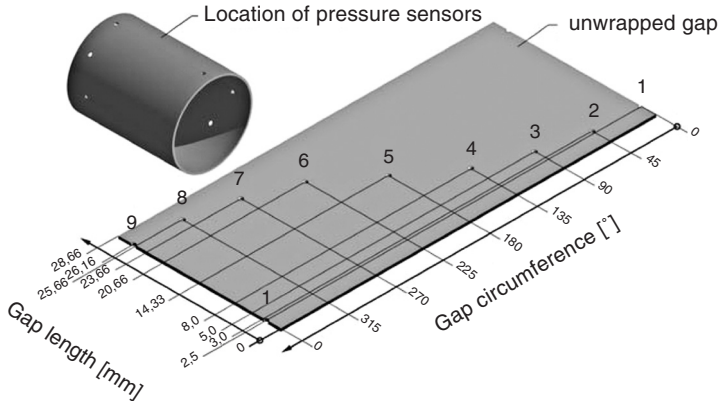


Figure 4: Placement of measurement points over gap length and gap circumference

Figure 5 shows the implemented pressure sensors and the thermocouples. The entire test set up used for the measurements is shown in Fig.6.

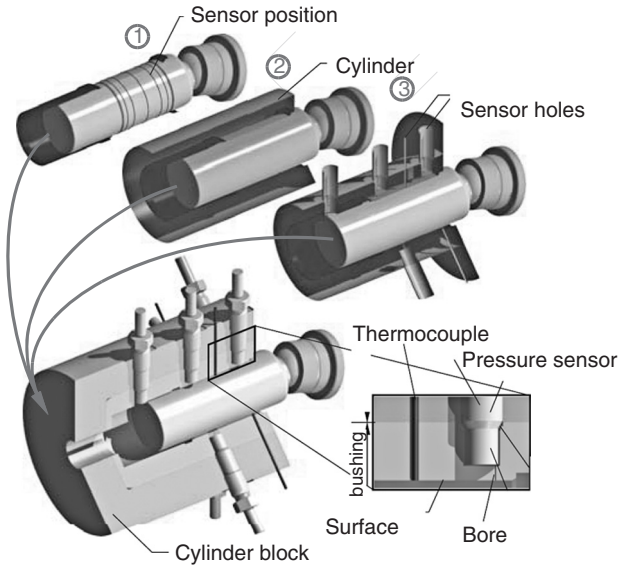


Figure 5: Sensor implementation in cylinder block

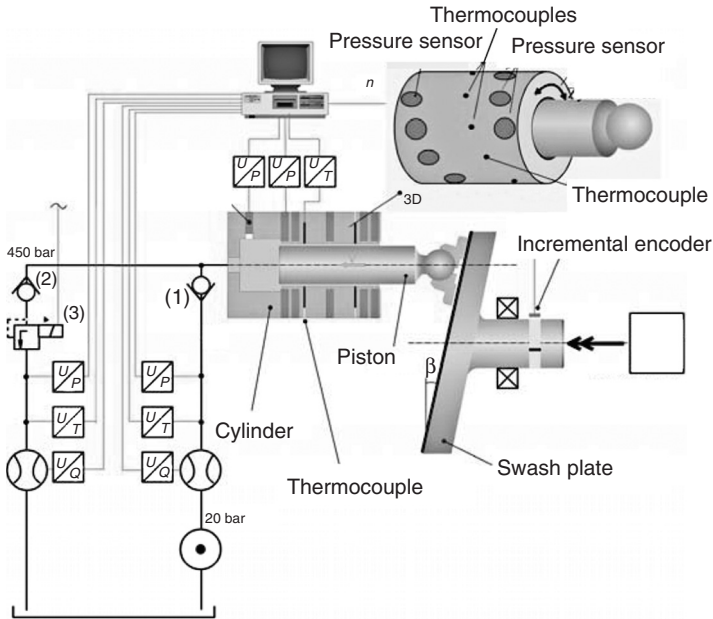


Figure 6: Scheme of the proposed measurement set up

1.3 Test Pump Design

A special test pump was designed for the measurements of pressure and temperature fields reported here. Figure 7 shows the proposed and realized locking device with the retainer pin on a fixed disc and the detent on the cylinder block. 180 unique angular combinations can be obtained by aligning a bore of the fixed disc with the bores of the turnable cylinder block and repeating this cycle twenty times. The developed locking device allows the controlled adjustment of the cylinder every 2° . Thus using 9 pressure sensors and nine thermocouples the measurement of pressure and temperature of 1620 points of the gap surface is possible. Figure 8 shows the entire design of the test pump. The cylinder block with the installed sensors is shown in Fig 9.

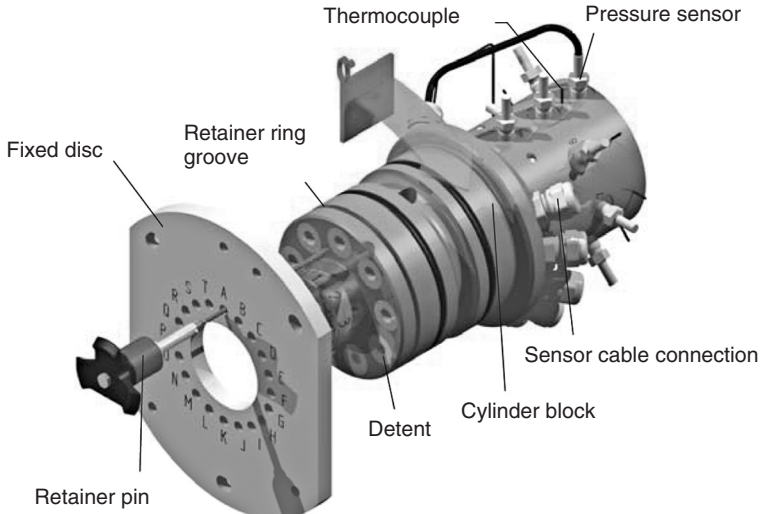


Figure 7: Locking device of the cylinder block

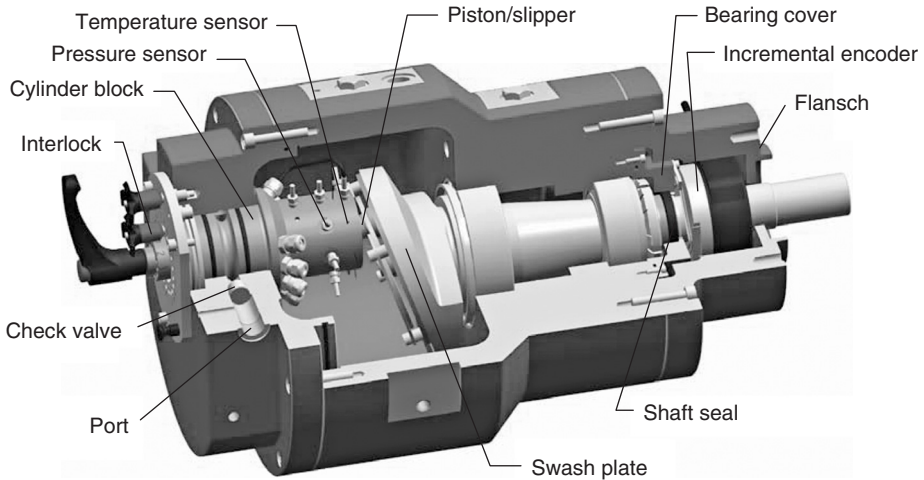


Figure 8: Test pump design

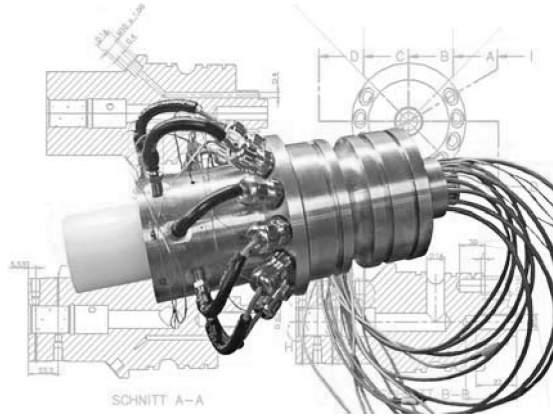


Figure 9: Cylinder block with implemented pressure sensors and thermocouples

1.4 Determination of angular position of swash plate

Figure 10 demonstrates the method applied for determination of the angular position of rotating swash plate. An incremental encoder ERN 120 from Heidenhain is used to trigger the sequential measurements of nine pressures and nine temperatures for each adjusted angular position of the cylinder block. Figure 10 shows that the incremental encoder is used to send a reference signal indicating the reference position of the piston at its outer dead point. The proposed method requires repeating the measurements at same steady state operating conditions (pump speed, inlet and outlet pressure and inlet temperature). The encoder is also used to measure the shaft speed. The angular resolution of the TTL signal of the encoder is

$$\pm \frac{360^\circ}{1240} \times \frac{1}{20} = \pm 0^\circ 01' 03'' \tag{1}$$

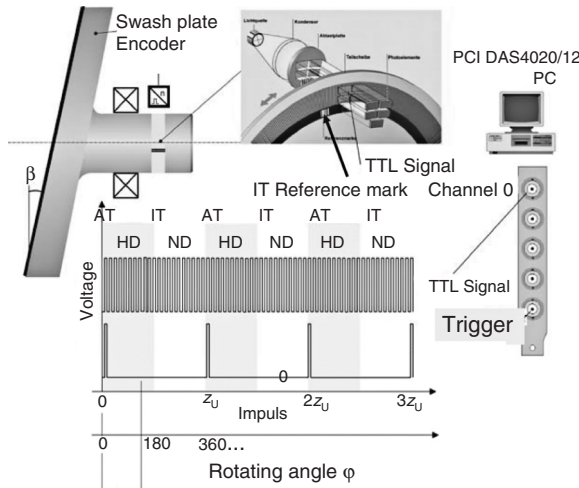


Figure 10: Method of measurement of angular position of swash plate

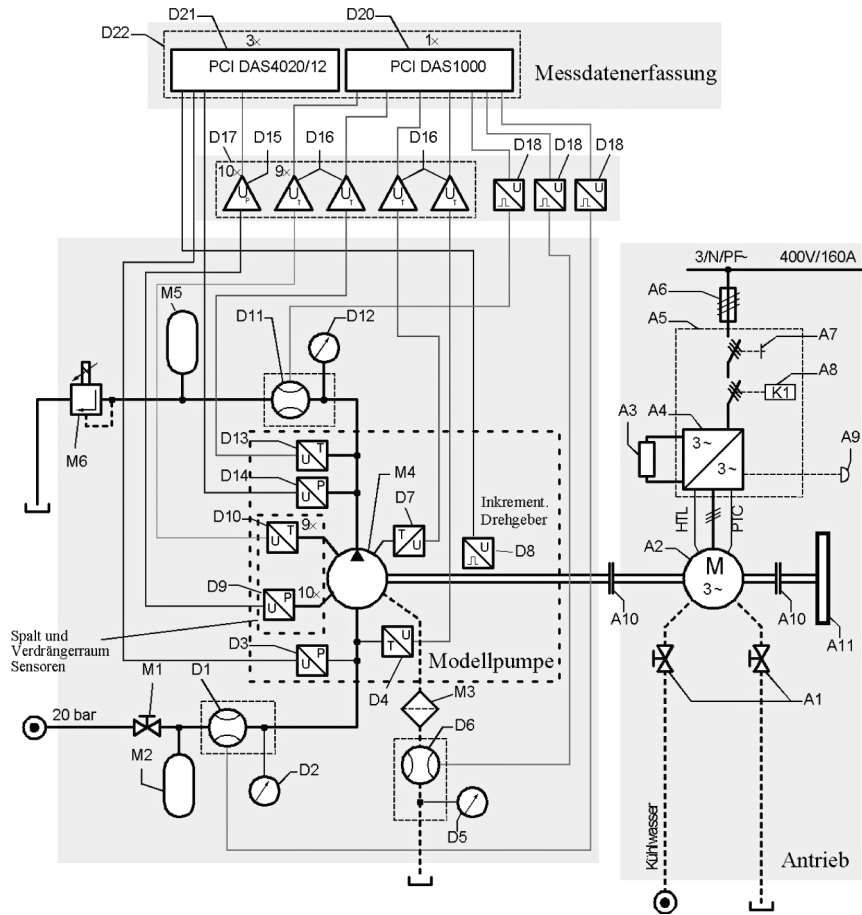


Figure 11: Hydraulic circuit of test rig

Figure 11 shows the hydraulic circuit including the data acquisition structure of the test rig. The test pump (M4) is driven by the frequency controlled electric motor (A2). The test pump works in open circuit. Accumulators (M2, M5) in both lines are used to reduce pressure pulsation at pump ports. The pump inlet and outlet temperature and pressure and the case temperature are directly measured on pump ports and the pump case respectively (measurement point D3, D4, D13, D14 und D7). The pressure is measured in the displacement chamber and at nine points in the gap between piston and cylinder using the piezoresistive pressure sensor 4065A with the amplifier 4618A from Kistler (D9). The temperature in the gap is measured by using nine thermocouples (D10). All time critical measurement signals are transferred) to the PC using three A/D boards PCI DAS4020/12 (D21). The remaining signals are transferred to the measurement PC using the A/D board PCI DAS 1000 (D20). In addition the flow rate at the pump inlet, pump outlet and in the case line are measured by gear flow meters (D1, D6 und D11).

2 MEASUREMENT RESULTS

The described test rig has been used for a first set of measurements of dynamic pressure fields. The temperature in the gap was also measured. The measurements were made at 1500 rpm pump speed and 150 bar pressure difference. The low pressure was kept constant at 25 bar. The fluid temperature at pump inlet was kept constant at 43 °C corresponding to a kinematic viscosity of 25 cSt. Figure 12 shows the pressure field measured for an angular position of the swash plate of $\varphi=180^\circ$, i.e. at the inner dead point of the piston. The pressure field is shown for the unwrapped gap. Unfortunately, two of the implemented pressure sensors failed and therefore the pressure over the gap length could be measured only on 7 points. The sensor position is marked accordingly. By turning the cylinder block 180 times finally 180 measurement points over the the gap circumference could be measured.

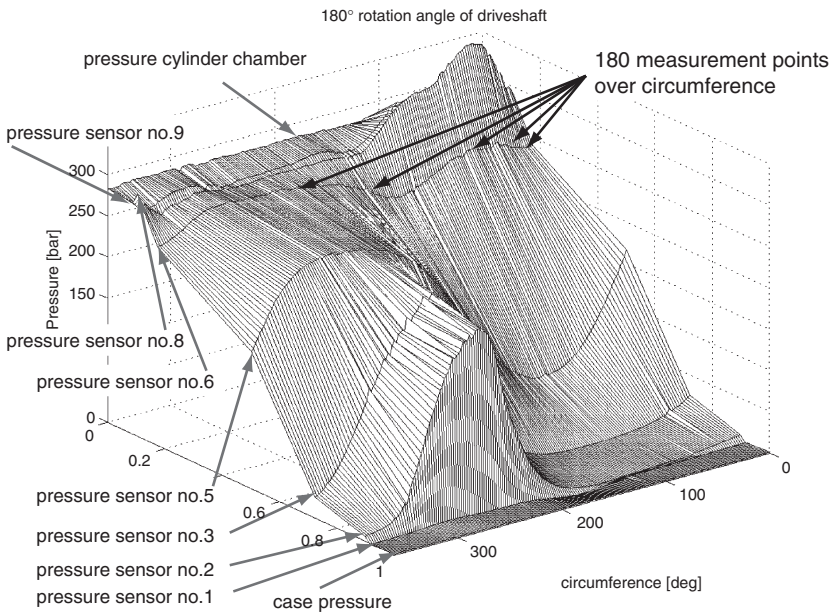


Figure 12: Measured pressure field between piston and cylinder for $p_{HP}=175$ bar, $n=1500$ rpm, 25 cST

Figure 13 shows the measured pressure fields for eight selected angular positions of the swash plate (eight different positions of piston during one shaft rotation). Measurements were made under steady state conditions of the pump keeping the inlet temperature constant at 43°C and the pump speed @ 1500 rpm. Inlet pressure was adjusted to 25 bar and outlet pressure to 175 bar.

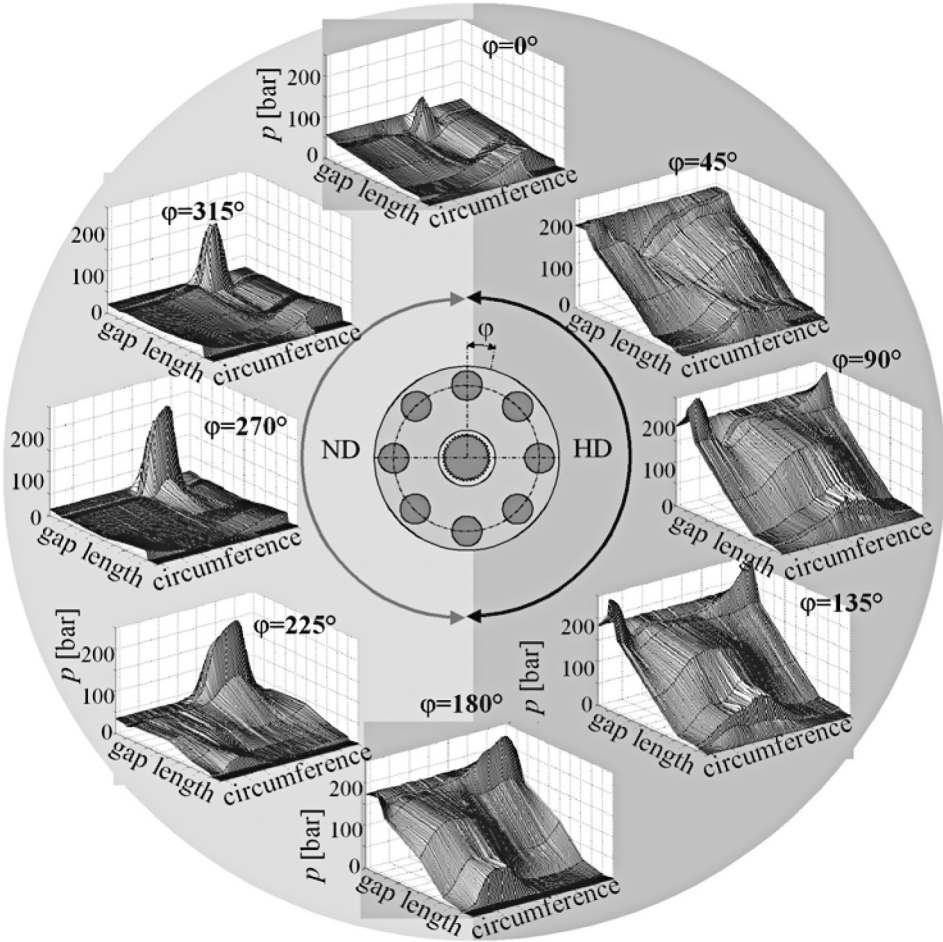


Figure 13: Measured pressure field between piston and cylinder for $p_{HP} = 175$ bar, $n = 1500$ rpm, 25 cSt

Figure 14 shows the measured pressure field for a second series of measurements made at 275 bar (high pressure). The inlet pressure was kept constant at 25 bar. The fluid temperature at the pump inlet was kept constant at 43 °C corresponding to a kinematic viscosity of 25 cSt. Figure 15 shows the measured temperature field for the measurements @ 275 bar high pressure. Because of variations in the room temperature the case temperature of the test pump did not remain constant during the 180 measurements. There were variations of ± 1 K. This explains the temperature field profile shown in Fig. 15. Note that the temperature field shown in Fig. 15 has been composed of 180 measurements each with 9 thermocouples over the gap length.

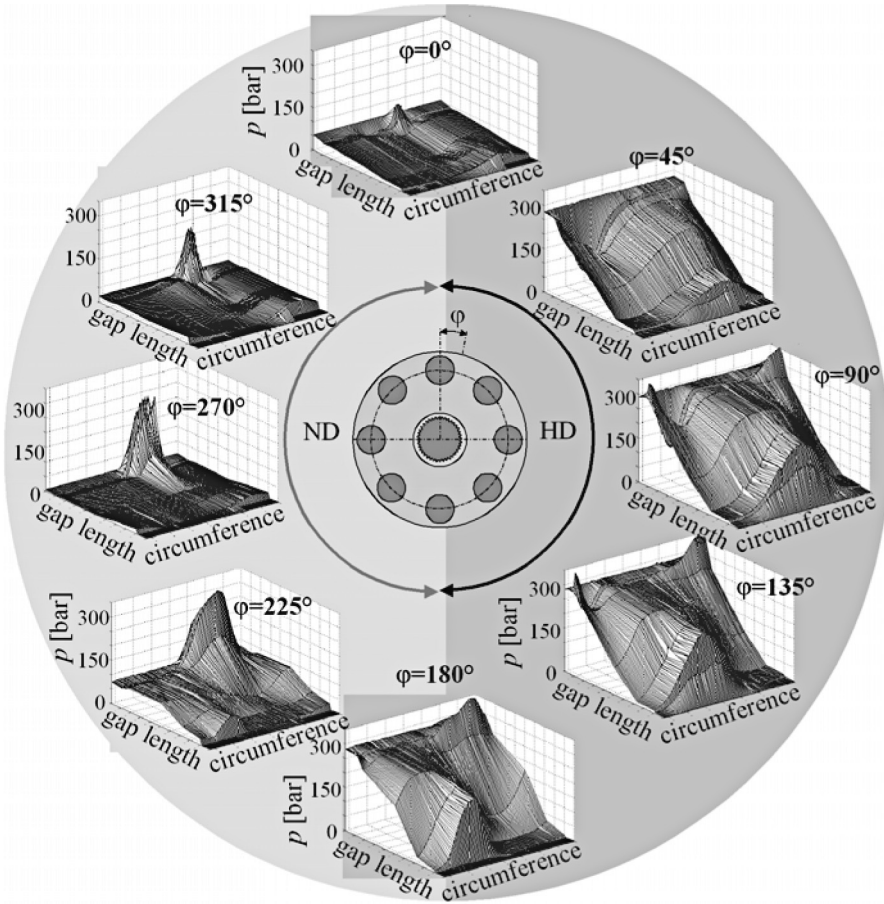


Figure 14: Measured pressure field between piston and cylinder for $p_{HP} = 275$ bar, $n = 1500$ rpm, 25 cST

3 COMPARISON OF MEASUREMENT AND EHD SIMULATION

For comparison of measurement and simulation, the special test rig conditions were considered in a specially modified simulation model of the EHD CASPAR version. The entire cylinder block is made from brass and the dimensions of the block differ from a standard unit. The inverse kinematic was considered, i.e. the piston of the test pump is not loaded by a centrifugal force. Figure 16 shows the modelled cylinder for determination of the stiffness matrix, which is used in CASPAR to calculate the surface deformation due to pressure field in the gap.

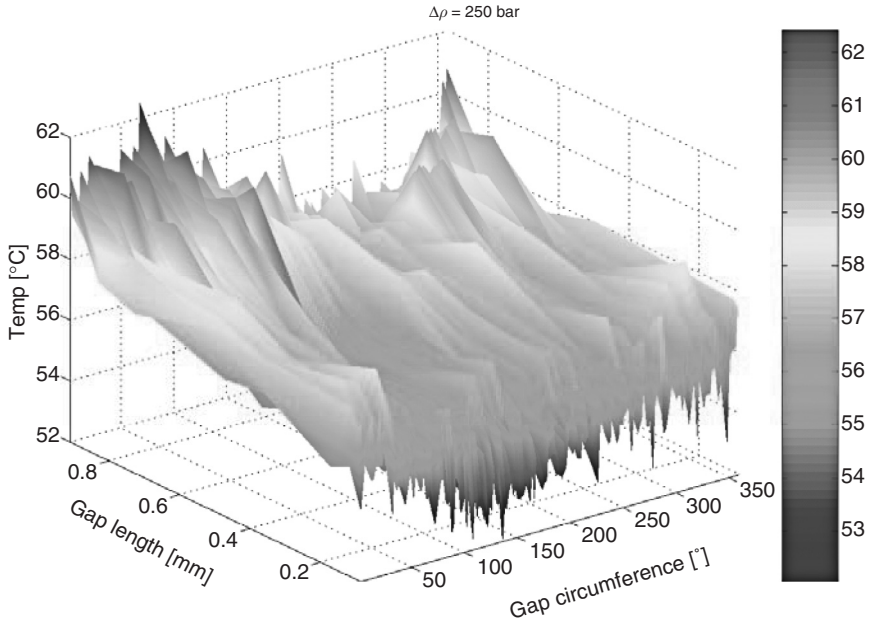


Figure 15: Measured temperature field between piston and cylinder for $p_{HP} = 275$ bar, $n = 1500$ rpm

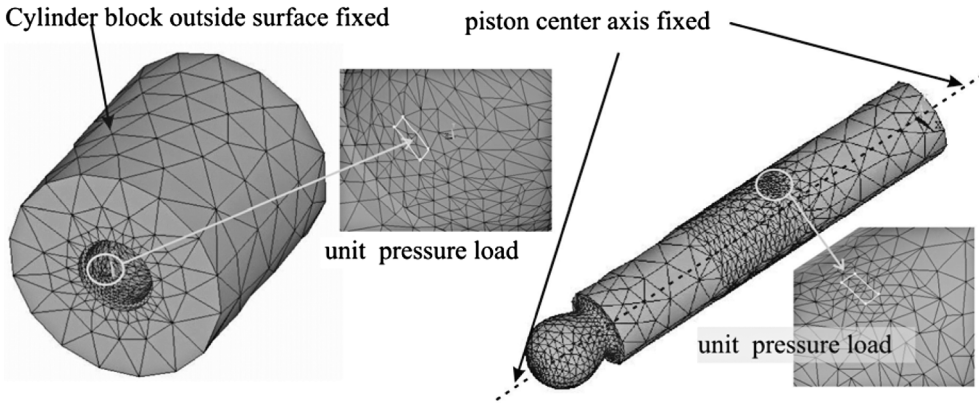


Figure 16: FEM model used for determination of stiffness matrix

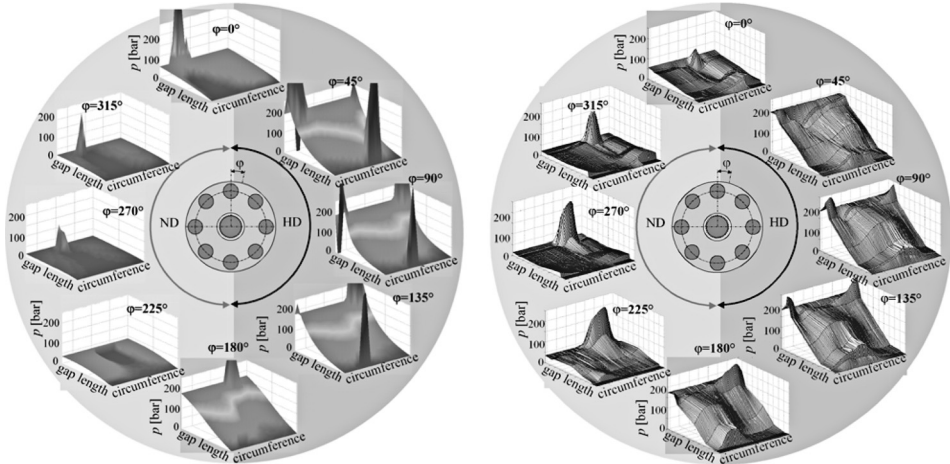


Figure 17: Pressure fields in the gap for different angular positions of the shaft, $p_{HP} = 175$ bar, $n = 1500$ rpm, $\nu = 25$ cSt (left: simulation with EHD model; right: measurement)

Figure 17 shows a comparison of the measured and calculated pressure field for the first set of measurements @ 175 bar high pressure. The model considers a relative motion of the piston, which contributes mainly to hydrodynamic pressure generation during the suction phase. Comparing measurement and simulation it can be concluded that the simulation model needs to be further improved to cover all the effects of the test pump. The current test pump EHD model neglects the influence of small sensor bores, which damp the pressure peaks. There are some other deviations which require further investigation.

4 CONCLUSION

This paper presents a new test rig for carrying out measurements of the dynamic pressure field in the gap between piston and cylinder using a wobble plate test pump design. The test rig also allows the measurement of the temperature field between piston and cylinder. The temperatures are measured in the fluid film. The pressure and temperatures can be measured on 1620 points of the gap surface by turning the cylinder block every 2° around the piston and using a special locking device. First measurement results have shown that the developed test pump works well and makes possible the measurement of pressure and temperature fields based on the proposed method. The measured pressure field has been compared with simulation results obtained using a modified EHD model to consider the special test pump design. Comparing the measured results with the applied simulation model it is obvious that the current model does not cover all physical effects and needs to be improved further.

REFERENCES

- [1] **Huang, C. and Ivantysynova, M.** 2003. A new approach to predict the load carrying ability of the gap between valve plate and cylinder block. *Bath Workshop on Power transmission and Motion Control PTMC 2003*, Bath, UK, pp. 225–239.
- [2] **Dowd, J. R. and Barwell, F. T.,** 1974. Tribological interaction between piston and cylinder of a model high pressure pump. *Transactions ASLE*, Vol. 18, pp.21–30.
- [3] **Ivantysynova, M. and Huang, C.** 2002 Investigation of the gap flow in displacement machines considering elastohydrodynamic effect, *Fifth JHPS International Symposium on Fluid Power*. Tokyo, Japan., pp. 219–229.
- [4] **Fang, Y and Shirakashi, M.** 1995. Mixed lubrication characteristics between piston and cylinder in hydraulic piston pump-motor. *Journal of Tribology, Trans. ASME*, Vol. 117, pp. 80–85.
- [5] **Manring, Noah, D.** 1999. Friction forces within the cylinder bores of swash-plate type axial-piston pumps and motors. *Journal of Dynamic Systems, Measurement and Control*, Vol. 121, pp. 531–537.
- [6] **Oberem, Richard.** 2002. *Untersuchung der Tribosysteme von Schrägscheibenmaschinen der HFA-Hydraulik*. Diss. RWTH Aachen, Germany.
- [7] **Patir, N. and Cheng, H. S.,** 1978. An average flow model for determining effects of three dimensional roughness on partial hydrodynamic lubrication. *ASME Journal of Lubrication Technology*, Vol. 100, pp. 12–17.
- [8] **Reiners, W.,** 1987. *Die Ausbildung elastohydrodynamischer Reaktionskräfte am Kolbenschaft unter Berücksichtigung der Primär- und Sekundärbewegung*. Dissertation, RWTH Aachen, Germany.
- [9] **Reynolds, O. et al,** 1886. *Hydrodynamische Theorie der Schmiermittelreibung*. Ostwald's Klassiker der exakten Wissenschaften. No. 218. Leipzig Akademische Verlagsgesellschaft.
- [10] **Tanaka K., Kyogoku K. and Nakahara, T.,** 1999. Lubrication characteristics on sliding surfaces between piston and cylinder in a piston pump and motor (Effects of running-in, profile of piston top and stiffness). *JSME International Journal, Series C (Mechanical Systems, Machine Elements and Manufacturing)*, Vol. 42 (1999) No. 4, pp. 1031–1040.
- [11] **Yamaguchi, A. and Matsuoka, H.,** 1992. A mixed lubrication model applicable to bearing/seal parts of hydraulic equipment. *Trans. ASME, J. Trib.* 114, pp. 116–121.
- [12] **Ivantysynova, M.** 2003. Prediction of pump and motor performance by computer simulation. *1st International Conference on Computational Methods in Fluid Power Technology*. Melbourne, Australia, pp. 505–522.
- [13] **Ivantysynova, M. and Lasaar, R.** 2004. An investigation into Micro- and macro geometric design of piston/cylinder assembly of swash plate machines. *International Journal of Fluid Power*. *International Journal of Fluid Power*, Vol. 5 (2004), No. 1, pp. 23–36.

Authors' Index

A

Almondo, A., 379

B

Balossini, Gualtiero, 3

Behr, Robert, 451

Bergstrom, Don, 223

Bideaux, E., 317

Brun, Xavier, 45

Burton, Richard, 163, 223

C

Chinniah, Yuvin, 163

Conrad, Finn, 117

D

Derkaoui, A., 317

E

Edamura, Kazuya, 269, 277

Ellman, A., 179

Esqué, S., 179

F

Fedde, T., 307

Fiedler, M., 255

Figliolini, Giorgio, 365

G

Gstöttenbauer, Norbert, 291

Guillemard, F., 317

H

Habibi, Saeid, 163

Harms, H-H., 307

Helduser, S., 255

Hös, Csaba, 193

Huang, Changchun, 451

Huhtala, K., 437

I

Ichiryu, K., 333

Ikeo, S., 333

Inberg, Juha, 59

Ito, K., 333

Ivantysynova, Monika, 451

J

Jacazio, Giovanni, 3

K

Kagawa, Toshiharu, 351

Kainz, Alexander, 291

Karjalainen, J-P., 437

Karjalainen, R., 437

Kawachi, Masashi, 277

Kawamura, K., 333

Kawashima, Kenji, 351

Koivula, Timo, 147

Kojima, E., 409

Koskinen, Kari T., 107

Koyabu, E., 333

Kullmann, László, 193

L

Laamanen, Arto, 91

Laffite, J., 317

Lang, T., 307

Lee, S., 333

Legrand, Xavier, 45

Liermann, Matthias, 17

Lin Shi, Xue-Fang, 45

Linjama, Matti, 29, 91, 133

M

Manhartsgruber, Bernhard, 291, 427

Marquis-Favre, W., 317

Mattiazzo, G., 395

Murrenhoff, Hubertus, 17

O

Okungbowa, Noreense, [223](#)

P

Pastorelli, Stefano, [365](#), [379](#)

Plummer, A.R., [75](#)

R

Rea, Pierluigi, [365](#)

Retif, Jean-Marie, [45](#)

Rinkinen, Jari, [147](#)

Roli, Francesco, [117](#)

Rüdiger, F., [255](#)

Rusanen, Heikki, [147](#)

S

Sairiala, Harri, [107](#)

Sampson, Eric, [163](#)

Scavarda, S., [317](#)

Scheidl, R., [209](#), [291](#)

Schultz, Albert, [243](#)

Shimoyama, H., [333](#)

Siivonen, Lauri, [133](#)

Smaoui, Mohamed, [45](#)

Soga, Tsutomu, [277](#)

Sorli, Massimo, [365](#), [379](#)

Steiner, B., [209](#)

T

Tadano, Kotaro, [351](#)

Takemura, Kenjiro, [269](#)

Terada, A., [409](#)

Thomasset, Daniel, [45](#)

V

Vilenius, Matti, [91](#), [107](#), [133](#), [437](#)

Virvalo, Tapio, [29](#), [59](#)

Y

Yamazaki, T., [409](#)

Yokota, Shinichi, [269](#), [277](#)

Yoshida, Kazuhiro, [277](#)

